Quantification of sediment fluxes from continental collision and slab detachment in the Carpathians foreland basin

Marion Roger

▶ **To cite this version:**

Marion Roger. Quantification of sediment fluxes from continental collision and slab detachment in the Carpathians foreland basin. Applied geology. Université Grenoble Alpes [2020-..], 2023. English. NNT : 2023GRALU022 . tel-04858789

HAL Id: tel-04858789

https://theses.hal.science/tel-04858789v1

Submitted on 30 Dec 2024

HAL is a multi-disciplinary open access archive for the deposit and dissemination of scientific research documents, whether they are published or not. The documents may come from teaching and research institutions in France or abroad, or from public or private research centers.

L'archive ouverte pluridisciplinaire **HAL**, est destinée au dépôt et à la diffusion de documents scientifiques de niveau recherche, publiés ou non, émanant des établissements d'enseignement et de recherche français ou étrangers, des laboratoires publics ou privés.

THÈSE

Pour obtenir le grade de

DOCTEUR DE L'UNIVERSITÉ GRENOBLE ALPES

École doctorale : STEP - Sciences de la Terre de lEnvironnement et des Planètes
Spécialité : Sciences de la Terre et de lEnvironnement
Unité de recherche : Institut des Sciences de la Terre

Quantification du flux de sédiments généré par la collision continentale et le détachement de slab dans les Carpates.

Quantification of sediment fluxes from continental collision and slab detachment in the Carpathians foreland basin.

Présentée par :

Marion ROGER

Direction de thèse :

Peter VAN DER BEEK Professeur, UGA	Directeur de thèse
Arjan DE LEEUW MAITRE DE CONFERENCES, Université Grenoble Alpes	Co-encadrant de thèse
Laurent HUSSON chercheur, CNRS	Co-encadrant de thèse

Rapporteurs :

Massimiliano ZATTIN
PROFESSEUR, Université de Padoue
Delphine ROUBY
CHARGE DE RECHERCHE, CNRS

Thèse soutenue publiquement le **29 juin 2023**, devant le jury composé de :

Peter VAN DER BEEK PROFESSEUR, Université de Potsdam	Directeur de thèse
Massimiliano ZATTIN PROFESSEUR, Université de Padoue	Rapporteur
Delphine ROUBY CHARGE DE RECHERCHE, CNRS	Rapporteure
Mary FORD PROFESSEUR DES UNIVERSITES, Université de Lorraine	Examinatrice
Christophe BASILE PROFESSEUR DES UNIVERSITES, UGA	Président du Jury
Laurent HUSSON DIRECTEUR DE RECHERCHE, CNRS	Co-directeur de thèse

Invités :

Arjan de Leeuw MAITRE DE CONFERENCES, ISTerre	Co-directeur de thèse

Charte anti-plagiat

Art 1 : Définition du plagiat

Le plagiat consiste à reproduire un texte, une partie d'un texte, une illustration ou des idées originales d'un auteur, sans lui en reconnaître la paternité par un référencement bibliographique ou iconographique adéquat (Cf. art. 3).

Art 2 : Objet des travaux universitaires

Sont considérés comme travaux universitaires tous les documents réalisés par les étudiants et les enseignants, les chercheurs et les enseignants-chercheurs dans le cadre des activités de formation et de recherche. Ces travaux universitaires doivent toujours avoir pour ambition de produire un savoir inédit et d'offrir une lecture critique, nouvelle et personnelle du sujet.

Art 3 : **Méthodologie de référencement bibliographique**

La méthodologie d'un travail universitaire implique que les emprunts (par exemple par copier/coller) soient clairement identifiés et que le nom de l'auteur et la source de l'extrait soient mentionnés.

Les citations textuelles y compris dans une traduction personnelle, doivent obligatoirement être placées entre guillemets et être accompagnées d'une référence bibliographique à la suite de la citation, ou en note de bas de page.

Les emprunts non textuels *(*tableaux, graphiques, photos, formules scientifiques, etc.) doivent également être accompagnés d'une référence bibliographique à leur suite ou en note de bas de page.

En complément, toutes les références des documents cités, empruntés ou adaptés, doivent figurer en bibliographie.

Art 4 : **Détection du plagiat**

L'Université Grenoble Alpes est dotée d'un outil permettant de contrôler systématiquement les travaux universitaires et de détecter les similitudes, dans le but de rechercher le plagiat.

Art 5 : **Sanctions disciplinaires pour plagiat**

Les auteurs présumés de plagiat seront traduits devant la section disciplinaire compétente qui pourra prendre des sanctions pouvant aller jusqu'à l'exclusion définitive de tout établissement d'enseignement supérieur. La procédure disciplinaire n'exclut pas d'éventuelles poursuites judiciaires.

Art. 6 : **Engagement**

Les étudiants et les personnels s'engagent à ne pas commettre de plagiat dans leurs travaux universitaires. À cette fin, ils reconnaissent avoir pris connaissance des obligations décrites dans les articles 2 et 3 de la présente charte et s'engagent à s'y conformer.

Je certifie, ...Marion ROGER.....*(indiquer nom prénom)*
avoir pris connaissance de la charte anti-plagiat et à la respecter.

Date et signature : 18/04 à Grenoble

Abstract

This manuscript is the result of the work on the "Quantification of sediment fluxes from continental collision and slab detachment in the Carpathian foreland basin". The subject initiated with the aim of quantifying the amount of sediments supplied to the pro-foreland during the erosion of the Carpathian belt, that were preserved in the foreland and/or subsequently transported in the Black Sea. The Carpathians foreland basin developed a south-eastward axial transport system and sediment delivered southward built the North-western Black Sea shelf during the middle-late Miocene. To retrace the timing of sediment delivery to the Black Sea, as well as quantifying the fluxes of sediment in and out of the foreland from middle Miocene to present, we retraced the exhumation of the orogenic wedge and the sedimentation of the pro-foreland.

The formation of the Carpathian belt occurred in the context of a retreating subduction zone. The European slab retreats toward the European Platform, leading to the accretion of a wedge and extension in a back-arc basin, the Pannonian Basin. The different sedimentary unit accreted in the wedge display a deep-marine facies sediment from Cretaceous to Paleogene, evolving toward more molassic sedimentary facies in the Oligocene and Miocene.

To understand the accretion-collision process in the Carpathians belt and constraining the onset of exhumation of the different nappes, we performed thermal modelling on low-temperature thermochronology data (AHe, AFT and ZHe) we dated from the Ukrainian Carpathians. Most of our AHe ages are reset by burial heating, the AFT data display some reseted ages and partially reset ages, and none of our ZHe ages are reset. With inverse modelling, we determine the time–temperature paths of six of the eight nappes composing the wedge. It reveals that most of the nappes were stacked in sequence starting around 34 Ma until 12 Ma. However, some out-of-sequence thrusting occurred during middle Miocene. The exhumation rate of the nappe increased toward the outer wedge leading to increase in sediment supply to the foreland basin in Miocene. With the non-reset ZHe ages we obtained, we identify the potential sediment sources of the Carpathian wedge. The main sources were the southwestern margin of the East European Platform and the sedimentary cover of the Inner Carpathian units.

We wanted to obtain the exhumation of the entire Carpathians belt to quantify erosion during the construction of the orogen. We built a comprehensive low-temperature thermochronology database of the Carpathians belt, from the Western to the South-eastern Carpathians and inverse-model the data, with a thermal kinematic model (Pecube), to obtain exhumation rates. We separated the belt in three regions: the Western Carpathians, the North-eastern Carpathians and the Eastern and South-eastern Carpathians. We run the model on time steps corresponding, as much as possible, to the chronostratigraphy of the Paratethys region, in order to compare directly the exhumation rates in the belt with the sedimentation rates in the foreland. We obtain an exhumation model which show a

diachronous pattern from the Northwest to the Southeast of the belt. The Western Carpathians exhumation peaked from 24 to 12.8 Ma, the North-eastern region exhumation peaked from 18 to 6.1 Ma and the Eastern and South-eastern region peak exhumation lasted from 8.6 Ma to present. Comparison with previous estimates of exhumation are coherent for the Western and North-eastern regions. However, some discrepancy is to note in the Eastern and south-eastern region.

To obtain the fluxes of sediment exiting the foreland basin during its development, we needed to constrain the thickness of the basin at each stage. The thickness maps of the foreland basin were obtain by the construction of a 3D model of the pro-foreland. In a geomodeller (PetEx, MOVE) we referenced geological maps and cross-sections as well as isodepth maps from wells measurement and interpreted seismic sections. From these maps we identified the depocenters of the foreland basin in time and space. We also estimated the volume of sediment from the Ukrainian foreland that were extensively eroded. The comparison of the location of sediment depocenters and the architecture of the lower plate display the influence of the lithosphere strength and age in the focus of subsidence/creation of accommodation space during foreland development.

The comparison of exhumation rates and sedimentation rate in the basin is not direct; the fluxes of sediment out of the belt were not all delivered to the foreland basin. We separated the eroded sediment fluxes from the belt in three categories, the sediment supplied to the retro-foreland, the sediment supplied to the pro-foreland, and among them, the sediment reintegrated into the nappes of the wedge. We then focussed on the comparison of the sediment supplied to the pro-foreland that were not reintegrated in the bet by further wedge propagation. The sediment fluxes supplied to the foreland display the same pattern as the exhumation rate model after the apportionment of sediment fluxes. We compared these latter fluxes to the sedimentation rates of the foreland basin. The spatial correlation of sediment erosion *loci* with the sediment depocenters shows the development of the axial transport system in the basin. The volumetric analysis show that from 16 to 11.6 Ma, sediments were accommodated everywhere in the foreland basin. However, most of the sediment supplied from the belt were accommodated in the southern part from 11-9 Ma to present. The balance of sediment volume indicate also that sediment started exiting the foreland basin at 8.6 Ma and that ~55.000 km^3 of sediment were transported to the North-western shelf of the Black Sea.

We conclude the study on the geodynamic development of the Carpathians region. We compare the exhumation of the belt with the extension of the Pannonian back-arc basin and the Neogene volcanism of the intra-Carpathian region. We also explain the development of the Focsani Depression with the new insight of our study and according to the retreat and sinking of the Vrancea slab. We integrated our results in the regional framework of the Carpathians: the influence of the slab retreat and dynamic uplift and subsidence on the belt development and on the accommodation of sediment in the foreland.

Résumé

Ce manuscrit est le résultat du travail sur la "Quantification du flux de sédiments généré par la collision continentale et le détachement de slab dans le bassin d'avant-pays des Carpates". Le sujet a pour but de quantifier la quantité de sédiments apportés à l'avant-pays pendant l'érosion de la chaîne des Carpates, qui ont été préservés dans l'avant-pays et/ou transportés par la suite dans la mer Noire. Le bassin d'avant-pays des Carpates a développé un système de transport axial vers le sud-est et les sédiments transportés vers le sud ont construit le plateau nord-ouest de la mer Noire au cours du Miocène moyen et tardif. Afin de retracer la chronologie du transport des sédiments vers la mer Noire et de quantifier les flux de sédiments entrants et sortant de l'avant-pays depuis le Miocène moyen jusqu'à aujourd'hui, nous avons retracé l'exhumation du prisme orogénique et la sédimentation de l'avant-pays.

La formation de la chaîne des Carpates s'est produite dans le contexte d'une zone de subduction en retrait. La plaque plongeante Européenne s'est retirée vers la plate-forme Européenne, entraînant l'accrétion d'un prisme et l'extension du bassin d'arrière-arc, le bassin Pannonien. Les différentes unités sédimentaires accrétées dans le prisme présentent un faciès marin profond du Crétacé au Paléogène, évoluant vers un faciès sédimentaire plus molassique à l'Oligocène et au Miocène.

Pour comprendre le processus d'accrétion-collision dans la chaîne des Carpates et déterminer le début de l'exhumation des différentes nappes, nous avons réalisé une modélisation thermique sur des données thermocrhonologiques à basse température (AHe, AFT et ZHe) que nous avons datées dans les Carpates Ukrainiennes. La plupart de nos âges AHe sont recuits par le réchauffement dû à l'enfouissement, les données AFT présentent des âges recuits et des âges partiellement recuits, et aucun de nos âges ZHe n'est recuit. Grâce à la modélisation inverse, nous déterminons les trajectoires temps-température de six des huit nappes composant le prisme orogénique. Cela révèle que la plupart des nappes ont été accrétées en séquence depuis environ 34 Ma jusqu'à 12 Ma. Toutefois, certains chevauchements hors séquence se sont produits au cours du Miocène moyen. Le taux d'exhumation des nappes a augmenté vers l'avant du prisme, ce qui a entraîné une augmentation de l'apport de sédiments dans le bassin d'avant-pays au Miocène. Grâce aux âges ZHe non recuits que nous avons obtenus, nous identifions les sources potentielles de sédiments du prisme des Carpates. Les principales sources sont la marge sud-ouest de la plate-forme Est-Européenne et la couverture sédimentaire des unités des Carpates internes.

Nous voulions obtenir l'exhumation de l'ensemble de la chaîne des Carpates pour quantifier l'érosion pendant la construction de l'orogène. Nous avons constitué une base de données complète de thermochronologie à basse température de la ceinture des Carpates, des Carpates de l'Ouest aux Carpates du Sud-est, et nous avons procédé à une modélisation inverse des données, à l'aide d'un modèle cinématique thermique (Pecube), afin d'obtenir les taux d'exhumation. Nous avons séparé la ceinture en trois régions : les Carpates de l'Ouest, les Carpates du Nord-est et les Carpates de l'Est et du Sud-est. Nous avons exécuté le modèle sur des pas de temps correspondant, dans la mesure du possible, à la

chronostratigraphie de la région de la Paratéthys, afin de comparer directement les taux d'exhumation dans la chaîne avec les taux de sédimentation dans l'avant-pays. Nous obtenons un modèle d'exhumation qui montre un schéma diachronique du nord-ouest au sud-est. L'exhumation des Carpates de l'Ouest a culminé entre 24 et 12,8 Ma, celle de la région Nord-est entre 18 et 6,1 Ma et celle des régions Est et Sud-est entre 8,6 Ma et aujourd'hui. La comparaison avec les estimations antérieures de l'exhumation est cohérente pour les régions Ouest et Nord-est. Cependant, certaines divergences sont à noter dans la région Est et Sud-est.

La comparaison des taux d'exhumation et de sédimentation dans le bassin n'est pas directe ; les flux de sédiments provenant de la ceinture n'ont pas tous été acheminés vers le bassin de l'avant-pays. Nous avons séparé les flux de sédiments érodés de la ceinture en trois catégories : les sédiments fournis au retro-basin, les sédiments fournis au pro-basin et, parmi eux, les sédiments réintégrés dans les nappes du prisme. Nous nous sommes ensuite concentrés sur la comparaison des sédiments apportés au pro-basin qui n'ont pas été réintégrés dans le prisme par sa propagation ultérieure. Les flux de sédiments fournis à l'avant-pays présentent le même schéma que le modèle d'exhumation après la répartition des flux de sédiments. Nous avons comparé ces derniers flux aux taux de sédimentation du bassin de l'avant-pays. La corrélation spatiale des lieux d'érosion de sédimentation montre le développement du système de transport axial dans le bassin. L'analyse volumétrique montre qu'entre 16 et 11,6 Ma, les sédiments ont été logés partout dans le bassin d'avant-pays. Toutefois, la plupart des sédiments provenant de la chaîne ont été transportés et préservés dans la partie Sud de l'avant-pays de 11 à 9 Ma jusqu'à aujourd'hui. Le bilan du volume de sédiments indique également que les sédiments ont commencé à sortir du bassin d'avant-pays vers 8,6 Ma et que ~55 000 km^3 de sédiments ont été transportés vers le plateau nord-ouest de la mer Noire.

Nous concluons l'étude sur le développement géodynamique de la région des Carpates. Nous comparons l'exhumation de la ceinture avec l'extension du bassin Pannonien d'arrière-arc et le volcanisme Néogène de la région intra-Carpates. Nous expliquons également le développement du bassin de Focsani grâce aux nouvelles connaissances acquises dans le cadre de notre étude et en fonction du retrait et de l'enfoncement de la plaque de Vrancea. Nous avons intégré nos résultats dans le cadre régional des Carpates : l'influence du retrait de la plaque plongeante et du soulèvement et de la subsidence dynamiques sur le développement de la ceinture et sur l'accommodation des sédiments dans l'avant-pays.

Remerciements

Je voudrais commencer mes remerciements en mentionnant mon jury de thèse. Je remercie en particulier Christophe Basile, président de ce jury, dont les compliments sur mon travail m'ont beaucoup réjouie. Je remercie également Delphine Rouby et Mary Ford pour leurs commentaires et questions sur mon travail, ainsi que pour leurs encouragements à le poursuivre. Je remercie également Massimiliano Zattin qui, malgré la distance, m'a beaucoup enrichi par ses questions et commentaires sur mon travail de thèse.

Je voudrais continuer en remerciant mes directeurs de thèse, Peter van der Beek, Arjan de Leeuw et Laurent Husson, de m'avoir confié ce sujet et de m'avoir permis d'en maîtriser le développement. Je tiens à les remercier pour tout ce que cette thèse m'a appris et pour leur aide dans ce processus d'apprentissage.

Merci à toutes les personnes qui ont participé et collaboré avec moi sur ce projet. Je vous suis redevable de cette expérience et de ce qu'elle m'a apporté.

Je tenais ensuite à remercier mes ami.e.s du laboratoire. Tout d'abords ce.lle.ux qui ont partagé le bureau 310 du troisième étage avec moi : Ou Xiong, avec qui je partages des siestes et les aléas de la thèse ; Manon Cantraine, qui, de loin au soleil, me soutenait ; Veleda Astarte Paiva Muller, qui a toujours su illuminer le bureau de bonne humeur ; Charline Coudun, que je soutiendrais jusqu'au bout de sa thèse ; Juan-Carlos Verano, gracias a quien recuerdo mi español.

Et aussi tous mes ami.e.s du laboratoire qui m'ont suivis pendant ces trois années et demi qui n'ont pas toutes été roses, mais grâce à e.lles.ux tout pouvait aller mieux. Merci à Marianna Corre, Maxime Bertauts, William Carlin, bravo a nous d'être maintenant tous docteur en sciences de la terre (ou quelquechose pas loin de ça). Nous pouvons être fier.e de nous. Merci à Boris Chauviré, Anta-Clarisse Sarr, Lorella Masci, Camille Litty, Camille Dusseaux et Loraine Gourbet, pour êtré déjà passer par là et m'avoir, nous avoir, soutenu, pris sous votre aile parfois, et surtout rassuré. J'aurais toujours un doux souvenir de mon parcours au laboratoire lié à vous tout.e.s.

Un autre merci à mes ami.e.s qui ne sont pas passé.e.s par le laboratoire mais dont la présences fut des plus réconfortante et dont le soutiens m'a grandment aidé. La liste n'est pas exhaustive mais merci à: Titouan, Coline, Marion, Lucie, Martin, Thibault, Christian, Jérôme, Aude, Audrey, Anaïs, Alicia, Baptiste, …

Finalement je voudrais remercier ma famille pour leur soutiens et pour avoir toujours considéré mes choix.

Table of Contents

Introduction

1 Alpine orogens and subduction zones in the Mediterranean region

It has long been suggested that the Mediterranean region retains contrasting alpine orogens (Royden and Burchfiel, 1989). The convergence rates, slab vergence, and thrusting style of these mountain ranges are directly influenced by lithospheric-scale differences, such as the thickness and rheology of the lithosphere or the boundary geometry, of the Adriatic and European plates (Wortel, 2000; Wortel and Spakman, 2000; Jolivet et al., 2021). Mediterranean orogens are classified into two categories: collisional orogens, characterised by thick-skinned thrusting, high-grade metamorphism, and high topography (e.g., the European Alps), and retreating subduction orogens, characterised by extension during thrusting, low-grade metamorphism, and low topography (e.g., Carpathians, Dinarides, and the Apennine-Calabrian Arcs). The coexistence of these two types of orogens along the deformation front of the Mediterranean realm confers to the region a great tectonic complexity.

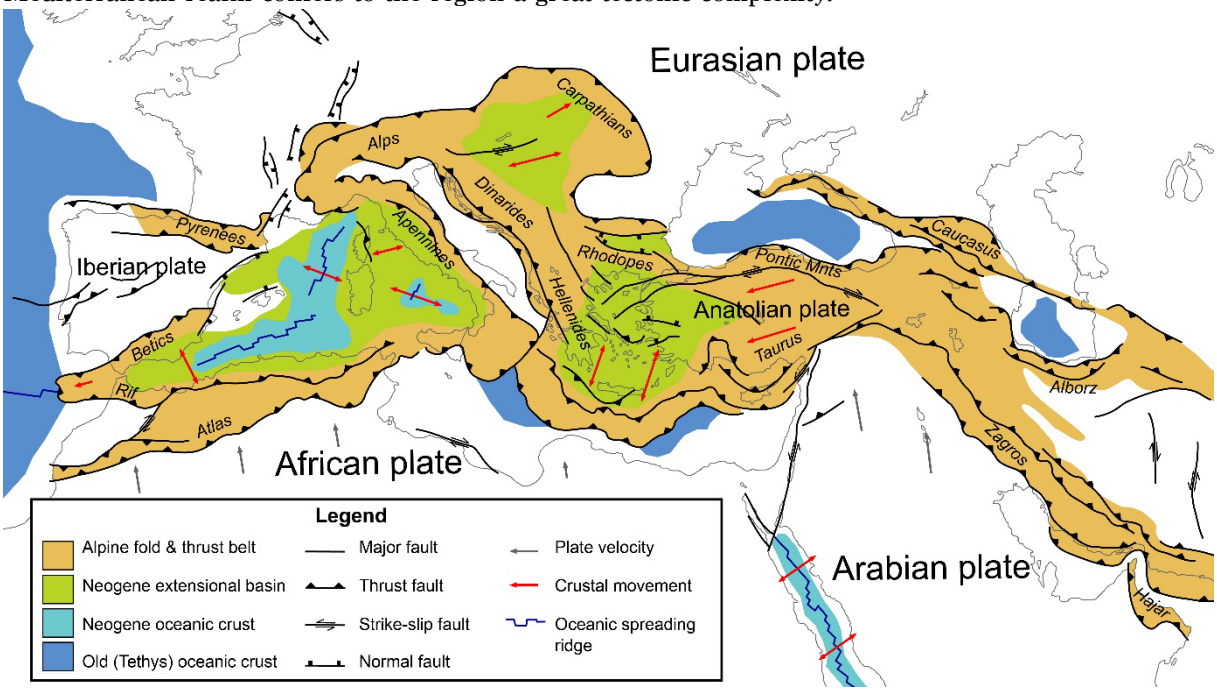

Figure 0.1: Alpine structures in the Mediterranean region. Only Alpine structures of the regions are shown. Source: Wikimedia Commons - Tectonic map Mediterranean.

The Cenozoic evolution of the Mediterranean domain records changes in subduction polarity and the retreat of subduction zones from the previous deformation front (Doglioni et al., 1999; Handy et al., 2015; Jolivet et al., 2021) During inward migration of plates, subduction-zone retreat causes crustal extension and lithospheric thinning behind the deformation front. The Apennine-Calabrian arc retreated about 800 km, resulting in the opening of the Ligurian and Tyrrhenian seas (Doglioni et al., 1999; Wortel and Spakman, 2000; Cifelli et al., 2007). The subduction retreat suggest that the location of the initial subduction front is further north, toward the Carpathians, i.e., the northern most subduction zones of the Mediterranean region.

The previous orogenic cycles record and preserve well thick-skinned deformation. The metamorphic rock gradient and crustal evidence of deformation are strongly imprinted in the crust and brought to the surface by erosion exhumation. However, in the case of a thin-skinned thrust belt of a retreating subduction zone, the crustal markers of deformation are less imprinted in the crust and often eroded or overprinted by new deformation event. Due to this poor conservation of tectonic and metamorphic markers the study of ended retreating subduction zone of precedent orogenic cycles is tedious. Therefore, the Carpathian arc, that provide along strike differences for active and inactive subduction front, may alone provide a better view of the development and termination of retreating subduction zones from the Mediterranean region.

2 The Carpathian belt and foreland basin.

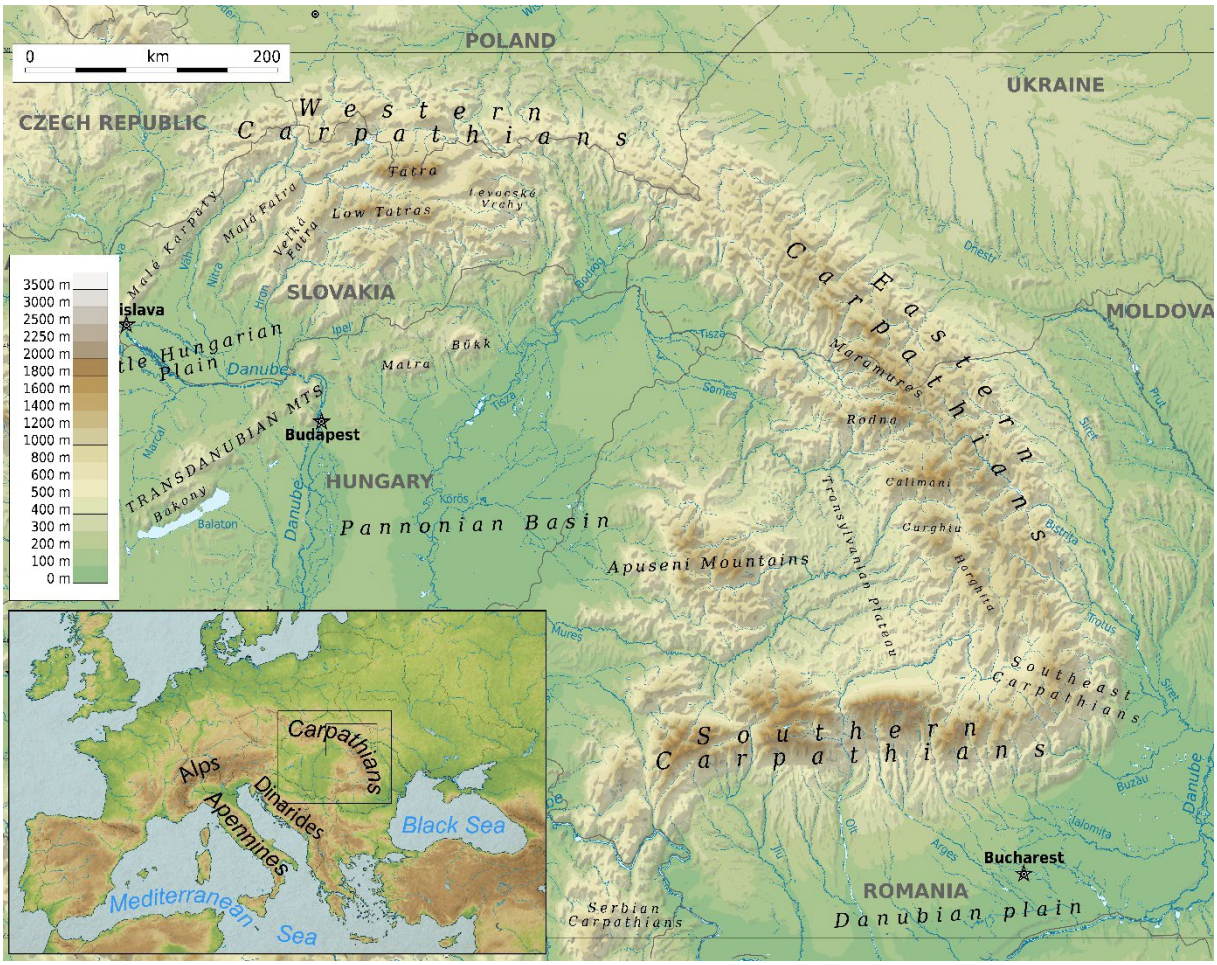

Figure 0.2: Geographic map of the Carpathians belt. Source: Wikimedia Commons – Geographic map of the Carpathians

To better understand the interest of the Carpathians in the study of retreating subduction zones, we briefly present the different characteristics and the main developmental steps of the Carpathian belt and foreland system.

The Carpathian Arc extends from the Czech Republic to Romania. It is divided into four sections: the Western Carpathians, located mainly in Slovakia and southern Poland; the Eastern Carpathians, located in Ukraine and Romania; the Southeastern Carpathians that cover the orogen bending zone, where localized deep seismicity is present nowadays; and the Southern Carpathians, wich comprise the E-W oriented zone in Romania, composed of different tectonic units and have higher topography. The Western, Eastern and South-eastern Carpathians regions are fold and thrust belts characteristic of a retreating subduction zone. The Southern Carpathians are of a different development history and do not provide sediments from the same basin (Moser et al., 2005; Fügenschuh and Schmid, 2005; Schmid et al., 2008).

The interior of the Carpathian arc comprises the Pannonian basin in central Hungary. To the east, the Transylvanian Basin subsided during convergence in the Carpathian thrust belt and is now uplifted (Tiliță et al., 2018). The Neogene Carpathian volcanic arc extends from the western to the eastern

Carpathian interior. The most recent volcanoes are the Calimani, Gurghui and Harghita mountains in Romania (Pécskay et al., 2006; Seghedi and Downes, 2011).

The Carpathian foreland extends from the Czech Republic into Poland, Ukraine, Romania and Moldova. This foreland is vast and widens towards the southeast (de Leeuw et al., 2020). The basin is drained by large rivers such as the Dniester, Prut and Siret. The foreland is elevated to ~300 m in Poland. In Ukraine, Moldova and Romania, the foreland is incised by up to 400-500 m. In contrast, just in front of the Southeast Carpathians in Romania, the foreland is at sea level and forms a flat and subsiding region (van der Hoeven et al., 2005).

According to reconstructions of the Carpathians, the formation of the belt and foreland, the Neogene volcanics and the extension of the Pannonian basin are due to the retreat of the subduction zone and the migration of several micro- plates into an ancient embayment. A remnant of the European slab remains attached to the SE Carpathians, allowing the contemporaneous effects of slab retreat over the Carpathian system to be observed and quantified in this region (Şengül-Uluocak et al., 2019).

3 Why use the Carpathians as a study case?

The Carpathian belt was accreted from the Oligocene to the middle Miocene and collided with the East European Plate from middle-Miocene to Pleistocene (Nemčok et al., 2006; Schmid et al., 2008; Handy et al., 2015). The location of the fold and thrust belt and its pro-foreland basin in the European continent is isolated from other Alpine orogens influence for sediment supply and tectonic overprint. Slab retreat was not affected by a change in slab polarity along the Carpathians front. Furthermore, arc development in the western and eastern Carpathians has reached quiescence, i.e., the slab has detached, and the belt is no longer active in these regions. However, the South-eastern Carpathian region is still active, with localized earthquakes at depth and the resulting uplift and subsidence linked to the remaining attached European slab.

In the Mediterranean region: the Carpathian foreland system developed with an active source (the Carpathian belt) and has only one outlet, the Black Sea. As the Danube did not connect with the Carpathian foreland system until the Pliocene (Matoshko et al., 2019; Krézsek and Olariu, 2021), the Middle Miocene to Pliocene foreland developed as a near-closed source-sink system with the Carpathian belt as the only active supplier of sediments. The source to sink system situation provides an opportunity to study the co-development of the Carpathian belt and its foreland basin as a typical retreating subduction-zone orogen. In addition, the thrust belt and foreland basin have been extensively studied and, therefore, a wealth of data is available as a base for the study.

4 How do we study the evolution of a fold and thrust belt and its foreland?

To study the development of the Carpathian Mountain belt and foreland system, we need to understand the development of the belt and its accretion, as well as the development of its foreland basin. We can access the development of the fold and thrust belt by tracing the rates of exhumation during accretion, collision and during the slab detachment along the Carpathian arc. Exhumation of the Carpathians can

be expressed in eroded sediment volumes over time and at different locations. Eroded sediment fluxes can be compared quantitatively to the sediments present in the foreland basin and can trace the sediment fluxes through time, during the development of the retreating subduction-zone orogen. The development of the foreland is synchronous with the erosion of the belt, but the sedimentary evolution of the basin can additionally provide insight into the more recent development of the system (up to the Pleistocene). The development of the fold and thrust belt start before the onset of the foreland development, a subsequent co-evolution period of orogenic activity and foreland development precede the end of convergence, a quiescence of the belt and post-orogenic foreland sedimentation. The locus of erosion and sediment deposition during the orogenic and foreland development is related to the activity of the upper plate and the dynamics of the lower subducting plate, respectively. By tracing the evolution of the sedimentary system from source to sink in space and time, we can retrace the development of the retreating subduction zone of the Carpathians, from the collision to the slab detachment.

5 How to retrieve sediment fluxes?

The exhumation pattern of a region quantifies the upward vertical path of rocks with respect to the surface. Exhumation in a fold and thrust belt can be quantified by modelling the time-temperature trajectories of rocks within the orogenic wedge, based on their thermochronology record. Inversion of a large number of thermochronology data across orogens allows tracing orogen development by quantifying the spatial and temporal pattern of exhumation (Morris et al., 1998; Thomson et al., 2010; Curry et al., 2021). Through monitoring the variation in exhumation rate over space and time, which can be achieved through the application of several thermochronometers, we can constrain the loci of exhumation during the development of the orogenic wedge. By mapping out a laterally varying exhumation pattern, we can, in the Carpathians in particular, determine the period of activity in the different regions of the orogen and observe their progressive inactivation as exhumation decreases.

Construction of a spatially controlled exhumation model requires a large thermochronological database, which can be constructed for the Carpathian belt as the orogen has been extensively studied using thermochronological methods. As erosion is the process of removing material from the surface, exhumation rates can be proxies for erosion rates if topographic surface is constant. Thus, quantification of sediment fluxes supplied by the belt to the foreland basin is possible.

Foreland-basin development can be deciphered by studying the lateral variation of sedimentary facies and the respective thicknesses of sedimentary units of a certain age. Constraining depositional ages is paramount for a complete model of foreland development. The Carpathian foreland basin has been extensively studied because of its resource potential and its paleogeographic environment. As a result, the stratigraphy of the basin is well constrained in age (Vasiliev et al., 2004, 2005, 2010; de Leeuw et al., 2010; Krijgsman et al., 2010; de Leeuw et al., 2013; Palcu et al., 2015, 2019; Van Baak et al., 2015) and paleo environment (Tărăpoancă et al., 2003; Oszczypko, 2006; Oszczypko and Oszczypko-Clowes, 2012; Dziadzio et al., 2006; Matoshko et al., 2016; Jorissen et al., 2018; Matoshko et al., 2019; de Leeuw et al., 2020; Lazarev et al., 2020). The Carpathian foreland contains the deepest basin on the European continent, the Focsani Depression, which is estimated to reach 10-12 km in depth (Tărăpoancă et al., 2003). The development of this depression and the volume of sediments deposited in this area are

intriguing, and expose the role of slab dynamics during foreland basin development (Royden and Karner,1984; Artyushkov et al., 1996). We intend to compare the volumes of sediments deposited in the foreland basin with the eroded sediment fluxes of the belt to recover its development using a quantitative approach.

This comparison can be achieved using geologic maps and geologic sections of the foreland, as well as existing isopach maps, to develop a 3D model that allows estimation of the sediment volumes deposited during each of the regional chronostratigraphic stages. From the foreland 3D model, quantification of volume of sediment preserved in the basin along time can be derived. We can compare the sediment volumes from the belt, derived from the exhumation model, and the volumes of sediment in the foreland during its development. The volumetric analysis of the Carpathians system, and the tracking of exhumation and deposition loci, can give insight on the co-evolution of fold and thrust belt and foreland in a retreating subduction zone.

6 Quantification of processes and objectives

In this work, we aim to quantify processes to distinguish the contribution of the geodynamic processes during the development of the Carpathian belt and foreland. The Carpathians are the result of interactions of the retreating slab with the upper plate and the European passive margin. From this perspective, we need to understand the development of the region through its tectonic and sedimentary archives, i.e., retrace the flux of sediments during exhumation and deposition in the Carpathian system. This overall goal leads to the following specific objectives for this thesis:

We must first understand the Carpathian accretionary system and the interactions within the orogenic wedge. We seek to decipher tectonic burial and nappe stacking in the Carpathian wedge using thermochronometry and time-temperature modelling.

Second, on a larger scale, the overall pattern of exhumation can provide important information about the drivers of rock uplift in the belt before and during collision with the passive margin. Quantifying exhumation rates will indicate the intensity of uplift/deformation across the various regions of the orogen, as well as highlight periods of strong erosion and thus high eroded sediment flux.

Third, a volumetric study of the foreland basin will clarify where and when the sediments were accommodated and preserved. Together with insights into the development of the foreland system, the pattern of deposition may reveal which geodynamic process controls sediment deposition in the foreland over space and time.

Fourth, comparison of belt and foreland sediment fluxes could indicate syn- or dia-chronicity in the development of each and reveal the timing and magnitude of sediment transfer out of the system.

Finally, identification of the processes influencing exhumation of the thrust sheets and those influencing accommodation in the foreland may help to constrain the time and space evolution of detachment of the European slab beneath the Carpathian front.

The history of accretion, erosion and deposition of sediments in the Carpathian system will provide an example of the development and termination of a retreating subduction-zone orogen of the Mediterranean realm.

7 Outline

I have divided the manuscript into five chapters describing the work carried out during the project: Quantification of sediment fluxes in the Carpathian belt and foreland from collision to slab detachment.

The first chapter introduces some theory related to the dynamics of accretionary and orogenic wedges and the development of the foreland-basin system as well as the thermochronology dating and use in geology and more specifically in orogenic wedges. It will continue with the geological context of formation of the Carpathian belt and a description of the stratigraphy of its thin-skinned nappes, which predominantly consist of flysch-type sediments. The sedimentary system of the foreland basin is also described following the sedimentary succession and facies evolution from the Badenian (mid-Miocene, 16-12.65 Ma) to the Early Pleistocene (2.58-1.8 Ma).

The second chapter is based on the published paper "Construction of the Ukrainian Carpathian Wedge from low-temperature thermochronology and tectono-stratigraphic analysis". In this chapter, the accretion and stacking of the nappes in the Ukrainian Carpathian wedge are recovered from time-temperature and time-depth trajectories. Through this analysis, we have developed a model explaining the sources of sediment to the Carpathian basin during its closure as well as the sedimentary and tectonic burial, exhumation and erosion of the nappes accreted in the Outer Carpathian Belt.

The third chapter of this thesis describes the construction of the exhumation model for the Carpathian belt. The model resulting from the inversion of a comprehensive set of thermochronological data from the mountain belt is first compared and contrasted with exhumation rates established by previous studies. After validation of our results, we integrate the variation of exhumation rates across the Carpathian belt into a geodynamic model. We highlight possible sources of the diachronous pattern of exhumation observed in the model.

In the fourth chapter, we present a 3D model of the Carpathian foreland basin and the resulting sediment thickness maps for each regional stratigraphic stage. We elaborate on the timing and location of the depocenters and their relationship to the features of the lower plate. We also discuss the development of the Focsani depression and the coevolutionary increase in slab pull and suction with sedimentation rates over time.

Finally, the fifth chapter of the thesis compares the eroded sediment fluxes from the belt to those deposited in the foreland basin. The sediment mass balance shows an outflow of sediment from the system and we determine when this occurred. Investigating lateral variation in crustal processes or rheological characteristics, conclusions are drawn about the roles of the subducting plate, the upper plate, and the passive margin during the construction of the Carpathian foreland fold and thrust belt system.

To complement the work in this thesis, we summarize the perspectives that were considered during the project. We also explain how the results of this project may be important in conceiving and approaching studies of the coevolution of foreland fold and the thrust belt. We present an initial implementation of a numerical model of slab detachment constrained by the exhumation rate model and the migration of foreland sediments to depocenters.

References

Artyushkov, E. V., Baer, M. A., and Mörner, N.-A.: The East Carpathians: Indications of phase transitions, lithospheric failure and decoupled evolution of thrust belt and its foreland, Tectonophysics, 262, 101–132, https://doi.org/10.1016/0040-1951(95)00207-3, 1996.

Cifelli, F., Mattei, M., and Rossetti, F.: Tectonic evolution of arcuate mountain belts on top of a retreating subduction slab: The example of the Calabrian Arc, J. Geophys. Res., 112, B09101, https://doi.org/10.1029/2006JB004848, 2007.

Curry, M. E., Beek, P. van der, Huismans, R. S., Wolf, S. G., Fillon, C., and Muñoz, J.-A.: Spatio-temporal patterns of Pyrenean exhumation revealed by inverse thermo-kinematic modeling of a large thermochronologic data set, Geology, 49, 738–742, https://doi.org/10.1130/G48687.1, 2021.

Doglioni, C., Gueguen, E., Harabaglia, P., and Mongelli, F.: On the origin of west-directed subduction zones and applications to the western Mediterranean, SP, 156, 541–561, https://doi.org/10.1144/GSL.SP.1999.156.01.24, 1999.

Dziadzio, P. S., Borys, Z., Kuk, S., Masłowski, E., Probulski, J., Pietrusiak, M., Górka, A., Moryc, J., Baszkiewicz, A., Karnkowski, P., Karnkowski, P. H., and Pietrusiak, M.: Hydrocarbon Resources of the Polish Outer Carpathians—Reservoir Parameters, Trap Types, and Selected Hydrocarbon Fields: A Stratigraphic Review, in: The Carpathians and Their Foreland: Geology and Hydrocarbon Researces: AAPG Memoir 84, edited by: Golonka, J. and Picha, F. J., The American Association of Petroleum Geologists, Tulsa, Oklahoma, U.S.A., 259–291, https://doi.org/10.1306/985611M843071, 2006.

Fügenschuh, B. and Schmid, S. M.: Age and significance of core complex formation in a very curved orogen: Evidence from fission track studies in the South Carpathians (Romania), Tectonophysics, 404, 33–53, https://doi.org/10.1016/j.tecto.2005.03.019, 2005.

Handy, M. R., Ustaszewski, K., and Kissling, E.: Reconstructing the Alps–Carpathians–Dinarides as a key to understanding switches in subduction polarity, slab gaps and surface motion, Int J Earth Sci (Geol Rundsch), 104, 1–26, https://doi.org/10.1007/s00531-014-1060-3, 2015.

van der Hoeven, A. G. A., Mocanu, V., Spakman, W., Nutto, M., Nuckelt, A., Matenco, L., Munteanu, L., Marcu, C., and Ambrosius, B. A. C.: Observation of present-day tectonic motions in the Southeastern Carpathians: Results of the ISES/CRC-461 GPS measurements, Earth and Planetary Science Letters, 239, 177–184, https://doi.org/10.1016/j.epsl.2005.09.018, 2005.

Jolivet, L., Baudin, T., Calassou, S., Chevrot, S., Ford, M., Issautier, B., Lasseur, E., Masini, E., Manatschal, G., Mouthereau, F., Thinon, I., and Vidal, O.: Geodynamic evolution of a wide plate boundary in the Western Mediterranean, near-field *versus* far-field interactions, BSGF - Earth Sci. Bull., 192, 48, https://doi.org/10.1051/bsgf/2021043, 2021.

Jorissen, E. L., de Leeuw, A., van Baak, C. G. C., Mandic, O., Stoica, M., Abels, H. A., and Krijgsman, W.: Sedimentary architecture and depositional controls of a Pliocene river-dominated delta in the semi-isolated Dacian Basin, Black Sea, Sedimentary Geology, 368, 1–23, https://doi.org/10.1016/j.sedgeo.2018.03.001, 2018.

Krézsek, C. and Olariu, C.: Filling of sedimentary basins and the birth of large rivers: The lower Danube network in the Dacian Basin, Romania, Global and Planetary Change, 197, 103391, https://doi.org/10.1016/j.gloplacha.2020.103391, 2021.

Krijgsman, W., Stoica, M., Vasiliev, I., and Popov, V. V.: Rise and fall of the Paratethys Sea during the Messinian Salinity Crisis, Earth and Planetary Science Letters, 290, 183–191, https://doi.org/10.1016/j.epsl.2009.12.020, 2010.

L. Royden (2), G. D. Karner (3): Flexure of Lithosphere Beneath Apennine and Carpathian Foredeep Basins: Evidence for an Insufficient Topographic Load, Bulletin, 68, https://doi.org/10.1306/AD461372-16F7-11D7-8645000102C1865D, 1984.

Lazarev, S., de Leeuw, A., Stoica, M., Mandic, O., van Baak, C. G. C., Vasiliev, I., and Krijgsman, W.: From Khersonian drying to Pontian "flooding": late Miocene stratigraphy and palaeoenvironmental evolution of the Dacian Basin (Eastern Paratethys), Global and Planetary Change, 192, 103224, https://doi.org/10.1016/j.gloplacha.2020.103224, 2020.

de Leeuw, A., Bukowski, K., Krijgsman, W., and Kuiper, K. F.: Age of the Badenian salinity crisis; impact of Miocene climate variability on the circum-Mediterranean region, Geology, 38, 715–718, https://doi.org/10.1130/G30982.1, 2010.

de Leeuw, A., Filipescu, S., Maţenco, L., Krijgsman, W., Kuiper, K., and Stoica, M.: Paleomagnetic and chronostratigraphic constraints on the Middle to Late Miocene evolution of the Transylvanian Basin (Romania): Implications for Central Paratethys stratigraphy and emplacement of the Tisza–Dacia plate, Global and Planetary Change, 103, 82–98, https://doi.org/10.1016/j.gloplacha.2012.04.008, 2013.

de Leeuw, A., Vincent, S. J., Matoshko, A., Matoshko, A., Stoica, M., and Nicoara, I.: Late Miocene sediment delivery from the axial drainage systemof the East Carpathian foreland basin to the Black Sea, Geology, https://doi.org/10.1130/G47318.1, 2020.

Matoshko, A., Matoshko, A., de Leeuw, A., and Stoica, M.: Facies analysis of the Balta Formation: Evidence for a large late Miocene fluvio-deltaic system in the East Carpathian Foreland, Sedimentary Geology, 343, 165–189, https://doi.org/10.1016/j.sedgeo.2016.08.004, 2016.

Matoshko, A., Matoshko, A., and de Leeuw, A.: The Plio–Pleistocene Demise of the East Carpathian Foreland Fluvial System and Arrival of the Paleo-Danube To The Black Sea, Geologica Carpathica, 70, 91–112, https://doi.org/10.2478/geoca-2019-0006, 2019.

Morris, Sinclair, and Yell: Exhumation of the Pyrenean orogen: implications for sediment discharge, Basin Research, 10, 69–85, https://doi.org/10.1046/j.1365-2117.1998.00053.x, 1998.

Moser, F., Hann, H. P., Dunkl, I., and Frisch, W.: Exhumation and relief history of the Southern Carpathians (Romania) as evaluated from apatite fission track chronology in crystalline basement and intramontane sedimentary rocks, Int J Earth Sci (Geol Rundsch), 94, 218–230, https://doi.org/10.1007/s00531-004-0456-x, 2005.

Nemčok, M., Pogácsás, G., and Pospíšil, L.: Activity Timing of the Main Tectonic Systems in the Carpathian–Pannonian Region in Relation to the Rollback Destruction of the Lithosphere, in: The Carpathians and Their Foreland: Geology and Hydrocarbon Researces: AAPG Memoir 84, edited by: Golonka, J. and Picha, F. J., The American Association of Petroleum Geologists, Tulsa, Oklahoma, U.S.A., 743–766, https://doi.org/10.1306/985627M843083, 2006.

Oszczypko, N.: Late Jurassic-Miocene evolution of the Outer Carpathian fold-and-thrust belt and its foredeep basin (Western Carpathians, Poland), 25, 2006.

Oszczypko, N. and Oszczypko-Clowes, M.: Stages of development in the Polish Carpathian Foredeep basin, Open Geosciences, 4, https://doi.org/10.2478/s13533-011-0044-0, 2012.

Palcu, D. V., Tulbure, M., Bartol, M., Kouwenhoven, T. J., and Krijgsman, W.: The Badenian–Sarmatian Extinction Event in the Carpathian foredeep basin of Romania: Paleogeographic changes in the Paratethys domain, Global and Planetary Change, 133, 346–358, https://doi.org/10.1016/j.gloplacha.2015.08.014, 2015.

Palcu, D. V., Vasiliev, I., Stoica, M., and Krijgsman, W.: The end of the Great Khersonian Drying of Eurasia: Magnetostratigraphic dating of the Maeotian transgression in the Eastern Paratethys, Basin Res, 31, 33–58, https://doi.org/10.1111/bre.12307, 2019.

Pécskay, Z., Lexa, J., Szakács, A., Seghedi, I., Balogh, K., Konečný, V., Zelenka, T., Kovacs, M., Póka, T., Fülöp, A., Márton, E., Panaiotu, C., and Cvetković, V.: Geochronology of Neogene magmatism in the Carpathian arc and intra-Carpathian area, 21, 2006.

Royden, L. and Burchfiel, B. C.: Are systematic variations in thrust belt style related to plate boundary processes? (The western Alps versus the Carpathians), Tectonics, 8, 51–61, https://doi.org/10.1029/TC008i001p00051, 1989.

Schmid, S. M., Bernoulli, D., Fügenschuh, B., Matenco, L., Schefer, S., Schuster, R., Tischler, M., and Ustaszewski, K.: The Alpine-Carpathian-Dinaridic orogenic system: correlation and evolution of tectonic units, Swiss J. Geosci., 101, 139–183, https://doi.org/10.1007/s00015-008-1247-3, 2008.

Seghedi, I. and Downes, H.: Geochemistry and tectonic development of Cenozoic magmatism in the Carpathian–Pannonian region, Gondwana Research, 20, 655–672, https://doi.org/10.1016/j.gr.2011.06.009, 2011.

Şengül-Uluocak, E., Pysklywec, R. N., Göğüş, O. H., and Ulugergerli, E. U.: Multidimensional Geodynamic Modeling in the Southeast Carpathians: Upper Mantle Flow-Induced Surface Topography Anomalies, Geochem. Geophys. Geosyst., 2019GC008277, https://doi.org/10.1029/2019GC008277, 2019.

Tărăpoancă, M., Bertotti, G., Maţenco, L., Dinu, C., and Cloetingh, S. A. P. L.: Architecture of the Focşani Depression: A 13 km deep basin in the Carpathians bend zone (Romania): ARCHITECTURE OF THE FOCŞANI DEPRESSION, Tectonics, 22, n/a-n/a, https://doi.org/10.1029/2002TC001486, 2003.

Thomson, S. N., Brandon, M. T., Reiners, P. W., Zattin, M., Isaacson, P. J., and Balestrieri, M. L.: Thermochronologic evidence for orogen-parallel variability in wedge kinematics during extending convergent orogenesis of the northern Apennines, Italy, Geological Society of America Bulletin, 122, 1160–1179, https://doi.org/10.1130/B26573.1, 2010.

Tiliţă, M., Lenkey, L., Maţenco, L., Horváth, F., Surányi, G., and Cloetingh, S.: Heat flow modelling in the Transylvanian basin: Implications for the evolution of the intra-Carpathians area, Global and Planetary Change, 171, 148–166, https://doi.org/10.1016/j.gloplacha.2018.07.007, 2018.

Van Baak, C. G. C., Mandic, O., Lazar, I., Stoica, M., and Krijgsman, W.: The Slanicul de Buzau section, a unit stratotype for the Romanian stage of the Dacian Basin (Plio-Pleistocene, Eastern Paratethys), Palaeogeography, Palaeoclimatology, Palaeoecology, 440, 594–613, https://doi.org/10.1016/j.palaeo.2015.09.022, 2015.

Vasiliev, I., Krijgsman, W., Langereis, C. G., Panaiotu, C. E., Maţenco, L., and Bertotti, G.: Towards an astrochronological framework for the eastern Paratethys Mio–Pliocene sedimentary sequences of the Focşani basin (Romania), Earth and Planetary Science Letters, 227, 231–247, https://doi.org/10.1016/j.epsl.2004.09.012, 2004.

Vasiliev, I., Krijgsman, W., Stoica, M., and Langereis, C. G.: Mio-Pliocene magnetostratigraphy in the southern Carpathian foredeep and Mediterranean-Paratethys correlations, Terra Nova, 17, 376–384, https://doi.org/10.1111/j.1365-3121.2005.00624.x, 2005.

Vasiliev, I., de Leeuw, A., Filipescu, S., Krijgsman, W., Kuiper, K., Stoica, M., and Briceag, A.: The age of the Sarmatian–Pannonian transition in the Transylvanian Basin (Central Paratethys), Palaeogeography, Palaeoclimatology, Palaeoecology, 297, 54–69, https://doi.org/10.1016/j.palaeo.2010.07.015, 2010.

Wortel, M. J. R.: Subduction and Slab Detachment in the Mediterranean-Carpathian Region, Science, 290, 1910–1917, https://doi.org/10.1126/science.290.5498.1910, 2000.

Chapter I: Scientific context

As an introduction to the studies reported in this thesis, this first chapter discusses the construction of orogenic wedges and foreland basins from a broad and theoretical point of view. We review the mechanisms of orogenic wedge formation and foreland-basin development. The theory and methodology of low-temperature thermochronology are also described. Finally, the geological context of the Carpathian belt and its foreland basin is developed with an emphasis on the different features that are important for the thesis subject. We discuss the migration of micro-plates into the Carpathian embayment and their coeval extension, leading to the formation of the Pannonian Basin. The stratigraphy of the Carpathian fold and thrust belt is detailed for each nappe of the outer wedge. Then we describe the foreland-basin stratigraphy, as well as the development of the axial sediment transport system. Finally, different geodynamic models for slab retreat in the Carpathian region are explained.

1 Principles and theory of thrust-belt and foreland-basin formation

This section will discuss the different concepts used for the analysis of the Carpathians belt formation and the foreland development. The different models discussed here whether conceptual, mechanical, or analytical, form a base for the discussion of the geodynamic evolution of the study region. More elaborate and specific geodynamic models for the Carpathian belt and its foreland will be presented in the respective chapters of the manuscript.

1.1 Orogenic wedges

1.1.1 Critical taper theory

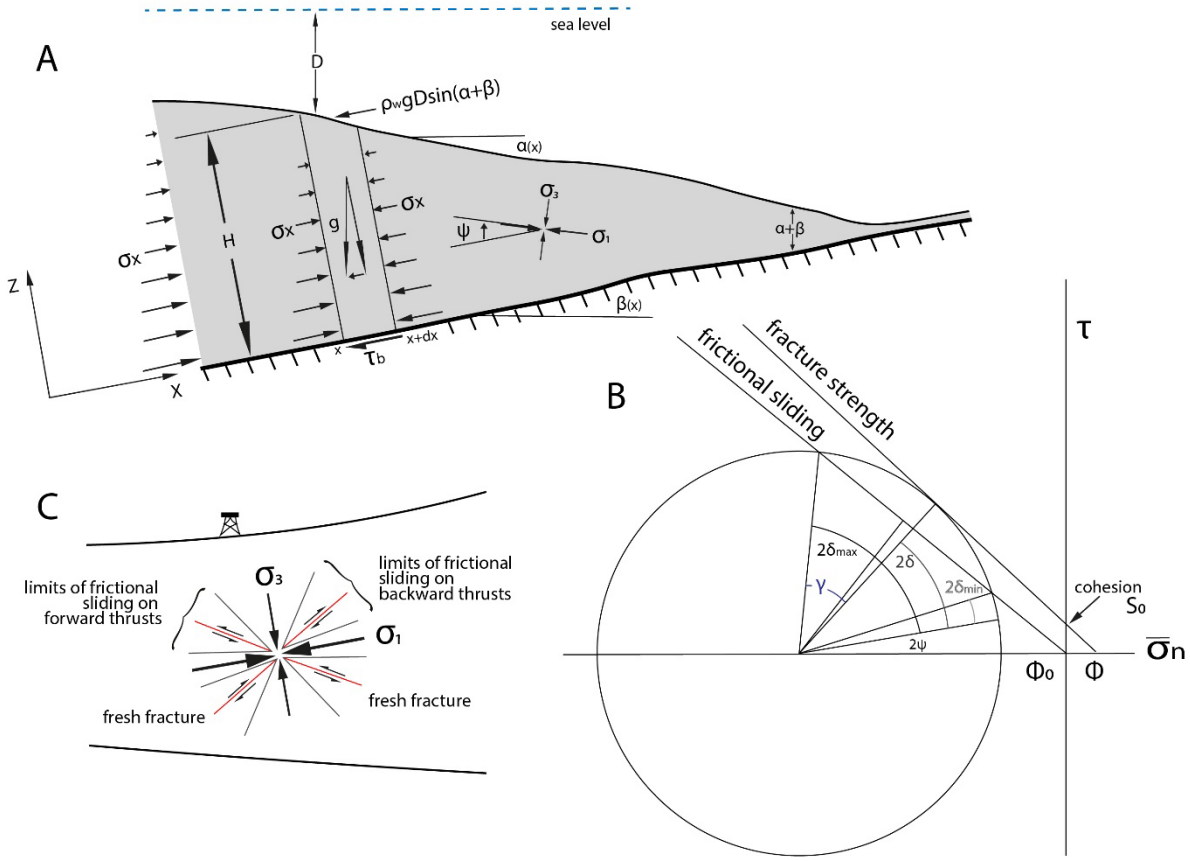

Figure I.1: A) Schematic diagram of a submerged critical wedge under horizontal compression, on the verge of Coulomb failure. The force balance applied on a rock column from x to x + dx and the orientation of the principal stresses (σ_1 and σ_3) are displayed. τ_b is the shear stress from traction at the basal decollement. From Davis et al. (1983, their Figure 5). B) Mohr-Coulomb diagram for a cohesive critical wedge; γ is the range of angles at which new thrusts can develop. δ_{max}, δ and δ_{min} are the maximum, optimal, and minimum angles at which sliding can occur on existing faults. C) Sketch of the stress orientation in a critical wedge and the limits of frictional sliding and fresh fracture formation. B) and C) from Dahlen et al. (1984, their Figure 17).

Several common characteristics have been observed through research on various types of thin-skinned accretionary prisms and orogenic wedges in convergence zones: a) a basal detachment of the prism material is dipping toward the hinterland; b) the materiel involved on top of the detachment is under horizontal compression and deformed; c) the overall shape is a wedge with a predictable taper angle, opening toward the hinterland (Chapple 1978). These characteristics are similar to what is observed in sandbox experiments with an inclined plane covered with sand and shortened against a backstop wall. The sand pile develops a critical taper, growing by deformation in the wedge to reach a state of stable sliding whilst growing self-similarly, called the steady state (Davis et al., 1983; Dahlen et al., 1984). Davis et al. (1983) showed that the critical taper shape is reached when the material in the wedge is on the verge of failure and under horizontal compressional forces everywhere. Wedges with a lower topographic angle α and/or basal detachment dip angle β than a critical taper will not slide but deform internally to reach this critical shape. Critical-wedge theory implies that a critically tapered orogenic wedge responds to four forces: a) lithostatic pressure of the rock pile; b) the potential overlying water pressure (pore pressure); c) the resistance to frictional sliding at the basal decollement; d) the horizontal compression. The stable shape of a non-cohesive Coulomb wedge is described by the equation:

$$\propto + R\beta = F$$

Where:

$$R = \frac{(1-\lambda)K}{\left(1-{}^{\rho_w}/_{\rho}\right)+(1-\lambda)K}$$

and

$$F = \frac{(1-\lambda_b)\mu_b}{\left(1-{}^{\rho_w}/_{\rho}\right)+(1-\lambda_b)K}$$

Where K is a dimensionless quantity of the integrated forces balanced in the wedge according to the stress orientation angle (ψ) in the z direction (Figure I.1), and the internal strength of the wedge (internal angle of friction ϕ). The stability of the wedge is, according to this equation, dependent on the basal friction coefficient, μ_b, and the pore fluid pressure both in the wedge (λ) and at the basal detachment (λ_b). Variation of basal friction, linked to the basal friction coefficient and/or the basal pore-fluid pressure variation, will provokes changes of shape in the wedge (i.e., variation of α and/or β). External phenomena as erosion and isostasy will decrease the topographic slope and the dip of the basal detachment, respectively, and critical taper shape can be reached by adjustment of the basal friction and overall deformation in response. The density ratio between the rock density ρ and the water density ρ_w is what makes the major difference between the shapes of emerged and submerged wedges. The emergence of the wedge above sea level may produce a drop of 1° in the surface slope angle α (Davis et al., 1983).

The theory is applicable to wedges that are in a regime of brittle deformation and frictional sliding. Thicker wedges with rocks reaching ductile behaviour at the base, or with specific rock properties in the basal detachment preventing normal frictional sliding (i.e., evaporites), are at the limit of this theory. In addition to the critical taper theory for non-cohesive Coulomb wedges, Dahlen et al. (1984), quantified

and experimented with the brittle deformation and effective stress regime in a Coulomb wedge. One property that arose is the type of fault deformation according to the basal angle and the frictional sliding of reactivated faults in wedges. A threshold in the cohesive strength parameter allows for sliding on fault or for the creation of new fractures in the wedge as a function of the stress regime in the Coulomb wedge (cohesive or non-cohesive; Dahlen, 1990). Wedge deformation can, accordingly, be due to creation of new faults, or by the propagation of existing faults through sliding.

1.1.2 Doubly vergent wedges

A critical taper shape fits most accretionary prisms and thin-skinned foreland fold and thrust belts. However, accretionary or collisional orogens frequently have a different shape, corresponding to a doubly vergent wedge. This shape was also observed in sandbox experiments where convergence is driven from below rather than from the side (Malavieille, 1984; Wang and Davis, 1992) and in numerical experiments (e.g., Willet et al., 1993). In the context of two rigid plates with a less competent layer of material on top and competent material at their base, the situation may be approximated as follows: one plate may be under-thrusting the other at a singularity point (S) where the upper incompetent materiel is bound to be deformed if the other plate is kept fixed and non-deformed (Figure I.2). The velocity of the under-thrusting plate, and thus the accretionary flux, is constant. Both the numerical and analog models show three stages of development: 1) From the singularity point S, materiel is being uplifted in a triangular shape and moved over S in the direction of materiel influx; 2) Deformation propagates as a shear zone on the pro-side (i.e., on the under-thrusting plate) with a basal decollement separating the accreted and deformed material on top of the rigid, undeformed under-thrusting plate; 3) A shear decollement also develops on the retro-side of the wedge (i.e. on the fixed plate) and may propagate in the direction of material influx on the upper layer of the fixed plate (Figure I.2). From critical wedge theory, the topographic angle on the pro-side is the maximum taper angle, whereas on the retro-side it displays the minimal taper angle. Material fluxes in the doubly vergent wedge propagate toward the retro-side via pathways of increasing slope. Deformation is located in the retro-wedge and pro-wedge shear zones, where material is thrusted. The shear zones join at the S point of the orogen (Figure I.2). The asymmetric transport of material in the wedge (from the proside to the retroside) confers an asymmetry in the total strain of the wedge as the retro-shear zone accumulates material transported from the pro-shear zone (Figure 2). Advection of heat in a wedge is also asymmetric, hotter material is advected from the base of the crust, and transported along the retro-shear zone.

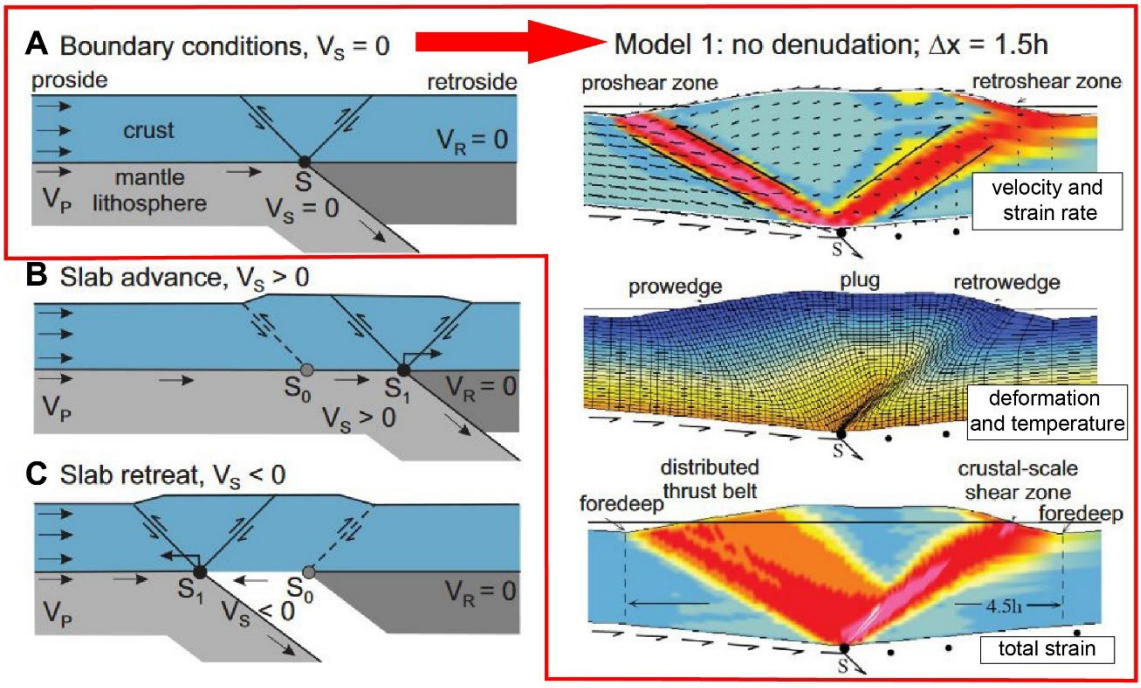

Figure I.2: A) boundary conditions for a standard S-point model for small cold collisional orogens (after Willet et al., 1993). Pro-side lithosphere moves to the right at velocity V_P and is subducted beneath retroside lithosphere which moves to the left with velocity V_R, with a detachment at the S-point (of velocity V_S). The model has $V_P>0$, $V_S=V_R=0$. (B,C) Variation on S-point velocity boundary condition with $V_S>0$ in conditions of slab advancing (B) and $V_S<0$ for conditions of slab retreat (C). Model 1 demonstrates the repartition of velocity and strain rate, deformation and temperature and the total strain in an active orogen with boundary conditions shown in A and no surface denudation (after Beaumont et al., 1994 and Jamieson and Beaumont 2013).

1.2 Accretion and soft collision

Orogenic wedges refer to the accretion of sedimentary material that builds the wedge and the topography in a convergent system during the subduction of oceanic and/or thinned continental crust. These systems are often contrasted with collisional orogens, where the continental crust of both margins is involved in the deformation process creating the topography. Nonetheless the conceptual limit between accretion and collision is very thin in subduction zone orogenic system and depends on time and scale of observation of the convergence zone (Royden and Faccenna, 2018; Van Staal and Zagorevski, 2020).

Accretion is defined as the juxtaposition of different units of allochthonous rocks, such as sediments or plutonic/volcanic terranes scraped-off from the downgoing plate. Collision is often thought of as a major event happening at the suture of an oceanic domain, between two continental margins and implying metamorphism and large-scale deformation in both plates (Figure I.3). However, in the case of soft collision, the continental crusts of the upper and the lower plates do come together, but without significant thick-skinned deformation and metamorphism, because convergence stops before this can occur (Figure I.3). Soft collision is often the case for retreating subduction zones where the driving

mechanism of convergence is the negative buoyancy of the downgoing plate and the retreating rate of the slab is higher than the convergence rate of the plates. The subduction orogens often occur where continent boundary display highly extended continental margins. The convergence resumes during subduction of oceanic crust and accretion at the upper plate margin. Once the highly extended continental margin is consumed in the subduction zone, thicker continental crust collides. However, collisional deformation does not significantly affect both continental margins unless convergence persisted. The collision end when the slab detached and/or convergence cease.

This situation applies to the Carpathian belt, where most of the oceanic slab is detached, the lower plate terranes are juxtaposed in the upper plate orogenic wedge and display low grade metamorphism and low degree of deformation. The soft type of collision can also be referred to as "docking" where only soft lithologies are deformed during convergence, and when hard, buoyant, and thick crust enters the subduction zone, the convergence stops or is redirected elsewhere. This is the case for most orogens categorised as "soft-collisions" such as the Carpathians and the Apennines (Royden and Burchfiel, 1989; Van Staal and Zagorevski, 2020). However, convergence zone commonly initiates by a stage of subduction of oceanic crust and/or rifted margin before reaching a continent-continent hard type of collision. Therefore, the "hard" collision orogens might all initiate with a soft collision (Royden and Faccenna, 2018).

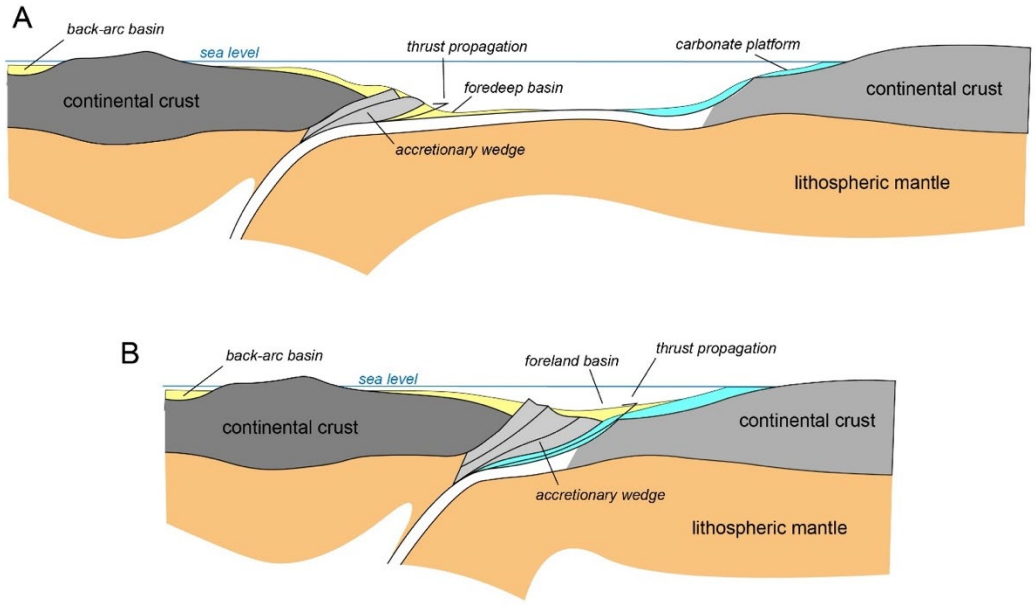

Figure I.3: Sketch showing accretion and soft-collision sketch. A: Accretion period for an accretionary wedge in a Continent-Ocean subduction zone;, sediments are scraped-off from the ocean floor and accreted to the wedge. B: When the rifted margin of a continent on the downgoing plate reaches the subduction zone, soft-collision in a Continent-Ocean subduction zone, time-evolution of A sketchstarts. The collision puts the upper plate terranes on top of the thinned continental crust of the lower plate craton and incorporates the terranes of the lower plate in the wedge by thrust propagation. As the deformation is migrates to the lower plate domain, the collision initiates (as inModified from van Staal and Zagorevski, 2020).

1.3 Pro-foreland architecture and characteristics in elastic flexure model paradigm

The term foreland basin refers to the depression that generally stretches out alongside a mountain belt and has the capacity to accumulate sediments. Foreland formation initiates where the lithosphere flexes downward in response to passive or active forces applied on the lithosphere during convergence. Flexural foreland basins are supplied with sediment from both margins and display specific characteristics depending on the depozone. In a foreland basin system, four types of depozones are identified (according to Beaumont, 1981; DeCelles and Giles, 1996; DeCelles, 2012):

The *wedge-top depozone* (Figure I.4) is located on the wedge toward the thrust front. This depozone can comprise thrust-top deposits or the foredeep sediments lying on top of the frontal thrust. Wedge-top sediments will generally be deposited unconformably on top of the underlying sedimentary succession of the wedge. Their proximal location within the wedge typically leads to coarse-grained, deformed and poorly consolidated sediments with multiple unconformities.

The next zone toward the stable foreland is the *foredeep zone* (Figure I.4). Accretionary system has a foredeep basin that is progressively integrated to the wedge if deformation propagates outward. This zone is situated outboard of the frontal thrust and inboard of the bulge that may form during the flexure of the lower plate. Foredeep sedimentation occurs generally in a deeper and/or more rapidly subsiding environment than in the other depozones. The depth of the zone depends on the topographic load of the wedge, the flexural rigidity of the downgoing plate and the mantle downward forces. These characteristics and forces can change as the foreland develops, which means that the deflection of the foredeep depozone may change over time. The foredeep sedimentation records the filling of the basin, resulting in the transition from a deep marine (flysch), to a shallow marine or fluvial (molasse) environment which may involve axial sediment transport (Sinclair, 1997). Sub-aerial basins are characterized by large fluvial systems migrating to the transition from the foredeep and the forebulge; the drainage basin of the fluvial system is usually limited by the bulge top (Garcia-Castellanos et al., 2003).

The *forebulge depozone* (Figure I.4) is on top of the flexural forebulge when it exists. This zone can be preserved in the stratigraphy or totally eroded over time by the foreland drainage system. The zone usually has a low topography and shallow water terrestrial deposits comprising condensed layers and eroded surfaces. Outward of the bulge zone, on the stable foreland, a shallow and broad depression, generated by a second but much shallower trough in the flexural profile, is the last depozone of the foreland system. The *back-bulge* (Figure I.4) is often referred to as a secondary basin with sediment

potentially coming from the bulge or the forebulge or the craton area, and deposited in a calm environment. The back-bulge depozone is usually as extended as the foredeep but much shallower.

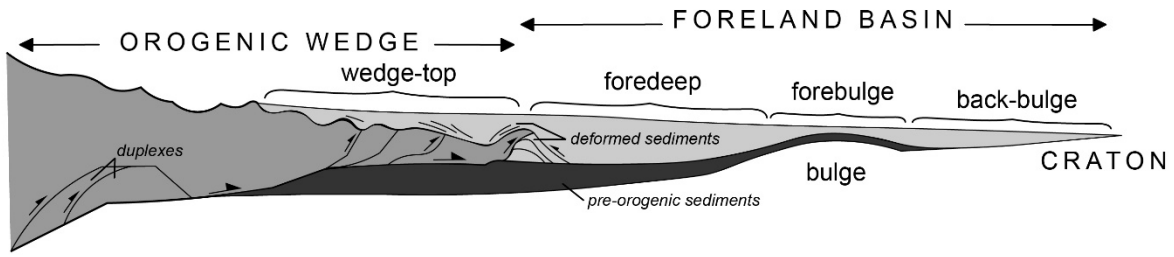

Figure I.4: Sketch of a foreland basin system according to an elastic flexure paradigm. Modified after DeCelles and Giles 1996; their figure 1.

Migration of the wedge and foreland system over time implies a stacking of the depozones in the foreland stratigraphy (Sinclair, 1997; 2012). Continuous convergence of both margins changes the location of the depozones over time. The downgoing lithosphere is also bound to increase in thickness and change from oceanic to continental lithosphere (a mix of both within an extended margin context) toward the stable foreland and the flexural profile of the foreland basin will enlarge, modifying depozone boundaries. According to the elastic flexure model (Decelles and Giles, 1996), outward migration due to propagation of thrusting should be recorded in the sediment column starting by a back bulge type of sedimentation, with calm- and shallow-environment deposits, to a forebulge, then thick foredeep flysch- or molasse-type sediments and finally typical coarse and deformed wedge-top sediments containing multiple unconformities. The foreland stratigraphy can thus record the development of the convergence zone and the migration of the bulge, allowing for a reconstruction of the orogenic wedge dynamic (Stockmal and Beaumont, 1986; Flemings and Jordan, 1989; Waschbusch and Royden, 1992a; Sinclair, 1997).

1.4 Pro-foreland basin formation with dynamic topography.

The downward motion of cold material in the earth mantle provokes a dynamic subsidence affecting the upper plates. Conversely, mantle upwelling at the base of the lithosphere creates dynamic uplift. The expression of topography is affected by these dynamic uplift and subsidence and by dynamic topography, especially in subduction zones (Zhong and Gurnis, 1995). The viscous coupling of the mantle and the plunging slab imply a downward flexure of the lithosphere. Therefore, foreland formation and development are impacted by a dynamic topography evolving during convergence and collision in orogens (Gurnis, 1992; Catuneanu et al., 1997; Burgess and Moresi, 1999). Some theorical experiments on the expression of dynamic topography in retreating subduction zones show the dynamic flexure of the foreland plate and formation of a viscous bulge on both side of the retreating trench (Husson et al., 2012; Figure I.5).

Examples of retro-arc foreland basins influenced in their architecture and shifting of depocenters due to dynamic topography are common in the North and South American regions (Painter and Carrapa, 2013; Liu et al., 2014; Flament et al., 2015). Using the stratigraphy and architecture of the foreland basin, a shift of depocenters is observed away from the deformation front (Painter and Carrapa, 2013; Liu et al., 2011, 2014). It is shown that the shift of sediment depocenter is due to the dynamic topography

of the subducting slab during its detachment/decoupling from the foreland plate lithosphere. The change of dip creates a dynamic subsidence over several hundred kilometres in the West Interior Basin in North America. The same pattern of sediment depocenter shift is observed in Chaco retro-arc basin in South America (Flament et al., 2015).

In pro-foreland basin, the dynamic topography due to a slab panel sinking affected the Ganges basin in the Himalaya. The continental collision advanced past the subducting slab, which reversed and detached, affecting the Indian plate and increasing subsidence and uplift (Husson et al., 2014).

In the Mediterranean region, influence of dynamic topography in the small-scale short-lived subduction zone is observed for the actives orogens (Husson, 2006; Faccenna and Becker, 2020). The dynamic topography is observed in retreating subduction zones such as the Apennines (Faccenna et al., 2014; Faccenna and Becker, 2020) and Hellenides arcs (Guillaume et al., 2009).

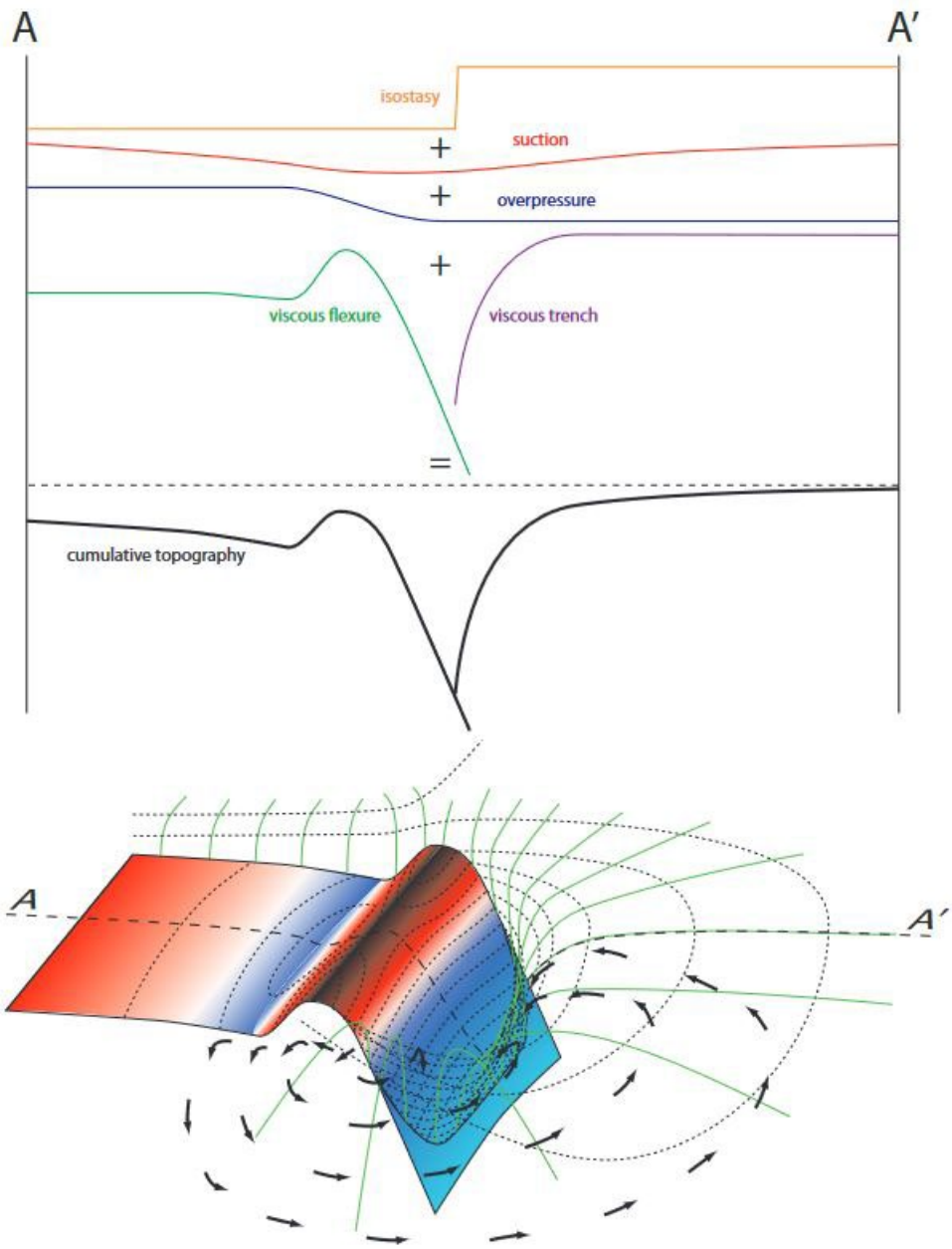

Figure I.5: Synthetic 3D sketch of the topography around a subduction zone (bottom) in the experiments (not to scale). Black dotted lines are isodepths curves, green curves follow the local maximum topographic gradients. Black arrows denote the flow pattern from below the slab on the foreside to above the slab on the backside. Top graph shows the isolated contributors along the central cross-section AA′: isostasy curve depict the isostatic component affecting topography; suction curve refer to the downgoing vertical slab motion affecting topography; overpressure curve refer to the vertical motion of the viscous material being compressed and extend in the foreside and backside of the retreating trench; viscous flexure and viscous trench curves are the purely viscous vertical motion across the trench (experiment in a purely viscous model).

1.5 Foreland system in retreating subduction zones

The retreat of the subduction zone implies a density driven slab sinking faster than the convergence of the plates (Royden, 1993). When the roll back of the subducting slab is faster than the convergence rate, the system compensates the difference by extension in the upper plate (Royden, 1993). This upper plate extension often occurs behind the collision/accretion front, and is accompanied by lithospheric thinning, normal faulting and advection of heat during asthenosphere upwelling.

Foreland fold and thrust belts in retreating subduction zones are typically narrow orogens with a low topography, being arcuate at both hinges (Royden, 1993; Doglioni et al., 1999). In this setting, the foredeep often records higher subsidence rates confined close to the deformation front than is expected from the topographic load due to the large slab pull flexing the downgoing plate (Royden, Karner, 1984). The forebulge often presents a carbonate shelf, and the back-bulge depozone is poorly developed in this setting (Sinclair, 1997; DeCelles, 2012).

In the case of the Carpathians, it has been long observed that the flexure of the foreland is not a result of flexural loading only and requires a dynamic subsidence of the foreland plate (Royden, 1993; Artyushkov et al., 1996). In retreating subduction zones, the foreland architecture is modified by the slab pull over time (Waschbusch and Royden, 1992b; Royden, 1993; Leever et al., 2006b; Sinclair and Naylor, 2012). When roll-back terminates, the slab breaks off in panels or through a slab tear that migrates laterally, increasing the slab pull effect over a smaller surface over time (Wortel and Spakman, 2000; Konečny et al., 2002; Tărăpoancă et al., 2004). The topography difference in the SE Carpathian region between the elevation of the Transylvanian basin and the foredeep basin is explain by current dynamic topography due to the steep slab remnant hanging under the region (Şengül-Uluocak et al., 2019).

1.6 Recycling of foreland sediments in foreland fold-and-thrust belt systems

In a convergent system, sediments are bound to be recycled in a succession of cyclic erosion-deposition-accretion events (Covey, 1986). The accretion phase brings the sediment into a prism or a wedge growing as the influx of sediments continues. After their accretion, sediments follow a curved particle path, the kinematics and curvature of which depending mainly on the internal dynamics of the wedge, the locus of erosion, fault propagation and the wedge basal friction (Konstantinovskaia and Malavieille, 2005). However, starting from an horizontal path of particle during accretion, a continuous increase of vertical exhumation is observed for particle paths in accretionary wedge (Konstantinovskaia and Malavieille, 2005). Sediments that are accreted later are bound to exhume through more vertical particle paths. Erosion balances the continual growth of the accretionary system, bringing the sediment particles out of the accretionary prism, once dynamic equilibrium is reached. Surface erosion is the most efficient process balancing topographic growth in natural examples of aerial wedges (Beaumont et al., 1994; Naylor and Sinclair, 2007). Eroded from the surface, sediments flow down the mountain bemts, radially, to fluvial or turbiditic axial drainage, ultimately being deposited in the pro-foreland basins (Figure I.6), or even exiting the system towards another sediment sink. Crustal material of the downgoing plate can enter the subduction channel and be brought deep into the earth (Vanucchi 2009). Reversely, crustal fragment

of the downgoing plate can be abraded by the wedge and accreted at the foot of the accretionary prism (Hilde, 1983). Crustal material of the upper plate can also be affected by tectonic abrasion at the base of the prism. The resulting materiel could enter the subduction channel or be underplated.

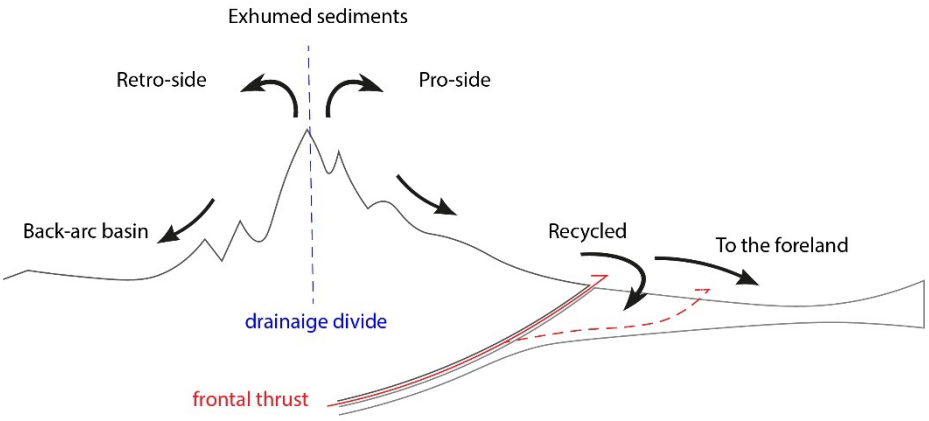

Figure I.6: sketch of the repartition of exhumed sediments from an accretionary wedge. From drainage divide (dashed blue line), sediments are provided to the pro or retro sides of the wedge. Sediments on the pro-side are ultimately deposited in the foreland, accretion can bring them into the subduction channel, underplate the sediment, or reintegrate it into the wedge as part of syn-orogenic sediments of a thrust sheet (recycled).

If preserved in the foredeep, sediment eroded from the wedge may be reintegrated into the accretionary system and repeat the particle pathway to the range's surface. Recycling occurs when the foreland sediments, eroded from the wedge, are reintegrated into the wedge by foreland accretion, due to forward propagation of the system (Figure I.6). This cycle may vary in duration depending on the particle path to the surface, the depozone, and the influx-outflux of the wedge, as well as the convergence rate. Short cycles would imply integration of young sediments at the toe of the wedge, with shallow burial and a quick path to surface along nearby faults, with erosion and deposition occurring in the vicinity of the accretion front. Such a short cycle can be observed in the cannibalism of molasse thrust sheets at the frontal thrust (Schlunegger 1997). Reversely, a long cycle would be characterised by a deep burial of the sediment, with a long path from the foot of the wedge and a long exhumation phase with low erosion rates and erosion with subsequent deposition in a distal part of the foreland basin (Covey, 1986). Sediment recycled in the belt can be eroded from the belt but transported to another basin or not being re-integrated afterward. The sediments exit the system, either by being underplated or subducted, or by being transported by the sediment system to another basin. This could either be the retro basin, or a down-dip basin not related to the orogenic wedge accretion front, e.g. from the Himalayas to the Indian Ocean, from the Carpathians to the Black Sea, or from the Alps to the North Sea.

In the following manuscript, the mention of foreland cannibalism or sediment recycling in the Carpathians system will refer to sediments eroded from the belt that resulted from the accretion of former foreland sediments.

1.7 Low-temperature thermochronology

1.7.1 Principle of thermochronology and low-temperature thermochronometers

Thermochronology groups different methods applied to specific minerals to constrain the time at which a rock cooled through a temperature called closure temperature (Tc) (Dodson, 1973). Tc is the temperature at which a given mineral matrix starts to trap the daughter element of a decaying radioactive isotope parent (or, in the case of fission tracks, preserve lattice damage). Thus, a thermochronological system (combination of a specific mineral and a specific parent-daughter pair) records, by daughter-product accumulation, the time that had passes since it cooled below the Tc to the present temperature. Conversely, the daughter product is removed (or the lattice damage annealed) as the mineral is heated above Tc.

Thermochronology techniques are used to constrain the time at which rocks crossed isotherms in the crust on their way to the surface (or subsurface). Closure temperatures vary between up to 900 °C for U/Pb in zircon and as low as 50 °C for (U-Th-Sm)/He in hematite (Ault et al., 2019). In this thesis, I will focus on four different low-temperature (LT) thermochronometers: apatite and zircon fission track (AFT and ZFT), and apatite and zircon (U-Th-Sm)/He (AHe and ZHe). These thermochronometers can resolve the thermal history of rocks over ~10 km of crust (ZFT Tc ≈ 200-250°C) and resolve cooling and exhumation down to ~2 km (AHe Tc ≈ 40-90°C).

1.7.2 Fission-track thermochronology

The AFT and ZFT thermochronometers have nominal Tc in the range of 100-130°C and 200-250 °C respectively (Ault et al., 2019). This method uses the spontaneous fission of ^{238}U creating damage zones (fission tracks) in a mineral lattice, which are visible under an optical microscope. To constrain the AFT or ZFT age of a sample using the external detector method (Hurford and Green, 1982), a mount of apatite or zircon grains covered with a mica detector is irradiated with a known neutron flux in a nuclear reactor to induce fission of ^{235}U in the grains. Induced tracks are present in both the grains and the detector, but spontaneous tracks are only present in the grains. Since tracks are only visible after etching, by etching the grains before irradiation and the detector after irradiation, the number of spontaneous and induced tracks in each grain can be separated. After irradiation, the detector is detached from the grains and placed next to them as a mirror image. The number of tracks both in the grain and the detector are counted under the microscope, on a given square area. From the obtained number of induced (Ni) and spontaneous (Ns) tracks, after calculation of different factors inherent to the irradiation (in particular the neutron dose; monitored with a dosimeter glass) and the human error while counting, the age of the grain can be calculated. Other parameters are measured during AFT analysis: the etch-pit width of a track at the grain surface (Dpar) records the annealing kinetics, depending on the chemistry of apatite grains. Track-length measurements allow to obtain more information on the cooling path of the rock sample (Gleadow et al., 1986; Green et al., 1986; Gallagher, 2012).

AFT and ZFT only give meaningful ages if sufficient grains are dated. From a population of grain ages, a central age (CA) and several (or a unique) population peak(s) (P1-Pn) can be statistically identified (Galbraith and Green, 1990).

1.7.3 (U-Th)/He thermochronology

The AHe and ZHe thermochronometers are based on the α-decay of ^{235}U to ^{207}Pb and ^{238}U to ^{206}Pb, as well as ^{232}Th to ^{208}Pb and ^{147}Sm to ^{143}Nd. All these decay chains produce α particles or ^{4}He atoms, the diffusion of which in the mineral lattice is temperature dependent. At high temperatures (above Tc) the diffusion of ^{4}He is sufficiently rapid for the atoms to escape from the crystal lattice, whereas at lower temperatures they are effectively trapped. The Tc for AHe ranges from 40-100°C and for ZHe it ranges from potentially as low as 30°C to 250°C (Ault et al., 2019). The Tc interval depends on the grain size and shape, as well as on the amount of accumulated α damage in the apatite or zircon grains, which itself depends on the U, Th and Sm concentration and the thermal history of the sample (e.g., Flowers et al., 2009; Gautheron et al., 2009; Guenthner et al., 2013).

For this method, ^{4}He is extracted from the grain by laser heating in a vacuum, the gas is mixed with purified ^{3}He and analysed with a noble-gas mass spectrometer (Farley et al., 1996). The U, Th and Sm content is subsequently measured by inductively coupled plasma mass spectrometry (ICP-MS). This method requires pristine grains, with no inclusions (especially for apatite; in zircons, inclusions are tolerated if they are small and do not touch the surface of the grain) or fractures (Flowers et al., 2023). The shape and size of the grain impact the ejection of ^{4}He particles upon their production and must be corrected in the final age calculation (Farley et al., 1996; Ketcham et al., 2011). The α-damage heritage (damage in the matrix) also perturbs the age measured for apatite by enhancing α-particle diffusion (Flowers et al., 2009; Gautheron et al., 2009).

1.7.4 Application of LT thermochronology to detrital samples

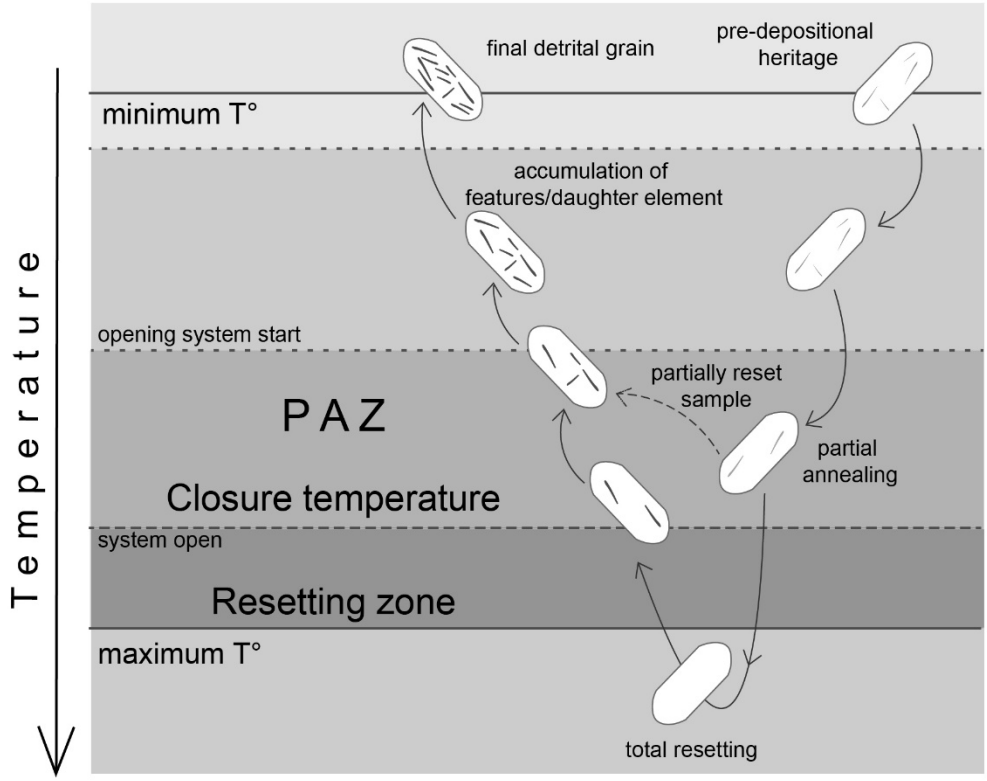

Figure I.7: Principle of detrital thermochronology. PAZ: partial annealing zone for fission-track thermochronometers; the equivalent for (U-Th-Sm)/He thermochronometers is known as PRZ (partial retention zone). The resetting zone occurs at temperatures above the Tc as the annealing of the pre-burial inherited tracks is dependent on the source and the time spent at higher temperature. This implies that grains with older pre-burial age will, in general, need to reach higher temperatures or spent more time at the Tc to fully reset.

LT thermochronology is widely used in geology and geomorphology. With this method the exhumation of mountain belts, valley incision, fault zone activity or basin infill can be constrained over time. An efficient way to constrain variations of erosion in time and space is to model the exhumation (as defined by England and Molnard, 1990) rates of a region and link it with its increase or decrease in topography to isolate the erosion rates.

In this thesis, I obtained LT thermochronology ages (ZHe, AFT and AHe) to unravel the exhumation and preceding sedimentary and/or tectonic burial of the different nappes of the Ukrainian Carpathians (Part II). I also used thermochronology data in regional inversions to constrain the variation in exhumation rates over time along the Carpathian fold and thrust belt (Part III). As a result, eroded sediment volumes can be quantified and compared to deposited sediment volumes in the foreland basin at the same period (Part V).

Since all data were collected in sedimentary units, it is important to explain the specificity of detrital thermochronology performed during my work and how we interpreted the results regarding the accretion-exhumation history of the Carpathians. To understand a thermochronologic age of a detrital sample, we have to compare the stratigraphic ages of these detrital samples to their thermochronometer

ages. If the thermochronologic age is younger than the stratigraphic age, the thermochronometer is said to be reset, i.e., the thermochronometer age records the last phase of cooling of the rock sample after deposition and burial (Figure I.7). A reset age also implies that the burial of the detrital sample was sufficient to reach the closure temperature (Tc) of the considered thermochronometer. In contrast, detrital samples with thermochronologic ages older than the stratigraphic age are non-reset; i.e., the sample did not reach Tc during post-depositional burial. These non-reset ages can be interpreted as recording the last phase of cooling of the source region of the sedimentary rock before its deposition (see Chapter II, section 6.4). Detrital thermochronologic ages can also be partially reset; i.e., the thermochronometer age is close to the stratigraphic age of the samples (Figure I.7). In this case, the sample records both pre- and post-depositional cooling and its thermochronologic age may not have a direct geologic significance.

For AFT and ZFT thermochronometers performed on detrital samples, the population peaks can have a large variety of ages depending on the sources of the sediment. The variation of sources in a detrital sample can imply a variation in the mineral chemistry and inherited fission tracks from the last cooling phase. The resulting CA (and related 2σ error) of the sample can fall in the partially reset samples as the variety of grains usually give several population peaks. To avoid misleading CA given by largely variable grain population, the minimum age of a sample can be use (Galbraith and Laslett, 1993; Vermeesch, 2019) as a significant age to date last exhumation event for fission-track thermochronology.

For (U-Th)/He in detrital apatite and zircon, the shape and size of the grains are the main limitations for finding good aliquots for measurement. Moreover, the eU (effective Uranium; amount of parent elements in the mineral decaying with ^{4}He ejection) of a grain depends on the source rock and varies from grain to grain in a detrital sample (Peyton and Carrapa, 2013). Because of this, (U-Th)/He single-grain ages in sedimentary rocks can be significantly dispersed in the same sample (see Part II).

1.7.5 Thermochronological age patterns in orogenic belts

In numerical models, a doubly vergent wedge can reach a state of equilibrium, where the influx of material is balanced by the eroded material. This flux steady state (as defined in Willett and Brandon, 2002) will be reached by the orogenic system after a specific response time, to tectonic or climatic changes. Different types of steady state can be defined, such as flux steady state (a balance between accreted and eroded material), or topographic steady state (a steady topographic elevation of the wedge despite active deformation). We will here discuss the notions of “thermal steady state” and “exhumation steady state” as presented in Willett and Brandon (2002).

It is important to specify that, while speaking of a wedge being in steady state, the time scale of observations can change the characterisation of the state. The adaptation of a wedge to a change is time -dependent. Thus, the characterisation of the state depends on the archive used to decipher the state of the wedge. The archive use that can be sensitive to a change within a quicker time laps than the response time needed for the orogenic system to reach steady state. Or conversely the archive use to characterize the change in the orogenic system need a long response-time to reach the steady state. A second point highlighted by Willett and Brandon (2002) is that, even in a case where steady state is not reached, the "maturity" of the system can be deduced from the degree to which it has approached steady state.

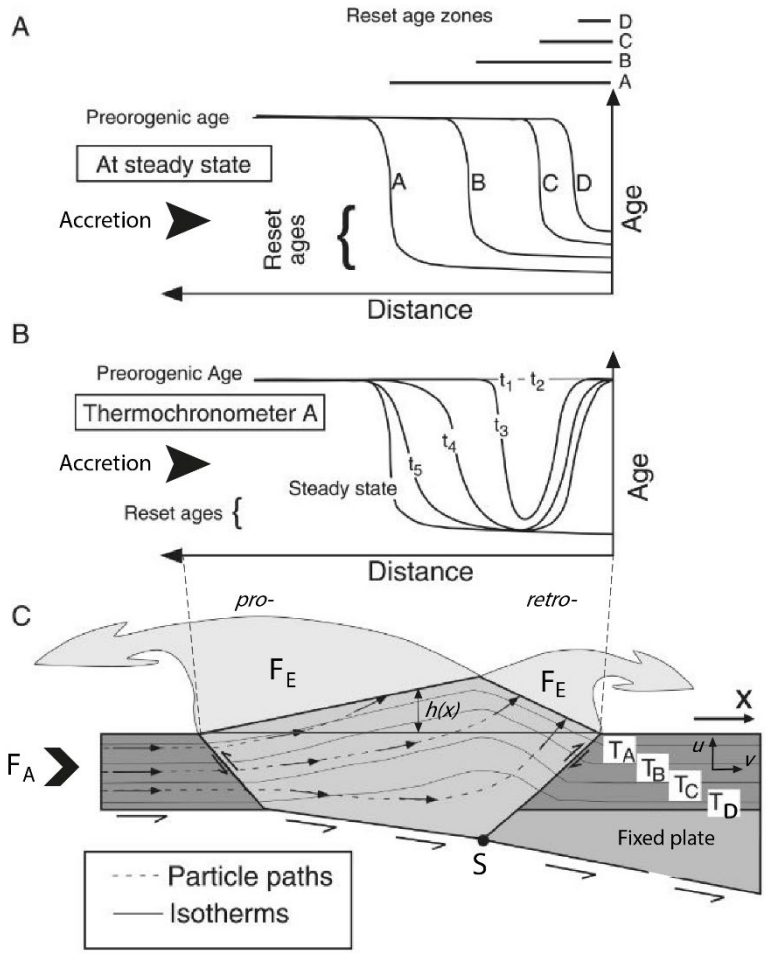

Figure I.8: A) Thermochronometers ages pattern on at the surface of a doubly vergent wedge, zones of resetting are attached to the retro-wedge side. B) Temporal evolution of the pattern of thermochronometer A ages, assuming a constant pre-orogenic age. Maturity of the wedge occurs when the a steady-state age pattern of aeis reach ed. C) Sketch of an orogenic doubly -vergent wedge. FA and FE refer to the accretionary flux of material, and the eroded flux of material respectively. Modified after Willet and Brandon (2002).

According to the evolution of accretionary systems, thermal and exhumation steady state are interdependent. Thermal steady state is reached when the thermal structure inside the wedge (which is affected by material advection and heat diffusion) is constant in time. Exhumation steady state is reached when thermochronometer ages of rocks at the surface reach time invariance. Exhumation steady state

requires topographic steady state as well as a thermal steady state; topographic steady state itself requires a balance of rock uplift, horizontal advection and erosion. Topographic steady state is often observable at the local scale (e.g., a drainage basin) but is harder to evaluate over an entire orogen. As both thermal and exhumation steady state are evaluated with thermochronology, assumption of a constant (steady) topography or accretion is often made to study an accretionary wedge.

Thermochronometers can be used independently to analyse the degree of maturity of the wedge as they are bound to reset their ages at different times, depending on their closure temperature (T_c). As shown in Figure I.8, the thermochronometers can reset their age from a pre-orogenic age from the retro-wedge to the accretionary front. In Figure I.8 B, the example for the thermochronometer A with the pattern of age on the surface of the wedge at different time period (t_n) display the pattern of a progressive reset of the age as the wedge grows in time. Evolution of the pattern is linked to the "maturity" of the wedge. Associating different thermochronometers, this can indicate the degree at which the wedge has approached exhumation steady state.

This pattern was demonstrated as relevant for both singly vergent and doubly vergent wedges to investigate the steadiness of orogenic wedges. In wedges with ongoing accretion the nested pattern of thermocrhonology ages younging toward the back thrust (or retro-shear zone) is observed for the Southern Alps (New Zealand) and display lateral variation in accretion of the orogen (Batt and Braun, 1999). The pattern is also observed in Taiwan, and when not, is used to understand the thermal adjustment and exhumation of the wedge, visible in the thermochronology ages (Beyssac et al., 2007). On the contrary, when the pattern is not observed in wedges, the kinematics of exhumation need to be investigated. In the Apennines, the lateral variation of the belt exhumation rates and erosion rates shows the inactive north-west side of the orogen correlates with vertical advection of material and variable erosion rates in the retro- and pro-side of the orogen (Thomson et al., 2010; Erlanger et al., 2022). The East side of the orogen display a nested pattern of thermochronology ages. The age-elevation correlation profile of the East Apennines displays an "orogenic wave" behaviour, where the exhumation rate derived from the thermochronology age displays the sab retreat and therefore, the "advancement" of the nested pattern toward the slab (Thomson et al., 2010).

2 Geological setting of the Carpathian Belt

The Carpathian Mountain belt extends from the Czech Republic, Poland and Slovakia at its Western end to SW Ukraine and Romania in the East and South-east. We are mainly interested in the thin-skinned Outer Carpathian flysch belt, which stretches out along the Western, Eastern and South-eastern Carpathians (see Introduction Figure 0.2). The Southern Carpathians have a different geology, exposing mostly crystalline rocks, (Schmid et al., 1998; Fügenschuh and Schmid, 2005; Moser et al., 2005). The Southern Carpathians play a major role in the variation of the environment of the Paratethys (Leever et al., 2011), but do not participate in the evolution of the foreland fold and thrust belt area we studied in this work. The Southern and South-eastern Carpathians are separated by the Intra-Moesian fault that separates the Moesian Platform from the Dobrogea Mountains. The South-eastern and Eastern Carpathians are delimited by the Trotus fault (Figure I.10). There seems to be no well-defined limit between the Western and Eastern Carpathians.

Hereafter, I describe the tectonic construction of the Carpathians and the stratigraphic evolution of the flysch belt across its different parts and explain their lateral correlation. The pre-orogenic structures influencing the foreland formation and the European slab dynamics are explained thereafter.

2.1 Paleogeography

2.1.1 Tethyan realm

Opening of the Alpine Tethys and transition to the Neotethys in the Alpine realm took place in the Late Jurassic (~150 Ma) and several oceanic digitations were opened, including the Piedmont-Liguria Ocean, Vardar Ocean and Ceahlau-Severin Ocean, bounding different micro-plates: 1) the AlCaPa (Alpine-Carpathians-Pannonian plate) was separated by the Piedmont-Liguria Ocean from the European margin to the north and attached to the Adriatic plate (Figure I.9). 2) The Tisza plate was separated from AlCaPa by the west Vardar Ocean and from Dacia by the East Vardar Ocean (Figure I.9). 3) The Dacia plate was separated from the European margin in the N and E by the Ceahlau-Severin Ocean. The NE end of the Piedmont-Liguria Ocean was a large embayment (the Carpathians embayment); a deep marine domain situated on oceanic to thinned continental crust with sedimentation starting from the Early Cretaceous (Figure I.9; Handy et al., 2015; Le Breton et al., 2021).

By the Santonian (~84 Ma), AlCaPa had moved northward with the Adriatic plate (Figure I.9). The Tisza and Dacia plates collided and closed the Vardar Ocean and the Ceahlau-Severin Ocean, accreting Vardar-derived and Ceahlau-Severin-derived sedimentary units onto both plates (Sandulescu, 1975). According to the reconstruction of Handy et al. (2015), a dextral transfer zone separated the AlCaPa and Tisza-Dacia plates (Figure I.9). From this period on, the Tisza-Dacia unit was moving into the Carpathian embayment by dextral strike-slip movement along the Timok and Cerna-Jiu faults (Figure I.10), which accommodated the clockwise rotation of both blocks (Ustaszewski et al., 2008b; Figure I.10).

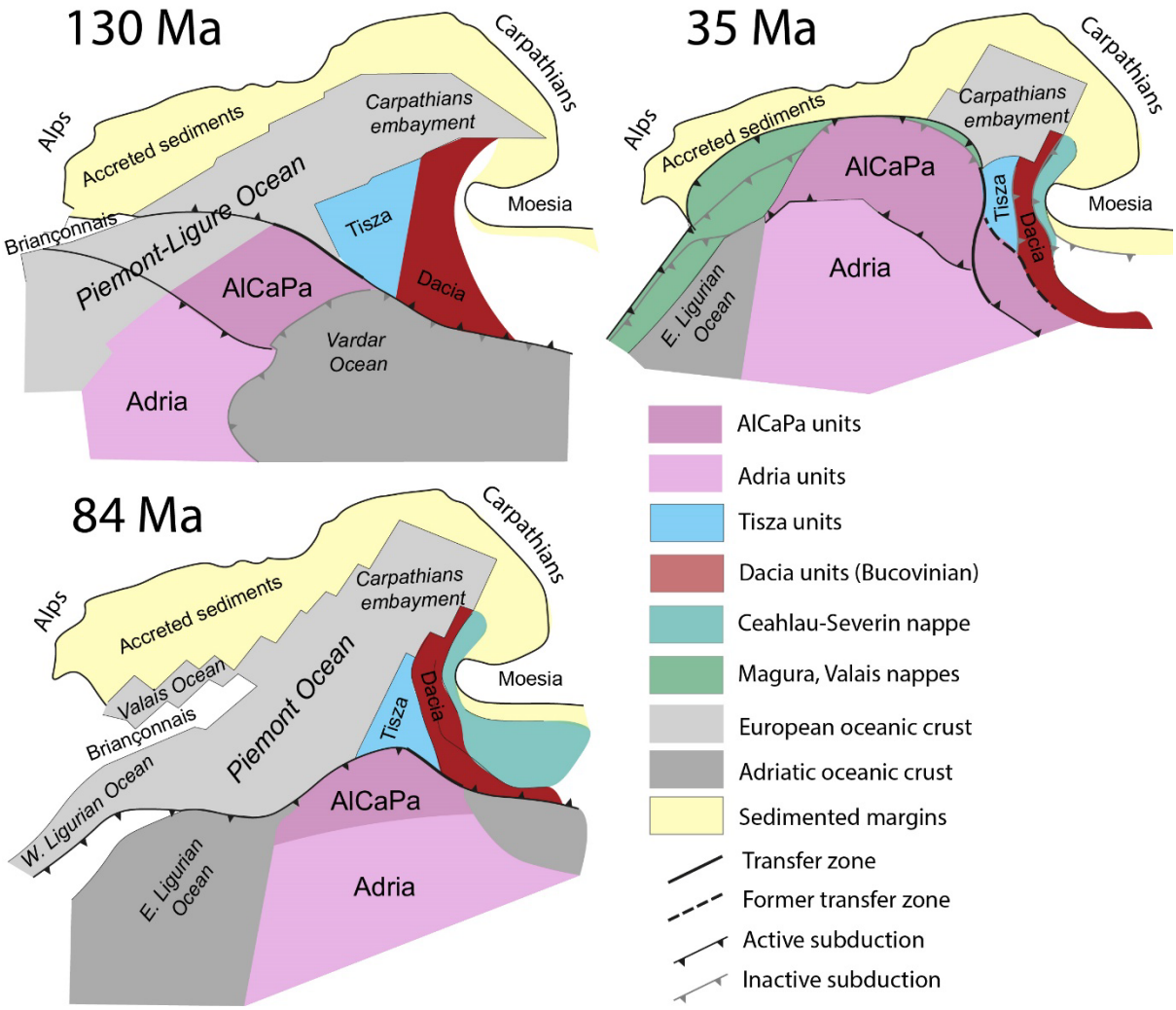

Figure I.9: Situation of the Adriatic plates in the Carpathians embayment at 130 Ma (after Le Breton et al., 2021), 84 Ma and 35 Ma (after Handy et al. (2015)).

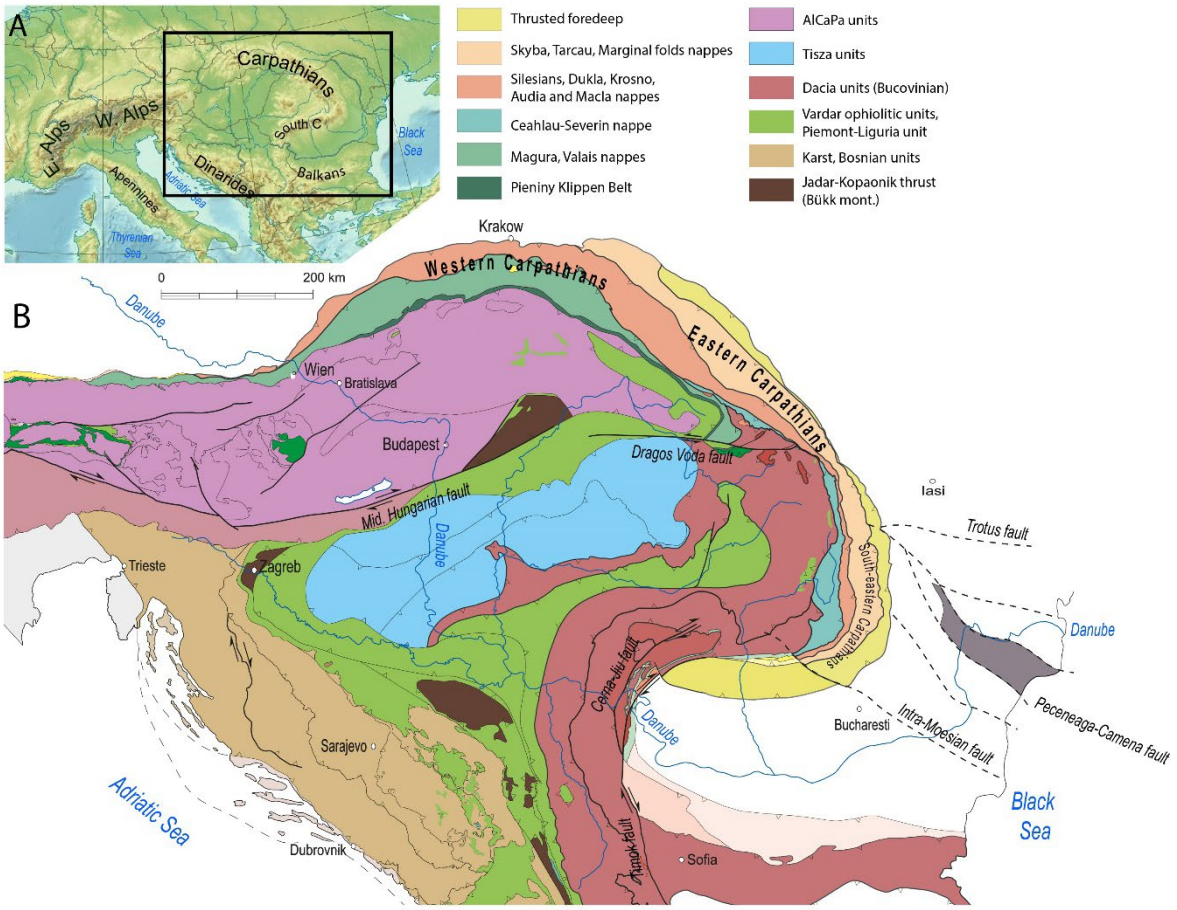

Figure I.10: A) Location of the Carpathians in Europe. B) Geological simplified map of the Carpathians-Pannonian-Dinarides region showing different domains and tectonic units. Modified after Schmid et al. (2008).

2.1.2 Migration in the Carpathian embayment

At the end of Eocene and beginning of Oligocene (~34 Ma), the tectonics of the Alpine realm changed: Alpine collision started in the Eastern Alps, leading to slab break-off and decoupling of the Adria and AlCaPa plates (Figure I.10; Sperner et al., 2002; Schmid et al., 2008). AlCaPa was pushed eastward by lateral extrusion of Adria and simultaneously pulled in a NE-ward direction by roll-back of the European slab (Figure I.9 and 10). According to Sperner et al. (2002); AlCaPa was rotating counter-clock-wise with transtensional sinistral structures oriented NNE-SSW during its migration into the Carpathians embayment in Late Oligocene. This led to a first pulse of extension along the northern rim of the future Pannonian Basin and compression along sinistral strike-slip faults along the Pieniny-Klippen belt (Figure I.10). The latter consists of AlCaPa derived sediments that were uplifted at this period (Kral, 1983). Rotation of AlCaPa was also enhanced by its collision with the Tisza-Dacia block in the east (Ustaszewski et al., 2008). As a result of these events, extension thus started in the AlCaPa plate and the European slab separated into an Alpine slab and a Carpathian slab (Figure I.19). Rotation and extension were precursors to later large-scale extension in the Pannonian Basin and created the

Paleogene basins (Tari et al., 1993; Kováč, 2016) south of the High Tatra Mountains in Slovakia (Figure.0.2; Sperner et al., 2002; Introduction Figure 0.2).

2.1.3 The construction of the Carpathians and the opening of the Pannonian Basin

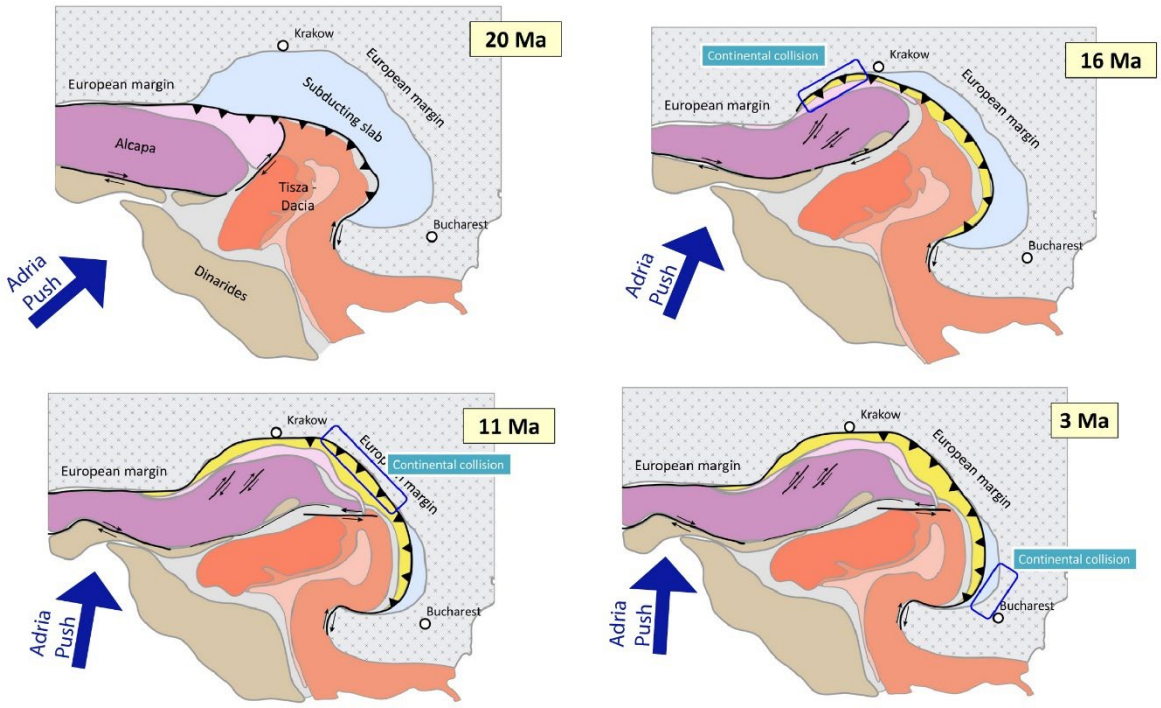

Figure I.11: Miocene to Pliocene motion of AlCaPa Tisza-Dacia plate into the Carpathians embayment. After Csontos, 1995.

Most of the contraction in the Western Carpathians was oblique to the East-European Margin (Schmid et al., 2008). However, most of the strike-slip deformation of the Carpathian flysch belt was concentrated in the western and central parts of the Pieniny-Klippen belt (Ratschbacher et al., 1993; Sperner et al., 2002; Ustaszewski et al., 2008; Castelluccio et al., 2016). ENE motion of the AlCaPa block was accommodated by the Mid-Hungarian Fault zone, a large sinistral strike-slip fault under the Pannonian Basin that forms the boundary between the AlCaPa and Tisza-Dacia blocks (Figure I.11). Handy et al. (2015) suggested that this fault zone contributed to asthenospheric upwelling lateral shift and thermal lithospheric thinning under the Pannonian Basin at ~20 Ma (Sclater 1980), which induced calc-alkaline magmatism dated at 22-8 Ma (Seghedi and Downes, 2011). The Mid-Hungarian Fault zone accommodated the differential eastward motion of AlCaPa and Tisza-Dacia blocks toward the embayment. The contraction in the Eastern Carpathians was more perpendicular to the East-European Margin; especially in the Ukrainian region. The Pieniny-Klippen belt and Magura-Valais units vanish in the north of the Eastern Carpathians and leave place to the Ceahlau-Severin (derived) units (Figure I.9). The basement units of Tisza-Dacia became involved in the collision with the East-European Margin in the vicinity of the present-day Ukrainian-Romanian border. Dacia-derived basement blocks are outcropping in the Maramureş Mountains and Rodna Horst region (Bucovinian units in Figure I.10; also see Figure 0.2 of the Introduction). Other E-W oriented strike-slip faults (e.g., Dragos-Voda fault,

Figure I.10) accommodated the Tisza-Dacia migration to the SE of the Carpathian embayment in later stages of convergence (~10 Ma; Figure I.10 and 11).

AlCaPa and the Western Carpathians have been inactive since 15 Ma (Mazzoli et al., 2010; Castelluccio et al., 2016) and, from this time on, collision was located in the Eastern Carpathians, where the Tisza-Dacia block continued moving eastward due to trench retreat and slab roll-back. This eastward movement was accompanied by Pannonian Basin extension and asthenospheric upwelling, which accommodated ~180 km of upper plate extension (Matenco and Bertotti, 2000; Schmid et al., 2008; Ustaszewski et al., 2008b; Balázs et al., 2016). There are no constraints on the timing of slab retreat and/or mantle flow acceleration under the Pannonian Basin, which means it is difficult to determine a cause-and-effect relation between the two phenomena. In any case, there was accelerated extension in the back arc after 15 Ma.

2.2 Stratigraphy of the Carpathians

2.2.1 Lateral correlation in the stratigraphy

The lateral correlation of the stratigraphy of the outer Carpathian belt, which we present here, is based on the work of Schmid et al. (2008), who reviewed the entire Carpathian-Pannonian-Dinaride system and related structural (co-)evolution. Based on the study of Schmid et al. (2008), the association of nappes described in the Carpathians, with similar paleogeography/accretion dynamics, are laterally correlated from west to east. In Figure I.10 the different nappes that were associated are shown in the map and in the legend, with the respective names from west to east.

2.2.2 The Pieniny Klippen Belt

The Pieniny Klippen Belt is a highly deformed melange of sediments that formed due to both sedimentary and tectonic events along the plate boundary of AlCaPa (Golonka et al., 2015, 2019, 2022).. Its composition and structure vary along the AlCaPa boundary. The Pieniny Klippen Belt is interpreted as a transfer zone, which allowed for the rotation and extension of AlCaPa during the Cretaceous and Paleogene (Ratschbacher et al., 1993; Nemcok and Nemcok, 1994; Sperner et al., 2002; Castelluccio et al., 2016). It also provided a backstop to the accretion of the early wedge of the Western Carpathian flysch belt. The Pieniny Klippen Belt vanishes in Ukraine; further to the east, the first accreted unit is the Ceahlau-Severin Nappe (Figure I.10), which played a similar role during rotation of the Tisza-Dacia plate into the embayment (Moser et al., 2005; Ustaszewski et al., 2008; Schmid et al., 2008).

Figure I.12: Stratigraphy of the Carpathian flysch belt derived from the stratigraphic columns of the state regional geological maps and the stratigraphy of Sandulescu, 1981; Oszczypko et al., 2005a; Oszczypko et al, 2006; Dziadzio et al., 2006; Merten et al., 2010. The scale of the left bar is in Time (Ma), whereas the scale of the stratigraphic columns is in thickness (m). The colour scale connects the stratigraphic columns to the time-scale on the left. Columns are aligned on the Eocene-Oligocene boundary. Sediments under the basal detachment line occur as massive blocks (olistoliths) in the overlying strata, or as slices of underplated sediments.

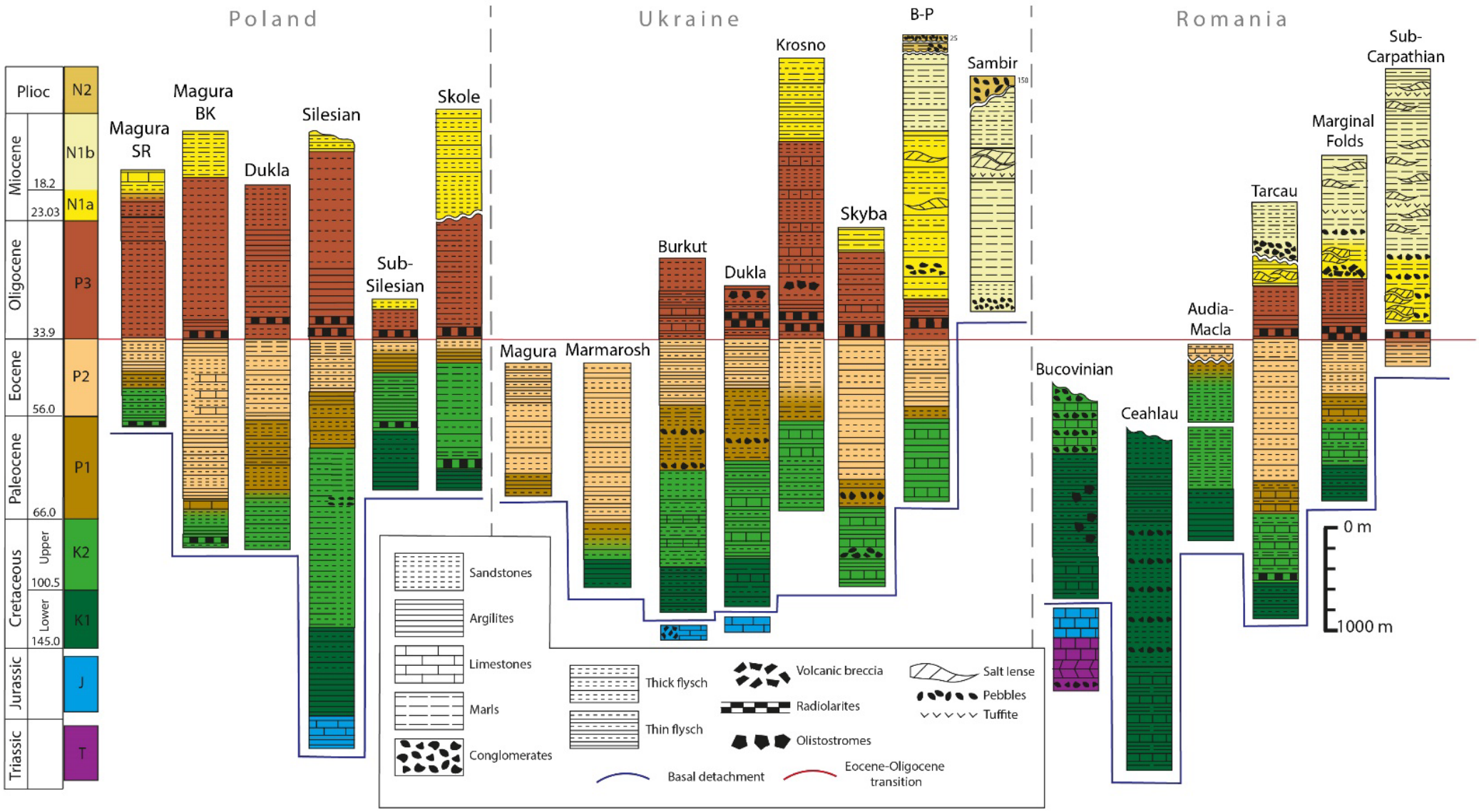
Poland
Ukraine
Romania
Plioc
N2
Miocene
N1b
18.2
N1a
23.03
Oligocene
P3
33.9
Eocene
P2
56.0
Paleocene
P1
66.0
Cretaceous
Upper
K2
100.5
Lower
K1
145.0
Jurassic
J
Triassic
T
Magura SR
Magura BK
Dukla
Silesian
Sub-Silesian
Skole
Magura
Marmarosh
Burkut
Dukla
Krosno
Skyba
B-P
Sambir
Bucovinian
Ceahlau
Audia-Macla
Tarcau
Marginal Folds
Sub-Carpathian
0 m
1000 m
Sandstones
Argilites
Limestones
Marls
Conglomerates
Thick flysch
Thin flysch
Volcanic breccia
Radiolarites
Olistostromes
Salt lense
Pebbles
Tuffite
Basal detachment
Eocene-Oligocene transition

2.2.3 The Western Carpathians

In the Western Carpathians, the Flysch belt can be divided into two domains, the Magura nappe and the Silesian nappe (Figure I.10). The stratigraphy of these two domains is different and they used to be separated by the Silesian Ridge, which ran through the Carpathian embayment, parallel to the east European margin and in the prolongation of the Bohemian massif (Oszczypko et al., 2006; Oszczypko and Oszczypko-Clowes, 2009; Kováč, 2016).

South of the ridge, the sediments of the Magura basin, which was linked to the Valais Ocean, were deposited on oceanic crust. The Magura Nappes regroup four units identified in the literature (Golonka and Picha, 2006; Oszczypko and Oszczypko-Clowes, 2009). Two stratigraphic logs are provided for the Magura Nappes in Figure I.12. The column labelled BK refers to the lithostratigraphy of Bistrica and Krynica subunits, The column labelled SR refers to Siary and Rača subunits of the Magura nappe. Both logs start with Late Cretaceous radiolarites and thin flysch deposits. In the Paleocene and Eocene, sediments evolve into thicker flysch with occurrences of calcareous beds in the external units of the basin. At the beginning of the Oligocene, the external units display the Menilites beds, organic-rich layers intercalated with siliceous layers and thin sandstones that accumulated across the Carpathian region and the Pannonian basin at this time. The interpretation of the depositional environment of this formation varies. In Poland, the organic matter is mainly from continental and/or lacustrine origin, but lateral variations of the sedimentary facies indicate environments with shallow marine and deltaic sedimentation (Dziadzio and Matyasik, 2021). During the rest of the Oligocene, thick sandstone beds were deposited in the Magura basin. In the early Miocene, deposition evolved into thinner flysch with calcareous layers and marls. Sedimentation ended in the Burdigalian (~18 Ma) for the Magura units. The logs show a difference in thickness between the internal and external units of the Magura Nappe; the Paleogene units of the latter being thicker with sandier sediments. This difference in thickness is interpreted to result from the more central position of the external units in the Magura Basin. The sandier facies is attributed to the proximity of the Silesian Ridge, a source of sediments for the Magura basin during the Paleogene as identified by paleocurrents in the deposits of the large sandstone fans of the external units (Oszczypko et al., 2006). The Dukla unit of the Western Carpathians was also located south of the Silesian Ridge, on its flank, and displays sand-rich sedimentation from the Late Cretaceous to middle Eocene, with some occurrences of argillite interbeds and marl layers. In the beginning of the Oligocene, the Menilite beds and a thick flysch series were deposited in this unit, a sedimentation pattern that remained until the late Oligocene (~28 Ma), which marked the end of sedimentation for this unit.

To the North of the Silesian Ridge, the next unit is the Silesian Nappe (Figure I.10 and I.12), which records sedimentation starting in the Jurassic with argillites and limestones. Early Cretaceous sediments evolved from argillites to thick flysch deposits and Late Cretaceous sediments are laterally varying from thick flysch to sandstones, with conglomerates and marls being deposited at the end of the Cretaceous. Thick flysch deposits and argillites or marls alternated in the Paleocene and Eocene of both units. As for the rest of the Silesian units, the early Oligocene begins with deposition of the Menilite Beds, followed by thick argillites and sandstones to the end of the Oligocene. The Sub-Silesian and Skole

Nappes have a similar stratigraphy, starting in the Early Cretaceous with argillites and evolving into siliceous layers in the Late Cretaceous, followed by deposition of thin flysch in the Sub-Silesian Nappe and thick flysch in the Skole Nappe. Both units are characterised by thin Paleocene and Eocene deposits, compared to the rest of the Carpathians. Argillites are followed by sandstone deposits during these epochs. In the beginning of the Oligocene, Menilites beds were deposited in both units and sedimentation continued with thick sandy flysch. Oligocene flysch and sandstones are tree times thicker in the Skole Nappe than in the Sub-Silesian Nappe. In the early Miocene, sandstones, and flysch from the Skole Nappe are thicker compared to the Sub-Silesian Nappe and in discordance with the underlying deposits. The observed difference in thickness in the external nappes of the Western region, from the Oligocene onward, is interpreted as resulting from syn-orogenic deposition, especially in the early Miocene, when the accretion and exhumation of the Inner Carpathians and the Magura Nappe had already started (Świerczewska and Tokarski, 1998; Oszczypko and Oszczypko-Clowes, 2009; Śmigielski et al., 2016; Kováč, 2016).

2.2.4 The Eastern Carpathians in Ukraine

The nappes from the Western and Eastern Carpathians can be correlated in the Ukrainian Eastern Carpathians: The Magura and Dukla nappes may be followed into this region from Poland and Slovakia and vanish further to the south-east, whereas some more external nappes come into being and then continue into the Romanian region.

The Magura Nappe (including the Marmarosh Domain, following Oszczypko et al., 2005) contains mostly Paleogene sediments, starting with thin-bedded Paleocene flysch, followed by an alternation of massive sandstone beds and thin-bedded flysch in the Eocene (Figure I.12). Sedimentation stopped at the Eocene-Oligocene boundary.

The Burkut and Dukla nappes display a very similar stratigraphy from the Lower Cretaceous to the Upper Eocene: Early Cretaceous sedimentation started with thin-bedded flysch and limestones as well as some breccia incorporating Jurassic limestones and volcanic rocks. These are followed by sandier deposits in the Upper Cretaceous. In the Paleocene, the sedimentation evolved into a sandy flysch with conglomerate intercalations, followed in the Eocene by thin-bedded flysch varying in thickness throughout the basin. Oligocene sedimentation started with argillites and limestones evolving into thick-bedded sandstones at the top of the Burkut Nappe. The youngest sediments of the Dukla Nappe consist of grey flysch with thick-bedded sandstones and radiolarites (known as the Menilites Beds), as well as olistostromes, all deposited in the Oligocene.

Sediments of the Krosno Nappe start with thick-bedded flysch in the Eocene. The siliceous Menilite Beds, mark the base of the Oligocene and are followed by grey argillites and siltstones. The Krosno Suite was deposited from the middle-Oligocene to the early Miocene, i.e. up to the regional Eggenburgian stage (~18.2 Ma). This particularly thick unit consists of 2 km of sandy flysch sequences with intercalations of olistostromes, argillites, siltstones, and some calcareous layers.

The following nappe in the pile is the Skyba Nappe (Figure I.12). It is composed of two depositional subunits, an internal unit resembling the Krosno Nappe in the Oligocene, and an external unit in

which Miocene sediments are missing. Sedimentation in both subunits started in the Late Cretaceous with a sequence of thin grey flysch and marl-limestone interbeds with conglomerate lenses. The overlying Paleogene sediments are divided into four suites, alternating between thick-bedded sandstones and thin-rhythmic flysch with conglomerate lenses at the base. These were followed in the Oligocene by the Menilites beds, which evolved into calcareous argillites, grey sandstones with black argillites, and thin sandstones with grey carbonaceous argillites for the internal units. This is topped by Miocene grey argillites with siltstone interbeds deposited until the end of the Eggenburgian (18.1 Ma) in the internal unit. For the external unit, Oligocene deposits, including the Menilites beds, are followed by marls and coarse layered batches of sandstones (Oszczypko, 2006).

Sedimentation in the Boryslav-Pokuttia unit began in the Late Cretaceous with argillites intercalated with limestones as well as with some conglomerate lenses (Figure I.12). In the Paleocene, thick sandstones were deposited, followed by an Eocene alternation between thin and thick-bedded flysch deposits. The Oligocene Menilites Beds are overlain by sandstones with calcareous siltstones. From the early Miocene to the end of the Eggenburgian, the Boryslav-Pokuttia Nappe accumulated siltstones and clays evolving into thin sandstones, with intercalations of clay. There are also some lenses of conglomerates. A thick layer of argillites and siltstone with lenses of salt was deposited on the nappe during the Ottnangian (18.1-17.2 Ma). After this time, sedimentation extended to the Sambir unit. While argillites with thin sandstone interbeds accumulated on the Boryslav-Pokuttia unit, conglomerates and sandstones were deposited on the Sambir unit (Andreyeva-Grigorovich et al., 2008). Sedimentation stopped at the end of the early Miocene in the Boryslav-Pokuttia unit, apart from several tens of meters of conglomerates thought to be Pliocene in age. Thick deposits of clay and marls evolving into tuffites and evaporites accumulated, on the other hand, in the Sambir unit during the Middle Miocene. Deposition continued to the end of the early Sarmatian (10.7 Ma) in that unit; the remaining Miocene deposits are syn-tectonic conglomerates dated around 9 Ma (Andreyeva-Grigorovich et al., 2008).

2.2.5 The Eastern and South-eastern Carpathians in Romania

The stratigraphy of the internal units in Romania is different from the rest of the Carpathians. The basement of the Bucovinian Nappes is overlain by Triassic and Jurassic sediments. The Lower Cretaceous of the Bucovinian nappes is composed of limestone with marl interbeds. The thin-skinned Transylvanian Nappes, which comprise more massive limestone facies, especially in the Tithonian and –the lower part of the Lower Cretaceous, were thrust eastwards onto Dacia during closure of the East Vardar Ocean at the end of the Early Cretaceous (Sandulescu, 1988; Krezsek and Bally, 2006). The thick skinned Bucovinian Nappes, derived from the basement of Dacia, were stacked approximately simultaneously. At this time Dacia was located west of Moesia (Figure I.9). The contact between the Bucovinian nappes and the overlying Transylvanian nappes is marked by the Aptian-Albian Wildflysch series containing olistostromes of Mesozoic sediments. The thrust is sealed by uppermost Albian to Cenomanian conglomerates.

The Ceahlau-Severin Nappe is composed of deep marine sediments of the former Ceahlau Ocean, a digitation of the Vardar Ocean that was located between Dacia and the Moesia platform (Figure I.9; (M. Sandulescu, 198875; Csontos et al., 1992; Krézsek and Bally, 2006; Schmid et al., 2008)). The

Ceahlau-Severin nappe was accreted to the east of the Bucovinian units. The Ceahlau-Severin nappe was accreted to the Bucovinian units and formed the early wedge in the Middle Cretaceous and further deformed during the migration of the Dacia block into the Carpathian embayment (Sandulescu, 1975; Moser et al., 2005) Sediments from this nappe are all from the Early Cretaceous and show marls intercalated with limestones at their base (Figure I.12). Sandstones and conglomerates follow, evolving into argillites and thin sandstones. The top of the Ceahlau-Severin Nappe is a thick horizon of sandy conglomerate, partially eroded.

The Audia-Macla Nappe consists of sediments that accumulated in the Carpathian embayment and displays Early Cretaceous argillites and flysch, evolving into sandstones with marl interbeds in the Late Cretaceous. A hiatus in sedimentation is observed (especially in the Macla unit of the nappe) in the Late Cretaceous. Sedimentation resumed with sandier sediments until the end of Paleocene. Eocene sediments, composed of sandy limestones, were deposited unconformably on top of this stratigraphy.

The Tarcau nappe is widespread in the Eastern and South-eastern Carpathians. Its stratigraphy begins in the Lower Cretaceous with thin flysch and continues into the Upper Cretaceous with siliceous beds followed by intercalated limestones and marls until the end of the Paleocene. Voluminous deposits of thick sandstones with argillite interbeds compose the early Eocene, and the facies change into sandstones and marls at the end of the Eocene. Similar to the other nappes of the Carpathian embayment, the Menilites Beds were deposited at the beginning of the Oligocene and followed by argilites and thick turbiditic sandstones known as the Kliwa and and Fusaru formations. The former were sourced from the craton located east of the basin, while the latter were sourced from the active margin of Dacia in the west (Roban et al., 2022). Early Miocene sediments of the Tarcau nappe are composed of argillites and evaporites, with middle-Miocene conglomerates and marly sandstones lying discordantly on top of the underlying stratigraphy.

The Marginal Folds Nappe displays a similar sedimentation history as the Tarcau Nappe, but strata are thinner, especially for the Upper Eocene, with sediments of this age consisting of marls and argillites. The Menilite beds are again present at the beginning of the Oligocene and followed by the Kliwa Sandstone. Early Miocene sedimentation started with volcanic breccia and conglomerates in the Marginal folds unit and evolved into evaporites and marls. Middle-Miocene deposits are in concordance with earlier deposits and display an alternation of conglomerates and tuffites with marls, and finally evaporites lenses.

The Sub-Carpathian Nappe is the most external nappe in the Romanian Eastern Carpathians. Eocene and Oligocene sediments are thin in this nappe and consist of marls and argillites, followed by the Menilites beds in the Oligocene. A hiatus occurs from the beginning of the Oligocene to the Early Miocene, when sedimentation resumed with thick evaporites or marls and conglomerates. Sedimentation continued into the late Miocene with thick marls intercalated with conglomerates at their base, followed by tuffites and evaporites. Toward the top of the nappe, the strata become thinner and consist of argillites and evaporites.

Late-Miocene sediments are only present in the Romanian south-east Carpathians, overlying the external nappes as wedge-top sediments, which are remarkably thick on top of the Subcarpathian nappe (Leever et al., 2006). Further north, late-Miocene wedge-top deposits are not present on the Tarcau and

Marginal Folds nappes; they may have never been deposited or have since been totally eroded. The late Miocene sediments display alternations of sandstones and marls, which accumulated in a shallow-water environment. These sediments are regarded as sediments from the former foredeep zone of the belt.

2.3 The East European margin

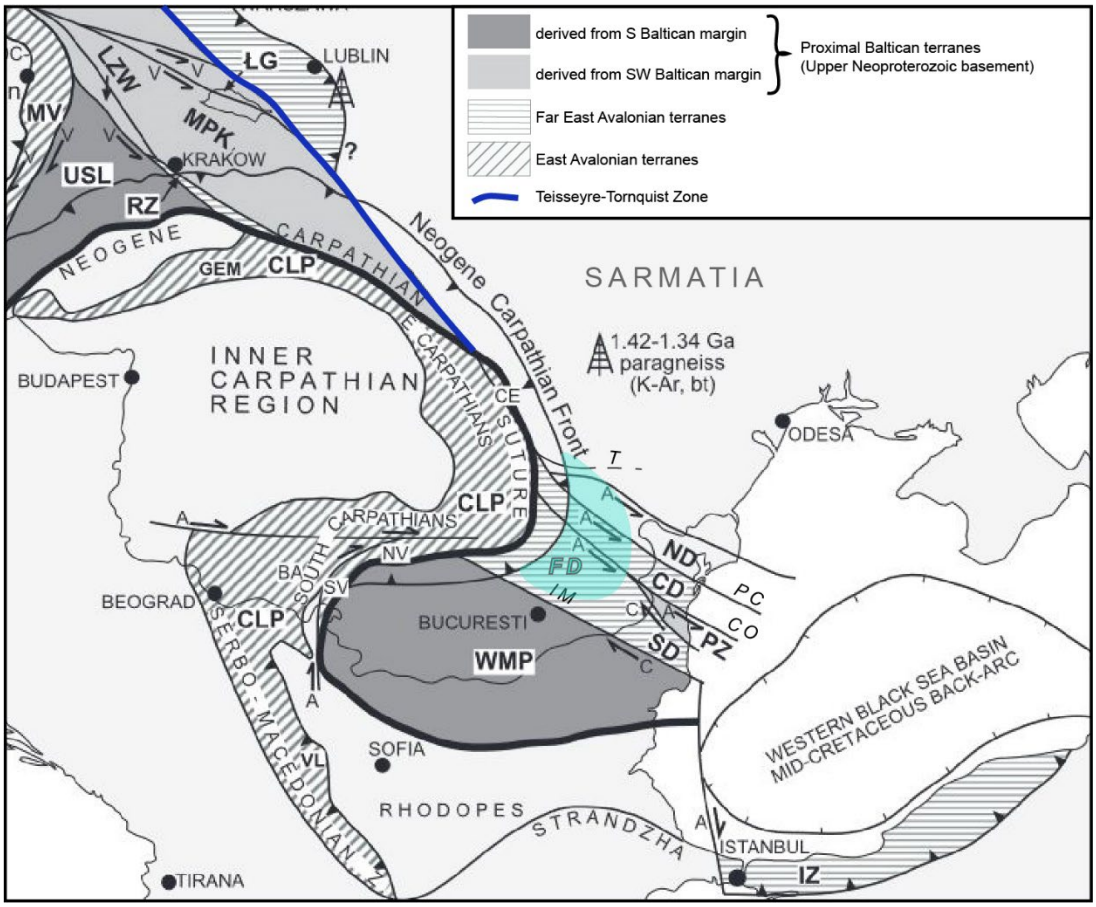

Figure I.13: Caledonian terranes on the southwestern margin of the East European craton. Proterozoic drill hole data after Marheine and ValverdeVaquero (2002) for Warszawa and Mînzatu et al. (1975) for the East Carpathian foredeep; 1.46–1.36 Ga granites in the Southwest Baltic Sea area after Åhäll et al. (1997), Tschernoster (2000), Cečys et al. (2002), and Obst et al. (2004); CD: Central Dobrogea; CE: Ceahlău ophiolites (Alpine); CLP: Carpathian lower Paleozoic; FEAAC :Far East Avalonian accretionary complex (thrust sheet on the Baltican crust); GEM: Gemerides (considered part of the CLP); IZ: Istanbul-Zonguldak; ŁG: Łysogóry; LZW: Lubliniec-Zawiercie-Wielun´; MPK: Małopolska; MV: Moravia; ND: North Dobrogea (Variscan); NSB: North Sea basement; NV: Novaci meta-granite (part of the CLP); RZ: Rzeszotary; SD: South Dobrogea; SV: Severin ophiolites (Alpine); USL: Upper Silesia; VL: Vlasina Complex (considered part of CLP); WMP—: West Moesian Platform. Letters A, C, and V next to transcurrent faults are indicative of Alpine, Caledonian, and Variscan times of displacement. T: Trotus Fault; PC: Peceneaga-Camena Fault; CO: Capidava-Ovidiu Fault; IM: Intra-Moesia Fault; Light blue area noted FD forindicates the : Focşani Depression After Oczlon et al., 2007

For a better understanding of the domain where the Carpathian collision occurred and where the foreland basin lies, we will here succinctly describe the different features of the East European Margin.

What we will call the East European Craton refers to the Sarmatia proto-continent of Baltica (Oczlon et al., 2007). This Precambrian domain is composed of different terranes as old as Archean in its core (oldest Tonalites dated in Sarmatia are 3.65 Ga, Claesson et al., 2006). Around the Archean terranes, several Proterozoic terranes were accreted to Sarmatia and successively metamorphosed by subsequent continental collisions (Figure I.13).

In the Late Ordovician – Early Silurian, several terranes of the Avalonia continent were accreted to the Baltica and Laurentia continents. Among them there were the Central and South Dobrogea terranes that accreted to the southwest of the East European Craton during the lower Ordovician (Oczlon et al., 2007; Figure I.13). Accretion of the three continents, Laurentia, Baltica and Avalonia, formed the Laurussia continent in the Silurian. The main feature remaining from this collision is the Trans-European Suture Zone (TESZ), a large faulted zone that separated Baltica and Avalonia and that dates from the Late Ordovician to Silurian (Janik et al., 2022). The TESZ crosscuts the European Continental plate from the North Sea to the Black Sea. The TESZ is made up by a series of thrust faults, as well as the Tornquist-Teisseyre Fault Zone (TTFZ) that records dextral strike-slip motion dated to the Silurian (Pharaoh, 1999). In the Carboniferous, during closure of the Rheic Ocean, North Dobrogea, which belongs to the Ligerian-Moldanubian domain, was accreted to the southern margin of Baltica (Oczlon et al., 2007; Seghedi, 2012).

During the Mesozoic opening of the Vardar Ocean, the Moesian Platform was detached from Baltica and was displaced along the southwest margin of the East European Craton. The following closure of the Tethys Ocean and resulting Alpine collision brought the Gondwana derived, AlCaPa, and East Avalonian derived, Tisza and Dacia terranes into the Carpathians embayment (Figure I.9).

In this setting, the Carpathian belt is emplaced on a variety of tectonic terranes making up the European margin. The thrust front has passed the TESZ and the TTFZ, which disappear underneath the Carpathians (Figure I.13), and thus touches the East European Craton in Ukraine. In Romania, the frontal thrust is bent at the transition from the craton to the Dobrogea terrane (indicated as the TESZ in Figure I.13). The Southeastern Carpathians are located in a zone delimited by major faults of the TESZ: the Intra-Moesia fault and the Trotus fault (Figure I.13).

3 Development of the Carpathian foreland basin

3.1 Geometry and limits of the Carpathian foreland basin

The Carpathian Foreland Basin (CFB) is situated on the pro side of the belt and developed from the middle Miocene (Karpatian to Badenian ~16 Ma) to the present day. The CFB is marked by differences in width along the basin. In the North-western CFB, in Poland, the sediments reach the city of Kraków to the west and extend to ~100 km from the frontal thrust. At the boundary with Ukraine, the basin is still narrow but widens East of Lviv (Figure I.10). The transition from a narrow to a wider foreland

allows to define a Western CFB (WCFB) and an Eastern CFB (ECFB). The CFB extends 250-300 km away from the frontal thrust in the rest of Ukraine. Toward the South, the CFB covers the Romanian and Moldovan territories and extends to the East of the South Bug River (Figure I.14; de Leeuw et al., 2020). To the South, the sediments reach the present-day borders of the NW Black Sea (BS) basin and the Dobrogea Massif. The CFB is again only a hundred kilometres wide between the Carpathians and the Dobrogea Massif.

The depth of the CFB also varies laterally. The NW CFB in Poland is up to 4 km deep (Oszczypko et al., 2006; Oszczypko and Oszczypko-Clowes, 2012). Where the CFB widens, the depth diminishes and foredeep sediments reach a maximum thickness of ~500 m (Oszczypko et al., 2006; Andreyeva-Grigorovich, 2008). Approximately 50 km north of the Ukrainian-Romanian border, a local Badenian (16-12.65 Ma) through developed into eroded Mesozoic sediments of the lower plate (Oszczypko et al., 2006, map 35-32b Ukraine). South of this through, the CFB sediments continuously thicken to reach 3-4 km in the North of Romania

Two other and sharper transitions in basin depth are also observed: the first occurs across the Trotuş and Peceneaga-Camena faults (Figure I.13; Tărăpoancă et al., 2003; Krézsek and Olariu, 2021) where the basin depth increases from ~4 km to 6 km on average. The foreland deepens very rapidly towards the belt and perpendicular to the lower plate faults to reach a depth close to 12-13 km. To the south, the basin depth diminishes at the Ovidiu fault zone to reach an average depth of 4-6 km again. To the SW, the Focsani Depression reaches the Intra-Moesian fault zone (Figure I.14), where the Dacian Basin depth is about 2-3 km (Krézsek and Olariu, 2021).

During this work, we limit our analysis of the CFB to the sedimentary system provided by the Western, Eastern and South-eastern Carpathian. Sediments provided by the South Carpathians are not integrated into the source-to-sink analysis. The southwestern extent of the CFB is then limited to the Focsani Depression (Tărăpoancă et al., 2003). The Romanian part of the Carpathian Foreland Basin is known as the Dacian Basin. The Western Dacian Basin constitutes the foreland of the South Carpathians. The exchange of sediment between the Western Dacian Basin and the CFB was limited until late Miocene-early Pliocene (Late Pontian ~5.6-4.7 Ma) when eustatic variations were the largest in the eastern Paratethys region (Popov et al., 2010) and when the Danube River started to prograde into the Focsani Depression (Stoica et al., 2013; Jorissen et al., 2018; Matoshko et al., 2019; Krézsek and Olariu, 2021). Because of the limited exchanges between the two basins and the different sources supplying sediment to them in the middle-late Miocene, the Western Dacian Basin was excluded from this study.

The eastern limit of our foreland analysis is located just to the east of the South Bug River in Ukraine. Sediments deposited beyond this boundary are roughly dated as Miocene-Pliocene (Figure I.14). These Miocene-Pliocene sediments could have been part of the forebulge or back-bulge of the CFB sedimentary system. Regarding the lack of data on these Miocene-Pliocene sediments and their sourcing (highly probable to be the East European Margin), we decided to limit the analysis of the CFB to the imprecisely dated sediments (mainly west of the South Bug River) and do not account for the sediments simply dated as “Miocene-Pliocene” in the rest of this work (Figure I.14).

The current border of the northwest Black Sea basin is the Southern limit of the CFB in our analysis. However, the limit of the Black Sea basin changed during the development of the foreland due to

eustatic variations (Popov et al., 2010) and/or reactivation of extensional faults (Khriachtchevskaia et al., 2010; Krezsek et al., 2016; Stovba et al., 2020). This major sink was inferred to have received sediment from the CFB (de Leeuw et al., 2020).

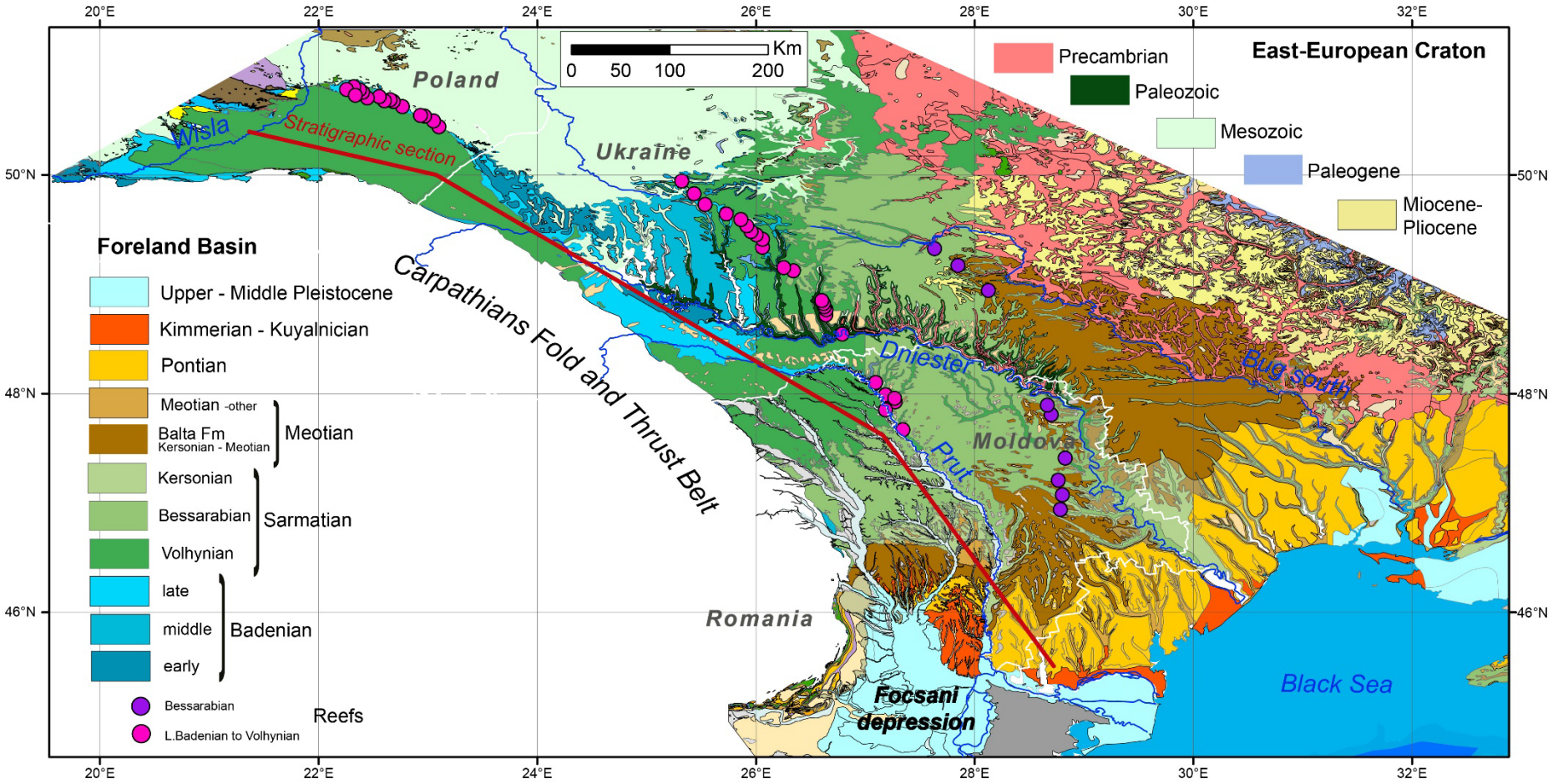

Figure I.14: Geological map of the Carpathian Foreland Basin (after de Leeuw et al., 2020 and in prep.).

3.2 Stratigraphy of the Carpathian Foreland basin

Paratethys stages are used to subdivide the stratigraphy of the Carpathian Foreland basin (CFB). The basins and sub-basins of the Paratethys sea had a poor connection to the open ocean and their variable water salinity confers them an endemic fauna. Local biostratigraphies were developed for these basins and until recently, correlating the regional stages to the global timescale was problematic. Early correlation frameworks such as those by Jones and Simmons (1996, 1997), Rögl (1998) and Steininger (1988) are frequently used, despite some lack of time constraints. During the last two decades, significant work has been carried out to update the chronostratigraphy of the Paratethys basins with paleomagnetic dating over long continuous sections in the South-eastern Carpathians and on the Taman Peninsula (Vasiliev et al., 2004, 2005, 2010, 2011; Krijgsman et al., 2010; Palcu et al., 2015, 2017, 2019, 2021; Lazarev et al., 2020; Matoshlo et al., submitted), as well as radio-isotopic dating of several key intervals (de Leeuw et al., 2010; Vasiliev et al., 2010, 2011; Mandic et al., 2012; van Baak et al., 2015). These studies provide a reliable chronostratigraphy for the Paratethys basins for the middle Miocene to Pliocene stages.

A reconstruction of sedimentation in the Carpathian foreland retraces the evolution of the region from early Miocene to present. The CFB is emerged at present, and notably tilted from NW to SE (Ionesi et al., 2005; Matoshko et al., 2016; de Leeuw et al., 2020). The eastern CFB sediments are eroded and incised by several rivers that end in the Black Sea basin. In the western CFB the Wisla River drains the basin and flows to the Baltic Sea. The following description of the stratigraphy is based on the interpretation of de Leeuw et al. (2020 and in prep).

The upper Karpatian to lower Badenian (late Burdigalian-Langhian, ~16.8- 15 Ma) *Debowiec Conglomerates* are the first widely distributed formation in the western CFB, and it contains flysch-derived clast (Oszczypko et al., 2006; Oszczypko and Oszczypko-Clowes, 2012). The rest of the Badenian (16-14.8 Ma) comprises the dark mud and sandy clay of the *Skawina formation* in the Western CFB. To the east, Badenian sediments that overlie the East European Platform are marls and clays (*Baranow Beds*). After this period, the connection of the Central Paratethys to the Mediterranean become restricted (~13.8-13.4 Ma; de Leeuw et al., 2010; 2018) and evaporite precipitated in the deeper parts of the Western CFB (*Wielician* and *Krzyzanowice beds;* Oszczypko et al., 2006; Peryt, 2006). Halite and gypsum/anhydrite layers of this age are also found in the East Carpathian Foreland and stretch all along the Carpathians (Peryt, 2006; de Leeuw et al., 2010, 2018), with occurrence of limestones and red-algal reefs in the late Badenian (~13.3 Ma, Figures I 14 & 15). The red-algal reefs mark the limit of the foredeep basin and the shoreface sediment facies with shallower and more carbonated depositional environment in the late Badenian (Figure I.15; de Leeuw et al., 2020). In the Western CFB, overlying the evaporites, are the *Machow formation* and the *Krakowiec clays* (~1500-300m; Kurovets et al., 2004; Oszczypko et al., 2006) These sediments correlate laterally to the east with the *Dashava formation*, which shows turbiditic clay and sand deposits at its base, evolving to sandier facies at the top of the Badenian (Kurovets et al., 2004; (Andreyeva-Grigorovich, 2008; Oszczypko and Oszczypko-Clowes, 2012). Both of these formations continue into the Sarmatian.

Deposition in the Ukrainian part of the CFB started in the Early Badenian with the *Baranov* and *Zhuriv beds* which were followed by evaporites in the Middle Badenian. The Late Badenian consists of the *Kosiv formation* in the deeper area closer to the Carpathians. The Volhynian (12.65 ~11.6 Ma) consists of the *Dashava formation* close to the mountain belt. This formation consists of turbiditic clay-sandy and deltaic sandstone deposits that are shallowing-upward (Figure I.15). This trend coincides, or possibly slightly post-dated, the installation of shoreface sand evolving into deltaic sediment deposits in the WCFB (Dziadzio et al., 2006). During the Volhynian, the ECFB extended onto the East European Platform and a wide area of shallow-water deposition was established in Ukraine. The so-called *Volyn beds*, made of sandy and shell-rich strata, are indicative of shoreface sedimentary facies and stretch out up to the Ukrainian-Moldavian boundary (de Leeuw et al., 2020). This is the uppermost formation present in the Ukrainian foreland to the north of Moldova, which is currently incised by rivers and prone to erosion. If any younger sediments were ever deposited, they have since been eroded.

A relatively thin series of mars and limestones deposited in the Romanian part of the ECFB during the late Badenian and Volhynian. These co-occur with reef limestones that crop out in a narrow zone close to the present-day Prut River in northern Romania. During the Bessarabian, the ECFB extended further south with the widespread deposition of *Cryptomactra* clays (~300-500 m thick; Nikonov, 1969; Ionesi et al., 2005). Reefs migrated a hundred kilometres eastward from their Volhynian position (Figure I.15, de Leeuw et al., 2020 and references therein). The map pattern of Bessarabian deposits (Figure I.14) displays this eastward enlargement and progradation of the CFB. Seismic images close to the mountain belt display prograding clinoforms progressively migrating to the south at this time (Taraponca et al., 2004). The juxtaposition of the *Bîrnova sands*, the *Scheia* and *Repedea formations* (~100 m thick; Saulea, 1965; Ionesi et al., 2005; Tabara and Chirila, 2009), with a laterally corresponding sand-clay and shell-rich pro-delta facies (Figure I.15, de Leeuw et al., 2020) also demonstrates the southward advance of deltaic system. Even further south (Figure I.14 and I.15), the *Congeria beds* display similar pro-delta facies in the upper Sarmatian (Kersonian, 9.6-8.3 Ma Palcu et al., 2021). The overlying *Mactra podolica* and *Mactra bulgarica* beds record a deeper depositional environment, with sands and mud containing endemic Paratethys fauna. At the Bessarabian-Kersonian transition, regional sea-level dropped (Popov et al., 2010), and the Eastern Paratethys became a wide brackish-water to hypersaline lake (Krijgsman et al., 2020; Palcu et al., 2021). During this transition, the central and south ECFB accumulated delta-top sediments, known as the *Balta formation* (de Leeuw et al., 2020; Matoshko et al., 2016, 2019). Palaeocurrents in the Balta formation are to the south and southeast, which provides evidence for axial sediment transport along the CFB at this time. Deposition of the *Balta formation* continued in the Eastern CFB up to the end of the Meotian stage (8.3-6.1 Ma). Intercalations of delta-front and proximal shelf sediments in the SE allow to retrace the paleo shoreline in the Black Sea basin (Figure I.15; Krijgsman et al., 2010b; Stoica et al., 2013; de Leeuw et al., 2020; Matoshko et al., 2023).

A transgression occurred at the onset of the Pontian (6.1-4.7 Ma; Popov et al., 2010), and the *Balta formation* is covered by littoral and shallow marine deposits. This flooding took place across the northern Black Sea margin and is dated at 6.1 Ma (Popov et al., 2004; Krijgsman and Piller, 2012). The shallow marine deposits are topped by paleosols, indicating a subsequent regression. At present, these deposits are incised by river valleys (Figure I.14).

More recent deposits are only present in the south-eastern portion of the basin, and date to the Kimmerian and Kuyalnician (4.7-1.8 Ma). These are valley-fill deposits and fluvial and deltaic sands called the *Porat formation* (~80 m; Matoshko et al., 2019 and references therein). These sediments are topped by paleosol and/or loess deposits that accumulated during the middle and late Pleistocene (Necea et al., 2013).

From the Badenian to the Pleistocene, the Focsani Depression was in constant subsidence according to tectono-stratigraphic reconstructions of the SE Carpathians (Matenco and Bertotti, 2000; Tărăpoancă et al., 2003; Leever et al., 2006a; Necea et al., 2021) and was thus a major depocenter. Recent studies reconstruct the depositional environment in the Focsani Depression based on integrated studies of faunas and sedimentary facies (Stoica et al., 2013; Van Baak et al., 2015; Jorissen et al., 2018; Lazarev et al., 2020; Matoshko et al., 2023) or geophysical imaging (Krézsek and Olariu, 2021). The clinoforms that prograded through the Eastern CFB in the Bessarabian-Kersonian continued their progradation into the Focsani Depression in the Kersonian-Meotian (Krézsek and Olariu, 2021). The deformed Kersonian sediments close to the frontal thrust present the same base-level drop as the CFB but display shoreface sediment facies with more distal depositional environment than present at this time in the Eastern CFB (Matoshko et al., 2016; Lazarev et al., 2020). In the early Meotian, the central Focsani Depression preserved southward advancing clinoforms (Krézsek and Olariu, 2021) with shoreface sediment facies (Lazarev et al., 2020). The late Meotian to Pontian transgression also influenced the Focsani Depression and changed the sedimentation to offshore facies of clay with benthic faunas (Krijgsman et al., 2010a; Stoica et al., 2013; Lazarev et al., 2020; Matoshko et al., 2023). A lake-level drop of approximately 100 m subsequently led to more proximal facies in the middle Pontian (Leever et al., 2006; Krijgsman et al., 2010; Stoica et al., 2013; Krezsek and Olariu, 2021; Matoshko et al., 2023), while the onset of the late Pontian is marked by a new transgression. There was subsequently a transition from deep water to deltaic sediment facies in the western Dacian Basin and the Focsani Depression in the late Pontian to Dacian (5.3-4.1 Ma; Stoica et al., 2013; Krézsek and Olariu, 2021). The Romanian (4.1-1.8 Ma) to Pleistocene sediments are predominantly fluvio-deltaic with shallow-water depositional facies (van Baak et al., 2015).

Figure I.15: Representation of the Carpathian foreland basin fill from de Leeuw et al. (2020 ; in prep). International chronostratigraphy is correlated with the regional chronostratigraphy of the Pannonian basin, the Dacian basin and the Black Sea basin. Formation abbreviations are all called in the section 2.4: Kry: Krzyzanowice beds Wie: Wieliczka salts; Mac: Machow formation; Ska: Skawina beds; Bar: Baranov beds; Zhu: Zhuriv beds; Kra: Krakowiec clays; Das: Dashava formation; Kos: Kosiv formation; Tyr: Tyras formation; Voly: Volyn beds; Cry: Cryptomactra clays; Co: Congeria beds; Bir: Bîrnova sands; Sch: Scheia formation; Rep: Repedea formation; Mpo: Mactra podolica beds; Mbu: Mactra bulgarica beds; Balta: Balta formation; Po1 and Po2: Porat formation.

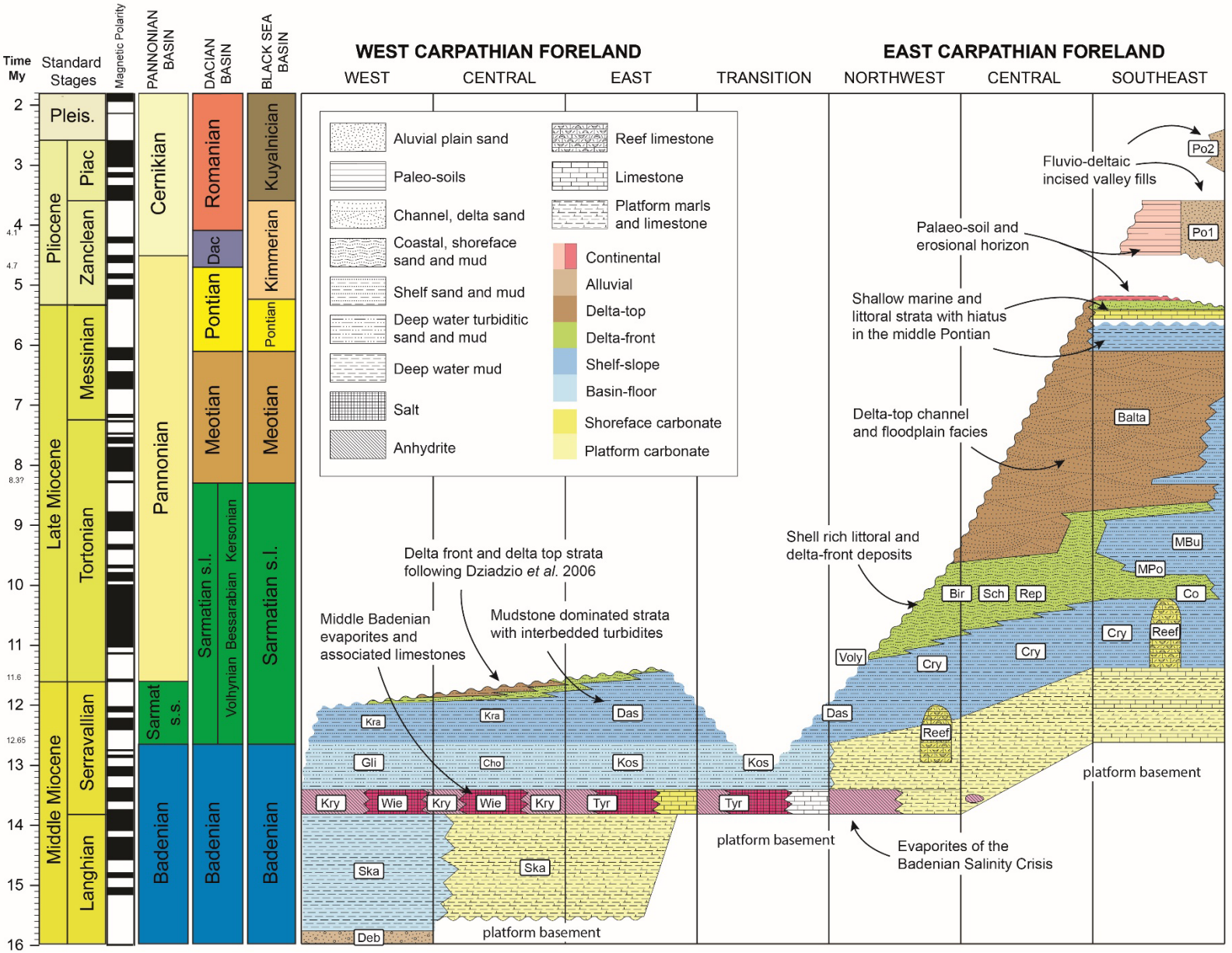
Time My
Standard Stages
Magnetic Polarity
PANNONIAN BASIN
DACIAN BASIN
BLACK SEA BASIN
WEST CARPATHIAN FORELAND
EAST CARPATHIAN FORELAND
WEST
CENTRAL
EAST
TRANSITION
NORTHWEST
CENTRAL
SOUTHEAST
Pleis.
Piac
Zanclean
Messinian
Tortonian
Serravallian
Langhian
Pliocene
Late Miocene
Middle Miocene
Cernikian
Pannonian
Sarmat s.s.
Romanian
Dac
Pontian
Meotian
Sarmatian s.l.
Volhynian
Bessarabian
Kersonian
Badenian
Kuyalnician
Kimmerian
Pontian
Meotian
Sarmatian s.l.
Badenian
Aluvial plain sand
Paleo-soils
Channel, delta sand
Coastal, shoreface sand and mud
Shelf sand and mud
Deep water turbiditic sand and mud
Deep water mud
Salt
Anhydrite
Reef limestone
Limestone
Platform marls and limestone
Continental
Alluvial
Delta-top
Delta-front
Shelf-slope
Basin-floor
Shoreface carbonate
Platform carbonate
Fluvio-deltaic incised valley fills
Po2
Po1
Palaeo-soil and erosional horizon
Shallow marine and littoral strata with hiatus in the middle Pontian
Delta-top channel and floodplain facies
Balta
Shell rich littoral and delta-front deposits
MBu
MPo
Co
Bir
Sch
Rep
Cry
Reef
Voly
Delta front and delta top strata following Dziadzio et al. 2006
Middle Badenian evaporites and associated limestones
Mudstone dominated strata with interbedded turbidites
Kra
Das
Gli
Cho
Kos
Kry
Wie
Tyr
Ska
Deb
platform basement
Evaporites of the Badenian Salinity Crisis

3.3 Sediments in Carpathian wedge-top and piggy-back basins

Piggy-back basins developed during the early Miocene on the Magura nappe in the Western Carpathians (WC) (Oszczypko and Oszczypko-Clowes, 2002; Oszczypko, 2006; Oszczypko et al., 2006). These basins are preserved today in the Polish Carpathian region. They contain early Miocene sediments of the *Zawada Formation* (Oszczypko and Oszczypko-Clowes, 2002). The basins had a water depth of some hundred meters and accumulated turbiditic sand and carbonate as well as marls and clays. Badenian to Early Sarmatian sediments, of fresh water molasse facies, were deposited discordantly at the NW limits of each basins (Oszczypko and Oszczypko-Clowes, 2002).

There are no piggy-back basins preserved in the Ukrainian Carpathians. The Sambir Nappe contains very young sediments (up to ~9 Ma; see Part II and references therein) from the distal margin embedded in the wedge. However, the Comăneşti wedge-top basin is a well-preserved basin comprising up to 800 m of Sarmatian to Meotian sediments in the Eastern CarpathiansCarpathians. It consists of three formations, the oldest composed of conglomerate and sandstone evolving into a sandstone and clay formation interbedded with occurrences of coal beds (Grasu et al., 1990; Micu et al., 2004). The upper formation of the basin is composed of volcanic tuff and cineritic sandstone (Grasu et al., 2004). The South-eastern Carpathians also expose some wedge-top sediments: Sarmatian shallow water sediments lie unconformably over the Tarcau nappe (Matenco and Bertotti, 2000). The toe of the wedge (i.e., the outer part of the sub-Carpathian nappe) is furthermore deeply buried under the foreland sediments in the Focsani Depression. These sediments are progressively deformed by the ongoing shortening of the area, and the frontal thrust is blind under the ten-kilometre thick foreland sediment package (Matenco and Bertotti, 2000; Tărăpoancă et al., 2003; Leever et al., 2006a).

3.4 Development of CFB axial transport system

Understanding each stage of the development of the foreland system is essential to our study of sediment supply from the belt to the foreland. Hereafter we describe the evolution of foreland sedimentary systems based on a review of sedimentary facies and field observations by Matoshko et al. (in prep.). The spatial distribution of sediments in the foreland basin includes a boundary where the siliciclastic sediments supplied by the Carpathian belt transitioned to more carbonated facies toward the distal margin.

During the **Badenian** (16-12.65 Ma), the CFB was isolated from the Black Sea by an emerged area. In the Early Badenian, deep-water predominantly siliciclastic sediments accumulated close to the present-day frontal thrust in Poland, Ukraine and northern Romania. During the Badenian the transition from siliciclastic to carbonate foreland sediments progressed eastward to the present-day Moldavian-Ukrainian border (Figure I.16). The eastward retreat of the boundary between siliciclastic and carbonate sediments indicates a deepening of the basin at the frontal thrust and progressive drowning of the platform; or advancement of the wedge onto the East European Margin and radial onlap of sediments onto the platform. Due to this widening of the basin, sediment was deposited further and further to the East. This is also noticeable in the displacement of the carbonate reefs from Badenian/Volhynian to the Bessarabian (Figure I.13; de Leeuw et al., 2020)

In the Volhynian, Bessarabian and Kersonian (12.65-8.37 Ma), the sediment transport system in the east Carpathian Foreland changed from radial to axial and from a deep-marine to a fluvio-deltaic system (de Leeuw et al., 2020; Matoshko et al., in prep). This occurred progressively from the northwest to the southeast. By the **Volhynian** (12.65 to ~11.22 Ma), carbonate sediments extended into Ukraine and to the current borders of the Black Sea basin (Figure I.16). The western CFB was infilled by the late Volhynian with the occurrence of coastal and fluvial sedimentary facies in the Polish foreland (Dziadzio et al., 2006) and north of the present Ukrainian-Moldovan border with the *Volyn beds*. Further north, in the Ukrainian foreland, some of the Volhynian sediments are eroded due to incision in this area. The carbonate and siliciclastic sediments of the distal margin are preserved to the north east of the eroded areas. They consist of shallow marine to littoral sediments with abundant molluscs, separated from the deeper water zone by a string of serpulid reefs. During the **Bessarabian** sub-stage (~11.6 to ~9.6 Ma), coastal sedimentary facies prograded to the south (Figure I.16). Deep-water sedimentary facies are restricted to the SW area of the Romanian foreland in the FD. The Bessarabian carbonate shelf extended to the present-day South Bug River and the Black Sea basin border. Toward the SW of the foreland, the clinoform system that developed in the northwest in the Volhynian, continued to prograde south to southwest-ward in the Bessarabian (mentioned in section 3.2). By the end of Bessarabian, the CFB sediments developed a shallowing upward sediment sequence (Figure I.15). From the **Kersonian** (~9.6 to 8.37 Ma), a fluvio-deltaic environment developed with the *Balta formation* (Figure I.15). Carbonate sediments are confined at the Black Sea border (Figure I.16). During the Kersonian, the shoreline migrated south and was located tens of kilometres inland from the present-day Black Sea coastline (de Leeuw et al., 2020). Kersonian eustatic variations in the Eastern and Central Paratethys (Popov et al., 2010; Palcu et al., 2021) could have enhanced the southward migration of the shoreline in the foreland.

During the **Meotian** (8.37-6.1 Ma), sea-level rose but the Balta formation continued its development and paleo-currents show a southeast-ward sediment-transport direction (Matoshko et al., 2016; de Leeuw et al., 2020). A late Meotian to early **Pontian** (6.1-4.7 Ma) transgressive event, known as the Pontian flooding, caused shore-line retreat during the high-stand. This event created significant accommodation space in the Focsini Depression. During the **Dacian** (4.7-4.1 Ma), the Danube delta prograded in the Dacian Basin toward the East; the Danube reached the Focsani Depression by the end of the Dacian. Later, in the **Romanian** (4.1-1.8 Ma), the Focsani Depression became overfilled. Both the Danube and the East Carpathian Foreland sediment systems were thus forced to deposit all of their sediment load in the down-stream Black Sea basin (Figure I.16; Jipa and Olariu, 2009; van Baak et al., 2015; Olariu et al., 2018; de Leeuw et al., 2018; Matoshko et al., 2019).

From the late Pontian to end of the early **Pleistocene** (2.58-1.8 Ma), sedimentary facies show shallowing upward; by the Pleistocene, a fluvial system was installed that incised the north and north-west foreland areas and infilled river valleys in the south, developing deltas in the Black Sea basin (Figure I.14; Kimmerian and Kyualnician; (Matoshko et al., 2009; Matoshko et al.,, 2019). In the SE Carpathian area, rivers draining the belt developed strath-terraces dated from Middle to Upper Pleistocene in the FD, which indicate significant recent incision of the SE belt (Necea et al., 2013).

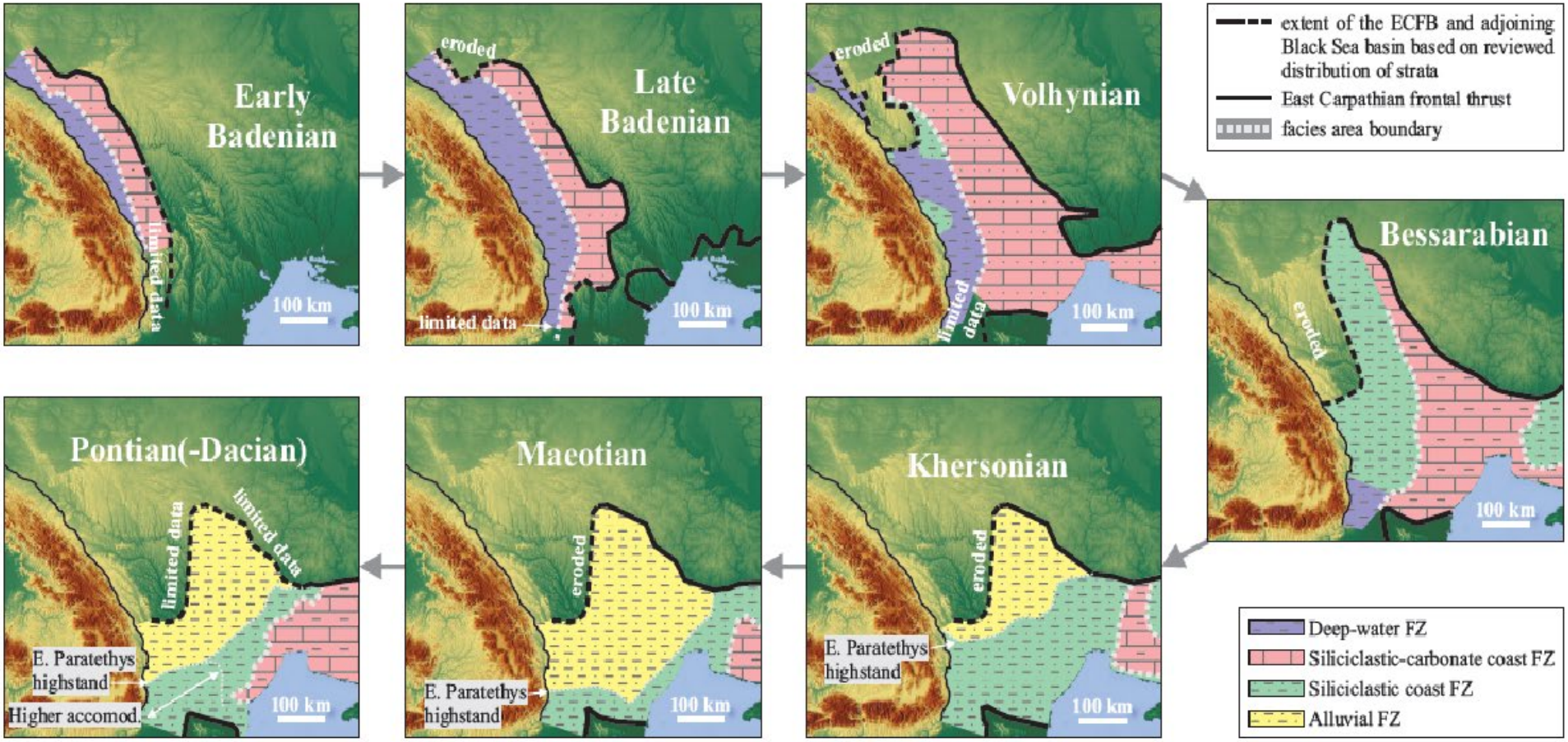

Figure I.16: Evolution of depositional environments in the East Carpathian Foreland Basin (ECFB) with the modern, reviewed, distribution of strata. The black bold line delimited the past extend of the East Carpathian Foreland Basin, when dashed, the limit was eroded. Dashed white line represent the limit of pure siliciclastic sedimentary facies and siliciclastic (50%) and carbonate (50%) From Matoshko et al. (in prep).

4 Retreat and detachment of the Carpathians slab

The development of the foreland-basin system of the Carpathians is tied to the evolution of the subduction system in the Pannonian-Carpathian region (Royden, 1993). As explained earlier, the Focsani Depression is the only part of the Carpathian foreland that is currently actively subsiding (van der Hoeven et al., 2005) and accumulated 12-13 km of sediments since the early Badenian (Matenco and Bertotti, 2003; Tarapoanca et al., 2004; Kreszek and Olariu, 2021). This zone reflects the Vrancea slab pull on the European plate. The Vrancea slab is the last remnant of the European slab that was involved in the closure of the Tethys oceanic domains and Alpine orogeny (Wortel and Spakman, 2000; Sperner et al., 2002; Handy et al., 2015). The Vrancea slab is imaged as a high seismic-velocity anomaly in the upper lithosphere (70-600 km) that outlines a vertically hanging (or delaminated) slab in tomographic images (Wortel and Spakman, 2000; Koulakov et al., 2010; Şengül-Uluocak et al., 2019).

Accretion and exhumation of the SE belt is impacted by the retreat and pull of the slab during late Miocene to Pliocene-Pleistocene time (Leever et al., 2006a; Matenco et al.,2007; Necea et al., 2013, 2021). The present-day slab efect is linked to the dynamic topography created at the bend zone. The current elevation of the Transylvanian basin and the Apuseni Mountains, and enhanced subsidence in the Focsani Depression and in the external nappes of the SE Carpathians (i.e., Sub-Carpathians nappes; Şengül-Uluocak et al., 2019; Necea et al., 2021) are consequences of the mantle circulation due to the slab retreat/hanging. Recent exhumation and erosion in the SE Carpathians is directly impacted by the slab evolution (Necea et al., 2021; this study), thus its effect on the belt and foreland system over the Northeastern and Eastern regions need to be assesed as well.

Slab subduction and detachment can happen in different ways in retreating subduction zones. It is commonly admitted in the European realm that most of the subduction zones are retreating due to the low convergence rates between the Africa and Europe since the Late Paleogene (Royden, 1993; Schmid et al., 2008; Jolivet et al., 2021). The European slab detached in the Western Alps around 35 Ma (Wortel and Spakman, 2000; Sperner et al., 2002; Schmid et al., 2008; Handy et al., 2015). Lateral propagation of the slab break-off was enhanced by asthenospheric readjustment (Horváth and Cloetingh, 1996; Handy et al., 2015; Tari et al., 2021). According to the model of slab detachment proposed by Wortel and Spakman (2000), retreating slabs break off by tearing large slab panels, the tear propagate laterally. At the surface, the slab tear is expressed by enhanced subsidence ahead of the tear and an uplifted area at the tail of the tear, linked to toroidal asthenospheric flow through the tear and isostatic rebound (Wortel and Spakman, 2000). In a slightly different model, Konečny et al. (2002) proposed subsequent break-off of three slab panels (Figure I.17), in the Northwest, East and Southeast of the Carpathian belt. The timing of slab break-off is also proposed based on the end of extension in the Pannonian basin and related volcanism in the intra-Carpathian region (Horváth and Cloetingh, 1996; Pécskay et al., 2006; Ustaszewski et al., 2008b; Kováč, 2016). According to this model, asthenospheric flow under the Pannonian Basin created a mantle upwelling under the Pannonian Basin lithosphere during high extension along former transform faults. The eastward advection of asthenosphere upwelling by the slab retreat enhanced the downgoing and detachment of slab panels under the Carpathians collision front.

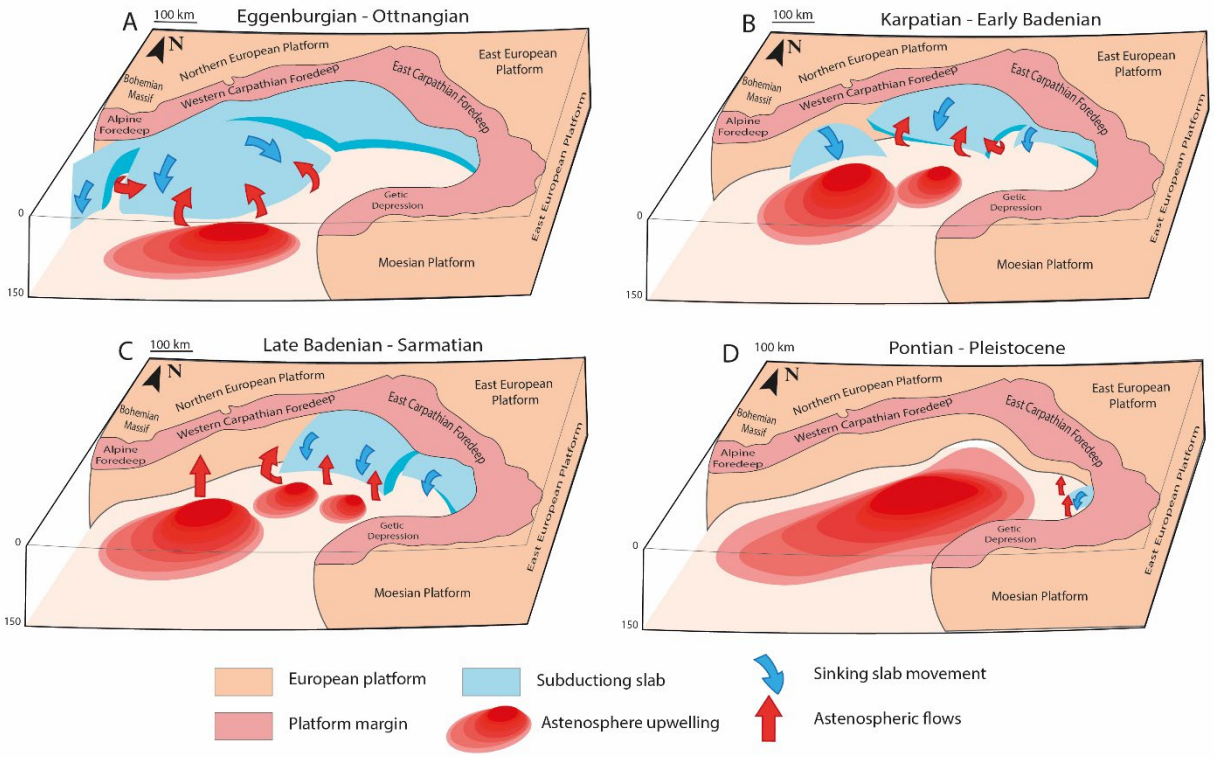

Figure I.17: Subduction model of the Carpathian slab: successive panels were detached under the Pannonian Basin during the development of the Carpathians belt. After Konečny et al., 2002.

From a larger reconstruction of the European subduction zones, Handy et al. (2015) propose a model of slab detachment led by gravity instability of the European slab and a broad lithosphere decoupling under the Pannonian basin. The decoupling explains the migration of AlCaPa and Tizsa-Dacia into the Carpathian embayment and the extension of the crust underlying the Pannonian Basin (Figure I.19). Previous models implied extrusion of the AlCaPa plate due to hard collision in the Western Alps and a push from the Adria Plate (Csontos et al., 1992; Royden, 1993; Sperner et al., 2002, section 2.1.2 and references therein). In the model proposed by Handy et al., 2015 model, the slab tear started at the collision point of the Western Alps and propagated laterally to detach a single large panel that destabilised due to the asthenospheric upwelling and the lateral asthenospheric flow under the Pannonian region. In this model, transform fault zones are the focus of mantle upwelling and lithospheric thinning. Slab delamination is proposed to be the process to progressively detach the sinking panel bit by bit until completed detachment of the slab. However, the model of lateral propagation of a tear in the slab panel, allowing a progressive sinking and detachment of the slab is proposed by Wortel and Spakman (2000) as a general mechanism for the Mediterranean realm subduction dynamic (Figure I.18). Decoupling of the crust from the lithospheric mantle in the Pannonian region is furthermore proposed to have lowered the resistance to northeast- and northward upper plate migration, thus facilitating the accretion of the fold-thrust belt and slab roll-back. Gögüs et

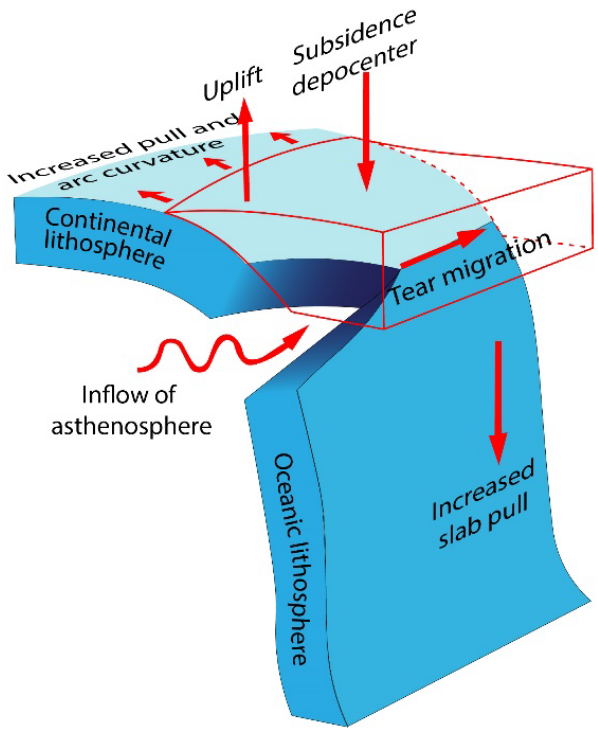

Figure I.18: Lateral migration of slab detachment. The slab pull forces increase laterally and causes a pattern of subsidence and uplift during its migration. Slab roll-back is enhanced by asthenospheric flows in the gap and around the slab. After Wortel and Spakman, 2000.

al. (2016) try to reproduce the surface uplift and subsidence and the lithosphere thickness observe in the SE Carpathians with numerical modeling of lithosphere delamination and slab break-off. The models revealed a good correlation between seismic evidence for thinner lithosphere under the Carpathian hinterland and thicker lithosphere under the Focsani depression, linked to lithosphere delamination and slab sinking dynamics. Models from Gögüs et al. (2016) display an evolution of the topography in the last 10 Ma in good aggrement with the quantification of exhumation and deposition rates of the Southeast Carpathians (Merten et al., 2010; Necea et al., 2021). Their model also correlate with the more modern observation and quantification of the dynamic topography of the SE Carpathians proposed by Şengül-Uluocak et al. (2019) (Figure I.20).

Processes of accretion and collision in the Carpathian region, as well as foreland subsidence and post-collisional exhumation loci are directly affected by subduction dynamics. In our study of the sediment fluxes of the Carpathians belt and foreland system, the slab position, rate of retreat, and pull over the European lithosphere are of major importance.

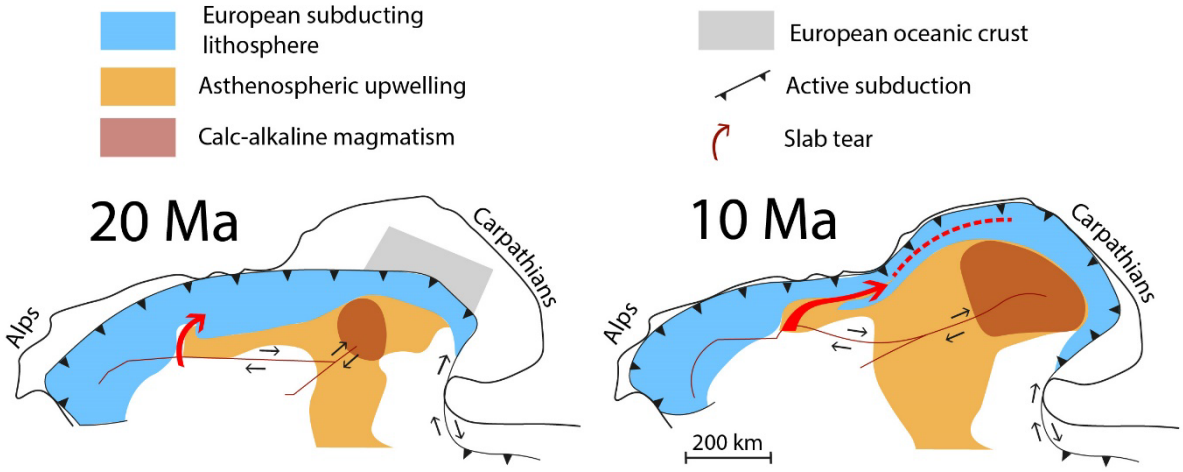

Figure I.19: Situation of the European and Adriatic slabs in the Alpine-Carpathian region at 20 and 10 Ma. After Handy et al. (2015).

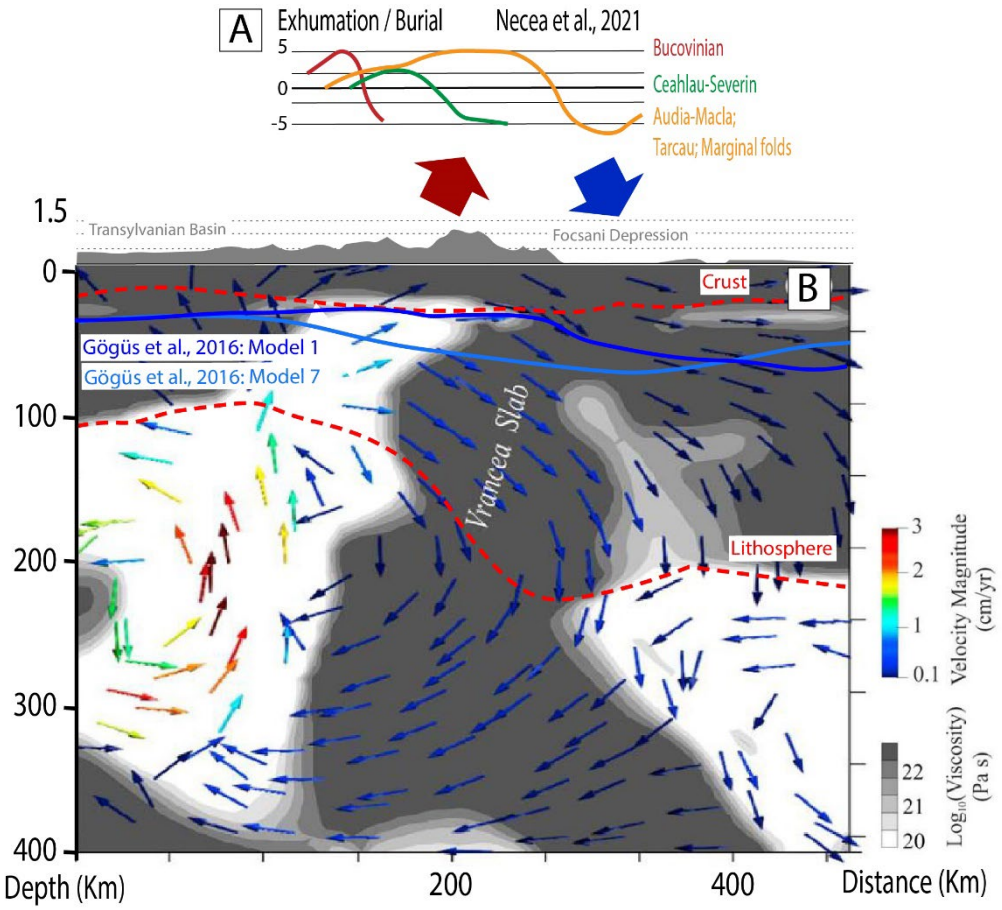

Figure I.20: A) Evolution of exhumation and subsidence across the nappes of the SE Carpathians, for three periods; Late Jurassic – Cretaceous (Bucovinian), middle Eocene (Ceahlau-Severin), late-Eocene – late Miocene (Audia-Macla, Tarcau, Marginal folds). After Necea et al, (2021). B) Mantle flow vectors and viscosity field of Model-2 from Şengül-Uluocak et al. (2019) underneath the Vrancea zone (SE Carpathians). Red dotted lines indicate crutal and lithosphere boundaries after Şengül-Uluocak et al. (2019). Full blue lines are the lower boundaries of upper-middle crust from model EXP-1 and EXP-7 at 10.1 Myr from Gögüs et al. (2016). The red and Blue arrows are respectively showing the loci of dynamic uplift and subsidence in the profil.

References

Andreyeva-Grigorovich, A. S.: New data on the stratigraphy of the folded Miocene Zone at the front of the Ukrainian Outer Carpathians, 36, 2008.

Artyushkov, E. V., Baer, M. A., and Mörner, N.-A.: The East Carpathians: Indications of phase transitions, lithospheric failure and decoupled evolution of thrust belt and its foreland, Tectonophysics, 262, 101–132, https://doi.org/10.1016/0040-1951(95)00207-3, 1996.

Ault, A. K., Gautheron, C., and King, G. E.: Innovations in (U–Th)/He, Fission Track, and Trapped Charge Thermochronometry with Applications to Earthquakes, Weathering, Surface-Mantle Connections, and the Growth and Decay of Mountains, Tectonics, 38, 3705–3739, https://doi.org/10.1029/2018TC005312, 2019.

Batt, G. E. and Braun, J.: The tectonic evolution of the Southern Alps, New Zealand: insights from fully thermally coupled dynamical modelling: Evolution of the S. Alps, Geophysical Journal International, 136, 403–420, https://doi.org/10.1046/j.1365-246X.1999.00730.x, 1999.

Beaumont, C.: Foreland basins, Geophysical Journal International, 65, 291–329, https://doi.org/10.1111/j.1365-246X.1981.tb02715.x, 1981.

Beaumont, C., Fullsack, P., and Hamilton, J.: Styles of crustal deformation in compressional orogens caused by subduction of the underlying lithosphere, Tectonophysics, 232, 119–132, https://doi.org/10.1016/0040-1951(94)90079-5, 1994.

Beyssac, O., Simoes, M., Avouac, J. P., Farley, K. A., Chen, Y.-G., Chan, Y.-C., and Goffé, B.: Late Cenozoic metamorphic evolution and exhumation of Taiwan: EXHUMATION OF THE TAIWAN MOUNTAIN BELT, Tectonics, 26, n/a-n/a, https://doi.org/10.1029/2006TC002064, 2007.

Burgess and Moresi: Modelling rates and distribution of subsidence due to dynamic topography over subducting slabs: is it possible to identify dynamic topography from ancient strata?: Identifying dynamic topography in the ancient record, Basin Research, 11, 305–314, https://doi.org/10.1046/j.1365-2117.1999.00102.x, 1999.

Castelluccio, A., Mazzoli, S., Andreucci, B., Jankowski, L., Szaniawski, R., and Zattin, M.: Building and exhumation of the Western Carpathians: New constraints from sequentially restored, balanced cross sections integrated with low-temperature thermochronometry: WESTERN CARPATHIANS TECTONIC EVOLUTION, Tectonics, 35, 2698–2733, https://doi.org/10.1002/2016TC004190, 2016.

Catuneanu, O., Beaumont, C., and Waschbusch, P.: Interplay of static loads and subduction dynamics in foreland basins: Reciprocal stratigraphies and the "missing" peripheral bulge, Geol, 25, 1087, https://doi.org/10.1130/0091-7613(1997)025<1087:IOSLAS>2.3.CO;2, 1997.

Claesson, S., Bibikova, E., Bogdanova, S., and Skobelev, V.: Archaean terranes, Palaeoproterozoic reworking and accretion in the Ukrainian Shield, East European Craton, Memoirs, 32, 645–654, https://doi.org/10.1144/GSL.MEM.2006.32.01.38, 2006.

Covey, M.: The Evolution of Foreland Basins to Steady State: Evidence from the Western Taiwan Foreland Basin, in: Foreland Basins, edited by: Allen, P. A. and Homewood, P., Blackwell Publishing Ltd., Oxford, UK, 77–90, https://doi.org/10.1002/9781444303810.ch4, 1986.

Dahlen: Critical taper model of fold-and-thrust belts and accretionary wedges, 1990.

Dahlen, F. A., Suppe, J., and Davis, D.: Mechanics of fold-and-thrust belts and accretionary wedges: Cohesive Coulomb Theory, J. Geophys. Res., 89, 10087–10101, https://doi.org/10.1029/JB089iB12p10087, 1984.

Davis, D., Suppe, J., and Dahlen, F. A.: Mechanics of fold-and-thrust belts and accretionary wedges, J. Geophys. Res., 88, 1153, https://doi.org/10.1029/JB088iB02p01153, 1983.

DeCelles, P. G.: Foreland Basin Systems Revisited: Variations in Response to Tectonic Settings, in: Tectonics of Sedimentary Basins, edited by: Busby, C. and Azor, A., John Wiley & Sons, Ltd, Chichester, UK, 405–426, https://doi.org/10.1002/9781444347166.ch20, 2012.

DeCelles, P. G. and Giles, K. A.: Foreland basin systems, Basin Research, 8, 105–123, https://doi.org/10.1046/j.1365-2117.1996.01491.x, 1996.

Dodson, M. H.: Closure temperature in cooling geochronological and petrological systems, Contr. Mineral. and Petrol., 40, 259–274, https://doi.org/10.1007/BF00373790, 1973.

Doglioni, C., Gueguen, E., Harabaglia, P., and Mongelli, F.: On the origin of west-directed subduction zones and applications to the western Mediterranean, SP, 156, 541–561, https://doi.org/10.1144/GSL.SP.1999.156.01.24, 1999.

Dziadzio, P. S. and Matyasik, I.: Sedimentological and geochemical characterisation of the Lower Oligocene Menilite shales from the Magura, Dukla, and Silesian nappes, Polish Outer Carpathians - A new concept, Marine and Petroleum Geology, 132, 105247, https://doi.org/10.1016/j.marpetgeo.2021.105247, 2021.

Erlanger, E. D., Fellin, M. G., and Willett, S. D.: Exhumation and erosion of the Northern Apennines, Italy: new insights from low-temperature thermochronometers, Solid Earth, 13, 347–365, https://doi.org/10.5194/se-13-347-2022, 2022.

Faccenna, C. and Becker, T. W.: Topographic expressions of mantle dynamics in the Mediterranean, Earth-Science Reviews, 209, 103327, https://doi.org/10.1016/j.earscirev.2020.103327, 2020.

Faccenna, C., Becker, T. W., Miller, M. S., Serpelloni, E., and Willett, S. D.: Isostasy, dynamic topography, and the elevation of the Apennines of Italy, Earth and Planetary Science Letters, 407, 163–174, https://doi.org/10.1016/j.epsl.2014.09.027, 2014.

Farley, K. A., Wolf, R. A., and Silver, L. T.: The effects of long alpha-stopping distances on (U-Th)/He ages, Geochimica et Cosmochimica Acta, 60, 4223–4229, https://doi.org/10.1016/S0016-7037(96)00193-7, 1996.

Flament, N., Gurnis, M., Müller, R. D., Bower, D. J., and Husson, L.: Influence of subduction history on South American topography, Earth and Planetary Science Letters, 430, 9–18, https://doi.org/10.1016/j.epsl.2015.08.006, 2015.

Flemings, P. B. and Jordan, T. E.: A synthetic stratigraphic model of foreland basin development, J. Geophys. Res., 94, 3851–3866, https://doi.org/10.1029/JB094iB04p03851, 1989.

Flowers, R. M., Zeitler, P. K., Danišík, M., Reiners, P. W., Gautheron, C., Ketcham, R. A., Metcalf, J. R., Stockli, D. F., Enkelmann, E., and Brown, R. W.: (U-Th)/He chronology: Part 1. Data, uncertainty, and reporting, GSA Bulletin, 135, 104–136, https://doi.org/10.1130/B36266.1, 2023.

Fügenschuh, B. and Schmid, S. M.: Age and significance of core complex formation in a very curved orogen: Evidence from fission track studies in the South Carpathians (Romania), Tectonophysics, 404, 33–53, https://doi.org/10.1016/j.tecto.2005.03.019, 2005.

Galbraith, R. F. and Green, P. F.: Estimating the component ages in a finite mixture, International Journal of Radiation Applications and Instrumentation. Part D. Nuclear Tracks and Radiation Measurements, 17, 197–206, https://doi.org/10.1016/1359-0189(90)90035-V, 1990.

Galbraith, R. F. and Laslett, G. M.: Statistical models for mixed fission track ages, Nuclear Tracks and Radiation Measurements, 21, 459–470, https://doi.org/10.1016/1359-0189(93)90185-C, 1993.

Gallagher, K.: Transdimensional inverse thermal history modeling for quantitative thermochronology: TRANSDIMENSIONAL INVERSE THERMAL HISTORY, J. Geophys. Res., 117, n/a-n/a, https://doi.org/10.1029/2011JB008825, 2012.

Garcia-Castellanos, D., Vergés, J., Gaspar-Escribano, J., and Cloetingh, S.: Interplay between tectonics, climate, and fluvial transport during the Cenozoic evolution of the Ebro Basin (NE Iberia):

TECTONICS, CLIMATE, AND DRAINAGE, J. Geophys. Res., 108, https://doi.org/10.1029/2002JB002073, 2003.

Gautheron, C., Tassan-Got, L., Barbarand, J., and Pagel, M.: Effect of alpha-damage annealing on apatite (U–Th)/He thermochronology, Chemical Geology, 266, 157–170, https://doi.org/10.1016/j.chemgeo.2009.06.001, 2009.

Gerin, C., Gautheron, C., Oliviero, E., Bachelet, C., Mbongo Djimbi, D., Seydoux-Guillaume, A.-M., Tassan-Got, L., Sarda, P., Roques, J., and Garrido, F.: Influence of vacancy damage on He diffusion in apatite, investigated at atomic to mineralogical scales, Geochimica et Cosmochimica Acta, 197, 87–103, https://doi.org/10.1016/j.gca.2016.10.018, 2017.

Gleadow, A. J. W., Duddy, I. R., Green, P. F., and Lovering, J. F.: Confined fission track lengths in apatite: a diagnostic tool for thermal history analysis, Contr. Mineral. and Petrol., 94, 405–415, https://doi.org/10.1007/BF00376334, 1986.

Glen S. Stockmal (2), Christopher B: Geodynamic Models of Convergent Margin Tectonics: Transition from Rifted Margin to Overthrust Belt and Consequences for Foreland-Basin Development, Bulletin, 70, https://doi.org/10.1306/94885656-1704-11D7-8645000102C1865D, 1986.

Golonka, J. and Picha, F. J.: The Carpathians and Their ForelandGeology and Hydrocarbon Resources, American Association of Petroleum Geologists, https://doi.org/10.1306/M84985, 2006.

Golonka, J., Krobicki, M., Waśkowska, A., Cieszkowski, M., and Ślączka, A.: Olistostromes of the Pieniny Klippen Belt, Northern Carpathians, Geol. Mag., 152, 269–286, https://doi.org/10.1017/S0016756814000211, 2015.

Golonka, J., Pietsch, K., Marzec, P., Kasperska, M., Dec, J., Cichostępski, K., and Lasocki, S.: Deep structure of the Pieniny Klippen Belt in Poland, Swiss J Geosci, 112, 475–506, https://doi.org/10.1007/s00015-019-00345-2, 2019.

Golonka, J., Waśkowska, A., Cichostępski, K., Dec, J., Pietsch, K., Łój, M., Bania, G., Mościcki, W. J., and Porzucek, S.: Mélange, Flysch and Cliffs in the Pieniny Klippen Belt (Poland): An Overview, Minerals, 12, 1149, https://doi.org/10.3390/min12091149, 2022.

Guillaume, B., Martinod, J., Husson, L., Roddaz, M., and Riquelme, R.: Neogene uplift of central eastern Patagonia: Dynamic response to active spreading ridge subduction?: DYNAMIC NEOGENE UPLIFT OF PATAGONIA, Tectonics, 28, n/a-n/a, https://doi.org/10.1029/2008TC002324, 2009.

Gurnis, M.: Rapid Continental Subsidence Following the Initiation and Evolution of Subduction, Science, 255, 1556–1558, https://doi.org/10.1126/science.255.5051.1556, 1992.

Handy, M. R., Ustaszewski, K., and Kissling, E.: Reconstructing the Alps–Carpathians–Dinarides as a key to understanding switches in subduction polarity, slab gaps and surface motion, Int J Earth Sci (Geol Rundsch), 104, 1–26, https://doi.org/10.1007/s00531-014-1060-3, 2015.

Hilde, T. W. C.: Sediment subduction versus accretion around the pacific, Tectonophysics, 99, 381–397, https://doi.org/10.1016/0040-1951(83)90114-2, 1983.

van der Hoeven, A. G. A., Mocanu, V., Spakman, W., Nutto, M., Nuckelt, A., Matenco, L., Munteanu, L., Marcu, C., and Ambrosius, B. A. C.: Observation of present-day tectonic motions in the Southeastern Carpathians: Results of the ISES/CRC-461 GPS measurements, Earth and Planetary Science Letters, 239, 177–184, https://doi.org/10.1016/j.epsl.2005.09.018, 2005.

Horváth, F. and Cloetingh, S.: Stress-induced late-stage subsidence anomalies in the Pannonian basin, Tectonophysics, 266, 287–300, https://doi.org/10.1016/S0040-1951(96)00194-1, 1996.

Husson, L., Guillaume, B., Funiciello, F., Faccenna, C., and Royden, L. H.: Unraveling topography around subduction zones from laboratory models, Tectonophysics, 526–529, 5–15, https://doi.org/10.1016/j.tecto.2011.09.001, 2012.

Husson, L., Bernet, M., Guillot, S., Huyghe, P., Mugnier, J.-L., Replumaz, A., Robert, X., and Van der Beek, P.: Dynamic ups and downs of the Himalaya, Geology, 42, 839–842, https://doi.org/10.1130/G36049.1, 2014.

Janik, T., Starostenko, V., Aleksandrowski, P., Yegorova, T., Czuba, W., Środa, P., Murovskaya, A., Zayats, K., Mechie, J., Kolomiyets, K., Lysynchuk, D., Wójcik, D., Omelchenko, V., Legostaieva, O., Głuszyński, A., Tolkunov, A., Amashukeli, T., Gryn', D., and Chulkov, S.: Lithospheric Structure of the East European Craton at the Transition from Sarmatia to Fennoscandia Interpreted from the TTZ-South Seismic Profile (SE Poland to Ukraine), Minerals, 12, 112, https://doi.org/10.3390/min12020112, 2022.

Jolivet, L., Baudin, T., Calassou, S., Chevrot, S., Ford, M., Issautier, B., Lasseur, E., Masini, E., Manatschal, G., Mouthereau, F., Thinon, I., and Vidal, O.: Geodynamic evolution of a wide plate boundary in the Western Mediterranean, near-field *versus* far-field interactions, BSGF - Earth Sci. Bull., 192, 48, https://doi.org/10.1051/bsgf/2021043, 2021.

Jorissen, E. L., de Leeuw, A., van Baak, C. G. C., Mandic, O., Stoica, M., Abels, H. A., and Krijgsman, W.: Sedimentary architecture and depositional controls of a Pliocene river-dominated delta in the semi-isolated Dacian Basin, Black Sea, Sedimentary Geology, 368, 1–23, https://doi.org/10.1016/j.sedgeo.2018.03.001, 2018.

Ketcham, R. A., Gautheron, C., and Tassan-Got, L.: Accounting for long alpha-particle stopping distances in (U–Th–Sm)/He geochronology: Refinement of the baseline case, Geochimica et Cosmochimica Acta, 75, 7779–7791, https://doi.org/10.1016/j.gca.2011.10.011, 2011.

Khriachtchevskaia, O., Stovba, S., and Stephenson, R.: Cretaceous–Neogene tectonic evolution of the northern margin of the Black Sea from seismic reflection data and tectonic subsidence analysis, SP, 340, 137–157, https://doi.org/10.1144/SP340.8, 2010.

Konecˇny, V., Kovacˇ, M., and Lexa, J.: Neogene evolution of the Carpatho-Pannonian region: an interplay of subduction and back-arc diapiric uprise in the mantle, 20, 2002.

Konstantinovskaia, E. and Malavieille, J.: Erosion and exhumation in accretionary orogens: Experimental and geological approaches: ACCRETIONARY OROGENS, Geochem. Geophys. Geosyst., 6, https://doi.org/10.1029/2004GC000794, 2005.

Koulakov, I., Zaharia, B., Enescu, B., Radulian, M., Popa, M., Parolai, S., and Zschau, J.: Delamination or slab detachment beneath Vrancea? New arguments from local earthquake tomography: DELAMINATION OR SLAB DETACHMENT BENEATH VRANCEA, Geochem. Geophys. Geosyst., 11, n/a-n/a, https://doi.org/10.1029/2009GC002811, 2010.

Kováč, M.: Paleogene palaeogeography and basin evolution of the Western Carpathians, Northern Pannonian domain and adjoining areas, Global and Planetary Change, 19, 2016.

Krézsek, C. and Bally, A. W.: The Transylvanian Basin (Romania) and its relation to the Carpathian fold and thrust belt: Insights in gravitational salt tectonics, Marine and Petroleum Geology, 23, 405–442, https://doi.org/10.1016/j.marpetgeo.2006.03.003, 2006.

Krézsek, C. and Olariu, C.: Filling of sedimentary basins and the birth of large rivers: The lower Danube network in the Dacian Basin, Romania, Global and Planetary Change, 197, 103391, https://doi.org/10.1016/j.gloplacha.2020.103391, 2021.

Krezsek, C., Schleder, Z., Bega, Z., Ionescu, G., and Tari, G.: The Messinian sea-level fall in the western Black Sea: small or large? Insights from offshore Romania, PG, 22, 392–399, https://doi.org/10.1144/petgeo2015-093, 2016.

Krijgsman, W., Stoica, M., Vasiliev, I., and Popov, V. V.: Rise and fall of the Paratethys Sea during the Messinian Salinity Crisis, Earth and Planetary Science Letters, 290, 183–191, https://doi.org/10.1016/j.epsl.2009.12.020, 2010a.

Krijgsman, W., Stoica, M., Vasiliev, I., and Popov, V. V.: Rise and fall of the Paratethys Sea during the Messinian Salinity Crisis, Earth and Planetary Science Letters, 290, 183–191, https://doi.org/10.1016/j.epsl.2009.12.020, 2010b.

Krijgsman, W., Palcu, D. V., Andreetto, F., Stoica, M., and Mandic, O.: Changing seas in the late Miocene Northern Aegean: A Paratethyan approach to Mediterranean basin evolution, Earth-Science Reviews, 210, 103386, https://doi.org/10.1016/j.earscirev.2020.103386, 2020.

L. Royden (2), G. D. Karner (3): Flexure of Lithosphere Beneath Apennine and Carpathian Foredeep Basins: Evidence for an Insufficient Topographic Load, Bulletin, 68, https://doi.org/10.1306/AD461372-16F7-11D7-8645000102C1865D, 1984.

Lazarev, S., de Leeuw, A., Stoica, M., Mandic, O., van Baak, C. G. C., Vasiliev, I., and Krijgsman, W.: From Khersonian drying to Pontian "flooding": late Miocene stratigraphy and palaeoenvironmental evolution of the Dacian Basin (Eastern Paratethys), Global and Planetary Change, 192, 103224, https://doi.org/10.1016/j.gloplacha.2020.103224, 2020.

Le Breton, E., Brune, S., Ustaszewski, K., Zahirovic, S., Seton, M., and Müller, R. D.: Kinematics and extent of the Piemont–Liguria Basin – implications for subduction processes in the Alps, Solid Earth, 12, 885–913, https://doi.org/10.5194/se-12-885-2021, 2021.

de Leeuw, A., Bukowski, K., Krijgsman, W., and Kuiper, K. F.: Age of the Badenian salinity crisis; impact of Miocene climate variability on the circum-Mediterranean region, Geology, 38, 715–718, https://doi.org/10.1130/G30982.1, 2010.

de Leeuw, A., Vincent, S. J., Matoshko, A., Matoshko, A., Stoica, M., and Nicoara, I.: Late Miocene sediment delivery from the axial drainage systemof the East Carpathian foreland basin to the Black Sea, Geology, https://doi.org/10.1130/G47318.1, 2020.

Leever, K. A., Matenco, L., Bertotti, G., Cloetingh, S., and Drijkoningen, G. G.: Late orogenic vertical movements in the Carpathian Bend Zone - seismic constraints on the transition zone from orogen to foredeep: Late orogenic vertical movements in the Carpathian Bend Zone, Basin Research, 18, 521–545, https://doi.org/10.1111/j.1365-2117.2006.00306.x, 2006a.

Leever, K. A., Bertotti, G., Zoetemeijer, R., Matenco, L., and Cloetingh, S. A. P. L.: The effects of a lateral variation in lithospheric strength on foredeep evolution: Implications for the East Carpathian foredeep, Tectonophysics, 421, 251–267, https://doi.org/10.1016/j.tecto.2006.04.020, 2006b.

Leever, K. A., Matenco, L., Garcia-Castellanos, D., and Cloetingh, S. A. P. L.: The evolution of the Danube gateway between Central and Eastern Paratethys (SE Europe): Insight from numerical modelling of the causes and effects of connectivity between basins and its expression in the sedimentary record, Tectonophysics, 502, 175–195, https://doi.org/10.1016/j.tecto.2010.01.003, 2011.

Liu, S., Nummedal, D., and Gurnis, M.: Dynamic versus flexural controls of Late Cretaceous Western Interior Basin, USA, Earth and Planetary Science Letters, 389, 221–229, https://doi.org/10.1016/j.epsl.2014.01.006, 2014.

M. Sandulescu: Essai de synthese structurale des Carpathes, Bulletin de la Société Géologique de France, 299-358., 1975.

Mandic, O., de Leeuw, A., Bulić, J., Kuiper, K. F., Krijgsman, W., and Jurišić-Polšak, Z.: Paleogeographic evolution of the Southern Pannonian Basin: 40Ar/39Ar age constraints on the Miocene continental series of Northern Croatia, Int J Earth Sci (Geol Rundsch), 101, 1033–1046, https://doi.org/10.1007/s00531-011-0695-6, 2012.

Matenco, L. and Bertotti, G.: Tertiary tectonic evolution of the external East Carpathians (Romania), Tectonophysics, 316, 255–286, https://doi.org/10.1016/S0040-1951(99)00261-9, 2000.

Matoshko, A., Gozhik, P., and Semenenko, V.: Late Cenozoic fluvial development within the Sea of Azov and Black Sea coastal plains, Global and Planetary Change, 68, 270–287, https://doi.org/10.1016/j.gloplacha.2009.03.003, 2009.

Matoshko, A., Matoshko, A., de Leeuw, A., and Stoica, M.: Facies analysis of the Balta Formation: Evidence for a large late Miocene fluvio-deltaic system in the East Carpathian Foreland, Sedimentary Geology, 343, 165–189, https://doi.org/10.1016/j.sedgeo.2016.08.004, 2016.

Matoshko, A., Matoshko, A., and de Leeuw, A.: The Plio–Pleistocene Demise of the East Carpathian Foreland Fluvial System and Arrival of the Paleo-Danube To The Black Sea, Geologica Carpathica, 70, 91–112, https://doi.org/10.2478/geoca-2019-0006, 2019.

Matoshko, A., de Leeuw, A., Stoica, M., Mandic, O., Vasiliev, I., Floroiu, A., and Krijgsman, W.: The Mio-Pliocene transition in the Dacian Basin (Eastern Paratethys): paleomagnetism, mollusks, microfauna and sedimentary facies of the Pontian regional stage, Geobios, S0016699523000244, https://doi.org/10.1016/j.geobios.2023.03.002, 2023.

Mazzoli, S., Jankowski, L., Szaniawski, R., and Zattin, M.: Low-T thermochronometric evidence for post-thrusting (<11 Ma) exhumation in the Western Outer Carpathians, Poland, Comptes Rendus Geoscience, 342, 162–169, https://doi.org/10.1016/j.crte.2009.11.001, 2010.

Merten, S., Matenco, L., Foeken, J. P. T., Stuart, F. M., and Andriessen, P. A. M.: From nappe stacking to out-of-sequence postcollisional deformations: Cretaceous to Quaternary exhumation history of the SE Carpathians assessed by low-temperature thermochronology: EXHUMATION HISTORY OF THE SE CARPATHIANS, Tectonics, 29, https://doi.org/10.1029/2009TC002550, 2010.

Moser, F., Hann, H. P., Dunkl, I., and Frisch, W.: Exhumation and relief history of the Southern Carpathians (Romania) as evaluated from apatite fission track chronology in crystalline basement and intramontane sedimentary rocks, Int J Earth Sci (Geol Rundsch), 94, 218–230, https://doi.org/10.1007/s00531-004-0456-x, 2005.

Naylor, M. and Sinclair, H. D.: Punctuated thrust deformation in the context of doubly vergent thrust wedges: Implications for the localization of uplift and exhumation, Geol, 35, 559, https://doi.org/10.1130/G23448A.1, 2007.

Necea, D., Fielitz, W., Kadereit, A., Andriessen, P. A. M., and Dinu, C.: Middle Pleistocene to Holocene fluvial terrace development and uplift-driven valley incision in the SE Carpathians, Romania, Tectonophysics, 602, 332–354, https://doi.org/10.1016/j.tecto.2013.02.039, 2013.

Necea, D., Juez-Larré, J., Matenco, L., Andriessen, P. A. M., and Dinu, C.: Foreland migration of orogenic exhumation during nappe stacking: Inferences from a high-resolution thermochronological profile over the Southeast Carpathians, Global and Planetary Change, 200, 103457, https://doi.org/10.1016/j.gloplacha.2021.103457, 2021.

Nemcok, M. and Nemcok, J.: Late Cretaceous deformation of the Pieniny Klippen Belt, West Carpathians, Tectonophysics, 239, 81–109, https://doi.org/10.1016/0040-1951(94)90109-0, 1994.

Oczlon, M. S., Seghedi, A., and Carrigan, C. W.: Avalonian and Baltican terranes in the Moesian Platform (southern Europe, Romania, and Bulgaria) in the context of Caledonian terranes along the southwestern margin of the East European craton, in: The Evolution of the Rheic Ocean: From Avalonian-Cadomian Active Margin to Alleghenian-Variscan Collision, Geological Society of America, https://doi.org/10.1130/2007.2423(18), 2007.

Oszczypko, N.: Late Jurassic-Miocene evolution of the Outer Carpathian fold-and-thrust belt and its foredeep basin (Western Carpathians, Poland), 25, 2006.

Oszczypko, N. and Oszczypko-Clowes, M.: Stages in the Magura Basin: a case study of the Polish sector (Western Carpathians), Geodinamica Acta, 22, 83–100, https://doi.org/10.3166/ga.22.83-100, 2009.

Oszczypko, N. and Oszczypko-Clowes, M.: Stages of development in the Polish Carpathian Foredeep basin, Open Geosciences, 4, https://doi.org/10.2478/s13533-011-0044-0, 2012.

Oszczypko, N. and Oszczypko-Clowes, M. A.: Newly discovered Early Miocene deposits in the Nowy Sącz area (Magura Nappe, Polish Outer Carpathians), 2002.

Oszczypko, N., Oszczypko-Clowes, M., Golonka, J., and Krobicki, M.: Position of the Marmarosh Flysch (Eastern Carpathians) and its relation to the Magura Nappe (Western Carpathians), Acta Geologica Hungarica, 48, 259–282, https://doi.org/10.1556/AGeol.48.2005.3.2, 2005.

Oszczypko, N., Krzywiec, P., Popadyuk, I., and Peryt, T.: Carpathian Foredeep Basin (Poland and Ukraine): Its Sedimentary, Structural, and Geodynamic Evolution, in: The Carpathians and Their Foreland: Geology and Hydrocarbon Researces: AAPG Memoir 84, edited by: Golonka, J. and Picha, F. J., The American Association of Petroleum Geologists, Tulsa, Oklahoma, U.S.A., 293–350, https://doi.org/10.1306/985612M843072, 2006.

Painter, C. S. and Carrapa, B.: Flexural versus dynamic processes of subsidence in the North American Cordillera foreland basin: FLEXURAL VERSUS DYNAMIC PROCESSES, Geophys. Res. Lett., 40, 4249–4253, https://doi.org/10.1002/grl.50831, 2013.

Palcu, D. V., Tulbure, M., Bartol, M., Kouwenhoven, T. J., and Krijgsman, W.: The Badenian–Sarmatian Extinction Event in the Carpathian foredeep basin of Romania: Paleogeographic changes in the Paratethys domain, Global and Planetary Change, 133, 346–358, https://doi.org/10.1016/j.gloplacha.2015.08.014, 2015.

Palcu, D. V., Golovina, L. A., Vernyhorova, Y. V., Popov, S. V., and Krijgsman, W.: Middle Miocene paleoenvironmental crises in Central Eurasia caused by changes in marine gateway configuration, Global and Planetary Change, 158, 57–71, https://doi.org/10.1016/j.gloplacha.2017.09.013, 2017.

Palcu, D. V., Vasiliev, I., Stoica, M., and Krijgsman, W.: The end of the Great Khersonian Drying of Eurasia: Magnetostratigraphic dating of the Maeotian transgression in the Eastern Paratethys, Basin Res, 31, 33–58, https://doi.org/10.1111/bre.12307, 2019.

Palcu, D. V., Patina, I. S., Şandric, I., Lazarev, S., Vasiliev, I., Stoica, M., and Krijgsman, W.: Late Miocene megalake regressions in Eurasia, Sci Rep, 11, 11471, https://doi.org/10.1038/s41598-021-91001-z, 2021.

Pécskay, Z., Lexa, J., Szakács, A., Seghedi, I., Balogh, K., Konečný, V., Zelenka, T., Kovacs, M., Póka, T., Fülöp, A., Márton, E., Panaiotu, C., and Cvetković, V.: Geochronology of Neogene magmatism in the Carpathian arc and intra-Carpathian area, 21, 2006.

Peryt, T. M.: The beginning, development and termination of the Middle Miocene Badenian salinity crisis in Central Paratethys, Sedimentary Geology, 188–189, 379–396, https://doi.org/10.1016/j.sedgeo.2006.03.014, 2006.

Peyton, S. L. and Carrapa, B.: An Introduction to Low-temperature Thermochronologic Techniques, Methodology, and Applications, in: Application of Structural Methods to Rocky Mountain Hydrocarbon Exploration and Development, American Association of Petroleum Geologists, https://doi.org/10.1306/13381688St653578, 2013.

Pharaoh, T. C.: Palaeozoic terranes and their lithospheric boundaries within the Trans-European Suture Zone (TESZ): a review, Tectonophysics, 314, 17–41, https://doi.org/10.1016/S0040-1951(99)00235-8, 1999.

Popov, S. V., Antipov, M. P., Zastrozhnov, A. S., Kurina, E. E., and Pinchuk, T. N.: Sea-level fluctuations on the northern shelf of the Eastern Paratethys in the Oligocene-Neogene, Stratigr. Geol. Correl., 18, 200–224, https://doi.org/10.1134/S0869593810020073, 2010.

Ratschbacher, L., Frisch, W., Linzer, H.-G., Sperner, B., Meschede, M., Decker, K., Nemĉok, M., Nemĉok, J., and Grygar, R.: The Pieniny Klippen Belt in the Western Carpathians of northeastern Slovakia: Structural evidence for transpression, Tectonophysics, 226, 471–483, https://doi.org/10.1016/0040-1951(93)90133-5, 1993.

Roban, R. D., Ducea, M. N., Mihalcea, V. I., Munteanu, I., Barbu, V., Melinte-Dobrinescu, M. C., Olariu, C., and Vlăsceanu, M.: Provenance of Oligocene lithic and quartz arenites of the East Carpathians: Understanding sediment routing systems on compressional basin margins, Basin Research, bre.12711, https://doi.org/10.1111/bre.12711, 2022.

Royden, L. and Burchfiel, B. C.: Are systematic variations in thrust belt style related to plate boundary processes? (The western Alps versus the Carpathians), Tectonics, 8, 51–61, https://doi.org/10.1029/TC008i001p00051, 1989.

Royden, L. and Faccenna, C.: Subduction Orogeny and the Late Cenozoic Evolution of the Mediterranean Arcs, Annu. Rev. Earth Planet. Sci., 46, 261–289, https://doi.org/10.1146/annurev-earth-060115-012419, 2018.

Royden, L. H.: Evolution of retreating subduction boundaries formed during continental collision, Tectonics, 12, 629–638, https://doi.org/10.1029/92TC02641, 1993.

Schmid, S. M., Berza, T., Diaconescu, V., Froitzheim, N., and Fügenschuh, B.: Orogen-parallel extension in the Southern Carpathians, Tectonophysics, 297, 209–228, https://doi.org/10.1016/S0040-1951(98)00169-3, 1998.

Schmid, S. M., Bernoulli, D., Fügenschuh, B., Matenco, L., Schefer, S., Schuster, R., Tischler, M., and Ustaszewski, K.: The Alpine-Carpathian-Dinaridic orogenic system: correlation and evolution of tectonic units, Swiss J. Geosci., 101, 139–183, https://doi.org/10.1007/s00015-008-1247-3, 2008.

Seghedi, A.: Palaeozoic Formations from Dobrogea and Pre-Dobrogea – An Overview, Turkish Journal of Earth Sciences, https://doi.org/10.3906/yer-1101-20, 2012.

Seghedi, I. and Downes, H.: Geochemistry and tectonic development of Cenozoic magmatism in the Carpathian–Pannonian region, Gondwana Research, 20, 655–672, https://doi.org/10.1016/j.gr.2011.06.009, 2011.

Şengül-Uluocak, E., Pysklywec, R. N., Göğüş, O. H., and Ulugergerli, E. U.: Multidimensional Geodynamic Modeling in the Southeast Carpathians: Upper Mantle Flow-Induced Surface Topography Anomalies, Geochem. Geophys. Geosyst., 2019GC008277, https://doi.org/10.1029/2019GC008277, 2019.

Sinclair, H.: Thrust Wedge/Foreland Basin Systems, in: Tectonics of Sedimentary Basins, edited by: Busby, C. and Azor, A., John Wiley & Sons, Ltd, Chichester, UK, 522–537, https://doi.org/10.1002/9781444347166.ch26, 2012.

Sinclair, H. D.: Flysch to molasse transition in peripheral foreland basins: The role of the passive margin versus slab breakoff, 4, 1997.

Sinclair, H. D. and Naylor, M.: Foreland basin subsidence driven by topographic growth versus plate subduction, Geological Society of America Bulletin, 124, 368–379, https://doi.org/10.1130/B30383.1, 2012.

Śmigielski, M., Sinclair, H. D., Stuart, F. M., Persano, C., and Krzywiec, P.: Exhumation history of the Tatry Mountains, Western Carpathians, constrained by low-temperature thermochronology: EXHUMATION HISTORY OF THE TATRy, Tectonics, 35, 187–207, https://doi.org/10.1002/2015TC003855, 2016.

Sperner, B., Ratschbacher, L., and Nemčok, M.: Interplay between subduction retreat and lateral extrusion: Tectonics of the Western Carpathians: TECTONICS OF THE WESTERN CARPATHIANS, Tectonics, 21, 1-1-1–24, https://doi.org/10.1029/2001TC901028, 2002.

Stoica, M., Lazăr, I., Krijgsman, W., Vasiliev, I., Jipa, D., and Floroiu, A.: Paleoenvironmental evolution of the East Carpathian foredeep during the late Miocene–early Pliocene (Dacian Basin; Romania), Global and Planetary Change, 103, 135–148, https://doi.org/10.1016/j.gloplacha.2012.04.004, 2013.

Stovba, S. M., Popadyuk, I. V., Fenota, P. O., and Khriachtchevskaia, O. I.: Geological structure and tectonic evolution of the Ukrainian sector of the Black Sea, Geofizicheskiy Zhurnal, 42, 53–106, https://doi.org/10.24028/gzh.0203-3100.v42i5.2020.215072, 2020.

Świerczewska, A. and Tokarski, A. K.: Deformation bands and the history of folding in the Magura nappe, Western Outer Carpathians (Poland), Tectonophysics, 297, 73–90, https://doi.org/10.1016/S0040-1951(98)00164-4, 1998.

Tărăpoancă, M., Bertotti, G., Maţenco, L., Dinu, C., and Cloetingh, S. A. P. L.: Architecture of the Focşani Depression: A 13 km deep basin in the Carpathians bend zone (Romania): ARCHITECTURE OF THE FOCŞANI DEPRESSION, Tectonics, 22, n/a-n/a, https://doi.org/10.1029/2002TC001486, 2003.

Tărăpoancă, M., Garcia-Castellanos, D., Bertotti, G., Matenco, L., Cloetingh, S. A. P. L., and Dinu, C.: Role of the 3-D distributions of load and lithospheric strength in orogenic arcs: polystage subsidence in the Carpathians foredeep, Earth and Planetary Science Letters, 221, 163–180, https://doi.org/10.1016/S0012-821X(04)00068-8, 2004.

Tari, G., Bada, G., Beidinger, A., Csizmeg, J., Danišik, M., Gjerazi, I., Grasemann, B., Kováč, M., Plašienka, D., Šujan, M., and Szafián, P.: The connection between the Alps and the Carpathians beneath the Pannonian Basin: Selective reactivation of Alpine nappe contacts during Miocene extension, Global and Planetary Change, 197, 103401, https://doi.org/10.1016/j.gloplacha.2020.103401, 2021.

Thomson, S. N., Brandon, M. T., Reiners, P. W., Zattin, M., Isaacson, P. J., and Balestrieri, M. L.: Thermochronologic evidence for orogen-parallel variability in wedge kinematics during extending convergent orogenesis of the northern Apennines, Italy, Geological Society of America Bulletin, 122, 1160–1179, https://doi.org/10.1130/B26573.1, 2010.

Ustaszewski, K., Schmid, S. M., Fügenschuh, B., Tischler, M., Kissling, E., and Spakman, W.: A map-view restoration of the Alpine-Carpathian-Dinaridic system for the Early Miocene, Swiss J. Geosci., 101, 273–294, https://doi.org/10.1007/s00015-008-1288-7, 2008.

Van Baak, C. G. C., Mandic, O., Lazar, I., Stoica, M., and Krijgsman, W.: The Slanicul de Buzau section, a unit stratotype for the Romanian stage of the Dacian Basin (Plio-Pleistocene, Eastern Paratethys), Palaeogeography, Palaeoclimatology, Palaeoecology, 440, 594–613, https://doi.org/10.1016/j.palaeo.2015.09.022, 2015.

Van Staal, C. and Zagorevski, A.: Accretion, Soft and Hard Collision: Similarities, Differences and an Application from the Newfoundland Appalachian Orogen, GS, 47, 103–118, https://doi.org/10.12789/geocanj.2020.47.161, 2020.

Vasiliev, I., Krijgsman, W., Langereis, C. G., Panaiotu, C. E., Maţenco, L., and Bertotti, G.: Towards an astrochronological framework for the eastern Paratethys Mio–Pliocene sedimentary sequences of the Focşani basin (Romania), Earth and Planetary Science Letters, 227, 231–247, https://doi.org/10.1016/j.epsl.2004.09.012, 2004.

Vasiliev, I., Krijgsman, W., Stoica, M., and Langereis, C. G.: Mio-Pliocene magnetostratigraphy in the southern Carpathian foredeep and Mediterranean-Paratethys correlations, Terra Nova, 17, 376–384, https://doi.org/10.1111/j.1365-3121.2005.00624.x, 2005.

Vasiliev, I., de Leeuw, A., Filipescu, S., Krijgsman, W., Kuiper, K., Stoica, M., and Briceag, A.: The age of the Sarmatian–Pannonian transition in the Transylvanian Basin (Central Paratethys), Palaeogeography, Palaeoclimatology, Palaeoecology, 297, 54–69, https://doi.org/10.1016/j.palaeo.2010.07.015, 2010.

Vasiliev, I., Iosifidi, A. G., Khramov, A. N., Krijgsman, W., Kuiper, K., Langereis, C. G., Popov, V. V., Stoica, M., Tomsha, V. A., and Yudin, S. V.: Magnetostratigraphy and radio-isotope dating of upper Miocene–lower Pliocene sedimentary successions of the Black Sea Basin (Taman Peninsula, Russia), Palaeogeography, Palaeoclimatology, Palaeoecology, 310, 163–175, https://doi.org/10.1016/j.palaeo.2011.06.022, 2011.

Vermeesch, P.: Statistics for Fission-Track Thermochronology, in: Fission-Track Thermochronology and its Application to Geology, edited by: Malusà, M. G. and Fitzgerald, P. G., Springer International Publishing, Cham, 109–122, https://doi.org/10.1007/978-3-319-89421-8_6, 2019.

Waschbusch, P. J. and Royden, L. H.: Episodicity in foredeep basins, 4, 1992a.

Waschbusch, P. J. and Royden, L. H.: Spatial and temporal evolution of foredeep basins: lateral strength variations and inelastic yielding in continental lithosphere, Basin Research, 4, 179–196, https://doi.org/10.1111/j.1365-2117.1992.tb00044.x, 1992b.

Wortel, M. J. R. and Spakman, W.: Subduction and Slab Detachment in the Mediterranean-Carpathian Region, Science, 290, 1910–1917, https://doi.org/10.1126/science.290.5498.1910, 2000.

Zhong, S. and Gurnis, M.: Mantle Convection with Plates and Mobile, Faulted Plate Margins, Science, 267, 838–843, https://doi.org/10.1126/science.267.5199.838, 1995.

Chapter II: Construction of the Ukrainian Carpathian wedge from low-temperature thermochronology and tectono-stratigraphic analysis

Marion Roger[1], Arjan de Leeuw[1], Peter van der Beek[2], Laurent Husson[1], Edward R. Sobel[2], Johannes Glodny[3], and Matthias Bernet[1]

[1]Institut des Sciences de la Terre (ISTerre), Université Grenoble Alpes, CNRS, IRD, 38000 Grenoble, France
[2]Institut für Geowissenschaften, Universität Potsdam, 14476 Potsdam, Germany
[3]GFZ German Research Centre for Geosciences, 14473 Potsdam, Germany

Received: 24 August 2022 – Discussion started: 30 August 2022
Revised: 6 January 2023 – Accepted: 8 January 2023 – Published: 23 February 2023
Solid Earth, 14, 153–179, 2023
https://doi.org/10.5194/se-14-153-2023

Context of the study:
The following Chapter is based on the published article cited above. The article focuses on the construction of the Ukrainian Carpathian wedge, especially on retracing the burial and exhumation history of the nappes. The study is conducted based on low-temperature thermochronology dating done on eleven samples collected during a field campaign in 2019. The initial project of the fieldwork was to collect samples in Ukraine to complete the thermochronology database introduce in Chapter III. To complete our analysis of the Carpathian belt exhumation (Chapter III), we wanted to understand the nappe stacking process during accretion and exhumation of the orogenic wedge, including the burial history of the nappes. In the following Chapter we present the result of the low-temperature thermochronology dating we re-used in the inversion model (see Chapter III). We also do a source analysis based on the non-reset ages of zircon dated by (U-Th)/He method.

Abstract.

The evolution of orogenic wedges can be determined through stratigraphic and thermochronological analysis. We used apatite fission-track (AFT) and apatite and zircon (U–Th–Sm)/ He (AHe and ZHe) low-temperature thermochronology to assess the thermal evolution of the Ukrainian Carpathians, a prime example of an orogenic wedge forming in a retreating subduction zone setting. Whereas most of our AHe ages are reset by burial heating, 8 out of 10 of our AFT ages are partially reset, and none of the ZHe ages are reset.

We inverse-modeled our thermochronology data to determine the time–temperature paths of six of the eight nappes composing the wedge. The models were integrated with burial diagrams derived from the stratigraphy of the individual nappes, which allowed us to distinguish sedimentary from tectonic burial. This analysis reveals that accretion of successive nappes and their subsequent exhumation mostly occurred sequentially, with an apparent increase in exhumation rate towards the external nappes. Following a phase of tectonic burial, the nappes were generally exhumed when a new nappe was accreted, whereas, in one case, duplexing resulted in prolonged burial. An early orogenic wedge formed with the accretion of the innermost nappe at 34 Ma, leading to an increase in sediment supply to the remnant basin. Most of the other nappes were accreted between 28 and 18 Ma. Modeled exhumation of the outermost nappe started at 12 Ma and was accompanied by out-of-sequence thrusting. The latter was linked to emplacement of the wedge onto the European platform and consequent slab detachment. The distribution of thermochronological ages across the wedge, showing non-reset ages in both the inner and outer part of the belt, suggests that the wedge was unable to reach dynamic equilibrium for a period long enough to fully reset all thermochronometers.

Non-reset ZHe ages indicate that sediments in the inner part of the Carpathian embayment were mostly supplied by the Inner Carpathians, while sediments in the outer part of the basin were derived mostly from the Teisseyre–Tornquist Zone (TTZ) or the southwestern margin of the East European Platform. Our results suggest that during the accretionary phase, few sediments were recycled from the wedge to the foredeep. Most of the sediments derived from the Ukrainian Carpathian wedge were likely transported directly to the present pro- and retro-foreland basins.

1 Introduction

Thin-skinned fold-and-thrust belts result from the accretion, stacking, and exhumation of sediments from pre-existing basins trapped in convergence zones. These basins frequently evolve from rifted passive margins to orogens (e.g., Stockmal et al., 1986), and their stratigraphy provides a record of convergence zone dynamics and the onset of orogeny, in particular when the sedimentary record is combined with subsequent exhumation paths that can be retrieved from detrital zircon and apatite grains using low-temperature thermochronology (e.g., Merten et al., 2010; Fillon et al., 2013; Vacherat et al., 2014; Andreucci et al., 2015; Castelluccio et al., 2016).

Sediments in the antecedent basin are brought to depth by sedimentary burial and integrated into the wedge through nappe stacking processes in two steps. Sediment deposition in the basin may bury older deposits under several kilometers of overburden. Sediment accumulation is bound to accelerate as the

orogenic belt propagates toward the basin through a combination of enhanced erosion of the growing wedge, the backstop and the forebulge area, and creation of accommodation space by flexure of the underlying plate (e.g., Simpson, 2006; Sinclair, 2012) and possible dynamic subsidence of the foreland (e.g., Husson et al., 2014; Flament et al., 2015). Tectonic nappe stacking integrates the pre-existing basin step by step into the growing wedge. When the frontal thrust propagates into the adjacent former basin, the latter becomes a nappe that overrides more external areas of the basin. Overthrusting of the basin by the orogenic wedge leads to tectonic burial in addition to initial sedimentary burial. As thrusting propagates outwards and the wedge evolves, the newly formed nappes are sequentially uplifted and exhumed. Syn-orogenic deposits that accumulate on the newly formed thrust sheet, i.e., wedge-top sediments, might also be progressively incorporated into the wedge and eventually buried. This process repeats until plate convergence stops (Davis et al., 1983; Dahlen et al., 1984; Konstantinovskaia and Malavieille, 2005; Hoth et al., 2007). Overthrusting of a nappe may entrain a phase of internal deformation in the orogenic wedge that causes rock and surface uplift (Hoth et al., 2007; Sinclair and Naylor, 2012). Steady state in the wedge may potentially be reached if the tectonic influx of material into the wedge and the outflow through erosion balance one another so that the elevation and width of the wedge remain constant (Willett et al., 1993). In the Carpathian fold-and-thrust belt, the main driver of foreland basin subsidence and frontal accretion is slab rollback rather than plate convergence (e.g., Royden and Faccenna, 2015). The elevation and width of the wedge provide an insufficient load to have created the observed foreland basin, which suggests that the subducting slab primarily drove subsidence (Royden and Karner, 1984; Royden and Burchfiel, 1989; Royden, 1993b; Krzywiec et al., 1997). Foreland subsidence was enhanced by the reactivation of pre-orogenic normal faults during the Miocene (Krzywiec, 2001; Tărăpoancă et al., 2003; Oszczypko et al., 2006), probably also predominantly due to flexure of the lithosphere through slab roll-back.

Previous studies in the eastern and southeastern Romanian Carpathians have focused on the timing of nappe stacking and exhumation of the wedge. Using low-temperature thermochronology to quantify the erosion pattern on both sides of the wedge, Sanders et al. (1999) concluded that the southeastern Carpathians can be treated as a doubly vergent critical wedge, where the back thrusts are covered by Neogene volcanic rocks and sediments that accumulated in the retro-foreland volcanic basin. Further studies, however, inferred that the doubly vergent wedge concept cannot be directly applied to the Romanian eastern and southeastern Carpathians and that this belt is a singly vergent wedge that evolved through forward propagation of deformation over the subducting plate followed by significant out-of-sequence thrusting (Matenco et al., 2010; Merten et al., 2010). In contrast, the Western Carpathians might correspond to a doubly vergent wedge as back thrusts are present and some involve basement blocks (Mazzoli et al., 2010; Castelluccio et al., 2016). These contrasting views imply that caution should be exerted when extrapolating interpretations of wedge dynamics along the Carpathian arc because the characteristics of the downgoing plate change markedly along-strike.

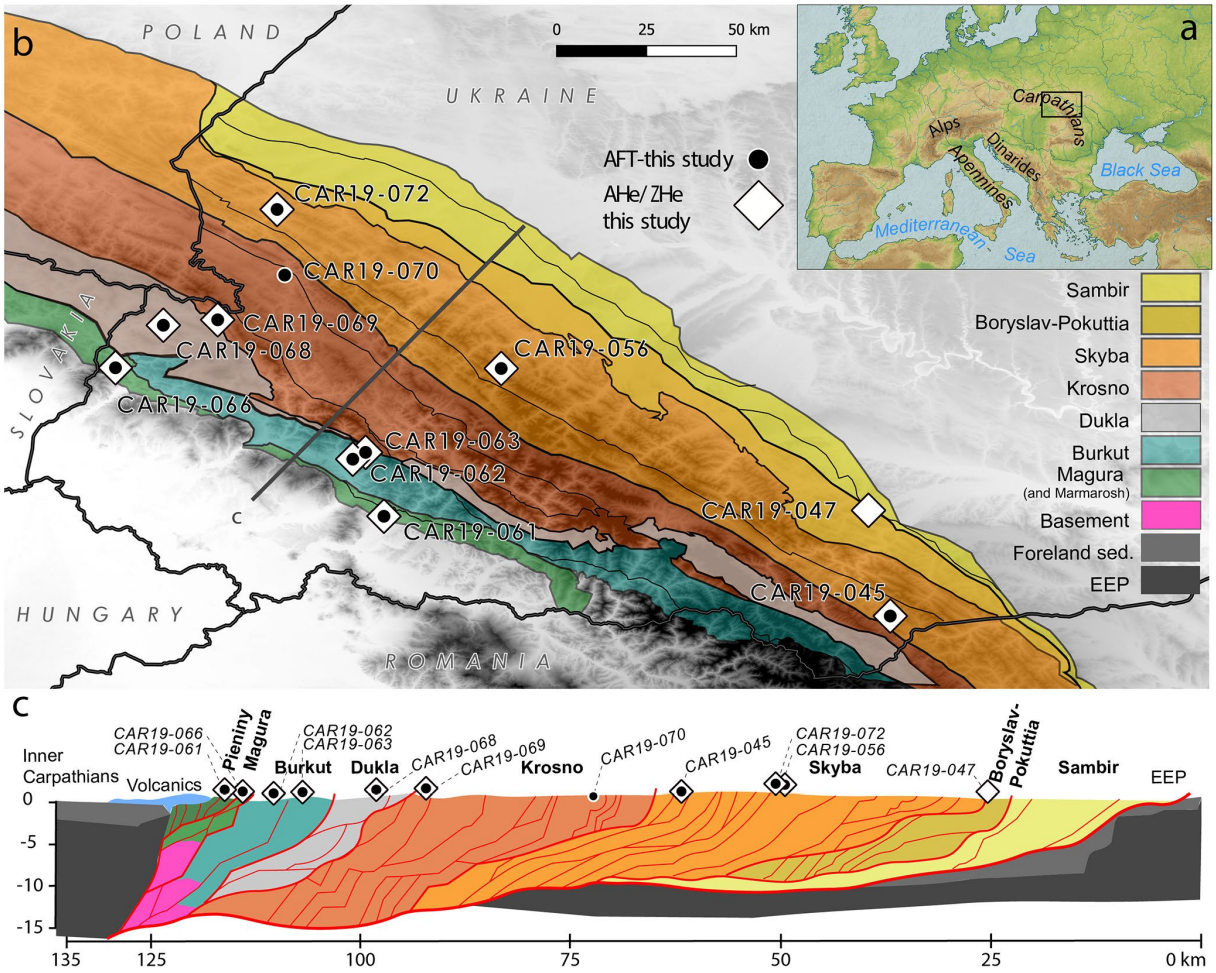

Figure II.**Error! Use the Home tab to apply 0 to the text that you want to appear here.**-1 Overview of the study area in the Ukrainian Carpathians, showing the main tectonic nappes and sample locations. (a) The inset shows the setting of the Carpathian belt in Europe and the location of the study region. (b) Simplified tectonic map; units are highlighted in different colors and follow Schmid et al. (2008), with revised names to more closely follow the regional designation of the lithostratigraphy. EEP: East European Platform. The Marmarosh and Magura nappes are both represented in green. Thin lines represent major intra-nappe faults. The thick grey line marks the location of the cross-section. The digital elevation model (DEM) file is from OpenTopography (https://doi.org/10.5069/G92R3PT9, Tozer et al., 2019) Simplified tectonic cross-section (after Nakapelyukh et al., 2018). Major faults delimiting the nappes are in bold red lines, and thin red lines indicate intra-nappe faults. Sample locations are projected onto the section.

Convergence in the Carpathians was mostly oblique to the East European Platform (EEP), except in the Ukrainian Carpathians, where it occurred perpendicular to the margin. This makes the Ukrainian Carpathians a promising site to resolve wedge dynamics, as well as the kinematics and drivers of nappe stacking. The structure and timing of nappe accretion in the Ukrainian Carpathians were previously studied by Nakapelyukh et al. (2018), employing balanced cross-sections and low-temperature thermochronology. Their study suggested very rapid convergence starting in the Miocene when most of the nappes were accreted and subsequently exhumed (Figure II.1). To better understand the dynamics of accretionary wedge formation during slab roll-back and to constrain sediment fluxes in this type of

orogen, we study the accretion–collision and exhumation phases of the Ukrainian Carpathian wedge from the Oligocene onward using thermal history modelling based on low-temperature thermochronology and stratigraphic analysis. In particular, we constrain the timing and amount of sedimentary and tectonic burial for each nappe, as well as its subsequent exhumation.

2 Geological context

The Carpathian belt is the result of the collision of the Tisza–Dacia and Alps–Carpathian–Pannonian (ALCAPA) microplates with the East European Platform (Csontos et al., 1992; Schmid et al., 2008). These two microplates jointly moved to the north from the Late Cretaceous (Santonian; ~84 Ma) to the Oligocene (~34 Ma). From then on, they moved northeast into the Carpathian embayment, a deepwater area of oceanic to thinned continental crust with intervening ridges formed during Tethyan rifting (Handy et al., 2015). Most of the microplate motion was accommodated by roll-back of the subducting European oceanic crust and rifted continental margin. ALCAPA motion was also promoted by extrusion from the convergence zone of the Alps (Sperner et al., 2002). Nappe accretion into the outer Carpathian thin-skinned wedge started in the Oligocene (Sandulescu, 1975; Nemčok et al., 2006; Schmid et al., 2008). The age of the terminal frontal thrust of the Outer Carpathians, which can be used as a proxy for collision, becomes younger from northwest to southeast along the orogen (Nemčok et al., 2006). Oblique collision occurred in the northwestern Carpathians from 17–15 Ma (Nemčok et al., 2006 and references therein). Subsequent subduction roll-back towards the east led to continued nappe accretion in front of the wedge, coincident with back-arc extension in the Pannonian Basin (Tari et al., 1992; Horváth and Cloetingh, 1996). This was followed by collision in the Ukrainian Carpathians at approximately 12 Ma (Gagała et al., 2012; Nakapelyukh et al., 2018) and in the Romanian Carpathians after 10 Ma (Matenco and Bertotti, 2000). The cessation of contraction in the belt has been linked to break-off of the European slab, which also propagated from northwest to southeast (Nemcok et al., 1998; Wortel and Spakman, 2000; Cloetingh et al., 2004; Handy et al., 2015). The slab is still attached in the southeasternmost corner of the Carpathians, known as the Vrancea Zone, where its pull on the overriding crust, in combination with the induced mantle flow, causes extremely rapid localized subsidence (Royden and Karner, 1984; ¸Sengül-Uluocak et al., 2019). Whereas this sequence of events explains most observables, other models exist, for instance including successive panels of the slab breaking off, activating mantle cells and upwelling in the Pannonian Basin (Konecný et al., 2002), or including lithosphere delamination and Neogene extension in the Pannonian realm leading to eastward extrusion of the Carpathian microplates by mantle flow (Kovács, 2012).

The Carpathians consist of an inner and an outer belt separated by the Pieniny Klippen Belt (PKB). The Inner Carpathians formed in the Cretaceous by thick-skinned stacking of nappes comprising the basement of the ALCAPA and Tisza–Dacia blocks as well as their Permian–Cretaceous sedimentary cover (Csontos and Vörös, 2004; Schmid et al., 2008). The Outer Carpathians are a thin-skinned accretionary prism, which developed from the Oligocene to the late Miocene and are composed of flysch nappes derived from the Carpathian embayment (Slaczka, 2005). In Ukraine, most of the thick-skinned inner Carpathian units are covered by the Neogene volcanics that erupted on the edge of the Pannonian Basin; they only crop out in a limited area next to the border with Romania. The PKB is the outermost unit of the Inner Carpathians outcropping in Ukraine. The PKB was thrust onto the Outer Carpathians

(Figure II.1) during early to middle Miocene convergence (Castelluccio et al., 2016). Whether the PKB accommodated strike-slip motion and/or back thrusting during the emplacement of the Inner Carpathians in Poland is debated (Ratschbacher et al., 1993; Nemčok et al., 2006; Castelluccio et al., 2016). The Ukrainian Carpathians mainly expose the outer flysch nappes of the belt (Figure II.1), which consist of a series of thin thrust sheets that contain Cretaceous to Miocene mostly deep-water clastic sediments. These outer nappes were accreted northeastward and then thrust onto the East European Platform during the early to middle Miocene (Figure II.1c). Each nappe groups several units that display similar sedimentary sequences and share the same décollement horizon (Figure II.2).

Convergence and accretion of the Carpathian wedge are thought to have started in the Oligocene in Ukraine, when the innermost nappes of the Outer Carpathians were integrated into the accretionary wedge (Gagała et al., 2012; Nakapelyukh et al., 2018). Total convergence in the Ukrainian Carpathians is around 340 km according to balanced cross-section restoration (Nakapelyukh et al., 2018). Low-temperature thermochronology data combined with balanced cross-sections have been interpreted to record two phases of shortening in Oligocene–Miocene times, as well as out-of-sequence thrusting in both the Western and Eastern Carpathians (Matenco et al., 2010; Merten et al., 2010; Mazzoli et al., 2010; Castelluccio et al., 2016; Nakapelyukh et al., 2018). These studies postulate a slower convergence phase before the emplacement of the outer Carpathian nappes onto the European Platform, followed by a rapid middle to late Miocene shortening phase with out-of-sequence thrusting during collision. In the Ukrainian Carpathians, the slow convergence phase took place from the middle Oligocene to the early Miocene (~32 to ~20 Ma). The subsequent rapid contraction phase occurred from the early to middle Miocene, with an estimated shortening rate of ~21 km Myr^{-1} (Nakapelyukh et al., 2018). The deformation of the inner Carpathian nappes provoked contraction in the adjacent basins and propagating thrusts scraped off sediment sheets from the down-going plate, imbricating them into the wedge. It is estimated that the Ukrainian Carpathians became quiescent at ~12 Ma, when roll-back of the European slab and foreland propagation of thrusting ended in the region (Nemčok et al., 2006).

Present-day surface heat flow in the Ukrainian Carpathians, the Pannonian back-arc basin, and the European foreland is well constrained. Heat flow in the Pannonian Basin is about 90–100mWm^{-2}, with the highest values recorded close to the Carpathian volcanic arc (Pospíšil et al., 2006). Heat flow diminishes across the fold-and-thrust belt from ~80mWm^{-2} at the contact with the innermost nappes to values between 40 and 70mWm^{-2} within the outer nappes (Pospíšil et al., 2006). It is possible that middle Miocene calc–alkaline volcanic intrusions adjacent to the inner nappes, emplaced between 13.8 and 9.1 Ma (Seghedi et al., 2001), provided a transient source of heat, although given the small dimension of the region affected (Horváth et al., 1986), this post-collisional volcanism is unlikely to have had a major impact on heat flow at a regional scale, in line with inferences for the Transylvanian back-arc basin in Romania, just to the south of our study area (Tiliță et al., 2018).

Another source of transient heat during emplacement of the Carpathian nappes may have been back-arc extension and asthenosphere upwelling under the Pannonian Basin between 19 and 15 Ma (Tari et al., 1992; Horváth and Cloetingh, 1996). However, Andreucci et al. (2015) showed that heating associated with Pannonian Basin extension did not affect the Carpathian nappes: low-temperature thermochronology and vitrinite reflectance data indicate a maximum paleotemperature of 170 °C for the inner part of the wedge, with temperatures decreasing from the middle part of the wedge towards the Pannonian Basin. Well data indicate present-day geothermal gradients in the Skyba nappe ranging from

20 to 24°C km^{-1} (Kotarba and Kołtun, 2006), in broad agreement with the values obtained in external domains of other mountain belts (e.g., Husson and Moretti, 2002). Because tectonic reconstructions of the belt at crustal and lithospheric scale indicate a cylindrical structure (Docin, 1963; Vashchenko et al., 2006; Gerasimov et al., 2005; Matskiv et al., 2008, 2009), we suggest that an average present-day near-surface geothermal gradient of 25°C km^{-1} may be extrapolated to the entire Carpathian wedge. However, a range of near-surface processes can distort the thermal field in orogenic domains. These include, in particular, the topography that imposes an irregular thermal boundary condition, heat advection in areas undergoing sustained erosion, and, conversely, the blanketing effect in domains with rapid sedimentation (e.g., Husson and Moretti, 2002). Because data are scarce, the magnitude of these perturbations and the associated uncertainties can only be inferred indirectly. Nevertheless, expected sedimentation and erosion rates as well as durations in the region are sufficiently low (<1 $mm.yr^{-1}$, Shlapinskyi 2007; Shlapinskyi, 2015; Figure II.2) to only perturb the thermal regime by a maximum of 10% to 15% (Husson and Moretti, 2002). Considering the present-day reference value, this implies that the geothermal gradient could have varied within an approximate range of 22 to 28 °$C.km^{-1}$. Thermo-kinematic models could help alleviate this uncertainty, but for the current study, we deem 25°C km^{-1} to be a reasonable estimate.

3 Stratigraphy of the Ukrainian Carpathians

As mentioned above, the Ukrainian Carpathians consist of a number of nappes or thrust sheets, which are differentiated based on their position, stratigraphy, and tectonic evolution (Sandulescu, 1988; Slaczka, 2005; Oszczypko, 2006). Whereas the stratigraphy of each nappe is to some degree distinct, there are some overarching similarities. Broadly speaking, the Carpathian embayment originated as a passive margin basin, subdivided by several mostly submarine ridges (known as cordilleras). Changes in sedimentation patterns in the adjacent parts of the Carpathian embayment indicate that these ridges were periodically uplifted during convergence, possibly by long-distance transfer of compressive stresses (Poprawa and Malata, 2006; Oszczypko, 2006). As all the nappes are derived from the Carpathian embayment, their stratigraphic relations retrace the convergence and evolution of the Ukrainian Carpathian wedge before and during accretion. Figure II.2 depicts the stratigraphy of the units containing our samples and other units useful for further interpretations. It is mainly based on Ukrainian geological maps (Docin, 1963; Vashchenko et al., 2006; Gerasimov et al., 2005; Matskiv et al., 2008, 2009) with some exceptions specified below.

In the study region, the Magura nappe (including the Marmarosh domain, following Oszczypko et al., 2005) contains mostly Paleogene sediments, starting with thin-bedded Paleocene flysch followed by an alternation of massive sandstone beds and thin-bedded flysch in the Eocene (Figure II.2). Sedimentation stopped at the Eocene–Oligocene boundary.

The Burkut and Dukla nappes display a very similar stratigraphy from the Lower Cretaceous to the upper Eocene: Early Cretaceous sedimentation started with thin-bedded flysch and limestones as well as some breccia incorporating Jurassic limestones and volcanic rocks. These are followed by sandier deposits in the Upper Cretaceous. In the Paleocene, the sedimentation evolved into a sandy flysch with conglomerate intercalations, followed in the Eocene by thin-bedded flysch varying in thickness

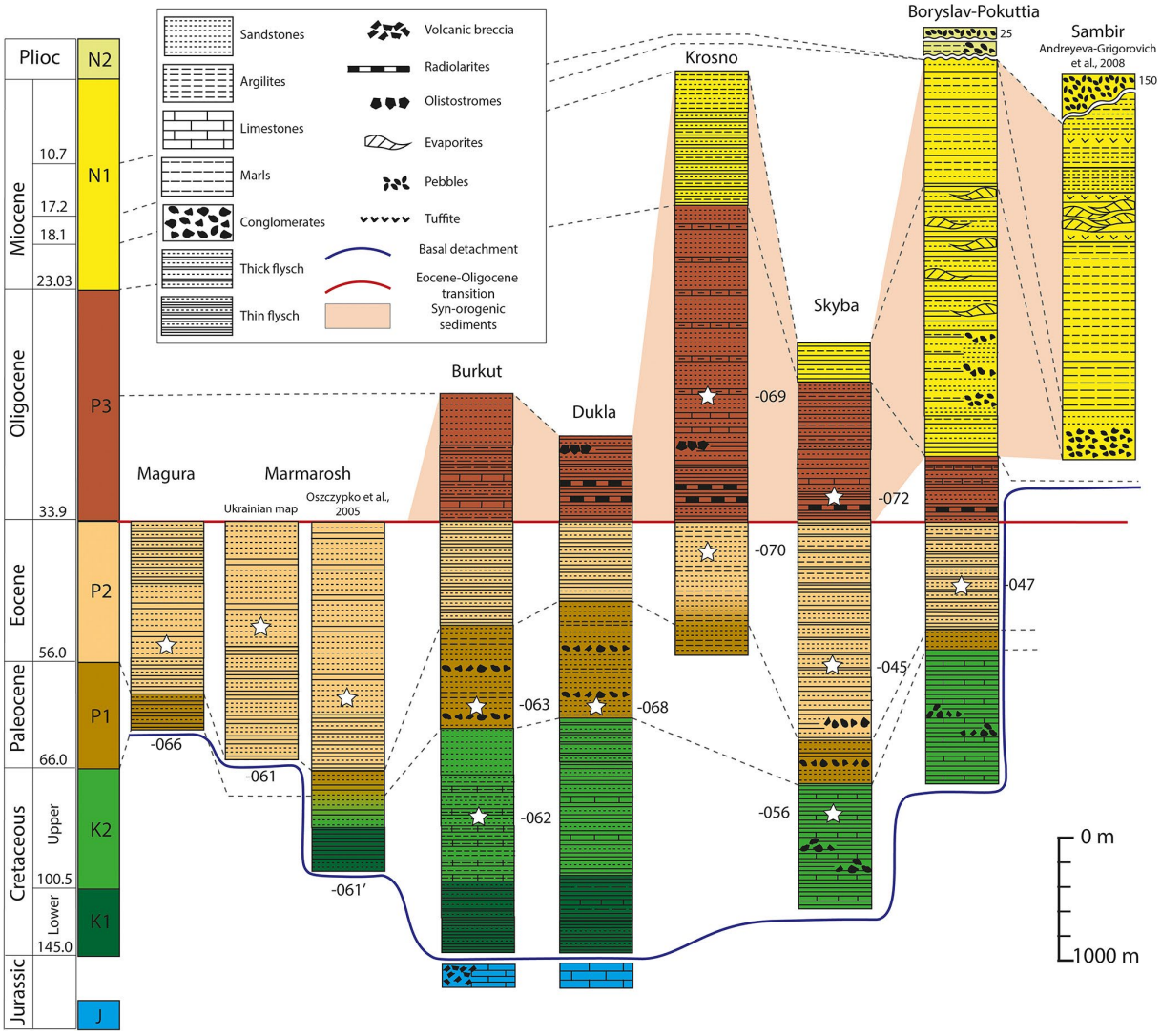

Figure II.2: Regional stratigraphy of the Ukrainian Carpathian nappes, mainly from Ukrainian geological maps (Docin, 1963; Vashchenko et al., 2006; Gerasimov et al., 2005; Matskiv et al., 2008, 2009). Stars mark the sample locations in the nappe stratigraphy; samples are identified by their suffix. The dark blue line marks the décollement horizon of the nappes. Jurassic rocks are integrated in the Burkut and Dukla nappes. Syn-orogenic sediments are indicated in the beige zone, and older deposits are regarded as pre-orogenic. Any syn-orogenic sediments on the Magura and Marmarosh nappes have been eroded. Two interpretations of the stratigraphy are indicated for the Marmarosh nappe: one from the Ukrainian geological map and the other from Oszczypko et al. (2005). The Sambir nappe stratigraphy is after Andreyeva-Grigorovich et al. (2008), adapted to the revised stratigraphic limits of Paratethys stages (Krijgsman and Piller, 2012). The stratigraphic columns depicted here are the closest ones available to the sampling site of each sample. Lateral variations in thickness or nature of deposition within individual nappes are not represented by these logs.

throughout the basin. Oligocene sedimentation started with argillites and limestones evolving into thick-bedded sandstones at the top of the Burkut nappe. The youngest sediments of the Dukla nappe consist of grey flysch with thick-bedded sandstones and radiolarites (known as Menilites beds), as well as olistostromes, all deposited in the Oligocene.

Sedimentation in the part of the basin represented by the Krosno nappe started in the Eocene with thick-bedded flysch. The siliceous Menilites beds, which can be followed throughout the Carpathians, mark the base of the Oligocene and are followed by grey argillites and siltstones. The Krosno beds were deposited from the middle Oligocene to the early Miocene, i.e., up to the regional Eggenburgian stage (~18.1 Ma). This particularly thick unit consists of 2 km of sandy flysch sequences with intercalations of olistostromes, argillites, siltstones, and some calcareous layers.

The following nappe in the pile is the Skyba nappe. It is composed of two depositional subunits, an internal unit with an Oligocene stratigraphy resembling that of the Krosno nappe and an external unit in which Miocene sediments are missing. The oldest sediments in both subunits are dated to the Late Cretaceous and comprise a sequence of thin grey flysch and marl–limestone interbeds with conglomerate lenses. The overlying Paleogene sediments are divided into four suites, alternating between thick-bedded sandstones and thin-rhythmic flysch with conglomerate lenses at the base. These were followed in the Oligocene by the Menilites beds, which evolved into calcareous argillites, grey sandstones with black argillites, and thin sandstones with grey carbonaceous argillites for the internal units. This sequence is topped by Miocene grey argillites with siltstone interbeds deposited until the end of the Eggenburgian (18.1 Ma) in the internal unit. For the external unit, Oligocene deposits, including the Menilites beds, are followed by marls and coarse layered batches of sandstones (Oszczypko, 2006).

Sedimentation in the Boryslav–Pokuttia area began in the Late Cretaceous with argillites intercalated with limestones as well as with some conglomerate lenses. In the Paleocene, thick sandstones were deposited, followed by an Eocene alternation between thin- and thick-bedded flysch deposits. The Oligocene Menilites beds are overlain by sandstones with calcareous siltstones. From the early Miocene to the end of the Eggenburgian, the Boryslav–Pokuttia area accumulated siltstones and clays evolving into thin sandstones, with intercalations of clay. There are also some lenses of conglomerates. A thick layer of argillites and siltstone with lenses of salt was deposited during the Ottnangian (18.1– 17.2 Ma, Figure II.2). After this time, sedimentation extended into the Sambir area; while argillites with thin sandstone interbeds accumulated in the Boryslav–Pokuttia area, conglomerates and sandstones were deposited in the area of the current Sambir nappe (Andreyeva-Grigorovich et al., 2008). Sedimentation stopped at the end of the early Miocene in the Boryslav–Pokuttia area, apart from several tens of meters of conglomerates thought to be Pliocene in age. Thick deposits of clay and marls evolving into tuffites and evaporites accumulated, on the other hand, in the Sambir area during the middle Miocene. Deposition there continued concordantly to the end of the early Sarmatian (10.7 Ma) with grey clays and sandstones with intercalated tuffites. These are overlain discordantly by syn-tectonic conglomerates dated around 9 Ma (Andreyeva-Grigorovich et al., 2008).

In the Ukrainian Carpathians, the middle to late Miocene foredeep is represented by the Bilche–Volytsa Zone, where the oldest sediments are of Badenian age (16–12.65 Ma; Andreyeva-Grigorovich et al., 2008). These show a similar facies as the Badenian deposits of the Sambir nappe, with marls and clays at the base and tuffites intercalated by evaporite layers. Early Sarmatian facies are also similar to those of the

Sambir nappe and constitute the uppermost preserved strata in the foredeep. The more distal foreland deposits are shallower-water equivalents of the foredeep sediments.

4 Methods

4.1 Low-temperature thermochronology

Low-temperature thermochronology can record the thermal evolution of mountain belts and the exhumation of rock in the crust over a large range of temperatures (30–300 °C), corresponding to depths of 1–10 km for an average geothermal gradient (e.g., Ault et al., 2019; Malusà and Fitzgerald, 2019). Here we use apatite fission-track and apatite and zircon (U–Th–Sm) = He low-temperature thermochronometers. These have nominal closure temperatures in the range of 80–120, <80, and <200 °C, respectively, depending on cooling rate, mineral composition, and accumulated α damage (e.g., Ault et al., 2019). When these methods are applied to sedimentary rocks (i.e., in detrital thermochronology), they either record information on the pre-depositional history of the sediments or on their post-depositional burial and subsequent exhumation, depending on the maximum burial temperature experienced by the samples (e.g., van der Beek et al., 2006; Fillon et al., 2013). In a flysch basin, detrital grains are derived from a variety of source rocks and therefore tend to show a wide range of chemical compositions and apparent cooling ages if they were not affected by full thermal resetting during burial heating. Thus, detrital thermochronology potentially allows tracing both the pre- and post-depositional history of the sampled sedimentary rocks if a sufficient number of grains can be analyzed per sample (e.g., van der Beek et al., 2006; Fillon et al., 2013; Malusà and Fitzgerald, 2020). The combined thermochronological data can also be used for thermal history modeling (see Sect. 4.2.1).

4.1.1 Sampling

A total of 14 samples, weighing 3–5 kg each, were collected from sandstones across three transects in the Ukrainian Carpathians (Table II.1). Sampling focused on areas that were not targeted in previous studies (Andreucci et al., 2015; Nakapelyukh et al., 2018), aiming to collect at least one sample per tectonic unit along each transect (Figure II.1). Samples were crushed and sieved, after which apatite and zircon were separated from other minerals with standard heavy liquid and magnetic separation techniques. Apatite grains were hand-picked under the microscope for subsequent apatite fission-track (AFT) and apatite (U–Th–Sm) = He (AHe) dating. Zircon (U–Th–Sm) = He (ZHe) dating was performed on the same samples. Most samples yielded sufficient apatite and zircon grains for all three analyses, but in some of the samples, one or two of the analyses were not possible (Table II.1).

Table II.1: Sample locations and characteristics

Sample	latitude °N	longitude °E	elevation m	Lithology	Tetonic unit	Stratigraphic age Ma	Thermochronometers
CAR19-045	47.9417	25.14956	731	coarse sandstone	Skyba	Lutetian-Bartonian (47.8-37.8)	AFT, AHe, ZHe
CAR19-047	48.3108	25.07353	366	greenish sandstone	Boryslav-Pokuttia	Ypresian (56-47.8)	AHe, ZHe
CAR19-056	48.806	23.79279	626	grey sandstone	Skyba	Upper-Cretaceous (96-66)	AFT, AHe, ZHe
CAR19-061	48.29	23.38376	223	fine, light grey sandstone	Marmarosh	Bartonian-Priabonian (41.2-33.9)	AFT, AHe, ZHe
CAR19-062	48.4893	23.27509	293	fine, light grey sandstone	Burkut	Cenomanian-Turonian (100.5-89.9)	AFT, AHe, ZHe
CAR19-063	48.5132	23.31984	455	grey sandstone	Burkut	Danian-Ypresian (65.8-47.8)	AFT, AHe, ZHe
CAR19-066	48.8085	22.44757	248	white sandstone	Magura	Lutetian-Bartonian (47.8-37.8)	AFT, AHe, ZHe
CAR19-068	48.957	22.61442	296	yellowish sandstone	Dukla	Campanian-Maastrichtian (83.6-66)	AFT, AHe, ZHe
CAR19-069	48.9759	22.8041	460	yellowish sandstone	Krosno	Aquitanian (27.8-23.03)	AFT, AHe, ZHe
CAR19-070	49.1321	23.03773	708	yellow sandstone	Krosno	Eocene (56-33.9)	AFT
CAR19-072	49.3612	23.01119	387	grey sandstone	Skyba	Rupelian (33.9-27.8)	AFT, AHe, ZHe

4.1.2 Fission-track thermochronometry

A total of 11 samples were prepared for AFT thermochronometry at the Geo-Thermo-Chronology platform of ISTerre, Grenoble (France), using the external detector method (Hurford and Green, 1982). Apatite crystals were mounted in resin, polished and etched with a 5.5M HNO^3 solution at 21 °C during 20 s, and attached to a mica detector. The mounted apatite crystals were irradiated at the Oregon State University Triga reactor (USA). A total of 10 samples contained sufficient countable grains for statistically meaningful dating; AFT ages were only calculated for samples with more than 30 counted grains. Three Durango and three Fish Canyon Tuff standards were used to determine a α-calibration value (Hurford and Green, 1983) of 28212 yr cm^2 for MR. Etch-pit width (Dpar) measurements were made on each analyzed grain in order to determine compositional variations in the apatites, which are known to have an influence on their kinetics (e.g., Carlson et al., 1999; Sobel and Seward, 2010).

4.1.3 (U–Th–Sm) = He thermochronometry

Sample	grains	ρ_s	N_s	ρ_i	N_i	ρ_d	$P(\chi^2)$	Dispersion	Central age	2 σ	U	TLn	MTL	Std	Dpar	Dpar err
		10^5 cm^{-2}		10^5 cm^{-2}		10^5 cm^{-2}		%	Ma		ppm		µm		µm	
CAR19-045	75	4.23	1371	18.30	5926	10.80	<<1	48	39.4	6.0	25.0	13.0	11.8	2.3	2.0	0.9
CAR19-056	61	5.03	1230	34.50	8450	10.59	<<1	53	20.3	3.6	49.0	10.0	13.1	2.3	1.7	0.7
CAR19-061	81	4.83	1535	15.50	4937	10.49	<<1	39	47.5	6.6	22.0	21.0	10.8	1.7	1.5	0.8
CAR19-062	67	1.90	488	18.70	4796	10.39	<<1	29	15.9	2.4	27.0	-	-	-	1.7	0.9
CAR19-063	67	1.45	350	16.60	3999	10.29	<<1	41	15.0	2.8	24.0	3.0	12.0	4.0	1.4	1.0
CAR19-066	68	6.55	1247	23.80	4528	10.19	<<1	47	41.1	6.6	35.0	10.0	10.2	2.2	1.5	1.0
CAR19-068	81	1.99	607	25.80	7875	10.09	<<1	25	11.1	1.52	38.0	3.0	8.5	1.6	1.5	1.0
CAR19-069	97	2.53	950	24.10	9043	9.98	<<1	62	16.0	2.8	36.0	9.0	10.5	2.8	1.6	0.6
CAR19-070	31	3.53	360	15.70	1605	9.88	<<1	65	28.1	8.2	24.0	1.0	8.5	0.0	1.5	0.6
CAR19-072	61	2.41	532	15.10	3337	9.78	<<1	59	21.7	4.6	23.0	2.0	13.7	1.2	1.5	0.8

Table II.2: Apatite fission-track data. ρ_s: spontaneous track density; N_s: number of spontaneous tracks counted in the sample; ρ_i: induced track density; N_i: number of induced tracks counted on the mica-detector; ρ_d: dosimeter track density; $P(\chi^2)$: Chi-square probability that the sample contains a single age population, U: Uranium content; TLn: number of track lengths measured; MTL: Mean track length; Std: standard deviation of track lengths measurement; Dpar: mean Dpar value for the sample; Dp err: mean error on the Dpar measurement.

Fracture- and inclusion-free apatite and zircon grains were picked under a microscope; their size was measured and their shape recorded. Of the 11 samples considered, 10 contained apatite and zircon suitable for (U–Th–Sm) = He dating, with one to five single grains of apatite and/or zircon per sample dated (Tables II.3 and 4). ^{4}He concentrations were measured at the University of Potsdam (Germany): crystals were encapsulated and heated by a laser to extract ^{4}He; after mixing with a known amount of purified ^{3}He gas, the gas mixture was analyzed in a quadrupole noble gas mass spectrometer. The crystals were dissolved and their U, Th, and Sm content determined by ICP-MS (inductively coupled plasma mass spectrometry) at the German Research Centre for Geosciences (GFZ), Potsdam (Germany), following the methodology of Galetto et al. (2021) and Zhou et al. (2017). AHe and ZHe ages were corrected for α ejection using the methods outlined by Ketcham et al. (2011).

Sample	grain	U	Th	Sm	eU	He	ESR	Ft	Uncorrected age	2 σ	Ft corrected ages
		ppm	ppm	ppm	ppm	nmol/g	mm		Ma	Ma	Ma
CAR19-045	045-a1	7.6	18.6	16.5	12.0	0.4	69.08	0.78	6.4	0.2	8.2
	045-a2	4.5	36.1	13.1	13.0	0.9	61.57	0.76	12.9	0.5	17.0
	045-a3	10.4	68.2	24.8	26.4	1.1	88.23	0.83	7.6	0.2	9.2
CAR19-047	*047-a1*	*9.4*	*2.1*	*60.8*	*9.9*	*0.0*	76.87	*0.80*	*0.1*	*0.1*	*0.1*
	047-a2	25.3	31.6	17.6	32.7	1.4	88.18	0.83	7.9	0.1	9.5
CAR19-056	056-a1	24.7	78.8	48.6	43.2	1.7	60.46	0.75	7.4	0.2	9.8
	056-a2	44.7	180.3	22.7	87.1	3.4	65.99	0.77	7.1	0.2	9.2
	056-a3	136.8	194.4	60.3	182.5	6.6	59.30	0.75	6.7	0.1	8.9
CAR19-061	061-a1	4.4	28.1	41.0	11.0	0.7	54.91	0.73	10.6	0.8	14.6
	061-a2	6.6	13.6	23.1	9.8	0.6	62.88	0.76	11.3	0.5	14.8
	061-a3	14.6	5.5	9.1	15.9	1.8	60.81	0.75	20.3	0.7	27.0
CAR19-062	062-a1	12.0	44.8	22.1	22.5	4.0	74.63	0.80	32.8	0.6	41.1
	062-a2	11.0	89.0	4.1	31.9	1.4	62.89	0.76	8.2	0.4	10.7
	062-a3	*1.8*	*45.5*	*5.4*	*12.5*	*0.2*	71.08	*0.79*	*2.7*	*0.1*	*3.5*
CAR19-063	063-a1	5.9	18.7	3.8	10.3	0.4	68.43	0.78	7.3	0.3	9.3
CAR19-066	066-a1	44.9	128.4	6.8	75.1	4.2	70.34	0.79	10.2	0.2	13.0
	066-a2	29.2	22.1	21.6	34.4	8.0	67.91	0.78	42.9	0.7	55.0
	066-a3	7.5	41.7	12.3	17.2	0.6	54.01	0.72	6.5	0.5	9.1
CAR19-068	068-a1	16.0	387.7	52.7	107.1	2.9	63.10	0.76	5.0	0.2	6.6
	068-a2	22.4	291.8	39.1	91.0	2.8	67.40	0.78	5.6	0.3	7.2
	068-a3	27.6	345.9	44.9	108.9	3.2	61.67	0.76	5.4	0.1	7.1
CAR19-069	069-a1	34.9	116.2	7.5	62.2	3.2	68.52	0.78	9.5	0.1	12.2
	069-a2	59.7	242.4	26.5	116.7	5.0	80.53	0.72	7.9	0.1	11.0
	069-a3	37.6	82.8	44.5	57.1	3.5	77.18	0.81	11.1	0.2	13.8
CAR19-072	072-a1	7.6	22.9	11.7	13.0	1.0	66.55	0.77	14.2	0.6	18.4
	072-a2	35.0	5.1	21.8	36.2	4.6	72.61	0.79	23.5	0.3	29.6

Table II.3: Apatite (U-Th-Sm)/He data. Ages in italics are considered outliers and were not used in the models and for interpretations. eU: equivalent Uranium content; ESR: equivalent spherical radius; 2σ: weighted 2σ analytical uncertainty from analysis of age standards.

Table II.4: Zircon (U-Th-Sm)/He data. Ages in italics are considered outliers and were not used in the models and for interpretations. eU: equivalent Uranium content; ESR: equivalent spherical radius; 2σ: weighted 2σ analytical uncertainty from analysis of age standards

Sample	grain	U	Th	Sm	eU	He	ESR	Ft	Uncorrected age	2 σ	Ft corrected ages
		ppm	ppm	ppm	ppm	nmol/g	mm		Ma	Ma	Ma
CAR19-045	*045-z1*	*2.3*	*28.6*	*0.7*	*9.0*	*0.9*	*79.5*	*0.80*	*19.2*	*0.6*	*24.2*
	045-z2	*0.8*	*5.3*	*0.3*	*2.0*	*0.1*	*57.6*	*0.77*	*8.5*	*2.4*	*11.0*
	045-z3	483.7	74.9	0.6	501.4	704.9	83.6	0.85	254.9	2.3	298.5
CAR19-047	047-z1	66.0	62.8	0.4	80.8	164.9	105.4	0.88	367.3	2.6	417.4
	047-z2	54.1	73.8	0.7	71.5	71.4	61.4	0.79	182.6	4.7	229.1
CAR19-056	056-z1	52.3	77.3	0.5	70.5	150.2	55.4	0.77	383.1	15.7	491.7
	056-z2	*2.4*	*70.1*	*2.5*	*18.8*	*1.2*	*70.8*	*0.81*	*11.8*	*0.8*	*14.6*
	056-z3	98.8	123.4	1.0	127.8	259.7	80.9	0.84	365.9	4.8	432.3
	056-z4	41.8	25.5	0.2	47.7	71.8	72.1	0.83	272.8	3.3	328.7
CAR19-061	061-z1	212.4	61.2	0.3	226.8	111.2	60.4	0.80	90.3	0.8	113.2
	061-z2	274.9	132.0	0.6	306.0	121.2	67.0	0.81	73.0	0.9	89.6
	061-z3	345.3	74.8	0.6	362.9	135.8	64.1	0.79	69.0	0.8	87.0
	061-z4	853.2	260.8	1.3	914.4	364.2	61.9	0.80	73.4	0.5	91.6
	061-z5	111.5	43.8	0.6	121.7	63.2	65.6	0.81	95.5	1.2	117.6
CAR19-062	062-z1	47.0	35.7	0.3	55.4	31.6	66.8	0.81	104.6	1.4	128.6
	062-z2	204.8	190.1	2.5	249.5	120.6	61.9	0.79	88.9	1.8	112.4
	062-z3	74.6	111.8	0.4	100.8	58.3	72.2	0.82	106.1	1.3	128.7
	062-z5	167.8	55.6	0.5	180.9	87.9	56.6	0.78	89.4	1.5	114.0
CAR19-063	063-z1	39.9	51.4	0.2	52.0	20.9	76.5	0.83	73.8	0.8	89.0
	063-z2	65.1	39.8	0.1	74.5	40.6	68.3	0.81	100.3	1.0	123.5
	063-z3	144.9	55.9	0.2	158.1	95.2	106.2	0.88	110.7	2.2	125.5
	063-z4	534.8	60.5	0.5	549.0	411.5	55.1	0.78	137.4	1.6	175.9
	063-z5	372.9	197.6	3.1	419.3	165.8	39.1	0.69	72.8	1.2	105.1
CAR19-066	066-z1	211.9	35.0	0.7	220.1	98.5	64.4	0.81	82.4	1.3	101.8
	066-z2	115.1	184.1	1.1	158.4	86.4	83.3	0.84	100.2	1.7	118.9
	066-z3	125.5	140.1	1.5	158.4	190.9	44.8	0.72	219.4	3.7	300.7
	066-z4	272.4	34.4	0.5	280.5	85.3	56.7	0.78	56.2	0.7	71.6
	066-z5	24.6	23.1	0.3	30.0	12.5	67.6	0.81	76.4	1.3	94.6
CAR19-068	068-z1	227.7	135.7	0.6	259.6	307.2	65.5	0.81	215.4	2.4	265.1
	068-z2	737.8	141.3	1.2	771.0	522.2	66.8	0.81	124.3	1.6	152.2
	068-z3	132.6	26.8	0.2	138.9	146.8	72.7	0.83	192.7	1.8	231.6
CAR19-069	069-z1	106.0	12.6	0.1	109.0	99.3	59.3	0.79	166.6	2.2	209.2
	069-z2	124.5	67.4	0.3	140.3	58.5	57.8	0.79	76.9	1.5	97.7
	069-z3	124.3	93.5	0.8	146.3	39.9	60.7	0.79	50.4	0.6	63.4
	069-z4	126.2	87.3	0.3	146.7	68.4	62.3	0.80	85.9	1.4	107.2
	069-z5	*0.7*	*8.6*	*2.9*	*2.7*	*0.5*	66.0	*0.80*	*34.5*	*1.8*	*43.4*
CAR19-072	072-z1	405.6	120.0	0.6	433.8	185.5	58.6	0.79	78.8	0.8	99.6
	072-z2	*0.5*	*3.4*	*2.1*	*1.3*	*0.8*	*60.1*	*0.78*	*105.5*	*4.0*	*135.0*
	072-z3	495.9	266.7	3.4	558.5	516.8	62.6	0.80	169.1	2.4	210.3

4.2 Time–temperature models and tectono-stratigraphic analysis

4.2.1 Thermal history modeling

We modeled the time–temperature (T-t) pathways constrained by one or more samples for each of the nappes using the QTQt (version 5.8.0) code (Gallagher, 2012), which employs a Markov chain Monte

Carlo inversion method. Inputs for the modeling consisted of our ZHe, AHe, and AFT dates, Dpar values, and depositional ages, as well as a limited number (<20 per sample) of fission-track lengths and angles to the c axis. We used the diffusion model of Gautheron et al. (2009) for AHe and that of Guenthner et al. (2013) for ZHe, as well as the multi-kinetic annealing model of Ketcham et al. (2007) for AFT. For all models we explore a temperature range of 0–300 °C and a time range of 350–0 Ma. We included a maximum of two constraints when exploring the T-t space: (1) samples should reside at surface temperatures (5±5 °C) at the depositional age of their host sediment, and (2) we imposed a 150±50 °C temperature constraint at 150±50 Ma for the samples belonging to the Magura, Burkut, and Dukla units. The latter was applied to force a (partial) reset of the ZHe system in these units before calculation of the burial temperatures after deposition, i.e., the scenario that best complies with our thermochronological results (see below). Inversions were run with 100 000 models for the burn-in and 150 000 models for the post-burnin phases. Model outcomes include a probability field for the range of thermal histories explored as well as several alternative "best-fit" models: the maximum likelihood model is the one that fits the input data the best out of all the burn-in and post-burn-in models, while the "maximum post" model is the post-burn-in model that best fits the data; both may show unwarranted structure, however (Gallagher, 2012). We therefore prefer the "expected" model, which reflects the average of all the tested models, weighted by posterior probability, and its 95% credibility interval to indicate the most probable thermal history recorded by our samples.

4.3 Tectono-stratigraphic analysis

The stratigraphy of the wedge (Figure II.2) contains important information on the pre-, syn-, and post-orogenic evolution of the Ukrainian Carpathians: the age, thickness, lithology, depositional environment, and provenance of the corresponding sediments provide insight into the former topography and tectonic activity in the region. To complete the post-depositional thermal history, we therefore compiled sedimentary burial diagrams for each sampled unit using the stratigraphy published on the 1 V 200000 scale geological maps of the Ukrainian Carpathians (Docin, 1963; Vashchenko et al., 2006; Gerasimov et al., 2005; Matskiv et al., 2008 and 2009), which is compiled in Figure II.2. It is notoriously difficult to date flysch deposits, which contain reworked fauna, and deformation complicates stratigraphic measurements in the wedge. Keeping this in mind, the stratigraphic data nevertheless provide a useful complement to the thermochronological results. The burial diagrams in Figures II. 6 to 9 indicate to which minimal depth samples were buried by sediment accumulation and when the sedimentation rates in the area of the future nappe changed; they also provide a maximum age for cessation of sedimentation. Combined with the thermal history models, this information allows discriminating sedimentary from tectonic burial and tracking the full burial–exhumation cycle for each nappe. As we are mainly interested in the timing and amount of maximum burial, we made no attempt to correct the burial curves for compaction effects. Sedimentary thicknesses shown in Figure II.2 are averaged for each tectonic unit, resulting in some uncertainty in the thickness of the sedimentary overburden for our samples that can be substantial and increases with progressive burial.

5 Results

5.1 Apatite fission-track ages

AFT data are reported in Table II.2 and Figure II.3. All samples are characterized by significant age dispersion and $P(\chi^2)$ values close to zero, indicating that they contain multiple age populations. This may be explained by inheritance of a wide variety of detrital grains in our sandstone samples in combination with partial resetting as a result of relatively low temperatures experienced since deposition. In our dataset, samples CAR19-056, CAR19-062, CAR19-063, and CAR19-068 appear to be relatively close to full resetting, as nearly all single-grain ages are younger than the depositional age (Figure II.3). The rest of the samples contain a large proportion of grains that are significantly older than, or in the range of, the depositional age. When dealing with significantly dispersed single-grain ages such as here, central ages (Figure II.3, CA) are not geologically meaningful. We therefore used the RadialPlotter program (Vermeesch, 2009) to determine major grain age components (peaks) by applying the mixture modeling algorithm of Galbraith and Green (1990) and determining the minimum age (Galbraith and Laslett, 1993) for each sample. Between one and three age peaks were detected in our AFT age distributions (Figure II.3). The youngest peak (P1) generally overlaps within error with the calculated minimum age component (Figure II.3). Minimum ages for samples from the Magura nappe (CAR19-061, CAR19-066) range from 24.0±3.3 to 31.0 ±3.7 Ma, indicating cooling of this nappe before the Miocene (Figure II.3). Samples CAR19-062, CAR19-063, and CAR19-068 from the Burkut and Dukla nappes are strongly reset and have very similar minimum ages of 11.0±3.0, 11.0±1.5, and 10.0±1.5 Ma, respectively (Figure II.3). These minimum ages are also similar to the 11.0±0.9 Ma minimum age of sample CAR19-069 from the adjacent Krosno nappe, which is partially reset. The minimum age of sample CAR19-070, which derives from a more external position on the Krosno nappe, is 13.0±4.4 Ma. Samples CAR19-045 and CAR19-056 from the Skyba nappe display minimum ages of 21.0±2.4 and 16.1±1.0 Ma, respectively, the latter being strongly partially reset. Sample CAR19-072, which comes from the same nappe, shows a younger but less precise minimum age of 12.0±6.6 Ma. In summary, the Magura nappe has partially reset populations with Oligocene minimum AFT ages, and the Burkut and Dukla nappes have strongly partially reset age distributions with late Miocene minimum ages, whereas the Krosno and Skyba nappes have partially reset age populations, with minimum ages that generally fall into the early to middle Miocene, except for the innermost part of the Krosno nappe, which has a late Miocene minimum age, more similar to the Burkut and Dukla nappes.

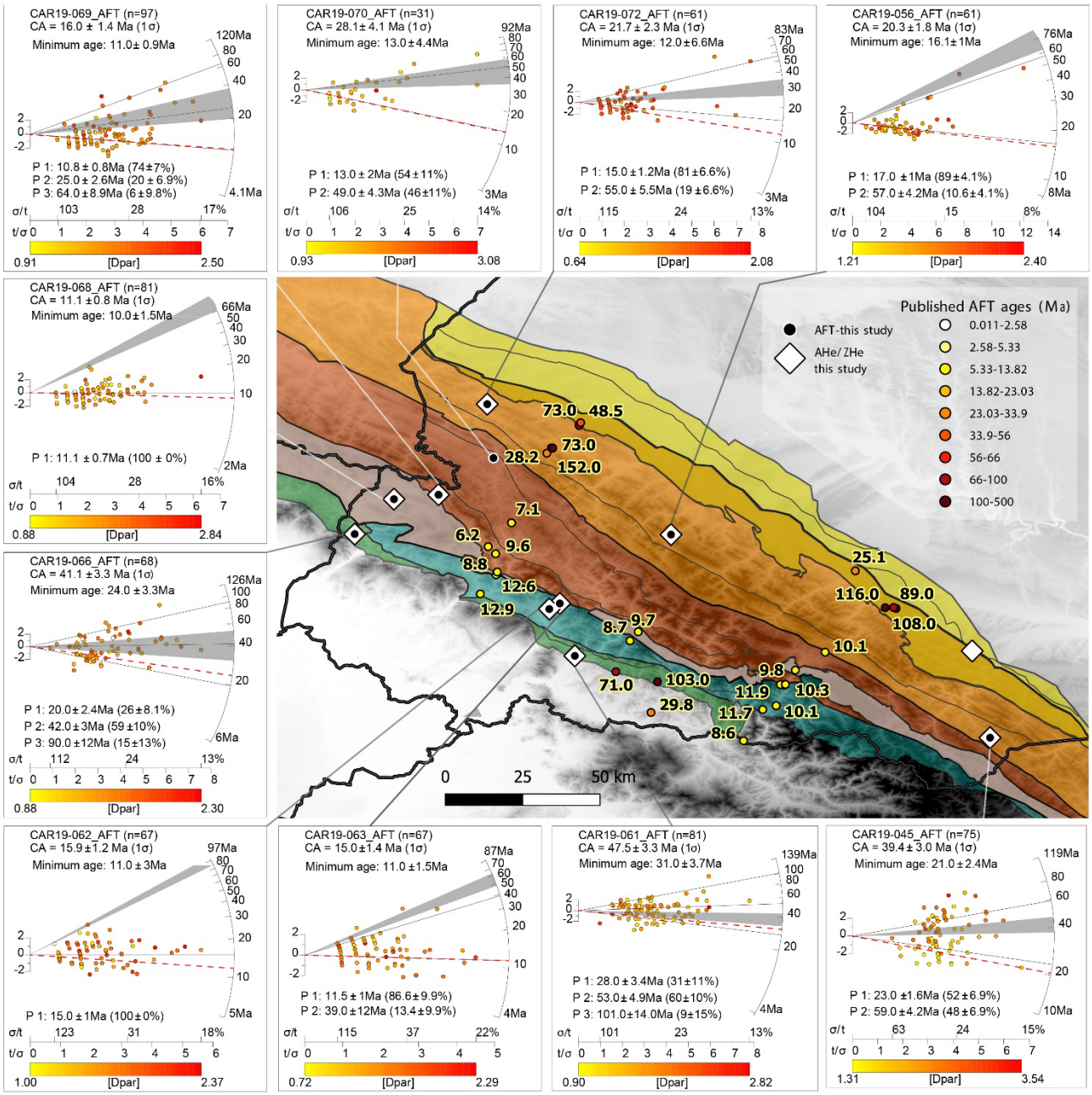

Figure II.3: AFT data from this study shown as radial plots (centred on the central age, which is reported below the sample code as CA); individual single-grain ages in radial plots are coloured according to Dpar value. Grey band in radial plots indicates depositional age, dashed lines are different age populations (P1, P2, etc.); red dashed line is minimum age. Coloured circles on map show AFT central ages from previous studies (Nakapelyukh et al., 2017, 2018; Andreucci et al., 2013, 2015). Base map shows different nappes, with colour scheme as in Figure II.1.

5.2 Apatite (U–Th–Sm) = He ages

AHe data are reported in Table 3 and Figure II.4. Whereas some samples (CAR19-056, CAR19-068, CAR19-069) show overlapping middle to late Miocene single-grain AHe ages, most samples have widely dispersed ages without a clear correlation with effective uranium content (eU) or grain size (Table S1 in the Supplement). Although this is to be expected in detrital samples in which grains are characterized by differences in size, eU, as well as pre-depositional thermal history (e.g., Fillon et al., 2013), there are a few single-grain ages that need to be treated with caution. We suspect He loss to have caused anomalously young single-grain ages in samples CAR19-047 and CAR19-62 (Table 3), which we do not consider further. Older AHe ages are to be considered taking into account partial resetting of the AHe system, given the potentially large diversity of radiation damage, grain size, and pre-depositional history. This can be the case for samples CAR19-061, CAR19-062, CAR19-066, and CAR19-072, which all have grains with either Paleogene or Miocene AHe ages. We find a relatively large spread of AHe single-grain ages in the Magura and Burkut nappe samples (CAR19-061, CAR19-066, CAR19-062, and CAR19-063). In contrast, samples from the Dukla, Krosno, and Skyba nappes, with the exception of CAR19-072, show less AHe age dispersion. If we do not take into account the AHe ages that are older than the minimum AFT ages of the respective samples and are therefore clearly partially reset, we find two prominent age peaks in our data: one at 13.5±2.0 and one at 8.8±2.0 Ma. These comprise 70% of the data.

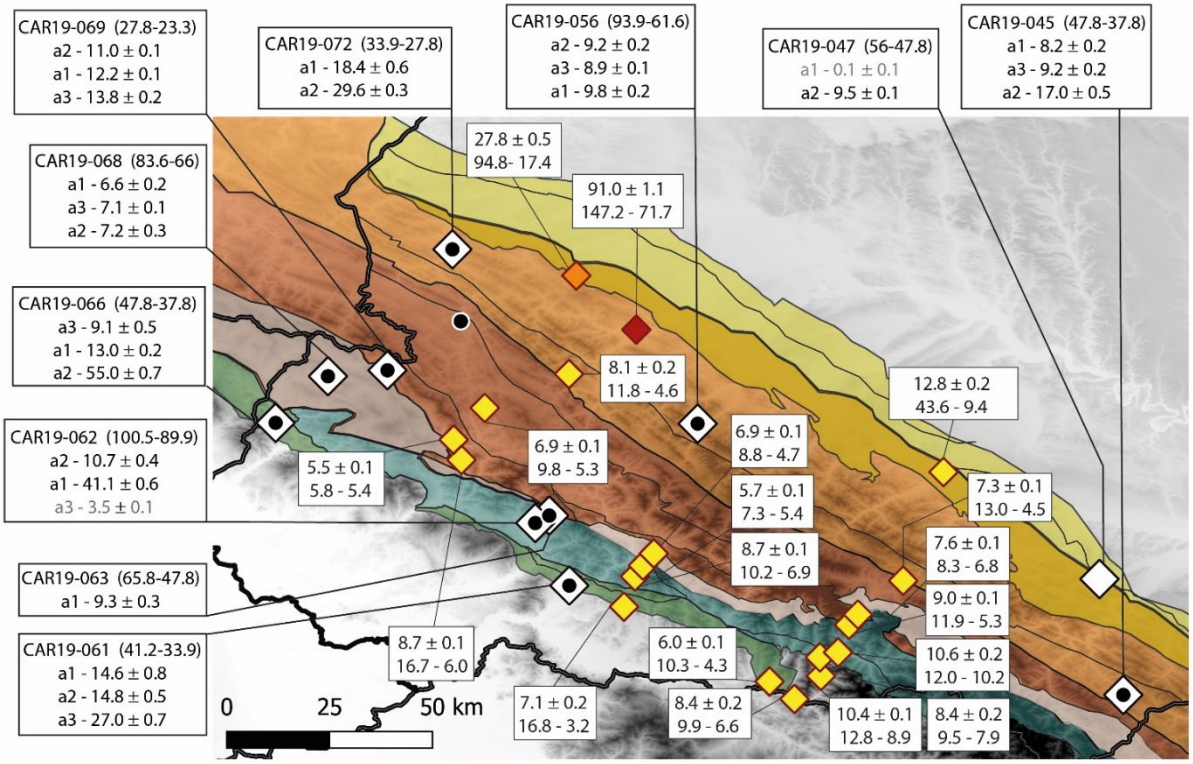

Figure II.4: Apatite (U-Th)/He ages in the Ukrainian Carpathians. Symbols and colour scale for the data are as indicated in Figure II.3. Single-grain ages, corrected for α-ejection, from this study are detailed next to the map frame (numbers in parentheses next to sample code denote the depositional age range). Previously published data (Andreucci et al., 2013, 2015; Merten et al., 2010) are reported on the map as the average age and associated uncertainty, with maximum and minimum single-grain ages below. Ages in grey are interpreted to be outliers and are not used in the models or in our interpretations.

5.3 Zircon (U–Th–Sm) = He ages

Zircon (U–Th–Sm) = He data are reported in Table 4 and Figure II.5. All but three of the single-grain ages are older than the depositional age of the samples and thus non-reset. Single grain ages show little correlation with eU or grain size (Figure II.A1). The three grains with young ZHe ages (two in sample CAR19-045 and one in CAR19-056) also have suspiciously low U and Th contents and anomalous U=Th ratios (Table 4). A grain from sample CAR19-069 has a ZHe age that is only slightly older than the depositional age and similar characteristics, while a grain from sample CAR19-072 also has very low U and Th content, even though its ZHe age is significantly older than the depositional age. We do not include these grains in our further discussion. Two clear populations of ZHe ages can be discerned in the remaining grains: 60–130Ma ZHe ages were obtained from samples from the inner nappes (Magura–Marmarosh, Dukla, Burkut, Krosno) and 230–450 Ma ZHe ages from the outer nappes (Skyba, Boryslav–Pokutia). Because the ZHe ages are demonstrably non-reset, these age groups likely relate to different provenance areas for the detrital zircons in these units.

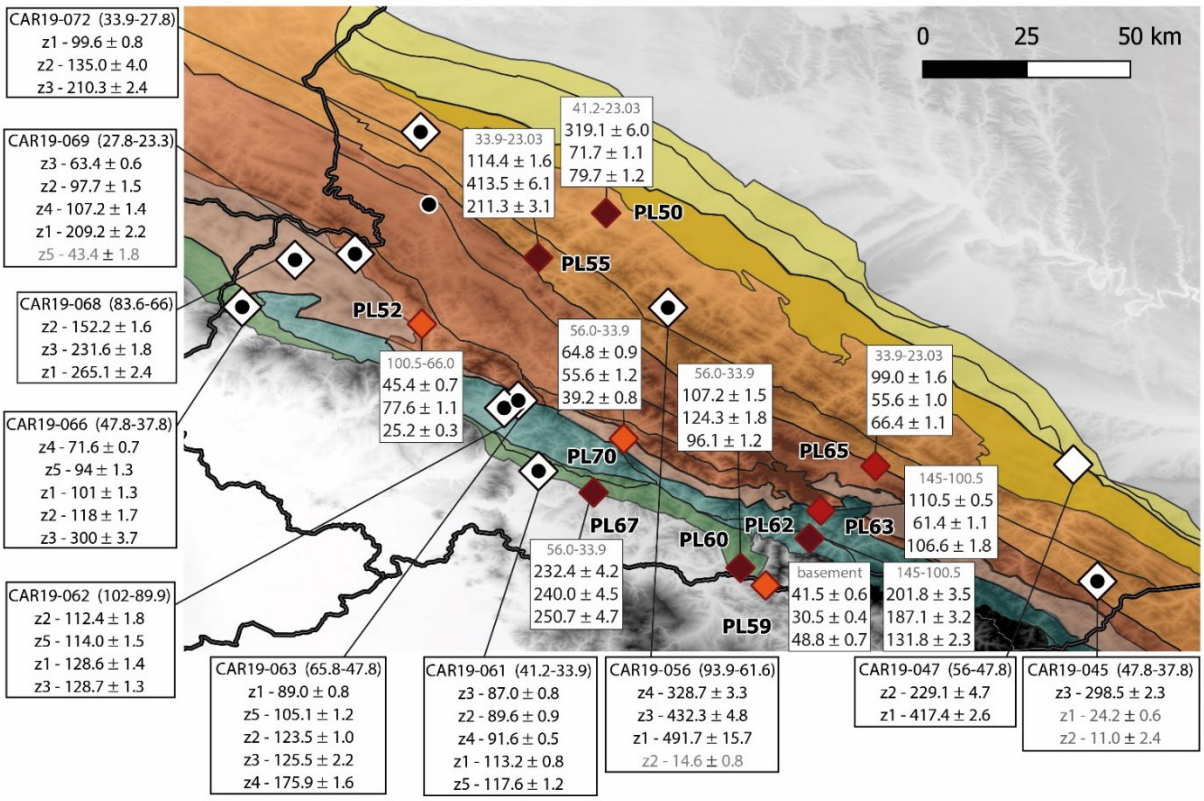

Figure II.5: Zircon (U-Th)/He ages in the Ukrainian Carpathians. Symbols and colour scale for the data are as indicated in Figure II.3. Single-grain ages, corrected for α-ejection, from this study are detailed next to the map frame (numbers in parentheses next to sample code denote the depositional age range). Previously published data (Andreucci et al., 2015) are reported on the map as follow: -depositional age range, - average age and associated uncertainty, - maximum single-grain age, - minimum single-grain age. Ages in grey are interpreted to be outliers and are not used in the models or in our interpretations.

5.4 Thermal history models and tectono-stratigraphy

We modeled time–temperature histories for eight samples and briefly summarize the results below, going from the internal to the external nappes. The depositional age of sample CAR19-066, from the Magura nappe, is Lutetian–Bartonian (48–38 Ma; Matskiv et al., 2008). After deposition, it underwent 800 ± 400m of sedimentary burial until the end of the Eocene (34 Ma). Thermal history modelling indicates that the sample reached its peak temperature of 85–105 °C around 24–18 Ma, i.e., more than 10 Myr after the end of sedimentation in this area (Figure II.6). The sample subsequently cooled at a constant rate until the present day. There are two interpretations of the stratigraphy of the laterally equivalent Marmarosh nappe (see Oszczypko et al., 2005; Matskiv et al., 2009), which influences the inferred amount of burial but not the depositional age of the corresponding sample CAR19-061. After deposition in the Bartonian–Priabonian (41–34 Ma), the sample underwent 800 ± 200m of pre-Oligocene burial according to the geological map (Matskiv et al., 2009), whereas 500m of additional sedimentary burial is inferred based on the Oszczypko et al. (2005) stratigraphy (Figure II.6). Time–temperature modelling of sample CAR19-061 suggests rapid syn- and postburial heating to a peak temperature of 85–

100 °C, which was reached around 31–29 Ma, with continuous cooling at a constant rate starting 4 Myr after sedimentation ended. Next in the direction of vergence of the belt is the Burkut nappe, from which samples CAR19-062 and CAR19-063 were modeled (Figure II.7). Sample CAR19-062 has a Cenomanian–Turonian depositional age (102–89 Ma) and shows a long burial phase under a total of 4000–5000m of sediment (Matskiv et al., 2009); sedimentation in this area ended in the mid-Oligocene (ca. 28 Ma). Thermal history modeling reveals a correspondingly long heating phase, with the peak temperature between 105 and 125 °C being reached around 40 Ma. The onset of cooling is difficult to pinpoint exactly for this sample, but the 95% credible intervals of the expected model show a clear cooling step at ~17.5 Ma. Subsequent cooling was intermittent, with a possible acceleration after 10 Ma (Figure II.7). Sample CAR19-063 has a Danian–Ypresian (65.8–47.8 Ma) depositional age and was buried under 2000–3000m of sediment until the mid-Oligocene (ca. 28 Ma; Matskiv et al., 2009). Thermal history modeling indicates that sample CAR19-063 reached a maximum temperature of 110 to 155 °C at 23–18Ma and began cooling immediately after. Cooling possibly slowed down at around 10 Ma. Sample CAR19-068 was modeled to retrieve a thermal history for the Dukla nappe (Figure II.8). After deposition in the Campanian–Maastrichtian (83.6–66 Ma), ~3000m of sediments accumulated on top of the sampled sandstone until the mid-Oligocene (ca. 28 Ma; Matskiv et al., 2008). Thermal history modeling indicates that heating lasted some 8 Myr longer; the sample reached a peak temperature of 100 to 130 °C at 13 ± 2 Ma, followed by rapid cooling at a constant rate. Sample CAR19-069 is from the Krosno nappe and was deposited in the Chattian (28–23 Ma). It was subsequently rapidly buried under an overburden of 2500 ± 500 m. Sedimentation in this area terminated in the early Miocene (Eggenburgian; 18 Ma; Matskiv et al., 2009). Thermal history modeling indicates that the peak temperature of 115 °C was reached shortly after (17 Ma), followed by continuous and rapid cooling. The outermost nappe for which we derived thermal history models is Skyba. Sample CAR19-045 was deposited in the Lutetian–Bartonian (48–38 Ma; Vashchenko et al., 2006) and accumulated an overburden of 1700 ± 400m of sediments until the Burdigalian, when sedimentation stopped. Thermal history modeling retrieves a most likely onset of burial heating at 45 Ma and a maximum temperature of 85–100 °C that was reached at 12 ± 1 Ma (Figure II.9). Subsequent cooling was rapid and continuous until the present. Sample CAR19-056 was deposited in the Turonian–Danian (94–62 Ma; Docin, 1963) and accumulated 4000–5000m of sediment until the early Miocene (Eggenburgian, 18 Ma). Thermal history modeling reveals both syn- and post-depositional heating from 68 to 16 Ma up to a maximum temperature of 120 °C, followed by rapid and continuous cooling to the present.

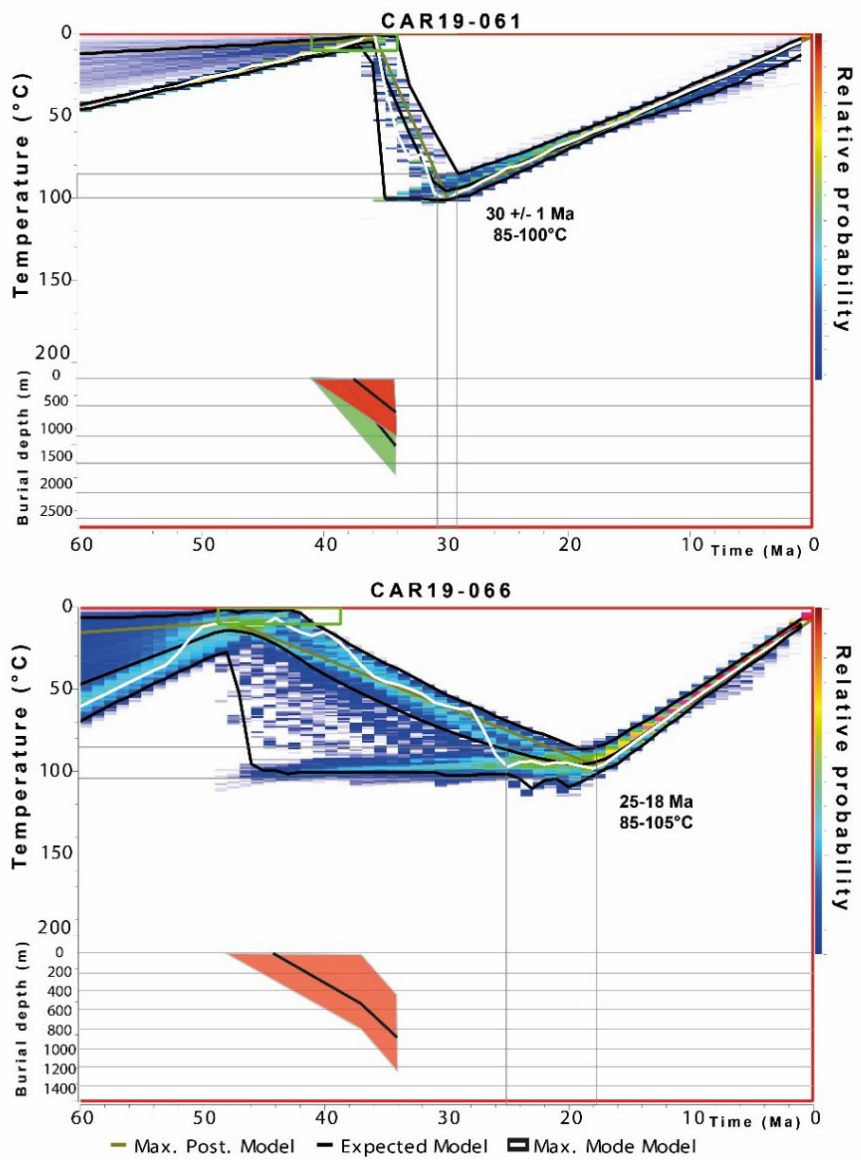

Figure II.6: Modelled thermal histories and associated burial diagrams for samples CAR19-061 and -066 from the Marmarosh and Magura nappes, respectively. For sample CAR19-061, burial diagrams are shown both for the stratigraphy from the Ukrainian geological map (orange) and the revised stratigraphy proposed by Oszczypko et al. (2005; green) as shown in Fig. 2. Peak burial temperature and time are highlighted by grey boxes.

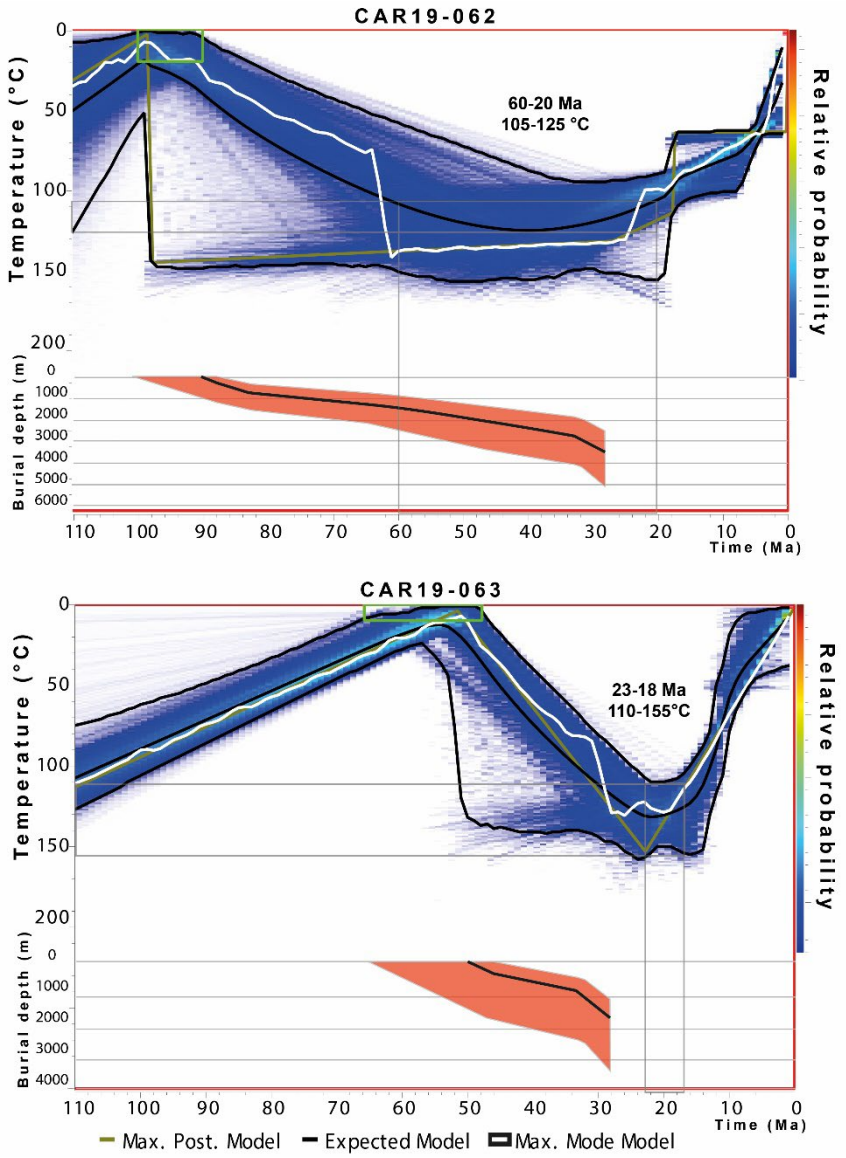

Figure II.7: Modelled thermal histories and associated burial diagrams for samples CAR19-062 and 063 from the Burkut nappe. Peak burial temperature and time are highlighted by grey boxes.

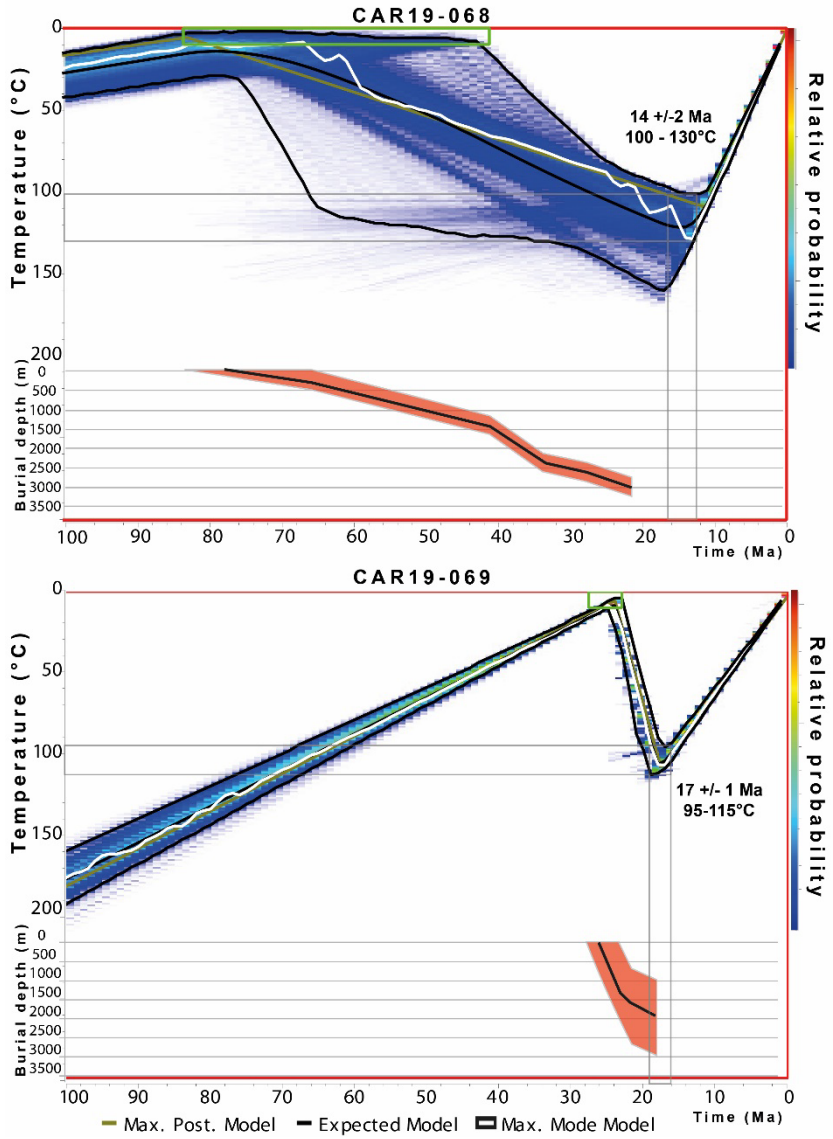

Figure II.8: Modelled thermal histories and associated burial diagrams for samples CAR19-068 and 069 from the Dukla and Krosno nappe, respectively, and associated burial diagrams. Peak burial temperature and time are highlighted by grey boxes.

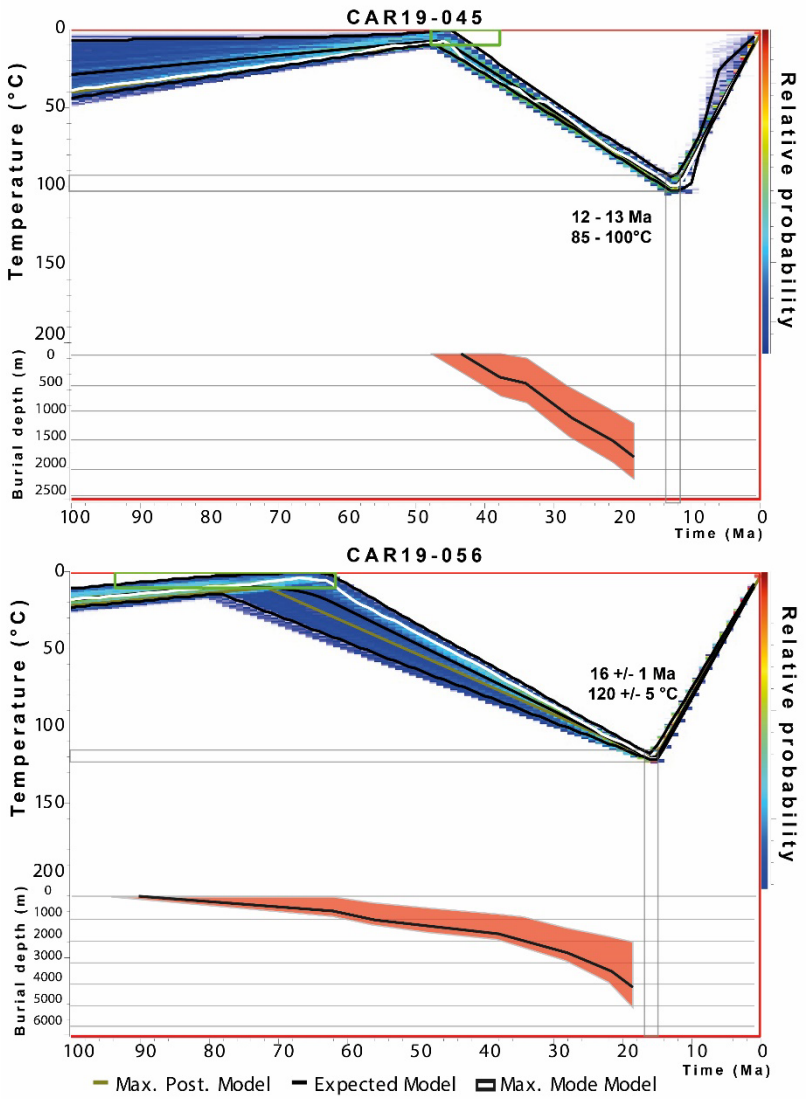

Figure II.9: Modelled thermal histories and associated burial diagrams for samples CAR19-045 and -056 from the Skyba nappe and associated burial diagrams. Peak burial temperature and time are highlighted by grey boxes.

6 Interpretation and discussion

6.1 Burial and exhumation pathways in the Ukrainian Carpathians

The burial diagrams and time–temperature models for the various nappes of the Ukrainian Carpathians obtained in our study provide enhanced insight into the evolution of the orogenic wedge. For several of our samples (CAR19- 045, CAR19-061, CAR19-066, CAR19-063, and CAR19-069), the peak temperature encountered during burial is very high when compared to the temperatures that would result from sedimentary overburden alone. Moreover, some samples show continued heating after sedimentation had terminated, requiring another process to explain this additional heating. We identify two ways in which this additional heating may be explained: first, part of the sediment column of the nappes may

have been eroded during the evolution of the wedge, which would imply that our burial diagrams are truncated and that heating due to sedimentary burial was more intense and continued for longer than we can determine. However, the nappes are internally deformed, so it is unlikely that none of the corresponding sediments would have been preserved in the cores of synclines or under intra-nappe thrusts. The only sediments likely to have been completely eroded are wedge-top deposits that may have accumulated unconformably on top of each of the nappes. There is some evidence that these existed in the form of the unconformable Radych conglomerate in the Ukrainian Carpathians (Andreyeva-Grigorovich et al., 2008) or the 850m thick Comane¸sti piggyback basin in Romania (Dumitrescu et al., 1962). However, accommodation space on the wedge top was probably too limited to explain the observed magnitude of additional heating (corresponding to additional burial of up to 2 km; Figure II.10). A second and more likely explanation for the additional heating is tectonic burial. In this scenario, the sedimentation rate first accelerated as the thrust front propagated over the basin (as shown by several of the burial diagrams; Figures II. 6–9) and then stopped when the site was overthrust by the advancing wedge. The absence of shallow-water facies at the top of the sedimentary column of all but the outermost two nappes (which contain sediments that were deposited on thicker crust) suggests that most of the nappes were overthrust in a deep-water environment. We infer from this observation that sedimentation did not end due to a lack of accommodation space. While we cannot exclude the possibility that part of the original sediment column has been eroded, we consider the observed additional heating to be due to tectonic burial. The amount of additional heating, as well as the time lag between the end of sedimentation and the onset of cooling, reflects the relative importance of tectonic thickening due to thrusting and surface erosion in thin-skinned fold-and-thrust belts (Husson and Moretti, 2002; Ehlers and Farley, 2003; Ter Voorde et al., 2004). To estimate how much tectonic burial a sample underwent, we used a geothermal gradient of 25 °C.km^{-1} for the evolving wedge, as justified in Sect. 2. This allows us to translate the modeled time–temperature paths based on the thermochronological data into depths of burial. We note that this approach neglects heat advection and blanketing effects during burial and exhumation. Inferred cooling rates for our samples are all ≤10 °Myr^{-1}, leading to maximum exhumation rates of 400 m.Myr^{-1} using the estimated geothermal gradient (see above). Maximum burial rates are significantly lower than that at <200 m.Myr^{-1} for all samples and in the range 50–70 m.Myr^{-1} for most of them. Such burial and exhumation rates, combined with a detachment depth of 10–15 km (Figure II.1), are not expected to significantly perturb the conductive thermal structure of the fold-and-thrust belt (Husson and Moretti, 2002; Braun et al., 2006). However, the inferred 15% uncertainty in the geothermal gradient (Sect. 2) would lead to a similar relative uncertainty in burial depths. The evolving topography of the wedge could also have affected the thermal structure recorded in particular by the low-temperature AFT and AHe thermochronometers (e.g., Braun et al., 2006). As the topographic evolution of the Ukrainian Carpathians is currently unconstrained, we neglected this effect. The resulting burial and exhumation paths are thus first order approximations of the evolution of the wedge. The amount and timing of sedimentary burial, as derived from the nappe stratigraphy, are indicated in the burial diagrams. The amount and timing of tectonic burial can thus be found by subtraction of this amount from the maximum burial inferred from the time–temperature path. The results are shown in Figure II.10. As seen in the regional cross-section in Figure II.1, internal thrusting affects each nappe; thus, the time–depth model represents only a particular internal thrust slice. Nevertheless, we consider the entire nappe to have behaved more or less according to the thermal models. Finally, assuming that

cooling of the sample from the maximum depth of burial to the present-day surface occurred by erosional unroofing, exhumation rates can be calculated for the different nappes of the wedge. This also allows calculation of the total amount of eroded sediment per nappe. Modeled thermal histories can thus be interpreted in terms of sedimentary and/or tectonic burial and subsequent exhumation of the nappe (or unit) they belong to. We use the expected model as the reference for all interpretations of sample pathways. Interpretation of the modeled thermal histories provides information on the evolution of the Ukrainian Carpathian wedge and highlights the different stages of tectonic burial and final exhumation of the wedge (Figure II.10). The Magura and Marmarosh nappes were accreted at approximately 34 Ma and had a stage of tectonic burial that lasted until 30 Ma in the SE (CAR19-061) and until 20 Ma in the NW (CAR19-066) of our study area. Overthrusting led to 2.5–3.0 km of tectonic burial in addition to the prior sedimentary burial. Subsequent exhumation amounted to 4 km at rates of 0.12–0.14 and 0.16–0.22 km.Myr^{-1}1, respectively. Accretion of the Burkut nappe occurred at 28 Ma for both samples (CAR19-063 and CAR19-062) and tectonic burial brought them to 5.0 and 5.5 km depth, respectively. The following exhumation stage occurred in two phases: a first phase between 18 and 10 Ma and a second phase after 10 Ma. The two samples from this nappe have different exhumation rates before 10 Ma (0.22 km.Myr^{-1} for CAR19-062 and 0.40 km.Myr^{-1} for CAR19-063); however, this difference may be linked to the lack of time constraints on the peak burial and the initiation of the exhumation stage (especially for CAR19-062), as the timing of the peak temperature directly impacts the exhumation rate estimate, which is interpolated from this peak to the next inflexion point of the cooling path. However, the post-10 Ma exhumation rate is 0.3 km Myr^{-1} for both samples and the thickest overburden (up to 5.5 km) was eroded from this nappe. The Dukla nappe shows a long tectonic burial stage from 28 to 14 Ma and started exhuming later than the Krosno and Skyba nappes, which are in a more external position. This timing suggests out-of-sequence thrusting in the Dukla nappe, in line with inferences by Roure et al. (1993). Exhumation of the Dukla nappe started around 12 Ma and occurred at a rate of 0.38 km Myr^{-1}. The samples of the Krosno nappe (CAR19-069) and the northwestern part of the Skyba nappe (CAR19-056) display very similar thermal histories, with a stage of tectonic burial (i.e., accretion) starting at 18 Ma, preceded by rapid syn-orogenic sedimentation on the Krosno nappe (Figure II.2; Shlapinskyi, 2015; Nakapelyukh et al., 2018). Exhumation of these nappes started not long after at 17 and 16 Ma, respectively. The southeastern part of the Skyba nappe (sample CAR19-045), on the other hand, continued its tectonic burial until 12 Ma. Exhumation rates for the Krosno and Skyba nappes were around 0.3–0.4 km Myr^{-1}, and 4–5 km of overburden was removed at a significantly higher rate than that of the Burkut and Dukla nappes. We have no thermal history models for the Boryslav–Pokuttia and Sambir nappes due to their much lower heating, which is below the level of AFT partial annealing. However, deposition in the Boryslav–Pokuttia area continued until 17.2 Ma (Andreyeva-Grigorovich et al., 2008), while AHe data indicate exhumation at 12.8–9.5 Ma. We thus observe an apparent increase in exhumation rates from the inner to the outer nappes in our models. However, this could simply be related to the later time of peak burial in the outer nappes, as the lack of track length measurements lowers the resolution of the thermal history at shallow depths, potentially failing to resolve earlier exhumation to the surface of samples in the inner nappes.

6.2 Evolution of the Ukrainian Carpathian wedge

Our combined tectono-stratigraphic and thermochronological analysis allows us to identify several sedimentary and tectonic events and to retrieve the activity of Ukrainian Carpathian wedge over time. We outline and discuss our main observations of the different stages below. Several of the burial diagrams show an increase in sedimentation rate just before the corresponding part of the antecedent basin was accreted into the wedge (Figure II.10). Such increasing sedimentation rates are expected in a pro-foreland basin adjacent to an approaching frontal thrust (Naylor and Sinclair, 2008), as has also been suggested for the Polish Carpathians (Poprawa et al., 2002; Oszczypko, 2006). In the Magura area, sedimentation rates increased in the early to middle Eocene, especially in the Marmarosh Unit, until the end of the Eocene (Figure II.2). In the Burkut and Dukla areas, the youngest sediments preserved are middle Oligocene in age; the approach of the active front toward the Burkut and Dukla areas is reflected by a coarsening of the grain size and the occurrence of olistostromes in the flysch, without a marked acceleration of the sedimentation rate. In the Krosno nappe, the 2 km thick Krosno beds show a rapid increase in sedimentation rate within the basin starting in the late Oligocene, probably due to high sediment supply from the internal Carpathians, uplifted as a result of the growing wedge. Sedimentation in the proximal units of the Skyba area was similar to the Krosno area, with Oligocene sandstones and Miocene syn-orogenic sediments. Miocene layers are absent from the more distal units of the Skyba nappe, where the stratigraphic successions ends with late Oligocene sediments, possibly because of erosion of the overlying strata or because the external part of the nappe was uplifted while it started to overthrust the Boryslav–Pokuttia area at this time (see Nakapelyukh et al., 2018). The Boryslav–Pokuttia and Sambir nappes preserve the majority of their Miocene deposits, with levels of sandstones and olistostromes followed by evaporite lenses and fossil-rich clays, marking the evolution toward a shallow marine environment in front of the wedge in the middle Miocene (Figure II.2). We observe diachronous building of the wedge with periods of increased tectonic activity. For the Magura nappe, the onset of accretion occurred at 34 Ma and exhumation was between 30 and 22 Ma, coeval with the accretion of the Burkut and Dukla nappes (around 28–22 Ma). Exhumation of the Burkut nappe started immediately afterwards at ca. 20 Ma (Figure II.7), and the next nappes in line, Krosno and Skyba, were being accreted at 18 Ma. Tectonic burial was very rapid for the Krosno nappe and exhumation started very shortly afterwards (ca. 16 Ma), whereas it occurred later, at around 12–8 Ma, for the Skyba nappe (Figures II. 8 and 9). Out-of-sequence thrusting in the wedge also occurred during this period, with the onset of exhumation in the Dukla nappe at 14 Ma (Figure II.8). In this scenario, the rapid middle to late Oligocene sedimentation in the Krosno area can be linked to the onset of Carpathian wedge growth and related erosion of the Inner Carpathians. Exotic pebbles of granite, amphibolite, gneiss, and limestone as well as large blocks of mafic volcanics are only found in the Burkut nappe and in the internal part of the Dukla nappe in mid-Cretaceous strata, which suggests that a ridge-like basement high was located in the Carpathian embayment in the vicinity of these nappes (Shlapinskyi, 2007; Nakapelyukh et al., 2017, 2018). It has been suggested that the arrival of the basement high at the subduction zone may have disrupted the propagation of the wedge and led to the formation of duplexes and out-of-sequence thrusting in the Dukla nappe (Roure et al., 1993). This may also have led to the markedly increased sediment flux to the Krosno area from the Oligocene onward. The basement high might correspond to a southeastward extension of the Polish Silesian ridge or a branch

of it known as the Bukowiec ridge in the vicinity of the Ukrainian border (Oszczypko, 2006). Apart from some minor Pliocene conglomerates, the youngest deposits within the Boryslav–Pokuttia nappe are dated to 17.2 Ma (Figure II.2), with local pockets of sediment only present in the most external parts of the nappe dated at 13.5 Ma (Andreyeva-Grigorovich et al., 2008). This absence of younger sediments indicates that most of the nappe was tectonically buried just after 17.2 Ma, while syn-tectonic deposition continued locally, in particular on the more external parts of the nappe, up to 13.5 Ma. The nappe started exhuming simultaneously with the Skyba nappe, as marked by its late Miocene AHe ages (12.8 ± 0.2 and 9.5 ± 0.1 Ma). Onset of exhumation probably happened when the wedge was thrust over the Sambir area. Badenian (16–12.65 Ma) sediments were found under the Carpathian wedge up to 70 km inward of the frontal thrust (Oszczypko et al., 2006), implying that the Sambir nappe overthrust the foreland by at least this distance after the Badenian. The thrust that delimits the eastern margin of the Sambir nappe, i.e., the Carpathian frontal thrust, crosscuts the early Sarmatian (12.65–11.5 Ma) Dashava formation and therefore must have been active until 11.5 Ma (Andreyeva-Grigorovich et al., 2008). Thrusting ceased afterwards (Nemčok et al., 2006; Nakapelyukh et al., 2018), coincident with the arrival of the wedge at the margin of the rigid East European Platform. Thick-skinned Mesozoic extensional faults on this margin were extensionally reactivated during the Badenian to early Sarmatian phase of wedge propagation and show up to 2.5 km of post middle Badenian offset (Krzywiec, 2001). Rheological variations at the margin of the East European Platform (e.g., elastic thickness varies from 40–80 km; Kaban et al., 2018) and the presence of pre-orogenic faults probably determined the location and magnitude of syn-orogenic extension, which occurred 50–70 km away from the orogenic front (Krzywiec, 2001; Tarapoanca et al., 2003, 2004; Leever et al., 2006). The vertical displacement on the normal faults appears to have been higher in the western part of the Ukrainian foreland, decreasing eastward (Oszczypko et al., 2006). The Badenian–Sarmatian depocenter that developed in the hanging wall of these normal faults (2 km) was subsequently overthrusted by the Sambir nappe.

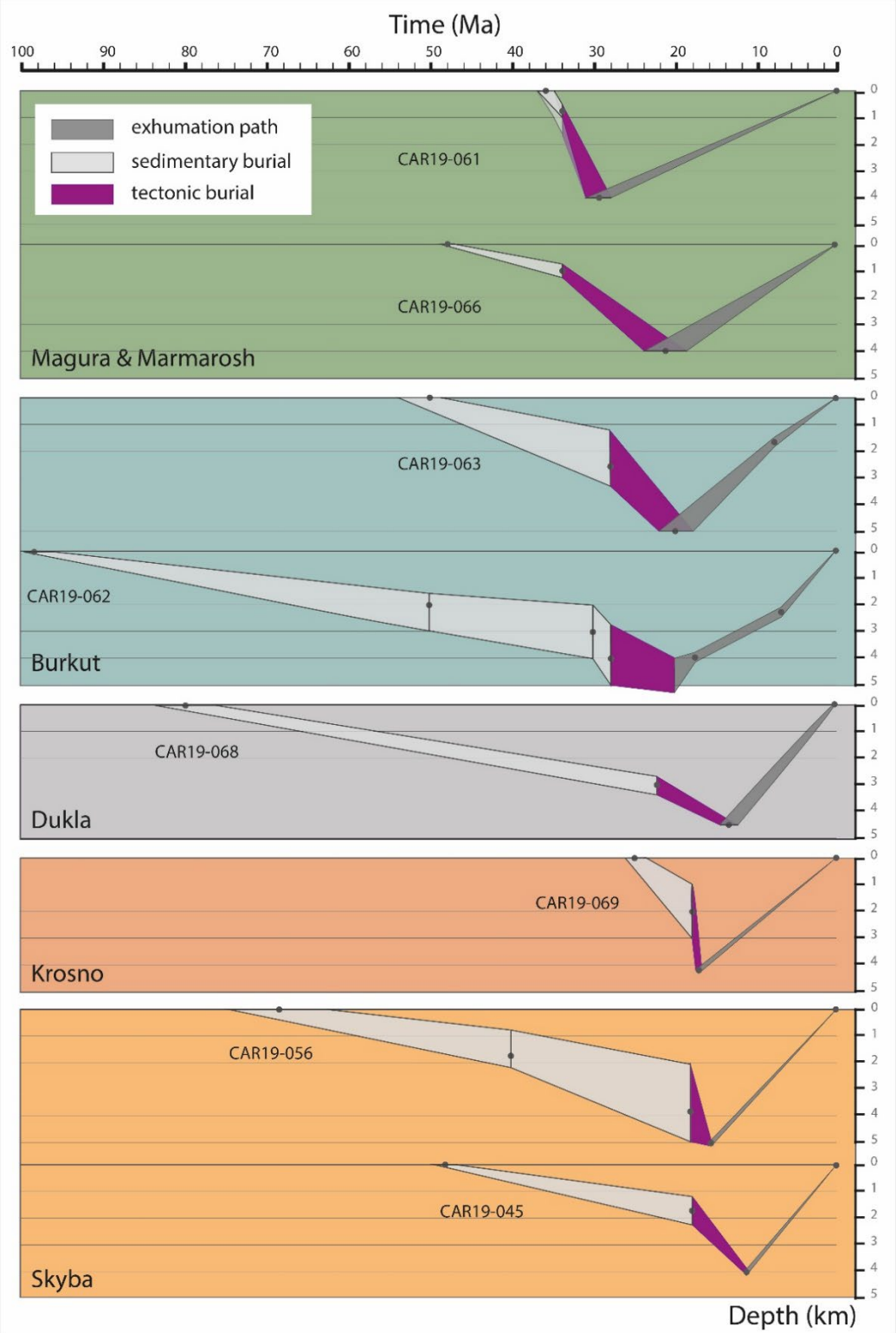

Figure II.10: Time-depth evolution of each sample. The depths of the samples through time was estimated from the burial diagrams and the thermal histories modelled in Figure II.7-10, using a geothermal gradient of 25°C/km. Tectonic burial refers to the accretion and burial by thrusting. Time-depth paths are sorted from the innermost (top) to the outermost sample (bottom) of this study. Box colours represent each tectonic nappe as in Figure II.1.

6.3 Thermochronometric age pattern and wedge dynamics

In line with previous low-temperature thermochronology data (Andreucci et al., 2015; Nakapelyukh et al., 2018), our results indicate partial resetting of the AFT system and fully reset AHe ages in the central nappes (Figure II.11). We find strong partial resetting of the AFT system and full resetting of the AHe system in the Burkut and Dukla nappes, while Andreucci et al. (2015) provided evidence for (strong) partial resetting of the ZHe system in these nappes. In contrast, the AHe and AFT systems are partially reset, and ZHe is nonreset in the innermost Magura nappe. For the more external Krosno and Skyba nappes, AFT samples are variably reset, with less resetting in the outer parts of these nappes. AHe ages, on the other hand, are fully reset in the Krosno nappe. The external part of the Skyba nappe reveals non-reset AHe ages, while the Boryslav–Pokuttia nappe has some reset AHe ages. This pattern of low-temperature thermochronology ages, showing burial heating to maximum temperatures in the core of the wedge (Figure II.11) and decreasing toward both the internal and external limits, is consistent with the exhumation pattern observed in other orogenic wedges including the Olympic Mountains (Brandon et al., 1998; Batt et al., 2001; Michel et al., 2019), Taiwan (Fuller et al., 2006; Beyssac et al., 2007), and the Apennines (Thomson et al., 2010; Erlanger et al., 2022). It also corresponds to the pattern reproduced in several modeling studies of orogenic wedges (Barr and Dahlen, 1990; Batt et al., 2001; Willett and Brandon, 2002). The increasing thermochronometer ages toward the innermost Magura nappe may indicate that the latter acted as a relatively stable backstop (e.g., Brandon et al., 1998) or that the Ukrainian Carpathians constituted an “immature” wedge, where steady state has either not been reached or has not been maintained sufficiently long to exhume reset thermochronometers within the inner wedge (e.g., Willet and Brandon, 2002; Konstantinovskaia and Malavieille, 2005). In a theoretical view of orogenic wedges, the accretion of nappes should decelerate over time; i.e., accretion and frontal thrust propagation should occur with a longer period of quiescence between events as the wedge grows (Naylor and Sinclair, 2007). This does not correspond to our model results. We infer from our time–depth diagrams (Figure II.11) that the accretion–exhumation phases are shorter in the period between 22 and 18 Ma when the main nappes (Burkut, Dukla, Krosno and Skyba) were accreted. The geodynamic context of this orogen may explain the observed discrepancy. In the Carpathians, the main driver of convergence is the retreat of the subduction zone linked to slab roll-back (Royden and Karner, 1984; Royden, 1993a; Wortel and Spakman, 2000; Konecný et al., 2002). Within this context, orogeny is governed by the dynamics of the slab, and therefore we infer that dynamic equilibrium of the orogenic wedge could have been impeded by the competition between the accretion of material and the retreat of the orogenic front due to slab roll-back, allowing no time for topography building, thermal re-equilibration, or internal deformation. In conclusion, the Ukrainian Carpathians record the competition of orogenic wedge growth and subduction retreat by slab roll-back.

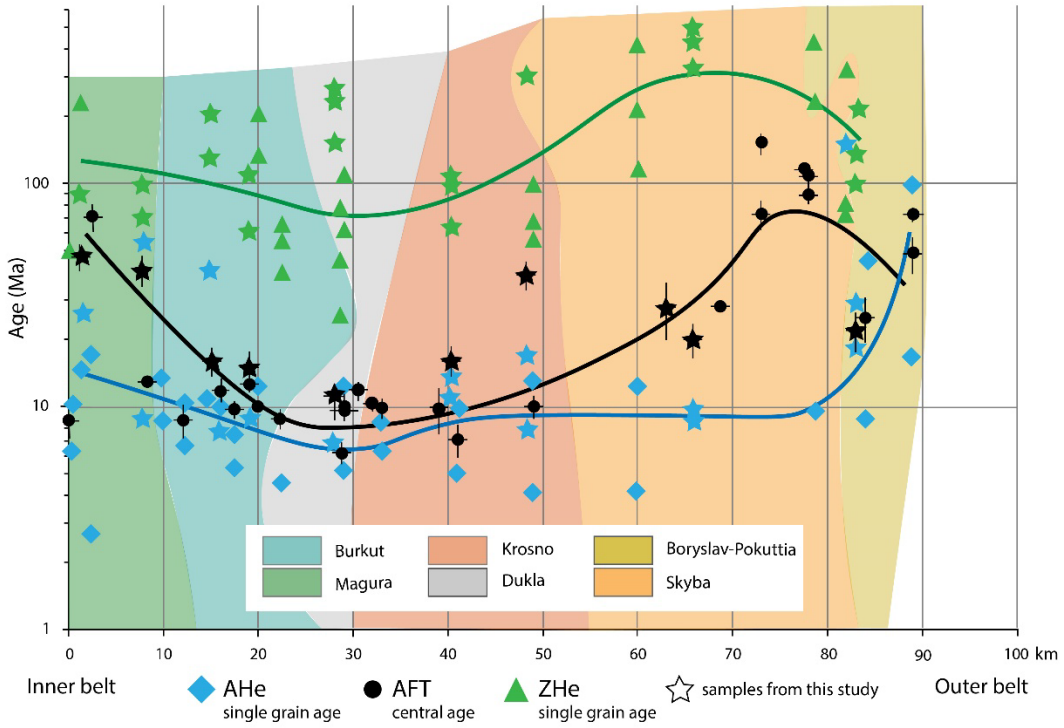

Figure II.11: Distribution of thermochronometer ages across the Ukrainian Carpathians as a function of distance, measured from the inner belt to the outer belt. The figure shows a compilation of previously published ages with symbols according to the system; samples from this study ages are shown with stars. Single-grain AHe and ZHe ages are shown; AFT data are represented as central ages together with the 2σ error. Note that the age axis is logarithmic. Curves outline the overall age pattern.

6.4 Sediment provenance from ZHe ages

While the reset and partially reset AFT and AHe thermochronometers provide insight into the sedimentary and tectonic evolution of the wedge, the non-reset ZHe ages provide insights into the sediment supply to the evolving wedge and its precursor deep-water basin (Figure II.12). ZHe ages of this study can be divided in two groups containing ages of 60–130 and 230–450 Ma. The younger age group is mainly found in the inner nappes (samples CAR19-061, CAR19- 062, CAR19-063; Figures II. 4, 12), while the older ZHe age population (230–450 Ma) is dominant in the outer nappes of the Ukrainian Carpathians (samples CAR19-045, CAR19-047, and CAR19-056; Figures II. 4, 12). Whereas ZHe ages reported by Andreucci et al. (2015) are (partially) reset in the core of the orogenic wedge (i.e., in the Burkut and Dukla nappes), their non-reset ZHe ages from the inner (232–250 Ma) and outer (55 and 413 Ma) parts of the wedge provide useful complementary information about sediment provenance. We interpret the source of the sediment in the inner nappes, characterized by 60–130Ma non-reset ZHe ages, to be the Bucovinian units of the Inner Carpathians (i.e., basement units of the Dacia plate; Sandulescu, 1988; Schmid et al., 2008) and their sedimentary cover. ZFT studies in the infra-Bucovinian units, located in the Maramures mountains, show fully reset ages recording a cooling phase that started in Cenomanian times (100 Ma), with another cooling event in the Coniacian–Campanian (90–72 Ma;

Gröger et al., 2008). Sedimentation in the Bucovinian units stopped in Barremian times (129–125 Ma; Iliescu and Kräutner, 1975), and the onset of thrusting is dated as Aptian–Albian (125–101 Ma) by the discordant deposition of the Wildflysch formation on top of both units (Sandulescu, 1975). For the Bucovinian and sub-Bucovinian units, which structurally overlie the infra-Bucovinian unit, the ZFT system is generally partially reset, depending on the tectonic overburden and stratigraphic position (Gröger et al., 2008). ZFT ages from the Bucovinian units are very similar to our 60–130 Ma ZHe ages for the innermost nappes, suggesting a source–sink relation. The 232–250 Ma ZHe ages present in the dataset of Andreucci et al. (2015) in the internal nappes may, on the other hand, signify that some zircons were derived from Triassic intrusions that are present in the basement of the inner Carpathian units. In line with our results, provenance analysis in the Western Carpathians showed that the Magura nappe received sediments from the inner units (Winkler and Slaczka, 1992). It is well documented that the Silesian, Bukowiec, and Dukla basement highs also supplied sediment to the basin, particularly during the Late Cretaceous and early Paleogene, as demonstrated by crystalline clasts and paleocurrents in the Burkut, Dukla, and Silesian nappes (Oszczypko, 2006). We nevertheless consider it more likely for the zircons with 60–130 Ma ZHe ages to have come from the inner Carpathian basement: supplying zircons with reset ZHe ages from the Dukla ridge would require approximately 6 km of exhumation, which seems unlikely considering that uplift of these ridges occurred due to far-field transmission of compressive stresses related to collision in the Inner Carpathians. Late Cretaceous to early Paleocene ZHe ages (60–130 Ma) are dominant in the Eocene to Oligocene of the Krosno nappe, which points towards an Inner Carpathians sediment source, while the basement high had been overthrust by the wedge by this time. In contrast, pre-Oligocene sediments of the Skyba and Boryslav–Pokuttia nappes exclusively display 230–450 Ma ZHe ages, and we infer that sediments in the outer nappes of the Ukrainian Carpathians were initially sourced from an area without significant exhumation (<6 km) since the mid-Triassic. Within the context of the Carpathians, the East European Craton and the Teisseyre–Tornquist Zone are the most plausible sources for these sediments (Pharaoh, 1999; Oszczypko, 2006; Roban et al., 2020). In the Oligocene sediments of the Skyba nappe, zircons from this older ZHe age population are joined by zircons from the 60–130 Ma ZHe age group, suggesting that, in addition to sediment supply from the East European Platform, the area started to receive sediments from the Inner Carpathians, either directly or recycled from the evolving wedge. Our results are in line with recent provenance analyses of sandstones in the Romanian Carpathians based on detrital zircon U–Pb ages, sedimentology, and petrography (Roban et al., 2020, 2022). These indicate that the Cretaceous sediments of the innermost Ceahlau–Severin and Teleajen nappes were sourced from the Bucovinian Units of Dacia basement, while those from the more external Audia, Tarcau, and Vrancea nappes were sourced from the European foreland (Roban et al., 2020). The Oligocene series of the Tarcau and Vrancea nappes display coarser-grained lithic-fragment rich sands and conglomerates that were sourced from both the growing orogenic wedge and thick-skinned nappes of the Inner Carpathians, while the finer-grained quartz-dominated sandstones of the Kliwa Fm on the more external part of the same nappes were sourced from the East European Platform (Roban et al., 2022). This mixed provenance signal during the Oligocene is analogous to that recorded in the Krosno and Skyba nappes.

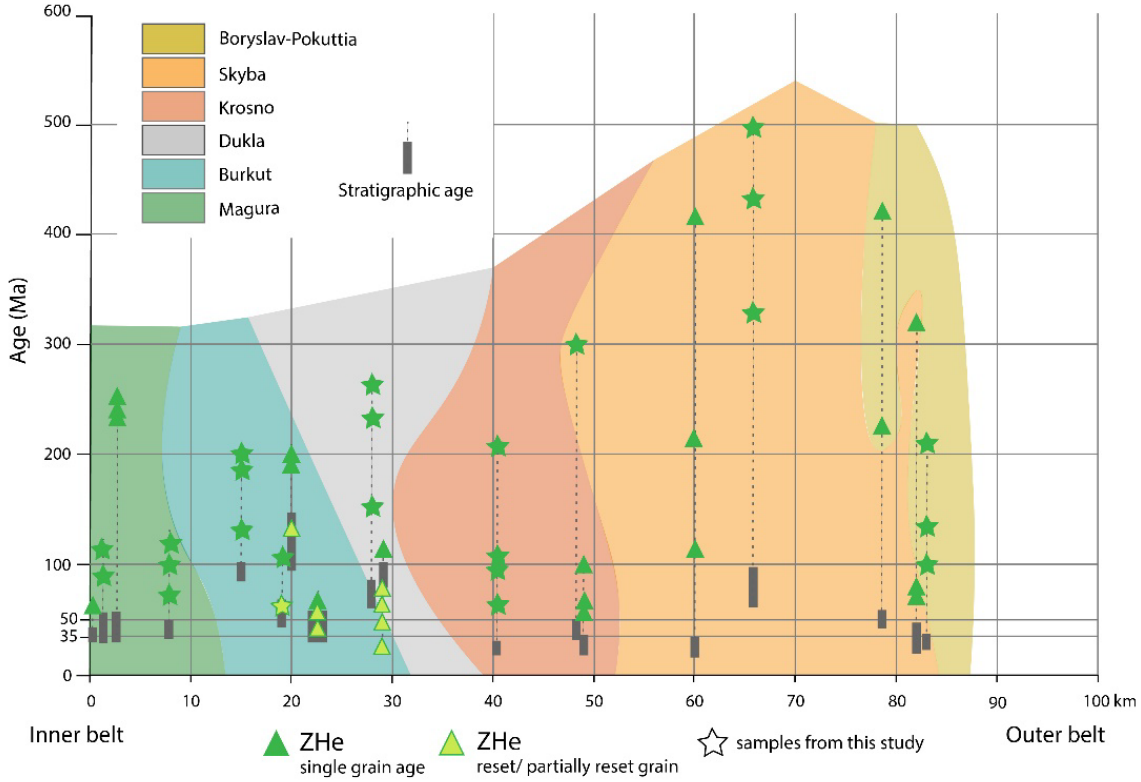

Figure II.12: Distribution of ZHe ages across the Ukrainian Carpathians as a function of distance from the inner to the outer belt. Stars represent data from this study; triangles are previously published data. Grey boxes indicate the stratigraphic age of the sample and dashed line mark the corresponding thermochronological ages. Coloured areas represent the different nappes.

6.5 Sediment recycling in the Carpathian wedge and sediment supply to the pro-foreland basin

Recycling of sediments is a major process in fold-and-thrust belts; quantifying the amount of eroded material and the timing of erosion can help retrieve sediment fluxes over time. Our study provides a view on the sediment fluxes in the Ukrainian Carpathian wedge from the classic model of a previously accreted nappe providing sediments to the next accreted nappe. A large volume of sediments accumulated in the part of the Carpathian embayment corresponding to the future Burkut, Dukla, Krosno, and Skyba nappes during the Oligocene. This sediment cannot have been sourced exclusively from the early thin-skinned wedge, as the amount of material exhumed from the inner nappes at that time was insufficient. Our thermal modeling indicates that during the Oligocene, only the Magura part of the wedge was exhuming. Multiplying the amount of exhumation of the growing wedge, with its width reconstructed from balanced cross-sections (Nakapelyukh et al., 2017, 2018), and comparing the thickness of the sediments over the width of the restored basin, we find an imbalance in the volume of material. In the 30–26 Ma interval, the Magura nappe was embedded in the wedge with a width of 20 and 0.8 km of exhumed sediment. In the same period, the restored basin carried 1.4 km of sediment over 140 km

based on restored sections of the region. For the 26–20 Ma period, the restored section allowed 80 km of width and 0.5 km of exhumation in the wedge. In comparison, the basin received 4 to 1.5 km of sediment over 30 and 80 km of restored width, respectively. Based on these estimates, the wedge may have provided only 8% and 17% of the basin's sediment during the 30–26 and 26–20 Ma periods, respectively. This imbalance suggests that much of the syn-orogenic sediment arriving in the basin was rather derived from the Inner Carpathians or the East European Platform. The growing wedge itself was a sediment source of minor importance at this time. The Boryslav–Pokuttia area accommodated little sediment after 17.2 Ma, except for deposition in some minor and very localized depocenters in its more external part until ca. 13.5 Ma (Figure II.2; Andreyeva-Grigorovich et al., 2008). However, at that time the Burkut, Dukla, Krosno, and Skyba nappes had mostly started exhuming. Hence, a large part of the sediments eroding from the wedge was transported to the Sambir area and/or to the modern Carpathian foreland basin (i.e., the Bilche-Volytsa zone; Figures II. 2, 13). In fact, the tectono-stratigraphic analysis, in combination with the kinematics of the Ukrainian Carpathians, indicates very little sediment recycling between the nappes. In the early stages of its development, the wedge provided a limited amount of sediment to the foreland area. During its subsequent rapid growth, most of the sediment eroded from it was first deposited in the Sambir area and, following its accretion, in the modern foreland basin. Preorogenic normal faults that were flexurally reactivated created significant accommodation space for the recycled sediment directly in front of the advancing wedge during the final stages of wedge emplacement (Oszczypko et al., 2006).

7 Conclusions

This study adds new constraints on the construction of the Ukrainian Carpathian wedge through low-temperature thermochronology and tectono-stratigraphic analysis. AFT and AHe single-grain ages show partial resetting in the most internal and external nappes and a progression to a very strong partial to total reset with young AHe ages (8–6 Ma) and minimum AFT ages (16–8 Ma) in the central part of the wedge (Burkut and Dukla nappes). ZHe ages are mainly non-reset, except in the central part of the wedge (i.e., Burkut and Dukla nappes), and shed light on the sediment source areas for the different preorogenic basins. A predominance of 130–60 Ma ZHe ages indicates that Eocene to Oligocene sediments in the Magura and Krosno nappes were supplied from the inner Carpathian basement and/or its sedimentary cover. Partial resetting of the ZHe system hampers provenance analysis for the Burkut and Dukla nappes, but sediment composition suggests that part of their Late Cretaceous to early Paleogene sediment was supplied by the intra-basinal Dukla ridge. In the more external Skyba and Boryslav–Pokuttia nappes, sediments older than 35 Ma show 230–450 Ma ZHe ages. We interpret these sediments to have been supplied from the East European Platform. From the Oligocene onwards, zircons from the 130–60 Ma age group also appear in the Skyba nappe, suggesting the arrival of sediment sourced from the Inner Carpathians. We elucidate the evolution of the wedge by combining burial diagrams and thermal history modeling, which allows distinguishing sedimentary from tectonic burial for each of the nappes involved. The Magura and Marmarosh areas accumulated sediment until the Eocene; their accretion and exhumation lasted from 34 to 30 Ma and from 34 to 20 Ma, respectively. The Burkut and Dukla areas record sedimentation until the Oligocene, while in the Krosno and Skyba areas sedimentation continued into the early Miocene. The Burkut and Dukla nappes started their

accretion as the inner nappes began their exhumation at around 28–20 Ma (Figure II.13). For the Burkut nappe, exhumation started at 20–18 Ma, corresponding to the onset of tectonic burial of the Krosno and Skyba nappes. However, the Krosno nappe and the northwestern part of the Skyba nappe started exhuming shortly after 18 Ma, in contrast to the southeastern part of the Skyba nappe that was exhumed around 12 Ma. The more internal Dukla nappe was also exhumed at 12 Ma, probably as a result of out-of-sequence thrusting. Early exhumation in the inner wedge from 34 Ma was slow, with a rate of 0.1 km Myr^{-1}. Following accretion at 28–18 Ma, exhumation occurred at an increasing rate for every progressive nappe (0.2–0.4 km Myr^{-1}). Final exhumation of the external nappes after 12 Ma was also rapid, with rates around 0.3 km Myr^{-1}. According to these rates and area estimates from balanced cross-sections, eroded sediments from the Ukrainian Carpathian wedge have mainly been transported into the Carpathian foreland basin, with little inter-nappe sediment recycling. Given the context of a retreating subduction zone and slab roll-back, the Ukrainian Carpathians can be seen as the product of the construction of an accretionary wedge in the Oligocene with collision in the late Miocene (Figure II.13). The low-temperature thermochronology pattern of reset versus partially reset ages across the wedge may indicate immature wedge dynamics, as resetting of the thermochronological systems toward the internal part of the wedge should have occurred during its accretion (Willet and Brandon, 2002). The inner nappes were accreted against the basement rocks of the active margin, which functioned as the backstop of the wedge. As convergence continued, the wedge grew through the accumulation of additional thrust sheets (the Burkut and Dukla nappes). The frontal thrust subsequently propagated over an intra-basinal high, which probably triggered the formation of out-of-sequence thrusts. The wedge further propagated during the accretion of the Krosno and Skyba nappes in the early Miocene. In the middle to late Miocene, rollback and associated slab suction increased subsidence of the foreland (more than the orogenic load) and reactivated preorogenic normal faults of the passive margin. It created an up to 2.5 km deep depocenter in front of the advancing wedge that facilitated its northward propagation, ultimately onto the East European Platform. The foreland was deformed by this last shortening episode until thrusting stopped at 11.5 Ma, coincident with slab detachment (Nemčok et al., 2006).

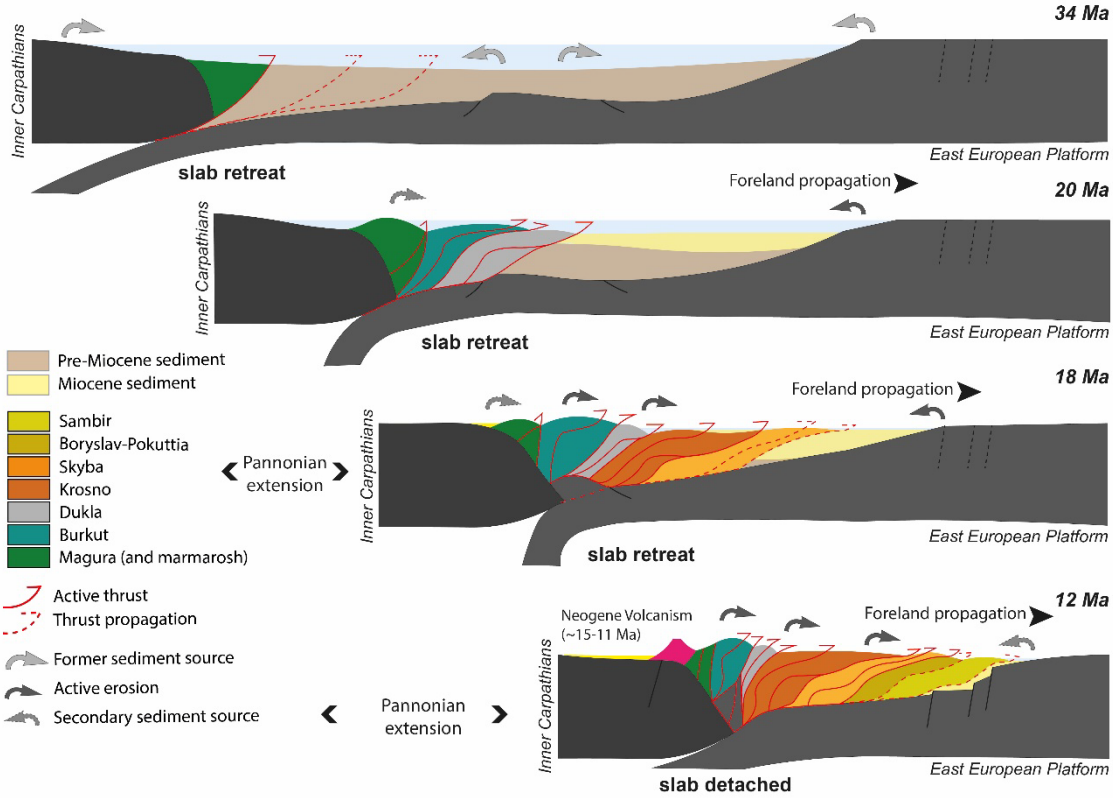

Figure II.13: Sketch of the construction of the Ukrainian Carpathian wedge from 34 Ma to 12 Ma. Dashed red line are thrusts that will propagate on the next time step. Full red lines with arrows on top are thrust that are active or will reactivate, full red lines without arrows are sealed. Light grey arrows show source of sediment supply to the different basins. Dark grey arrows are for the active erosion of the nappe. For 12 Ma sketch, foreland propagation terminated around 11.5 Ma (Nemčok et al., 2006). Not to scale.

Appendix A

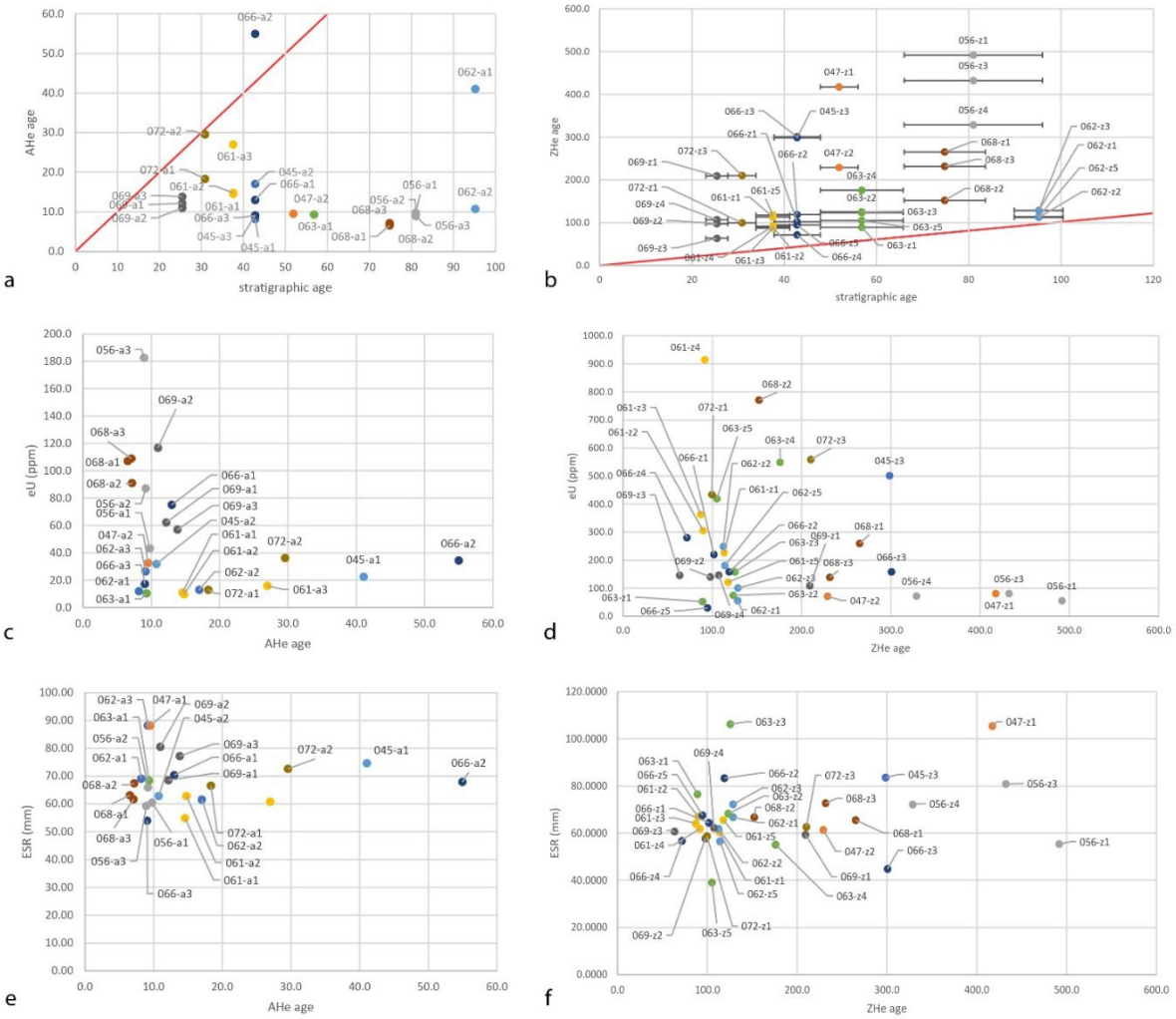

A 1: Circle colour refer to a sample, the same colour code is applied for all graphs. a) Graphic of the AHe single grain age compared to the stratigraphic age. CAR19-066_a2 is the only non-reset grain. b) ZHe single grain age compared to the stratigraphic age. ZHe are non-reset and mark the sediment source age of exhumation. c) AHe single grain age as a function of eU (ppm) content. d) ZHe single grain age as a function of eU (ppm) content. e) AHe single-grain age as a function of ESR (equivalent sphere radius, in mm). f) ZHe single-grain age as a function of ESR.

Data availability.

Data will be available from https://www.pangaea.de/ (last access: 10 January 2023). The DEM file is from OpenTopography and can be found at the following DOI: https://doi.org/10.5069/G92R3PT9 (Tozer et al., 2019).

Supplement.

The supplement related to this article is available online at: https://doi.org/10.5194/se-14-153-2023-supplement.

Author contributions.

AdL acquired funding for the project; AdL and MR planned the field campaign and sampled; MR and MB performed AFT analyses; ERS, MR, and JG performed the AHe and ZHe measurements; ERS, MB, and PvdB analyzed the data; MR modeled the data and wrote the paper draft; AdL, PvdB, LH, ERS, and MB reviewed and edited the paper.

Competing interests.

The contact author has declared that none of the authors has any competing interests.

Disclaimer.

Publisher's note: Copernicus Publications remains neutral with regard to jurisdictional claims in published maps and institutional affiliations.

Acknowledgements.

We thank Anton Matoshko for his help during the sampling campaign and Francis Coeur, Francois Senebier, and Melanie Balvay of the GTC platform at ISTerre for their help with sample processing, mineral separation, and fission-track thermochronology. Constructive reviews by Piotr Krzywiec and an anonymous reviewer helped to significantly improve the paper.

Financial support.

This work is supported by the French National Research Agency in the framework of the "Investissements d'avenir" program (ANR-15-IDEX-02) and is part of the IDEX QUANTIFLUX project. Review statement. This paper was edited by Stefano Tavani and reviewed by Piotr Krzywiec and one anonymous referee.

References

Andreucci, B., Castelluccio, A., Jankowski, L., Mazzoli, S., Szaniawski, R., and Zattin, M.: Burial and exhumation history of the Polish outer Carpathians: discriminating the role of thrusting and post-thrusting extension, Tectonophysics, 608, 866–883, https://doi.org/10.1016/j.tecto.2013.07.030, 2013.

Andreucci, B., Castelluccio, A., Corrado, S., Jankowski, L., Mazzoli, S., Szaniawski, R., and Zattin, M.: Interplay between the thermal evolution of an orogenic wedge and its retro-wedge basin: An example from the Ukrainian Carpathians, Geol. Soc. Am. Bull., 127, 410–427, https://doi.org/10.1130/B31067.1, 2015.

Andreyeva-Grigorovich, A. S., Oszczypko, N., S´ la ̨czka, A., Oszczypko-Clowes, M., Savitskaya, N. A., and Trofimovicz, N.: New data on the stratigraphy of the folded Miocene zone at the front of the Ukrainian outer Carpathians, Acta Geol. Pol., 58, 325–353, 2008. Ault, A. K., Gautheron, C., and King, G. E.: Innovations in (U–Th) = He, fission track, and trapped charge thermochronometry with applications to earthquakes, weathering, surface-mantle connections, and the growth and decay of mountains, Tectonics, 38, 3705–3739, https://doi.org/10.1029/2018TC005312, 2019.

Barr, T. D. and Dahlen, F. A.: Constraints on friction and stress in the Taiwan fold-and-thrust belt from heat flow and geochronology, Geology, 18, 111–115, https://doi.org/10.1130/0091-7613(1990)018<0111:cofasi>2.3.co;2, 1990. Batt, G. E., Brandon, M. T., Farley, K. A., and Roden-Tice, M.: Tectonic synthesis of the Olympic Mountains segment of the Cascadia wedge, using two-dimensional thermal and kinematic modelling of thermochronological ages, J. Geophys. Res., 106, 26731– 26746, https://doi.org/10.1029/2001jb000288, 2001.

Beyssac, O., Simoes, M., Avouac, J.-P., Farley, K. A., Chen, Y.- G., Chan, Y.-C., and Goffé, B.: Late Cenozoic metamorphic evolution and exhumation of Taiwan, Tectonics, 26, TC6001, https://doi.org/10.1029/2006tc002064, 2007.

Brandon, M. T., Roden-Tice, M. K., and Garver, J. I.: Late Cenozoic exhumation of the Cascadia accretionary wedge in the Olympic Mountains, northwest Washington State, Geol. Soc. Am. Bull., 110, 985–1009, https://doi.org/10.1130/0016-7606(1998)110<0985:lceotc>2.3.co;2, 1998.

Braun, J., van der Beek, P., and Batt, G. E.: Quantitative Thermochronology: Numerical methods for the interpretation of thermochronological data, Cambridge University Press, 271 pp., https://doi.org/10.1017/CBO9780511616433, 2006.

Carlson, W. D., Donelick, R. A., and Ketcham, R. A.: Variability of apatite fission-track annealing kinetics: I. Experimental results, Am. Mineral., 84, 1213–1223, 1999. Castelluccio, A., Mazzoli, S., Andreucci, B., Jankowski, L., Szaniawski, R., and Zattin, M.: Building and exhumation of the Western Carpathians: New constraints from sequentially restored, balanced cross sections integrated with lowtemperature thermochronometry, Tectonics, 35, 2698–2733, https://doi.org/10.1002/2016TC004190, 2016.

Cloetingh, S. A. P. L., Burov, E., Matenco, L., Toussaint, G., Bertotti, G., Andriessen, P. A. M., Wortel, M. J. R., and Spakman, W.: Thermo-mechanical controls on the mode of continental collision in the SE Carpathians (Romania), Earth Planet. Sc. Lett., 218, 57–76, https://doi.org/10.1016/S0012821X(03)00645-9, 2004.

Csontos, L. and Vörös, A.: Mesozoic plate tectonic reconstruction of the Carpathian region, Palaeogeogr. Palaeocl., 210, 1–56, https://doi.org/10.1016/j.palaeo.2004.02.033, 2004.

Csontos, L., Nagymarosy, A., Horváth, F., and Kovac, M.: Tertiary evolution of the Intra-Carpathian area: a model, Tectonophysics, 208, 221–241. 1992.

Dahlen, F. A., Suppe, J., and Davis, D.: Mechanics of fold-and-thrust belts and accretionary wedges: Cohesive Coulomb Theory, J. Geophys. Res., 89, 10087–10101, https://doi.org/10.1029/JB089iB12p10087, 1984.

Davis, D., Suppe, J., and Dahlen, F. A.: Mechanics of fold-andthrust belts and accretionary wedges, J. Geophys. Res., 88, 1153, https://doi.org/10.1029/JB088iB02p01153, 1983.

Docin, G.D.: State geological map of Ukraine (M34-30) scale 1 V 200 000, State geological research institute UkrSGRI, 1963.

Dumitrescu, I., Mir˘auj˘a, O., S˘andulescu, M., Stef˘anescu, M., Bandrabur, T.: Harta Geologic˘a Republica Socialist˘a România, scara 1 V 200:000, tiraj 2000, 1962.

Ehlers, T. A. and Farley, K. A.: Apatite (U–Th) = He thermochronometry: methods and applications to problems in tectonic and surface processes, Earth Planet. Sc. Lett., 206, 1–14, https://doi.org/10.1016/S0012-821X(02)01069-5, 2003.

Erlanger, E. D., Fellin, M. G., and Willett, S. D.: Exhumation and erosion of the Northern Apennines, Italy: new insights from low-temperature thermochronometers, Solid Earth, 13, 347–365, https://doi.org/10.5194/se-13-347-2022, 2022.

Fillon, C., Gautheron, C., and van der Beek, P.: Oligocene–Miocene burial and exhumation of the Southern Pyrenean foreland quantified by low-temperature thermochronology, J. Geol. Soc. London, 170, 67–77, https://doi.org/10.1144/jgs2012-051, 2013.

Flament, N., Gurnis, M., Müller, R. D., Bower, D. J., and Husson, L.: Influence of subduction history on South American topography, Earth Planet. Sc. Lett., 430, 9–18, https://doi.org/10.1016/j.epsl.2015.08.006, 2015.

Fuller, C. W., Willett, S. D., Fisher, D., and Lu, C. Y.: A thermomechanical wedge model of Taiwan constrained by fission-track thermochronometry, Tectonophysics, 425, 1–24, https://doi.org/10.1016/j.tecto.2006.05.018, 2006.

Gagała, Ł., Vergés, J., Saura, E., Malata, T., Ringenbach, J.-C., Werner, P., and Krzywiec, P.: Architecture and orogenic evolution of the northeastern Outer Carpathians from crosssection balancing and forward modeling, Tectonophysics, 532–535, 223–241, https://doi.org/10.1016/j.tecto.2012.02.014, 2012.

Galbraith, R. F. and Green, P. F.: Estimating the component ages in a finite mixture, International Journal of Radiation Applications and Instrumentation. Part D. Nuclear Tracks and Radiation Measurements, 17, 197–206, https://doi.org/10.1016/1359-0189(90)90035-V, 1990.

Galbraith, R. F. and Laslett, G. M.: Statistical models for mixed fission track ages, Nucl. Tracks Rad. Meas., 21, 459–470, https://doi.org/10.1016/1359-0189(93)90185-C, 1993.

Galetto, A., Georgieva, V., García, V. H., Zattin, M., Sobel, E. R., Glodny, J., Bordese, S., Arzadún, G., Bechis, F., Caselli, A. T., Becchio, R.: Cretaceous and Eocene rapid cooling phases in the Southern Andes (36–37 S): Insights from low-temperature thermochronology, U-Pb geochronology, and inverse thermal modeling from Domuyo area, Argentina, Tectonics, 40, e2020TC006415, https://doi.org/10.1029/2020TC006415, 2021.

Gallagher, K.: Transdimensional inverse thermal history modelling for quantitative thermochronology, J. Geophys. Res., 117, B02408, https://doi.org/10.1029/2011JB008825, 2012. Gautheron, C., Tassan-Got, L., Barbarand, J., and Pagel, M.: Effect of alpha-damage annealing on apatite (U–Th) = He thermochronology, Chem. Geol., 266, 157–170, https://doi.org/10.1016/j.chemgeo.2009.06.001, 2009. Gerasimov L. S., Makarov B. O., Chayi S. V., and Gerasinova I.I.: State geological map of Ukraine (M34-24) scale 1 V 200 000, State geological research institute UkrSGRI, 2005.

Gröger, H. R., Fügenschuh, B., Tischler, M., Schmid, S. M., and Foeken, J. P. T.: Tertiary cooling and exhumation history in the Maramures area (internal eastern Carpathians, northern Romania): thermochronology and structural data, Geological Society, London, Special Publications, 298, 169–195, https://doi.org/10.1144/SP298.9, 2008.

Guenthner, W. R., Reiners, P. W., Ketcham, R. A., Nasdala, L., and Giester, G.: Helium diffusion in natural zircon: Radiation damage, anisotropy, and the interpretation of zircon (U-Th) = He thermochronology, Am. J. Sci., 313, 145–198, https://doi.org/10.2475/03.2013.01, 2013.

Handy, M. R., Ustaszewski, K., and Kissling, E.: Reconstructing the Alps–Carpathians–Dinarides as a key to understanding switches in subduction polarity, slab gaps and surface motion, Int. J. Earth Sci., 104, 1–26, https://doi.org/10.1007/s00531-014-1060-3, 2015.

Horváth, F. and Cloetingh, S.: Stress-induced late-stage subsidence anomalies in the Pannonian basin, Tectonophysics, 266, 287–300, https://doi.org/10.1016/S0040-1951(96)00194-1, 1996.

Horváth, F., Szalay, A., Dovenyi, P., Rumpler, J., and Burrus, J.:Structural and thermal evolution of the Pannonian basin: an overview. Thermal Modelling in Sedimentary Basins, J. Burrus, Ed, Technip, Paris, 339–358, 1986.

Hoth, S., Hoffmann-Rothe, A., and Kukowski, N.: Frontal accretion: An internal clock for bivergent wedge deformation and surface uplift, J. Geophys. Res., 112, B06408, https://doi.org/10.1029/2006JB004357, 2007.

Hurford, A. J., and Green, P. F.: A users' guide to fission track dating calibration, Earth Planet. Sc. Lett., 59, 343–354, 1982.

Husson, L. and Moretti, I.: Thermal regime of fold and thrust belts – an application to the Bolivian sub Andean zone, Tectonophysics,345, 253–280, https://doi.org/10.1016/s0040-1951(01)00216-5, 2002.

Husson, L., Bernet, M., Guillot, S., Huyghe, P., Mugnier, J.-L., Replumaz, A., Robert, X., and van der Beek, P.: Dynamics ups and downs of the Himalaya, Geology, 42, 839–842, https://doi.org/10.1130/G36049.1, 2014.

Iliescu, V. and Kräutner, H. G.: Contributions to the knowledge of the palynological assemblages and the age of the metamorphic formations in the Rodna and Bistrita Mountains, Dari de seama ale sedintelor Institutului de Geologie si Geofizica, Bucharest, v.61/4, 11–25, 1975 (in Romanian).

Kaban, M. K., Chen, B., Tesauro, M., Petrunin, A. G., El Khrepy, S., and Al-Arifi, N.: Reconsidering Effective Elastic Thickness Estimates by Incorporating the Effect of Sediments: A Case Study for Europe, Geophys. Res. Lett., 45, 9523–9532, https://doi.org/10.1029/2018GL079732, 2018.

Ketcham, R. A., Carter, A., Donelick, R. A., Barbarand, J., and Hurford, A. J.: Improved modeling of fissiontrack annealing in apatite, Am. Mineral., 92, 799–810, https://doi.org/10.2138/am.2007.2281, 2007.

Ketcham, R. A., Gautheron, C., and Tassan-Got, L.: Accounting for long alpha-particle stopping distances in (U–Th–Sm) = He geochronology: Refinement of the baseline case, Geochim. Cosmochim. Ac., 75, 7779–7791, https://doi.org/10.1016/j.gca.2011.10.011, 2011.

Konecný, V., Kovác, M., Lexa, J., and Šefara, J.: Neogene evolution of the Carpatho-Pannonian region: an interplay of subduction and back-arc diapiric uprise in the mantle, EGU Stephan Mueller Special Publication Series, 1, 105–123, 2002.

Konstantinovskaia, E. and Malavieille, J.: Erosion and exhumation in accretionary orogens: Experimental and geological approaches, Geochem. Geophys. Geosyst., 6, Q02006, https://doi.org/10.1029/2004GC000794, 2005.

Kotarba, M. J. and Kołtun, Y. V.: The origin and habitat of hydrocarbons of the Polish and Ukrainian parts of the Carpathian Province, in: The Carpathians and Their Foreland: Geology and Hydrocarbon Resources, edited by: Golonka, J. and Picha, F. J., AAPG Memoir 84, 395–442, 2006.

Kovács, I.: Seismic anisotropy and deformation patterns in upper mantle xenoliths from the central Carpathian–Pannonian region: Asthenospheric flow as a driving force for Cenozoic extension and extrusion?, Tectonophysics, 514–517, 168–179, https://doi.org/10.1016/j.tecto.2011.10.022, 2012.

Kräutner, H. G., Sassi, F. P., Zirpoli, G., and Zulian, T.: The pressure characters of the pre-Alpine metamorphisms in the East Carpathians (Romania), Neu. Jb. Mineral. Abh., 125, 278–296, 1975.

Krijgsman, W. and Piller, W. E.: Central and Eastern Paratethys. The Neogene Period, in: The Geologic Time Scale, edited by: Gradstein, F., Ogg, J., Schmitz, M., and Ogg, G., 935–937, 2012. Krzywiec, P., Jochym, P. T., Kusmierek, J., Lapinkiewicz, A. P., MackowskP, T., and Stefaniuk, M.: Quantifying

effects of parameter variations on results of flexural modelling of continental collision zones: Polish Outer Carpathians, 1997.

Krzywiec, P.: Contrasting tectonic and sedimentary history of the central and eastern parts of the Polish Carpathian foredeep basin results of seismic data interpretation, in: Marine and Petroleum Geology, 18, Elsevier, 13–38, 2001.

Leever, K. A., Bertotti, G., Zoetemeijer, R., Matenco, L., and Cloetingh, S. A. P. L.: The effects of a lateral variation in lithospheric strength on foredeep evolution: Implications for the East Carpathian foredeep, Tectonophysics, 421, 251–267, https://doi.org/10.1016/j.tecto.2006.04.020, 2006.

Malusà, M. G. and Fitzgerald, P. G.: From Cooling to Exhumation: Setting the Reference Frame for the Interpretation of Thermochronologic Data, in: Fission-Track Thermochronology and its Application to Geology, edited by: Malusà, M. and Fitzgerald, P., Springer Textbooks in Earth Sciences, Geography and Environment, Springer, Cham, https://doi.org/10.1007/978-3-319-89421-8_8, 2019.

Malusà, M. G. and Fitzgerald, P. G.: The geologic interpretation of the detrital thermochronology record within a stratigraphic framework, with examples from the European Alps, Taiwan and the Himalayas, Earth-Sci. Rev., 201, 103074, 2020.

Matenco, L. and Bertotti, G.: Tertiary tectonic evolution of the external East Carpathians (Romania), Tectonophysics, 316, 255–286, https://doi.org/10.1016/S0040-1951(99)00261-9, 2000.

Matenco, L., Krézsek, C., Merten, S., Schmid, S., Cloetingh, S., and Andriessen, P.: Characteristics of collisional orogens with low topographic build-up: an example from the Carpathians, Terra Nova, 22, 155–165, https://doi.org/10.1111/j.1365-3121.2010.00931.x, 2010.

Matskiv B. V., Pukach B. D., Kovalof Y. V., and Vorobkanich V. M.: State geological map of Ukraine (M34-29, M34-35, L34-5) scale 1 V 200 000, State geological research institute UkrSGRI, 2008.

Matskiv B. V., Pukach B. D., Vorobkaniv V. M., Pastukhanoa S. V., and Gnilko O. M.: State geological map of Ukraine (M34-36, M35-31, L34-6, L35-1) scale 1 V 200000, State geological research institute UkrSGRI, 2009.

Mazzoli, S., Jankowski, L., Szaniawski, R., and Zattin, M.: Low-T thermochronometric evidence for postthrusting (<11 Ma) exhumation in the Western Outer Carpathians, Poland, C. R. Geosci., 342, 162–169,https://doi.org/10.1016/j.crte.2009.11.001, 2010.

Merten, S., Matenco, L., Foeken, J. P. T., Stuart, F. M., and Andriessen, P. A. M.: From nappe stacking to outof-sequence postcollisional deformations: Cretaceous to Quaternary exhumation history of the SE Carpathians assessed by low-temperature thermochronology, Tectonics, 29, TC3013, https://doi.org/10.1029/2009TC002550, 2010.

Michel, L., Glotzbach, C., Falkowski, S., Adams, B. A., and Ehlers, T. A.: How steady are steady-state mountain belts? A reexamination of the Olympic Mountains (Washington state, USA), Earth Surf. Dynam., 7, 275–299, https://doi.org/10.5194/esurf-7-275-2019, 2019.

Nakapelyukh, M., Bubniak, I., Yegorova, T., Murovskaya, A., Gintov, O., Shlapinskyi, V., and Vikhot, Y.: Balanced geological cross-section of the outer Ukrainian Carpathians along the pancake profile, J. Geodyn., 108, 13–25, https://doi.org/10.1016/j.jog.2017.05.005, 2017.

Nakapelyukh, M., Bubniak, I., Bubniak, A., Jonckheere, R., and Ratschbacher, L.: Cenozoic structural evolution, thermal history, and erosion of the Ukrainian Carpathians fold-thrust belt, Tectonophysics, 722, 197–209, https://doi.org/10.1016/j.tecto.2017.11.009, 2018. Naylor, M. and Sinclair, H. D.: Punctuated thrust deformation in the context of doubly vergent thrust wedges: Implications for the localization of uplift and exhumation, Geology, 35, 559–562, https://doi.org/10.1130/G23448A.1, 2007.

Naylor, M. and Sinclair, H. D.: Pro- vs. retro-foreland basins, Basin Res., 20, 285–303, https://doi.org/10.1111/j.1365-2117.2008.00366.x, 2008.

Nemcok, M., Pospisil, L., Lexa, J., and Donelick, R. A.: Tertiary subduction and slab break-off model of the Carpathian–Pannonian region, Tectonophysics, 295, 307–340, https://doi.org/10.1016/S0040-1951(98)00092-4, 1998.

Nemčok, M., Pogácsás, G., and Pospíšil, L.: Activity Timing of the Main Tectonic Systems in the Carpathian–Pannonian Region in Relation to the Rollback Destruction of the Lithosphere, in: The Carpathians and Their Foreland: Geology and Hydrocarbon Researces: AAPG Memoir 84, edited by: Golonka, J. and Picha, F. J., The American Association of Petroleum Geologists, Tulsa, Oklahoma, USA, 743–766, https://doi.org/10.1306/985627M843083, 2006.

Oszczypko, N.: Late Jurassic-Miocene evolution of the Outer Carpathian fold-and-thrust belt and its foredeep basin (Western Carpathians, Poland), Geol. Q., 50, 169–194, 2006. Oszczypko, N., Oszczypko-Clowes, M., Golonka, J., and Krobicki, M.: Position of the Marmarosh Flysch (Eastern Carpathians) and its relation to the Magura Nappe (Western Carpathians), Acta Geologica Hungarica, 48, 259–282, https://doi.org/10.1556/AGeol.48.2005.3.2, 2005.

Oszczypko, N., Krzywiec, P., Popadyuk, I., and Peryt, T.: Carpathian Foredeep Basin (Poland and Ukraine): Its Sedimentary, Structural, and Geodynamic Evolution, in: The Carpathians and Their Foreland: Geology and Hydrocarbon Researces: AAPG Memoir 84, edited by: Golonka, J. and Picha, F. J., The American Association of Petroleum Geologists, Tulsa, Oklahoma, U.S.A., 293–350, https://doi.org/10.1306/985612M843072, 2006.

Pharaoh, T. C.: Palaeozoic terranes and their lithospheric boundaries within the Trans-European Suture Zone (TESZ): a review, Tectonophysics, 314, 17–41, https://doi.org/10.1016/S0040-1951(99)00235-8, 1999.

Poprawa P., Malata T., and Oszczypko N.: Ewolucja tektoniczna basenów sedymentacyjnych polskiej czêoeci Karpat zewnêtrznych w oewietle analizy subsydencji, Prz. Geol., 11, 1092–1108, 2002 (in Polish with English abstract).

Poprawa, P., Malata, T., Pécskay, Z., and Kusiak, M. A.: Geochronology of the Crystalline Basement of theWestern Outer Carpathians' Source Areas-Constraints from K=Ar Dating of Mica and Th–U–Pb Chemical Dating of Monazite from the Crystalline'Exotic'Pebbles, Geolines, 20, 110, 2006.

Pospíšil, L., Ádám A., Bimka J., Bodlak P., Bodoky T., Dövényi P., Granser H., Hegedüs E., Joo I., Kendzera A., Lenkey L., Nemčok M., Posgay K., Pylypyshyn B., Sedlák J., Stanley W. D., Starodub G., Szalaiová V., Šály B., Šutora A., Várga G., and Zsíros T.: Crustal and lithospheric structure of the Carpathian – Pannonian region – A geophysical perspective: Regional geophysical data on the Carpathian – Pannonian lithosphere, in: The Carpathians and their foreland: Geology and hydrocarbon resources, edited by: Golonka, J. and Picha, F. J., AAPG Memoir 84, 651–697, 2006.

Ratschbacher, L., Frisch, W., Linzer, H.G., Sperner, B., Meschede, M., Decker, K., Nemčok, M., Nemčok, J., and Grygar, R.: The Pieniny Klippen Belt in the western Carpathians of northeastern Slovakia: structural evidence for transpression, Tectonophysics 226, 471–483, https://doi.org/10.1016/0040-1951(93)90133-5, 1993.

Roban, R. D., Ducea, M. N., Ma?enco, L., Panaiotu, G. C., Profeta, L., Krézsek, C., Melinte-Dobrinescu, M. C., Anastasiu, N., Dimofte, D., Apotrosoaei, V., and Francovschi, I.: Lower Cretaceous Provenance and Sedimentary Deposition in the Eastern Carpathians: Inferences for the Evolution of the Subducted Oceanic Domain and its European Passive Continental Margin, Tectonics, 39, e2019TC005780, https://doi.org/10.1029/2019TC005780, 2020.

Roban, R. D., Ducea, M. N., Mihalcea, V. I., Munteanu, I., Barbu, V., Melinte-Dobrinescu, M. C., Olariu, C., and Vl˘asceanu, M.: Provenance of Oligocene lithic and quartz arenites of the East Carpathians: Understanding sediment routing systems on compressional basin margins, Basin Res., 35, 244–270, https://doi.org/10.1111/bre.12711, 2022.

Roure, F., Roca, E., and Sassi, W.: The Neogene evolution of the outer Carpathian flysch units (Poland, Ukraine and Romania): kinematics of a foreland/fold-and-thrust belt system, Sediment. Geol., 86, 177–201, https://doi.org/10.1016/0037-0738(93)90139-V, 1993.

Royden, L. and Burchfiel, B. C.: Are systematic variations in thrust belt style related to plate boundary processes? (The western Alps versus the Carpathians), Tectonics, 8, 51–61, https://doi.org/10.1029/TC008i001p00051, 1989.

Royden, L. and Faccenna, C.: Subduction orogeny and the Late Cenozoic evolution of the Mediterranean Arcs, Annu. Rev. Earth Pl. Sc., 46, 261–289, https://doi.org/10.1146/annurevearth-060115-012419, 2015.

Royden, L. and Karner, G. D.: Flexure of lithosphere beneath Apennine and Carpathian foredeep basins: Evidence for an insufficient topographic load, Am Assoc. Petrol. Geol. Bull, 68, 704–712, https://doi.org/10.1306/ad461372-16f7-11d7-8645000102c1865d, 1984.

Royden, L. H.: The tectonic expression of slab pull at continental convergent boundaries, Tectonics, 12, 303–325, https://doi.org/10.1029/92tc02248, 1993a.

Royden, L. H.: Evolution of retreating subduction boundaries formed during continental collision, Tectonics, 12, 629–638, https://doi.org/10.1029/92TC02641, 1993b.

Sanders, C. A. E., Andriessen, P. A. M., and Cloetingh, S. A. P. L.: Life cycle of the East Carpathian orogen: Erosion history of a doubly vergent critical wedge assessed by fission track thermochronology, J. Geophys. Res., 104, 29095–29112, https://doi.org/10.1029/1998JB900046, 1999.

Sandulescu, M.: Essai de synthèse structurale des Carpathes, Bull. Soc. Géol. France, 299–358, 1975. Sandulescu, M.: Cenozoic Tectonic History of the Carpathians, in: The Pannonian Basin: A Study in Basin Evolution, edited by:

Royden, L. H. and Horváth, F., Am. Assoc. Pet. Geol. Memoir, 45, 17–25, 1988.

Schmid, S. M., Bernoulli, D., Fügenschuh, B., Matenco, L., Schefer, S., Schuster, R., Tischler, M., and Ustaszewski, K.: The Alpine-Carpathian-Dinaridic orogenic system: correlation and evolution of tectonic units, Swiss J. Geosci., 101, 139–183, https://doi.org/10.1007/s00015-008-1247-3, 2008.

Seghedi, I., Downes, H., Pécskay, Z., Thirlwall, M. F., Szakács, A., Prychodko, M., and Mattey, D.: Magmagenesis in a subduction-related post-collisional volcanic arc segment: the Ukrainian Carpathians, Lithos, 57, 237–262, https://doi.org/10.1016/S0024-4937(01)00042-1, 2001.

Sengül-Uluocak, E., Pysklywec, R. N., Gö ̆güş, O. H., and Ulugergerli, E. U.: Multidimensional Geodynamic Modeling in the Southeast Carpathians: Upper Mantle Flow-Induced Surface Topography Anomalies, Geochem. Geophys. Geosyst., 20, 2019GC008277, https://doi.org/10.1029/2019GC008277, 2019.

Shlapinskyi, V.: Geological map of the Ukrainian Carpathians, scale 1 V 100000. Transcarpathian, Ivano–Frankivsk, Lviv, Tscernivtsi regions, in: Zvit ZAO “Koncern Nadra”, edited by: Krupsky, Y. Z., Kyiv, 228 pp., 2007 (in Ukrainian).

Shlapinskyi, V.: The Geological Architecture of the Skyba, Krosno, DuklyaChornogora Nappes of the Ukrainian Carpathians and Prospects of Oil and Gas (unpublished doctoral thesis), Institute of Geology and Geochemistry of Combustible Minerals, Lviv, 2015 (in Ukrainian).

Simpson, G. D. H.: Modelling interactions between fold-thrust belt deformation, foreland flexure and surface mass transport, Basin Res., 18, 125–143, https://doi.org/10.1111/j.1365-2117.2006.00287.x, 2006.

Sinclair, H.: Thrust Wedge/Foreland Basin Systems, in: Tectonics of Sedimentary Basins, edited by: Busby, C. and Azor, A., John Wiley & Sons, Ltd, Chichester, UK, 522–537, https://doi.org/10.1002/9781444347166.ch26, 2012.

Sinclair, H. D. and Naylor, M.: Foreland basin subsidence driven by topographic growth versus plate subduction, Geol. Soc. Am. Bull., 124, 368–379, https://doi.org/10.1130/B30383.1, 2012.

S´ la ̨czka, A.: Bukowiec Ridge: a cordillera in front of the Dukla Basin (Outer Carpathians), Mineralia Slovaca, 37, 255–256, 2005.

Sobel, E. R. and Seward, D.: Influence of etching conditions on apatite fission-track etch pit diameter, Chem. Geol., 271, 59–69, https://doi.org/10.1016/j.chemgeo.2009.12.012, 2010.

Sperner, B., Ratschbacher, L., and Nemčok, M.: Interplay between subduction retreat and lateral extrusion: Tectonics of the Western Carpathians, Tectonics, 21, 1051, https://doi.org/10.1029/2001TC901028, 2002.

Stockmal, G. S., Beaumont, C., and Boutilier, R.: Geodynamic models of convergent margin tectonics: Transition from rifted margin to overthrust belt and consequences for foreland-basin development, Am. Assoc. Petrol. Geol. Bull., 70, 181–190, https://doi.org/10.1306/94885656-1704-11d7-8645000102c1865d, 1986.

T˘ar˘apoanc˘a, M., Bertotti, G., Matenco, L., Dinu, C., and Cloetingh, S. A. P. L.: Architecture of the Foc ̧sani Depression: A 13 km deep basin in the Carpathians bend zone (Romania), Tectonics, 22, 1074, https://doi.org/10.1029/2002TC001486, 2003.

T˘ar˘apoanc˘a, M., Garcia-Castellanos, D., Bertotti, G., Matenco, L., Cloetingh, S. A. P. L., and Dinu, C.: Role of the 3-D distributions of load and lithospheric strength in orogenic arcs: polystage subsidence in the Carpathians foredeep, Earth Planet. Sc. Lett., 221, 163–180, 2004.

Tari, G., Horváth, F., and Rumpler, J.: Styles of extension in the Pannonian Basin, Tectonophysics, 208, 203–219, 1992. Ter Voorde, M., de Bruijne, C. H., Cloetingh, S. A. P. L., and Andriessen, P. A. M.: Thermal consequences of thrust faulting: simultaneous versus successive fault activation and exhumation, Earth Planet. Sc. Lett., 223, 395–413, https://doi.org/10.1016/j.epsl.2004.04.026, 2004.

Thomson, S. N., Brandon, M. T., Reiners, P. W., Zattin, M., Isaacson, P. J., and Balestrieri, M. L.: Thermochronologic evidence for orogen-parallel variability in wedge kinematics during extending convergent orogenesis of the northern Apennines, Italy, Geol. Soc. Am. Bull., 122, 1160–1179, https://doi.org/10.1130/b26573.1, 2010.

Tilit, ˘a, M., Lenkey, L., Mat,enco, L., Horváth, F., Surányi, G., and Cloetingh, S.: Heat flow modelling in the Transylvanian basin: Implications for the evolution of the intra-Carpathians area, Global Planet. Change, 171, 148–166, https://doi.org/10.1016/j.gloplacha.2018.07.007, 2018.

Tozer, B., Sandwell, D. T., Smith, W. H. F., Olson, C., Beale, J. R., and Wessel, P.: Global bathymetry and topography at 15 arc sec: SRTM15+, Distributed by OpenTopography [data set], https://doi.org/10.5069/G92R3PT9 (last access: 8 June 2022), 2019.

Vacherat, A., Mouthereau, F., Pik, R., Bernet, M., Gautheron, C., Masini, E., Le Pourhiet, L., Tibari, B., and Lahfid, A.: Thermal imprint of rift-related processes in orogens as recorded in the Pyrenees, Earth Planet. Sc. Lett., 408, 296–306, https://doi.org/10.1016/j.epsl.2014.10.014, 2014.

van der Beek, P., Robert, X., Mugnier, J.-L., Bernet, M., Huyghe, P., and Labrin, E.: Late Miocene – Recent exhumation of the central Himalaya and recycling in the foreland basin assessed by apatite fission-track thermochronology of Siwalik sediments, Nepal, Basin Res., 18, 413–434, https://doi.org/10.1111/j.1365-2117.2006.00305.x, 2006.

Vashchenko, V. O., Turchynova, S. M., and Turchynov, I. I.: State geological map of Ukraine M-35-XXV (Ivano-Frankivsk) scale 1 V 200 000, Scientific-Editorial Council of the Department of Geology and Subsurface Use of the Ministry of Ecology and Natural Resources of Ukraine on June 8, 2006.

Vermeesch, P.: RadialPlotter: A Java application for fission track, luminescence and other radial plots, Radiat. Meas., 44, 409–410, 2009.

Willett, S., Beaumont, C., and Fullsack, P.: Mechanical model for the tectonics of doubly vergent compressional orogens, Geology, 21, 371–374, 1993.

Willett, S. D. and Brandon, M. T.: On steady states in mountain belts, Geology, 30, 175–178, https://doi.org/10.1130/0091-7613(2002)030<0175:ossimb>2.0.co;2, 2002.

Winkler, W. and Slaczka, A.: Sediment dispersal and provenance in the Silesian, Dukla and Magura flysch nappes (Outer Carpathians, Poland), Geol. Rundsch., 81, 371–382, https://doi.org/10.1007/BF01828604, 1992.

Wortel, M. J. R., and Spakman,W.: Subduction and slab detachment in the Mediterranean-Carpathian region, Science, 290, 1910–1917, https://doi.org/10.1126/science.290.5498.1910, 2000.

Zhou, R., Schoenbohm, L. M., Sobel, E. R., Davis, D. W., and Glodny J.: New constraints on orogenic models of the southern Central Andean Plateau: Cenozoic basin evolution and bedrock exhumation, Geol. Soc. Am. Bull., 129, 152–170, 2017

Chapter III: Exhumation of the Carpathian fold-and-thrust belt

The following part is focused on the exhumation of the Carpathian fold-and-thrust belt along its entire length, from Poland to Romania, over the last 34 My. The aim is to understand how exhumation evolved in space and time and to quantify the volumes of material eroded from the belt. In Chapter V we will subsequently compare the sediment fluxes from the belt with the pattern and rates of deposition in the pro-foreland of the Carpathians, which will be quantified in Chapter IV.

To quantify exhumation, we compiled a comprehensive low-temperature (LT) thermochronology database, including the new data we reported in Chapter II, and used this as input in an inverse thermal-kinematic model (Pecube; Braun et al., 2012). We separated the LT thermochronology data per tectonic unit and per region in order to perform inversions for units that we suppose to exhume relatively homogeneously and to test for diachronicity in the evolution of the belt, using an approach similar to that of Curry et al. (2021). We divided the exhumation period in different time steps, corresponding as much as possible to the stratigraphic intervals that are discerned in the Carpathian foreland basin. This approach allows obtaining exhumation rates for the different nappes over the same time steps. We describe our preferred model of exhumation and discuss its implications for the development of the Carpathians, comparing it with previous studies of exhumation, tectonic or erosion processes in the different regions of the Carpathians, including our own results on the Ukrainian Carpathians described in Chapter II.

1 Low-temperature thermochronology data in the Carpathians

The Carpathian belt is an excellent target for a low-temperature (LT) thermochronology-based exhumation model. The belt has a large and homogeneous data cover. A previous data gap in Ukraine was filled by complementary data from our 2019 field campaign. We compiled all the data available from the belt, including the new results presented in Chapter II. This database is presented in the appendix of the manuscript and described hereafter.

1.1 Database description

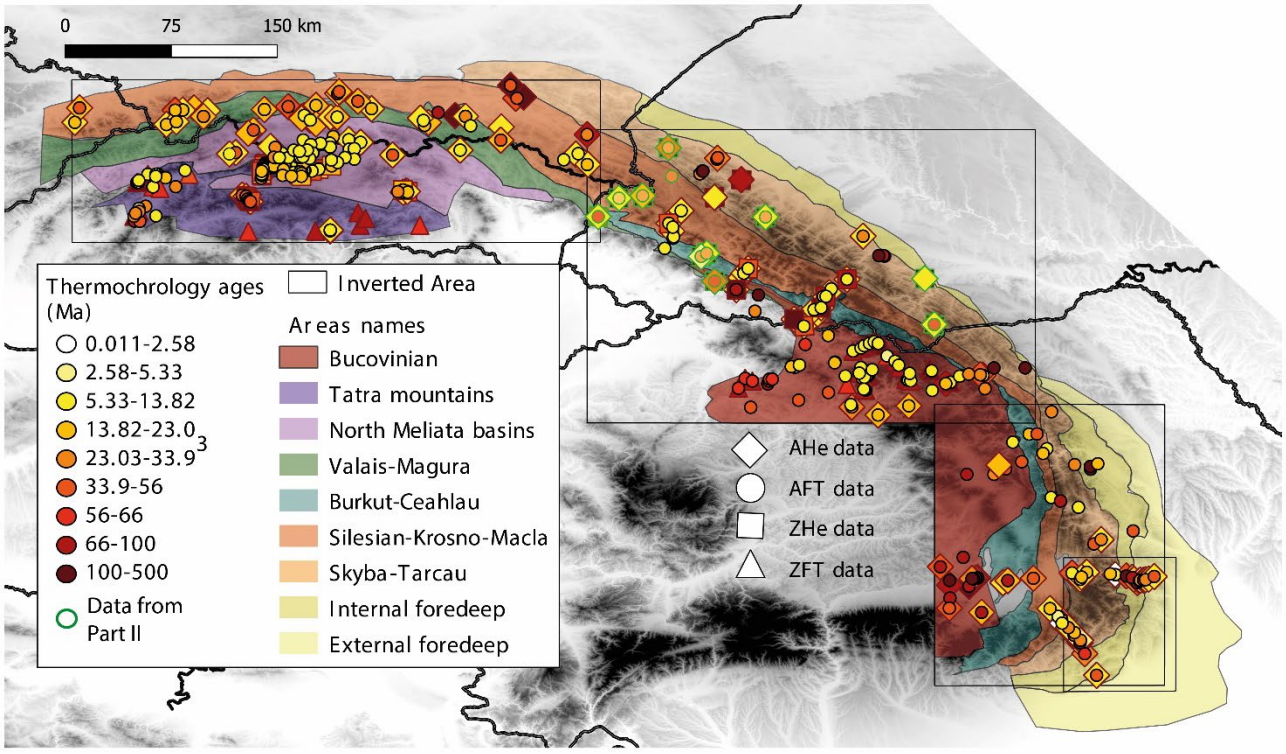

Figure III.1: LT-thermochronology data from the Carpathians. The age scale for the thermochronological data follows the geological timescale. Separate areas follow the identification of geological domains in the Carpathian region by Schmid et al. (2008); names refer to regional nappes/massifs throughout the belt from NW to SE. Data points contoured in green are from section II of this thesis.

A compilation of more than three hundred data points was created (Figure III.1); because many data points include dates from more than one thermochronology system, the compilation comprises a total of >500 ages. This database compiles apatite (AFT) and zircon (ZFT) fission-track as well as apatite (AHe) and zircon (ZHe) (U-Th)/He data from a dozen studies. The complete database is provided in the appendix of this manuscript. We classified the data by author, country, and thermochronometer. To our knowledge, all available data present in the literature were compiled.

For AFT and ZFT, whenever possible, we provide the location and elevation, the central age and related uncertainty, the stratigraphic age of the sampled unit, the grain count, the total number of induced and spontaneous tracks and their related densities, the age dispersion and the uranium concentration. When

complementary data were provided in the publication, such as track-length and Dpar (etch-pit diameter) measurements, these were also added to the database.

For (U-Th)/He data, we compiled the sampling locations and elevation, mean ages and single-grain ages with their related errors, stratigraphic ages of the sampled unit, and the concentration of uranium, thorium, and samarium (when measured) as well as the equivalent uranium concentration (eU, in ppm) of each sample. If the size and mass of the grains were provided, these were also added to the database.

In the following, the thermochronometry ages from the database are described according to their author's interpretation as reset, non-reset or partially reset (see Chapter I section 1.6.5 for definition).

As the main use of this database was to invert the data to obtain exhumation rates per tectonic unit and per region in the Carpathians, the tectonic unit to which the data pertains is also recorded.

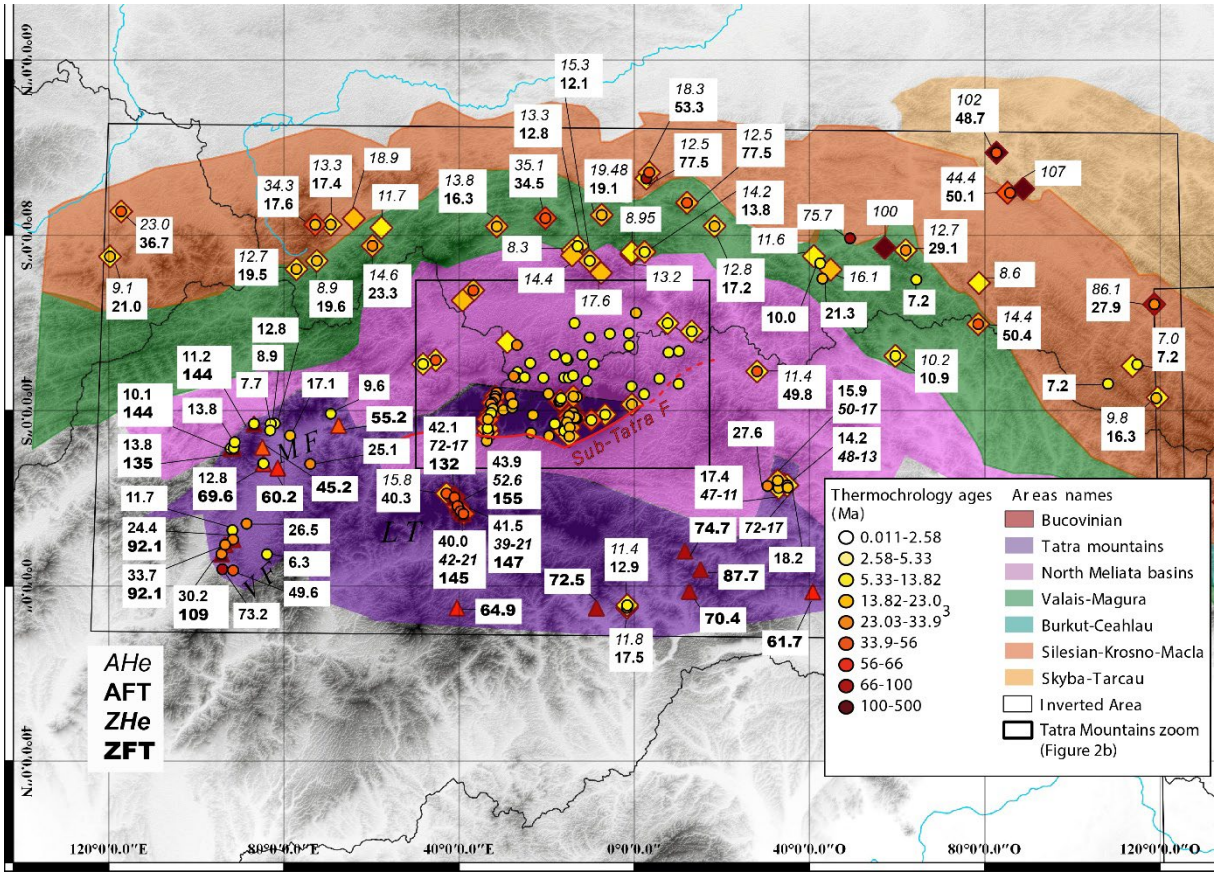

Figure III.2: LT thermochronology data from the Western Carpathian (WC) region; ZFT, AFT, ZHe and AHe thermochronometer ages are indicated for each sample. Data from the Tatra mountains are presented in Figure III.3. Red line represents the Sub-Tatra Fault. Data symbols are as in Figure III.1. MF: Male Fatra Mountains; LT: Low Tatra Mountains.

1.2 Distribution of thermochronometer data across the belt

1.2.1 The Western region

The Western region covers most of the Polish Outer Carpathians, parts of the Slovakian mountains and basins in the north of the country, and the easternmost part of the Czech Republic (Figure III.2). Previous authors constrained the thermal regime of the crust during Pannonian extension with thermochronology in this region (Anczkiewicz et al., 2013, 2015; Danišík et al., 2008b). Other studies also used LT thermochronometry to unravel the Miocene extension of the Northern Pannonian basin and related basement exhumation in the Central Carpathian Paleogene Basin (CCPB).

In Slovakia, most of the data were collected from the basement of the AlCaPa block. Most ZFT ages from the Mala Fatra and Low Tatra mountains are non-reset (> 100 Ma); ZHe ages are early Eocene to late Oligocene (~ 45-20 Ma; Figure III.2 and S1). In the valley between Mala Fatra and Low Tatra, and south of the Low Tatra massif, both the ZFT and ZHe thermochronometers show younger ages of ~70-45 Ma and ~15 Ma, respectively (Figure III.2). AFT ages in the Mala Fatra mountains are mid-Miocene (~17-7 Ma); they are older (~50-25 Ma) in the Low Tatra mountains and south of Velkà Fatra (Danišík et al., 2008a, 2008b, 2010, 2011; Plašienka et al., 2012; Figure S1).

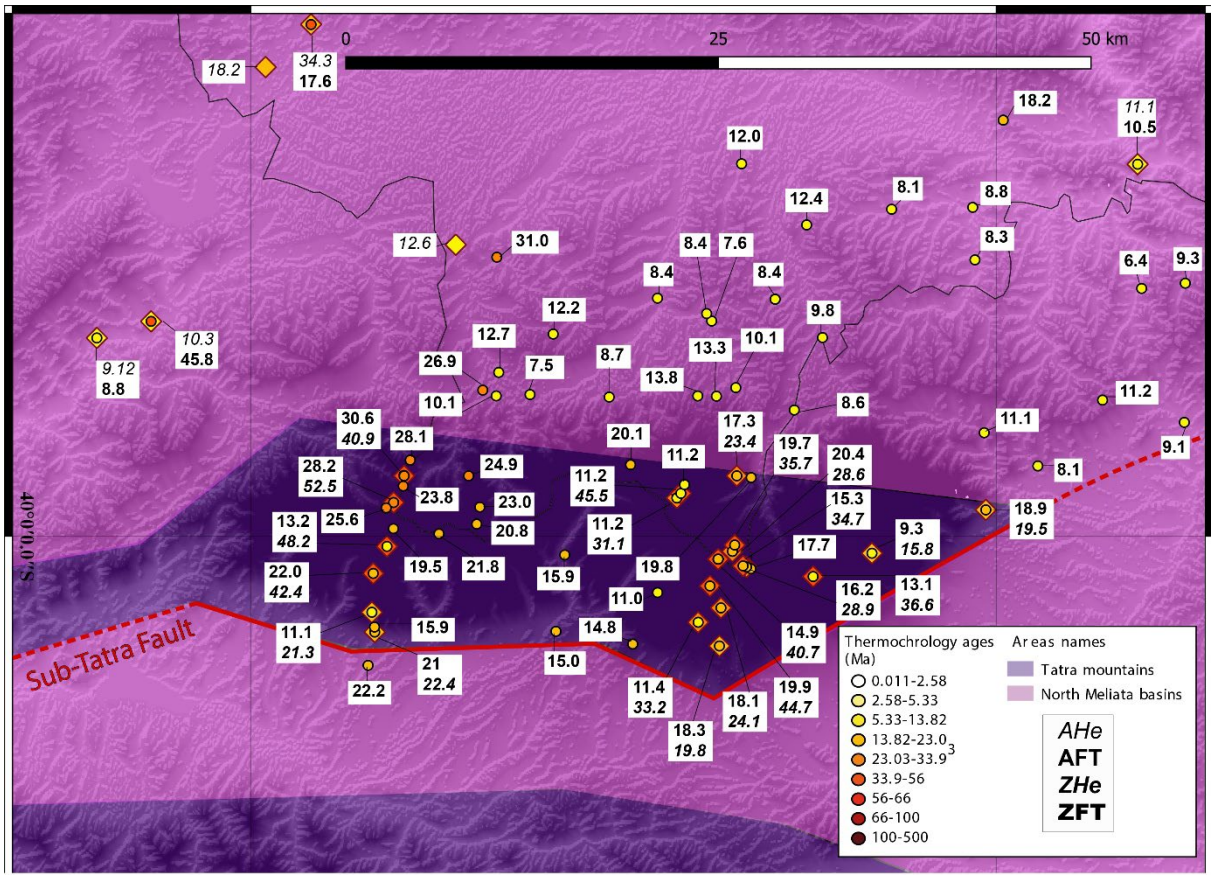

Figure III.3: LT thermochronology data from the Western Carpathian (WC) region, zoomed on the Tatra Mountains units, showing ZFT, AFT, ZHe and AHe thermochronometer ages of each sample. Data symbols are as in Figure 1.

The Tatra Mountains, located at the Slovakia-Poland border, have been intensively studied using thermochronology and thermal modelling to unravel the exhumation, tectonic activity and structure of the massif (Figure III.3). The ZHe system is reset in this massif and displays Eocene-late Oligocene ages between 50-23 Ma (Śmigielski et al., 2016); AFT is fully reset with ages between 28-10 Ma (Buchart, 1972; Kral', 1977; Śmigielski et al., 2016; Anczkiewicz et al., 2015; Králiková et al., 2014). Strikingly, AFT data from the eastern Tatra mountains show middle Miocene age (~20-9 Ma) but ZHe ages in this region are younger than elsewhere: late Oligocene-Miocene (from 30-15 Ma; Anczkiewicz et al., 2015; Śmigielski et al., 2016). These authors estimated that AFT and ZHe samples from the eastern Tatra mountains encountered temperatures of >200°C in the Late Cretaceous and ~150 °C in the Eocene-Oligocene. Those younger ages to the east are attributed to the reactivation of the Sub-Tatra fault (south of the Tatra mountains; Figure III.2), an important tectonic feature in the development of the Inner Western Carpathians (Anczkiewicz et al., 2015; Castelluccio et al., 2016).

The thermal history of the Central Carpathian Paleogene Basins (CCPB) north of the Tatra Mountains is constrained mostly by AFT and some AHe data (Figure III.3; Anczkiewicz et al., 2013). AFT ages span from ~30-6 Ma and AHe range from ~17-11 Ma. Younger ages are observed towards the east of CCPB, with central ages from ~13-6 Ma. Samples from north of the CCPB region have fully reset AFT ages but the samples yield older AHe ages (e.g., 17.6, 15.3 Ma for AHe on samples with AFT ages of 12.1 and

12.8 Ma; Figure III.2 and 3). This northward increase in ages for AHe was interpreted as a lesser degree of exhumation at these locations (Anczkiewicz et al., 2013).

Most thermochronology studies conducted in the Western Outer Carpathians, consisting of the Magura and Silesian nappes, were aimed at constraining the burial and exhumation of the region in the Miocene (Mazzoli et al., 2010; Zattin et al., 2011; Andreucci et al., 2013; Castelluccio et al., 2016). The Magura nappe shows mainly early- to middle-Miocene AHe and AFT ages (20-10 Ma), with late-Miocene ages from 10-7 Ma concentrated in the east of the Polish Carpathians and attributed to post-thrusting extension (Mazzoli et al., 2010). Nonetheless, several samples have ages older than Miocene; these include three AFT ages from 50.4-34.0 Ma and two AHe ages of 35.1 and 100 Ma.

In the Silesian unit in Poland, several AFT ages are partially reset (77.5 and 75.7 Ma) indicating that a temperature of ~100 °C was encountered during burial. Associated AHe ages are middle to late Miocene (~18-7 Ma). In the external area, east of the Silesians units, AHe data are non-reset with ages from 107-44.4 Ma, implying differential heating and/or burial from the inner to the outer areas in the Miocene.

1.2.2 North-Eastern Carpathians

The North-eastern region comprises the outer Carpathians of Ukraine and the Bucovinian units of north Romania (Figure III.4). The Bucovinian unit of the internal Carpathians was sampled in the vicinity of faults of the Maramures Mountains to constrain the timing and amount of deformation/exhumation of the different horsts and grabens in this area (Gröger et al., 2013). In the Bucovinian unit, ZFT ages are reset and range from Late Jurassic to Cenomanian (162.3-96.1 Ma). A sub-group of younger (Paleogene; ~60 Ma) ZFT ages is found in the NW of the unit; these ages are attributed to hydrothermal activity (Gröger et al., 2013). The AFT system is also reset in this unit and displays middle- to late-Miocene central ages (12.7-7.3 Ma), with some very young (3.4 and 4.0 Ma) ages attributed to overprinting by Neogene volcanism (Gröger et al., 2008). Toward the west of the Maramures Mountains, AFT ages are older (67.5-38.0 Ma) and interpreted as recording a Cretaceous exhumation event. South of the Maramures Mountains, AFT and AHe ages yield similar early to middle Miocene dates (25.0-18.8 Ma). These ages were interpreted as recording rapid cooling during the Miocene (Gröger et al., 2008). Only two AFT ages are available from the Romanian outer Carpathian units in the north-eastern region. The samples are on the Skyba-Tarcau nappe (Figure III.4) and show ages of >100 Ma. These ages are interpreted as non-reset (Sanders et al., 1999).

Data from previous studies on the Ukrainian outer Carpathians are discussed in Chapter II of this manuscript. Here we recapitulate the main conclusions regarding the thermochronometer ages from this region. The AFT and AHe thermochronometers record Miocene ages; early to middle Miocene for the reset AFT ages and middle to late Miocene for the reset AHe ages. The outermost nappes, i.e., the Skyba and Boryslav-Pokuttia nappes, display some non-reset AFT and AHe ages. Some AFT samples from the Krosno nappe are partially reset. Most of the ZHe ages are non-reset and record exhumation of the sources of the sediments now exposed in the Ukrainian Carpathian wedge.

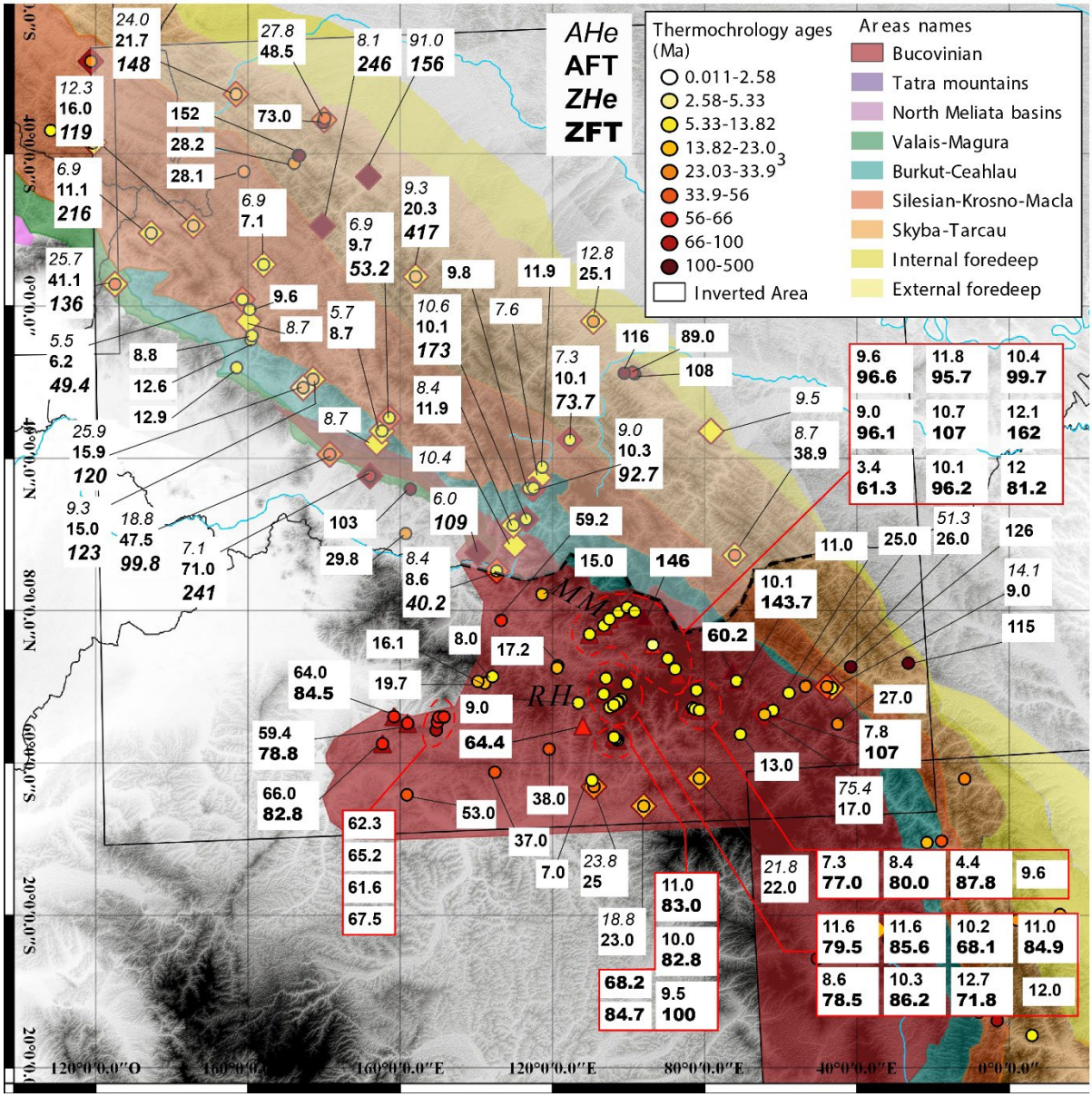

Figure III. 4: LT thermochronology data from the North-East Carpathian (NEC) region with ZFT, AFT, ZHe and AHe thermochronometer ages for each sample. The covered area is the Ukrainian Carpathian wedge detailed in Part II of this manuscript as well as the Maramures Mountains (MM) in northern Romania. Data symbols are as in Figure 1.

1.2.3 Eastern and South-eastern Carpathians

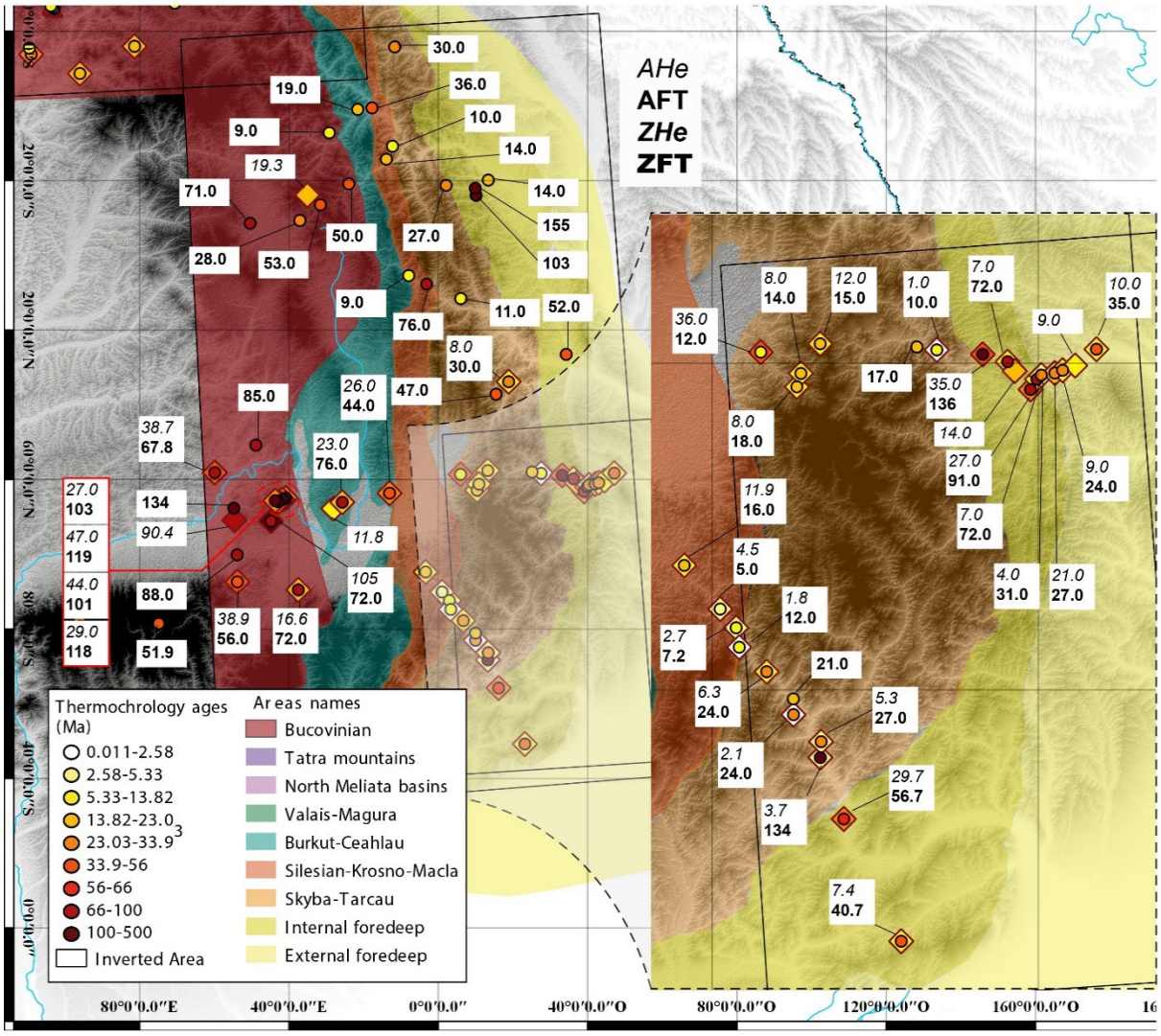

Figure III.5: LT thermochronology data from the Eastern and South-eastern Carpathian (E-SEC) region. For this area, only AFT and AHe data have been reported. The inset shows a zoom on the South-eastern Carpathian region, also known as the bend zone. Data symbols are as in Figure 1.

Only AFT and AHe thermochronometer data have been reported form the Eastern and South-eastern Carpathians in Romania, except for the Maramureş Mountains that are here, for the consistency of the inversions, attributed to the North-eastern Carpathians (Figure III.5).

Excluding the South-eastern bend zone, AFT ages in this region fall in the range of 155-5.0 Ma. Partially to non-reset AFT ages are found in the southern part of the Bucovinian units (central ages of >100 Ma). In contrast, AFT samples from the northern part of the Bucovinian unit in Romania are reset, with Paleogene to Oligocene (53.0-28.0 Ma; one Miocene - 9.0 Ma) ages. AFT ages from the Ceahlau, Audia and Tarcau nappes show an eastwards-younging trend (from 76 to 9 Ma) with reset (27.0-9.0 Ma), partially reset (44.0-30.0 Ma) and non-reset samples(76.0-52.0 Ma). In the most external Subcarpathian nappe, AFT samples are non-reset to partially reset (central ages >100 Ma; Figure III.5). AFT samples from the Audia-Macla and Tarcau nappes in the Bend Zone have totally reset ages between 37.0-12.0

Ma, with only one exception; an age of 134 Ma in the south (Figure III.5; Sanders et al., 1999). The Sub-Carpathian nappe bears only non-reset AFT data with ages from ~130-30 Ma (Merten et al., 2010; Necea et al., 2021).

Recent studies focused on the South-eastern Carpathians (i.e., Merten et al., 2010; Necea et al., 2021) used thermochronometry to decipher the exhumation of the zone with time-temperature modelling and reconstruct the history of nappe stacking. Numerous AHe ages have been reported from the Eastern and South- regions, generally associated to AFT ages from the same samples. The AHe ages become younger going from the west to east of the region. In the Bucovinian Units, AHe ages range from ~47.0-16.6 Ma, with some non-reset ages of 80->100 Ma. In the Ceahlau-Severin nappe, AHe ages are reset and range from 44.0 to 11.8 Ma (Figure III.5). In the Audia-Macla nappe, AHe ages are late Miocene to Pleistocene (12.0-1.8 Ma). AHe ages of the external nappes are reset at 6 to 13 Ma and at 1-2 Ma in the Tarcau and Marginal folds nappe, respectively. Some unreset AHe samples with ages from 32 to 37 Ma are found in these nappes (Merten et al., 2010; Necea et al., 2021). AHe samples from the Subcarpathian nappe are reset or partially reset, with ages spreading from 35.0 to 4.0 Ma. The use of LT thermochronometry and the analysis of grain populations as well as the reconstruction of thermal histories indicate that this zone is currently active with ongoing accretion and exhumation (Matenco et al., 2010, 2016; Merten et al., 2010; Necea et al., 2013, 2021).

2 Inversion of the thermochronology database

In this section we present the method to constrain the exhumation model by inversion of LT thermochronology data. The objective of this modelling exercise is to constrain the timing of the peak exhumation along the Carpathians arc. The hypothesis is that the development of this belt is diachronous from early-middle Miocene in the Western Carpathians (Mazzoli et al., 2010; Zattin et al., 2011; Andreucci et al., 2013; Castelluccio et al., 2016) to late Miocene or even Pliocene in the South-east Carpathians (Sanders et al., 1999; Matenco et al., 2010; Merten et al., 2010; Necea et al., 2021). Preceding work describing the lateral variation of exhumation in the Pyrenees, also using the Pecube code (Curry et al., 2021), has inspired the idea to search for a specific pattern of exhumation along the Carpathian arc. Specifically, we use Pecube to constrain time-varying exhumation rates for different parts of the arc, defined by nappe units and regions, which are then combined to visualise the spatio-temporal evolution of exhumation. An additional objective of the thermo-kinematic inversions was to constrain the amount of exhumed material, eroded of the belt and supplying the Carpathian foreland basin (CFB) and the Black Sea basin. The axial sediment transport system of this pro-foreland also shows a NW-SE evolutionary pattern (de Leeuw et al., 2020). Thus, the model setup aims to test the hypothesis of a diachronic co-evolution of the Carpathian fold-and-thrust belt and its foreland.

To observe lateral variations in exhumation rates, the orogen was separated in the regions described in the preceding section (1.2), i.e., the Western (WC), North-eastern (NEC) and Eastern and South-eastern Carpathian (E-SEC) regions. We further separated these regions into tectonic units (nappes) as defined by Schmid et al. (2008). The different nappes of the fold-and-thrust belt are correlated laterally, based on their paleo-geographic setting and tectonic evolution during accretion of the belt. The intra-regional

sub-division allows to combine samples that encountered a similar burial and exhumation history in the inversions.

2.1 Thermal-kinematic inversion with Pecube

2.1.1 What is Pecube?

The Pecube program traces the time-temperature histories (T-t path) of rock particles for a given (input) tectonic and geomorphic scenario, and predicts thermochronometric ages at specific locations. This thermal-kinematic code solves the heat production-diffusion-advection equation in three dimensions (Braun et al., 2012). Pecube can resolve the thermal history of a region by calculating the time evolution of the temperature field. It solves the heat equation allowing for vertical and/or horizontal heat advection, radiogenic heat production, and time-varying topography. These model inputs are determined by the user, together with the boundary conditions such as the surface and basal temperature.

Pecube can also be used to constrain the exhumation and/or relief evolution in mountain belts with an inverse approach that uses the Neighbourhood Algorithm (NA; Sambridge, 1999a, b). The NA inversions allow us to explore the variation of topographic and tectonic (kinematic) parameters within a pre-defined range (prior). The program searches the prior range of parameter values to find the combination of parameters that minimises the misfit between observed and predicted data (thermochronological ages; Figure III.6).

2.1.2 Output of the program

The output of the Pecube-NA inversion consists of a set of parameters with their associated fit statistics. The prior model (ranges of input parameters values) is reported, as well as the posterior model or best-fit scenario, which is the combination of parameters giving the lowest misfit between the predicted and the observed data.

The Pecube-NA inversion proceeds in two stages: the first stage samples a prior model space, defined by the range of values for the inverted parameters, to search for the best-fitting parameter combination. The parameter space is sampled over a series of iterations; at each iteration the parameter space to be searched is refined based on the misfit values. The misfit value (Φ) is an indicator of the fit of the predicted ages ($Pred_i$) of a model run to the observed ages (Obs_i). It corresponds to the reduced Chi-square value that considers the number of data points (n) and the uncertainty on the observed age of the thermochronometer (σ_i):

$$\Phi = \frac{1}{n}\sqrt{\sum_{i=1}^{n}\frac{(Obs_i - Pred_i)^2}{\sigma_i}} \quad (1)$$

During the second stage of the analysis, From the the probability distribution of each of the inverted parameters is calculated from the outcomes of the complete set of model runs performed, using a Bayesian approach and expressed as the marginal probability density function (PDF) for each parameter (Sambridge, 1999b). statistical estimators of the optimal parameter values, such as the mean, median or mode as well as the standard deviation can be derived from the marginal PDFs of the posterior model.

The model results can be represented by scatter plots in which the horizontal and vertical axes represent tested model parameters, and each tested parameter combination is shown as a point with a colour representing the resulting misfit value (Figure III.6). The marginal PDF of each of the two parameters, calculated from the ensemble of model outcomes, may additionally be visualised alongside the scatterplot axes. This visualisation also allows us to show the mean, median or mode of the posterior PDF model result together with the best-fit parameter combination (Figure III.6). One can choose which of these results are considered more representative of the best-fit tectono-geomorphic scenario for given a case-study. In well-constrained inversions the best-fit model should be close to the mode of the posterior parameter pdf, but this is not always the case (Figure III.6).

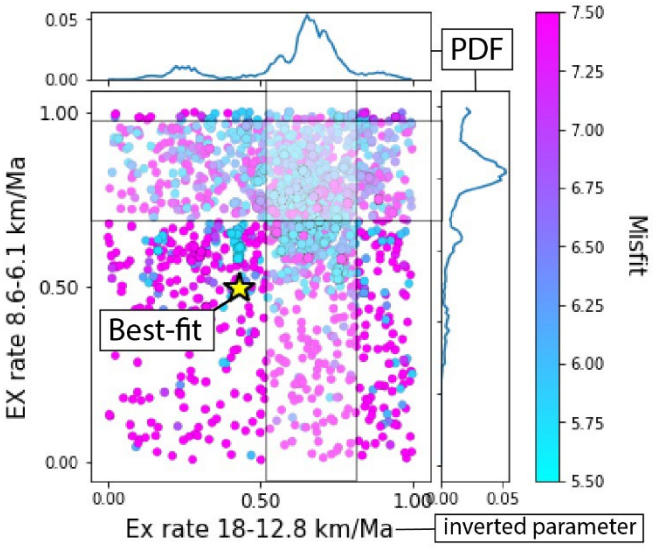

Figure III.6: Example plot of Pecube-NA inversion output. The corresponding posterior parameter PDFs are plotted alongside the scatter plot. Each dot in the scatterplot corresponds to an individual forward model, with the model misfit in colour (colour scale to the right; lower misfit values correspond to better fitting models). The yellow star shows the best-fit model, i.e., the parameter combination leading to the overall lowest misfit found during inversion and is here offset from the modes of the posterior parameter PDF's, which correspond to the region of general lower misfit values in the parameter space (white bands).

2.2 Modelling exhumation of the Carpathians with Pecube

To model the exhumation of the Carpathian belt using Pecube, we compiled the thermal parameters of the belt required by the code. We inverted for the exhumation rates of specific nappes over defined

timesteps, based on the stratigraphy of the Carpathian foreland basin. The method of selection of the data, the separation of regions and the definition of the timesteps are explained in this sub-section.

2.2.1 Model parameters

The Pecube code requires several input parameters, which include parameters controlling the thermal structure of the crust, the model thickness and the surface temperature (see Table 1). The crustal parameters are harmonized over the Outer Carpathians to represent the mean values of the crustal thickness and the basal temperature (Pospisil and Adam, 2006). Exceptions are made for the Tatra mountains, North Meliata and Sub-Carpathian units: the crustal thickness was adapted to reflect the thicker crust of Tatra Mountains and North Meliata units, and the thinner crust of the Sub-Carpathian nappe. We accordingly change the basal temperature to keep a constant geothermal gradient in the model. In the literature, a geothermal gradient of 20-30 °C/km is commonly cited for the Carpathians. We decided on a general geothermal gradient of 24°C/km, assuming that the gradient has not varied significantly over the last 34 My. This geothermal gradient is based on present-day well temperatures (Kolunt and Kotarba 2006), crustal thicknesses estimations (Pospisil et al 2006, Pospisil and Adam 2006) and previous thermo-kinematic modelling (Andreucci et al., 2015).

Pecube parameters for inversions		
Thermal parameters		
Thickness of the crust	30*	km
Thermal diffusivity	30	km²/My
Basal temperature	720*	°C
Sea level temperature	10	°C
Heat production	0.95	°C/My
Inversion parameters		
Number of time steps	2 to 4	
Number of runs	10900	
Sample size 1st iteration	100	
For all other iterations	90	
Re-sampled cells	70	

Table III.1: Pecube parameters for the exhumation model applied to the Carpathians. Values with an asterisk are varying in some inversions (see text for details).

2.2.2 Modelling strategy

The Pecube program allows the construction of models that separate data by fault structures. However, for the Carpathians, regions separated by major faults (i.e., nappes) are very elongated and arcuate along the belt. This structure cannot be well implemented in the Pecube program, where faults should be straight and defined by two points at the surface. We therefore chose to run separate models for each tectonic unit (i.e., nappe) in each region. By inverting the data per tectonic unit, we avoided having to make assumptions about fault locations and geometry, and restricted inverted parameters to the exhumation rates. However, the downside of this approach is that the trajectory of a rock particle from depth to the surface is assumed to be vertical. In the case of the Carpathians, i.e., an accretionary prism evolving into an orogenic wedge, trajectories of rocks evolve through time, depending on the mechanical properties of the prism and the influx of material in the wedge (see Chapter I section 2.2; Konstantinovskaia and Malavieille, 2005). Taking into account this assumption (which would not be

necessary if horizontal advection (i.e., faults) were implemented in the simulation), the exhumation rates presented here are estimates of the vertical component of the velocity of rock particles in the wedge. This restriction to vertical exhumation rates is thought to not impact the results we are seeking. We want to constrain the eroded overburden in time and space to estimate the fluxes of sediments from the orogen. These two parameters are directly linked to the vertical component of the exhumation path of rocks. Here we constrain rock uplift (as defined in England and Molnar, 1990) as topography is supposed constant during inversion.

The division in regions allows studying the diachronous evolution of the belt and the sub-division in tectonic units allows constraining exhumation rate without the implementation of faults. We thus ran twelve separate inversions on parts of the Carpathian dataset: dividing each of the three regions into four tectonic units. The following section describes the division and nomenclature of the different models.

In the WC, the inner part of the belt was split in two groups of data: (1) samples from the Tatra Mountains basement (TNM, Figure III.1 and 2) and (2) samples from the North Meliata Paleogene basins lying on the Tatra basement (NNM, Figure III.1 and 2). The outer part of the belt was equally split into two groups: (1) data from the Valais-Magura nappe, were grouped with those from the Pieniny Klippen belt (PMV, Figure III.1 and 2); and the most external data from the Silesian nappes (PAM, Figure III.1 and 2).

Data from the NEC are also divided into four datasets. The first contains the data from the Bucovinian basement (UBC, Figures 1 and 4). The second consists of data from the Magura unit together with the Burkut nappe, which are laterally correlated with Ceahlau-Severin nappe in Romania (UCS, Figure III.1 and 4). The data from the Krosno nappe is inverted on their own (UAM, Figure III.1 and 4). The final group contains the data from the most external nappes in Ukraine; i.e., the Skyba and Boryslav-Pokuttia nappes (named Internal foredeep in Figure III.1 and 3; UMT).

In the E-SEC, data from the Bucovinian sedimentary cover is modelled separately (RBC, Figure III.1 and 5) while the Ceahlau-Severin nappe is combined with the Audia-Macla nappe due to an insufficient amount of data on the latter (RAM, Figure III.1 and 5). The Marginal folds and Tarcau nappes (Tarcau on Figure III.1 and 5) are also modelled together (RMT). The data in the Subcarpathian nappes of the SE Carpathians are spatially very dense, compared to the other datasets (Figure III.5); we modelled them on a smaller area to increase the resolution of the model of the Subcarpathian nappe (Internal and External foredeep, Figure III.5). These areas are grouped together as RSE.

2.2.3 Division in time steps

The time steps during which we constrain exhumation rates were calibrated to represent the chronostratigraphic scale, to facilitate later comparison of exhumation from the mountain belt with deposition in the foreland basin (see Chapter I). However, the time steps chosen do not always completely correspond to the chronostratigraphic stages of the Paratethys stratigraphy. The time boundaries were adapted to obtain a distribution of the data among the time steps allowing a sufficient resolution of exhumation rates during each time step. The number of data inverted during a time step

greatly influences performance through the inversion process. This effect is particularly evident for the early time steps, as they have fewer thermochronology data, and in consequence, the largest time period for inversion. We used four timesteps to explore the temporal variation of exhumation for most dataset, with the exception of the E-SEC region, where the RSE model has only two time step due to young thermochronometer ages. In Figures III.7-9 we display the LT thermochronology data age frequency to illustrate the choice of time step per tectonic unit.

We started our inversion of exhumation rates at 34 Ma or, more specifically, to base the model on chronostratigraphic periods, the beginning of the Oligocene (33.9-23.03 Ma). The next time-step limit is placed at 24 Ma, which approximates the beginning of the Miocene (23.03-5.33 Ma). The period between 20-12 Ma is largely represented in our dataset all around the Outer Carpathians. Thus, we shortened the time steps in this period to a get finer depiction of the variation of exhumation rates over this period. The 18 Ma time-step limit is during the Ottnangian stage of the Black Sea chronostratigraphy (19-17 Ma; Krijgsman and Piller, 2012). The next time boundary is set to the beginning of Badenian stage, at 16 Ma. The following boundary is placed near the beginning of the Sarmatian stage (12.65-8.3 Ma) at 12.8 Ma. Another time boundary is placed near the end of the Sarmatian stage at 8.6 Ma, slightly departing from the stage limits. At the end of Meotian (8.3-6.1 Ma) another time boundary is set at 6.1 Ma. The last time-step limit we implemented corresponds to the base of the Pleistocene at 1.8 Ma for the SE Carpathians. We compile the different time step with the foreland stratigraphy in a supplementary figure (Figure S2).

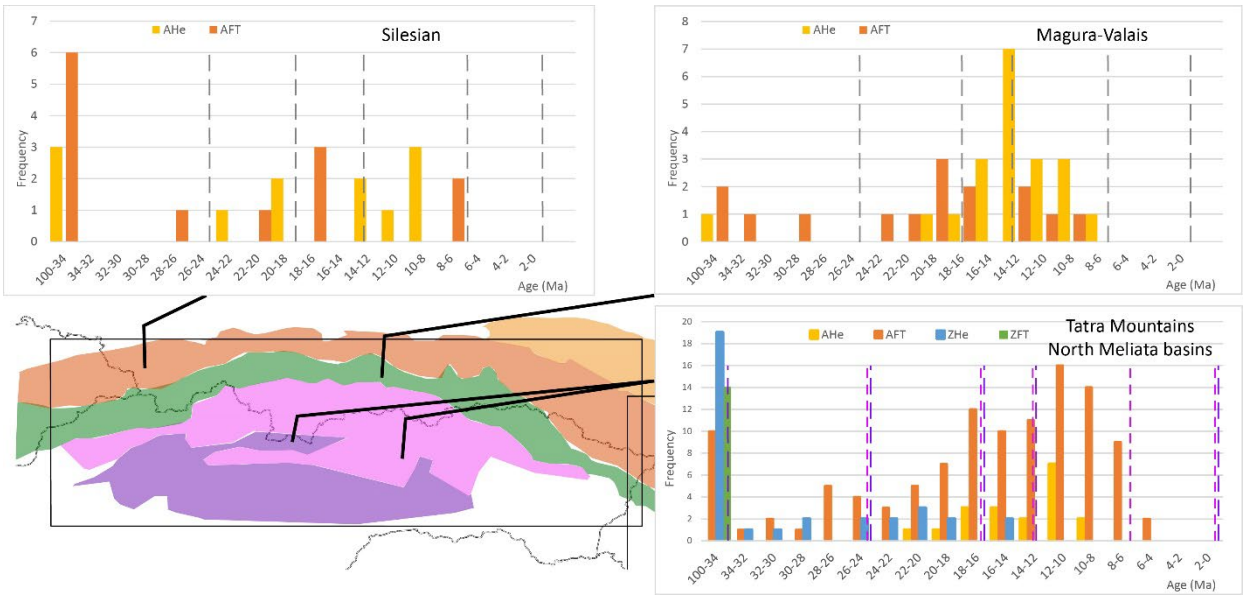

Figure III.7: Age-frequency diagram of LT thermochronology data of the different datasets of the WC region of the exhumation model. Bars in x-axis delimit the time steps. On the bottom right graph, purple bars delimit (Figure III.2) dataset and lilac bars the North Meliata basins dataset (Figure III.2).

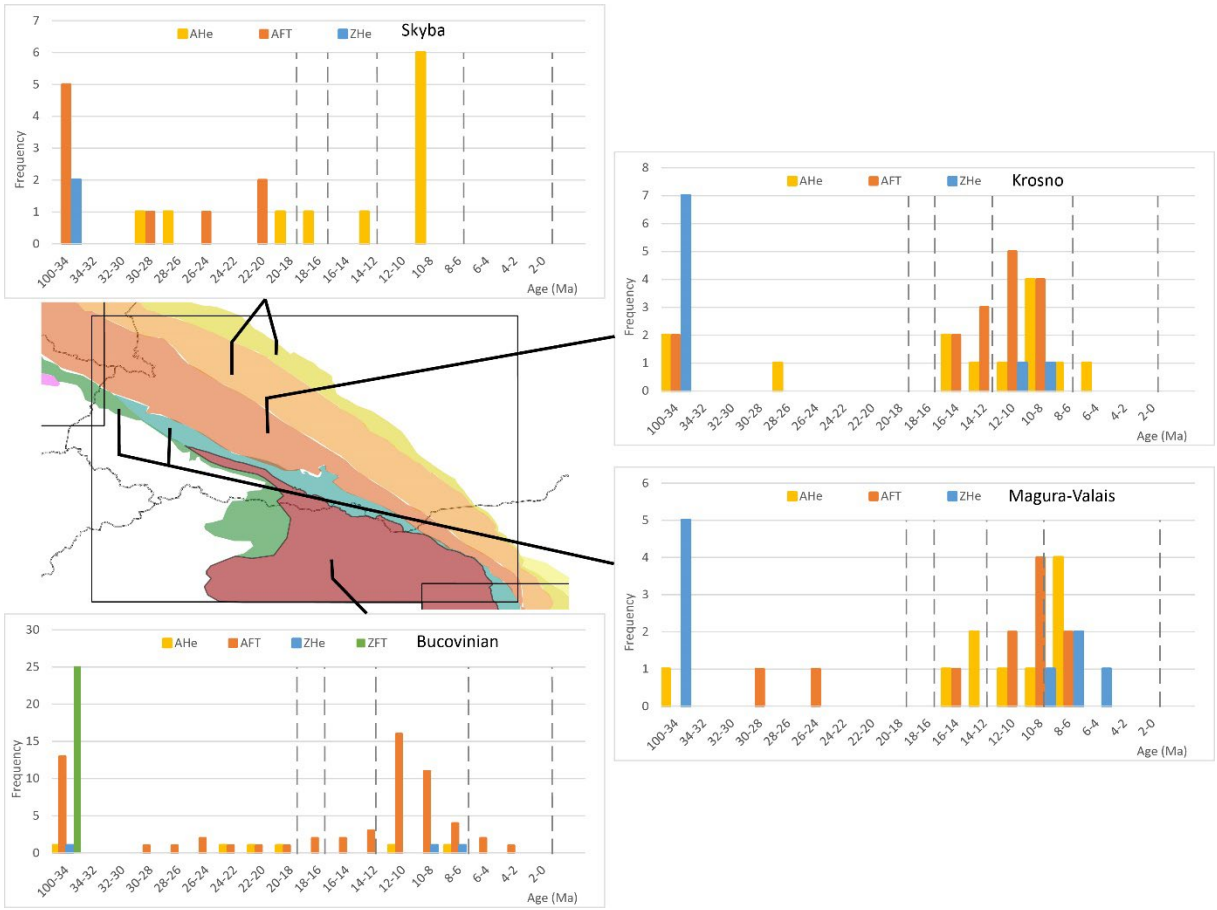

Figure III.8: Age-frequency diagram of LT thermochronology data of the different datasets of the NEC region of the exhumation model. Bars in x-axis delimit the time steps.

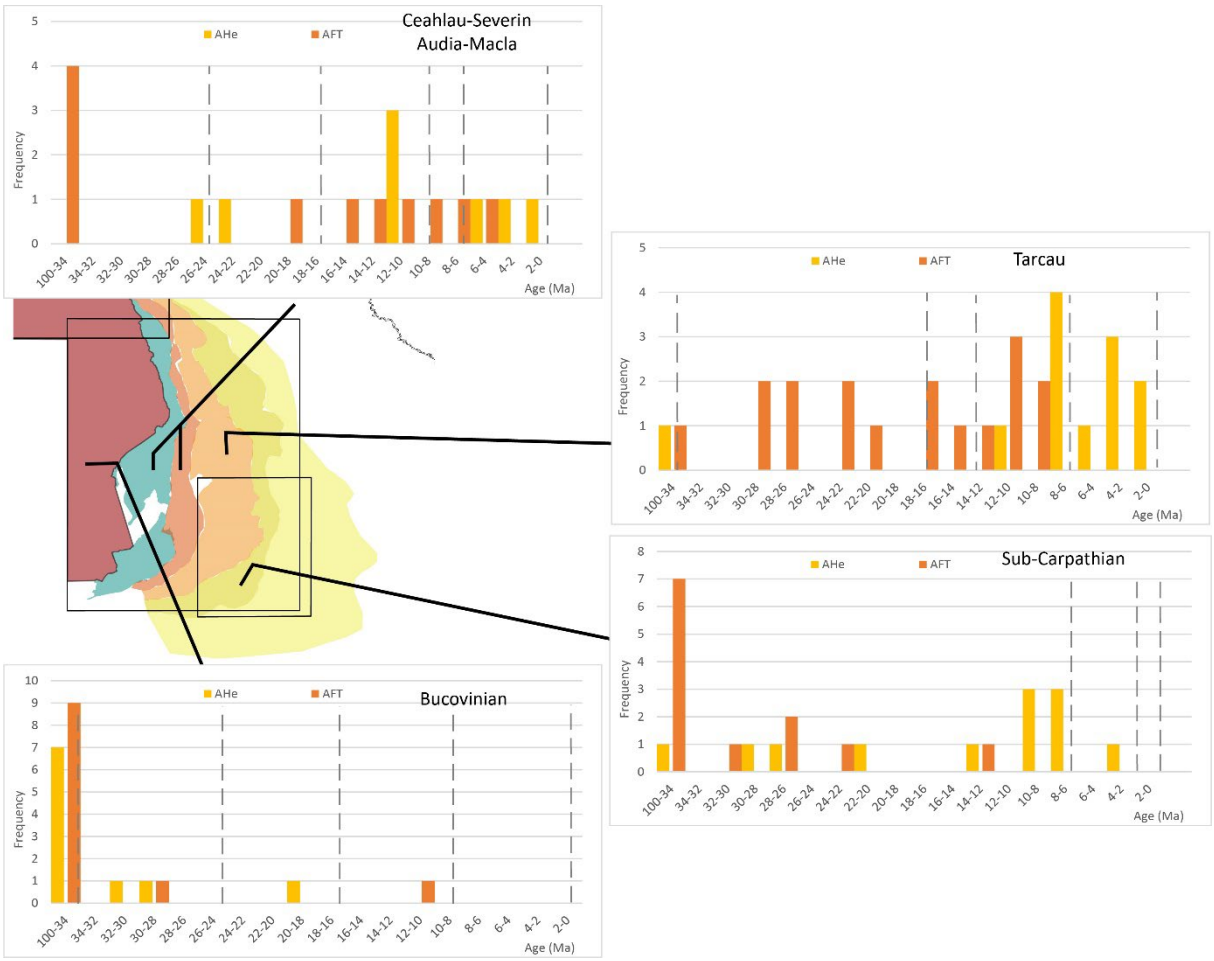

Figure III.9: Age-frequency diagram of LT thermochronology data of the different datasets of the E-SEC region of the exhumation model. Bars in x-axis delimit the time steps.

3 Exhumation of the Carpathian fold-and-thrust belt

The exhumation model of the Carpathian belt represents the evolution of the wedge over 34 My. In the following section we describe the results of the Pecube inversions for the twelve datasets as a comprehensive exhumation history. The variation over time and space of the exhumation rates indicates a diachronous development of the wedge.

Table III.2: Pecube-NA inversion results for the region of the Western Carpathians region. Name of the runs are presented in section 2.2.2 of this study. "Post" and "Prior" refer to the posterior and prior model, respectively; the table reports mean exhumation rates (in km/My) during the different time steps and their standard error. The overall best-fit exhumation rate for each time step is also reported.

Nappe run	Time step	Post		Prior		Best-fit
	Ma	mean	std err	mean	std err	km/My
TNM07	34-24	0.17	0.06	0.50	0.29	0.20
	24-16	0.55	0.06	1.00	0.29	0.50
	16-12.8	0.42	0.13	0.45	0.20	0.49
	12.8-0	0.21	0.04	0.50	0.29	0.20
NNM04	24-16	0.82	0.18	0.50	0.29	0.99
	16-12.8	0.94	0.06	0.50	0.29	0.99
	12.8-6.1	0.40	0.07	0.50	0.29	0.46
	6.1-0	0.05	0.04	0.50	0.29	0.00
PMV X1	24-16	0.45	0.21	0.50	0.29	0.16
	16-12.8	0.64	0.18	0.50	0.29	0.54
	12.8-6.1	0.32	0.15	0.50	0.29	0.78
	6.1-0	0.18	0.17	0.50	0.29	0.05
PAM23	24-18	0.61	0.18	0.50	0.29	0.68
	18-12.8	0.54	0.20	0.50	0.29	0.41
	12.8-8.6	0.29	0.19	0.50	0.29	0.42
	8.6-0	0.17	0.11	0.50	0.29	0.14

Table III.3: Pecube-NA inversion results for the region of the North-eastern Carpathians region. Name of the runs are presented in section 2.2.2 of this study.

Nappe run	Time step	Post		Prior		Best-fit
	Ma	mean	std err	mean	std err	km/My
UBC20	34-18	0.15	0.04	0.50	0.29	0.13
	18-12.8	0.71	0.04	0.50	0.29	0.74
	12.8-6.1	0.66	0.02	0.50	0.29	0.65
	6.1-0	0.10	0.04	0.50	0.29	0.03
UCS 20	18-16	0.70	0.13	0.50	0.29	0.85
	16-12.8	0.43	0.15	0.50	0.29	0.39
	12.8-8.6	0.41	0.12	0.50	0.29	0.38
	8.6-0	0.28	0.12	0.50	0.29	0.13
UAM 25	18-16	0.73	0.01	0.50	0.29	0.82
	16-12.8	0.31	0.01	0.50	0.29	0.07
	12.8-8.6	0.50	0.02	0.50	0.29	0.55
	8.6-0	0.38	0.02	0.50	0.29	0.35
UMT24	18-16	0.13	0.05	0.50	0.29	0.08
	16-12.8	0.75	0.07	0.50	0.29	0.78
	12.8-6.1	0.27	0.05	0.50	0.29	0.26
	6.1-0	0.08	0.09	0.50	0.29	0.07

Table III.4: Pecube-NA inversion results for the region of the Eastern-South-eastern Carpathians region. Name of the runs are presented in section 2.2.2 of this study.

Nappe run	Time step	Post		Prior		Best-fit
	Ma	mean	std err	mean	std err	km/My
RBC06	34-24	0.36	0.01	0.50	0.29	0.38
	24-16	0.01	0.01	0.50	0.29	0.01
	16-8,6	0.01	0.01	0.50	0.29	0.00
	8,6-00	0.01	0.01	0.50	0.29	0.01
RAM10	28-16	0.23	0.03	0.50	0.29	0.25
	16-8,6	0.04	0.03	0.50	0.29	0.00
	8,6-6,1	0.87	0.12	0.50	0.29	1.00
	6,1-0,0	0.10	0.06	0.50	0.29	0.07
RMT05	34-16	0.02	0.01	0.50	0.29	0.01
	16-12,8	0.01	0.01	0.50	0.29	0.01
	12,8-6,1	0.01	0.01	0.50	0.29	0.01
	6,1-0,0	0.74	0.01	0.50	0.29	0.74
RSE07	6,1-1,8	0.41	0.03	0.50	0.29	0.45
	1,8-0,0	0.09	0.06	0.50	0.29	0.03

3.1 Results of Pecube-NA inversions

The result of the Pecube-Na inversions of the 12 datasets are reported in this section. Tables 2-4 display the prior and posterior models as well as the best-fitting exhumation rates for each timestep and each inverted dataset. The improvement of the posterior model on the prior can be assessed by comparing the prior and posterior standard errors. We thus aimed for a standard error on the exhumation rates lower than 0.20 km/My, given the general 0.29 km/My error of the prior model (related to a prior range of 1 km/My for the exhumation rates). For the WC region this is not the case in the PMV X1 run (Table 2) where the error on the exhumation rate at time step 24 to 16 Ma is 0.21 km/My. The other regions (Tables 3 and 4) have errors significantly lower than the WC. Exhumation rates of the E-SEC region display very low values associated with relatively high errors (up to 100%; Table 4). We interpret these high errors and low exhumation as an inactive phase (i.e., no rock uplift). The detailed scatter plots and run performance are displayed in the supplementary figures of this part (Annexes S3-S5).

3.2 Model evaluation

The model performance can be assessed by the fit to the data for each thermochronometer (Figure III.10), which provides additional spatio-temporal information to the general performance of each model as evaluated by the misfit value (section 2.1.2, equation (1)) and the PDFs of exhumation rates. The normalized difference (Δ) between the observed (*Obs*) and predicted (*Pred*) ages (equation (2)) of each thermochronometer allows to assess if the model over- or under-predicts the age for each data point (a):

$$\Delta = \frac{Obs_a - Pred_a}{Obs_a} \quad (2)$$

The age difference of the exhumation model (Figure III.10) displays a general trend of under-predicted ages for all thermochronometers. The AFT and AHe thermochronometers are better constrained by the code. Strong underprediction of some of the ZFT and ZHe ages results from the non-reset nature of these thermochronometers in many samples. The general under-prediction of ages implies that the exhumation model of the Carpathians presented in this work should be interpreted as a maximum model.

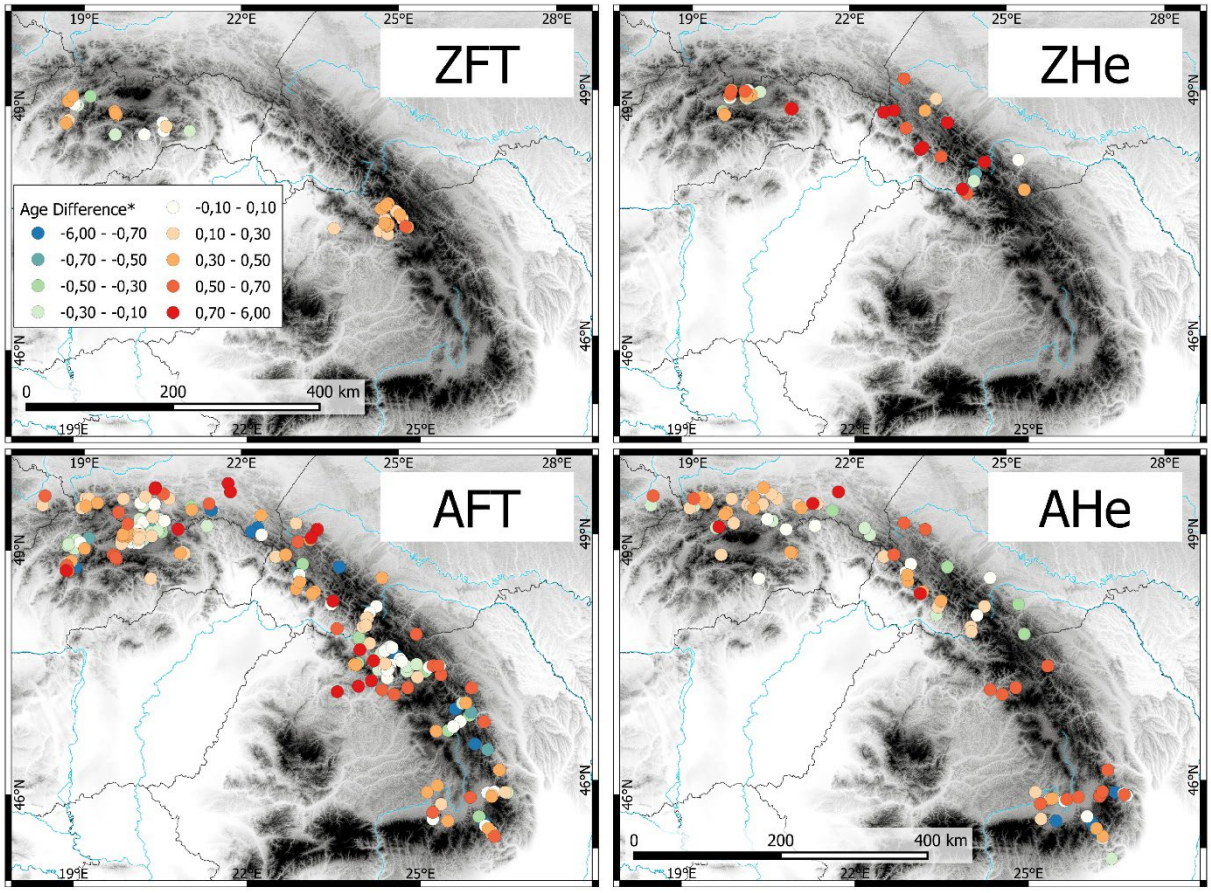

Figure III.10: Age difference (as defined in equation 2) of the exhumation model of the Carpathians for the four different thermochronometers. The difference is normalised by the observed age to allow the comparison between thermochronometers.

3.3 Variation of exhumation from NW to SE

The overall temporal and spatial evolution of exhumation that we obtain from our Pecube-NA inversions of the data (Figure III.11) displays diachronicity in exhumation rates from the inner to the outer units of the wedge, and especially a NW-SE propagation in the timing of most rapid exhumation.

The spatial variation of the exhumation rates over the Carpathian belt is illustrated in the maps of Figure III.12. At the onset of the model, between **34-24 Ma**, exhumation was limited to the innermost units of the Carpathians in the different regions. Exhumation rates were generally low (< 0.2 km/My), except in the Bucovinian unit in the E-SEC region. In the next time step, **24-18 Ma**, exhumation accelerated throughout the WC region to rates > 0.4 km/My. In comparison, other regions were

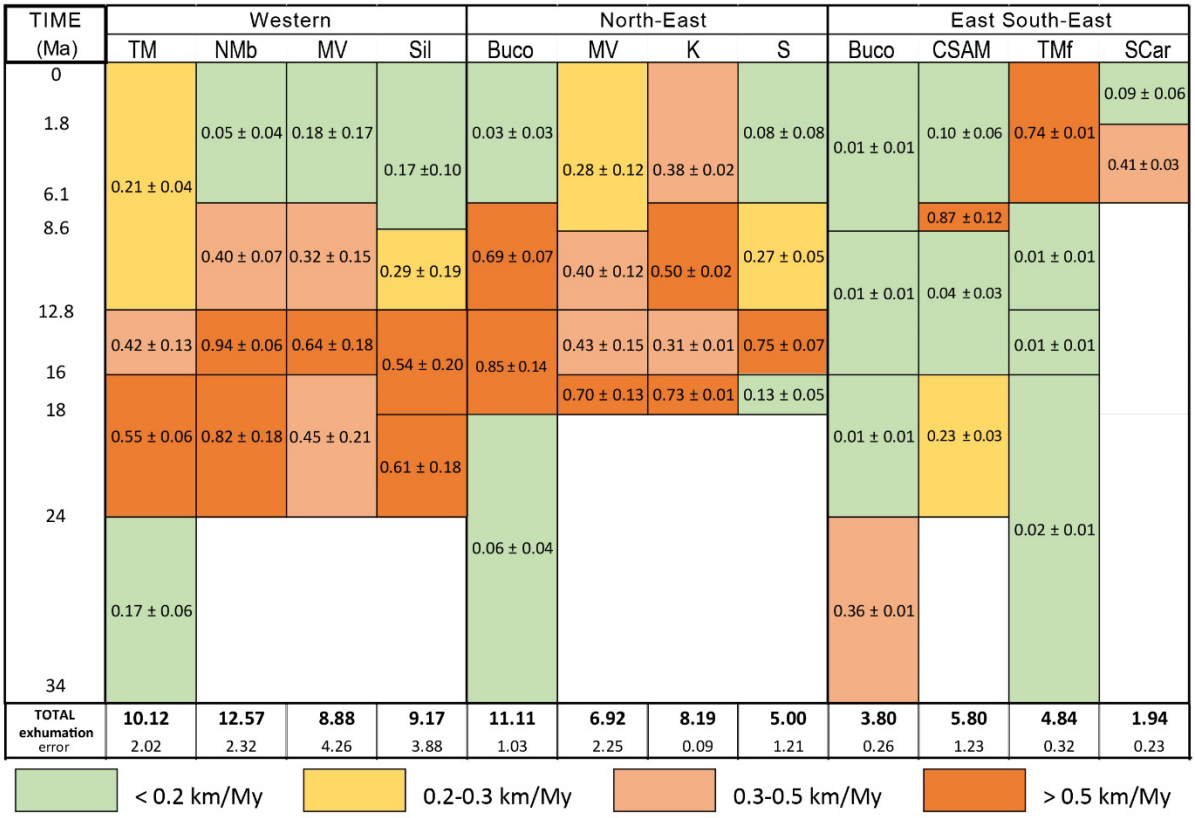

Figure III.11: Temporal variation of exhumation rates constrained by the Pecube inversions for the twelve datasets of the Carpathians. The exhumation rates over time are grouped by regions and ordered from the innermost to the outermost nappes. TNM: Tatra Mountains; CCPB: North Maliata basins from AlCaPa terranes; MV: Magura-Valais nappe; Sil: Silesian and Sub-silesian nappes; Buco: Bucovinian units; MB: Magura and Burkut nappes; DK: Dukla and Krosno nappes; SBP: Skyba and Boryslav-Pokuttia nappes; CSAM: Ceahlau-Severin and Audia-Macla nappes; TMf: Tarcau and Marginal folds nappes; SCar: Subcarpathian nappe. The nappe names correspond to the global database map in Figure III.1.

exhuming at lower rates of < 0.1 km/My, except for CSAM in the E-SEC, or are not constrained, mostly in the NEC. In the **18-16 Ma** time-step, most units of the NEC (except SBP) started to exhume at high rates (> 0.5 km/My). The rates also remained high in the WC (> 0.4 km/My) but low in the E-SEC (< 0.3 km/My). During the next time-step, **16-12.8 Ma**, the models predict propagation of high exhumation rates in the NEC to the Skyba and Boryslav-Pokuttia nappe (SBP at 0.75 km/My; Figure III.11). Both the WC and NEC still experienced rapid exhumation (0.4 – 0.85 km/My) during this time, with the exception of the Dukla-Krosno nappe where exhumation rates decreased from 0.73 km/My during the preceding time step to 0.31 km/My at this time step. Exhumation rates in the E-SEC remained < 0.1 km/My during this period. The **12.8-8.6 Ma** time-step displays a major change in the exhumation pattern as only the Bucovinian and the Dukla-Krosno units of the NEC show rapid exhumation (0.5 – 0.7 km/My) during this time. Exhumation rates decreased in the WC and the outer nappes of the NEC to 0.2 – 0.4 km/My during this time. Exhumation in the Dukla-Krosno unit accelerated during this time step after a deceleration in the preceding step. This result is coherent with the time-temperature modelling performed on data of the Dukla and Krsono nappes in Chapter II of the manuscript. The onset of rapid exhumation in the E-SEC region occurs during the **8.6-6.1 Ma** time-step. The Ceahlau-

Severin and Audia-Macla units are exhuming at 0.87 km/My during this period. Exhumation rates in the WC drop to ≤ 0.2 km/My after **6.1 Ma** for all units except the Tatra Mountains, where they remained at 0.21 km/My. The NEC units show deceleration at this time as well, although exhumation rates in the Dukla-Krosno unit were still ~0.4 km/My. In contrast, the Tarcau-Marginal fold and Sub-Carpathians units of the E-SEC started exhuming rapidly (0.4 – 0.7 km/My) during this time. The last time step, **1.8-0 Ma**, is only constrained for the Sub-Carpathians unit; the exhumation rate drops to 0.09 km/My for this time step.

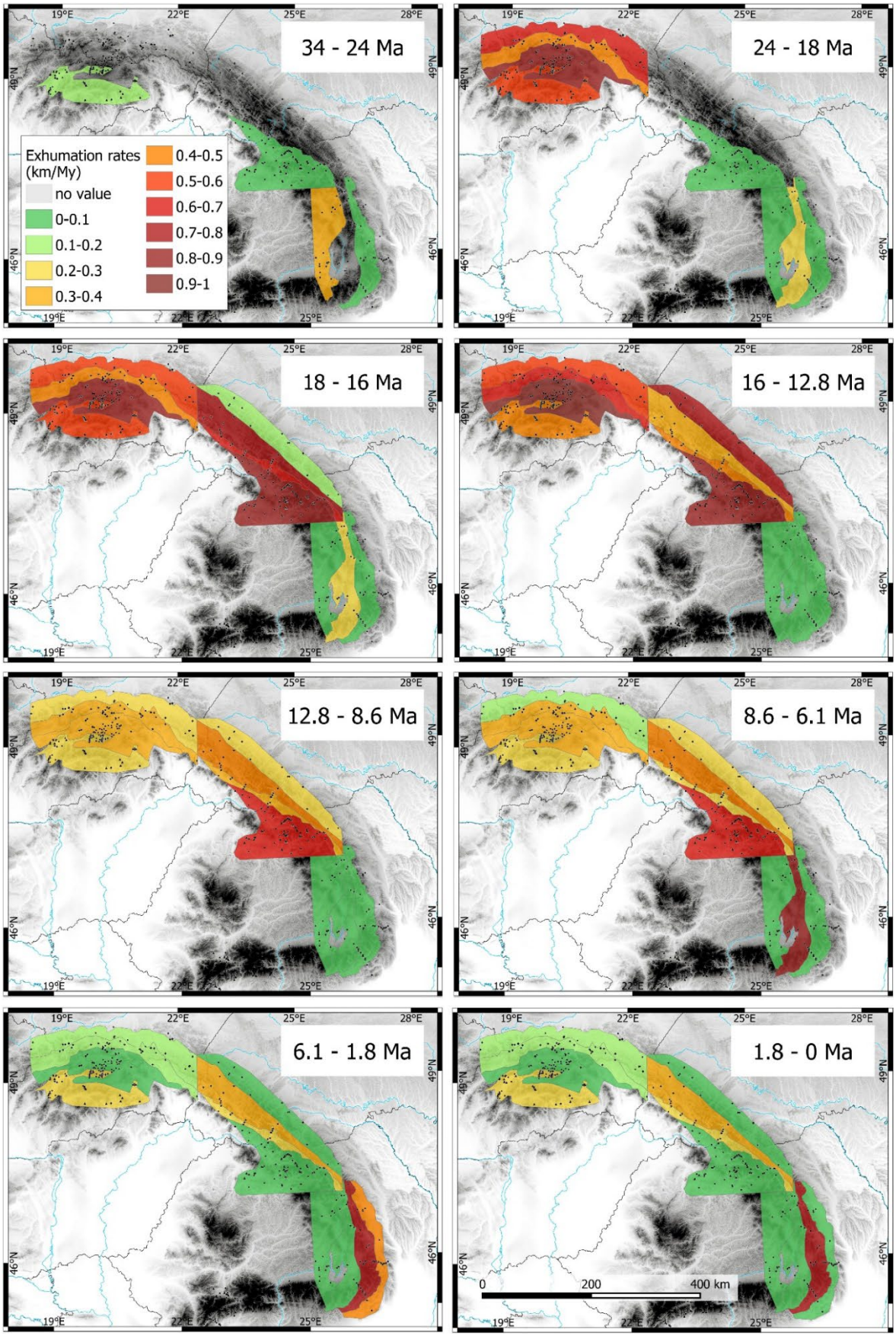

Figure III. 12: Map of the modelled exhumation rates over different time steps throughout the Carpathians.

3.4 Total amount of exhumation in the Carpathians.

The exhumation model for the Carpathian fold-and-thrust belt developed above also allows us to calculate the total amount of exhumation for each modelled unit. The horizontal advection and the curved path to surface in orogenic wedge exhume material to surface erosion during a long period of time (Batt and Braun, 1997, 1999). The cumulative amount of material eroded at the surface is much larger than the vertical amount of exhumation encountered by a rock sample (Batt and Brandon, 2002). Therefore, the total amount of exhumed material in the Carpathians is larger than the overburden interpreted from isotherm depth of reset and partially reset thermochronometers Figure III.13 shows the cumulative exhumation of the units in the different regions of the Carpathians.

In the WC, the maximum amount of exhumation is recorded in the Tatra Mountains and North Meliata basin. Both units have fully reset AFT systems as well as reset Miocene ZHe ages. The total amount of exhumation over the last 34 Ma is >10 km for both units, in good agreement with the reset ZHe ages. For the Outer Carpathians nappes of the WC, i.e. the Magura-Valais and Silesian units of the model, total exhumation is lower, but still sufficient to reset the AFT and AHe thermochronometers of these units. Total exhumation in the Silesian unit amounts to 9.17 ± 3.88 km (Figure III.13). We attribute this large error on the total amount of exhumation to the partial reset of most of the AFT data in this dataset.

In the NEC region, the inner Bucovinian units show the largest eroded overburden (11.11 ± 1.03 km; Figure III.13). This is explained by the regional tectonics of the Maramures Mountains and the Rodna Horst, which were exhumed mainly along E-W oriented strike slip fault zones and sub vertical normal faults (Gröger et al., 2008, 2013; Ustaszewski et al., 2008) allowing rapid and deep exhumation of basement rocks as recorded by reset middle-late Miocene ZFT and AFT ages. The Magura-Burkut and Dukla-Krosno units show ~7 km of total exhumation (6.92 ± 2.25 km and 6.93 ± 0.26 km respectively). The Skyba and Boryslav-Pokuttia nappes record an amount of exhumation (5.0 ± 1.2 km) that is coherent with the partially reset AFT and reset AHe data given the 24°C/km geothermal gradient we assumed. This gradient would imply a temperature of ~120 °C at 5 km depth; however, the non-reset samples of the set could explain the relatively large error on the total amount of exhumation. The lower limit of exhumation for this unit corresponds to 3.8 km or a temperature of ~90 °C, not sufficient for total resetting of the AFT system, but sufficient to reset the AHe thermochronometer.

The E-SEC region displays early exhumation of the Bucovinian units (from 34 to 24 Ma) followed by quiescence, with exhumation resuming in the Ceahlau-Severin and Audia-Macla unit at 8.6 Ma. The low total amount of exhumation of these units is required by the AFT and AHe ages older than Oligocene in the respective datasets (Figure III.5). These ages cannot constrain the exhumation during the period of inversion, therefore, the total amount of exhumation of our model (3.80 ± 0.26 km and 5.80 ± 1.23 km for the Bucovinian and Ceahlau-Severin / Audia-Macla, respectively) is a minimum estimate. Samples from the Audia-Macla nappe that display AFT ages of 5.0 to 16.0 Ma and AHe ages from 4.5 to 12.0 Ma require the relatively high exhumation rate at 8.6-6.1 Ma (Figure III.5). The Tarcau-Marginal folds and Subcarpathian units have a comparatively low total amount of exhumation, which

is consistent with the recent onset of exhumation in these nappes and the mostly unreset AFT ages encountered in these units (Figure III.13).

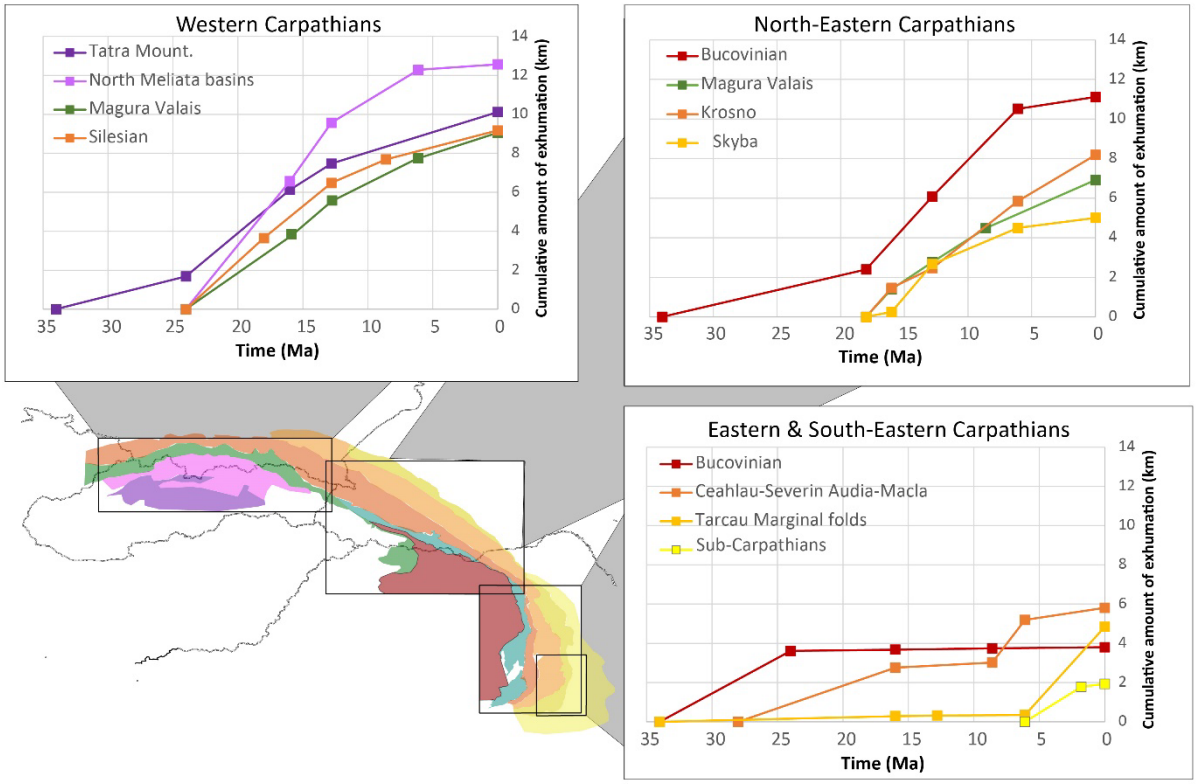

Figure III.13: Cumulative exhumation (km) by region and per tectonic unit in the Carpathians from inversion of thermochronology datasets. The colours of the lines correspond to those of the tectonic units on the simplified map of the Carpathians in the lower left corner, as in Figure 1.

4 Discussion

4.1 Modelling assumptions and simplifications

The approach we took in our inversion of the Carpathian LT thermochronology dataset is a simplification of the process of fold-and-thrust belt construction. Horizontal advection is neglected over the vertical (exhumation) component rock-particle paths in the process. We are mainly interested in the exhumation of material from the Carpathian belt, and its connection to the flux of eroded sediment shed to the pro-foreland basin. Thus, the horizontal displacement of rock particles, explored in restored sections across the WC and NEC region (Gągała et al., 2012; Castelluccio et al., 2016; Nakapelukh et al., 2017; 2018), is not constrained in the model.

Previous studies that have attempted to retrace the exhumation history over an entire mountain range have often found indications for lateral variations in the timing and amount of exhumation (Morris et al., 1998; Thomson et al., 2010; Fox et al., 2014, 2016; Curry et al., 2021). Recently, the lateral variation of exhumation in the Pyrenees was constrained through a relatively similar modeling strategy to that

applied here (Curry et al., 2021). The results of this latter study indicated a synchronous onset of exhumation throughout the mountain belt, and Curry et al. (2021) tested if a division of the thermochronology data by tectonic unit or by region led to better model predictions. The model in which the mountain belt was divided into four regions along north-south trending boundaries predicted lower misfits and was used to explain the evolution of the range in Cenozoic times. In contrast with this study, the spatial distribution of data in the Carpathian belt and the elongated shape of the orogen allowed to constrain both a regional approach and a separation by tectonic units.

Unlike the study of Curry et al. (2021), we assume a constant topography throughout the modelled time span in the Carpathian region and inverted only for the exhumation rates. The overall low elevation of the belt and the long accretion phase (from the Oligocene to late Miocene) suggest the formation of a submarine wedge that emerged in Miocene (see section 4.3 of this discussion). The SE Carpathians region is currently active, and its highest peaks reach ~1500 m. Considering the topography in the remaining active region and the overall moderate exhumation rates of the orogen (< 1 km/My), the evolution of the topography was neglected in the model setup.

However, the grouping of thermochronology data in tectonic units allows us to explore the exhumation of regions separated by complex fault zones. We constrained the diachronicity of along strike onset of exhumation. This procedure could be adapted to other orogens than the Carpathians or the Pyrenees.

4.2 Comparison with previous studies in the Carpathians

4.2.1 Exhumation of the WC, NEC and E-SEC studies

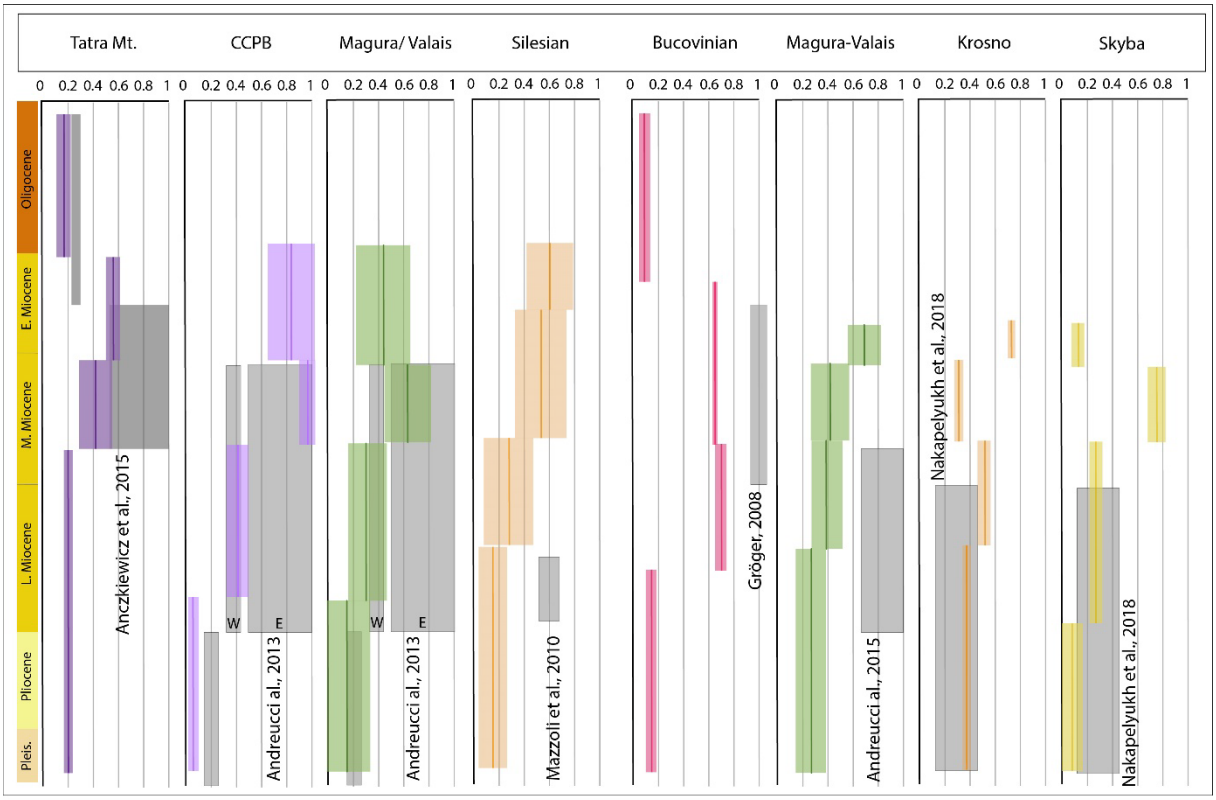

Figure III.14: Comparison of exhumation rates inferred for the Western and North-eastern Carpathians with estimates from previous studies.

The database comprises thermochronometry ages from previous studies, and the inverse modelling should therefore be comparable to the previously established exhumation rates or histories. In the WC region, several studies were conducted on the Tatra Mountains. Anczkiewicz et al. (2015) established two periods of cooling for the massif, an early episode of with cooling of 1-5 °C/My in the 30-20 Ma period and a younger and more rapid cooling episode of 10-20 °C/My in the middle-late Miocene (~16-9 Ma). In the highest area of the Tatra, thermochronology data indicate an exhumation rate of 0.2 km/My during the Oligocene-early Miocene (Anczkiewicz et al., 2015). The correspondence with our 0.21 km/My rate is good. However, as Anczkiewicz et al. (2015) assume a geothermal gradient of 20°C/km, their peak exhumation rates of approximately 0.25 km/My in the 30-20 Ma period corresponds to our estimate of 0.17±0.06 km/My obtained with a higher (24 °C/km) geothermal gradient (Figure III.14). The early-middle Miocene exhumation rate estimated by Anczkiewicz et al. (2015) is 0.5-1 km/My, also higher than our results (0.55 ± 0.06 km/My at 24-16 Ma and 0.42 ± 0.13 km/My at 16-12.8 Ma) but still within error. Andreucci et al. (2013) modelled the cooling history of the North Meliata basins (CCPB) and the Magura-Valais nappe and suggested that exhumation varied longitudinally, the Western area being exhumed at 0.4 km/My (supposing a geothermal gradient of 18°C/km) from 15-10 Ma and the Eastern

area having a higher exhumation rate of 0.4-1.1 km/My from 15-5 Ma. The rate subsequently decreased to 0.2 km/My until present-day. Our models are congruent with the exhumation rates estimated by Andreucci et al. (2013) from the Eastern region, at 0.82-0.94 km/Ma between 24 Ma and 12.8 Ma. For the period 12.8-6.1 Ma, our models correlate with the exhumation rates inferred by Andreucci et al. (2013) for both areas (Figure III.14). For the outer belt, Mazzoli et al. (2010) inferred an exhumation rate of 0.6 km/My around 7 Ma in the Silesian nappe, supposing a geothermal gradient of 25 °C/km. The rate we obtain for the late Miocene in these nappes is significantly lower, with 0.36 ± 0.13 km/My in the Magura nappe and 0.17 ± 0.10 km/My in the Silesian nappe from 8.6 Ma to present (Figure III.14).

In the Bucovinian unit of the NEC region, late Miocene (12.7-7.3 Ma) exhumation rates of about 1 km/My were inferred by Gröger (2008) for the Rodna horst and the Maramureş Mountains. This in good agreement with the exhumation rates that we obtained in the innermost unit, which are 0.85 ± 0.14 km/My for the 18-12.8 Ma and subsequently 0.69 ± 0.07 km/My for the 12.8-6.1 Ma time steps (Figure III.14). Exhumation rates for the outer Carpathians were estimated by Andreucci et al. (2015) and Nakapelyukh et al. (2018). For the Burkut and Krosno nappe, cooling rates were estimated by Andreucci et al. (2015) to be between 15-30 °C/My during the period 12-5 Ma, before decreasing to 3-6 °C/My from 5 Ma to present. These cooling rates would correspond to an exhumation rate of 0.7-1.0 km/My in the middle Miocene for the Burkut and Krosno nappe, which is in disagreement with our model, which predicts that exhumation rates in the Magura-Valais and Krosno nappes decreased earlier, from rates of ~0.7 km/My during the 18-16 Ma time step to 0.3-0.5 km/My after 16 Ma, before decreasing further at 8.6 Ma (Figure III.14). This difference in variation of exhumation rates over time can be explained by the correlation of several thermochronometers in the inversion compared to the time-temperature model of Andreucci et al. (2015) which was based on only two samples. Nakapelyukh et al. (2018) combined a restored structural-geological cross section and thermochronology data to estimate that over the last 12 My, 3.5-4.5 km of overburden was removed from the Ukrainian wedge. These results are, however, difficult to compare with ours because they account for a higher geothermal gradient of 30 °C/km over the last 12 My, while we computed the exhumation path since 18 Ma with a constant geothermal gradient of 24 °C/km (Figure III.14).

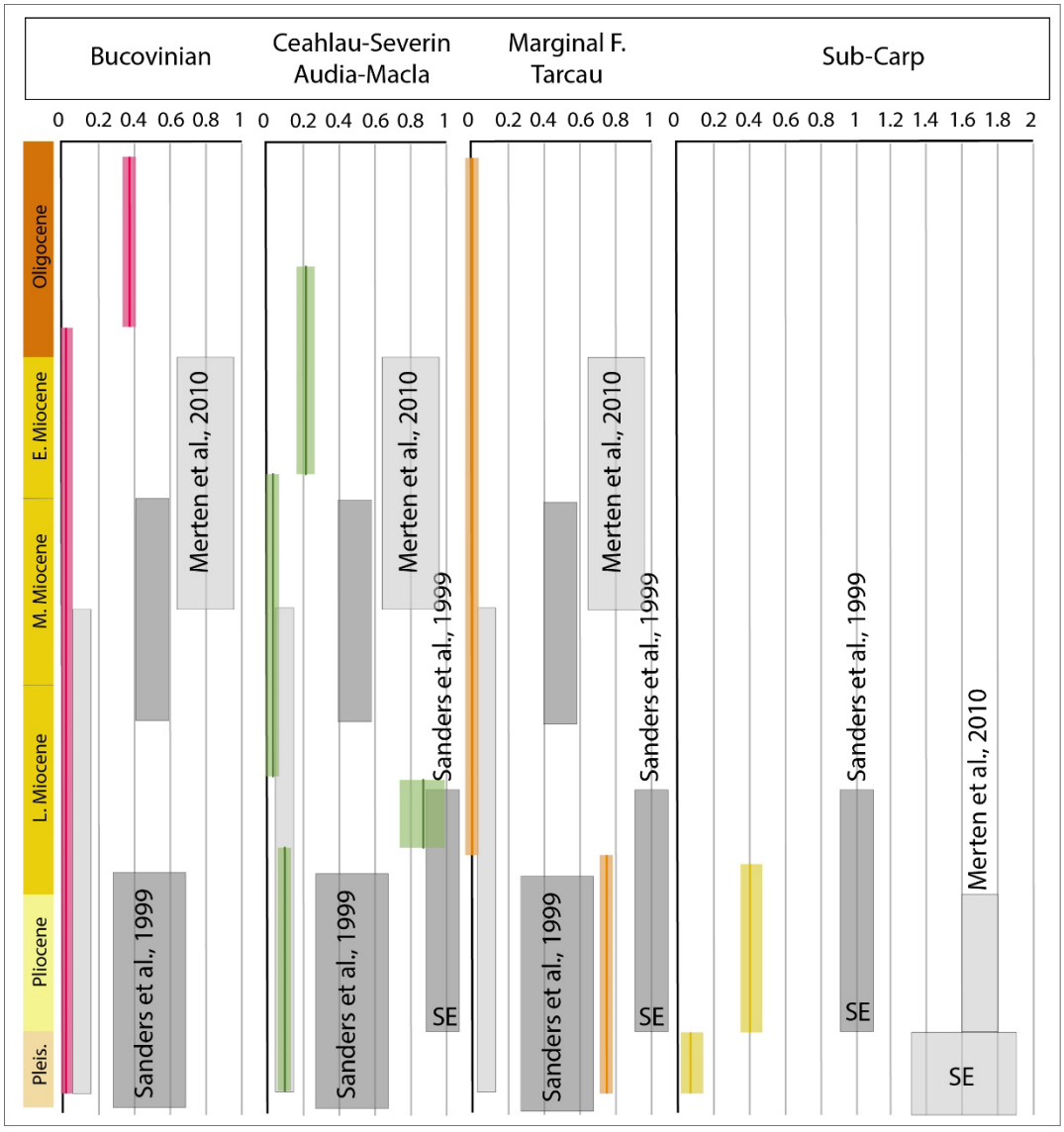

Figure III.15: Comparison of exhumation rates from previous studies on the Eastern and South-eastern Carpathians region.

In the E-SEC region, exhumation rates were estimated at 0.5±0.1 km/My from 15 to 11 Ma, subsequently declining to ~0.5 km/My at 5-0 Ma (Sanders et al., 1999; Figure III.15). In the South-eastern zone of the belt, exhumation rates were inferred to be ~1 km/My during the period 7-2 Ma. The total exhumation inferred by Sanders et al. (1999) amounts to 4±1 km for the middle Miocene-Pliocene (15-5 Ma) and 2 km for Pliocene-Quaternary (Figure III.15). Merten et al. (2010) proposed more detailed exhumation-rate estimates; they inferred the Ceahlau-Severin nappe to have exhumed at 0.7-0.4 km/My in the Paleogene, and the rest of the fold-and-thrust belt to have been exhumed in the early-middle Miocene at 0.8±0.4 km/My for about 4 My to amount for 3.2 ± 0.5 km of total exhumation. Merten et al. (2010) also differentiate the SE Carpathians bend zone from the rest of the E-SEC region; they infer that SE Carpathians were exhumed at 1.7 km/My during the late-Miocene and Pliocene. In our models, Paleogene exhumation of the Ceahlau-Severin nappe is unconstrained due to the younger ages of the thermochronometers. However, we found the most rapid exhumation rates during the 8.6-6.1 Ma time

step for the Ceahlau-Severin and Audia-Macla unit (0.87 ± 0.12 km/My), and during the 6.1-1.8 Ma time step for the Tarcau nappe (0.74 ± 0.01 km/My). Both these estimates are lower than the exhumation rates inferred by Merten et al. (2010) but are coherent with the rates estimated by Sanders et al. (1999) for the SE Carpathians (Figure III.15). For the Subcarpathian nappe, for which data are available only in the SE Carpathians, we infer a lower exhumation rate than the previously published rates (Figure III.15). The exhumation scenario proposed by Merten et al. (2010) considers two phases of exhumation separated by a Sarmatian burial phase. As a consequence of this assumption, the exhumation rates are higher in their model for the late Miocene-Pliocene period. A more detailed explanation on the difference in the SE Carpathians exhumation is proposed in the Supplementary Information of the manuscript.

In general, the model reproduces the data quite well and is consistent with most previous estimates of exhumation or cooling rates around the Carpathian Mountain belt. Our exhumation model is most at odds with previous studies of the South-eastern Carpathians (E-SEC). In a broader view, peak exhumation rates in the Carpathians are generally between 0.5-1 km/My in all studies, including our inverse model, and reveal a diachronous NW-SE wave of peak exhumation within the belt.

4.2.2 Comparison of exhumation models for the Ukrainian Carpathians

Whereas in the previous section, the exhumation histories obtained with the Pecube inversions were compared with those from the literature, here we specifically compare the exhumation history of the Ukrainian Carpathians derived from the Pecube models with the time-temperature histories obtained with QTQt modelling in Chapter II. For this comparison, one should note that for the inversion we grouped several units together, which were treated individually in Chapter II. In particular, the Magura and Burkut nappes were combined, as were the Dukla and Krosno nappes, and the Skyba and Boryslav-Pokuttia nappes. Second, we cannot make a one-to-one comparison because the time-temperature models are inferred for single samples, whereas the Pecube inversions take all the data present within a modelled region into account. Moreover, the Pecube inversions return independent exhumation rates for the different time steps input into the model, whereas the QTQt models predict continuous time-temperature histories.

For the innermost Magura, Marmarosh and Burkut nappes, the average exhumation rate over the last 18 My modelled by Pecube-NA inversion of the database is 0.38 ± 0.12 km/My. In comparison the exhumation rates estimated for samples CAR19-061, CAR19-066, CAR19-062 and CAR19-063 (Figures 6 and 7 from Chapter II) of the corresponding nappe are 0.12-0.14 km/My, 0.16-0.22 km/My, 0.22 km/My and 0.40 km/My respectively. The AFT and AHe ages of these samples are somewhat somewhat older than the average published AFT and AHe ages in these tectonic units (see Figure III.3 of Chapter II). This difference can explain the somewhat higher exhumation rates inferred from the Pecube inversions, as the older ages input into the time-temperature model led to an older onset of exhumation and thus a lower exhumation rate predicted by that model. For the Dukla and Krosno nappes, the QTQt models predict an onset of exhumation at ~14 and ~18 Ma respectively, at a rate of 0.3 to 0.4 km/My (Chapter II, Figure III.8). The average exhumation rate predicted by the Pecube-NA inversion is 0.38 ± 0.06 km/My over 18 My, which is similar. For the Skyba and Boryslav-Pokuttia nappes, the average

exhumation rate over the last 18 My predicted by the Pecube inversions is about 0.27 ± 0.06 km/My, but the inferred time-temperature histories suggest onset of exhumation of the Skyba nappe from 16-12 Ma with an exhumation rate of 0.3-0.4 km/My. The onset of exhumation is older and lower exhumation rate predicted by the Pecube-NA inversion is notably due to the mostly partially to non-reset ages making up the previously published data of these nappes implemented in the inversion model (Figure III.3).

Globally, the two approaches predict similar exhumation rates, taking into account the grouping of data in different sets for the Pecube inversions and the representativeness of each thermochronometer age in their respective dataset. In other words, if our data are younger (older) than most other published ages in the dataset, inferred rates from the Pecube-NA inversion will be slower (faster) than from the time-temperature modelling using QTQt. Our models for the exhumation of the Ukrainian Carpathians both show advantages. The time-temperature histories obtained with QTQt, and constrained by the stratigraphic record, provide a more detailed history on burial phase of the nappes. The Pecube-NA inversions translate an exhumation of material, not only a cooling of the rock.

4.3 Diachronous exhumation in the Carpathian belt

In the light of the dynamics of accretion-collision in the Carpathian belt, and the constraints on exhumation rates over time that arise from our inverse model, the construction of the Carpathian belt is diachronous from NW to SE. The times of peak exhumation rates migrate from NW to SE: most rapid exhumation rates occur from 24 Ma to 12.8 Ma in the WC, in the NEC region from 18 Ma to 6.1 Ma, and in E-SEC (Romania) from 8.6 Ma to 1.8 Ma (Figure III. 11 and 12). This diachronicity also shows up within the regions, especially in the E-SEC, where reset thermochronometer ages show differences of ten millions of years (e.g., 14 Ma to 5 Ma difference in Tarcau nappe for AFT ages) from north to south (Figure III.4).

The total amount of exhumation in the Carpathian units also decreases from NW to SE. The WC region records a little less than 10 km of exhumation for the Magura-Valais and Silesian units, whereas the NEC region records total exhumation between 8-5 km for the same units (Figure III.13). The variation of the total amount of exhumation is even more explicit in the E-SEC region, where rapid exhumation took place most recently in the Ceahlau-Severin and Audia-Macla, Tarcau and Sub-Carpathians units, and total exhumation is the lowest (6-2 km; Figure III.13). The difference in total exhumation can be explained by two phenomena: (1) the diachronous onset of exhumation from NW to SE could explain the difference of total exhumation if exhumation rates are similar along the Carpathian belt. (2) Exhumation of the Carpathians generally shows high rates (around 0.5-0.8 km/My) in the early time steps, which then decrease to 0.1-0.4 km/My for more recent time steps (Figure III.11). For the E-SEC region, this decrease is less clear for the Tarcau unit because of the recent onset of exhumation (Figure III.11). Such a laterally propagating transient phase of rapid exhumation could lead to an equal total amount of exhumation across the belt despite a diachronous onset of exhumation. However, by comparing the variation of rates (Figure III.11) and the total amount of exhumation (Figure III.13) suggests a combination of both effects. The high exhumation rates (> 0.5 km/My) propagate like a wave from NW-SE in time, but exhumation continuous to the present at lower rates (~0.1-0.2 km/My) for a

longer time in the NW than in the SE. The resulting total amount of exhumation is different and records both a diachronous onset of exhumation and its decrease to lower rates, but not to a total quiescence (i.e., zero exhumation) of the area.

5 Conclusion

We unravelled the exhumation history of the Carpathian arc through inversion of a LT thermochronology database using Pecube-NA (Braun et al., 2012). The division of the dataset by tectonic unit and by region allows observing a diachronous exhumation pattern from the NW to the SE. The exhumation rates we obtain are coherent with previous studies conducted on specific areas around the belt, with a difference in the Eastern and South-eastern Carpathians region. The onset of the exhumation differs from one region to another, with a pattern of earlier exhumation in the NW (24-18 Ma) and later in the SE (8.6-6.1 Ma). The total amount of exhumation for the Carpathians is around 10-8 km in the WC, 8-5 km in the NEC and 6-2 km in the E-SEC. The diachronous exhumation of the Carpathian belt is put in context with the development of the Pannonian Basin and the Neogene volcanics in Chapter V of this manuscript.

Annexes

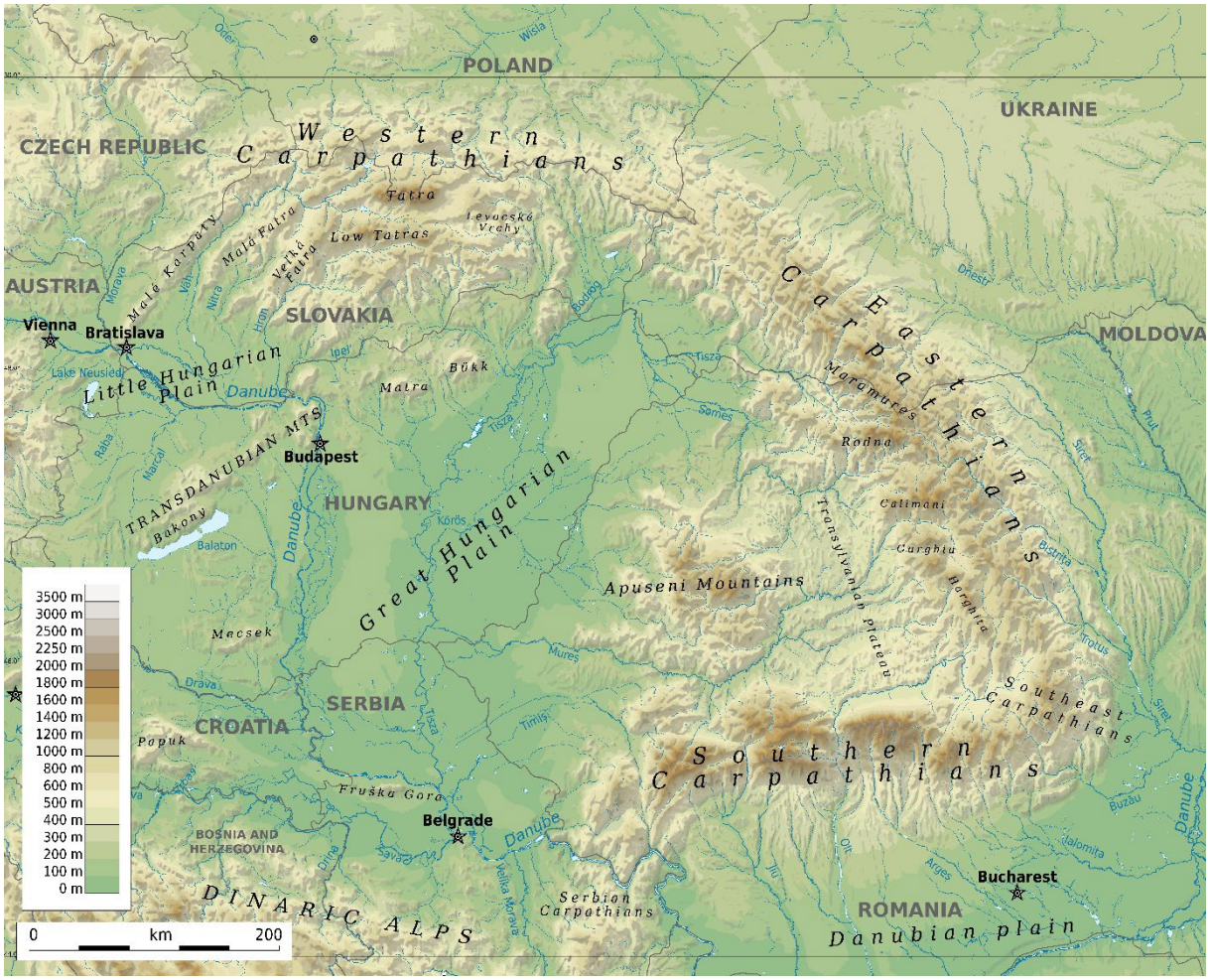

S 2: Geographic map of the Carpathians.

https://commons.wikimedia.org/wiki/File:Geographic_map_of_Carpathian_mountains.svg

Ikonact, CC BY-SA 4.0 <https://creativecommons.org/licenses/by-sa/4.0>, via Wikimedia Commons

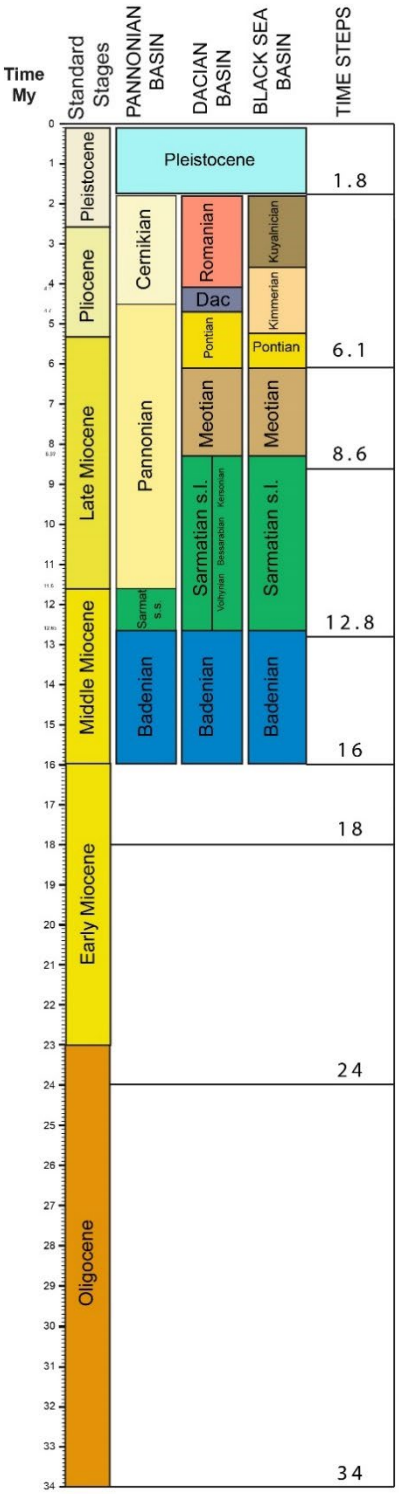

S 3 Time steps of inversion compared to the regional stratigraphy of the Carpathians region (sedimentary basins).

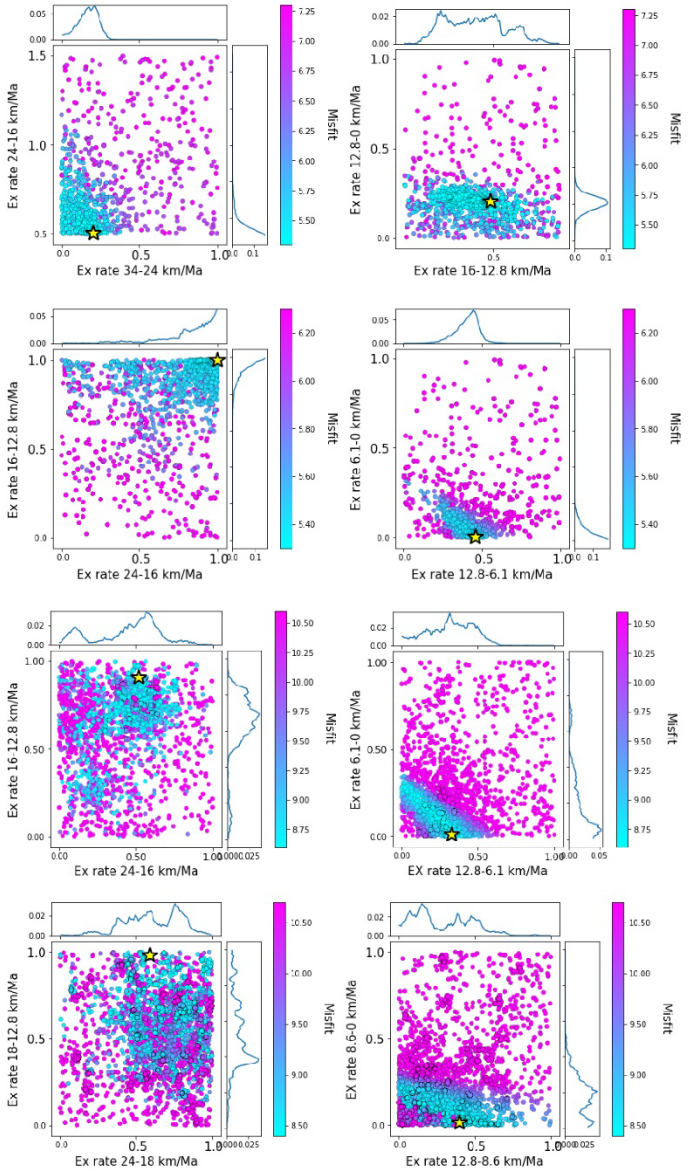

TNM07

Lowest misfit found: 5.31
Average misfit over all models: 7.26

	Posterior		Prior	
Parameters	Mean	Stn err	Mean	Stn err
34-24	0.17	0.06	0.50	0.29
24-16	0.55	0.06	1.00	0.29
16-12.8	0.42	0.13	0.45	0.20
12.8-0	0.20	0.04	0.50	0.29

NNM04

Lowest misfit found: 5.35
Average misfit over all models: 6.22

	Posterior		Prior	
Parameters	Mean	Stn err	Mean	Stn err
24-16	0.82	0.18	0.50	0.29
16-12.8	0.94	0.06	0.50	0.29
12.8-6.1	0.40	0.07	0.50	0.29
6.1-0	0.05	0.04	0.50	0.29

PMVX1

Lowest misfit found: 8.63
Average misfit over all models: 9.37

	Posterior		Prior	
Parameters	Mean	Stn err	Mean	Stn err
24-16	0.45	0.21	0.50	0.29
16-12.8	0.64	0.18	0.50	0.29
12.8-6.1	0.32	0.15	0.50	0.29
6.1-0	0.18	0.17	0.50	0.29

PAM23

Lowest misfit found: 8.47
Average misfit over all models: 10.54

	Posterior		Prior	
Parameters	Mean	Stn err	Mean	Stn err
24-18	0.61	0.18	0.50	0.29
18-12.8	0.54	0.20	0.50	0.29
12.8-8.6	0.29	0.19	0.50	0.29
8.6-0	0.17	0.11	0.50	0.29

S 4: Scatter plots and PDF of Pecube-Na inversion performance in the Western Carpathians region.

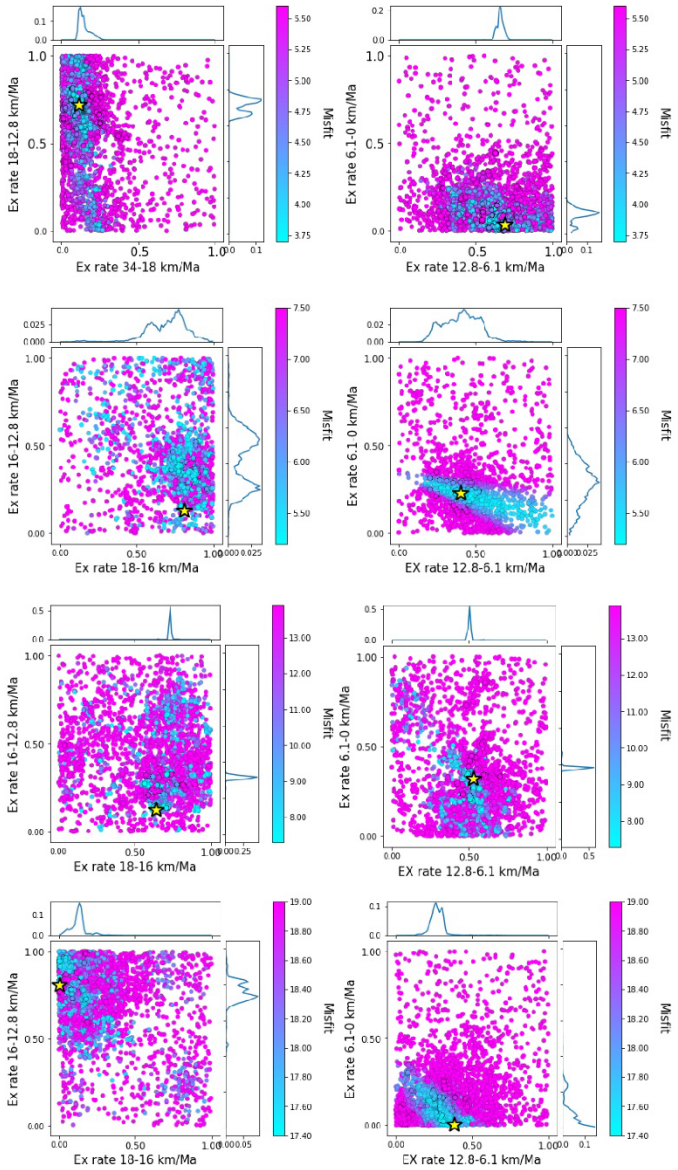

UBC20

Lowest misfit found: 3.74
Average misfit over all models: 4.70

	Posterior		Prior	
Parameters	Mean	Stn err	Mean	Stn err
34-18	0.15	0.04	0.50	0.29
18-12.8	0.71	0.04	0.50	0.29
12.8-6.1	0.66	0.02	0.50	0.29
6.1-0	0.10	0.04	0.50	0.29

UCS20

Lowest misfit found: 5.29
Average misfit over all models: 6.13t

	Posterior		Prior	
Parameters	Mean	Stn err	Mean	Stn err
18-16	0.70	0.13	0.50	0.29
16-12.8	0.43	0.15	0.50	0.29
12.8-6.1	0.41	0.12	0.50	0.29
6.1-0	0.28	0.12	0.50	0.29

UAM25

Lowest misfit found: 7.27
Average misfit over all models: 12.93

	Posterior		Prior	
Parameters	Mean	Stn err	Mean	Stn err
18-16	0.73	0.01	0.50	0.29
16-12.8	0.31	0.01	0.50	0.29
12.8-6.1	0.50	0.02	0.50	0.29
6.1-0	0.38	0.02	0.50	0.29

UMT24

Lowest misfit found: 17.46
Average misfit over all models: 18.83

	Posterior		Prior	
Parameters	Mean	Stn err	Mean	Stn err
18-16	0.13	0.05	0.50	0.29
16-12.8	0.75	0.07	0.50	0.29
12.8-6.1	0.27	0.05	0.50	0.29
6.1-0	0.08	0.09	0.50	0.29

S 5: Scatter plots and PDF of Pecube-Na inversion performance in the North-eastern Carpathians region

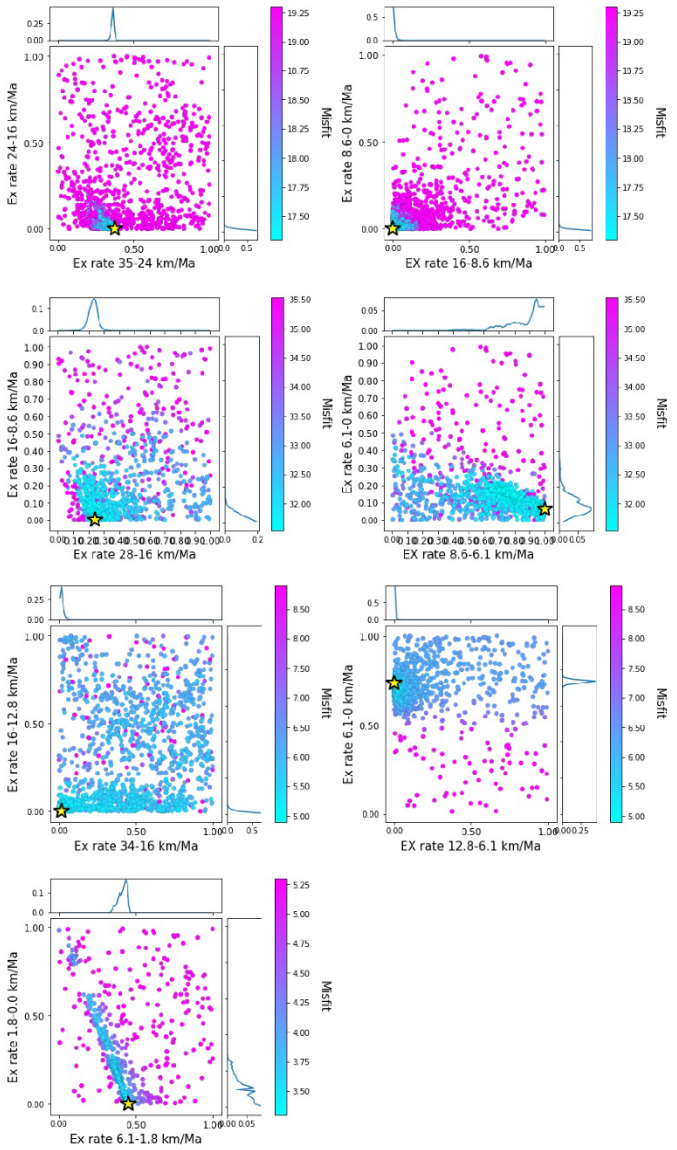

RBC06

Lowest misfit found: 17.29
Average misfit over all models: 19.17

	Posterior		Prior	
Parameters	Mean	Stn err	Mean	Stn err
34-24	0.36	0.01	0.50	0.29
24-16	0.01	0.01	0.50	0.29
16-8.6	0.01	0.01	0.50	0.29
8.6-0	0.01	0.01	0.50	0.29

RAM10

Lowest misfit found: 31.55
Average misfit over all models: 35.48

	Posterior		Prior	
Parameters	Mean	Stn err	Mean	Stn err
28-16	0.23	0.03	0.50	0.29
16-8.6	0.04	0.03	0.50	0.29
8.6-6.1	0.87	0.12	0.50	0.29
6.1-0	0.10	0.06	0.50	0.29

RMT05

Lowest misfit found: 5.0
Average misfit over all models: 6.52

	Posterior		Prior	
Parameters	Mean	Stn err	Mean	Stn err
34-16	0.02	0.01	0.50	0.29
16-12.8	0.01	0.01	0.50	0.29
12.8-6.1	0.01	0.01	0.50	0.29
6.1-0	0.73	0.01	0.50	0.29

RSE07

Lowest misfit found: 3.56
Average misfit over all models: 4.75

	Posterior		Prior	
Parameters	Mean	Stn err	Mean	Stn err
6.1-1.8	0.41	0.03	0.50	0.29
1.8-0	0.09	0.06	0.50	0.29

S 6: Scatter plots and PDF of Pecube-Na inversion performance in the Eastern and South-eastern Carpathians region.

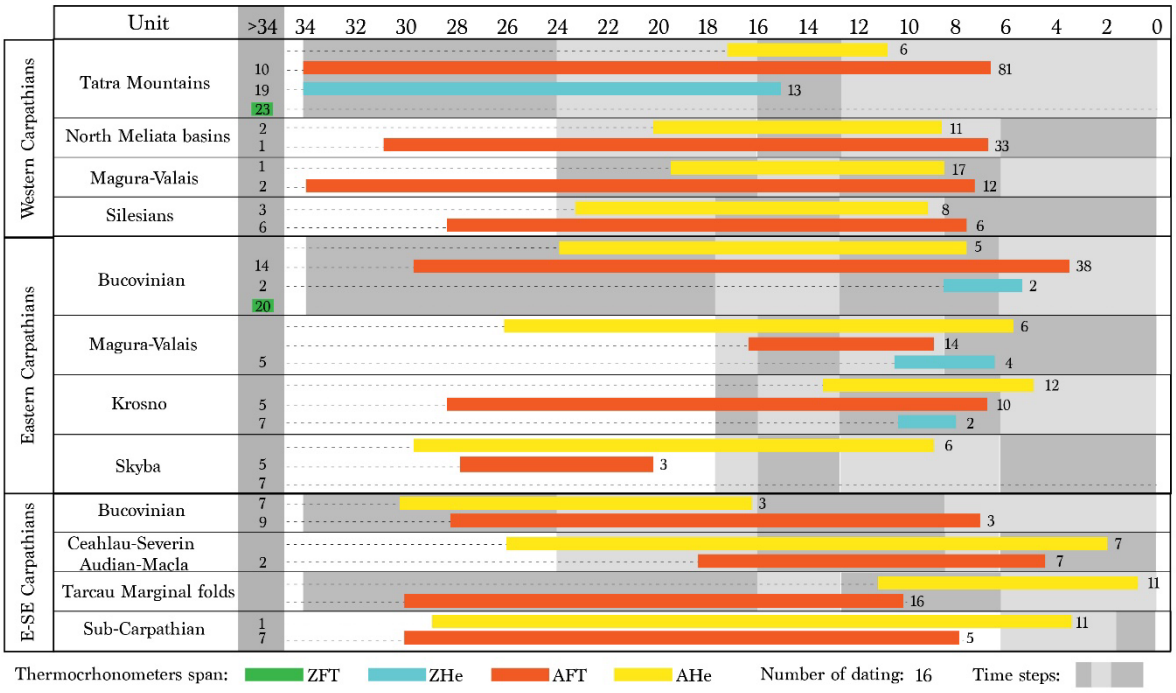

S 7: Table of thermochronology data repartition in the dataset of the inverse exhumation model.

References

Anczkiewicz, A. A., Środoń, J., and Zattin, M.: Thermal history of the Podhale Basin in the internal Western Carpathians from the perspective of apatite fission track analyses, Geologica Carpathica, 64, 141–151, https://doi.org/10.2478/geoca-2013-0010, 2013.

Anczkiewicz, A. A., Danišík, M., and Środoń, J.: Multiple low-temperature thermochronology constraints on exhumation of the Tatra Mountains: New implication for the complex evolution of the Western Carpathians in the Cenozoic: MULTIPLE EVOLUTION OF THE TATRA MOUNTAINS, Tectonics, 34, 2296–2317, https://doi.org/10.1002/2015TC003952, 2015.

Andreucci, B., Castelluccio, A., Jankowski, L., Mazzoli, S., Szaniawski, R., and Zattin, M.: Burial and exhumation history of the Polish Outer Carpathians: Discriminating the role of thrusting and post-thrusting extension, Tectonophysics, 608, 866–883, https://doi.org/10.1016/j.tecto.2013.07.030, 2013.

Andreucci, B., Castelluccio, A., Corrado, S., Jankowski, L., Mazzoli, S., Szaniawski, R., and Zattin, M.: Interplay between the thermal evolution of an orogenic wedge and its retro-wedge basin: An example from the Ukrainian Carpathians, Geological Society of America Bulletin, 127, 410–427, https://doi.org/10.1130/B31067.1, 2015.

Batt, G. E. and Brandon, M. T.: Lateral thinking: 2-D interpretation of thermochronology in convergent orogenic settings, Tectonophysics, 349, 185–201, https://doi.org/10.1016/S0040-1951(02)00053-7, 2002.

Batt, G. E. and Braun, J.: On the thermomechanical evolution of compressional orogens, Geophysical Journal International, 128, 364–382, https://doi.org/10.1111/j.1365-246X.1997.tb01561.x, 1997.

Batt, G. E. and Braun, J.: The tectonic evolution of the Southern Alps, New Zealand: insights from fully thermally coupled dynamical modelling: Evolution of the S. Alps, Geophysical Journal International, 136, 403–420, https://doi.org/10.1046/j.1365-246X.1999.00730.x, 1999.

Braun, J., van der Beek, P., Valla, P., Robert, X., Herman, F., Glotzbach, C., Pedersen, V., Perry, C., Simon-Labric, T., and Prigent, C.: Quantifying rates of landscape evolution and tectonic processes by thermochronology and numerical modeling of crustal heat transport using PECUBE, Tectonophysics, 524–525, 1–28, https://doi.org/10.1016/j.tecto.2011.12.035, 2012.

Castelluccio, A., Mazzoli, S., Andreucci, B., Jankowski, L., Szaniawski, R., and Zattin, M.: Building and exhumation of the Western Carpathians: New constraints from sequentially restored, balanced cross sections integrated with low-temperature thermochronometry: WESTERN CARPATHIANS TECTONIC EVOLUTION, Tectonics, 35, 2698–2733, https://doi.org/10.1002/2016TC004190, 2016.

Curry, M. E., Beek, P. van der, Huismans, R. S., Wolf, S. G., Fillon, C., and Muñoz, J.-A.: Spatio-temporal patterns of Pyrenean exhumation revealed by inverse thermo-kinematic modeling of a large thermochronologic data set, Geology, 49, 738–742, https://doi.org/10.1130/G48687.1, 2021.

Danišík, M., Pánek, T., Matýsek, D., Dunkl, I., and Frisch, W.: Apatite fission track and (U-Th)/He dating of teschenite intrusions gives time constraints on accretionary processes and development of planation surfaces in the Outer Western Carpathians, Zeit fur Geo, 52, 273–289, https://doi.org/10.1127/0372-8854/2008/0052-0273, 2008a.

Danišík, M., Kohút, M., Dunkl, I., Hraško, L., and Frisch, W.: Apatite fission track and (U-Th)/He thermochronology of the Rochovce granite (Slovakia) – implications for the thermal evolution of the Western Carpathian-Pannonian region, Swiss J. Geosci., 101, 225–233, https://doi.org/10.1007/s00015-008-1279-8, 2008b.

Danišík, M., Kadlec, J., Glotzbach, C., Weisheit, A., Dunkl, I., Kohút, M., Evans, N. J., Orvošová, M., and McDonald, B. J.: Tracing metamorphism, exhumation and topographic evolution in orogenic belts by multiple thermochronology: a case study from the Nízke Tatry Mts., Western Carpathians, Swiss J Geosci, 104, 285–298, https://doi.org/10.1007/s00015-011-0060-6, 2011.

Danišík, M., Kohút, M., Dunkl, I., and Frisch, W.: Thermal evolution of the Žiar Mountains basement (Inner Western Carpathians, Slovakia) constrained by fission track data, 12, n.d.

Fox, M., Herman, F., Willett, S. D., and May, D. A.: A linear inversion method to infer exhumation rates in space and time from thermochronometric data, Earth Surf. Dynam., 2, 47–65, https://doi.org/10.5194/esurf-2-47-2014, 2014.

Fox, M., Herman, F., Willett, S. D., and Schmid, S. M.: The Exhumation history of the European Alps inferred from linear inversion of thermochronometric data, American Journal of Science, 316, 505–541, https://doi.org/10.2475/06.2016.01, 2016.

Gągała, Ł., Vergés, J., Saura, E., Malata, T., Ringenbach, J.-C., Werner, P., and Krzywiec, P.: Architecture and orogenic evolution of the northeastern Outer Carpathians from cross-section balancing and forward modeling, Tectonophysics, 532–535, 223–241, https://doi.org/10.1016/j.tecto.2012.02.014, 2012.

Gröger, H. R., Fügenschuh, B., Tischler, M., Schmid, S. M., and Foeken, J. P. T.: Tertiary cooling and exhumation history in the Maramures area (internal eastern Carpathians, northern Romania): thermochronology and structural data, Geological Society, London, Special Publications, 298, 169–195, https://doi.org/10.1144/SP298.9, 2008.

Gröger, H. R., Tischler, M., Fügenschuh, B., and Schmid, S. M.: Thermal history of the Maramureş area (Northern Romania) constrained by zircon fission track analysis: Cretaceous metamorphism and Late Cretaceous to Paleocene exhumation, Geologica Carpathica, 64, 383–398, https://doi.org/10.2478/geoca-2013-0026, 2013.

Konstantinovskaia, E. and Malavieille, J.: Erosion and exhumation in accretionary orogens: Experimental and geological approaches: ACCRETIONARY OROGENS, Geochem. Geophys. Geosyst., 6, https://doi.org/10.1029/2004GC000794, 2005.

Králiková, S., Vojtko, R., Sliva, U., Minár, J., Fügenschuh, B., Kováč, M., and Hók, J.: Cretaceous—Quaternary tectonic evolution of the Tatra Mts (Western Carpathians): constraints from structural, sedimentary, geomorphological, and fission track data, Geologica Carpathica, 65, 307–326, https://doi.org/10.2478/geoca-2014-0021, 2014.

de Leeuw, A., Vincent, S. J., Matoshko, A., Matoshko, A., Stoica, M., and Nicoara, I.: Late Miocene sediment delivery from the axial drainage systemof the East Carpathian foreland basin to the Black Sea, Geology, https://doi.org/10.1130/G47318.1, 2020.

Matenco, L., Krézsek, C., Merten, S., Schmid, S., Cloetingh, S., and Andriessen, P.: Characteristics of collisional orogens with low topographic build-up: an example from the Carpathians: Collision of orogens with low topographic build-up, Terra Nova, 22, 155–165, https://doi.org/10.1111/j.1365-3121.2010.00931.x, 2010.

Matenco, L., Munteanu, I., ter Borgh, M., Stanica, A., Tilita, M., Lericolais, G., Dinu, C., and Oaie, G.: The interplay between tectonics, sediment dynamics and gateways evolution in the Danube system from the Pannonian Basin to the western Black Sea, Science of The Total Environment, 543, 807–827, https://doi.org/10.1016/j.scitotenv.2015.10.081, 2016.

Mazzoli, S., Jankowski, L., Szaniawski, R., and Zattin, M.: Low-T thermochronometric evidence for post-thrusting (<11 Ma) exhumation in the Western Outer Carpathians, Poland, Comptes Rendus Geoscience, 342, 162–169, https://doi.org/10.1016/j.crte.2009.11.001, 2010.

Merten, S., Matenco, L., Foeken, J. P. T., Stuart, F. M., and Andriessen, P. A. M.: From nappe stacking to out-of-sequence postcollisional deformations: Cretaceous to Quaternary exhumation history of the SE Carpathians assessed by low-temperature thermochronology: EXHUMATION HISTORY OF THE SE CARPATHIANS, Tectonics, 29, https://doi.org/10.1029/2009TC002550, 2010.

Morris, Sinclair, and Yell: Exhumation of the Pyrenean orogen: implications for sediment discharge, Basin Research, 10, 69–85, https://doi.org/10.1046/j.1365-2117.1998.00053.x, 1998.

Nakapelukh, M., Bubniak, I., Yegorova, T., Murovskaya, A., Gintov, O., Shlapinskyi, V., and Vikhot, Y.: Balanced geological cross-section of the outer ukrainian carpathians along the pancake profile, Journal of Geodynamics, 108, 13–25, https://doi.org/10.1016/j.jog.2017.05.005, 2017.

Nakapelyukh, M., Bubniak, I., Bubniak, A., Jonckheere, R., and Ratschbacher, L.: Cenozoic structural evolution, thermal history, and erosion of the Ukrainian Carpathians fold-thrust belt, Tectonophysics, 722, 197–209, https://doi.org/10.1016/j.tecto.2017.11.009, 2018.

Necea, D., Fielitz, W., Kadereit, A., Andriessen, P. A. M., and Dinu, C.: Middle Pleistocene to Holocene fluvial terrace development and uplift-driven valley incision in the SE Carpathians, Romania, Tectonophysics, 602, 332–354, https://doi.org/10.1016/j.tecto.2013.02.039, 2013.

Necea, D., Juez-Larré, J., Matenco, L., Andriessen, P. A. M., and Dinu, C.: Foreland migration of orogenic exhumation during nappe stacking: Inferences from a high-resolution thermochronological profile over the Southeast Carpathians, Global and Planetary Change, 200, 103457, https://doi.org/10.1016/j.gloplacha.2021.103457, 2021.

Plašienka, D., Broska, I., Kissová, D., and Dunkl, I.: Zircon fission-track dating of granites from the Vepor-Gemer Belt (Western Carpathians): constraints for the Early Alpine exhumation history, Jour. Geosci., 113–123, https://doi.org/10.3190/jgeosci.009, 2012.

Sambridge, M.: Geophysical inversion with a neighbourhood algorithm—I. Searching a parameter space, Geophysical Journal International, 138, 479–494, https://doi.org/10.1046/j.1365-246X.1999.00876.x, 1999a.

Sambridge, M.: Geophysical inversion with a neighbourhood algorithm—II. Appraising the ensemble, Geophysical Journal International, 138, 727–746, https://doi.org/10.1046/j.1365-246x.1999.00900.x, 1999b.

Sanders, C. A. E., Andriessen, P. A. M., and Cloetingh, S. A. P. L.: Life cycle of the East Carpathian orogen: Erosion history of a doubly vergent critical wedge assessed by fission track thermochronology, J. Geophys. Res., 104, 29095–29112, https://doi.org/10.1029/1998JB900046, 1999.

Śmigielski, M., Sinclair, H. D., Stuart, F. M., Persano, C., and Krzywiec, P.: Exhumation history of the Tatry Mountains, Western Carpathians, constrained by low-temperature thermochronology: EXHUMATION HISTORY OF THE TATRy, Tectonics, 35, 187–207, https://doi.org/10.1002/2015TC003855, 2016.

Thomson, S. N., Brandon, M. T., Reiners, P. W., Zattin, M., Isaacson, P. J., and Balestrieri, M. L.: Thermochronologic evidence for orogen-parallel variability in wedge kinematics during extending convergent orogenesis of the northern Apennines, Italy, Geological Society of America Bulletin, 122, 1160–1179, https://doi.org/10.1130/B26573.1, 2010.

Ustaszewski, K., Schmid, S. M., Fügenschuh, B., Tischler, M., Kissling, E., and Spakman, W.: A map-view restoration of the Alpine-Carpathian-Dinaridic system for the Early Miocene, Swiss J. Geosci., 101, 273–294, https://doi.org/10.1007/s00015-008-1288-7, 2008.

Zattin, M., Andreucci, B., Jankowski, L., Mazzoli, S., and Szaniawski, R.: Neogene exhumation in the Outer Western Carpathians: Neogene exhumation in the Outer Western Carpathians, Terra Nova, 23, 283–291, https://doi.org/10.1111/j.1365-3121.2011.01011.x, 2011.

Chapter IV: The Carpathian Foreland Basin sediments over time and space

The pro-foreland basin of the Carpathian fold-thrust belt has developed since the middle-Miocene and extends from South Poland to Southeast Romania and South Ukraine. Recent observations, lateral correlation of sediment facies, map analysis, and micro-biostratigraphy (de Leeuw et al., 2013; Stoica et al., 2013; Matoshko et al., 2016, 2019; de Leeuw et al., 2012, 2020) revealed that the basin is up to 300 km wide, also includes Moldova and stretches slightly beyond the South Bug River in Ukraine (Figure IV.1). This new understanding of the Carpathian pro-foreland basin (CFB) raised questions about the transport system delivering the sediments 250-300 km away from the frontal thrust, onto the East European Margin (EEM) and ultimately to the Black Sea (BS) basin (de Leeuw et al., 2020). In our study of the Carpathian foreland fold-thrust belt system we want to establish a volumetric estimation of the sediments in the pro-foreland basin. A comparison of sediment sourced from the exhumation and erosion of the belt and the sediment deposition in the basin along time and space will allow to construct the history of the CFB development over the Miocene-Pleistocene. To constrain sediment thickness maps, we compiled geological maps and cross sections of the region in a 3D modeler, and we obtained the architecture of the infill of the CFB. Sediment thickness per age is subsequently used to trace sediment depocenters in the foreland over time and space. In the following Chapter, we provide a quantification and timing on the development of the sediment transport system from the north-western to the south-easterns part of the foreland. At the end of this part, we discuss the implication of the lower plate in the architecture of the basin and the loci of sediment depocenters over time.

1 Carpathians Foreland Basin (CFB) model and data

Extended studies around the Carpathian Foreland Basin (CFB) gave a good insight into the basin stratigraphy and a high resolution biostratigraphic subdivision of the stratigraphy (~1 My). However, the studies of the foreland sedimentary system were confined to the different territories it lies on. The harmonisation of the basin sediments system was therefore limited to each country which prevented the development of a large comprehensive point of view on its development. Recent efforts have overcome this local view of the CFB stratigraphy (Matoshko et al., 2016, in prep; de Leeuw et al., 2020) and allow for a more integrated approach of the basin evolution (Chapter I and references therein). Hereafter, we describe the data we implemented in a 3D geomodeler to retrieve the architecture of the CFB sedimentary system.

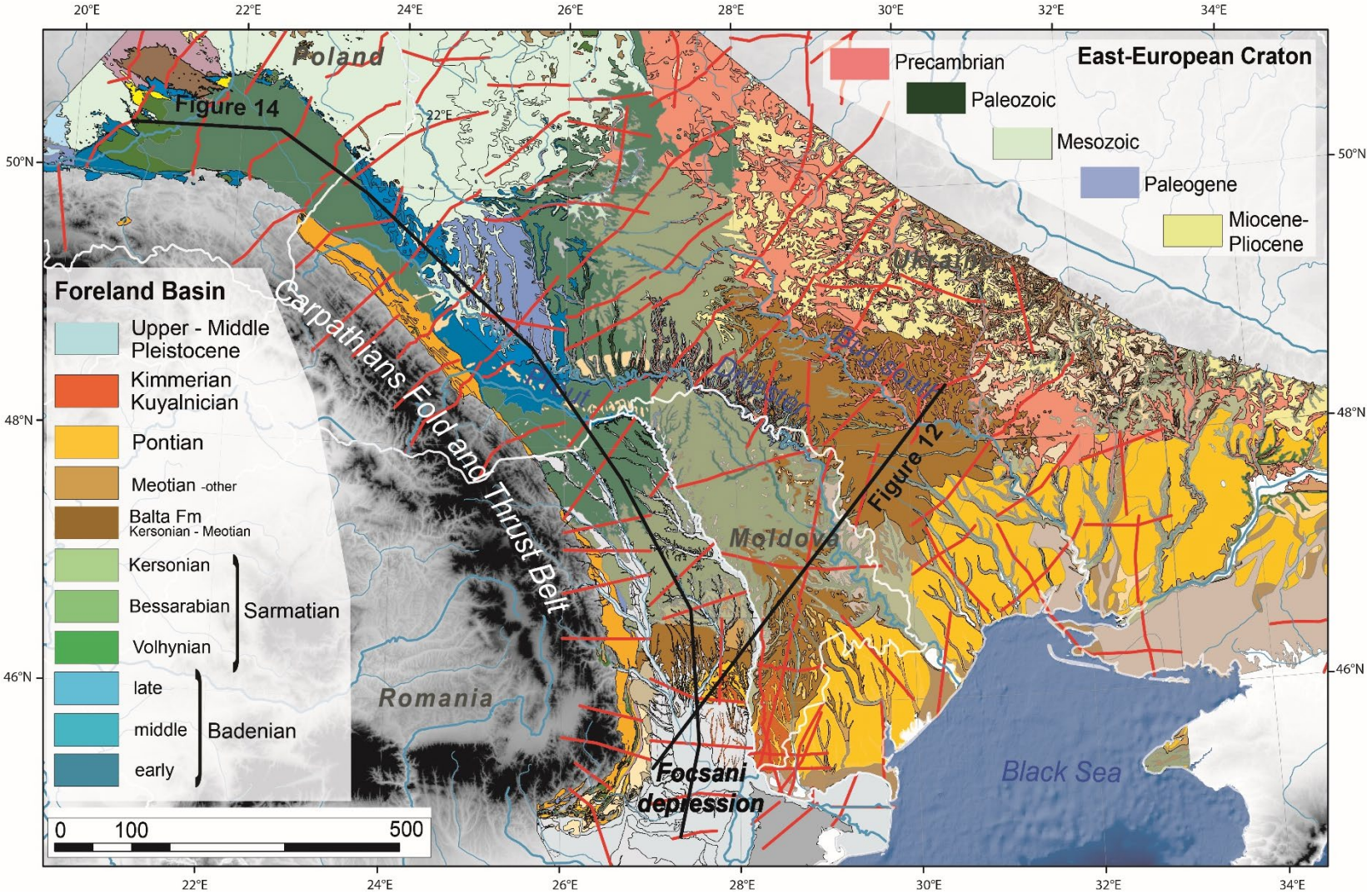

Figure IV.1: Carpathians Foreland Basin (CFB) map (de Leeuw et al., in prep) with location of geological cross-section from the 3D model (red lines). Black lines are section traces from Figure IV.12 and 14.

1.1 3D model data for the CFB

Sediment thicknesses throughout the foreland were determined by interpolating geologic maps and cross sections, which were combined with existing thickness maps for the Focsani Depression and the Polish foreland basin. In the following, we present the different methods we used to recover sediment thickness for each stage and sub-stage of the CFB. We also present an estimate of the sediment thickness recovered from the strongly eroded areas of the Ukrainian foreland.

1.1.1 Imported data

Geological maps (scale 1: 200k) of the Romanian, Moldavian, Ukrainian and Polish territories were imported into the MOVE software (PetEx). We georeferenced the geological sections of the state maps. Harmonization between sedimentary stages through CFB, transliteration of sediment formation names, their description and the classification of sediment horizons was done prior to my work by Elza Dugamin (internship in 2018). We added to the geologic maps thickness maps of the Polish foreland constrained by well data (Ney et al., 1974) and thickness maps from Tărăpoancă (2004) based on seismic sections, constrained with well data along the margin of the Focşani Depression in the SW of the CFB (Figure

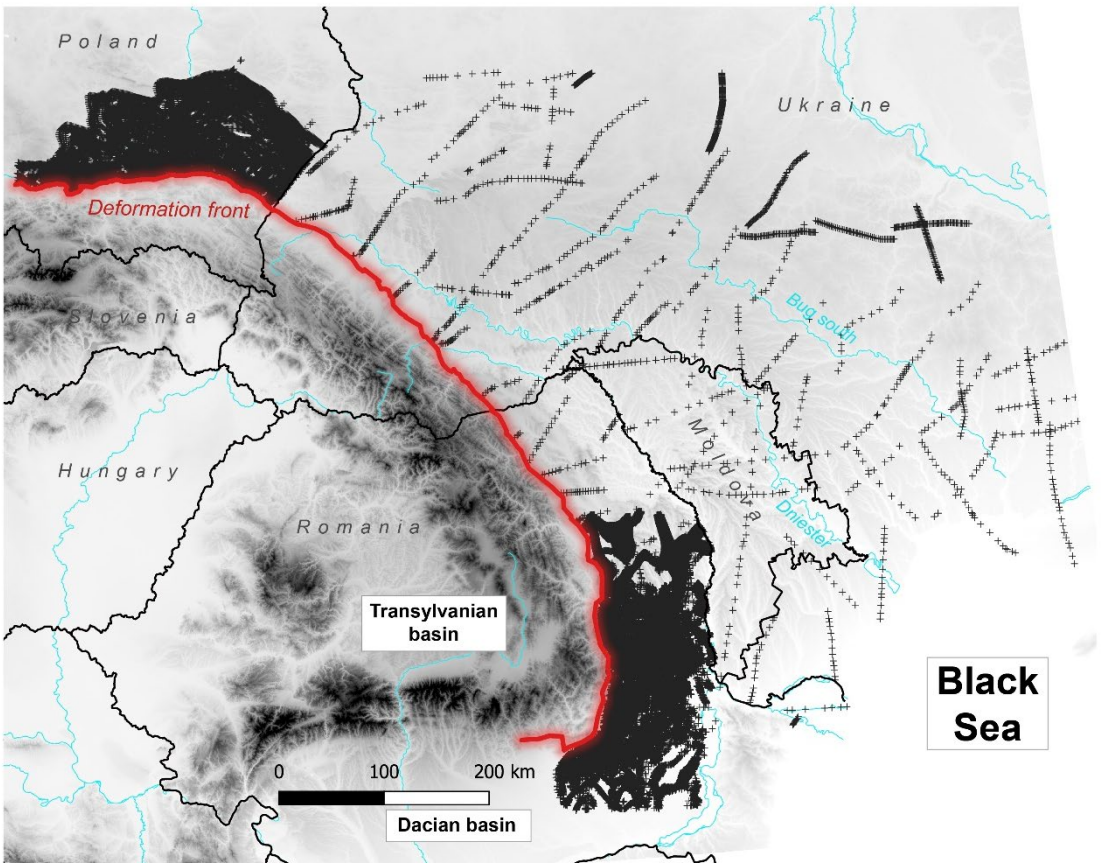

Figure IV.2: Data of the CFB model. Each cross represents a sediment thickness data point. In Poland, the density of data is high, due to the implementation of maps from Ney et al., 1974. In Romania, the density of data is high in the Focsani Depression due to the implementation of thickness maps from Tărăpoancă, 2004.

IV.2). However, the deepest part of the Focsani Depression was not reached by the wells and its stratigraphy was interpreted from interpolation of the data at its margins.

1.1.2 Separation of sediment layers

At several locations in the foreland, the stratigraphic intervals, as depicted on the geological cross sections, had to be subdivided to match those on adjacent maps. Lateral correlation of sedimentary formations with specific sedimentary faciès or the disappearance of subdivisions on geologic sections as the sediment layer thinned eastward in the basin prevented interpolation of sediment thicknesses. Nonetheless, we have divided the problematic horizons to obtain the most likely division of sediments in the foreland basin, as indicated below.

Sarmatian sediments

The Sarmatian sediments are subdivided into three substages. Since the Sarmatian period is a key to changes in the CFB sediment transport system (Matoshko et al., 2016, 2019; de Leeuw et al., 2020) we wanted to obtain volumetric estimates of accumulated sediment in the basin and thickness maps of each sub-stage. However, in sections of the Romanian foreland, these subdivisions are not indicated, and the sedimentary horizons are combined under the name Sarmatian. In addition, time constraints are not defined for all the Sarmatian sub-stages (Krijgsman and Piller, 2012). We adjusted the Sarmatian sub-stage boundaries as follow: the Volhynian stage spans from 12.65 Ma to 11.6 Ma. Its upper limit was tentatively placed at 11.6 Ma to correspond with the Sarmatian-Pannonian boundary in the Central Paratethys (ter Borgh et al., 2013; Magyar, 2021). The Bessarabian then lasted from 11.6 Ma to 9.6 Ma, resulting in a duration of 2 My. The Kersonian in our division started at 9.6 Ma and ended at 8.37 Ma, to be consistent with age brackets that were used during the exhumation modelling of chapter 3, even though we are aware that these ages were recently updated to 9.6-7.65 Ma (Palcu et al., 2021). On most of the geological maps of the CFB sediments are explicitly attributed to the Volhynian, Bessarabian and Kersonian substages and the thickness of these respective time-intervals is thus clear. The Sarmatian is, on the other hand, not subdivided on some of the Romanian maps and on the thickness maps of Tărăpoancă (2004). Based on outcrop observations and extensive study of deltaic sediment formation in the CFB, we subdivided the thickness of Sarmatian sediments according to the proportional duration ratio of time of the sub-stages, dependent on the deposition time of all sub-stages, i.e., the sedimentation rate over Sarmatian is supposed constant for the separation of the sediment thickness. For example, in the Polish Carpathian foreland, the currently preserved sediments belong to the Volhynian sub-stage. Volhynian and Bessarabian are preserved in the Ukrainian foreland, east of Bochkivtsi (Figure IV.3). In the case where only Volhynian and Bessarabian sediments overlapped, the thicknesses of undivided Sarmatian sediments in the cross-sections were divided between the two sub-stages. In instances where all three substages overlapped, the same process was followed. The Focsani Depression is the location where the Sarmatian is not separated in sub-stages. This area displays similar sedimentation rates over the three sub-stages (Figure IV.5, 6 and 7) due to the time ratio apply for thickness division. Our sub-division of the Sarmatian stage in the southwest of the CFB is sharp but allows to correlate the sub-stages

thicknesses throughout the CFB. Nevertheless, this division might impact the analysis on depositional rate in Romania during the Sarmatian. Our approach assumes a constant sedimentation rate over the course of Sarmatian, which may not always be realistic, but we currently lack means for a more accurate approach.

Balta formation

The Balta Formation is well identified in the foreland by its fluvio-deltaic sedimentary facies (Matoshko et al., 2016). However, dating of these sediments is arduous, and thus the division of the thickness of the formation has required some thought. The foreland stratigraphy places the development of the Balta Formation from the late Bessarabian-early Kersonian to the late Meotian (Matoshko et al., 2016; de Leeuw et al., 2020). Quite arbitrarily, based solely on depositional time, we assigned one-quarter of the thickness of the Balta sediments to the Kersonian in places where Meotian and Kersonian alluvial facies might have overlapped, and the remainder to the Meotian. In places where the Kersonian was clearly identified as coastal/marine sediments, the complete thickness of the Balta Formation was assigned to the Meotian stage.

1.2 Interpolation of data

We interpolated the section data through a GIS software and obtained the sediment thicknesses per stage. We used an inverse distance weighting (IDW) method for the interpolations. This retrieves sediment thickness where it has been eroded (i.e., in incised riverbeds) based on the calculation of an average value with the thicknesses of surrounding data points. This means that present-day incised river valleys, of < 20 km width, do not influence the thickness distributions. Across the basin, the resolution of our data sets can vary, especially after the addition of the very dense Ney et al. (1974) and Tărăpoancă (2004) datasets.

1.3 Retrieved sediment thickness in eroded areas

In the Ukrainian Carpathian foreland, the sediments have been extensively eroded north of Bochkivtsi to the Polish border (Figure IV.3). Using the dataset we compiled, we wanted to find the thickness of eroded sediments in this area. We used two different methods: 1) using the surrounding stratigraphic column with preserved upper fluvio-deltaic sediments at Bochkivtsi and at the edge of the Polish border (Dziadzio et al., 2006), we propagated the thickness of the strata through the eroded area considering the differences in lithosphere deflection. Spatial integration of the stratigraphy allowed us to calculate a volume of eroded sediment over the Ukrainian foreland. 2) Using the calculated thicknesses by age, we accumulated sediment thickness to the youngest fluvio-deltaic sediment stage in the region. We created a selected data set preserving most of the sediment thickness and interpolated over the eroded area (Figure IV.3). We subtracted the preserved sediment thickness from the recovered sediment

thickness and obtained estimates of the eroded sediments in the region (Figure IV.3). Both methods provided similar results, as would be expected.

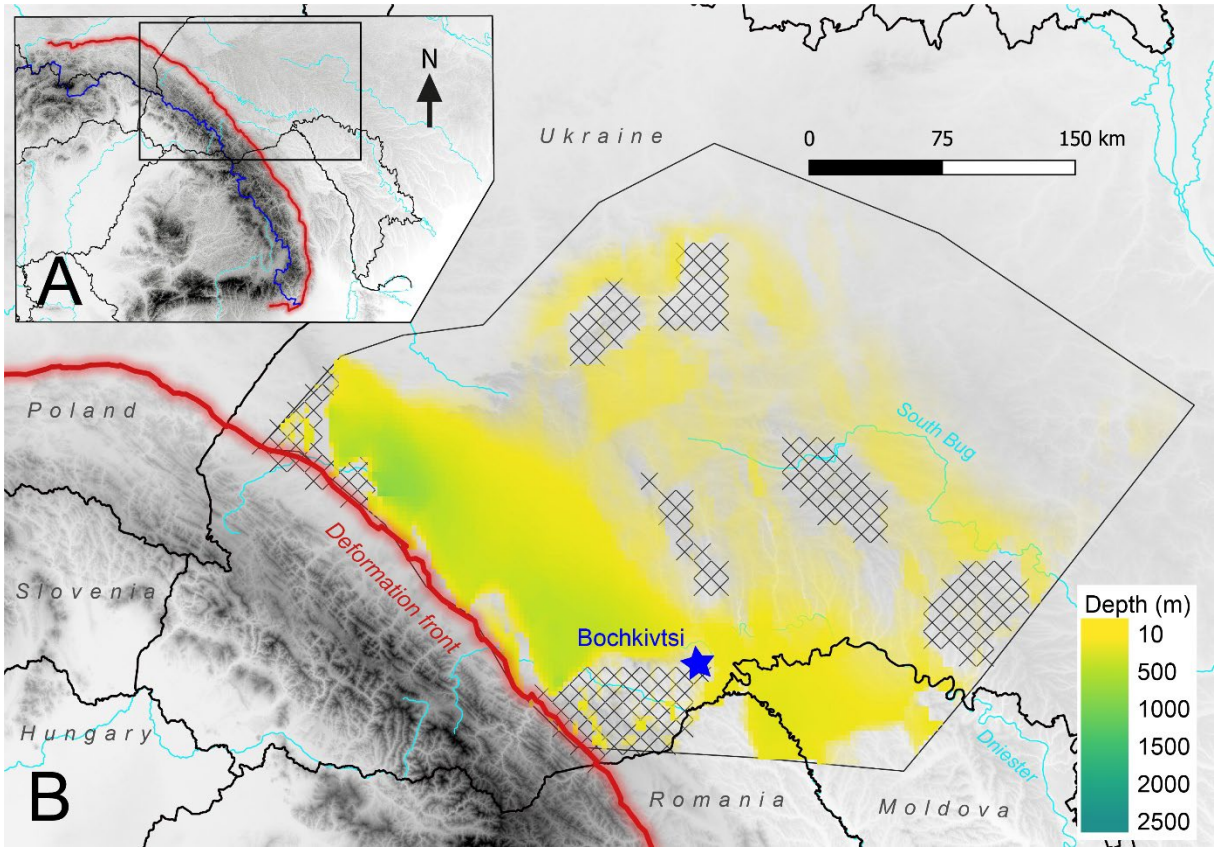

Figure IV.3: Sediment thickness map of the eroded sediments in the Ukrainian Foreland area. A) location of the retrieved sediment areas. B) Map of the retrieved sediments thickness. The crossed areas preserved (most of) the stratigraphy of the Ukrainian foreland and were used to constrain the interpolation on the missing sediment thickness. Map results show an intense erosion of ~500m of sediment in the Ukrainian foreland up to 50 km from the deformation front.

2 Sediment thicknesses in the CFB

We describe sediment thickness maps by stage and sub-stage in the CFB in detail in the following. It should be taken into account that during the underfilled stage sedimentation rates underestimate subsidence rates, while during progradation/aggradation of the sediment system, they overestimate subsidence rates. The maps also indicate the major depocenters in the basin.

2.1 Sediment thickness maps

Volumetric analysis of the **Badenian** stage (16-12.65 Ma) of the CFB needs special attention. Badenian sediments are present not only in the foreland, but also in the outermost nappes of the fold and thrust belt. These sediments are embedded in the nappe stratigraphy, not preserved as wedge-top sediments.

Moreover, Badenian sediments were overthrust by the Carpathian wedge for 70 km in the Ukrainian Foreland (Oszczypko, 2006; Oszczypko and Oszczypko-Clowes, 2012; see see Chapter II). During Badenian deposition, the Carpathian wedge was still accreting, thus the sediments were either reintegrated, overthrust, or preserved in the foreland. The thickness map described here corresponds, according to our interpretation, to the sediments deposited on the edges of the foreland during the Badenian. This is demonstrated, in the Polish and Ukrainian foreland where more distal facies are observed in Badenian outcrops (de Leeuw et al., 2020).

Badenian sediments are preserved up to 100-150 km from the deformation front (Figure IV.4). Sediment thickness increases south-eastward along the deformation front. The thickest estimated Badenian sediments are found in the Focsani Depression. However, because wells do not reach the base of the Focsani Depression, the bottom sediments thickness is interpreted from well data from its margin. The basin remained underfilled in the Badenian and due to ongoing convergence, the water depth in our study area was likely increasing at the time. The observed depositional rates thus underestimate subsidence rates in the vicinity of the frontal thrust (FT). The preservation of Badenian reefs on the distal margin is more indicative of the relative water depth. However, reefs of Badenian age are not directly observable at the surface in the South and SW of the basin (Figure I.14). They are preserved at the surface of the current basin in the Northernmost part of Romania along the Prut River (Figure I.14).

Sedimentation during the **Badenian** appears to have been concentrated in the SW of the basin (Figure IV.4). Accounting the convergence of the belt during this stage, and the diachronous cessation of thrusting along the Carpathian front (Chapter III and references therein), the Badenian depocentres in the Western and North-eastern regions may have been subducted/integrated into the wedge. Therefore, in the west and north of the CFB basin, the Badenian map is showing the sediment thickness of the distal margin that was preserved from erosion. The Badenian basin to the SE appears to have been less affected by the advancing wedge after deposition because the depo-centre is preserved. In this light, the thickness map of preserved sediments at this period (Figure IV.4) may bias the identification of the Badenian depocenters.

In the **Volhynian** substage (12.65-11.6 Ma), most of the preserved sediments are found in the Polish Carpathian foreland (Figure IV.5). The sediments extended over the East European Platform up to 300 km from the orogen, but have since been eroded along a 100 km wide central strip, where the Volhynian is now absent . Preserved sediments are again found at the Ukrainian-Romanian border and a 2 km deep trough holds mainly Volhynian sediments in northern Romania (Figure IV.5). The sediments were deposited in thick layers (~ 500 m) in the Romanian foreland and thin out towards Moldova. Another depositional centre is identified in the north of Focsani Depression for this sub-stage. Sedimentary facies indicate that the Polish part of the foreland basin became overfilled during the Volhynian (Dziadzio et al., 2006), which means sedimentation rates shown on the map exceeded subsidence rates, whereas the rest of the Carpathian foreland basin remained underfilled.

Bessarabian (11.6-9.6 Ma) sediments, if deposited, were not preserved in the western CFB (Figure IV.6). The northernmost sediments of this substage are found in the Ukrainian foreland in thin strata (<100 m). They correspond to coastal sediments bordering a potential ancient deltaic system, now eroded.

Thicker Bessarabian deposits (100-500 m) are found throughout the Romania and Moldova foreland. These sediments are interpreted as prograding clinoforms and indicate the onset of foreland infill of the accommodation space previously created (i.e., during Badenian and Volhynian underfilled stages). Clinoform height suggests approximately 400 m water depth close to the frontal thrust of the Romanian East Carpathians (de Leeuw et al., 2020) was progressively filled during the sub-stage. In the Bessarabian, sedimentation rates exceeded subsidence rates in the eastern CFB. On the other hand, the sediments extending eastward correspond to a a mix of siliciclastic and carbonate sediment that developed on the distal margin. The location of the carbonate platform is restricted to the E and SE of the CFB. The main centre of deposition at this time is the Focsani Depression, with 1500-2000 m of sediment accumulated (Figure IV.6). Sediments were also deposited on the borders of the current Black Sea basin. This indicates a potential transit of siliciclastic sediments to the Black Sea basin at this stage, particularly during the late Bessarabian lowstand (Popov et al., 2010; de Leeuw et al., 2020).

During the **Kersonian** sub-stage (9.6-8.37 Ma), less sediment was deposited and preserved in the CFB (Figure IV.7). A rather homogeneous sedimentary stratum of ~100 m of sediments is identified in Romania, Southern Moldova and Southern Ukraine, along the BS borders. Despite the homogeneous sedimentary cover of this stage, a higher sedimentation rate and a potentially larger accommodation space allow the identification of the Focsani Depression depocenter on the thickness map (Figure IV.7). Another patch of sediment is found in the north due to the Balta sediments attributed to the Kersonian stage.

In the **Meotian** (8.37-6.1 Ma), the sediments preserved in the CFB are limited to the southern part of the basin (Figure IV.8). The northernmost sedimentary strata (~100 m) are part of the Balta Formation. The shallow sedimentary strata (<100 m) east of the South Bug River are thin continental clays. In the Focsani Depression, sediment thickness is, as for the Kersonian, relatively homogeneous with a maximum of 1500 m deposited near the belt's frontal thrust. The Focsani Depression depocenter seems to extend more to the south starting from this stage, in line with inferences by Jipa and Olariu (2009). Prograding clinoforms imaged in seismic sections indicate that the Focsani Depression started to be overfilled during the Meotian (Krezsek and Olariu, 2021), which means that sedimentation outpaced subsidence.

Sedimentation rates were high (up to 1.2 km/My) in the **Pontian** (6.1-4.7 Ma) and located in the centre of the Focsani Depression (Figure IV.9). The Pontian depocenter in the Focsani Depression is located farther from the frontal thrust than for previous stages. After the infill of the CFB during the Meotian, accommodation space seems to have been limited in Pontian, leading to sediment preserved mostly in the Focsani Depression in thick layers and as a thin veneer further to the east. Early Pontian sediment cover the underlying strata transgressively up to 100 km inlands of the present-day Black Sea coastline (Popov et al., 2010; Krezsek et al., 2016). The "flooding" event from this period deposited sediments in the Black Sea north-western sedimentary platform, thus covering the CFB, up to 100 km landward of the Black Sea borders with thinner sediments of shallow marine facies during highstand stage. The middle Pontian (Portaferian) regression incised the foreland, transporting sediment farer in the Black Sea basin (Krijgsman et al., 2010; Stoica et al., 2013; Matoshko et al., 2023). Terrestrial faciès were deposited in the Focsani Depression. Lake-level rose again in the late Pontian, transgression in the platform allow for deposition of littoral sediment in the incised valley on the current borders of the

Black Sea basin. The Focsani Depression return to the deposition of shallow marine to deltaic faciès (Matoshko et al., 2023).

Our final map aggregates **Pliocene** and **Pleistocene** (4.7-0.0117 Ma) sediment thicknesses (Figure IV.10). During this period, a large accommodation space in the Focsani Depression allowed for up to 4500 m of sediment preservation. The depositional centre of the Focsani Depression for these stages is located around the Carpathian bend zone, a little more south than in previous stages. The thickest estimates are found below the town of Focşani. Deltas/estuaries also developed at the Black Sea basin borders at this time (Matoshko et al., 2009; Matoshko et al., 2019). Sediment supplied by the Danube played a role in the Focsani Depression during the Dacian (4.7-4.2 Ma) and Romanian (4.2-1.8 Ma) stages (Matenco et al., 2016; Matoshko et al., 2019; Krézsek and Olariu, 2021). The CFB axial transport system was also providing sediment to the Focsani Depression and the Black Sea basin, competing with the Danube River, through the Porat (Matoshko et al., 2019). The remaining Porat sediments are found at the northeast rim of the Focsani Depression but also in Moldova. Patches of sediments (Figure IV.10), in the north of Moldova correspond to Porat sediment preserved on cliffs on Balta Fm, as top sediments. Aside from CFB sediments, other deposit, are shown on the Plio-Pleistocene map (Figure IV.10). These sediments are not attributed to the volumetric analysis in our study. They are present on the map as punctuated deposit found on top of cliffs. Most of these sediments are interpreted as alluvial deposit (terraces) and preserved from river erosion. The delta of the Dniester River is also observable, as a triangle zone with thicker sediments (~100 m; Figure IV.10) in the BS basin borders. On the Dniester River course, in the north of Moldova, some Gelasian (2.6-1.8 Ma) terraces are preserved. The sediments on the South Bug River and Dnieper River course are Pleistocene terraces. Sediments attributed to continental erosion (red-brown clay formation) are not displayed in the Plio-Pleistocene maps. These sediments are thin deposit (≤20 m) and are found overlying (but sometime underlying) older formations, like Balta Fm, Sarmatian or Pontian sediments. Therefore, their exact age is not well constrained.

Quaternary river terraces are excluded from our sediments thickness analysis, these sediments are found in Romania, but the lack of resolution do not allow us to constrain their extent and their thickness (terraces up to 300m thick; Petrescu, 1966).). The loess sediments capping the terraces are also out of our scope for this study. The loess sediments are a produce of the erosion linked to glaciation-deglaciation during Quaternary. Their thickness can be up to ~30 m at the top of some cliffs (Necea et al., 2013).

In conclusion, the sediment thickness maps of the CFB trace the evolution of deposition in the foreland from the middle Miocene to the Pleistocene. Badenian sediments were mostly preserved in the Romanian foreland to the SW. The advancing wedge, at the time, reintegrated or overthrust the Badenian in the western and north-eastern regions. Since the Volhynian sub-stage was deposited throughout the foreland, as well in Poland as in Ukraine, this confirms that the Badenian sediments must have been cannibalized during the late convergence phase of the belt. The extend of the Volhynian deposits also mark the widening of the foreland to the east. The following Bessarabian sub-stage indicates the migration of deposits to the main depocenter of the CFB, the Focşani Depression as well as an extension of the basin further to the east. Bessarabian deposits progressively covered the sill that still separated the CFB from the Black Sea during the Badenian. These sediments were mostly transported by the axial sediment system that developed in the Polish part of the CFB in the Volhynian (Dziadzio

et al., 2006) and prograded throughout the eastern foreland over the course of the Bessarabian and Kersonian (Matoshko et al., 2016; de Leeuw et al., 2020). Sediment thicknesses are consistent from the north, where delta-top deposits (Balta Fm) are observed, to the edge of the BS, where the deposits are sediments with coastal/marine facies. During the Sarmatian, the CFB shifted from an underfilled foreland, where deep-water facies sediments dominated, to a foreland that is occupied by fluvio-deltaic sediments and large clinoforms that formed a prograding sediment transport system to the BS basin. By the Meotian, the Balta Formation sediments demonstrated the south-eastward progression of the foreland system deposits. The preservation of the Balta Fm on the distal margin can be interpreted as the eastward end of the main foreland river. The differential surface uplift linked to post-collisional slab detachment might be the cause of erosion of these strata closer to the mountain belt and preservation further away. However, the Focsani Depression depocenter still had higher sedimentation rates during the Meotian. During the Pontian, the foreland transport system was affected by changes in the base level of the Black Sea and sediment thickness maps no longer mark deposition toward the NE of the CFB. Most of the Pontian coastal sediments are related to the transgression event. The highstand sediments were deposited along the Black Sea, up to 100 km from the current coastline. Ongoing Carpathian belt erosion and foreland transport system were providing sediments to the Focsani Depression continuously during Pontian stage. The very high depositional rates thus reflect the high subsidence rates in the Focsani Depression, and the lack of accommodation space in the rest of the foreland basin against a background of continuing sediment supply. In the Plio-Pleistocene, the deltaic transport system resumes and marks the development of the Danube and Dniester deltas to reach the present-day coasts. The Danube River entered the Focsani Depression at the end of Pontian (Krézsek and Olariu, 2021) and developed a delta next to the Dobrogea Massif in Pleistocene. Despite the formation of large deltas at the Black Sea borders, the depositional rates remained high in the Focsani Depression in this recent stage.

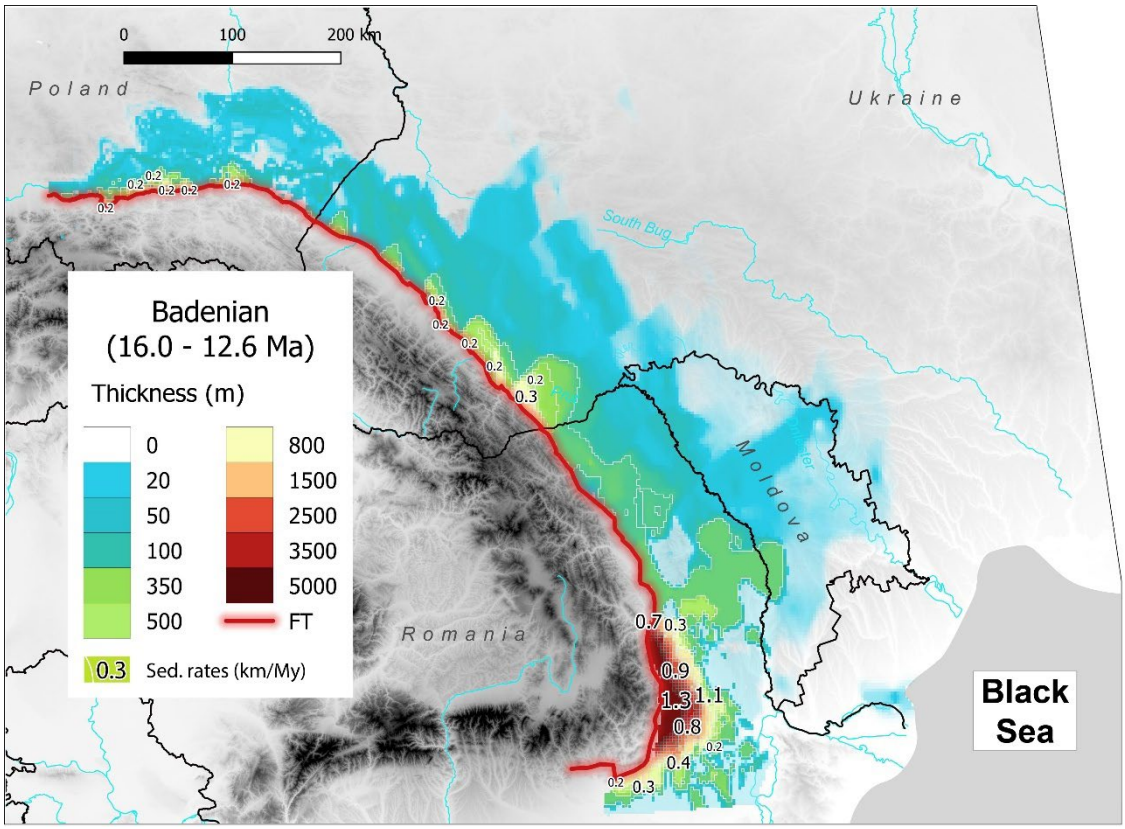

Figure IV.4: Badenian map of present-day sediment thickness in the CFB.

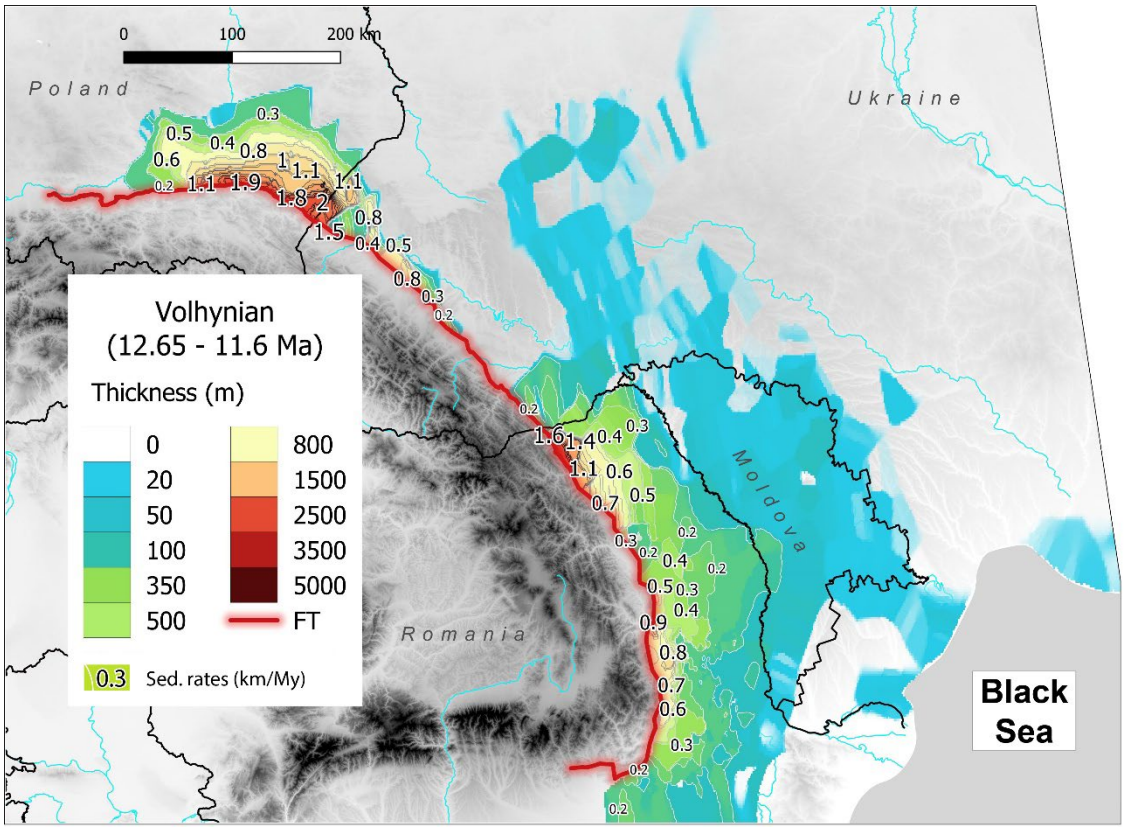

Figure IV.5: Volhynian map of present-day sediment thickness in the CFB.

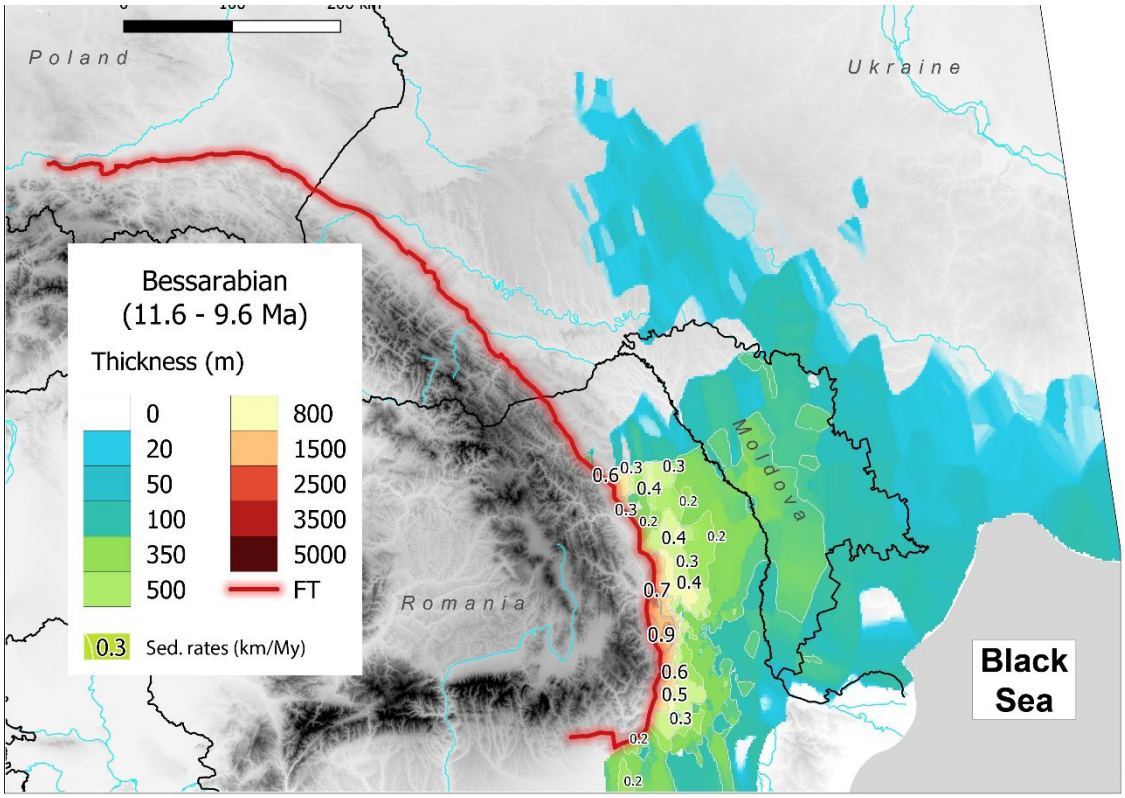

Figure IV.6: Bessarabian map of present-day foreland sediment thickness in the CFB.

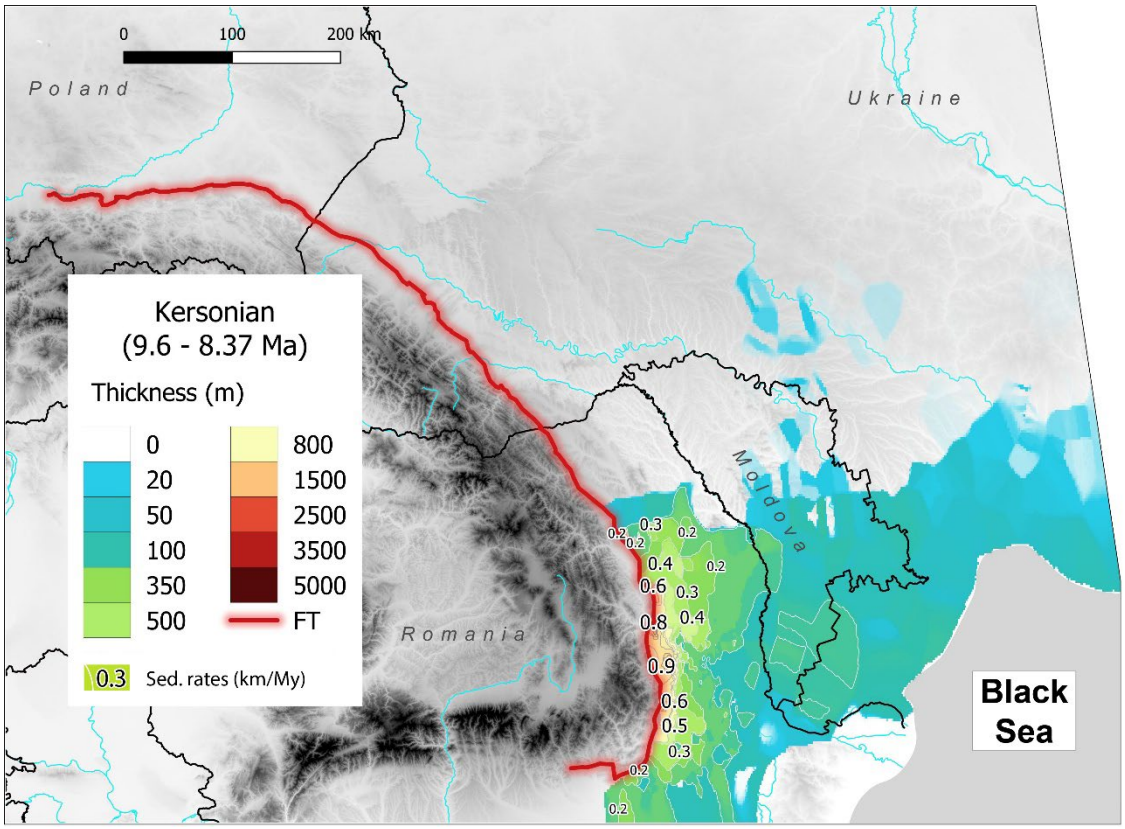

Figure IV.7: Kersonian map of present-day sediment thickness in the CFB.

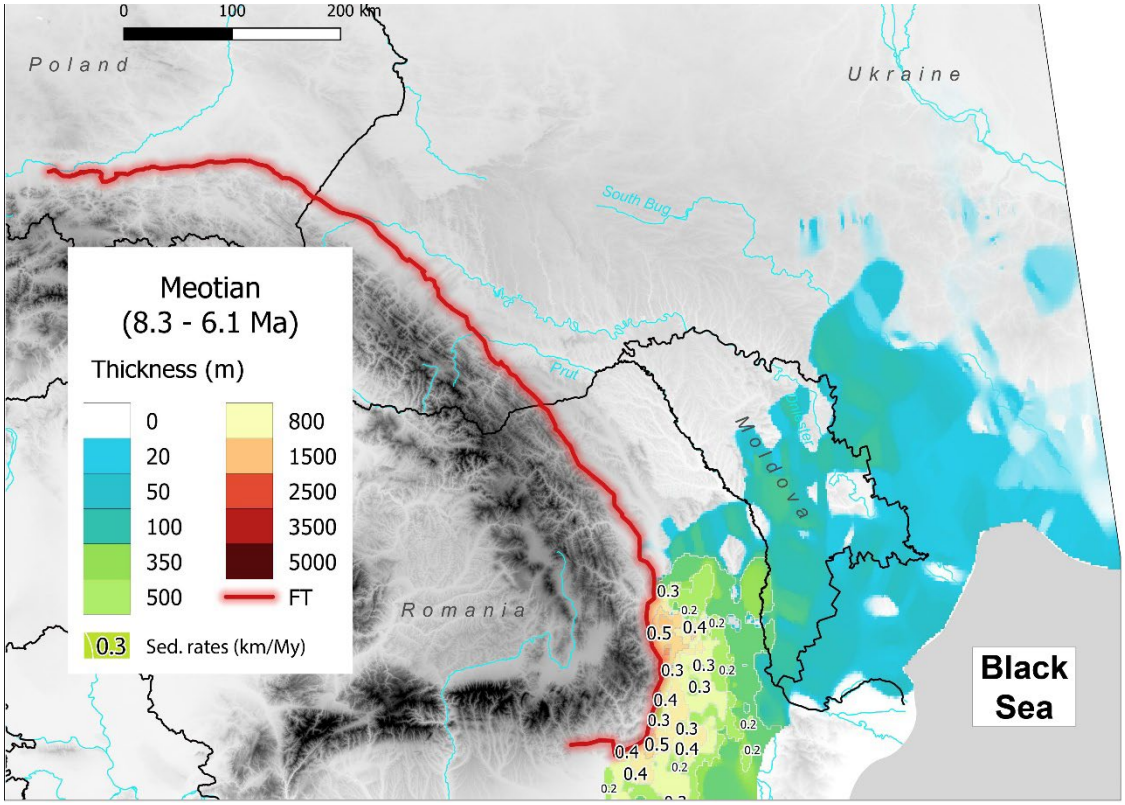

Figure IV.8: Meotian map of present-day sediment thickness in the CFB.

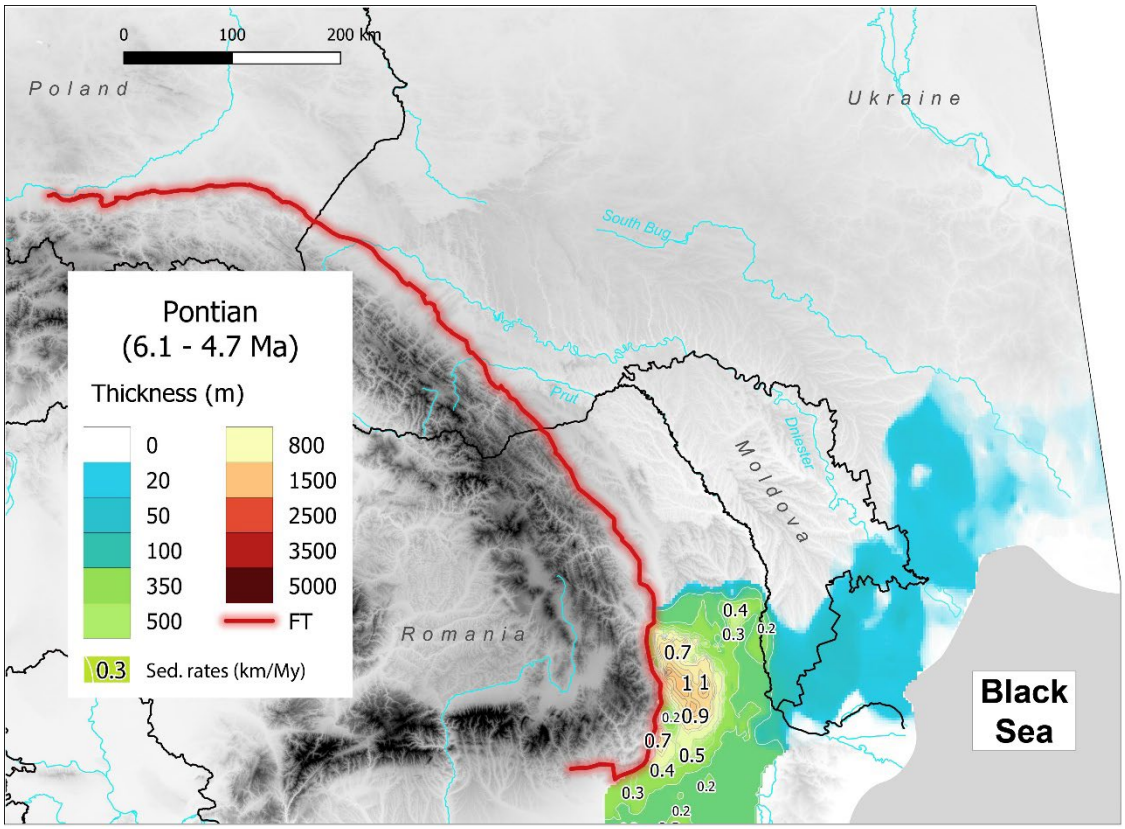

Figure IV.9: Pontian map of present-day sediment thickness in the CFB.

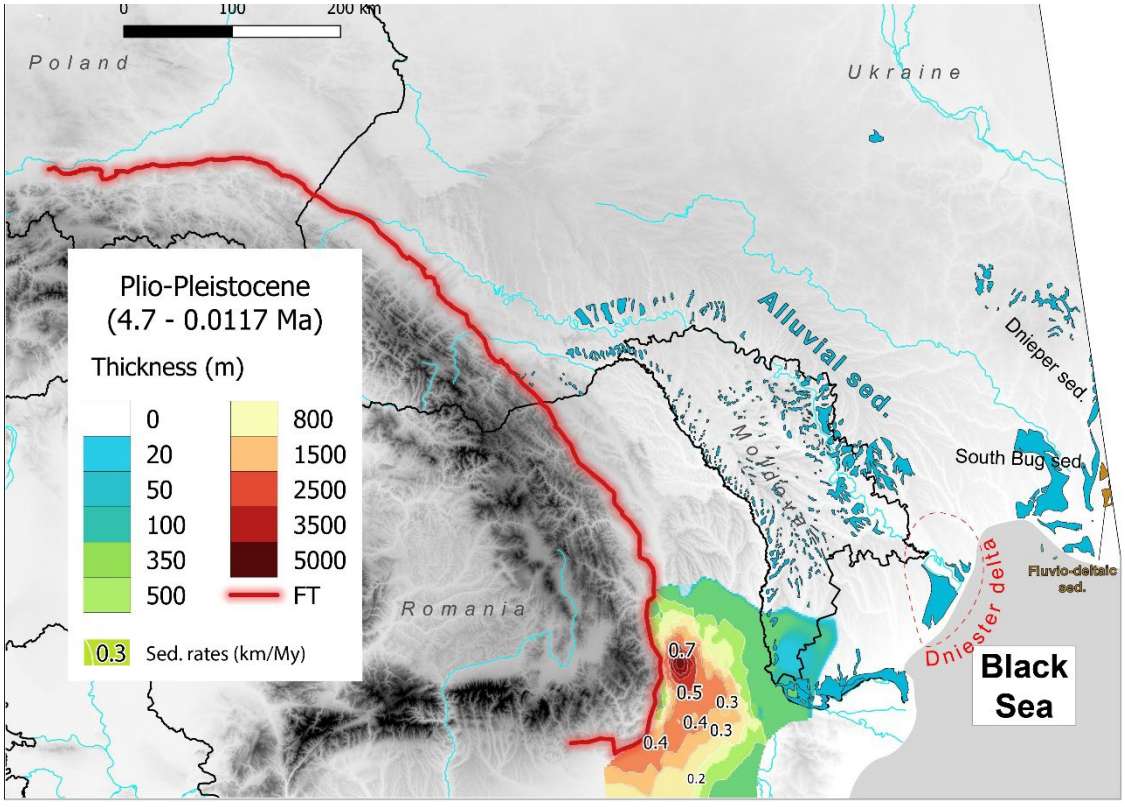

Figure IV.10: Plio-Pleistocene map of present-day sediment thickness in the CFB. Polygons in Blue represent the alluvial sediment preserved in the foreland at this period. Brown polygons are fluvio-deltaic sediment of this age. The polygons are extracted from the geological maps.

2.2 Foreland sections from the sediment thickness model

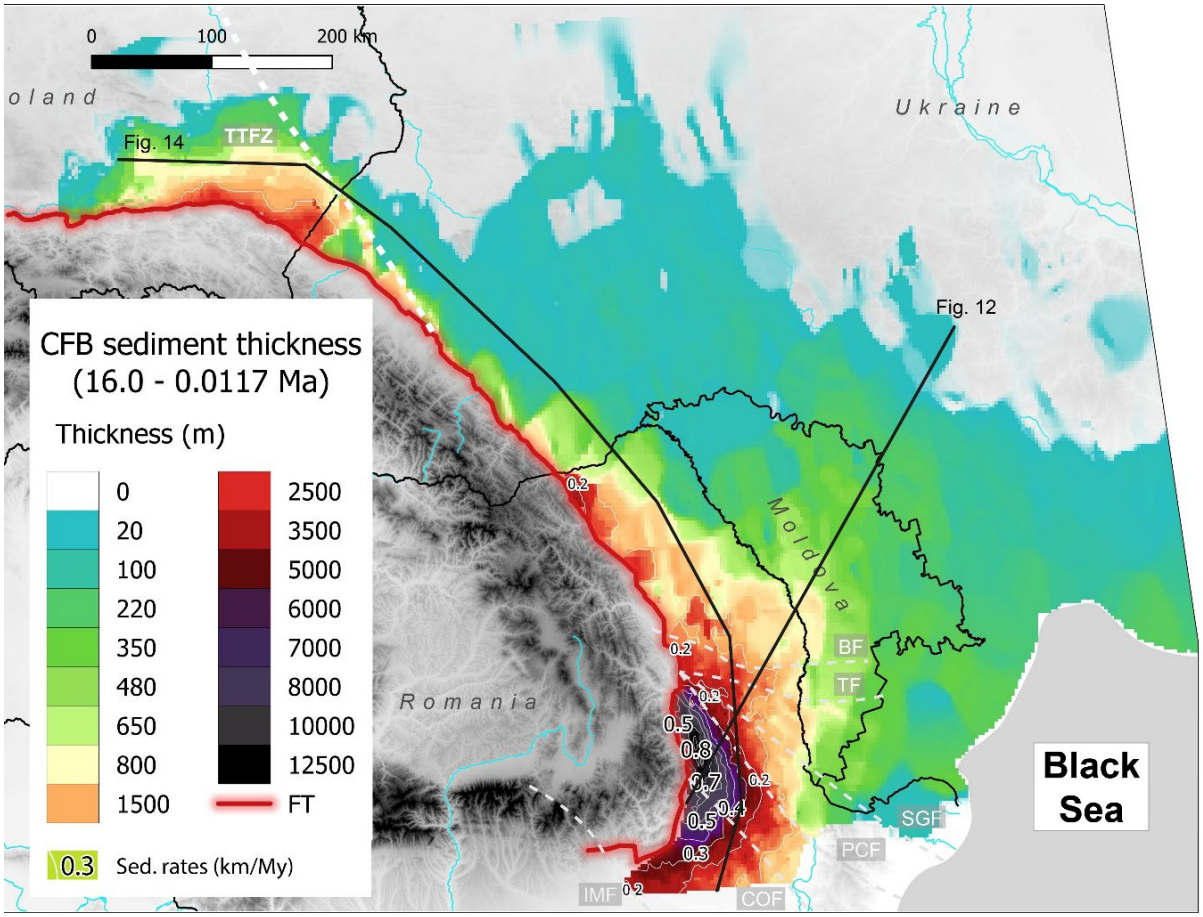

Figure IV.11: CFB sediments thickness map (of present-day preserved sediments). All thicknesses presented above were stacked to represent the foreland sediments from the Badenian to the Plio-Pleistocene. This map does not account for the Quaternary sediments. Black lines are the sections from Figure IV.12 and 14. White dashed lines represent the main faults in the foreland. TTFZ: Tornquist-Teisseyre Fault Zone; BF; Bistriţa Fault; TF: Trotus Fault; SGF: Saint George Fault; PCF: Peceneaga-Camena Fault; COF: Capidava-Ovidiu Fault; IMF: Intra-Moesia Fault; FT: Frontal thrust

The sediment thickness maps, once stacked, are a model of the 3D sediment thickness of the whole CFB. We exploit this model to observe the apparent organisation of the sediment in the pro-foreland. This model does not take into account the main faults of the lower crust. However, we can observe major thickness changes at the location of the main faults (Figure IV.12). The Focsani Depression depocenter distinguishes itself from the overall foreland. The depositional rates over the foreland exceed the 0.2 km/My around the Focsani Depression, the Polish trough and the Badenian trough in the north of Romania (Figure IV.11). Mean sedimentation rates are maximal in the Focsani Depression, in between the Peceneaga-Camena Fault (PCF) and the Capidava-Ovidiu Fault (COF; Figure IV.11). The stage-by-stage development of the foreland, and the map of Figure IV.11 suggest that the overall subsidence of the Focsani Depression was around 0.6-0.8 km/My in its deepest parts.

To explore the CFB development, two sections were extracted from the sediment thickness model. One section through the foreland (Figure IV.12) crosses the Focsani Depression, and ends on the East-

European Craton, running parallel to the edges of the BS. The NE part of the section is shallow, and the sedimentary layers are thinned. The most identifiable layers along the section are those pertaining to the Bessarabian and Volhynian substages, due to their consistent thickness from west to east. The Volhynian is very extended to the east but overall thin compared to the other stages toward the west. The Kersonian, as already discussed for the thickness maps, seems to have lesser sediment than the rest of the Sarmatian sub-stages. The Kersonian is also less extended to the east, maybe due to the attribution of Balta Fm sediment to the Meotian stage. Meotian layers of the Balta Formation crop out in Moldova and Ukraine, with an average thickness of ~100 m of sediment. Pontian sediments in the east are present in incised valleys. Some Plio-Pleistocene sediments from Porat cap the hills formed by the Meotian strata. The Badenian is completely covered in this section. It is found sparsely in Moldova, where the Badenian sediments are mixed carbonates and siliciclastics from the distal margin. Some of the Badenian sediments in this section may correspond to the reefs that formed at the edge of the zone of shallow marine mixed carbonate-siliciclastic deposition; approximately 100-150 km from the FT (Saulea, 1965; Górka et al., 2012; de Leeuw et al., 2020).

The section crosses the deepest point of the Focsani Depression (~12.5 km) and shows the spatial organization of the sedimentary layers. The Focsani Depression deepens greatly in two places, west of the Moldavian-Romanian border, and then, 100 km from the Carpathian thrust front (Figure IV.12). These step-increases in thickness coincides with the location of lower plate main faults (Figure IV.11). The flexure of the passive margin was promoted by pre-existing faults reactivated during the retreat of the subduction zone in the Carpathian embayment (Krzywiec, 2001a; Tărăpoancă et al., 2003; Leever et al., 2006). The Focsani Depression depocentre was already effective in the Badenian, as suggested by the difference in sediment thicknesses inside and outside the depression. Even if the Polish and Ukrainian foreland have preserved less Badenian sediments due to overthrusting of the foreland, the sedimentation rates in the Focsani Depression in the Badenian are higher than the average (Figure IV.12). This implies a greater subsidence during this stage or a deeper basin already present. Subsequently, the Volhynian sediments also appear to be affected by this difference in basin depth. The Volhynian thickness only increase at the Focsani Depression and to the western border. In contrast, the Bessarabian and Kersonian sediment thickness does not appear to be affected by a drastic increase in thickness at the borders of the depression. The sediment thickens progressively toward the centre of the depression. This even thickening of both stages could be an artefact of the Sarmatian sediment thickness division in the Romanian foreland (see section 1.2.2.). The difference in thickness becomes increasingly apparent in the Meotian, and then in the Pontian, when the strata beyond the depression are less than 100 m and about 1 km in the Focsani Depression (Figure IV.12). The change in sediment spatial accumulation at the end of the Sarmatian support the hypothesis of a growing axial sediment system delivering sediments to the Black Sea basin at the transition from Sarmatian to Meotian (de Leeuw et al., 2020). The Pontian sedimentation rates are higher than the average and sign a potential faster subsidence of the Focsani Depression at the time. But during the Pontian, the foreland axial system was perturbed by large eustatic variation (Popov et al., 2010). The Balta formation was incised, and sediments were transferred to the Black Sea basin during lowstand. Therefore, the Focsani Depression was infilled by shallow marine and delta facies during early and late Pontian and middle Pontian sediments were transferred downstream during highstand ((Stoica et al., 2013; Matoshko et al., 2023). During the Plio-Pleistocene a deepening of the central Focsani Depression occurred, and 4.2 km of

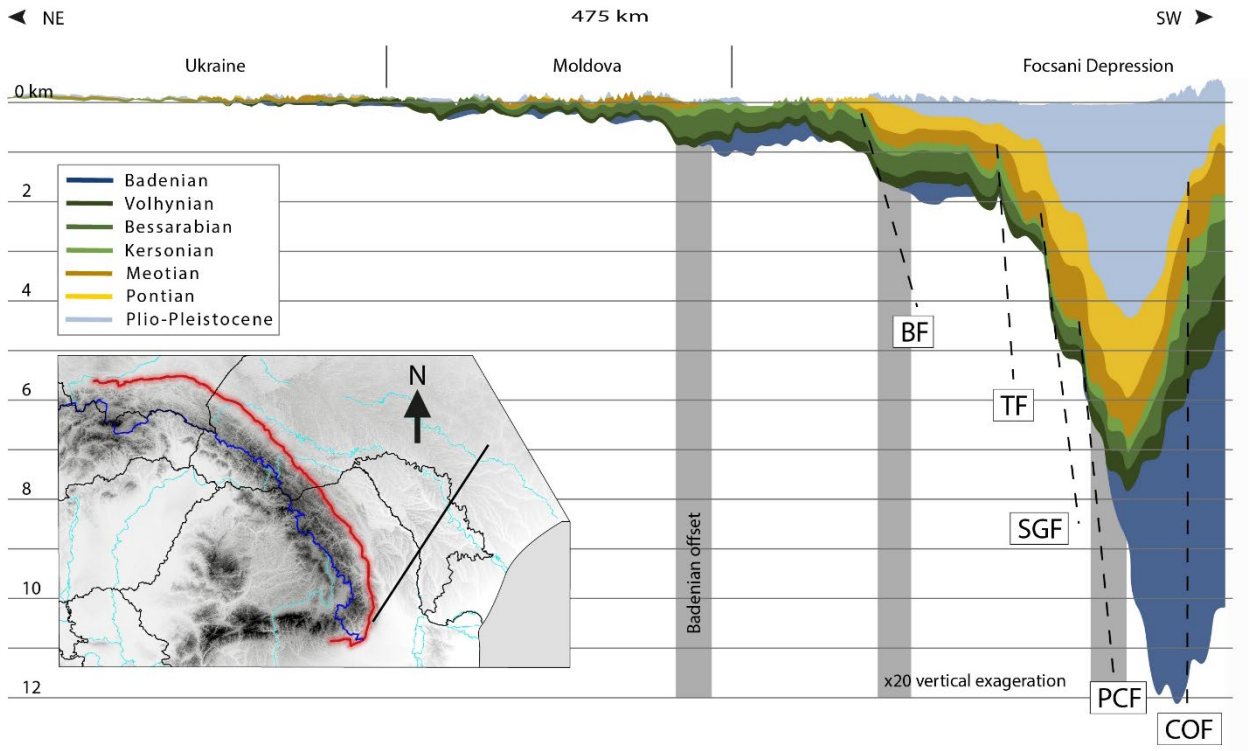

Figure IV.12: Section from the sediment thickness model of the CFB. The section crosses the Focsani Depression at its deepest point (in the model). BF; Bistriţa Fault; TF: Trotus Fault; SGF: Saint George Fault; PCF: Peceneaga-Camena Fault; COF: Capidava-Ovidiu Fault.

sediment accumulated. The Focsani Depression was shallow in Pontian (Krézsek and Olariu, 2021), thus the sedimentation rates mirror the subsidence of the depression for the latest stages (Figure IV.13).

The maximum sedimentation rates in the Focsani Depression, based solely on sediment accumulation and not corrected from sediment compaction or water depth at deposition time, was approximately 1.1 km/My, from Badenian to Kersonian (Figure IV.13). This could indicate the constant subsidence during this period. But taking into account the shallowing up of sediment facies in the Romanian Foreland, the subsidence is likely decreasing or sediment supply increase and infilled the accommodation space. In comparison, the maximum sedimentation rates from the Meotian to the Pontian were from 0.8 to 1.2 km/My. The drop of sedimentation rate at the Kersonian-Meotian transition can indicate the overfilling of the depression, a decrease of subsidence. The difference in rate can imply an increase of the subsidence in the Focsani Depression during Pontian. Combined with the observation of sediment facies shallowing up, the maximal sedimentation rates in the Focsani Depression are a potential proxy for the subsidence over the area from Meotian to Pontian (Figure IV.13).

A second section along the basin, 50 km from the frontal thrust, shows the NW to SE arrangement of the sedimentary system (Figure IV.14). The section shows four very different zones in the CFB: the Polish trough has Badenian sediments and thick layers of Volhynian sediments. Along the section trace, the Ukrainian foreland shows very sparse Badenian sediments, and the other layers are extensively eroded. Preservation of the stratigraphy is the best at the Ukrainian thrust front and towards the Romanian border where the Badenian is respectively overlain by Volhynian turbiditic to deltaic sediments (Kurovets et al., 2004) and Volhynian littoral sediments(Andreyeva-Grigorovich, 1997; de

Leeuw et al., 2020). The Romanian foreland shows a progressive deepening of the depth to basement from north to south and an increase in preserved sedimentary layers. The Focsani Depression is the area with the thickest sedimentary infill. This section does not cross the deepest point of the Focsani Depression, but rather runs along its margins. Unlike the previous section, we see thinner Badenian in the Focsani Depression, as we are on the edge of the depocenter of this age. Volhynian sediments along the foreland show that the depocenter was to the west, where the sediments are a kilometres thick (Figure IV.14). The Volhynian thickness resumes in the Romanian foreland with ~500 m of sediment and thins on the margins of the Focsani Depression. Similarly, the Bessarabian is very thick in the Romanian foreland (~800 m) and thins in the Focsani Depression (~500 m). The Bessarabian sediments are less preserved to the north. These two Sarmatian sub-stages illustrate the progression of the sedimentary system to the southeast and to the Focsani Depression. The Kersonian is shallow throughout the CFB and is slightly more preserved to the north than the Meotian layers in this section. The Pontian and Meotian sediments appear thicker (~1000 m and 600 m respectively) in the Focsani Depression than the older deposits. For these stages, the foreland depositional zone covers most of the Focsani Depression. Plio-Pleistocene sediments are the thickest deposits in the Focsani Depression in this section (~ 2 km). Comparison with the preceding section (Figure IV.12) shows that the locus of maximum deposition in the Focsani Depression shifted over time.

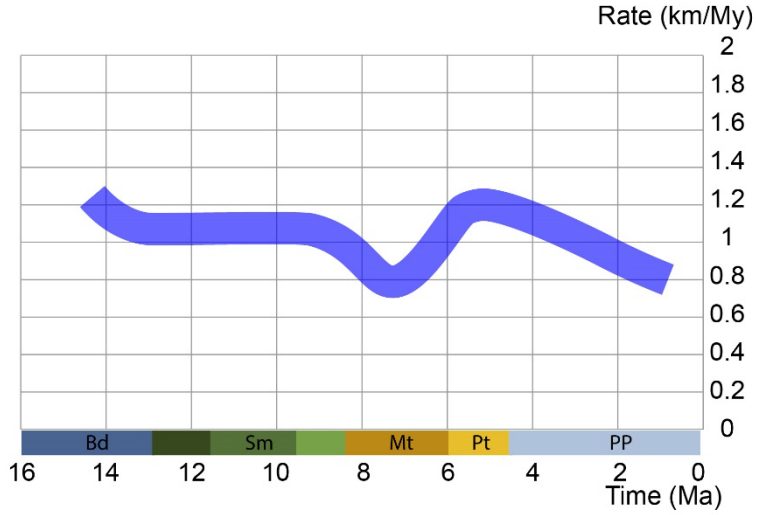

Figure IV.13: Maximum sedimentation rate over the Focsani Depression.

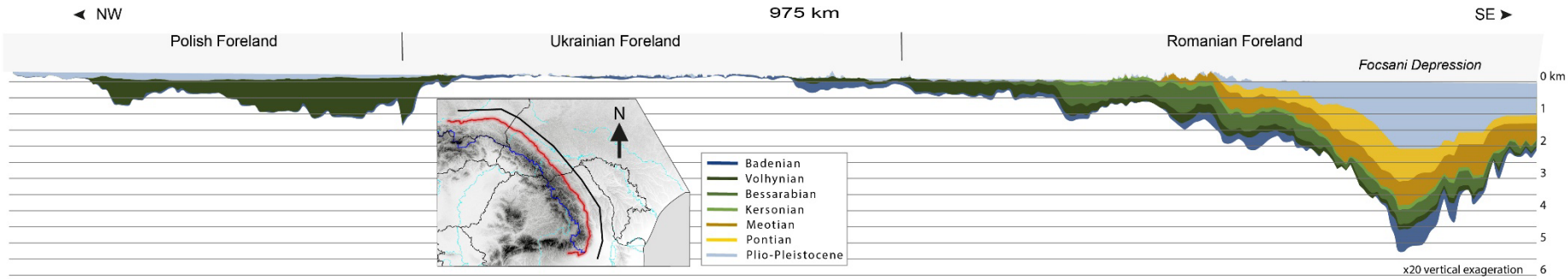

Figure IV.14: Section of the Carpathian foreland basin 3D model of sediment thickness at 50 km from the deformation front. The vertical scale is exaggerated twenty times. The Polish trough accumulated and preserved Volhynian sediments mainly, the transition to the Ukrainian craton shows an eroded area with some Badenian-Volhynian sediments preserved, but the depth of the actual basin in this region is close to zero. In Romania, especially in the Focsani Depression, sediments are well-preserved and were accumulated in large volumes during the Plio-Pleistocene (4.7-0.0117 Ma).

2.3 South-West Carpathian foreland

The architecture of the CFB is particularly interesting in its southwestern part, in the bend zone of the south-eastern Carpathian belt. In a recent basin analysis by Krézsek and Olariu (2021), a regional seismic and well log dataset covering the whole Dacian Basin, i.e. the Romanian part of the CFB, was used to interpret its architecture and the evolution of the depositional environment. The study overlaps the Focsani Depression SW part of our study area and is interpreted from new seismic and well data, allowing us to compare sediment thicknesses found in the Focsani Depression.

Section 3 of Krézsek and Olariu (2021) (Figure IV.15, B1), crosses the edge of the Focsani Depression and reaches the Carpathian deformation front a few tens of kilometres north of our section (Figure IV.12, 15 A) of the CFB. Our model does not include the fault traces but does reveal a step-increase in sediment thickness and depth. We display sediment thicknesses in kilometres while Krézsek and Olariu (2021) display depth in two way travel time (TWT) on their sections. Therefore, direct comparison of sediment thicknesses is not possible. However, architectural comparison of the two sections shows similarities in the sediment layer that deepens very rapidly at about 30 km from the thrust front due to displacement on the Miocene basement fault. At the edges of the Focsani Depression, the step-increases in sediment thickness are comparable on both sections (Figure IV.15), in location and in lateral variation of relative sediment thicknesses. The offset is due to activation of the Peceneaga-Camena fault zone according to Krézsek and Olariu (2021). The eastward evolution shows similarities in sediment architecture with thinning of sedimentary layers, especially post-Pontian sediments. Both sections (Figure IV.15 and 12) show a deeper sedimentary platform east of the Focsani Depression, where the foreland sediments are nearly flat until another step-increase in basement depth occurs near the Romanian border across an extensional fault (probably the Capidava-Ovidiu Fault).

Our foreland longitudinal section is comparable in its last Romanian part to section B2 (Figure IV.15) of Krézsek and Olariu (2021). In the S-N oriented part of their section, the Focsani Depression sediments show thinning of the Sarmatian-Badenian layer in the northern and southern boundaries of the Focsani Depression, consistent with our sediment thickness section. The other striking similarity is the relative lateral variation in sediment thickness in the two sections where the Pontian increases in thickness toward the north of the Focsani Depression while the Meotian increases in thickness in the south of the Focsani Depression. Another comparable layer is the post-Pontian sediments, which are for the two sections thickest in the Focsani Depression and cover the lateral step-increases in basement depth. At the southern boundary of the Focsani Depression, there are also similarities in both sections, as the sediments begin to lie flat on the Moesian platform, with little or no Badenian-Sarmatian sediments and conservation of Meotian and Pontian sediment thickness.

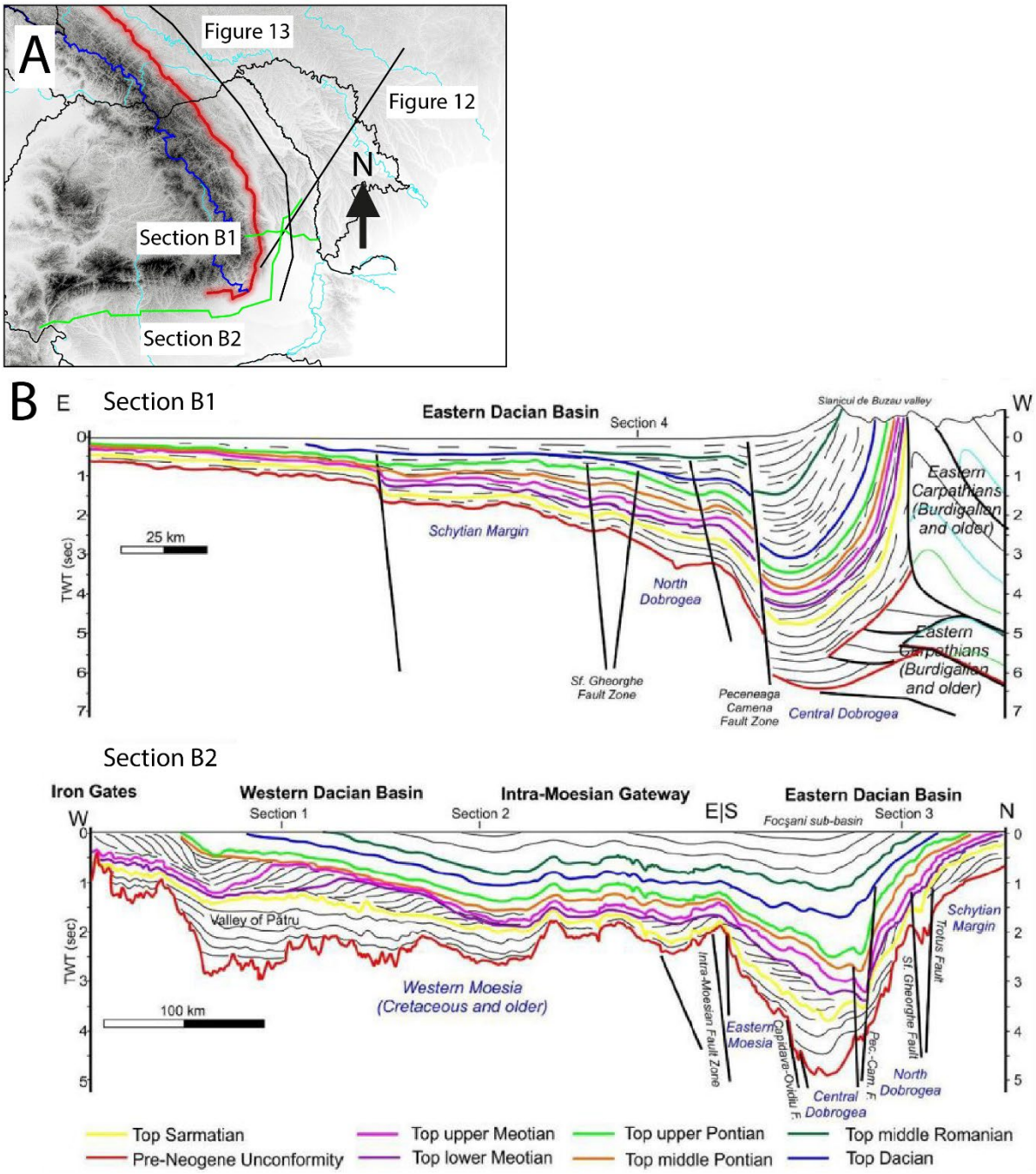

Figure IV.15: A) Location of sections in the CFB; green lines: Krézsek and Olariu (2021); black lines: this study; red line: Carpathians deformation front; blue line: Carpathians main drainage divide. B) section interpreted from the seismic data and well logs by Krézsek and Olariu (2021) as their Figure IV.4.

3 Limitation on the CFB model

3.1 Resolution across the foreland

We used several sets of data to complete the foreland model. However, the resolution and constraints on the sediment thickness vary from one set to another. The state geological maps and sections are based on wells and surface mapping. However, most of the spatial arrangement of sediment layers is up to the authors interpretations of the observations. Some thicknesses are minimum thickness as wells could not reach the basement. This happens mostly in the Romanian foreland at the rims of the Focsani Depression. The precisions on the data from Ney et al. (1974) and from Tărăpoancă (2004) increased the resolution in the Polish through and the Focsani Depression respectively. However, the isopach maps provided in the Tărăpoancă (2004) study were difficult to georeference, which may have induced a small geographic offset with respect to the rest of the maps. Its impact on volume estimates would, on the other hand, be negligible at the basin scale that we consider here. The contrast in resolution across the basin is smoothed by the IDW interpolation method, and sediment loss by river incision in narrow valleys (< 20 km) is overcome by interpolation. In shallow areas of the CFB, interpolation of sediment thickness is estimated to have the greatest error due to the large distances between the geological sections that were used to constrain thicknesses.

3.2 Compaction of sediments

The sediment thickness model we constructed is non-decompacted, i.e., sediments undergoing compaction during burial do not return to their original pre-burial thickness. We consider that this non-decompaction mainly affects clay and silt deposits undergoing shallow burial (< 2000m), reducing the porosity of the rock ~40% (Giles, 1997), thus reducing the thickness of sedimentary layers. The porosity loss also affects sandstone but to a lesser degree (up to 15% of porosity loss in lithic sand from 0-2 km depth; Chuhan et al., 2002). Once cementation of quartz begins (> 2-4 km depth), porosity loss decreases (Figure IV.16); this is primarily dependent on the temperatures reached by the sediments at depths greater than 2 km and thus on sedimentation rates in the basin (Chuhan et al., 2002; Marcussen et al., 2010). Regarding porosity loss as first factor of strata compaction, the greatest changes happen in the first two kilometres, and compaction decreases with further burial (Giles, 1997).

The evolution of CFB sediment facies can help deciphering the regions the most affected by the non-decompaction. Deep-water facies are thought to be more fine sediment like clay and mud. This facies is deposited mainly in the early stage of development of the CFB, thus sediments might be more buried and prone to compaction. The Polish through and the Focsani Depression are areas where sediments are consistently thicker than 2 km (Figure IV.11). Moreover, these locations contain mainly deep-water sediments, until the Volhynian. For the Focsani Depression the transition to a coastal sedimentary facies with alternation of fine sand and clay sediments, is progressive from Kersonian to Pontian. The Focsani Depression is then covered by ~2 km of Plio-Pleistocene sediments (Figure IV.14) of shallower facies that are more sand-dominated.

In conclusion, the Polish through is dominated by clayey sediments and they reach ~2 km of thickness, therefore they are very affected by compaction. The Focsani Depression is, on the other hand, the location that could be the most affected by decompaction. If decompaction is applied, the thickness variation should be equivalent for all strata except the Plio-Pleistocene, where sediments are, for most, at shallower depth than 2 km. For the rest of the foreland, sediments thickness is < 2 km. These sediments are in the range of depth affected by compaction, however. We recognize that decompaction of sediments in the Focsani Depression could affect the total thickness of sedimentary layers and their analysis. Indeed, sedimentation rates and sediment thicknesses are underestimated for this area. Even though, compared to locations less affected by sediment compaction, the Focsani Depression is undeniably the greatest area of sediment accommodation in CFB, the rates and thicknesses estimated in this study represent only minimal values.

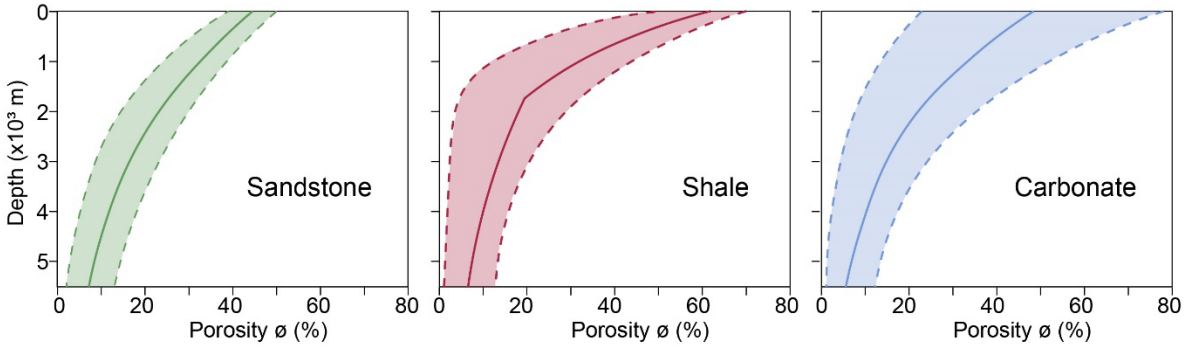

Figure IV.16: Compaction curves for sandstone, shale and carbonate rocks. Bold lines represent the mean trend and is defined by exponential function. Colored areas represent the range of compaction (from Giles, 1997).

3.3 Sources of errors in sediment thicknesses and their interpretation.

Basin stratigraphy determines the assignment of sediments to an age period and classifies the sediments in formation in the foreland basin. A sedimentary system evolves spatially in facies and deposition rates depending on the nature of the sediment (e.g., sand, silt, clay, carbonate, etc.) and its depositional environment (e.g., delta, flood plain, beach, offshore, etc.). Absolute dating of a sedimentary formation in the foreland is not obvious, and assigning sediments to a formation and age period over a wide area requires fine mapping and extensive study of the sedimentary system. In our case study, the stratigraphic ages of the CFB are relatively well constrained (age limits with precision < 1 My). However, there was no fully harmonious stratigraphic approach across the different countries of the Carpathian foreland. For example, Romanian maps have no preserved Plio-Pleistocene terraces (Figure IV.10), whereas, Moldova has many preserved cliff-top terraces.

The thickness of sediment of a stage does directly reflect the amount of subsidence in the foreland when the local water depth changes during deposition (assuming no absolute water-level changes). When the basin is underfilled, more accommodation space is created than sediments deposited and water depth

increases. Therefore, if water depth increases during deposition, the thickness of the sediments of that stage represents the minimum subsidence of the basin at that time. Over the course of the Badenian, water-depth increased throughout the Carpathian Foreland (Krezsek and Olariu, 2021; Matoshko et al., in prep.; see Chapter I), so the thickness of preserved sediment reflects the minimum subsidence of the basin for this stage. During filling of a certain part of the basin (such as during the Volhynian in Poland, during the Bessarabian in the northern Romanian foreland, and the Moldavian foreland in Kersonian), sedimentation rates exceed subsidence rates. Eventually, the excess sediment is transported to the next accommodation zone in the system. Therefore, sedimentation rates in progradation phases, are not representative of the accommodation space created by the system, as sediments infill the foreland areas that were underfilled in previous stages. When the depositional depth remains equal or the foreland is overfilled and excess sediment transferred further downstream, sedimentation rates do directly reflect the available accommodation space. Sediment thicknesses are therefore not a direct tool to foreland subsidence. Thickness of sediment require an interpretation in basin depth according to the sediment facies and the former water depth must be taken in account for the following stage. The area of accumulation also varies and change the relation of the sedimentation rates along time. Finally, the sediment thickness or sedimentation rates are directly dependent on the sediment supplied by the main source, therefore, a complete foreland analysis requires insights on the erosion rates variation of the providing belt.

The sediment that constitutes parts of the shelf in the north-western Black Sea have been supply by the CFB axial transport system from the Bessarabian to the Meotian-Pontian (de Leeuw et al., 2020). Subsequently, the Danube arrived to the area (Leever et al., 2011; Matoshko et al., 2019; Krézsek and Olariu, 2021) and thus contributed to the platform sediments. The Plio-Pleistocene (4.7-0.0117 Ma) and Romanian (4.2-1.8 Ma) ages overlap in our CFB model and in the Dacian Basin, therefore, at this period, distinguishing the source of sediments supplied by the Danube or by the CFB drainage system to the Focsani Depression and then to the Black Sea is tedious. Complete tracing of the foreland sedimentary system should incorporate the north-western Black Sea sedimentary platform to obtain accurate sediment volumes and a comparable source-sink budget, but sediments supplied by the Dnieper River and the Danube River must be identified and removed.

4 Implication of shifting depocenters

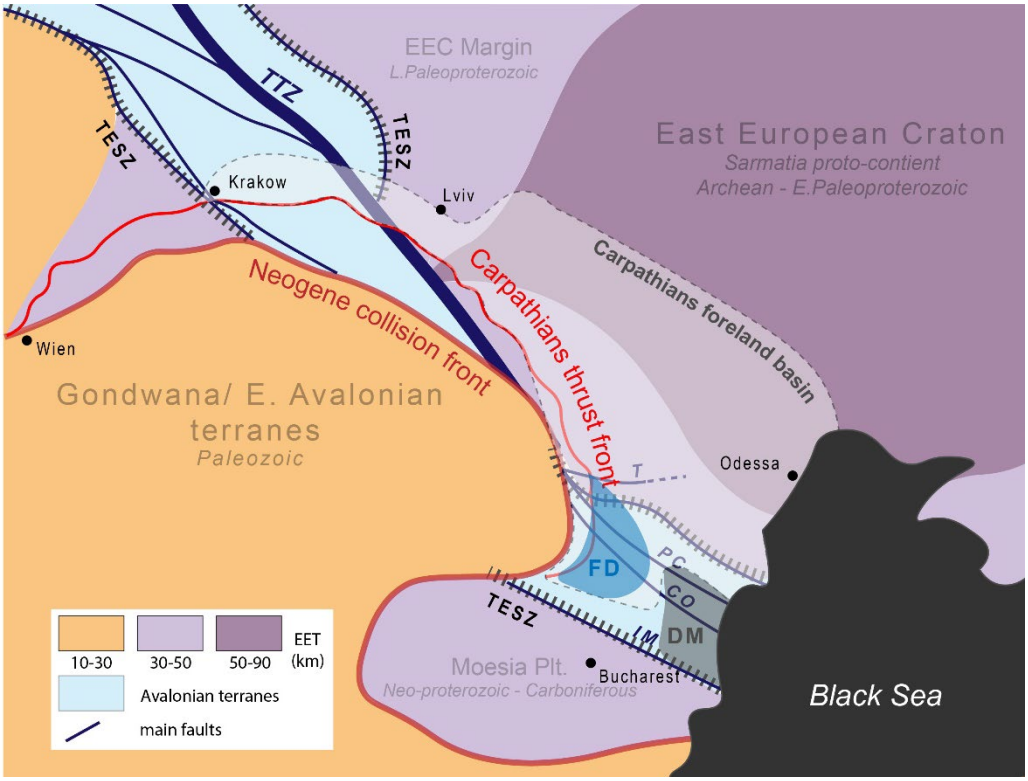

Figure IV.17 Terranes map of The Carpathians region. TTZ: Tornquist-Teisseyre Fault Zone; TESZ: Trans-European Suture *Zone;* . T: Trotus *Fault; PC*: Peceneaga-Camena Fault; CO: Capidava-Ovidiu Fault; IM: Intra-Moesia Fault; *FD:* Focsani Depression ; DM : Dobrogea Massif ; EET : Effective Elastic Thickness . (Modified after Oczlon, (2006): Terrane Map of Europe, 1st edition, Gaea Heidelbergensis, v 15)

4.1 Heritage of the lower plate and *loci* of depo-centers.

The plate underlying the CFB has a large variation in effective elastic thickness (EET) and includes a major structure of the European continental plate: the Trans-European Suture Zone (TESZ). Following, we detail these characteristics and how we think they have affected the development of the Foreland Basin.

The European platform is traversed from the North Sea to the BS by the TESZ, a zone of accreted terranes separated by transpressive lithospheric faults such as the Tornquist-Teisseyre Zone (TTZ), identified in the territories of Poland and Ukraine (Pharaoh, 1999; Krzywiec et al., 2017; Janik et al., 2022)). The suture zone marks the accretion of the Avalonian terranes to the Sarmatian Craton during the Late Ordovician (Chapter I section 3.1. and references therein). The difference in EET across the foreland crust is due to this difference in terranes (Starostenko et al., 2020; Janik et al., 2022). The estimated EET of the East European Craton (Sarmatia terranes) is about 80 km in the interior and is surrounded by terranes decreasing to 50 km of EET. For the European plate (Avalonian terranes) the

EET is estimated at 25-35 km (Kaban et al., 2018; Figure IV.17). In the southern part of the CFB, the Dobrogea Massif, which is also part of the Avalonian terranes, is flanked by strike-slip lithospheric faults separating the South, Central, and North Dobrogea units (Figure IV.17). These faults were active during the late Jurassic and Cretaceous (Tărăpoancă et al., 2003). The present-day outer Carpathian belt was thrust onto the TESZ and part of the East European platform (Figure IV.17).

We can explain the discontinuity in foreland sediment thickness and depositional locations during foreland filling by the heritage of the lower plate of the foreland basin. The deepest parts of the basin are found where the EET of the lower plate is moderate to low (25 - 50 km; Figure IV.17), in our case the Polish basin and the Romanian foreland. According to a purely flexural model estimates, the transition zones of contrasting lithospheric characteristics are destined to concentrate more lithospheric stress during contraction (Leever et al., 2006). The limit between the European plates and the Ukrainian craton provides both a sudden change in EET and pre-existing faults. However, the dynamic subsidence induced by the slab also affect the foreland basin during its formation. According to the models of development of retreating subduction zone including dynamic subsidence (presented in Chapter I section 4), the downward deflexion of the foreland increases with the slab pull and downward mantellic flow. We could not erase the correspondence between the deepest parts of the foreland and large accumulation of sediments. The accretion of the Carpathian belt triggered the reactivation of pre-existing faults and allowed significant movements along them (Krzywiec, 2001b; Tărăpoancă et al., 2003). But the vertical motion of the foreland lithosphere (East European Platform) could be enhanced by dynamic subsidence due to the downgoing slab and the mantle convection (Husson, 2006; Guillaume et al., 2013; Husson et al., 2012).

4.2 Focsani Basin evolution over time

The most developed depositional centre in the CFB is the Focsani Depression. From the Badenian to the present, this depression has received most of the sediment shed by the Carpathian belt. The size and amplitude of the Focsani Depression has intrigued for a long time (Royden and Karner, 1984; Waschbusch and Royden, 1992; Royden, 1993; Artyushkov et al., 1996), because such a deep basin could not have resulted from the accretion of the Carpathians alone and their loading on the subducting plate. The Focsani Depression was created over time by the rollback of the European slab and its steepening once the rollback was halted. The cumulative effect of slab pull, mantle dynamics, and loading by the Southeast Carpathians thickens crust led to the creation of the Focsani Depression (see Chapter I, section 4; Wortel and Spakman, 2000; Cloetingh et al., 2004; Göğüş et al., 2016; Şengül-Uluocak et al., 2019).

Periods of major sediment accumulation in the Focsani Depression indicate that during the Badenian and Pontian, subsidence/sedimentation rates were the highest (see section 2.2). The Romanian foreland basin was deepening during Badenian as recorded by the sediment facies (see Chapter I; Krezsek and Olariu, 2021) but kept nearly the same shallow water depth during the Pontian. The sedimentation rates in the Focsani Depression in the Pontian could reflect the subsidence of the foreland basin, while Badenian sedimentation rates reflect the accumulation of material in the foredeep. The Bessarabian consists of prograding marine to coastal sediments with clinoforms in the northern edge of the Focsani

Depression, indicating a southward (toward the centre of the Focsani Depression) advancing sediment transport system. Sedimentation at this age may have been enhanced by the large accommodation space already present in the region.

References

Andreyeva-Grigorovich, A. S.: New data on the stratigraphy of the folded Miocene Zone at the front of the Ukrainian Outer Carpathians, 36, 2008.

Artyushkov, E. V., Baer, M. A., and Mörner, N.-A.: The East Carpathians: Indications of phase transitions, lithospheric failure and decoupled evolution of thrust belt and its foreland, Tectonophysics, 262, 101–132, https://doi.org/10.1016/0040-1951(95)00207-3, 1996.

Chuhan, F. A., Kjeldstad, A., Bjùrlykke, K., and Hùeg, K.: Porosity loss in sand by grain crushingÐexperimental evidence and relevance to reservoir quality, Marine and Petroleum Geology, 2002.

Cloetingh, S. A. P. L., Burov, E., Matenco, L., Toussaint, G., Bertotti, G., Andriessen, P. A. M., Wortel, M. J. R., and Spakman, W.: Thermo-mechanical controls on the mode of continental collision in the SE Carpathians (Romania), Earth and Planetary Science Letters, 218, 57–76, https://doi.org/10.1016/S0012-821X(03)00645-9, 2004.

Dziadzio, P. S., Borys, Z., Kuk, S., Masłowski, E., Probulski, J., Pietrusiak, M., Górka, A., Moryc, J., Baszkiewicz, A., Karnkowski, P., Karnkowski, P. H., and Pietrusiak, M.: Hydrocarbon Resources of the Polish Outer Carpathians—Reservoir Parameters, Trap Types, and Selected Hydrocarbon Fields: A Stratigraphic Review, in: The Carpathians and Their Foreland: Geology and Hydrocarbon Researces: AAPG Memoir 84, edited by: Golonka, J. and Picha, F. J., The American Association of Petroleum Geologists, Tulsa, Oklahoma, U.S.A., 259–291, https://doi.org/10.1306/985611M843071, 2006.

Göğüş, O. H., Pysklywec, R. N., and Faccenna, C.: Postcollisional lithospheric evolution of the Southeast Carpathians: Comparison of geodynamical models and observations, Tectonics, 35, 1205–1224, https://doi.org/10.1002/2015TC004096, 2016.

Guillaume, B., Husson, L., Funiciello, F., and Faccenna, C.: The dynamics of laterally variable subductions: laboratory models applied to the Hellenides, Solid Earth, 4, 179–200, https://doi.org/10.5194/se-4-179-2013, 2013.

van der Hoeven, A. G. A., Mocanu, V., Spakman, W., Nutto, M., Nuckelt, A., Matenco, L., Munteanu, L., Marcu, C., and Ambrosius, B. A. C.: Observation of present-day tectonic motions in the Southeastern Carpathians: Results of the ISES/CRC-461 GPS measurements, Earth and Planetary Science Letters, 239, 177–184, https://doi.org/10.1016/j.epsl.2005.09.018, 2005.

Husson, L.: Dynamic topography above retreating subduction zones, Geol, 34, 741, https://doi.org/10.1130/G22436.1, 2006.

Husson, L., Guillaume, B., Funiciello, F., Faccenna, C., and Royden, L. H.: Unraveling topography around subduction zones from laboratory models, Tectonophysics, 526–529, 5–15, https://doi.org/10.1016/j.tecto.2011.09.001, 2012.

Husson, L., Bernet, M., Guillot, S., Huyghe, P., Mugnier, J.-L., Replumaz, A., Robert, X., and Van der Beek, P.: Dynamic ups and downs of the Himalaya, Geology, 42, 839–842, https://doi.org/10.1130/G36049.1, 2014.

Janik, T., Starostenko, V., Aleksandrowski, P., Yegorova, T., Czuba, W., Środa, P., Murovskaya, A., Zayats, K., Mechie, J., Kolomiyets, K., Lysynchuk, D., Wójcik, D., Omelchenko, V., Legostaieva, O., Głuszyński, A., Tolkunov, A., Amashukeli, T., Gryn', D., and Chulkov, S.: Lithospheric Structure of the

East European Craton at the Transition from Sarmatia to Fennoscandia Interpreted from the TTZ-South Seismic Profile (SE Poland to Ukraine), Minerals, 12, 112, https://doi.org/10.3390/min12020112, 2022.

Kaban, M. K., Chen, B., Tesauro, M., Petrunin, A. G., El Khrepy, S., and Al-Arifi, N.: Reconsidering Effective Elastic Thickness Estimates by Incorporating the Effect of Sediments: A Case Study for Europe, Geophys. Res. Lett., 45, 9523–9532, https://doi.org/10.1029/2018GL079732, 2018.

Krézsek, C. and Olariu, C.: Filling of sedimentary basins and the birth of large rivers: The lower Danube network in the Dacian Basin, Romania, Global and Planetary Change, 197, 103391, https://doi.org/10.1016/j.gloplacha.2020.103391, 2021.

Krijgsman, W., Stoica, M., Vasiliev, I., and Popov, V. V.: Rise and fall of the Paratethys Sea during the Messinian Salinity Crisis, Earth and Planetary Science Letters, 290, 183–191, https://doi.org/10.1016/j.epsl.2009.12.020, 2010.

Krzywiec, P.: Contrasting tectonic and sedimentary history of the central and eastern parts of the Polish Carpathian foredeep basin Ð results of seismic data interpretation, Marine and Petroleum Geology, 26, 2001a.

Krzywiec, P.: Contrasting tectonic and sedimentary history of the central and eastern parts of the Polish Carpathian foredeep basin Ð results of seismic data interpretation, Marine and Petroleum Geology, 26, 2001b.

Krzywiec, P., Gągała, Ł., Mazur, S., Słonka, Ł., Kufrasa, M., Malinowski, M., Pietsch, K., and Golonka, J.: Variscan deformation along the Teisseyre-Tornquist Zone in SE Poland: Thick-skinned structural inheritance or thin-skinned thrusting?, Tectonophysics, 718, 83–91, https://doi.org/10.1016/j.tecto.2017.06.008, 2017.

L. Royden (2), G. D. Karner (3): Flexure of Lithosphere Beneath Apennine and Carpathian Foredeep Basins: Evidence for an Insufficient Topographic Load, Bulletin, 68, https://doi.org/10.1306/AD461372-16F7-11D7-8645000102C1865D, 1984.

de Leeuw, A., Filipescu, S., Maţenco, L., Krijgsman, W., Kuiper, K., and Stoica, M.: Paleomagnetic and chronostratigraphic constraints on the Middle to Late Miocene evolution of the Transylvanian Basin (Romania): Implications for Central Paratethys stratigraphy and emplacement of the Tisza–Dacia plate, Global and Planetary Change, 103, 82–98, https://doi.org/10.1016/j.gloplacha.2012.04.008, 2013.

de Leeuw, A., Vincent, S. J., Matoshko, A., Matoshko, A., Stoica, M., and Nicoara, I.: Late Miocene sediment delivery from the axial drainage systemof the East Carpathian foreland basin to the Black Sea, Geology, https://doi.org/10.1130/G47318.1, 2020.

Leever, K. A., Bertotti, G., Zoetemeijer, R., Matenco, L., and Cloetingh, S. A. P. L.: The effects of a lateral variation in lithospheric strength on foredeep evolution: Implications for the East Carpathian foredeep, Tectonophysics, 421, 251–267, https://doi.org/10.1016/j.tecto.2006.04.020, 2006.

Leever, K. A., Matenco, L., Garcia-Castellanos, D., and Cloetingh, S. A. P. L.: The evolution of the Danube gateway between Central and Eastern Paratethys (SE Europe): Insight from numerical modelling of the causes and effects of connectivity between basins and its expression in the sedimentary record, Tectonophysics, 502, 175–195, https://doi.org/10.1016/j.tecto.2010.01.003, 2011.

Marcussen, Ø., Maast, T. E., Mondol, N. H., Jahren, J., and Bjørlykke, K.: Changes in physical properties of a reservoir sandstone as a function of burial depth – The Etive Formation, northern North Sea, Marine and Petroleum Geology, 27, 1725–1735, https://doi.org/10.1016/j.marpetgeo.2009.11.007, 2010.

Matenco, L., Munteanu, I., ter Borgh, M., Stanica, A., Tilita, M., Lericolais, G., Dinu, C., and Oaie, G.: The interplay between tectonics, sediment dynamics and gateways evolution in the Danube system from the Pannonian Basin to the western Black Sea, Science of The Total Environment, 543, 807–827, https://doi.org/10.1016/j.scitotenv.2015.10.081, 2016.

Matoshko, A., Matoshko, A., de Leeuw, A., and Stoica, M.: Facies analysis of the Balta Formation: Evidence for a large late Miocene fluvio-deltaic system in the East Carpathian Foreland, Sedimentary Geology, 343, 165–189, https://doi.org/10.1016/j.sedgeo.2016.08.004, 2016.

Matoshko, A., Matoshko, A., and de Leeuw, A.: The Plio–Pleistocene Demise of the East Carpathian Foreland Fluvial System and Arrival of the Paleo-Danube To The Black Sea, Geologica Carpathica, 70, 91–112, https://doi.org/10.2478/geoca-2019-0006, 2019.

Matoshko, A., de Leeuw, A., Stoica, M., Mandic, O., Vasiliev, I., Floroiu, A., and Krijgsman, W.: The Mio-Pliocene transition in the Dacian Basin (Eastern Paratethys): paleomagnetism, mollusks, microfauna and sedimentary facies of the Pontian regional stage, Geobios, S0016699523000244, https://doi.org/10.1016/j.geobios.2023.03.002, 2023.

Necea, D., Fielitz, W., Kadereit, A., Andriessen, P. A. M., and Dinu, C.: Middle Pleistocene to Holocene fluvial terrace development and uplift-driven valley incision in the SE Carpathians, Romania, Tectonophysics, 602, 332–354, https://doi.org/10.1016/j.tecto.2013.02.039, 2013.

Oszczypko, N.: Late Jurassic-Miocene evolution of the Outer Carpathian fold-and-thrust belt and its foredeep basin (Western Carpathians, Poland), 25, 2006.

Oszczypko, N. and Oszczypko-Clowes, M.: Stages of development in the Polish Carpathian Foredeep basin, Open Geosciences, 4, https://doi.org/10.2478/s13533-011-0044-0, 2012.

Palcu, D. V., Patina, I. S., Şandric, I., Lazarev, S., Vasiliev, I., Stoica, M., and Krijgsman, W.: Late Miocene megalake regressions in Eurasia, Sci Rep, 11, 11471, https://doi.org/10.1038/s41598-021-91001-z, 2021.

Pharaoh, T. C.: Palaeozoic terranes and their lithospheric boundaries within the Trans-European Suture Zone (TESZ): a review, Tectonophysics, 314, 17–41, https://doi.org/10.1016/S0040-1951(99)00235-8, 1999.

Popov, S. V., Antipov, M. P., Zastrozhnov, A. S., Kurina, E. E., and Pinchuk, T. N.: Sea-level fluctuations on the northern shelf of the Eastern Paratethys in the Oligocene-Neogene, Stratigr. Geol. Correl., 18, 200–224, https://doi.org/10.1134/S0869593810020073, 2010.

Royden, L. H.: The tectonic expression slab pull at continental convergent boundaries, Tectonics, 12, 303–325, https://doi.org/10.1029/92TC02248, 1993.

Royden, L. H. and Husson, L.: Subduction with Variations in Slab Buoyancy: Models and Application to the Banda and Apennine Systems, in: Subduction Zone Geodynamics, edited by: Lallemand, S. and Funiciello, F., Springer Berlin Heidelberg, Berlin, Heidelberg, 35–45, https://doi.org/10.1007/978-3-540-87974-9_2, 2009.

Şengül-Uluocak, E., Pysklywec, R. N., Göğüş, O. H., and Ulugergerli, E. U.: Multidimensional Geodynamic Modeling in the Southeast Carpathians: Upper Mantle Flow-Induced Surface Topography Anomalies, Geochem. Geophys. Geosyst., 2019GC008277, https://doi.org/10.1029/2019GC008277, 2019.

Starostenko, V., Janik, T., Mocanu, V., Stephenson, R., Yegorova, T., Amashukeli, T., Czuba, W., Środa, P., Murovskaya, A., Kolomiyets, K., Lysynchuk, D., Okoń, J., Dragut, A., Omelchenko, V., Legostaieva, O., Gryn, D., Mechie, J., and Tolkunov, A.: RomUkrSeis: Seismic model of the crust and upper mantle across the Eastern Carpathians – From the Apuseni Mountains to the Ukrainian Shield, Tectonophysics, 794, 228620, https://doi.org/10.1016/j.tecto.2020.228620, 2020.

Stoica, M., Lazăr, I., Krijgsman, W., Vasiliev, I., Jipa, D., and Floroiu, A.: Paleoenvironmental evolution of the East Carpathian foredeep during the late Miocene–early Pliocene (Dacian Basin; Romania), Global and Planetary Change, 103, 135–148, https://doi.org/10.1016/j.gloplacha.2012.04.004, 2013.

Tărăpoancă, M., Bertotti, G., Maţenco, L., Dinu, C., and Cloetingh, S. A. P. L.: Architecture of the Focşani Depression: A 13 km deep basin in the Carpathians bend zone (Romania): ARCHITECTURE OF THE FOCŞANI DEPRESSION, Tectonics, 22, n/a-n/a, https://doi.org/10.1029/2002TC001486, 2003.

Waschbusch, P. J. and Royden, L. H.: Spatial and temporal evolution of foredeep basins: lateral strength variations and inelastic yielding in continental lithosphere, Basin Research, 4, 179–196, https://doi.org/10.1111/j.1365-2117.1992.tb00044.x, 1992.

Wortel, M. J. R. and Spakman, W.: Subduction and Slab Detachment in the Mediterranean-Carpathian Region, Science, 290, 1910–1917, https://doi.org/10.1126/science.290.5498.1910, 2000.

Chapter V: Co-evolution of the Carpathian fold-thrust belt and its foreland

This Chapter presents our conclusions from the study of the construction and exhumation of the Carpathian fold-thrust and the resulting sediment fluxes to the foreland. We summarize most important aspects of our exhumation model based on inversion of the low-temperature thermochronology database (Chapter III) and we discuss our approach to split the eroded flux from the belt to obtain the sediment flux supplied to the pro-foreland basin, i.e., the Carpathian foreland basin. We compare the pro-foreland sediment flux supplied from the belt with the sediment volumes calculated from the thickness maps we constructed in Chapter IV. Based on the comparison of sediment fluxes supplied by the mountain belt and the volume of sediment preserved in the Carpathian foreland basin, we discuss the source-to-sink system of the Carpathians from the middle Miocene to the Pleistocene. From the mass balance of the Carpathian system, we elaborate on the co-evolution of the belt and the foreland. We retrieve the routing of sediments from the belt to the foreland. Finally, we elaborate on the timing and amount of sediments exiting the Carpathian fold-thrust belt and foreland. We discuss the links between the slab detachment, the lower plate features, and the development of the Carpathian fold-thrust belt and foreland. We moreover try to decipher the impacts of the diachronicity of slab detachment and the lateral variation of the lower plate features on the development of the Carpathian fold-thrust belt and foreland.

1 Introduction

We here repeat the main conclusions regarding the accretion and exhumation of the fold-and-thrust belt and the development of the Carpathian foreland studied in the previous Chapters:

Contraction of the orogen, when perpendicular to the passive margin as observed in the Ukrainian part of the belt had the characteristics of a single-vergent wedge with in-sequence thrusting during most of the accretionary time. The accretion lasted from Cretaceous to late Oligocene – early Miocene. The exhumation initiated in the innermost nappes around 30-24 Ma. Exhumation progressively propagated towards the foreland. The last major pulse of exhumation started at 12 Ma coincident with the end of foreland propagation of faulting. At this time, out-of-sequence thrusting in the inner nappes of the wedge (in Dukla nappe) also created duplexes that thickened the wedge. Accretion-collision in the Outer Carpathian belt brought the sediments of the nappes to the depth of the AFT thermochronometer reset zone, i.e., 120°C or 4-5 km, in most cases. The ZHe thermochronometer was not reset by accretion, allowing us to distinguish the provenance of sediments from different nappes through their pre-orogenic ZHe ages. The main sources identified are the sedimentary cover of the Inner Carpathian nappes, the intra-basinal ridges and the East European Platform. From the reconstruction of the accretion of the wedge, using time-depth diagrams (Chapter II), we approximated the ageonset of sediment discharge into the Carpathians foreland basin (CFB) from the Ukrainian wedge at ~12 Ma.

We developed an exhumation model of the Carpathian belt from 34 Ma to the present through inversion of a comprehensive low-temperature thermochronology database (Chapter III). We obtained exhumation rates for twelve tectonic units across three regions of the Carpathians: The Western Carpathians (WC), the North-eastern Carpathians (NEC) and the Eastern and South-eastern Carpathians (E-SEC). We compared the result of our model with previous studies establishing exhumation and/or erosion rates over the Carpathians and overall good agreement with the inversion model is found for the Western and the North-eastern Carpathians. The Eastern and South-eastern region shows some differences with previously published studies: 1) the onset of exhumation of the Tarcau nappe is later (Figure III.15) and 2) average exhumation rates and cumulative exhumation are lower. The reason is that we grouped thermochronological ages from the Romanian Carpathians to have sufficient data to constrain the inversion in the Eastern and South-eastern Carpathian region. The exhumation history of the Southeast Carpathians is to some degree imposed on the Romanian East Carpathians. Despite this minor discrepancy in the southeast, our exhumation model highlights the diachronous exhumation of the Carpathian belt since the Late Oligocene. Exhumation rates peaked in the Western Carpathians between 24 and 12.8 Ma. The most rapid exhumation took place from 18-8.6 Ma in the North-eastern Carpathian region, and around 8.6-0 Ma for the Eastern and South-eastern Carpathians. The observed diachronicity in peak exhumation can be linked with the lateral variation in the onset of collision with the East-European Platform.

The CFB developed in the middle Miocene, progressively expanded east and southeast-wards, and was gradually filled in by an axial sediment transport system during the Late Miocene (de Leeuw et al., 2020). At present, the former basin is being incised by rivers, except in the Focsani Depression, where subsidence continues. By combining geological maps, cross-sections and well data in a geomodelling package (PetEx MOVE), the foreland sedimentary system was modelled in 3D. Sediment thickness maps

extracted from this model allowed us to analyse the spatial distribution of sediments from the middle Miocene to the Pleistocene (16 Ma – 12 Ka). We identified several depocenters in the CFB during its development. The principal one is the Focsani Depression, whose evolution through time indicates a strong influence of lower plate inheritance and slab dynamics on the foreland sedimentary system (Chapter IV).

2 Estimation of eroded and deposited sediment volumes.

The following section describes the methods used to calculate the sediment volumes eroded from the Carpathian belt and the volumes of sediment preserved in the Carpathian foreland basin. We use the inversion model presented in Chapter III of this manuscript to estimate eroded sediment volumes. The volumes of the sediments preserved in the foreland are calculated using the sediment thickness maps of each stratigraphic stage generated in Chapter IV. We also assess the proportion of carbonate sediments in the Carpathian foreland basin; these need to be left out of the source-sink comparison since they do not derive from erosion of the belt.

2.1 Exhumation rates to erosion rates

From the exhumation model of the Carpathian fold-and-thrust belt, we aim to obtain an estimate of the volume of exhumed (and eroded) rocks during accretion and collision. Previously, we asserted that the Carpathians are a primarily mono-vergent orogenic wedge, with accretion and uplift occurring by stacking of sedimentary thrust-sheets (Chapter II and III; references therein). The principal driver of exhumation of rock material in orogenic wedges is erosion (Dahlen and Suppe, 1988). We obtained exhumation rates assuming a constant (present-day) topography of the belt. During collision of the wedge with the East-European Platform, the maximum topography was probably higher than at present. We constrain exhumation rates assuming vertical rock-particle paths within the orogenic wedge (see Chapter III, section 2). Exhumation rates are the vertical motion of rock material relative to the surface. The assumption of constant topography directly links the exhumation rate to erosion, i.e. on a period time (time step) particles exhumed are eroded at the surface to maintain a stable topography. Therefore, we assumed that in the Carpathians fold-and-thrust belt, the exhumation rates we calculated over a period of time can be directly used as erosion rates.

	Nappe	Surface (km²)	Volume (km³) exhumed per time step (Ma)								Total per nappe (km³)
			34-24	**24-18**	**18-16**	**16-12.8**	**12.8-8.6**	**8.6-6.1**	**6.1-1.8**	**1.8-0**	
Western Carpathian	Tatra	8 492	14 437	28 025	9 342	11 414	7 490	4 458	7 669	3 210	86 044
	North Meliata	10 570	0	52 005	17 335	31 119	17 758	10 570	2 273	951	132 011
	Magura-Valais	7 467	0	4 480	4 928	7 885	27 598	6 720	11 559	4 839	68 009
	Silesian	10 225	0	37 424	11 043	17 669	12 454	4 346	7 475	3 129	93 539
North-eastern Carpathian	Bucovinian	12 743	7 646	4 587	21 662	34 660	36 928	21 981	1 644	688	129 795
	Magura-Valais	2 919	0	0	3 619	5 791	7 968	5 691	2 761	1 156	26 986
	Krosno	9 578	0	0	13 985	9 502	20 115	11 973	15 651	6 552	66 264
	Skyba	9 623	0	0	2 502	23 096	10 913	6 496	3 310	1 386	47 703
Eastern and South-eastern Carpathian	Bucovinian	8 255	29 717	495	165	264	347	206	355	149	31 698
	Ceahlau-Severin and Audia-Macla	6 671	0	9 206	3 069	854	1 121	14 510	2 869	1 201	32 830
	Tarcau	6 578	0	395	132	210	276	164	20 931	8 762	30 870
	Subcarpathian	9 854	0	0	0	0	0	0	17 373	1 596	18 969
Total for the belt (km³)			51 800	136 618	84 333	147 674	130 094	84 962	95 104	34 135	764 719

Table V.1: Volumes of exhumed/eroded rocks from the Carpathian fold-thrust belt.

2.2 Sediment fluxes from the belt

We obtained the volume of material eroded from each tectonic unit during a certain time period by multiplying the area of the tectonic unit by its exhumation (erosion) rate during this time step and by the duration of the time step. The estimated sediment volumes eroded over time (Table V.1) can be summed to arrive at cumulative eroded volumes for any region of interest, or for the entire belt.

Figure V.1 shows the eroded sediment flux over time for the Western Carpathians, North-eastern Carpathians and Eastern and South-eastern Carpathians, as well as for the entire Carpathian fold-thrust belt. The peak sediment fluxes follow the pattern described in Chapter III (section 3). Marked erosion started in the Western Carpathians in the late Oligocene. Sediment fluxes from this region increased to a peak of ~22.500 km³/My from 22 to 14 Ma, after which the sediment flux decreased ~5.000 km³/My in the Pliocene-Pleistocene (<4 Ma), marking the end of tectonic activity in the region. Erosion in the North-eastern region started between ~18 and 7 Ma to reach a maximum eroded sediment flux of ~25.000 km³/My at 14 Ma. After that, eroded sediment fluxes decreased somewhat, to ~17.000 km³/My at 7 Ma, and then decreased more rapidly to ~5.000 km³/My at 4 Ma. Eroded sediment fluxes from the Eastern and South-eastern region were very low, not exceeding 5.000 km³/My until ~7 Ma, when erosion of the Tarcau and Sub-Carpathian nappes initiated (Table V.1 and Chapter III). Eroded sediment fluxes

from this region reached a peak at ~4-3 Ma with a flux of 10.000 km^3/My, after which sediment fluxes decreased to ~5.000 km^3/My at the present day (Figure V.1).

Cumulative sediment fluxes for the entire Carpathian belt display two peaks. The first occurs between 18 and 12 Ma, with a maximum flux of ~48.000 km^3/My at 14 Ma. The second peak reached an erosional flux of ~35.000 km^3/My at 7 Ma, and then decreaseddecreased to ~23.000 km^3/My at 4 Ma.

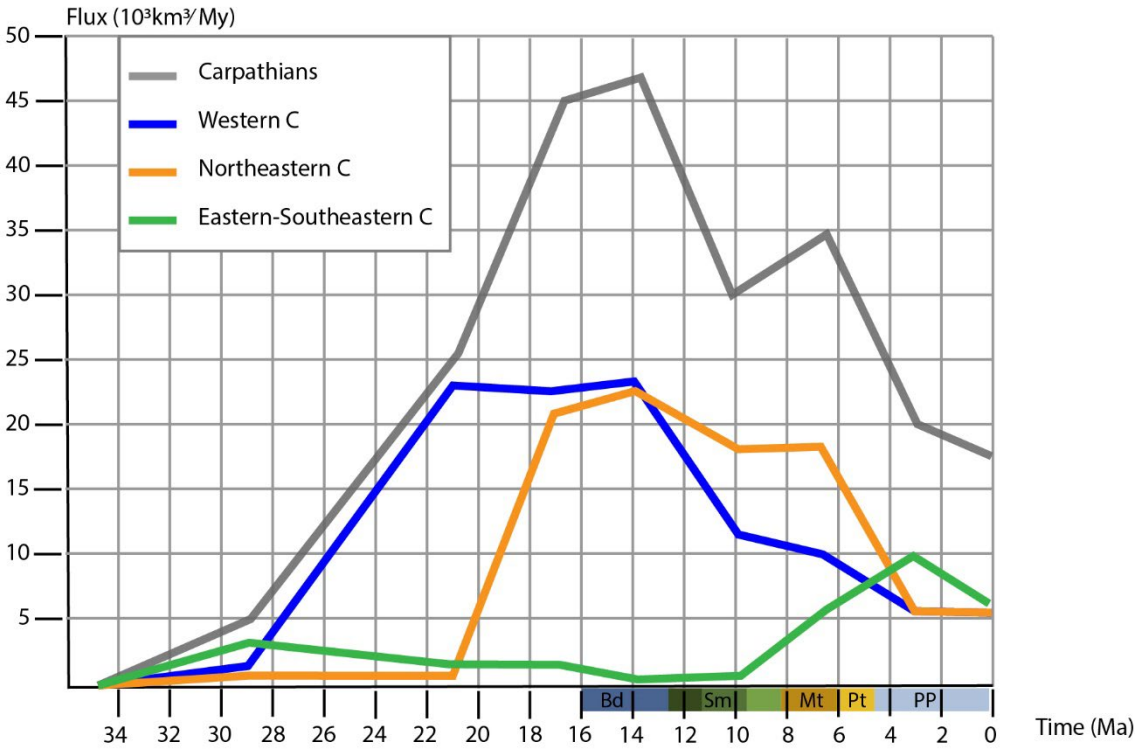

Figure V.1: Fluxes of sediment eroded from the Carpathian belt over time. The different coloured lines correspond to different parts of the mountain belt. The grey line represents the cumulative sediment flux from the entire belt. The coloured bars along the x-axis represent the stages of the foreland stratigraphy: Bd: Badenian; Sm: Sarmatian; Mt: Meotian; Pt: Pontian; PP: Plio-Pleistocene.

2.3 Sediment volumes in the Carpathian Foreland Basin (CFB)

2.3.1 Estimated volumes of sediments deposited in the pro-foreland basin

Sediment volumes deposited within the basin over time werewere calculated from the previously presented thickness maps (Chapter IV) using Qgis. The volumes were partitioned into three areas across the basin, the Northern, Central and Southern foreland (Figure V.2). The Northern foreland is situated in Poland. The Central Foreland is located in northwest Ukraine and the Southern foreland includes part of Romania, Moldova and southwest Ukraine (Figure V.2). Obtained sediment volumes are reported in Table V.2.

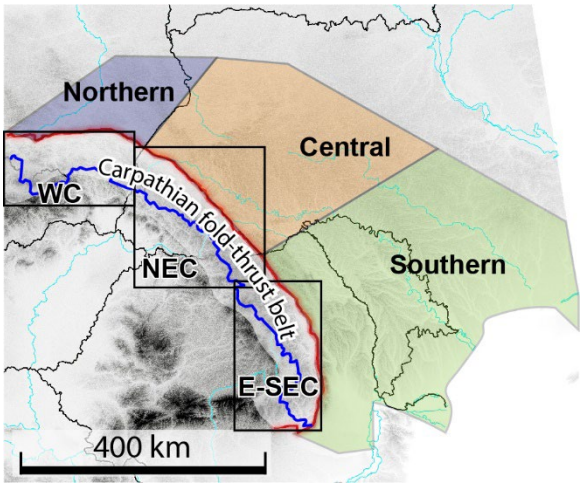

Figure V.2: Areas used for assessing CFB sediment volumes and areas of the exhumation model. Red line is the deformation front, blue line is the drainage divide of the Carpathians.

The record of sedimentation in the foreland does not go back as far as the erosion record because a large part of the former foreland was progressively overthrust by the advancing mountain belt or incorporated into it. As explained in Chapter IV, deposition in the present-day foreland started in the Badenian, (~16 Ma), for which there is an incomplete record due to continued convergence afterwards. The highest cumulative depositional fluxes to the foreland occurred in the Volhynian, at ~30.500 km^3/My, with relatively similar sediment volumes in the Northern and Southern forelands. Subsequently, during the Bessarabian and Kersonian stages, the cumulative depositional fluxes to the Carpathian foreland basin were ~12.000 km^3/My, but without any preserved sediments in the Northern foreland (Table V.2). In comparisoncomparison with the preceding stages, more sediments were retained in the Southern foreland. During the Meotian and Pontian stages, sediments were deposited only in the Southern foreland and cumulative depositional fluxes were around 9.000 km^3/My. The sediment flux to the Southern foreland is exceptionally high during the Plio-Pleistocene whereas the overall depositional flux in the CFB decreased to ~6.200 km^3/My (Table V.2). The latter may be linked to the cessation of tectonic activity in the Western and North-eastern Carpathian regions, and the resulting decrease in eroded sediment fluxes (Figure V.1). Note that the Central foreland received a few hundred km^3 of sediments during the Plio-Pleistocenesee, but these mostly constitute aeolian deposit and river terraces (see Chapter IV, sections 2 and 4 for a description and discussion of sediment distribution in the foreland basin).

STAGES (MA)	VOLUME (KM^3) Northern foreland	Central foreland	Southern foreland	Total CFB	Flux of sediment (km^3/My)
BADENIAN (16-12.65)	1 320	3 817	20 461	25 598	7 641
VOLHYNIAN (12.65-11.6)	11 982	3 625	16 395	32 001	30 477
BESSARABIAN (11.6-9.6)	0	796	23 258	24 054	12 027
KERSONIAN (9.6-8.37)	0	11	14 905	14 917	12 127
MEOTIAN (8.37-6.1)	0	11	18 986	18 997	8 369
PONTIAN (6.1-4.7)	0	0	13 018	13 018	9 299
PLIO-PLEISTOCENE (4.7-0.0117)	0	518	28 674	29 192	6 227
TOTAL	13 302	8 779	135 697	157 778	9 861

Table V.2: Volume of sediment present in the Carpathian foreland basin (km^3), per stage and per region. The column on the far right shows the total flux of sediment (km3/my) to the cfb over time.

2.3.2 Carbonate sediments in the Carpathian Foreland Basin

As indicated on maps of the Carpathian foreland basin (Chapter I Figure I.15), some sedimentary strata of the foreland contain carbonaceous sediments: a mixed carbonate-siliciclastic facies is often present along the distal margin of the basin (Figure I.16). We estimated the volume percentage of siliciclastic-carbonate sedimentary facies in the basin from facies and thickness maps for each stratigraphic stage (Figure V.3). For most stages, less than 10% of the total sediment volume is composed of the mixed siliciclastic-carbonate facies. Only the sediments of the Bessarabian sub-stage contain ~17% siliciclastic-carbonate sedimentary facies. Considering, in addition, that these mixed facies contain only up to 50% carbonate, primarily derived from molluscs, and an equal or even larger proportion of siliciclastic grains, we decided to neglect these carbonates in our volumetric analysis of the Carpathian foreland basin for now (but see section 4.3).

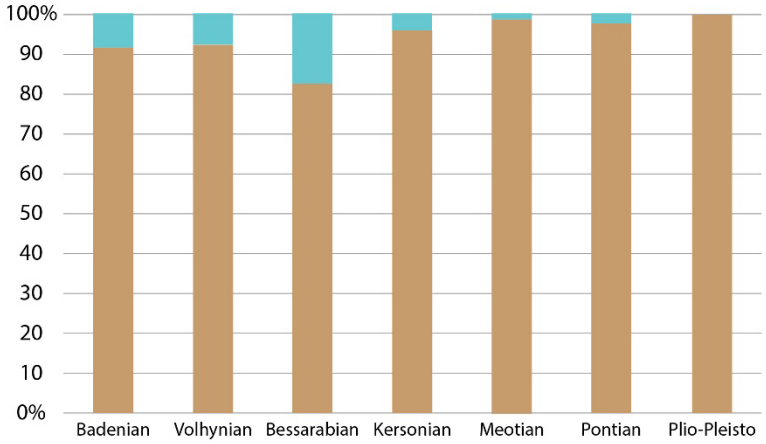

Figure V.3: Proportion of siliciclastic-carbonate sediments compared to siliciclastic sediment per time period in the CFB (data from Matoshko et al., in prep).

3 DistributionDistribution of eroded sediment fluxes

The fluxes of sediments eroded from the Carpathian belt were delivered to different areas: sediments were transported both to the pro- and the retro-forelands (Sanders et al., 2002; Krézsek and Bally, 2006; de Leeuw et al., 2013; Matenco et al., 2016). We also have to account for the amount of material deposited in the foreland basin, but re-integrated in the wedge by forward propagation of deformation. To compare the eroded sediment fluxes supplied by the Carpathian belt to the volume of sediment preserved in the Carpathian foreland basin, we separated the eroded sediment fluxes into three different fluxes. We distinguished between sediments supplied to the pro- and retro- foreland, and sub-divided the sediments supplied to the pro-foreland in sediments reintegrated into the belt by accretion (Covey, 1986; Schlunegger et al., 1997; see Chapter I section 1.5) and those deposited in the current foreland basin. Hereafter, we describe how we proceeded to obtain the fluxes of eroded sediment to the pro-foreland.

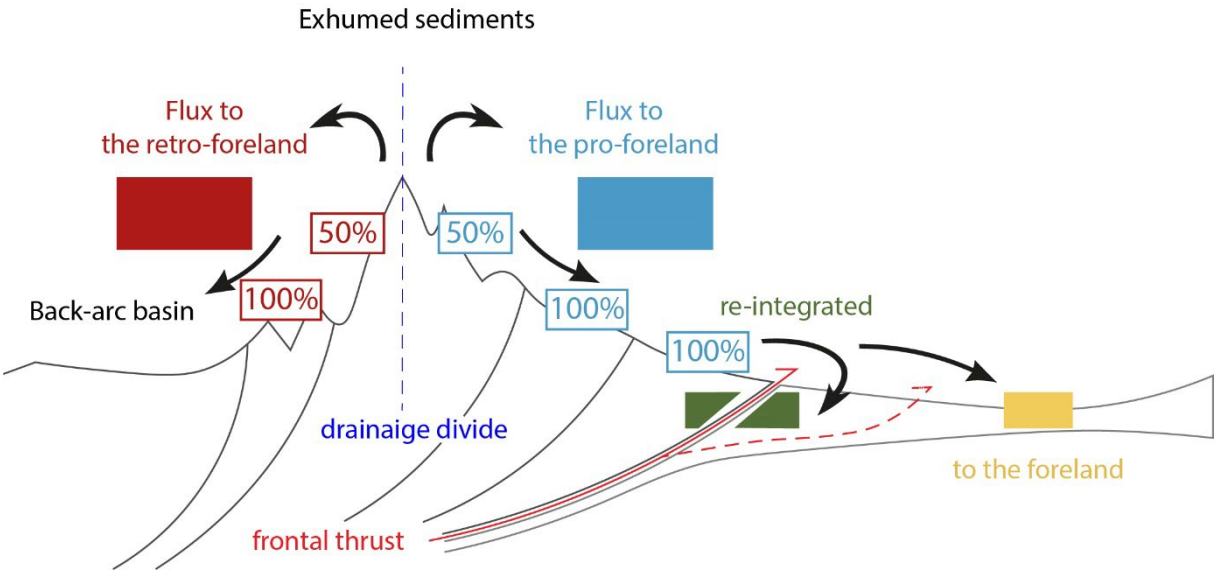

Figure V.4: Apportionment of eroded sediment flux. Sediment eroded from the tectonic unit containing the main drainage divide is divided in half between the pro-foreland and the retro-foreland. Tectonic units on the pro-side supply the pro-foreland, whereas units on the retro-side supply the retro-foreland. The main drainage divide can migrate during the following time step if the tectonic unit with the highest exhumation rates changes. Sediment fluxes supplied to the pro-foreland are differentiated between sediments re-integrated into the wedge by foreland cannibalism (Covey, 1986) and sediment preserved in the foreland. Modified after Figure I.5.

3.1 Sediment routing to the pro-foreland/retro-foreland

In our interpretation of the apportionment of the eroded sediment fluxes, we assumed that these are divided between fluxes to the pro- and to the retro-foreland basin at the drainage divide of the orogenic wedge. The divide migrates during advection of material (Willett et al., 2001). Migration of the drainage divide can, however, be affected by variations in erosion efficiency across the divide (Whipple et al., 2017; Schildgen et al., 2022), variations in rock erodibility and the location of active faults (Gailleton et

al., 2021; Scherler and Schwanghart, 2020). Since the latter factors are difficult to constrain for the Carpathian wedge in the past, we adopt a simple first-order approach and assumed that (1) the tectonic unit with the highest exhumation rate in a region during a time step contains the main drainage divide. The volume of eroded sediment from the nappe holding the main drainage divide is split in half between the sediment supplied to the pro- and to the retro-foreland (Figure V.4). (2) The position of the other tectonic units (in the same region, during the same time step) with respect to the drainage divide determines if they supply their eroded sediment to the pro- or retro-foreland (Figure V.4). (3) When the region reached a quiescent stage (i.e., when exhumation rates of all the tectonic units are lower than ~0.3 km/My, see Chapter III), the modern drainage divide of the Carpathian belt is used to separate the eroded volumes of sediment supplied to the pro- or retro-foreland.

We recognize some shortcomings in this procedure for dividing sediment fluxes: (1) the erodibility of various lithologies within the wedge can significantly affect the location of the drainage divide (Gailleton et al., 2021). However, based on the current location of the divide, it appears that the tectonic units with the highest recent exhumation rates, in each region, are those that hold the largest portion of the main drainage divide. (2) Intramountain basins permanently block sediment within. However, the volume of sediment retained by these basins is estimated to be low compared to the volume of exhumed sediment.

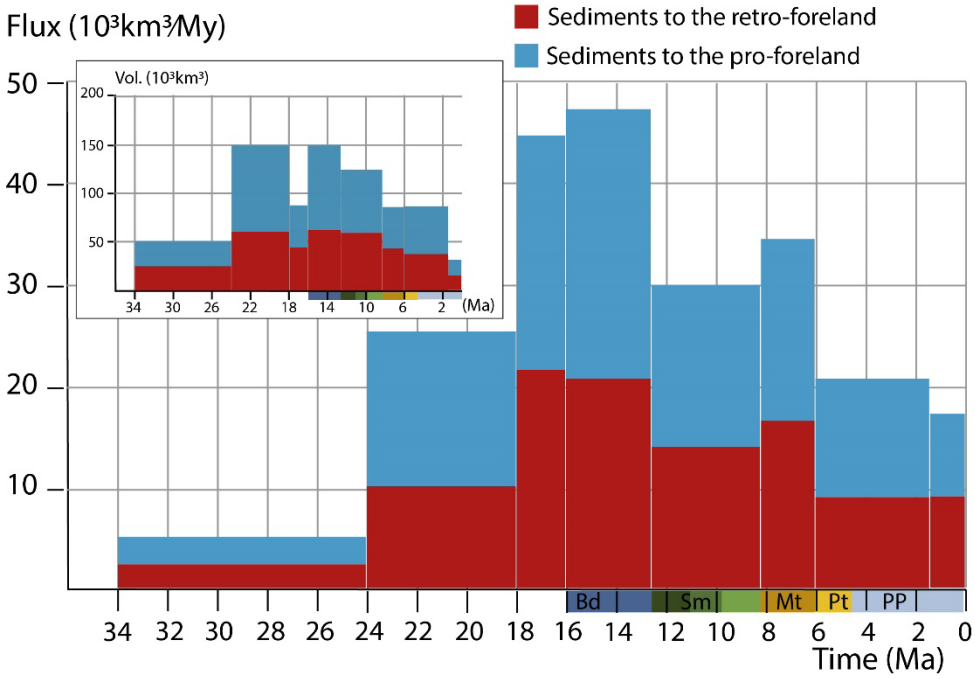

Figure V.5: Division of the eroded sediment fluxes from the Carpathian belt between sediments shed to the retro- and the pro-side of the wedge, respectively. The coloured bars along the x-axis represent the stages of the foreland stratigraphy: Bd: Badenian; Sm: Sarmatian; Mt: Meotian; Pt: Pontian; PP: Plio-Pleistocene.

3.2 Recycling of sediment into the wedge

When sediments are eroded from the wedge and deposited in the pro-foreland basin, they can subsequently be reintegrated during forward propagation of the wedge (Covey, 1986; Schlunegger et al.,

1997). The reintegration of sediment previously eroded from the wedge is referred to as sediment recycling (see Chapter I section 1.5). To compare only sediment delivered to the modern foreland, and not account twice the sediment recycled as sediment supplied to the foreland, we separated the volume of sediment delivered to the foreland and the sediment re-integrated into the wedge. We proceeded as follows:

Using the stratigraphy of the Carpathian belt nappes (Figure I.11), we estimated the average thickness of syn-orogenic sediments and multiplied it by the area of the paleo-basin. The width of the paleo-basin was estimated on the basis of restored cross-sections (Roure et al., 1993; Gągała et al., 2012; Castelluccio et al., 2016; Nakapelyukh et al., 2018). The length of the paleo-basin is expected to be comparable to the length of the current nappe since most of the deformation was by frontal accretion. We thus calculated the volume of syn-orogenic sediments reintegrated into the wedge. Most re-integration of sediments into the wedge occurred during the Oligocene and early Miocene (Chapter II, references therein). However, we focus below on the sediments recycled during the formation of the current pro-foreland (middle Miocene to present).

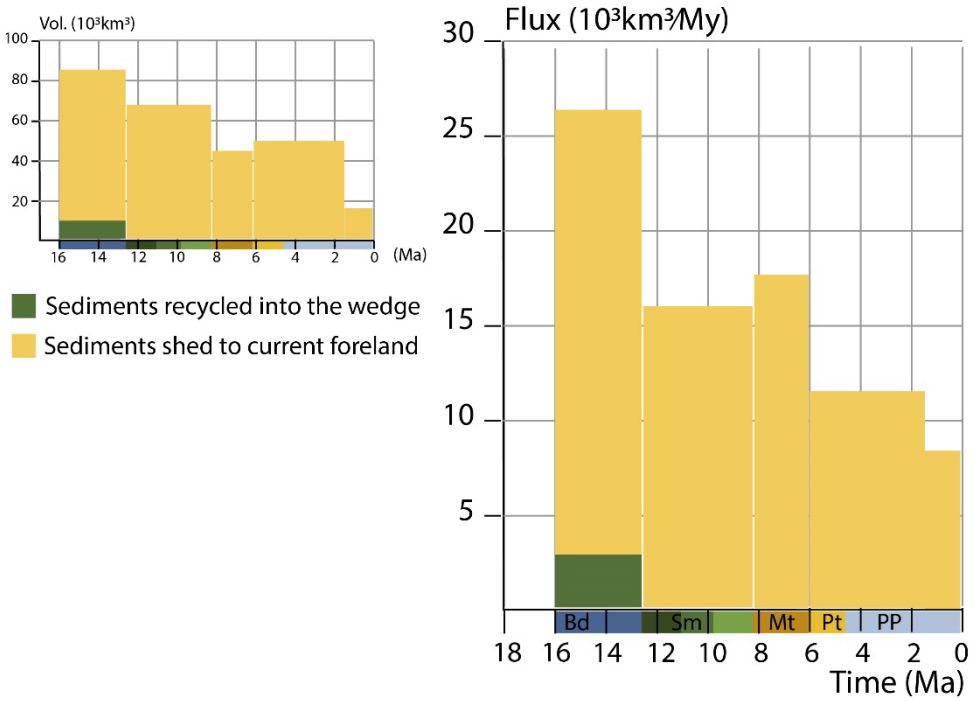

Figure V.6: Sediments volumes and fluxes shed to the pro-foreland, divided into sediment provided to the current foreland (yellow) and sediment "recycled" into the wedge (green). The coloured bar on the x-axis represents the stages of the foreland stratigraphy: Bd: Badenian; Sm: Sarmatian; Mt: Meotian; Pt: Pontian; PP: Plio-Pleistocene.

Since the middle Miocene, few sediments were recycled into the wedge (Figure V.6). Only significant amounts of Badenian sediments were re-integrated into the outermost nappes of the wedge, as well as in the stratigraphy of the Outer Carpathian Belt (Chapter I, Figure I.11 and references therein). Since the Badenian, reintegration of sediments into the wedge has been negligible, because foreland propagation of thrusting stopped along most of the Carpathian arc in the Sarmatian. In the South-eastern Carpathians, however, the Sub-Carpathian nappe contains Sarmatian sediments (Matenco and

Bertotti, 2000). Existing cross sections (e.g., Matenco et al., 2010) nevertheless indicate that the volume of these is very minor compared to the Sarmatian fill of the Focsani Depression.. The deposits of the Focsani Depression, which thus partially overlies the Subcarpathian Nappe, were accounted for as foreland deposits as indicated in Chapter IV. In our analysis we furthermore assume that Sarmatian and Meotian wedge-top sediments present in the East and Southeast Carpathians have a negligible volume.

4 Sediments fluxes from the belt to the foreland

In the following section we compare the fluxes or volumes of eroded and deposited sediments in the Carpathian region from the middle Miocene to present. We intend to trace the co-development of the belt and foreland basin through the identification of depocentres in the basin and erosion "hotspots" in the Carpathian belt. The inversion model of Carpathian exhumation and the sedimentation-rate maps of the foreland are combined for each stratigraphic stage. We then use the mass balance of the Carpathian system to constrain when sediment started to exit the Carpathian foreland and how much sediment has been removed from the system.

4.1 Comparison of eroded and deposited sediment volumes over time.

Figure V.7 shows the cumulative volume of material eroded from the Carpathian belt, and of each region (WC, NEC and E-SEC), together with the cumulative volume of sediment preserved in the Carpathian foreland basin, and in each foreland area (Northern, Central and Southern foreland), from 16 Ma to the present.

The volume of sediment eroded from the belt and supplied to the pro-foreland is higher than the volume of sediment contained in the foreland basin. The WC and NEC regions provided the highest, and similar, volumes of sediments from 16 to 6.1 Ma. Eroded volumes were high in the Badenian, when these regions delivered ~50,000 km^3 and ~30,000 km^3 of sediment, respectively. During the Sarmatian and Meotian, both regions delivered another approximately 50,000 km^3 of sediment. The sediment supply from both regions decreased after 6.1 Ma, with only ~15,000 km^3 of sediment delivered to the foreland during the Pontian and Plio-Pleistocene (Figure V.7). In contrast to the previous regions, the E-SEC region started supplying sediment to the pro-foreland basin during the Meotian. The region discharged ~40,000 km^3 of sediment during the Meotian, Pontian, and Plio-Pleistocene (Figure V.7).

In the Carpathian foreland basin, the Southern foreland area (Fig. V.2) accumulated the largest volume of sediments since 16 Ma (Figure V.7). The cumulative sediment volume of the Southern foreland suggests relatively low accumulation during the Badenian and Volhynian stages. However, sediment accumulation increased in the Bessarabian. The cumulative sediment volume of the Southern foreland then increased at a relatively constant rate until the Plio-Pleistocene (Figure V.7). The Northern and Central foreland areas show much less sediment accumulation than the Southern foreland. The Northern foreland accumulated ~13.000 km^3 of sediment in the Volhynian, after which the foreland received no other sediments from the belt. The Central foreland accumulated up to ~8.000 km^3 of sediment until the Bessarabian (Figure V.7). Note, however, that these figures do not take into account

any sediment that accumulated in the North and Central foreland after the Volhynian and Bessarabian, but that has been eroded since then due to basin inversion.

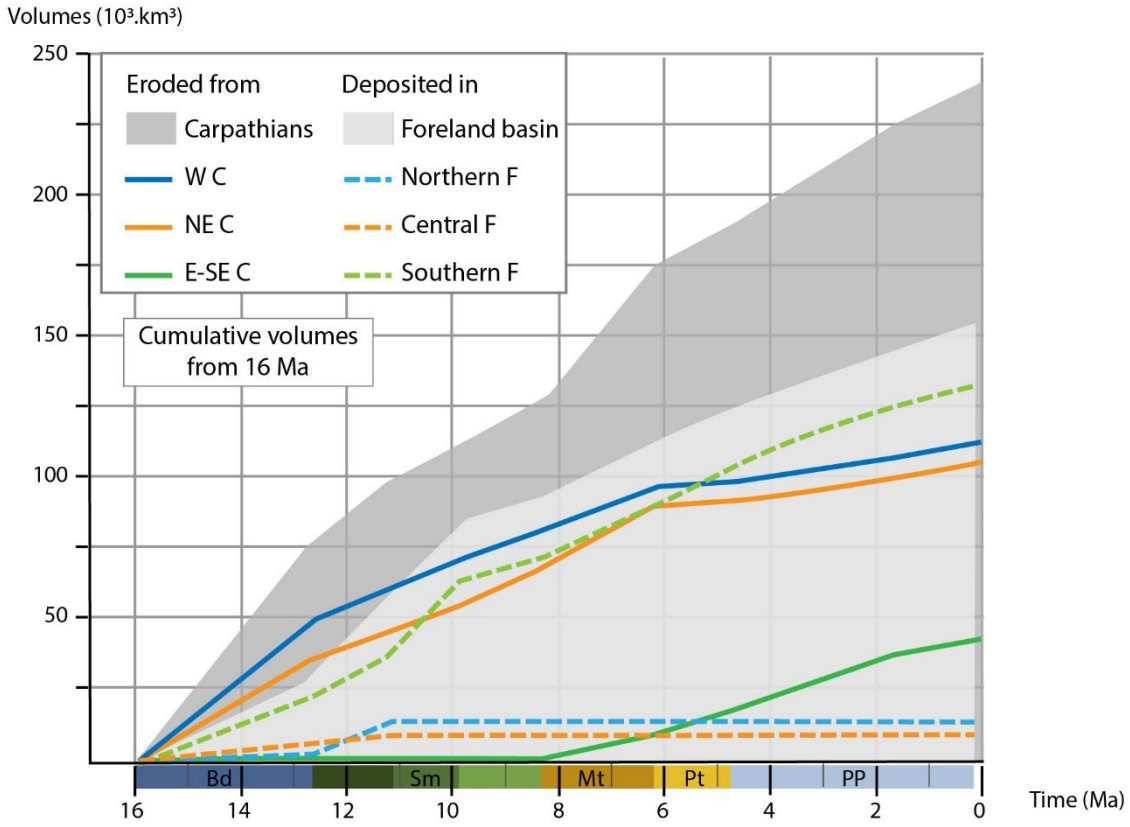

Figure V.7: Cumulative volumes of sediments eroded from the belt and deposited in the foreland basin according to the regions and foreland areas. Full lines and dark area refer to the volume of sediment eroded from the belt and transported to the pro-foreland. Dashed lines and light grey area refer to the volume of sediment deposited in the foreland. The colores bar on the x-axis represents the stages of the foreland stratigraphy: Bd: Badenian; Sm: Sarmatian; Mt: Meotian; Pt: Pontian; PP: Plio-Pleistocene.

The cumulative amounts of eroded and deposited sediments are offset, implying that, over the last 16 My, the Carpathian belt has provided ~80,000 km^3 of sediment that were not preserved in the foreland. The maximal difference between the volume of sediment supplied by the belt and the volume of sediment preserved in the foreland is seen in the Badenian, when the belt shed three times more sediment, at a rate of ~22.000 km^3/My, than the foreland retained. However, during this stage the thrust front was still active along the orogen and, therefore, a substantial amount of Badenian sediment is present beneath the mountain belt (see Chapters II and IV). We suggest that this missing sediment explains the divergence between eroded and deposited volumes in the Badenian despite of the closed nature of the source-sink system at this time, when paleogeographic reconstructions indicate that the Carpathians were surrounded by a shallow sea and there was no sediment transport to the Black Sea basin yet (Popov et al., 2004; Kováč et al., 2007; de Leeuw et al., 2020). Another pulse of divergence between cumulative volumes of erosion and deposition occurs in the Meotian. Given that post-Meotian shortening was very limited in the Carpathians, this latter divergence suggests that sediment was exported from the foreland basin (de Leeuw et al., 2020).

4.2 Sediment routing to the pro-foreland basin

We combined the exhumation rate and sedimentation rates maps, for the middle Miocene to present, resulting from our study (Figures V. 8-15). These maps allow identifying how the locus of exhumation in the belt and the main sediment depocenter in the pro-foreland basin shifted over time and if these shifts are coherent between the two. This source-to-sink analysis can also provide a qualitative notion of the routing of the sediments to the foreland. A quantitative comparison of sediment fluxes supplied by the belt and preserved in the foreland is shown in Figure V.16, where eroded and deposited sediment volumes are distinguished by region over the last 16 My.

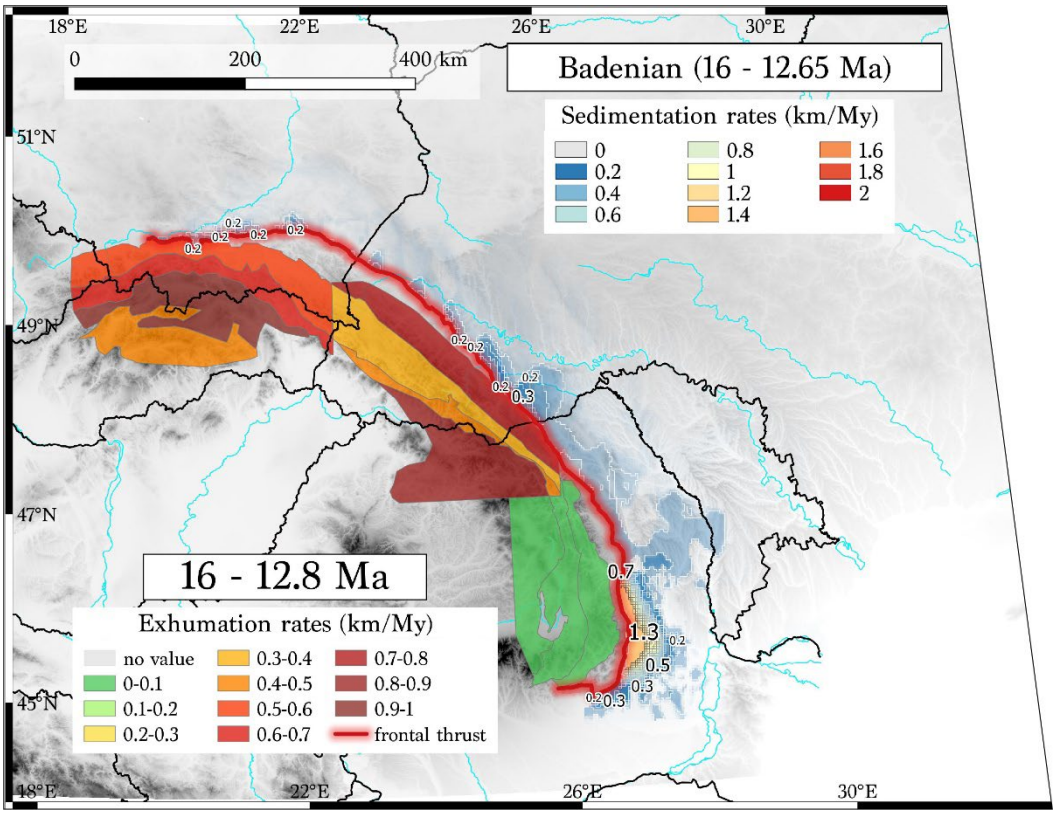

Figure V.8: Map of exhumation and sedimentation rates during the Badenian in the Carpathian system.

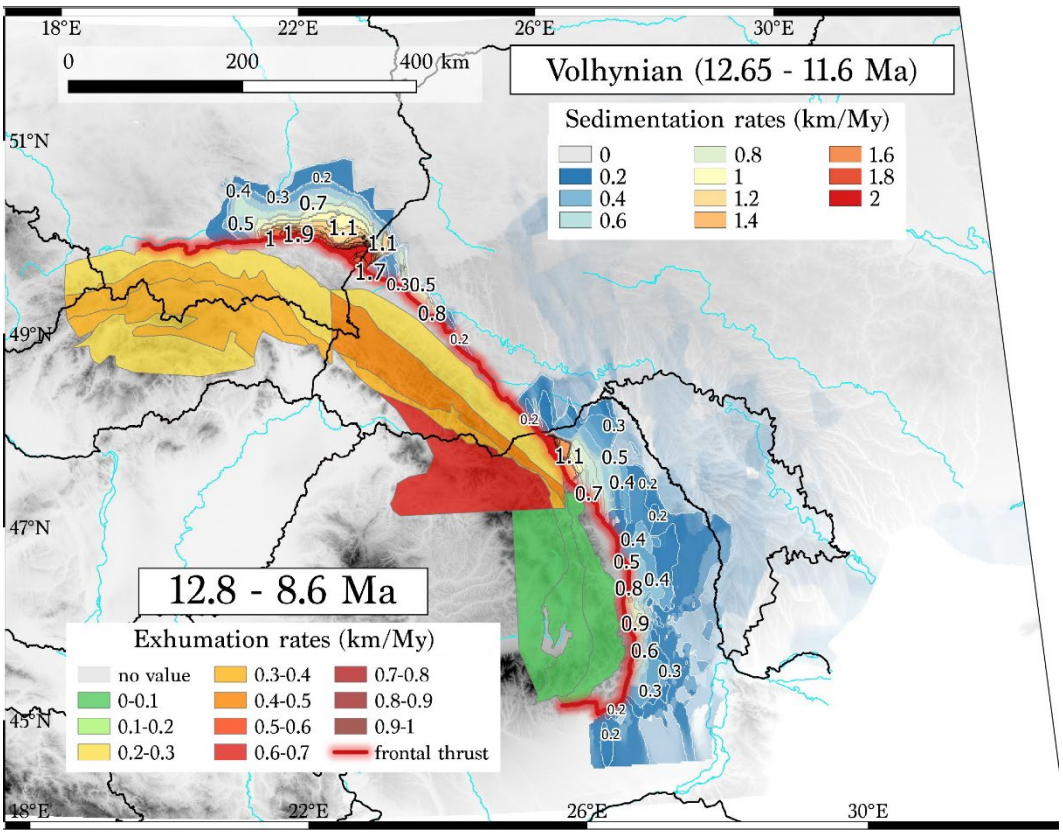

Figure V.9: Map of exhumation and sedimentation rates during the Volhynian in the Carpathian system.

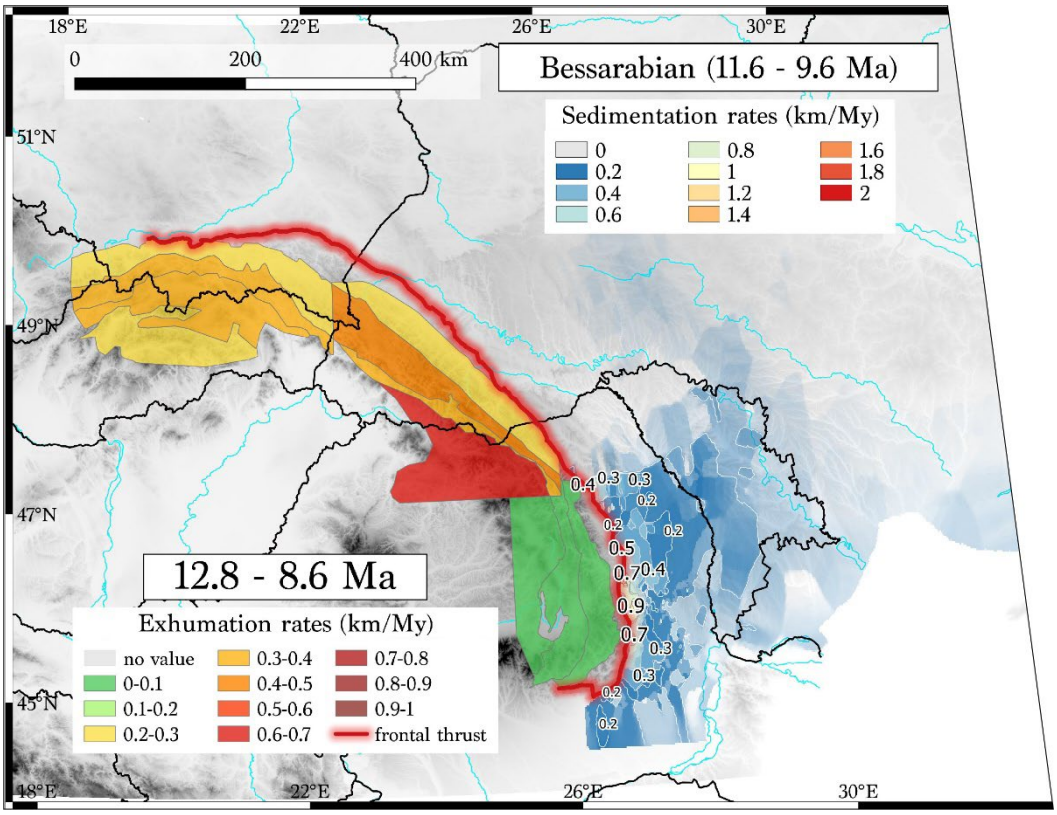

Figure V.10: Map of exhumation and sedimentation rates during the Bessarabian in the Carpathian system.

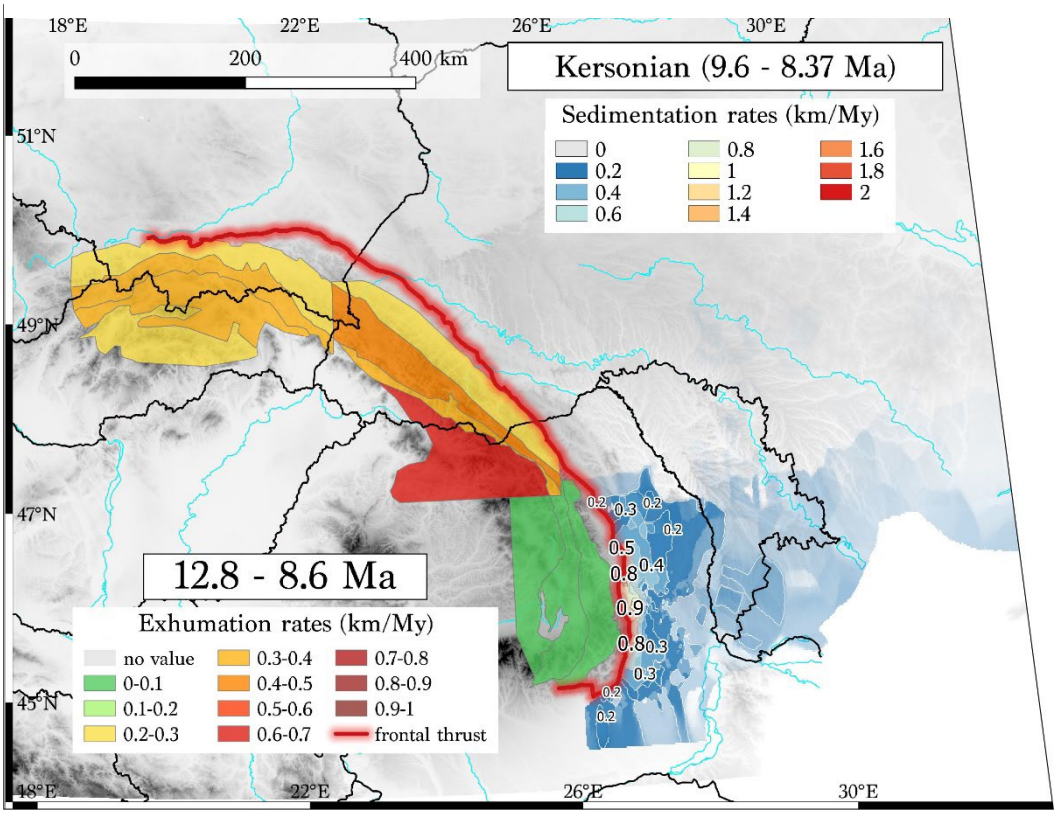

Figure V.11: Map of exhumation and sedimentation rates during the Kersonian in the Carpathian system.

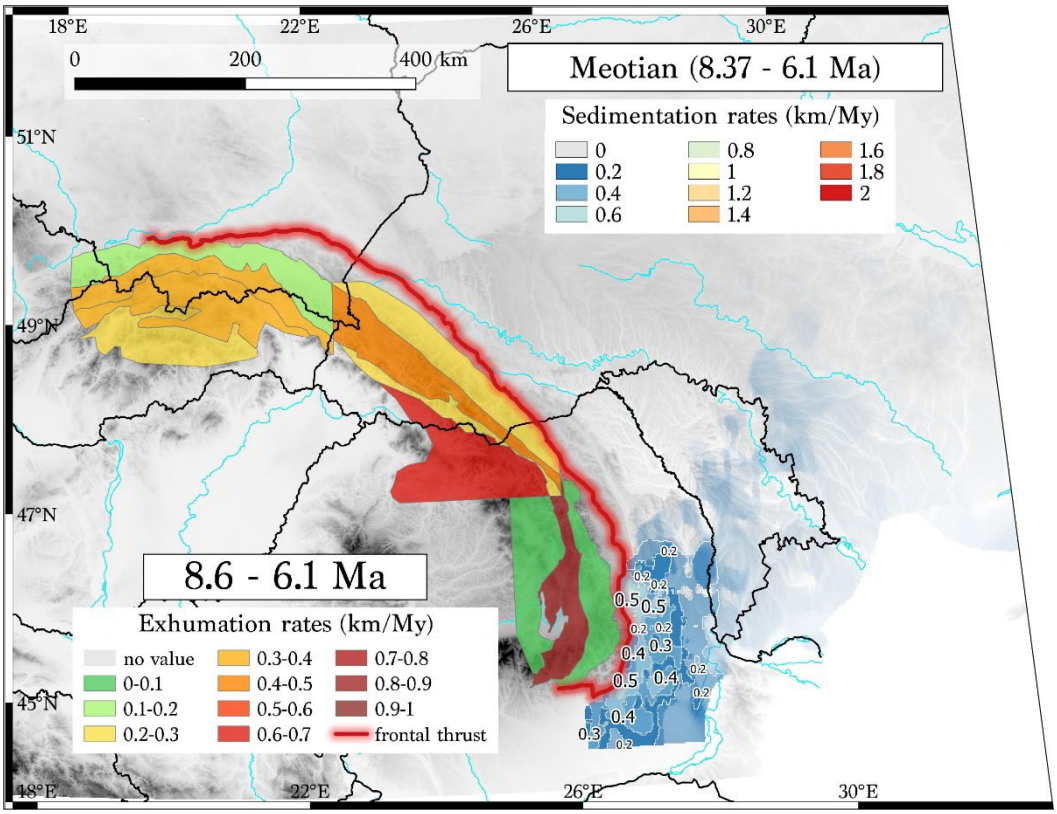

Figure V.12: Map of exhumation and sedimentation rates during the Meotian in the Carpathian system.

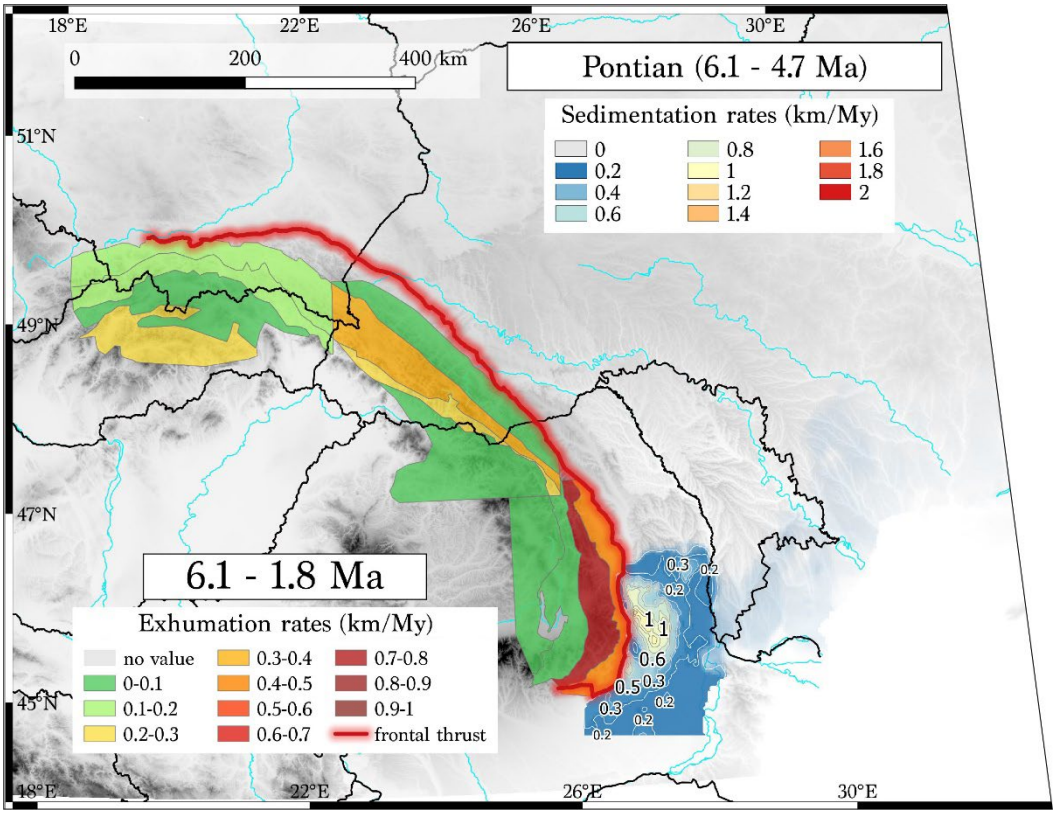

Figure V.13: Map of exhumation and sedimentation rates during the Pontian in the Carpathian system.

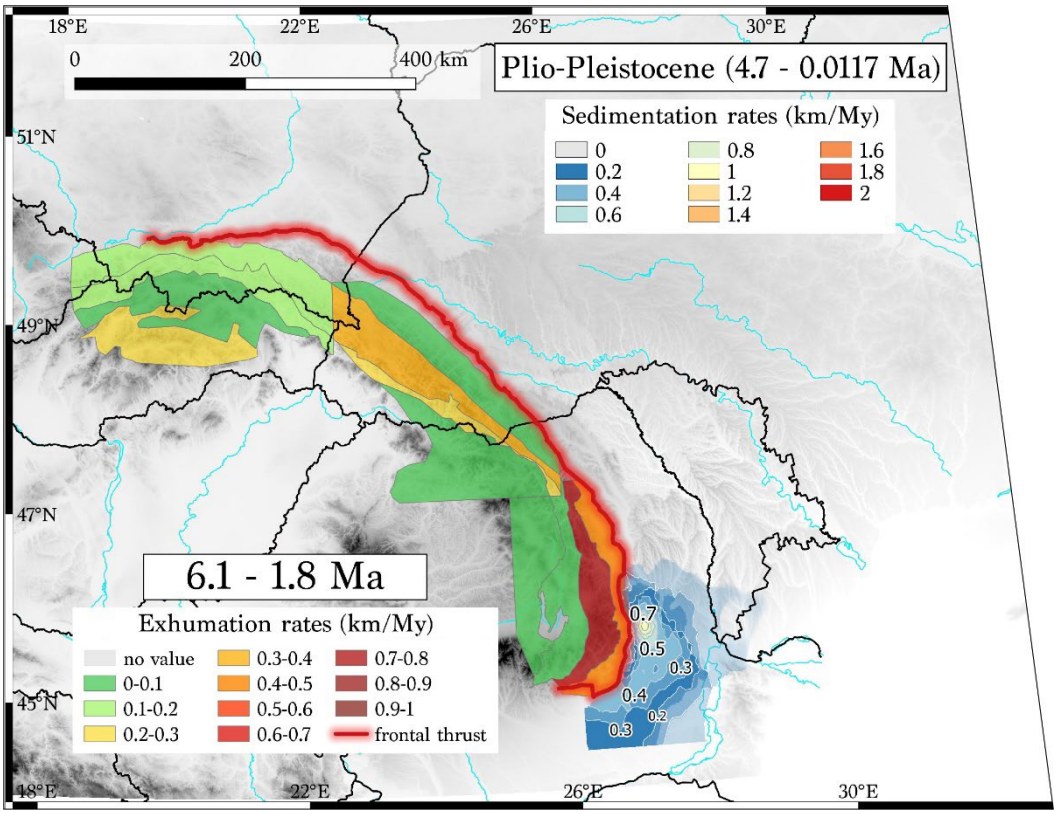

Figure V.14: Map of exhumation and sedimentation rates during the Plio-Pleistocene (until 1.8 Ma) in the Carpathian system.

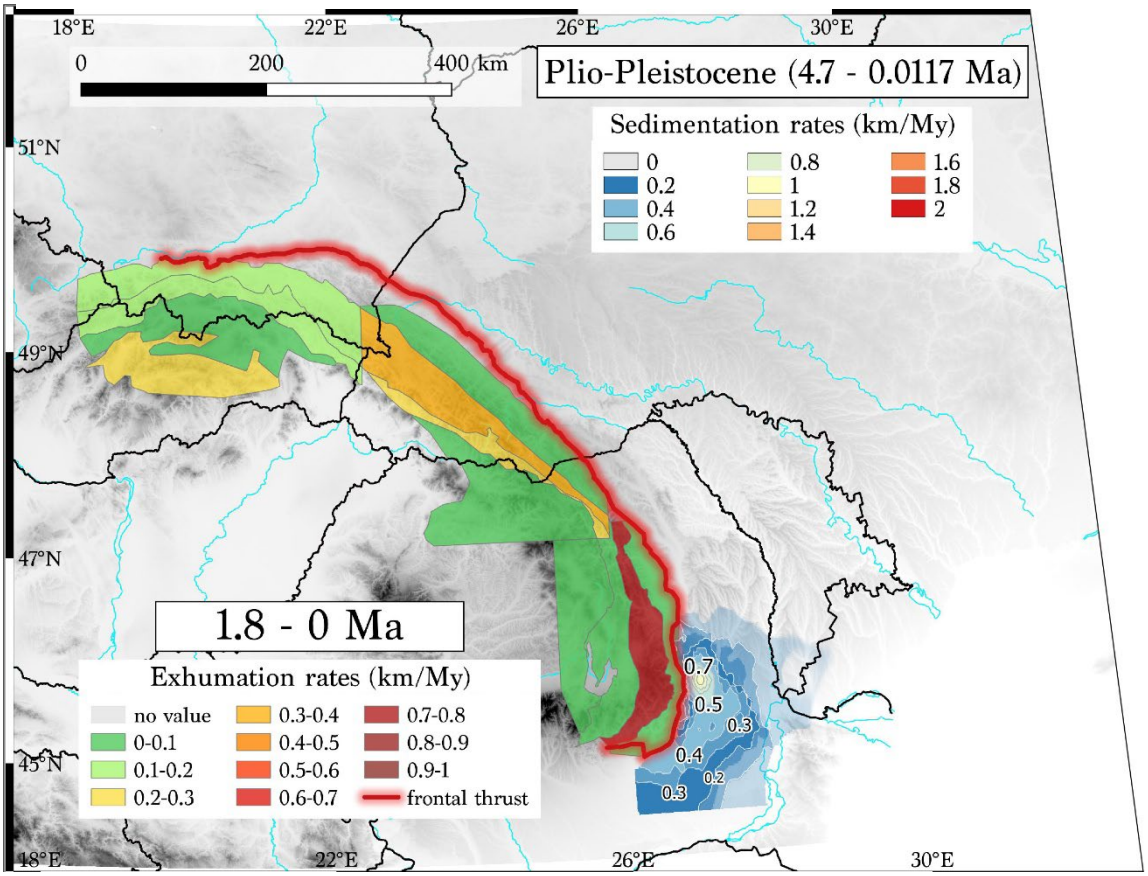

Figure V.15: Map of exhumation and sedimentation rates during the Plio-Pleistocene (since 1.8 Ma) in the Carpathian system.

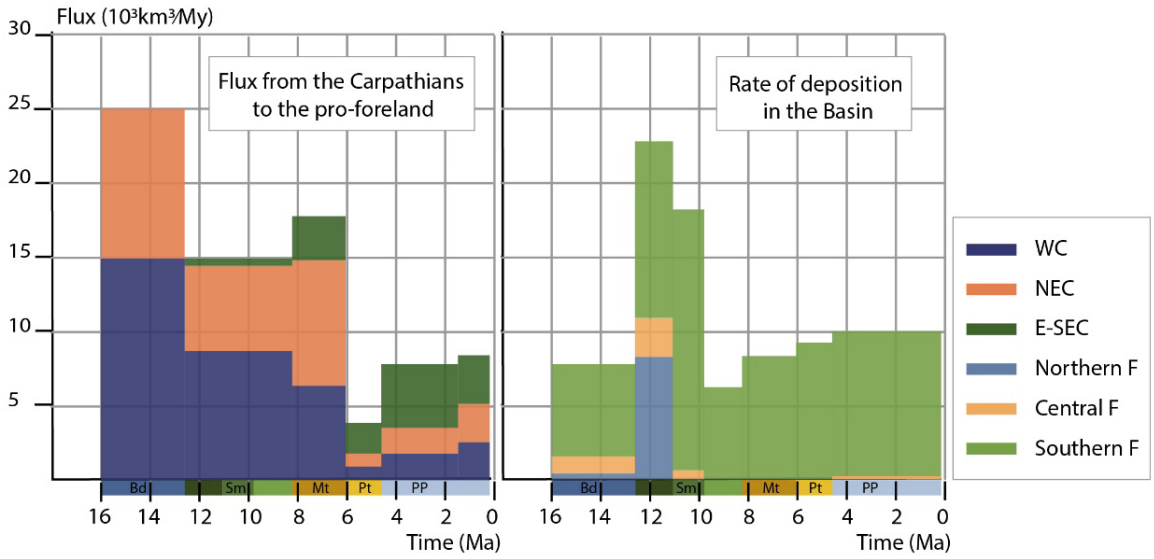

Figure V.16: Left) Sediment fluxes from the Carpathians to the pro-foreland basin. Eroded sediment fluxes are distinguished per region. Right) Sedimentation rates in the CFB distinguished by area as shown in Figure V.2. Note that the flux of sediments eroded over the Sarmatian period was divided among the three sub-stages. The coloured bar along the x-axis represents the stages of the foreland stratigraphy: Bd: Badenian; Sm: Sarmatian; Mt: Meotian; Pt: Pontian; PP: Plio-Pleistocene

Sediments deposited during the Badenian were derived from the WC and NEC regions, which were both rapidly exhumed (> 0.5 km/My) during this stage. The E-SEC region was not supplying sediments during this period (Figure V.8). Badenian sediments are preserved in the foreland mainly close to the frontal thrust; the main depocenter is the Focsani Depression. As discussed previously, difference between eroded and deposited volumes is largest in the Badenian (Figure V.7), which we attribute to sediment buried under the frontal thrust (see Chapter IV, Oszczypko, 2006; Figure V.6).

Whereas we constrained deposited sediment volumes for the Volhynian, Bessarabian, and Kersonian sub-stages, inversion of thermochronology data to constrain exhumation rates was performed for the entire Sarmatian stage (12.65-8.37 Ma), or more precisely for a time step spanning 12.8 to 8.6 Ma ((see Chapter III). Therefore, our model does not have the resolution to distinguish between potentially varying sediment sources during these sub-stages (Figures V. 9-11 and 16). Sediments were still derived primarily from the WC and NEC regions during the Sarmatian, with a greater contribution from the WC region than the NEC, due to higher exhumation rates (> 0.4 km/My; Figure V.16). The maps reveal a marked south-eastward shift of depocenters, we discuss it in section 4.4. In the Volhynian, deposition is distributed along the entire Carpathian front, with a large accumulation of sediments in the Northern foreland (Figure V.9). During the Bessarabian, sediments are no longer preserved in the Northern and Central forelands, but the depocenter shifts to the Southern Foreland, which in addition extends far onto the East European Platform (Figure V.10). The depocenter in the Kersonian is similar to that of the Bessarabian stage (Figure V.11). The WC and NEC regions could have provided sediments to the North and Central forelands during the Volhynian. Nonetheless, the sediment deposited in the Southern foreland during the Sarmatian period should also be sourced from the WC and NEC region because exhumation rates in the E-SEC region remained very low (Figure V.16). Therefore, an axial system transporting sediment from the actively eroding regions (i.e., regions with exhumation rates >0.3 km/My)

to these *loci* of deposition developed during the Volhynian stage and prograded along the foreland in the Bessarabian and Kersonian sub-stages (Figures V.10-11 and 16), in line with field observations (de Leeuw et al., 2020).

During the Meotian, the WC region provided less sediment than the NEC region (Figure V.12 and 16). The E-SEC region began to exhume and supply the Southern foreland. Most of the foreland no longer had accommodation space for sediments at this time and Meotian sediments only accumulated in the Southern foreland. The axial transport system developed in the Bessarabian continued to actively transport sediment from the WC and NEC region to the Southern foreland and specifically to the Focsani Depression (Figure V.12 and 16).

During the Pontian and Plio-Pleistocene, the erosional flux was highest out of the E-SEC region (Figure V. 13-16). The WC and NEC regions were close to inactive and provided less sediment than the E-SEC (Figure V.16). Sediment predominantly accumulated in the Focsani Depression during these stages (Figure 13-15). There was renewed accommodation space for Pontian sediments along the border of the Black Sea basin due to a transgressive event (see Chapter IV and references therein).

The overall source-to-sink system in the Carpathians shows a gradual shift in the locus of exhumation to the SE of the belt. The contribution of the WC region to the sediment supply decreased since 12.8 Ma. Sediment supply from the NEC region decreased around 6.1 Ma, while the E-SEC region started supplying sediments around 8.6 Ma (Figure V.16). In contrast, the shift in sediment deposition was abrupt and appears to have occurred during the Bessarabian (Figure V.16), when sediments began to be preserved primarily in the Southern foreland and no longer in the Northern foreland. At the time of this depocenter shift, the main *loci* of erosion were located significantly to the NW of the main sink in the foreland basin. The lateral offset between erosion and sediment deposition implies the existence of an axial sediment transport system along the Carpathian Foreland since this time (de Leeuw et al., 2020).

4.3 Sediments exiting the system

We performed a mass-balance calculation for the Carpathians source-to-sink system by subtracting the volumes of sediment preserved in the foreland basin from the volumes of sediment supplied by the belt to the pro-foreland (Figure V.17) over time. Excess eroded or deposited sediment volumes in the Carpathian system can indicate if, when, and how much sediment eroded from the Carpathian belt leaves the Carpathian foreland basin, or if sediment from elsewhere entered the foreland basin.

The mass balance plot (Figure V.17) shows a clear excess of eroded sediment volume during the Badenian. We assume that the imbalance for the Badenian stage is due to the reasons mentioned previously: the Badenian sediments are found up to 70 km under the mountain belt, so much of the Badenian foreland basin was overthrusted by the wedge (see Chapter IV, section 2 and 3). When averaged out over the Sarmatian, erosion and deposition are nearly in balance with an excess of 9.500 km^3 and 1.600 km^3 of sediment deposited during the Volhynian and Bessarabian sub-stages respectively, but an excess of around 7.500 km^3 sediment eroded in the Kersonian (Figure V.17, S1). The overall excess deposited volume over the Sarmatian stage is ~3.600 km^3. Considering that a portion of this volume,

especially for the Bessarabian sub-stage, is in the siliciclastic-carbonate sediment facies (Section 2.2.2), the excess volume deposited can be attributed to intra-basinal carbonate production, which generated approximately 3.600 km^3 of sediment over these stages according to our calculation above. The difference in exhumation rates for the Romanian East Carpathians between our study and foregoing ones suggest that we underestimate the exhumation rate of the E-SEC region during the Sarmatian in our inverse model (see Chapter III, section 4.2), which may offer a further explanation for the slight excess of sediment deposited. We can infer that the source-to-sink system was closed during the Sarmatian. Since the Meotian, the system shows excess erosion. During the Meotian, the excess volume of eroded sediment is ~25,000 km^3 (Figure V.17), while for the Pontian and the Pliocene (up to the Romanian stage at 1.8 Ma), the imbalance is smaller with ~3,000 km^3 and ~4.000 km^3 of excess eroded sediment volume, respectively. This small imbalance suggests that most of the sediment eroded during these stages accumulated in the foreland basin, more specifically in the Focsani Depression. The rest of the sediment must have excited the system. During the last 1.8 My, the excess eroded volume again reaches ~15,000 km^3, creating a total excess eroded volume of ~47,000 km^3 from the Meotian to the Pleistocene.

The volume of sediment retrieved from erosion of the Ukrainian foreland (see chapter IV section 1.1.4) is at least ~8.000 km^3. If we add the retrieved volume to the excess eroded volume of sediment since Meotian, the total reaches 55.000 km^3. These sediments eroded from the Carpathian belt and foreland basin were delivered to the Black Sea basin. The volume of the North-western platform of the BS was estimated to reach ~60.000 km^3 of sediment (de Leeuw et al., 2020), which is consistent with our estimate of sediment exiting the Carpathian system. The foreland stratigraphy reveals a large axial sediment transport system that came into being in the Sarmatian and prograded up to the Black Sea during the Meotian (Matoshko et al., 2016; de Leeuw et al., 2020). Evidence for this progradation is present in the *Balta* and *Porat formations* (Figure I.14; see Chapter I, section 3.2), which accumulated when onshore accommodation space became available during lake-level highstands. During the marked intervening lowstands (Popov et al., 2010; Krezsek et al., 2016; Palcu et al., 2021), sediment must have been shed into the Black Sea, as previously inferred by de Leeuw et al. (2020).

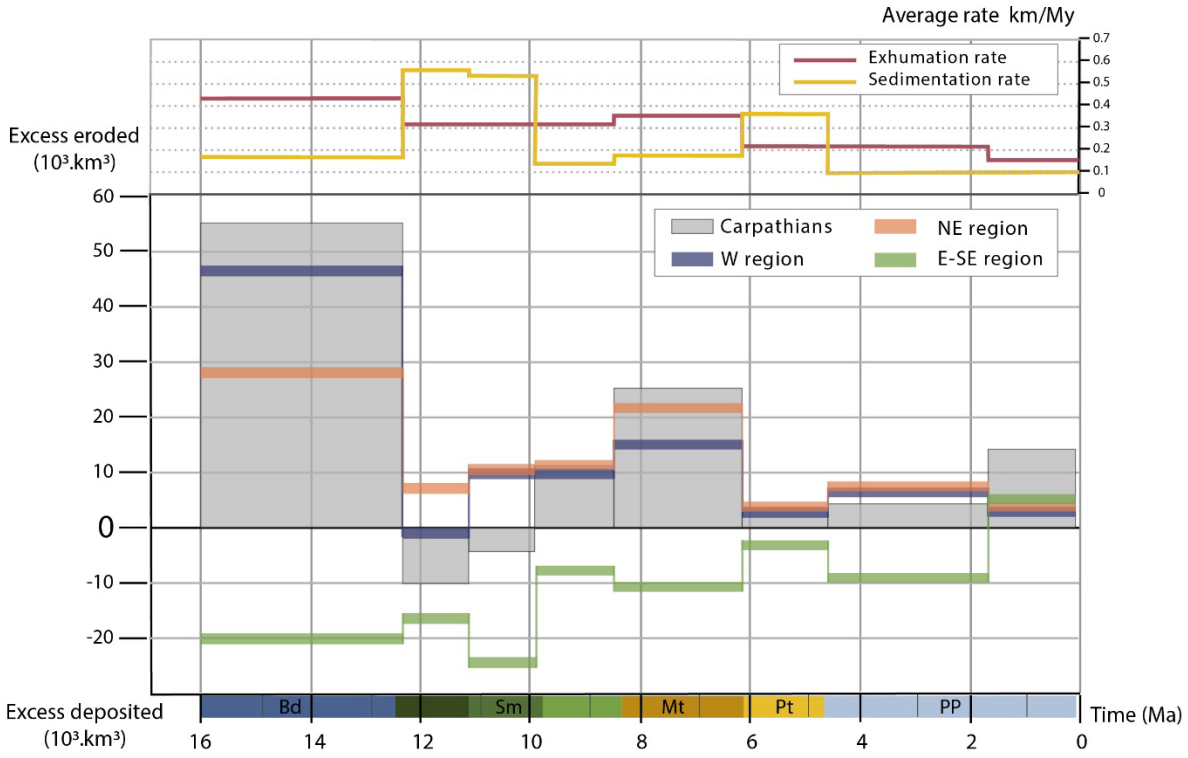

Figure V.17: Mass balance for the Carpathian fold-thrust belt and its foreland. Top) average exhumation and sedimentation rates over the last 16 Ma, from the exhumation model of the Carpathian belt and the sediment thickness model of the CFB, respectively. Note that the modelled exhumation rate is constant during the Sarmatian, but sedimentation rates vary during this stage. Bottom) Balance of the volumes of sediment eroded from the Carpathian belt and deposited in the CFB. Grey areas represent the total volume difference, whereas coloured bars indicate the volume difference for the different regions (blue: WC region and Polish foreland; Orange: NEC and Ukrainian Foreland; Green: E-SEC and Romanian foreland). The coloured bar on the x-axis represents the stages of the foreland stratigraphy: Bd: Badenian; Sm: Sarmatian; Mt: Meotian; Pt: Pontian; PP: Plio-Pleistocene.

5 Evolution of the sediment fluxes in the Carpathians source-to-sink system

We summarize the evolution of the Carpathian source-to-sink system based on our analysis of provenance shifting loci of exhumation and deposition, as well as the mass balance performed in this study.

First, the Badenian sediments present in the foreland reflect only a fragment of the paleo-basin that was present in front of the Carpathian wedge during the Badenian. A substantial amount of sediment supplied by the belt during this stage is beneath the mountain belt, i.e., overthrust, and are not accounted

for in the mass balance. However, based on balanced cross sections and paleo-basin reconstructions (Oszczypko, 2006; Oszczypko and Oszczypko-Clowes, 2012; Gągała et al., 2012; Nakapelyukh et al., 2018), the Badenian foreland should have been located all around the Carpathian arc, uniform deposition in a deep foreland basin. The Badenian sediments were provided by the WC and NEC regions and distributed radially in the Carpathian foreland basin. The Southern foreland is the area retaining most of the sediments of this stage, indicating already the predominance of the Focsani Depression as a depocenter of the area at the time (Figures V.8). The East European Platform east of the Focsani Depression is also receiving a large portion of the sediments in the Badenian.

During the Sarmatian, the Carpathian foreland basin transport system changed from a radial to an axial system (Figure V.18). In the Volhynian, sediments were deposited and accommodated in all foreland areas (Figures V.9 and 16) but sediment deposition shifted to the South-East of the foreland basin in the Bessarabian (Figure V.10). Sediments were largely accommodated in the Southern foreland; Northern and Central forelands seem to be overfilled at this time (see Chapter I and IV). By the Kersonian, sediments were only deposited in the Southern foreland (Figures V.11 and 16), despite being sourced from the WC and NEC. The Focsani Depression accommodated 70% of the sediments, while the other 30% were deposited over a wide area stretching up to the mouth of the Dnieper River (Figure V.12). In the Kersonian and Meotian, the axial transport system dominated in the East Carpathian foreland basin and delivered sediments to the Focsani Depression (Figure V.12) but also to more distal parts of the Southern foreland and to the Black Sea (Matoshko et al., 2016; de Leeuw et al., 2020). Most of the Southern foreland had developed into a delta-top environment (Matoshko et al., 2016). Our results show that the sediments for this system were sourced mainly from the NEC region and secondarily from the E-SEC and WC regions (Figure V.16). The fluvial system transported excess sediments to the Black Sea basin where they built the North-western Black Sea shelf.

Base level variations in the Paratethys region (Popov et al., 2010; Krezsek et al., 2016; Palcu et al., 2021) likely perturbed the sediment transport system in the Carpathian foreland basin (de Leeuw et al., 2020) during the late Miocene. The fluvial system of the foreland was incised during lake-level lows in the Kersonian, Meotian and Pontian, whereas lake-level highstands created onshore accommodation space and led to the deposition of the delta-top sediments of the Balta and Porat formations. Over the course of the Kersonian and Meotian, the shelf edge prograded across the Focsani Depression (Krezsek et al., 2021), which turned it into shallow environment (Matoshko et al., 2023). The shelf also prograded into the Black Sea. In the Pontian, the E-SEC region started to provide more sediments than the other regions. Sediments were only deposited in the Southern foreland. The Focsani Depression continued to be an important depocenter. During late Pontian flooding (Popov et al., 2010), however, the incised valleys of the platform were filled and sediment accumulated over a wide area stretching along the borders of the Black Sea. In the following Plio-Pleistocene stages, the SE-ward axial sediment transport system continued to be active, albeit with a strongly diminished sediment flux compared to the Sarmatian and Meotian (Fig V. 16). It also entered in competition with the Danube River transport system, which arrived in the Dacian Basin (see Chapter IV, discussion; de Leeuw et al., 2018; (Olariu et al., 2018; Matoshko et al., 2019; de Leeuw et al., 2020; Krézsek and Olariu, 2021). During the Plio-Pleistocene, sediment deposition was concentrated in the Focsani Depression and shifted to the south compared to the Pontian depocenter. The E-SEC region is the only one considered active in the belt

during these last two stages. It supplied half of the sediments discharged in the Carpathian foreland, the rest being derived from the relatively quiescent areas of the mountain chain further north. However, the overall volume of exhumed material diminishes in the last stages (Figure V.16 and 18). From 1.8 Ma to present, sediments supplied by the belt seem to be less preserved in the foreland (Figure V.16) and are transported to the Black Sea. This is logical because the Focsani Depression has been overfilled since the onset of the Romanian (~4.7 Ma).

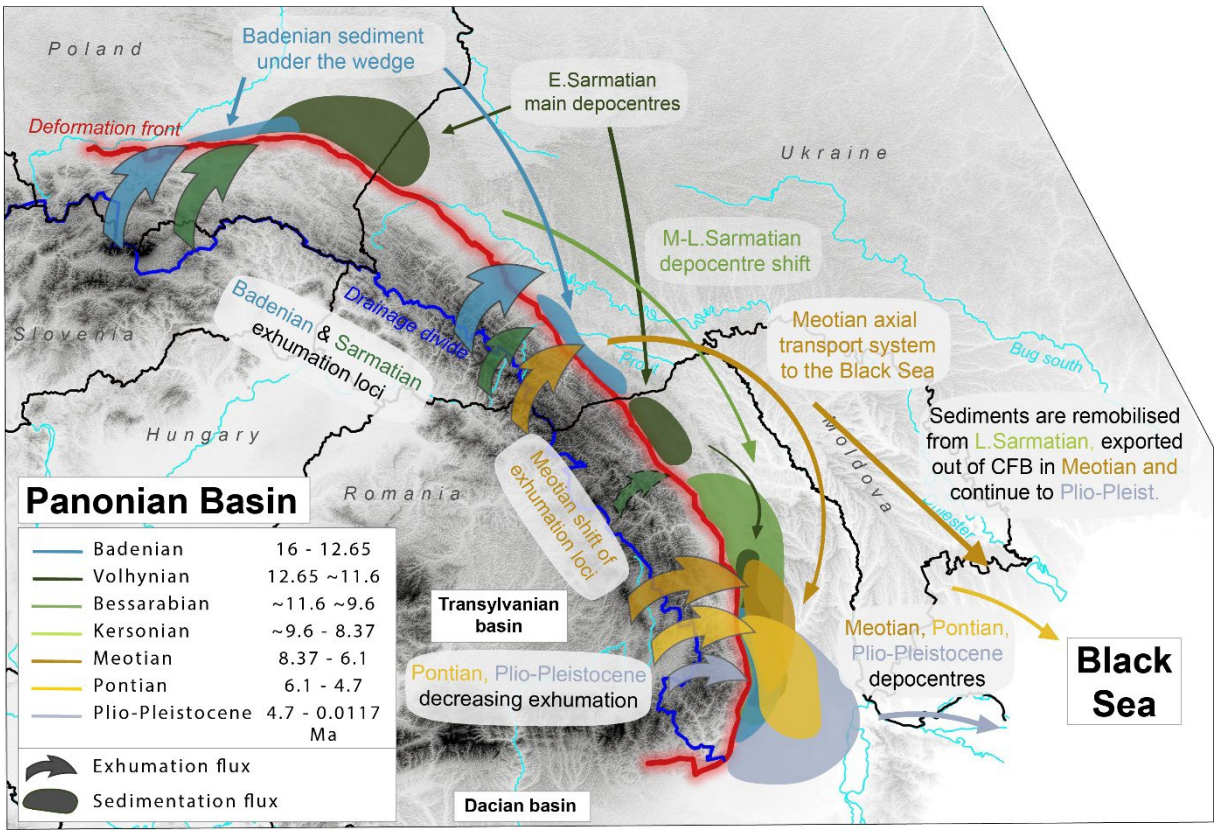

Figure V.18: Synthetic map of the sediment routing in the Carpathian fold-thrust belt and foreland system from the Badenian to the Plio-Pleistocene.

6 Regional framework of the Carpathian orogen

The following section discusses the development of the Carpathian fold-and-thrust belt and its retro-foreland, including the Pannonian Basin and the Neogene volcanic arc. The retro-foreland developed as a direct consequence of the retreat and detachment of the East-European slab. However, the architecture and syn-orogenic development of the Carpathian foreland basin is also influenced by the pre-orogenic structural inheritance of the lower plate (see Chapter I, section 2.3 and Chapter IV, section 4). We therefore also describe the development of the Focsani Depression in this section. In order to qualitatively compare the influence of pre-orogenic inheritance and slab detachment in the Carpathian region, we discuss the lateral evolution of different regional features.

6.1 Regional geodynamics of the intra-Carpathian region

Diachronous exhumation along the Carpathian arc is intimately linked to the evolution of the Pannonian-Carpathian region, including slab retreat, Neogene volcanism, lithospheric thinning and

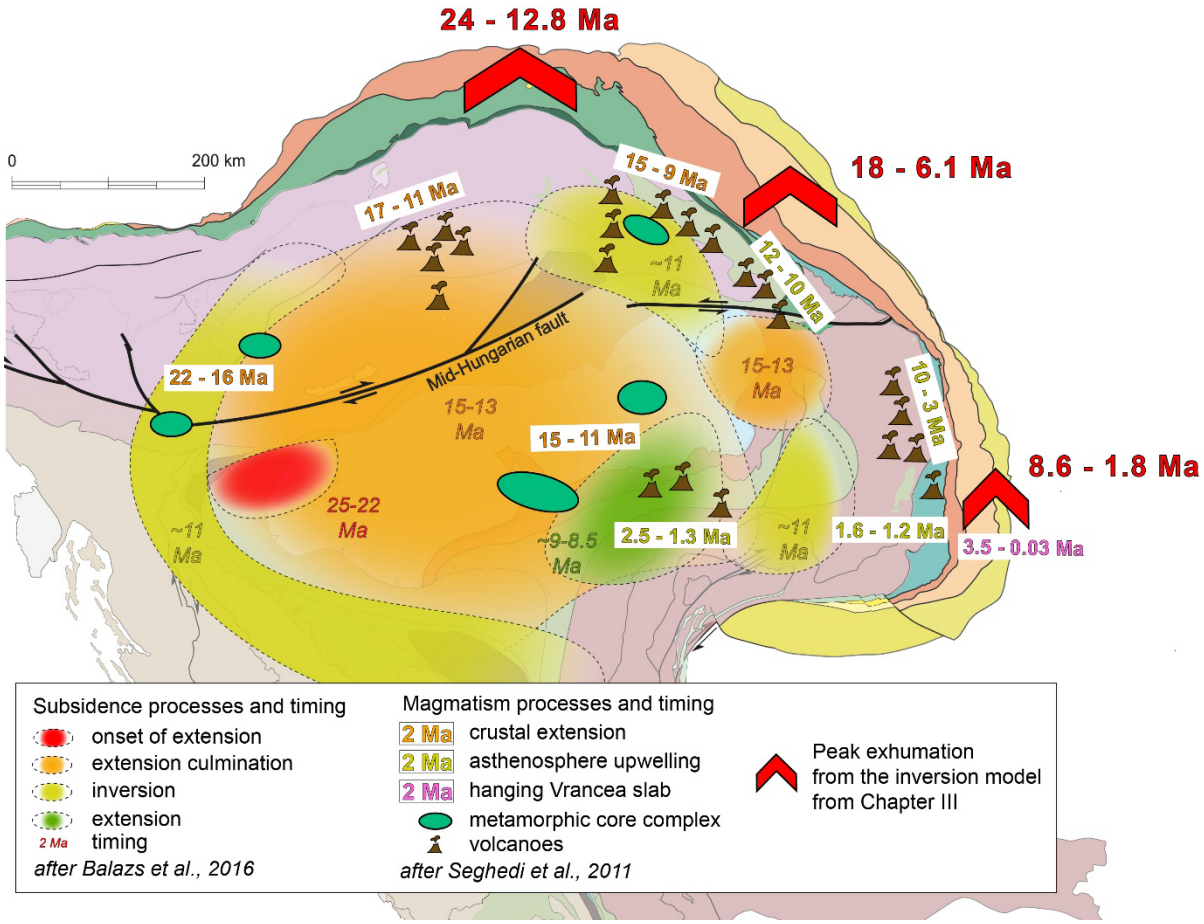

Figure V.19: Map of the Carpathian region showing the timing of volcanic events and subsidence in the Pannonian and Transylvanian basins, compared to the peak exhumation periods in the Carpathian belt constrained by our inversion of low-temperature thermochronology data. Base map is modified after Schmid et al. (2008).

delamination (Wortel and Spakman, 2000; Konečny et al., 2002; Ustaszewski et al., 2008; Handy et al., 2015; Göğüş et al., 2016; Bracco Gartner et al., 2020; Şengül-Uluocak et al., 2019).

The movement of the Tisza and Dacia blocks into the Carpathian embayment was driven by the north-eastward roll-back of the European slab (Chapter I, section 2.1 and references therein). Alpine collision to the west of the embayment changed the regime in the Pannonian-Carpathian region (Sperner et al., 2002; Handy et al., 2015). Collision in the Eastern Alps and Western Carpathians triggered tearing of the Carpathian slab. The onset of slab tearing was synchronous with the onset of Pannonian Basin extension (see Chapter I, section 4 and references therein). Back-arc extension was facilitated by slab roll-back until the thicker, more rigid and more buoyant lithosphere of the East-European plate arrived at the front of the subduction zone (Figure V.20 A). Calc-alkaline volcanism initiated in the northern Pannonian Basin at 17-11 Ma. The eruptive ages become younger towards the east-southeast (Figure

V.19; Seghedi and Downes, 2011). The main extensional phase in the Pannonian Basin occurred during the middle Miocene (~15-13 Ma), with 150-200 km of extension and associated crustal thinning (Ustaszewski et al., 2008; Balázs et al., 2016).

The resistance to further subduction of the European lithosphere led to a readjustment of the forces in the orogenic wedge, generating a marked pulse of exhumation and related sediment supply to the foreland (Figure V.20 B1). While extension and shortening continued at the back of the collision front, the slab steepened and increased the dynamic subsidence in the retro-side of the wedge and uplift in the pro-side (Figure V20 B2). At the border of Slovakia, Poland and Ukraine, calc-alkaline felsic events occurred between 15-13 Ma and volcanic edifices are also forming eastward, with intermediate calc-alkaline composition, from 14-9 Ma in the backstop of the Ukrainian Carpathians. The development of this segment of the Neogene volcanic arc is interpreted to result from asthenospheric upwelling into the space vacated when the slab steepened and tore (Figure V.20 B2; Seghedi and Downes, 2011; Kovacs et al., 2017). Peak exhumation of the NEC region in our model (18-8.6 Ma) is concordant in timing with the main extension phase (15-13 Ma) in the Pannonian Basin (Balázs et al., 2016) and with the formation of the Ukrainian Neogene volcanic arc (15-9 Ma; Figure V. 19).

The slab retreat produced lithospheric delamination and dynamic uplift of the Transylvanian basin and SE Carpathians (Figure V20.C'; Girbacea and Frisch, 1998; Krézsek and Bally, 2006). An uplift phase on the exterior of the Pannonian Basin coincided with continued extension shifting to the East of the basin, where slab roll-back could still occur (Horváth et al., 2015; Balázs et al., 2016). The exhumation resumed, but to a lesser degree and in the outer units of the wedge of the E-SEC region. The volcanic arc became inactive, and compression was transferred to the Dinarides front which currently takes up convergence (Figure V.20 C). Dynamic uplift also affected the Transylvanian basin over the last ~8 My (Matenco et al., 2016; Balázs et al., 2016; Şengül-Uluocak et al., 2019). In the southernmost volcanoes of Romania, melt generation is interpreted as a result of asthenospheric upwelling associated to decompression as a result of the retreat and the hanging Vrancea slab (Figure V.20 C'; Seghedi and Downes, 2011; Kovacs et al., 2017; Molnár et al., 2019; Bracco Gartner et al., 2020). Other volcanoes of the E-SEC back-arc (Figure V.19, volcanic event dates 2.5-1.3 and 1.6-1.2 Ma) have the same origin that required low amount of melting under a thinned lithosphere (~50 km), to produce basaltic melts during asthenosphere upwelling (Bracco Gartner and McKenzie, 2020). The most recent exhumation period (6.1-0 Ma) in the E-SEC region in our exhumation model corresponds with active collision and a dynamic uplift and subsidence over the SE Carpathians (Şengül-Uluocak et al., 2019; Necea et al., 2021). The Tarcau unit was rapidly exhumed over the last 6.1 My; however, exhumation of the Sub-Carpathian unit occurred at a moderate rate (~0.4 km/My) from 6.1 to 1.8 Ma) and practically stopped (< 0.1 km/My) in the last 1.8 My (see Chapter III, Figure III. 10). We interpret the activity of the Tarcau and Sub-Carpathian nappe in the late-Miocene to be a result of collision and retreat of the slab. It was accompanied by a dynamic topography wave in the Transylvanian-Carpathian region; asthenospheric upwelling and magmatism as well as downgoing viscous material created uplift and subsidence pattern in the SE Carpathians (see chapter I section 4 and references therein).

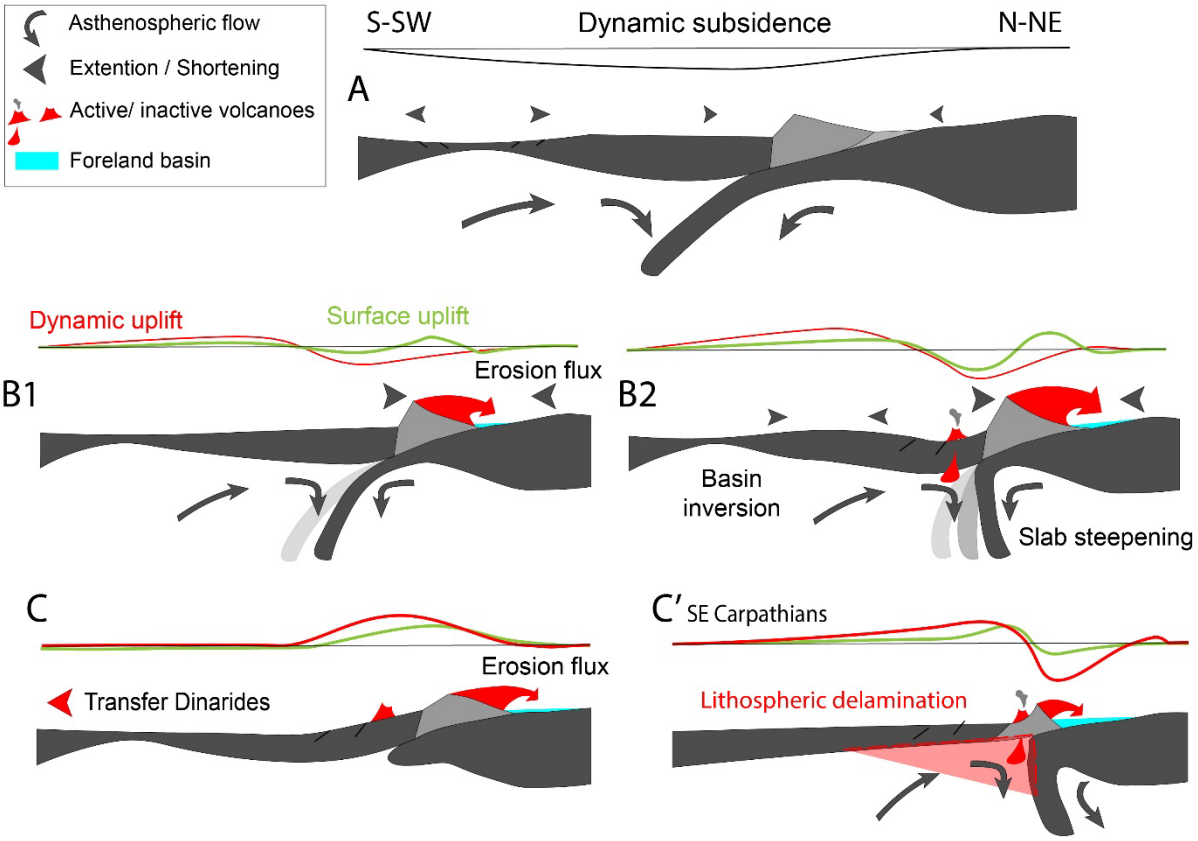

Figure V.20: Sketch of the regional dynamics in the Pannonian-Carpathian region. A) Regime during accretion and slab roll-back. Dynamic subsidence is represented here as the lithosphere response to mass density and buoyancy differences. B1) Change of regime during peak exhumation. Shortening at the Carpathian front is due to collision with the East-European plate. Ongoing back-arc extension and asthenospheric upwelling lead to dynamic uplift of the Pannonian Basin. The surface is uplifted by the wave of dynamic uplift and the collision with the East-European plate. B2) Slab steepening (with or without lithospheric delamination) increases dynamic subsidence and propagates as a wave toward the exterior of the Pannonian-Carpathian region. Erosional fluxes from the orogenic wedge are high. Slab steepening enhances mantle upwelling and asthenospheric flow to the base of the lithosphere, creating the back-arc volcanism. C) after slab detachment, exhumation is linked to the isostatic re-adjustment of the lithosphere and volcanic activity ceased. C') In the SE Carpathians region, the surface is uplifted due to lithospheric delamination under the wedge and the foreland subside due to slab sinking (see text for references).

6.2 Geodynamic development of the Southern Carpathian foreland

The evolution of the Carpathian foreland, as displayed in the Chapter IV, indicates the predominance of the Focsani Depression as a major sediment sink. Hereafter we discuss the evolution of the depression regarding the pro-foreland development and the SE Carpathians dynamics and inheritance.

We can consider that the transition from deposition to incision in the foreland represents an isostatic rebound due to slab detachment, as convergence also ceased in the Western and North-eastern Carpathians during Sarmatian (see Chapter II and III and references therein). The increase in subsidence of the Focsani Depression in the late Pontian (see Chapter IV) can be a consequence of slab tear and detachment in the North-eastern Carpathians (~6 Ma). The remaining slab panel is attached to the European lithosphere and drastically increases bending in the Southern foreland. The isostatic rebound of the foreland (after slab break-off), lifted the Northern and Central forelands, creating a tilted sedimentary platform that is intensively eroded in the Ukrainian region (Wortel and Spakman, 2000). Isostatic rebound may have been effective on a large wavelength on the Ukrainian craton where the EET is greatest. Contrastingly, the Northern foreland is less eroded. Dynamic topography in the SE Carpathians displays an ongoing subsidence of the Focsani Depression and an uplift of the Carpathian belt (Şengül-Uluocak et al., 2019). Based on the theorical model of others (Royden and Husson, 2009; Husson et al., 2012) and their interpretations (Göğüş et al., 2016), the decoupling of the slab from the intra-Carpathian plates under the Transylvanian-Carpathian increased the dynamic uplift in this region. The hanging (to overturned) slab under the pro-foreland create subsidence in the SE Carpathian foreland. The difference in isostatic uplift in the Northern and Central forelands, combined with dynamic subsidence on the Focsani Depression, has resulted in a north-west to south-eastward axial transport system and accommodation space, filling the Focsani Depression to the present (Figure V.21).

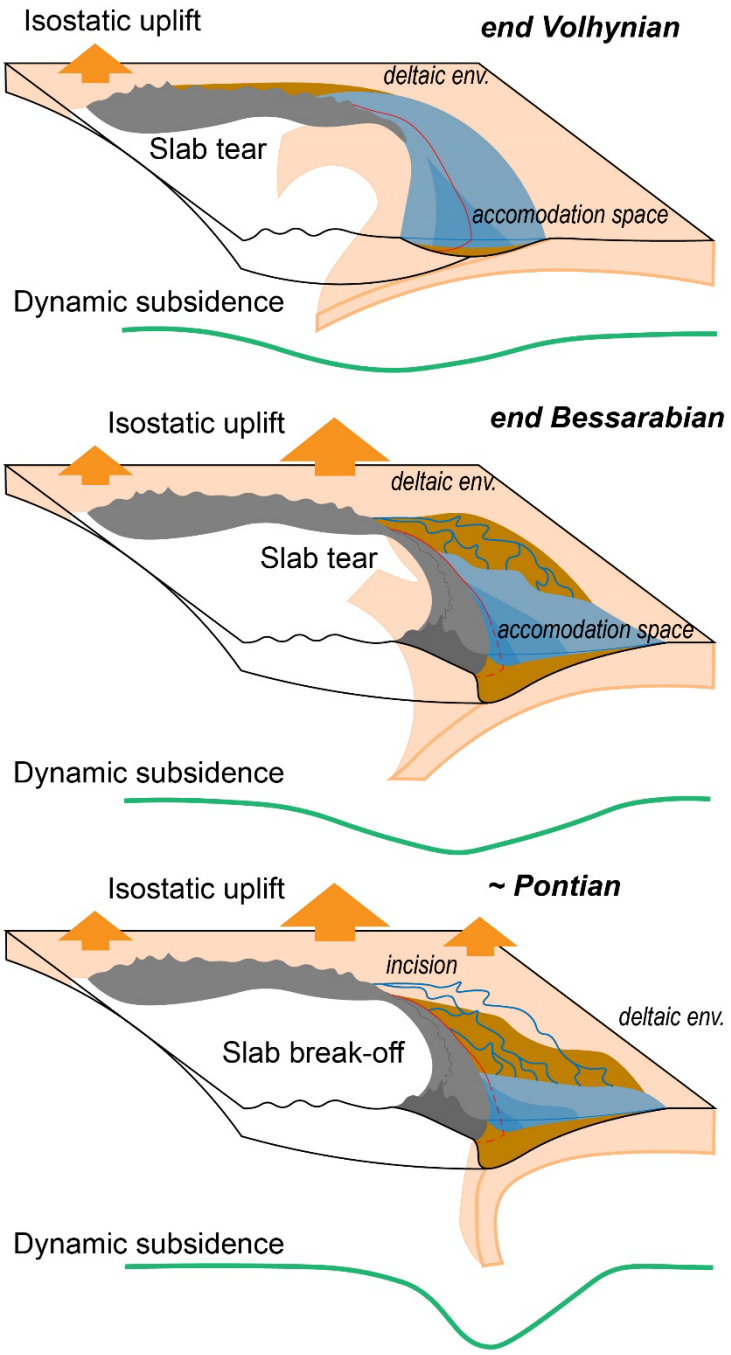

Figure V.21: Scheme of the Focsani Depression evolution. Top, situation during Volhynian, SE Carpathians are not exhumed and the Focsani Depression has accommodation space. Middle, situation in Bessarabian, The slab is torn in the NW and/or detached, the foreland is uplifted. Eastern Carpathians are exhuming, and the slab is retreating to the east. Bottom, situation in Pontian, the slab is verticalized and pull on the upper plate, creating dynamic subsidence focused on the Focsani Depression, thus creating accommodation space. Isostatic uplift of the Western and North-eastern Carpathians after slab break-off tilts the CFB and allows for erosion of the foreland. Red line is the frontal thrust, dashed red line is the blind frontal thrust.

6.3 Influence of pre-orogenic inheritance on the Carpathian region

The Carpathian foreland consist of an aggregation of plates with different effective elastic thickness (EET). In Chapter IV, we have shown that marked depocentres in the Carpathian foreland generally coincide with areas with low EET. We here dwell on the different processes in the Carpathian source-to-sink system that could also have been affected by the lateral variation of lithospheric features: the topography of the belt, the sediment thickness and distribution in the foreland, the peak of exhumation in the belt, the back-arc volcanism. The lateral variation of these processes is shown in Figure V.22.

The lateral variation of the total sediment thickness preserved in the foreland basin, 50 km from the deformation front, coincides well with the lateral variation in EET. A lower EET allows for greater sediment accommodation in a flexural paradigm. A higher EET is consistent with a shallower but wider flexural basin. However, total sediment thickness in the Focsani Depression is five times greater than in the other zones, despite a comparable EET. The accommodation of sediment is then not only dependent on the EET variation. This difference is explained by the flexural and dynamic subsidence of the slab in this region (Şengül-Uluocak et al., 2019).

Carpathian foreland basin sediments can be split into those deposited near the thrust front (< 100 km) and those deposited far from it (> 100 km) (Figure V.22). Where EET is high (in the NEC region and Central foreland), a larger proportion of sediment accumulated (or was better preserved) away from the thrust front. It is the only area where more sediment is preserved far (>100 km) from the thrust front than close to it. A notable feature is that, although the EET in the WC and E-SEC regions is similar (~20-40 km), sediments preserved far from the thrust front are present, and in great volume, only in the Southern foreland. This difference in sediment distribution in the pro-foreland can be explained by: (1) Thermal subsidence along the margin of the Black Sea back-arc basin (Maynard and Erratt, 2020) or (2) the increase in dynamic subsidence due to the downward pull of the European slab, which is detached in the WC region, but is still attached in the E-SEC region. Isostatic rebound following slab detachment led to erosion of the Northern foreland (Figure V.21).). The second proposition may explain the preferential accumulation of sediment away from the thrust front in the Southern foreland, in contrast to the Northern foreland, despite a similar lithospheric EET.

The lateral variation in EET does not appear to affect the timing or intensity of exhumation, nor the development of the volcanic arc in the retro-foreland (Figure V.22). These processes are rather influenced by diachronous detachment of the slab (Webb et al., 2017). However, the location of sediment depocenters along the frontal thrust appears to be equally affected by slab detachment and EET variations (Figure V.22). The locus of sedimentation is concentrated on the regions with lower EET, as long as the slab remains attached. In the Badenian and Volhynian, the slab is present under the entire Carpathian wedge and sediment depocenters are located where EET is lower. During the Bessarabian and Kersonian, the slab becomes detached in the WC and accumulation of sediment in the foreland is focused on the Central and Southern foreland. Sediment deposition starts to be concentrated in the Focsani Depression in the Kersonian and, during subsequent stages, only the Southern foreland accommodates sediments. The EET variation had an influence on the loci of sediment preservation, but the diachronous slab detachment over the region caused migration of the depocenters to the SE of the Carpathian foreland basin and enhanced the subsidence in the SE Carpathians.

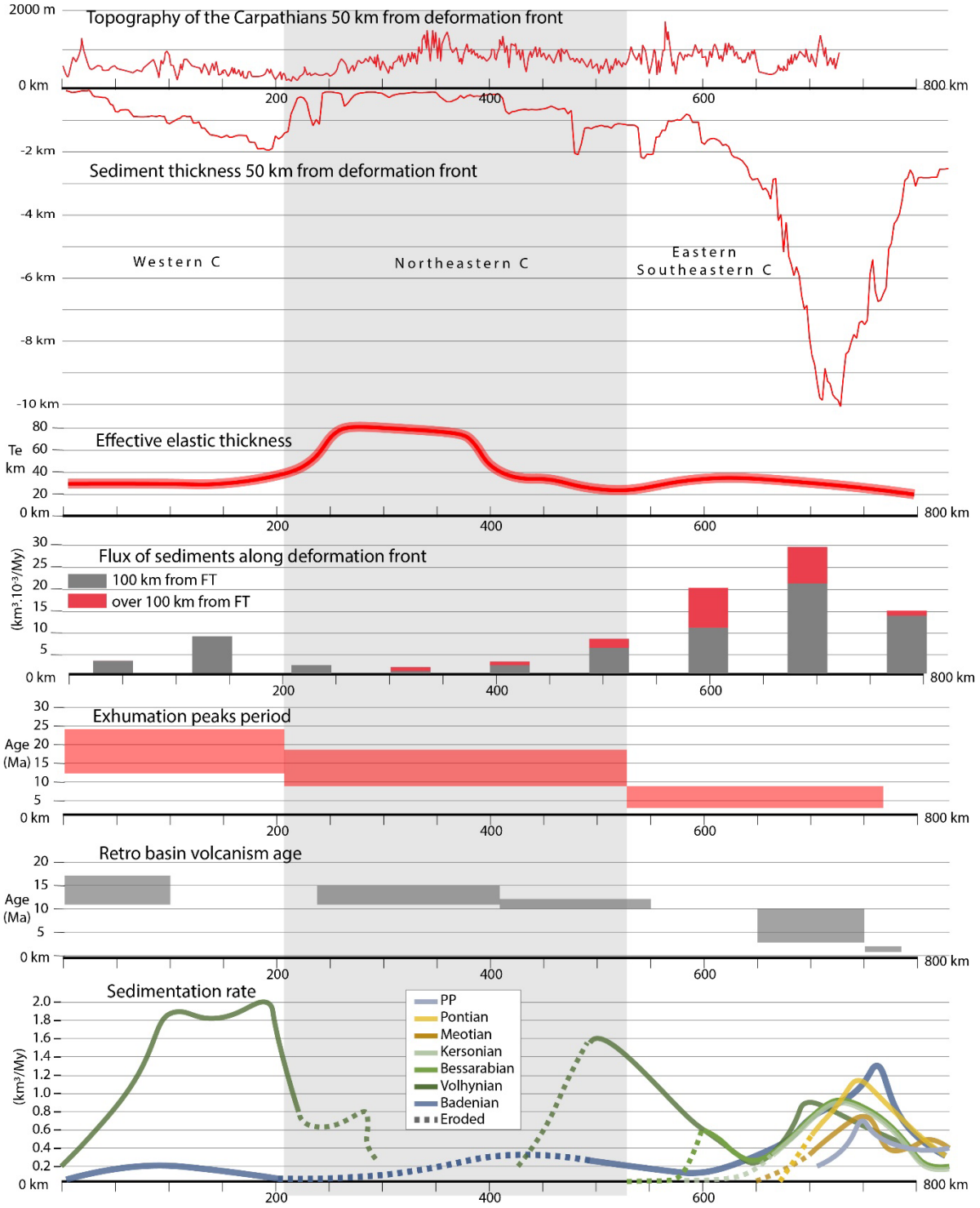

Figure V.22: Lateral variation of features and processes in the Carpathian region. The topography of the Carpathians is taken 50 km inboard of the deformation front. In comparison, the sediment thickness along the Carpathian foreland is taken 50 km outboard from the deformation front. Sediment thickness data are extracted from the 3D model of the CFB described in Part IV of this work. The lateral variation of EET is based on Kaban et al., 2018. Fluxes of sediment deposited in the foreland are extracted from the 3D model of the CFB from Part IV. Times of peak exhumation are based on the results of the exhumation model of the Carpathians (Chapter III). Ages of volcanism in the retro-foreland are from Seghedi et al., 2011. Sedimentation rates are from the model of sediment thickness of the Carpathians (Chapter IV). The rates are the maximum rate within the 50 km from the frontal thrust. PP: Plio-Pleistocene.

6.4 Drivers of the Carpathian fold-thrust belt and foreland system development

Based on our results and in line with the previous conclusions drawn in the different Chapters of this study, we can deduce that the Carpathian fold-and-thrust belt, and its associated foreland basin, has developed as follows:

- Retreat of the European slab led to the accretion of most of the nappes in the Carpathian embayment, from the Cretaceous to the Eocene.
- Subduction retreat slowed down when the buoyant and thicker lithosphere of the East European Platform arrived at the subduction zone and resisted flexure. North-eastward retreat of the subduction zone stopped, and soft collision started.
- This led to a peak in erosion and related sediment supply to the foreland. This sediment pulse leads to overfilling of the foreland basin. The radial sediment transport evolved into an axial transport system discharging sediment to the south-east of the Carpathian foreland basin.
- When the slab steepened and eventually tore, the retro-foreland volcanic arc developed by asthenospheric upwelling and related melting at the base of the lithosphere. Slab steepening also enhanced dynamic uplift in the belt and subsidence in the pro-foreland basins.
- Collision (and to a lesser degree dynamic uplift) of the orogenic wedge led to exhumation; the exhumed material was shed to the pro-foreland basin. The sediment depocenters were focused on areas with lower EET, but the lateral (and diachronous) tearing and detachment of the slab induced the migration of the sediment depocenter toward the south-east of the Carpathian foreland. Significant sediment was also accommodated over wide areas with higher EET, far from the orogen.
- When the slab breaks off, the belt gradually returns to isostatic equilibrium while dynamic depression decreases. This upliftrebound uplifts the belt, which then discharges more sediment into the foreland. The foreland is eventually also uplifted and becomes incised by the river system.
- The sediments that are remobilised from the incised areas of the foreland basin first find their way to subsiding areas further along the arc, and finally exit the foreland to the Black Sea basin.
- Steepening of the current Vrancea slab towards its position under the Focsani Depression generated a wave of dynamic uplift and subsidence that migrated toward the pro-foreland.

According to our reconstruction of the Carpathian region, the European slab was the main driver of the development of the Carpathian source-to-sink system. It also drove the diachronous construction of the entire system, with slab detachment occurring diachronously from NW to SE. Subduction dynamics, slab retreat and subsequent detachment, and reorganisation of mantle flow patterns set was directly related to: (1) accretion of the Carpathian wedge, (2) diachronous onset of collision, (3) extension of the Pannonian basin, (4) development of the volcanic arc in the retro-foreland, (5) dynamic uplift of the Carpathian belt, (6) dynamic subsidence and flexure of the lower plate, (7) migration of foreland depocenters and accommodation of sedimentation in the areas of lower EET of the CFB, and finally (8) return to isostatic equilibrium during the slowdown of subduction dynamics which tilted the foreland.

Using the chronology of the different processes in the Carpathian fold-thrust belt and foreland system, we can decipher the timing of cessation of slab retreat and slab detachment under the Carpathian arc. In the western Carpathian region, slab retreat ended in the early to middle Miocene, based on the peak in exhumation rates (ca. 24-12 Ma). The slab detachment occurred in the Bessarabian, when the foreland was uplifted and incised, and sediments eroded from the WC were transferred eastward. In the Ukrainian Carpathian region, slab retreat may have halted between 18 Ma and 12 Ma, according to onset of peak exhumation and volcanism in the retro-foreland. The uplift of the Ukrainian foreland is difficult to decipher because of the extensive erosion over the area but based on the interpretation of the sedimentary facies of the Balta Formation south of the extensively eroded area, the Ukrainian foreland may have been uplifted during the Kersonian and early Meotian (~9-5 Ma). Finally, in the E-SEC region, peak exhumation occurred at 8.6 Ma and exhumation of the sub-Carpathian nappe decreased after 1.8 Ma. In the northern Romanian foreland, uplift may have been during the Pontian, as sediments were restricted to the Focsani Depression starting from this stage (6.1-4.7 Ma). During the transgressive stage the sediment were deposited 100 km inlands from the Black Sea present-day border. However, the current erosion of the now tilted CFB do not allow for a precise dating of the uplift of the foreland. Currently, the south-eastern Carpathians are exhuming, and the Focsani Depression is still subsiding (van der Hoeven et al., 2005; Şengül-Uluocak et al., 2019) due to the Vrancea slab sinking beneath.

References

Bracco Gartner, A. J. J., Seghedi, I., Nikogosian, I. K., and Mason, P. R. D.: Asthenosphere-induced melting of diverse source regions for East Carpathian post-collisional volcanism, Contrib Mineral Petrol, 175, 54, https://doi.org/10.1007/s00410-020-01690-4, 2020.

Bracco Gartner, A. J. J. and McKenzie, D.: Estimates of the Temperature and Melting Conditions of the Carpathian-Pannonian Upper Mantle From Volcanism and Seismology, Geochem. Geophys. Geosyst., 21, https://doi.org/10.1029/2020GC009334, 2020.

Castelluccio, A., Mazzoli, S., Andreucci, B., Jankowski, L., Szaniawski, R., and Zattin, M.: Building and exhumation of the Western Carpathians: New constraints from sequentially restored, balanced cross sections integrated with low-temperature thermochronometry: WESTERN CARPATHIANS TECTONIC EVOLUTION, Tectonics, 35, 2698–2733, https://doi.org/10.1002/2016TC004190, 2016.

Covey, M.: The Evolution of Foreland Basins to Steady State: Evidence from the Western Taiwan Foreland Basin, in: Foreland Basins, edited by: Allen, P. A. and Homewood, P., Blackwell Publishing Ltd., Oxford, UK, 77–90, https://doi.org/10.1002/9781444303810.ch4, 1986.

Dahlen, F. A. and Suppe, J.: Mechanics, growth, and erosion of mountain belts, in: Processes in Continental Lithospheric Deformation, vol. 218, edited by: Clark, S. P., Jr., Burchfiel, B. C., and Suppe, J., Geological Society of America, 0, https://doi.org/10.1130/SPE218-p161, 1988.

Gągała, Ł., Vergés, J., Saura, E., Malata, T., Ringenbach, J.-C., Werner, P., and Krzywiec, P.: Architecture and orogenic evolution of the northeastern Outer Carpathians from cross-section balancing and forward modeling, Tectonophysics, 532–535, 223–241, https://doi.org/10.1016/j.tecto.2012.02.014, 2012.

Gailleton, B., Sinclair, H. D., Mudd, S. M., Graf, E. L. S., and Maţenco, L. C.: Isolating Lithologic Versus Tectonic Signals of River Profiles to Test Orogenic Models for the Eastern and Southeastern Carpathians, J. Geophys. Res. Earth Surf., 126, https://doi.org/10.1029/2020JF005970, 2021.

Göğüş, O. H., Pysklywec, R. N., and Faccenna, C.: Postcollisional lithospheric evolution of the Southeast Carpathians: Comparison of geodynamical models and observations, Tectonics, 35, 1205–1224, https://doi.org/10.1002/2015TC004096, 2016.

Handy, M. R., Ustaszewski, K., and Kissling, E.: Reconstructing the Alps–Carpathians–Dinarides as a key to understanding switches in subduction polarity, slab gaps and surface motion, Int J Earth Sci (Geol Rundsch), 104, 1–26, https://doi.org/10.1007/s00531-014-1060-3, 2015.

van der Hoeven, A. G. A., Mocanu, V., Spakman, W., Nutto, M., Nuckelt, A., Matenco, L., Munteanu, L., Marcu, C., and Ambrosius, B. A. C.: Observation of present-day tectonic motions in the Southeastern Carpathians: Results of the ISES/CRC-461 GPS measurements, Earth and Planetary Science Letters, 239, 177–184, https://doi.org/10.1016/j.epsl.2005.09.018, 2005.

Horváth, F. and Cloetingh, S.: Stress-induced late-stage subsidence anomalies in the Pannonian basin, Tectonophysics, 266, 287–300, https://doi.org/10.1016/S0040-1951(96)00194-1, 1996.

Husson, L., Guillaume, B., Funiciello, F., Faccenna, C., and Royden, L. H.: Unraveling topography around subduction zones from laboratory models, Tectonophysics, 526–529, 5–15, https://doi.org/10.1016/j.tecto.2011.09.001, 2012.

Konecˇny, V., Kovacˇ, M., and Lexa, J.: Neogene evolution of the Carpatho-Pannonian region: an interplay of subduction and back-arc diapiric uprise in the mantle, 20, 2002.

Kováč, M., Andreyeva-Grigorovich, A., Bajraktarević, Z., Brzobohatý, R., Filipescu, S., Fodor, L., Harzhauser, M., Nagymarosy, A., Oszczypko, N., Pavelić, D., Rögl, F., Saftić, B., Sliva, U., and Studencka, B.: Badenian evolution of the Central Paratethys Sea: paleogeography, climate and eustatic sea-level changes, 2007.

Kovacs, M., Seghedi, I., Yamamoto, M., Fülöp, A., Pécskay, Z., and Jurje, M.: Miocene volcanism in the Oaş–Gutâi Volcanic Zone, Eastern Carpathians, Romania: Relationship to geodynamic processes in the Transcarpathian Basin, Lithos, 294–295, 304–318, https://doi.org/10.1016/j.lithos.2017.09.027, 2017.

Krézsek, C. and Bally, A. W.: The Transylvanian Basin (Romania) and its relation to the Carpathian fold and thrust belt: Insights in gravitational salt tectonics, Marine and Petroleum Geology, 23, 405–442, https://doi.org/10.1016/j.marpetgeo.2006.03.003, 2006.

Krézsek, C. and Olariu, C.: Filling of sedimentary basins and the birth of large rivers: The lower Danube network in the Dacian Basin, Romania, Global and Planetary Change, 197, 103391, https://doi.org/10.1016/j.gloplacha.2020.103391, 2021.

Krezsek, C., Schleder, Z., Bega, Z., Ionescu, G., and Tari, G.: The Messinian sea-level fall in the western Black Sea: small or large? Insights from offshore Romania, PG, 22, 392–399, https://doi.org/10.1144/petgeo2015-093, 2016.

de Leeuw, A., Filipescu, S., Maţenco, L., Krijgsman, W., Kuiper, K., and Stoica, M.: Paleomagnetic and chronostratigraphic constraints on the Middle to Late Miocene evolution of the Transylvanian Basin (Romania): Implications for Central Paratethys stratigraphy and emplacement of the Tisza–Dacia plate, Global and Planetary Change, 103, 82–98, https://doi.org/10.1016/j.gloplacha.2012.04.008, 2013.

de Leeuw, A., Vincent, S. J., Matoshko, A., Matoshko, A., Stoica, M., and Nicoara, I.: Late Miocene sediment delivery from the axial drainage systemof the East Carpathian foreland basin to the Black Sea, Geology, https://doi.org/10.1130/G47318.1, 2020.

Matenco, L. and Bertotti, G.: Tertiary tectonic evolution of the external East Carpathians (Romania), Tectonophysics, 316, 255–286, https://doi.org/10.1016/S0040-1951(99)00261-9, 2000.

Matenco, L., Munteanu, I., ter Borgh, M., Stanica, A., Tilita, M., Lericolais, G., Dinu, C., and Oaie, G.: The interplay between tectonics, sediment dynamics and gateways evolution in the Danube system from the Pannonian Basin to the western Black Sea, Science of The Total Environment, 543, 807–827, https://doi.org/10.1016/j.scitotenv.2015.10.081, 2016.

Matoshko, A., Matoshko, A., de Leeuw, A., and Stoica, M.: Facies analysis of the Balta Formation: Evidence for a large late Miocene fluvio-deltaic system in the East Carpathian Foreland, Sedimentary Geology, 343, 165–189, https://doi.org/10.1016/j.sedgeo.2016.08.004, 2016.

Matoshko, A., Matoshko, A., and de Leeuw, A.: The Plio–Pleistocene Demise of the East Carpathian Foreland Fluvial System and Arrival of the Paleo-Danube To The Black Sea, Geologica Carpathica, 70, 91–112, https://doi.org/10.2478/geoca-2019-0006, 2019.

Maynard, J. R. and Erratt, D.: The Black Sea, a Tertiary basin: Observations and insights, Marine and Petroleum Geology, 118, 104462, https://doi.org/10.1016/j.marpetgeo.2020.104462, 2020.

Nakapelyukh, M., Bubniak, I., Bubniak, A., Jonckheere, R., and Ratschbacher, L.: Cenozoic structural evolution, thermal history, and erosion of the Ukrainian Carpathians fold-thrust belt, Tectonophysics, 722, 197–209, https://doi.org/10.1016/j.tecto.2017.11.009, 2018.

Necea, D., Juez-Larré, J., Matenco, L., Andriessen, P. A. M., and Dinu, C.: Foreland migration of orogenic exhumation during nappe stacking: Inferences from a high-resolution thermochronological profile over the Southeast Carpathians, Global and Planetary Change, 200, 103457, https://doi.org/10.1016/j.gloplacha.2021.103457, 2021.

Olariu, C., Krezsek, C., and Jipa, D. C.: The Danube River inception: Evidence for a 4 Ma continental-scale river born from segmented ParaTethys basins, Terra Nova, 30, 63–71, https://doi.org/10.1111/ter.12308, 2018.

Oszczypko, N.: Late Jurassic-Miocene evolution of the Outer Carpathian fold-and-thrust belt and its foredeep basin (Western Carpathians, Poland), 25, 2006.

Oszczypko, N. and Oszczypko-Clowes, M.: Stages of development in the Polish Carpathian Foredeep basin, Open Geosciences, 4, https://doi.org/10.2478/s13533-011-0044-0, 2012.

Palcu, D. V., Patina, I. S., Şandric, I., Lazarev, S., Vasiliev, I., Stoica, M., and Krijgsman, W.: Late Miocene megalake regressions in Eurasia, Sci Rep, 11, 11471, https://doi.org/10.1038/s41598-021-91001-z, 2021.

Popov, S. V., Bugrova, E. M., Amitrov, O. V., Andreyeva-Grigorovich, A. S., Akhmetiev, M. A., Zaporozhets, N. I., Nikolaeva, I. A., Sychevskaja, E. K., and Shcherba, I. G.: Biogeography of the Northern Peri-Tethys from the Late Eocene to the Early Miocene. Part 3. Late Oligocene-Early Miocene. Marine Basins, 38, 64, 2004.

Popov, S. V., Antipov, M. P., Zastrozhnov, A. S., Kurina, E. E., and Pinchuk, T. N.: Sea-level fluctuations on the northern shelf of the Eastern Paratethys in the Oligocene-Neogene, Stratigr. Geol. Correl., 18, 200–224, https://doi.org/10.1134/S0869593810020073, 2010.

Roure, F., Roca, E., and Sassi, W.: The Neogene evolution of the outer Carpathian flysch units (Poland, Ukraine and Romania): kinematics of a foreland/fold-and-thrust belt system, Sedimentary Geology, 86, 177–201, https://doi.org/10.1016/0037-0738(93)90139-V, 1993.

Royden, L. H. and Husson, L.: Subduction with Variations in Slab Buoyancy: Models and Application to the Banda and Apennine Systems, in: Subduction Zone Geodynamics, edited by: Lallemand, S. and Funiciello, F., Springer Berlin Heidelberg, Berlin, Heidelberg, 35–45, https://doi.org/10.1007/978-3-540-87974-9_2, 2009.

Sanders, C., Huismans, R., van Wees, J. D., and Andriessen, P.: The Neogene history of the Transylvanian basin in relation to its surrounding mountains, Stephan Mueller Spec. Publ. Ser., 3, 121–133, https://doi.org/10.5194/smsps-3-121-2002, 2002.

Scherler, D. and Schwanghart, W.: Drainage divide networks – Part 2: Response to perturbations, Earth Surf. Dynam., 8, 261–274, https://doi.org/10.5194/esurf-8-261-2020, 2020.

Schildgen, T. F., van der Beek, P. A., D'Arcy, M., Roda-Boluda, D., Orr, E. N., and Wittmann, H.: Quantifying drainage-divide migration from orographic rainfall over geologic timescales: Sierra de Aconquija, southern Central Andes, Earth and Planetary Science Letters, 579, 117345, https://doi.org/10.1016/j.epsl.2021.117345, 2022.

Schlunegger, F., Matter, A., Burbank, D. W., and Klaper, E. M.: Magnetostratigraphic constraints on relationships between evolution of the central Swiss Molasse basin and Alpine orogenic events, Geological Society of America Bulletin, 109, 225–241, https://doi.org/10.1130/0016-7606(1997)109<0225:MCORBE>2.3.CO;2, 1997.

Seghedi, I. and Downes, H.: Geochemistry and tectonic development of Cenozoic magmatism in the Carpathian–Pannonian region, Gondwana Research, 20, 655–672, https://doi.org/10.1016/j.gr.2011.06.009, 2011.

Şengül-Uluocak, E., Pysklywec, R. N., Göğüş, O. H., and Ulugergerli, E. U.: Multidimensional Geodynamic Modeling in the Southeast Carpathians: Upper Mantle Flow-Induced Surface Topography Anomalies, Geochem. Geophys. Geosyst., 2019GC008277, https://doi.org/10.1029/2019GC008277, 2019.

Sperner, B., Ratschbacher, L., and Nemčok, M.: Interplay between subduction retreat and lateral extrusion: Tectonics of the Western Carpathians: TECTONICS OF THE WESTERN CARPATHIANS, Tectonics, 21, 1-1-1–24, https://doi.org/10.1029/2001TC901028, 2002.

Ustaszewski, K., Schmid, S. M., Fügenschuh, B., Tischler, M., Kissling, E., and Spakman, W.: A map-view restoration of the Alpine-Carpathian-Dinaridic system for the Early Miocene, Swiss J. Geosci., 101, 273–294, https://doi.org/10.1007/s00015-008-1288-7, 2008.

Webb, A. A. G., Guo, H., Clift, P. D., Husson, L., Müller, T., Costantino, D., Yin, A., Xu, Z., Cao, H., and Wang, Q.: The Himalaya in 3D: Slab dynamics controlled mountain building and monsoon intensification, Lithosphere, L636.1, https://doi.org/10.1130/L636.1, 2017.

Whipple, K. X., Forte, A. M., DiBiase, R. A., Gasparini, N. M., and Ouimet, W. B.: Timescales of landscape response to divide migration and drainage capture: Implications for the role of divide mobility

in landscape evolution, J. Geophys. Res. Earth Surf., 122, 248–273, https://doi.org/10.1002/2016JF003973, 2017.

Willett, S. D., Slingerland, R., and Hovius, N.: Uplift, Shortening, and Steady State Topography in Active Mountain Belts, Am J Sci, 301, 455–485, https://doi.org/10.2475/ajs.301.4-5.455, 2001.

Wortel, M. J. R. and Spakman, W.: Subduction and Slab Detachment in the Mediterranean-Carpathian Region, Science, 290, 1910–1917, https://doi.org/10.1126/science.290.5498.1910, 2000.

Supplementary Material

Chapter II supplements

Sect. S1

From supplementary figure S1, we discriminate the reset and partially reset samples from the non-reset samples (S1, a). CAR19-061 is the only non-reset samples we have in our set, but CAR19-045 and CAR19-066 are very close to the limit and the 2σ error fall in the left part of the limit line. Repartition of the AFT age as a function of the elevation of the sampling site mark a pattern of increased altitude for older ages, apart from the samples from Magura nappe (i.e., CAR19-061 and CAR19-066). The difference in elevation is low (≈ 500m) for our data set. Usually more elevated samples tend to have younger ages due to the thermal regime in mountains belt where elevated area possess higher heat production (concentration of crust material in the high elevated areas) and faster heat advection (by active topography building and thrusting/fault activity). Strikingly the oldest and highest samples are beared in the more external nappes (Krosno and Skyba nappes) and as elevation decrease, the youngest samples are toward the internal nappes (Burkut and Dukla nappes). The Magura nappe, which is the back stop of our wedge, is showing the oldest ages and the lowest elevation in the dataset, implying less burial coupled with a longer period of exposition to erosion for this nappe. For the rest of the units, the increase of age toward the outer belt and the higher elevation is coherent with the dynamic of the retreating subduction zone and a thermally "immature" wedge building in the Ukrainian Carpathians (Dahlen et al., 1984; Royden, 1993a, b; Willett and Brandon, 2002; Husson and Moretti, 2002). The mean track length (MTL) compared to the age of the AFT samples don't display any pattern of shorter tracks in younger samples. High dispersion (> 30%) is present for all our samples (except for CAR19-068 with 25% and CAR19-062 with 29%) and samples often show two to three grain populations. This high difference inside each sample can lead to no correlation in track length measurement and AFT age, especially when track length measurement is low (in our case no more than 21 track measured in a sample).

Sect. S2 and S3

AHe single-grain age from our study show non-reset ages (CAR19-066_a2 and for CAR19-072_a2) and some partial reset ages (see A1 a), c) and e)). Most of the AHe ages are around 10 Ma when reset. The AHe with ages close to the CA of the corresponding AFT can be the result of the differential annealing between the grain population (this is the case for sample CAR19-061, -066 and -072). Comparing the ESR (equivalent spherical radius) and the eU (equivalent Uranium content) to the AHe single-grain age show no correlation of these parameters. Old AHe ages are in the mean range for the eU content (10-

60 ppm) and the ESR (60-80 μm) and AHe ages around 10 Ma pertain the maximum and minimum in both characteristics. Sample CAR19-068 has the smallest differences among grains for eU and ESR, in accordance with a single population in AFT ages (25 % of dispersion).

ZHe ages compared to the stratigraphic age (A1 b)) show the clear non-reset of the thermochronometer in our data. We also identified a population of ages around 100 Ma, and one older ranging from 200 – 400 Ma. As for AHe single grain, there are no evident correlations between the ZHe ages and ESR or eU content. It is worth noticing that for zircons, CAR19-068 show a larger dispersion of grains characteristics, unlike CAR19-061 and CAR19-062 that display great similarities between grains (except for CAR19-061_z4) which do not show for the apatite grains.

References

Dahlen, F. A., Suppe, J., and Davis, D.: Mechanics of fold-and-thrust belts and accretionary wedges: Cohesive Coulomb Theory, J. Geophys. Res., 89, 10087–10101, https://doi.org/10.1029/JB089iB12p10087, 1984.

Husson, L. and Moretti, I.: Thermal regime of fold and thrust belts—an application to the Bolivian sub Andean zone, Tectonophysics, 345, 253–280, https://doi.org/10.1016/S0040-1951(01)00216-5, 2002.

Royden, L. H.: The steady state thermal structure of eroding orogenic belts and accretionary prisms, J. Geophys. Res., 98, 4487–4507, https://doi.org/10.1029/92JB01954, 1993a.

Royden, L. H.: The tectonic expression slab pull at continental convergent boundaries, Tectonics, 12, 303–325, https://doi.org/10.1029/92TC02248, 1993b.

Willett, S. D. and Brandon, M. T.: On steady states in mountain belts, Geol, 30, 175, https://doi.org/10.1130/0091-7613(2002)030<0175:OSSIMB>2.0.CO;2, 2002.

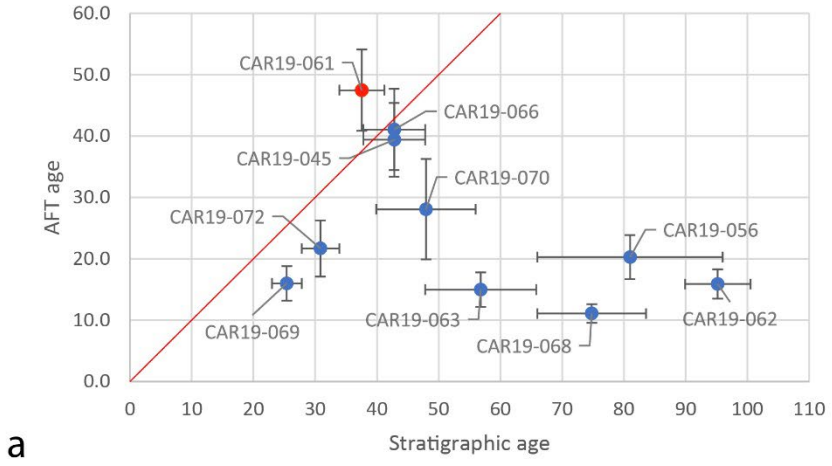

a

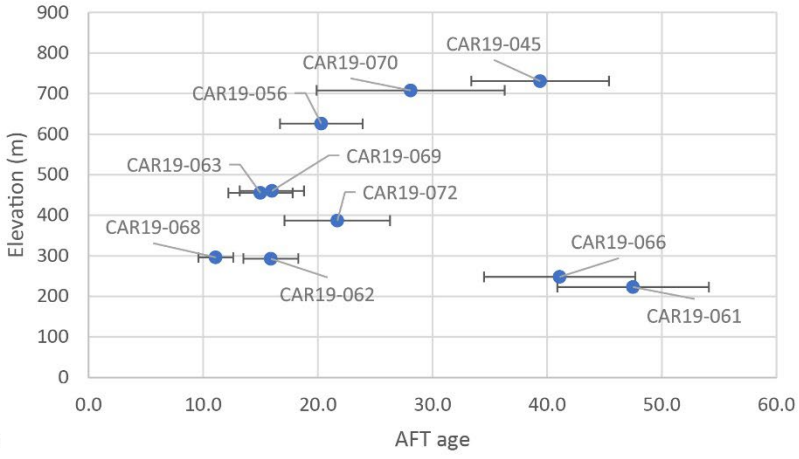

b

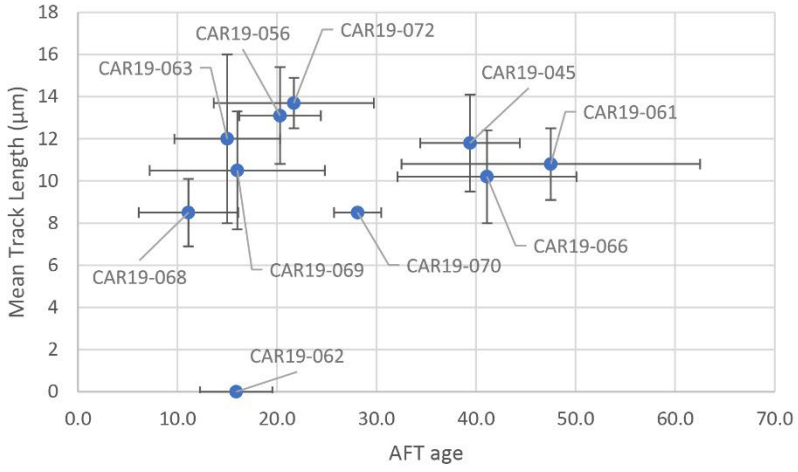

c

S 8: a) Graphic of AFT age vs. Stratigraphic age, both scales are in My. The red line shows the delimitation for: on the left non-reset samples (here only CAR19-061); on the right reset and partially reset samples. CAR19-045 and CAR19-066 samples display very poor partial resetting compared to the reset of the "reset" samples. b) AFT age vs. Elevation of the sampling site. Elevation and topography are supposed to have remained low in the Ukrainian Carpathians region. The older AFT ages are at a higher elevation in our case, is we speak in terms of nappes, the external nappes Krosno and Skyba (CAR19-

045, -056, -069, -070, -072) have higher elevation and older AFT central age. Burkut and Dukla samples (CAR19-062, -063, -068) are more internal and les elevated but also younger for AFT thermochronometer. The samples out of the trend of younger AFT ages toward low elevation are the samples from Magura nappe (CAR19-061, -066), both showing non-rest or very poor partial resetting. c) AFT age vs. Mean track length (CAR19-062 has no track length counted). Mean track length should align with the degree of resetting of each sample i.e., annealing of tracks is due to higher burial temperature or long residence at the PAZ, and should correspond to higher degree of resetting of the AFT. This pattern isn't obvious in our dataset. Non-reset, or very poorly reset sample (CAR19-061, -066, -045) have MTL of 10-12 µm, comparable to the MTL of CAR19-063 and CAR19-069, which display more resetting.

Sample	mineral	Ft corrected Age, Ma	2s analytic err., Ma	weighted 2s analytic err., Ma	U (ppm)	Th (ppm)	147Sm (ppm)	[U]e	Th/ 238U	He (nmol/g)	mass (ug)	Ft	ESR (mm)
Dur930_a1	Apatite	40.6410	1.5143	1.0937	1.6224	27.5233	3.6929	8.0903	17.5284	1.7959	37.5024	1.0000	121.8247
Dur930_a2	Apatite	30.6691	1.1054	0.8652	3.5240	70.2528	8.9501	20.0334	20.5975	3.3550	25.3718	1.0000	107.0631
Dur930_a3	Apatite	29.6255	0.3847	0.2803	3.6537	64.1073	7.3323	18.7189	18.1287	3.0262	33.7372	1.0000	115.2892
CAR19-63_a1	Apatite	9.3098	0.4653	0.2995	5.9116	18.7023	3.8020	10.3066	3.2687	0.4069	6.5145	0.7808	68.4279
CAR19-62_a1	Apatite	41.0700	1.0824	0.6261	11.9649	44.8312	22.0715	22.5002	3.8713	4.0394	8.3652	0.7990	74.6325
CAR19-62_a2	Apatite	10.7433	0.5395	0.3764	10.9541	88.9777	4.0780	31.8638	8.3926	1.4163	5.1058	0.7615	62.8878
CAR19-62_a3	Apatite	3.4658	0.2089	0.1355	1.7702	45.4976	5.3992	12.4622	26.5551	0.1859	7.1869	0.7890	71.0808
CAR19-56_a1	Apatite	9.7806	0.3043	0.1691	24.6810	78.8466	48.6459	43.2099	3.3007	1.7365	4.6311	0.7519	60.4649
CAR19-56_a2	Apatite	9.1818	0.3653	0.2125	44.7140	180.2646	22.6570	87.0762	4.1654	3.3541	5.9541	0.7727	65.9914
CAR19-56_a3	Apatite	8.9343	0.2880	0.1100	136.8446	194.3596	60.2509	182.5191	1.4675	6.6015	4.3863	0.7471	59.3007
CAR19-69_a1	Apatite	12.1729	0.3960	0.1241	34.8693	116.1868	7.4685	62.1732	3.4427	3.2048	6.4073	0.7811	68.5161
CAR19-69_a2	Apatite	9.6729	0.2208	0.1316	19.7150	79.9881	8.7512	38.5122	4.1919	1.6454	10.4309	0.8137	80.5269
CAR19-69_a3	Apatite	13.8216	0.2591	0.1614	37.6026	82.7747	44.5435	57.0546	2.2744	3.4600	9.4982	0.8056	77.1795
CAR19-45_a1	Apatite	8.1836	0.2041	0.1793	7.6135	18.5761	16.5109	11.9789	2.5209	0.4199	6.7071	0.7829	69.0783
CAR19-45_a2	Apatite	17.0282	0.9147	0.5099	4.4731	36.0914	13.1468	12.9546	8.3365	0.9134	4.9951	0.7564	61.5710
CAR19-45_a3	Apatite	9.1607	0.3834	0.2432	10.4214	68.1773	24.7579	26.4430	6.7593	1.0989	15.3844	0.8300	88.2276
CAR19-47_a1	Apatite	0.1376	0.1018	0.1006	9.3638	2.1437	60.8062	9.8675	0.2365	0.0062	9.0567	0.8049	76.8677
CAR19-47_a2	Apatite	9.5252	0.1954	0.1369	25.3028	31.6357	17.6197	32.7372	1.2918	1.4045	13.7679	0.8299	88.1766
CAR19-47_a3	Apatite												58.9836
CAR19-72_a1	Apatite	18.3523	0.7660	0.6159	7.5814	22.9412	11.7066	12.9726	3.1265	1.0064	5.9513	0.7746	66.5509
CAR19-72_a2	Apatite	29.5703	1.2009	0.3223	35.0301	5.1192	21.7665	36.2331	0.1510	4.6153	7.9205	0.7934	72.6115
0	Apatite												
CAR19-68_a1	Apatite	6.5524	0.2327	0.1858	15.9909	387.7030	52.7088	107.1011	25.0504	2.9204	5.4076	0.7623	63.1033
CAR19-68_a2	Apatite	7.1685	0.3440	0.2577	22.4447	291.8276	39.0549	91.0242	13.4338	2.7653	6.3322	0.7774	67.3988
CAR19-68_a3	Apatite	7.0698	0.1375	0.1116	27.5763	345.8539	44.8668	108.8519	12.9582	3.1739	4.8811	0.7568	61.6704
CAR19-61_a1	Apatite	14.5630	0.9784	0.7508	4.4300	28.1176	41.0434	11.0376	6.5579	0.6532	3.4885	0.7268	54.9090
CAR19-61_a2	Apatite	14.7863	0.7559	0.5105	6.5782	13.6280	23.1122	9.7808	2.1405	0.6074	5.1637	0.7615	62.8820
CAR19-61_a3	Apatite	26.9930	1.0998	0.6561	14.6078	5.4670	9.1366	15.8926	0.3867	1.7545	4.5442	0.7533	60.8114
CAR19-66_a1	Apatite	12.9991	0.4361	0.2163	44.9248	128.3676	6.8123	75.0912	2.9523	4.1610	7.3172	0.7867	70.3385
CAR19-66_a2	Apatite	54.9751	1.6715	0.7189	29.1782	22.0699	21.6131	34.3646	0.7815	8.0182	6.7318	0.7791	67.9059
CAR19-66_a3	Apatite	9.0592	0.6903	0.4977	7.4556	41.6717	12.3364	17.2484	5.7749	0.6155	3.3438	0.7223	54.0127

S2: Table of raw result for AHe

Sample	mineral	Ft corrected Age, Ma	2s analytic err., Ma	weighted 2s analytic err., Ma	U (ppm)	Th (ppm)	147Sm (ppm)	[U]e	Th/ 238U	He (nmol/g)	mass (ug)	Ft	ESR (mm)
FCT102020_z1	zircon	33.0779	7.5619	0.5257	321.8962	234.3351	0.6548	376.9649	0.7522	45.8849	3.0250	0.6803	37.7482
FCT102020_z2	zircon	31.3226	1.9049	0.3733	170.1877	108.8041	0.3445	195.7567	0.6605	26.7201	8.2809	0.8058	64.3600
CAR19-45_z1	zircon	23.2087	2.6997	0.5494	1.8720	23.7099	0.5864	7.4438	13.0863	0.7789	9.4819	0.8290	79.4660
CAR19-45_z2	zircon	11.0089	4.7565	2.4292	0.7659	5.3431	0.3388	2.0215	7.2083	0.0933	5.8554	0.7714	57.6151
CAR19-45_z3	zircon	298.5007	14.4691	2.3075	483.7465	74.9364	0.6139	501.3565	0.1601	704.9022	17.0114	0.8506	83.6214
CAR19-47_z1	zircon	417.4372	11.6336	2.6335	66.0032	62.7623	0.4220	80.7523	0.9825	164.9278	25.4927	0.8763	105.4407
CAR19-47_z2	zircon	229.0865	35.9548	4.7439	54.1031	73.8241	0.6663	71.4518	1.4098	71.4482	6.6352	0.7941	61.4000
CAR19-56_z1	zircon	491.6974	131.7172	15.6788	52.3130	77.3411	0.5332	70.4882	1.5275	150.1569	4.8454	0.7726	55.3641
CAR19-56_z2	zircon	14.5933	1.0015	0.7795	2.3507	70.0850	2.5334	18.8207	30.8048	1.2061	8.6971	0.8063	70.7670
CAR19-56_z3	zircon	432.2861	8.9814	4.8452	98.7732	123.3666	1.0325	127.7643	1.2905	259.7290	14.9714	0.8419	80.8705
CAR19-56_z4	zircon	328.7016	13.6658	3.3071	41.7588	25.1998	0.1921	47.6807	0.6235	71.8003	10.7437	0.8259	72.1294
CAR19-61_z1	zircon	113.2196	7.9114	0.8262	212.4424	61.1805	0.3456	226.8198	0.2975	111.2387	6.6005	0.7956	60.4300
CAR19-61_z2	zircon	89.5871	2.9808	0.9347	274.9460	132.0132	0.6069	305.9691	0.4961	121.2298	9.7467	0.8139	67.0477
CAR19-61_z3	zircon	85.3967	6.8046	0.7392	269.5291	58.3756	0.4471	283.2473	0.2238	106.0204	9.0958	0.8071	64.1158
CAR19-61_z4	zircon	91.6023	10.4021	0.4673	853.1514	260.7592	1.2641	914.4299	0.3158	364.1913	6.5445	0.8001	61.9002
CAR19-61_z5	zircon	117.6210	21.2997	1.2492	111.4603	43.7683	0.5569	121.7459	0.4057	63.2141	8.3012	0.8104	65.6077
CAR19-62_z1	zircon	128.5603	82.7970	1.3623	47.0322	35.7300	0.3093	55.4287	0.7849	31.5564	8.8623	0.8121	66.8114
CAR19-62_z2	zircon	112.4478	7.9154	1.7741	204.8089	190.1343	2.4967	249.4904	0.9592	120.6091	5.2782	0.7893	61.8883
CAR19-62_z3	zircon	128.6948	13.6738	1.3362	74.5673	111.7824	0.3609	100.8362	1.5489	58.2647	9.4946	0.8232	72.2393
0	zircon												
CAR19-62_z5	zircon	114.0263	10.5994	1.5466	167.8298	55.6044	0.5294	180.8968	0.3423	87.8688	6.3486	0.7823	56.6021
CAR19-63_z1	zircon	89.0035	8.2054	0.7706	39.9423	51.3777	0.1557	52.0160	1.3290	20.8521	10.4026	0.8284	76.5229
CAR19-63_z2	zircon	123.4546	32.1377	1.0357	65.0884	39.8401	0.1333	74.4508	0.6324	40.6004	7.1852	0.8105	68.2861
CAR19-63_z3	zircon	125.4800	4.9690	2.1780	144.9479	55.8809	0.2032	158.0799	0.3983	95.2225	24.2811	0.8807	106.2383
CAR19-63_z4	zircon	175.9403	5.6787	1.5882	534.7861	60.4791	0.5327	548.9987	0.1168	411.5353	6.3745	0.7781	55.1181
CAR19-63_z5	zircon	105.0599	2.6387	1.1643	372.8938	197.6002	3.0968	419.3298	0.5475	165.7593	1.8374	0.6914	39.0679
CAR19-66_z1	zircon	101.8189	3.9205	1.2964	211.8903	34.9907	0.6925	220.1132	0.1706	98.5079	9.5454	0.8082	64.4005
CAR19-66_z2	zircon	118.9471	5.9535	1.6693	115.1342	184.1259	1.0811	158.4037	1.6523	86.4236	12.6139	0.8415	83.3290
CAR19-66_z3	zircon	300.7198	26.6695	3.7096	125.4931	140.1285	1.5333	158.4233	1.1537	190.9245	2.9231	0.7248	44.8215
CAR19-66_z4	zircon	71.5560	1.9735	0.6672	272.3742	34.4460	0.5183	280.4690	0.1307	85.3193	6.0038	0.7839	56.7080
CAR19-66_z5	zircon	94.5718	16.5509	1.2561	24.6033	23.1122	0.3031	30.0347	0.9706	12.4679	7.4494	0.8071	67.6022
CAR19-72_z1	zircon	99.6084	6.3806	0.8453	405.5592	119.9780	0.5541	433.7540	0.3057	185.5380	4.4553	0.7897	58.6497
CAR19-72_z2	zircon	134.9585	12.0625	3.9770	0.4980	3.3625	2.1418	1.2882	6.9760	0.7507	6.5902	0.7803	60.0615
CAR19-72_z3	zircon	210.2957	13.5552	2.3957	495.8861	266.6524	3.4043	558.5494	0.5556	516.7891	7.4460	0.8012	62.6400
CAR19-68_z1	zircon	265.0770	6.0549	2.4480	227.7122	135.7231	0.6312	259.6071	0.6158	307.2216	8.1180	0.8092	65.5176
CAR19-68_z2	zircon	152.2001	15.5668	1.5932	737.7957	141.2934	1.2249	770.9996	0.1979	522.2199	8.4707	0.8145	66.7699
CAR19-68_z3	zircon	231.6371	11.3381	1.8068	132.6312	26.8340	0.2381	138.9372	0.2090	146.8286	12.5871	0.8290	72.7415
CAR19-69_z1	zircon	209.2321	34.0198	2.2033	106.0072	12.6138	0.0877	108.9714	0.1229	99.2956	6.1915	0.7929	59.3174
CAR19-69_z2	zircon	97.6811	9.1464	1.4804	124.4586	67.3612	0.3279	140.2885	0.5592	58.5293	6.7173	0.7854	57.7745
CAR19-69_z3	zircon	63.3571	2.7175	0.6286	124.3378	93.4843	0.8481	146.3066	0.7768	39.9275	6.9708	0.7942	60.6918
CAR19-69_z4	zircon	107.1800	4.8733	1.4282	126.1544	87.3496	0.3179	146.6816	0.7154	68.4215	7.0839	0.7996	62.3308
CAR19-69_z5	zircon	43.3743	3.5820	1.8252	0.6895	8.5991	2.9336	2.7102	12.8864	0.5136	9.5696	0.7960	66.0010

S3: Table of raw result for ZHe

Chapter III supplements

Low temperature thermochronology database of the Carpathians

The following tables display the thermochronological data we compiled for the Carpathian belt. The description of the database is provided in section 1.1 of the Chapter III of this manuscript.

Database name	AFT COMPILATION																	
								Calculation						Dosimeter		Age		
	Source	Sample	lat	long	(m)	lithology	stratigraphic age (Ma)	Tectonic units	Ngr	ρs (10^6/cm²)	Ns	ρi (10^6/cm²)	Ni	ρd (10^6/cm²)	Nd	P(χ²) %	Central age	1σ
ROMmer11_RO-02	Merten Thesis	RO-02	45.1264855	26.45489553	339	sandstone	11.5-10.5	foredeep	80	0.372	1742	1.403	6570			0		
ROMmer11_RO-04		RO-04	45.29951944	26.35936638	285	sandstone	10.5-8.5	Foredeep	51	0.593	1056	2.177	3879			0		
ROMmer11_RO-05		RO-05	45.38603641	26.3215152	357	sandstone	37.2-23.0	Tarcau nappe	37	0.399	534	2.042	2732			0		
ROMmer11_RO-06		RO-06	45.44731927	26.27465184	892	sandstone	65.5-40.4	Tarcau nappe	76	0.199	1056	1.455	7719			0		
ROMmer11_RO-07		RO-07	45.57168741	26.17371538	873	sandstone	65.5-40.4	Tarcau nappe	40	0.055	205	1.321	4895			0		
ROMmer11_RO-08		RO-08	45.753733354	25.86549867	522	conglomerate	130.0-112.0	Ceahlau nappe	21	0.092	96	1.242	1291			1		
ROMmer11_RO-09		RO-09	45.84205295	25.42930894	922	conglomerate	98.9-93.5	post-cretaceous cover	78	0.426	1681	1.026	4045			0		
ROMmer11_RO-10		RO-10	45.851065113	25.27249693	520	schist		Bucovinian nappe	32	0.265	354	0.418	559			59		

ROMmer11_RO-11		RO-11	45.99706252	25.19859701	470	sandstone	16.0-12.5	transylvanian hinterland	43	0.586	913	2.218	3458			0
ROMmer11_RO-12		RO-12	45.8690895	25.70147691	763	conglomerate	125.0-112.0	Baraolt nappe	55	0.305	829	1.023	2786			7
POLand13_PL_25*	Andreiucci 2013 B	PL_25*	49.62108333	20.08341667	492	sandstone	27.82-15.97	Krosno beds	11	1.52	28	23.47	433	11.5	5405	94.3
POLand13_PL_31		PL_31	49.45158333	20.3166	667	sandstone	13.82-7.24	Andesites Mount Wzar	20	0.39	22	5.01	286	11.19	5318	100
POLand13_PL_46		PL_46	49.42295	21.66365	513	sandstone	27.82-23.03	Magura sand stone	20	10.24	376	35.6	1308	10.94	5201	0
POLand13_PL_47		PL_47	49.46768333	22.35785	376	sandstone	27.82-23.03	Krosno beds	20	5.7	239	29.2	1224	10.88	5172	0
UKRand14_PL_39	Andreiucci 2014	PL_39	49.278	23.406	402	sandstone	56.0-33.9	internal foredeep	11							0 73 ± 9.1
UKRand14_PL_50		PL_50	49.10535	23.59728	394	sandstone	41.2-23.03									
UKRand14_PL_52		PL_52	48.7549	23.01528	375	sandstone	89.8-66.0	audia nappe	20							0.71 6.2 ± 0.7
UKRand14_PL_53		PL_53	48.69062	23.03987	334	sandstone	56.0-33.9									
UKRand14_PL_54		PL_54	48.85612	23.11432	754	sandstone	33.9-23.03	Marginal fold	21							0.95 7.1 ± 1.2

UKRand14_PL_55		PL_55	48.9642	23.38268	577	sandstone	33.9-23.03					
UKRand14_PL_56		PL_56	48.65198	24.57653	408	sandstone	23.03-11.63	external foredeep	21		0	25.1 ± 5.8
UKRand14_PL_58		PL_58	48.0019	24.18608	442	basement	420-298					
UKRand14_PL_59		PL_59	47.92877	24.10122	358	basement	420-298	Ceahlau-severin	14		0.53	8.6 ± 1.4
UKRand14_PL_60		PL_60	47.98445	24.02183	312	sandstone	56.0-33.9					
UKRand14_PL_61		PL_61	48.06155	24.18275	582	sandstone	145-125	audia nappe	15		0.79	11.6 ± 1.7
UKRand14_PL_62		PL_62	48.07738	24.2403	471	sandstone	145-125	audia nappe	19		0.5	10.1 ± 1.3
UKRand14_PL_63		PL_63	48.1651	24.27502	551	sandstone	145-125	Marginal fold	15		0.51	9.8 ± 1.4
UKRand14_PL_64		PL_64	48.19787	24.3037	577	sandstone	89.8-56					
UKRand14_PL_65		PL_65	48.30572	24.44802	877	sandstone	33.9-23.03	Marginal fold	22		0.66	10.1 ± 1.2
UKRand14_PL_67		PL_67	48.22262	23.55803	206	sandstone	56.0-33.9	audia nappe	20		0	71 ± 10.1
UKRand14_PL_68		PL_68	48.31918	23.59305	423	sandstone	89.8-56					

UKRand14_PL_69		PL_69	48.3542	23.61838	459	sandstone	145-125	Marginal fold	20									0.18	8.7	±	0.9
UKRand14_PL_70		PL_70	48.39232	23.65317	530	sandstone	56.0-33.9	Marginal fold	20									0.25	9.7	±	1.5
SLOdan10_MF-1	Danisik 2010	MF-1	49.14861111	18.82583333	658	granite	420-298		25	0.2546	319	2.4427	3061	0.664	3929	95	11.2		0.7			
SLOdan10_MF-3		MF-3	49.08333333	18.7375	606	granite	420-298		25	0.4158	217	3.1754	1657	0.6713	3929	52	13.8		1.4			
SLOdan10_MF-4		MF-4	49.17972222	19.12527778	546	granite	420-298		25	0.241	319	2.6536	3616	0.6713	3929	95	9.6		0.6			
SLOdan10_MF-5		MF-5	49.15083333	18.90694444	862	granite	420-298		25	0.1453	128	1.2403	1093	0.6783	3929	95	12.8		1.2			
SLOdan10_MF-6		MF-6	49.08444444	18.74944444	672	granite	420-298		25	0.288	382	3.1708	4205	0.6853	3929	92	10.1		0.6			
SLOdan10_MF-7		MF-7	49.09972222	18.7525	721	granite	420-298		25	0.203	280	1.2922	1782	0.5166	4936	95	13.8		1			
SLOdan11_BT-222	Danisik 2011	BT-222	49.004	20.879	757	tonalitic gneiss	358-298	North Meliata	20	0.4425	236	2.8236	1506	0.7098	3315	95	17.4		1.3			
SLOdan11_BT-485		BT-485	49.011	20.913	733	tonalite	358-298	PKB	20	0.6844	344	5.3601	2694	0.7093	3315	95	14.2		0.9			
SLOdan11_BT-487		BT-487	49.023	20.876	966	granodiorite	358-298	PKB	22	0.1709	222	1.1891	1545	0.7084	3315	66	15.9		1.2			
SLOdan11_BT-490		BT-490	49.005	20.915	651	sandstone	33-28	PKB	33	0.3495	265	2.1352	1619	0.7089	3315	49	18.2		1.3			

SLOdan11_BT-491		BT-491	49.009	20.836	524	sandstone	37-33	North Meliata	50	0.3822	677	1.6289	2885	0.7102	3315	0	27.6		2.2
ROMtis06_1	Tischler 2006 (dans groger thesis)	1	47.52537778	24.60943506	2020	-	-	Bucovinian nappe	24	0.441	539	6.571	8030			8	11.6	±	0.7
ROMtis06_2		2	47.52099137	24.59792073	1465	-	-	Bucovinian nappe	20	0.255	357	5.469	7646			10	11	±	0.8
ROMtis06_3		3	47.51742742	24.59216357	1310	-	-	Bucovinian nappe	20	0.248	496	4.858	9716			13	11.6	±	0.7
ROMtis06_4		4	47.51550836	24.58503566	1155	-	-	Bucovinian nappe	20	0.038	50	0.83	1096			99	10.2	±	1.5
ROMtis06_5		5	47.51221856	24.57050568	945	-	-	Bucovinian nappe	20	0.094	111	1.589	1873			79	8.6	±	0.9
ROMgro08_M01	Groger 2008	M01	47.72979	24.49667	540	-	-	Bucovinian nappe	25	0.049	73	11.221	16596	119.59	6511	10	9.6		1.2
ROMgro08_M02		M02	47.75372	24.56071	580	-	-	Ceahlau-severin	20	0.094	114	13.873	16842	98.14	6511	32	11.8		1.2
ROMgro08_M03		M03	47.77254	24.58664	630	-	-	audia nappe	15	0.112	64	14.809	8471	77.35	3606	55	10.4		1
ROMgro08_M04		M04	47.79145	24.6281	680	-	-	audia nappe	20	0.129	129	3.566	3580	14.1	4605	58	9		0.9
ROMgro08_M05		M05	47.8043	24.66709	745	-	-	audia nappe	20	0.224	168	2.873	2155	7.74	4223	99	10.7		0.9
ROMgro08_M06		M06	47.79085	24.69859	790	-	-	audia nappe	3	0.051	10	8.759	1708	116.61	4196	39	12.1		3.9

ROMgro08_M08		M08	47.690263	24.770543	820	-	-	audia nappe	2	0.098	4	4.39	180	8.52	4451	60	3.4	1.7
ROMgro08_M09		M09	47.647505	24.833619	1660	-	-	audia nappe	16	0.053	31	9.019	5276	96.19	5773	99	10.1	1.8
ROMgro08_M13		M13	47.571246	25.12822	930	-	-	audia nappe	20	0.044	64	0.857	1261	10.81	4451	99	9.8	1.3
ROMgro08_M14		M14	47.478662	25.27951	850	-	-	audia nappe	20	0.134	152	3.243	3668	10.5	4451	26	7.8	0.7
ROMgro08_P1		P1	47.430957	23.57476	315	-	-	Bucovinian nappe	20	0.306	297	0.84	815	10.23	4223	65	66	4.9
ROMgro08_P2		P2	47.509842	23.628772	215	-	-	vahic	20	0.633	713	1.679	1892	8.93	4223	9	59.4	3.7
ROMgro08_P3		P3	47.488712	23.686807	610	-	-	vahic	20	0.693	671	1.818	1760	9.37	4223	5	64	4.6
ROMgro08_P4		P4	47.465312	23.810507	350	-	-	Valais	22	0.109	150	2.693	3724	94.57	6511	43	67.5	6
ROMgro08_P5		P5	47.488947	23.81726	390	-	-	vahic	20	1.813	2489	4.493	6169	8.5	4223	5	61.6	3
ROMgro08_P6		P6	47.503686	23.82454	430	-	-	vahic	20	1.412	1028	3.789	2758	9.8	4223	5	65.2	4
ROMgro08_P7		P7	47.503894	23.846548	380	-	-	vahic	20	0.484	456	1.572	1482	11.44	4451	94	62.3	0.8
ROMgro08_R1-1		R1-1	47.59786	24.55936	1550	-	-	Bucovinian nappe	20	0.058	41	1.186	837	14.55	4766	97	12.7	2.1

ROMgro08_R2-2		R2-2	47.41492	24.59726	1105	-	-	Infrabucivinian	20	0.041	63	9.325	14333	121.63	4196	92	9.5	1.2
ROMgro08_R2-4		R2-4	47.4193	24.59043	705	-	-	Infrabucivinian	20	0.052	51	10.836	10717	118.28	4196	88	10	1.4
ROMgro08_R3-1		R3-1	47.533782	24.620652	2020	-	-	Bucovinian nappe	24	0.441	539	6.571	8030	9.78	4451	8	11.6	0.7
ROMgro08_R3-2		R3-2	47.42329	24.58285	1465	-	-	Infrabucivinian	20	0.255	357	5.469	7646	13.04	4766	10	11	0.8
ROMgro08_R3-3		R3-3	47.52893	24.60899	1310	-	-	Bucovinian nappe	20	0.248	496	4.858	9716	12.79	4766	13	11.6	0.7
ROMgro08_R3-4		R3-4	47.52633	24.60445	1155	-	-	Bucovinian nappe	20	0.038	50	0.83	1096	12.54	4766	99	10.2	1.5
ROMgro08_R3-6		R3-6	47.51869	24.58798	945	-	-	Bucovinian nappe	20	0.094	111	1.589	1873	8.17	4223	79	8.6	0.9
ROMgro08_R4-2		R4-2	47.49816	24.93105	1305	-	-	Bucovinian nappe	20	0.072	85	3.819	4499	13	4451	46	4.4	0.5
ROMgro08_R4-3		R4-3	47.49471	24.94101	980	-	-	Bucovinian nappe	20	0.202	216	5.345	5730	12.48	4451	84	8.4	0.6
ROMgro08_R4-4		R4-4	47.49043	24.96023	700	-	-	Bucovinian nappe	20	0.089	73	2.652	2185	12.27	4451	95	7.3	0.9
ROMgro08_R5-1		R5-1	47.552021	24.546451	1150	-	-	Bucovinian nappe	20	0.131	93	2.094	1487	9.26	4451	93	10.3	1.1
ROMgro08_R5-3		R5-3	47.55026	24.95187	1400	-	-	Bucovinian nappe	20	0.302	218	5.172	3734	9.22	4557	8	9.6	0.9

ROMgro08_S1		S1	47.854	24.29636	550	-	-	Ceahlau-severin	38	0.269	514	4.123	7884	12.91	4605	29	15		0.9
ROMgro08_S2		S2	47.78221	24.11195	350	-	-	Infrabucivinian	39	0.925	1787	3.357	6489	10.97	4605	5	59.2		5
ROMgro08_S3		S3	47.64102	24.35165	530	-	-	Bucovinian nappe	40	0.721	1500	3.293	6850	12.27	4605	5	48.6		3
ROMgro08_S4		S4	47.63513	24.34837	555	-	-	Bucovinian nappe	21	0.161	174	2.152	2320	12.59	4605	12	17.2		1.6
ROMgro08_S5		S5	47.59906	24.03017	555	-	-	Bucovinian nappe	36	0.148	242	12.953	21178	94.83	4196	5	19.7		2.2
SLOkra14_SKAN	Kralikova 2014	SKAN	49.04927778	19.04980556	589	granodiorite	358-298	Tatric basement	23	0.3352	428	1.928	2462	0.8583	17220	23	25.1	±	2.2
SLOkra14_B1		B1	49.04730556	18.86569444	518	granite pebbles	5.33-2.58	turiec group	22	0.1283	63	1.699	834	0.9138	3000	100	12.8	±	2.1
SLOkra14_B2		B2	49.04725	18.86730556	503	granite pebbles	5.33-2.58	turiec group	30	0.2472	105	3.379	1435	0.8668	3000	100	11.8	±	1.7
SLOkra14_SBB		SBB	49.12086111	18.96816667	444	clay	12.6-4.7	turiec group	40	0.3062	1203	2.101	8252	0.8583	17720	0	17	±	1.7
SLOkra14_SJAN		SJAN	49.14961111	18.89138889	405	granodiorite	358-298	tatric besament	30	0.2653	755	4.245	12080	0.8583	17720	47	8.9	±	0.7
SLOkra14_SHSB		SHSB	48.81469444	18.89086111	662	Rhyolite tuff	12.6-4.7	turiec group	15	0.1679	93	3.838	2126	0.8583	17720	100	6.3	±	0.8
SLOkra14_SVC		SVC	48.89166667	18.80822222	468	granite pebbles	2.58-0.017	turiec group	15	0.9261	1042	5.002	5628	0.8583	17720	59	26.5	±	2

SLOkra14_SBUD		SBUD	48.87375	18.75383333	483	sand/gravel	2.58-0.017	aluvial fan	16	0.3578	281	3.259	2559	0.8583	17720	0	11.7	±	2.7
SLOkra14_SDS		SDS	49.13258333	18.88958333	476	granite pebbles	2.58-0.017	river terrace	40	0.1016	295	2.114	6139	0.8583	17720	0	7.7	±	1.1
ROMsan99_15	sanders 1999	15	46.73966652	25.41128457	800	amphibolite		Bucovinian nappe	31	0.3877	545	0.8984	1263	ff0278	2068		71		6
ROMsan99_16		16	47.06230273	25.91236203	600	sandstone	129-100	Marginal fold	39	0.1151	117	0.9169	932	0.0261	1944		19		4
ROMsan99_21		21	47.24254642	26.09260572	600	sandstone	33.9-23.03	external foredeep	15	0.0914	25	0.6181	169	0.0261	1944		30		8
ROMsan99_23		23	47.06410516	25.97544732	600	sandstone	145-100	Marginal fold	48	0.0535	63	0.2556	301	0.0261	1944		36		6
ROMsan99_24		24	46.945144433	26.05475454	600	sandstone	56-33.9	Marginal fold	34	0.0604	53	0.9204	807	0.0261	1944		10		2
ROMsan99_25		25	46.907293115	26.02411311	600	sandstone	56-41	Marginal fold	14	0.071	37	0.8582	447	0.0278	2068		14		3
ROMsan99_26		26	46.781122257	26.40622974	400	sandstone	33.9-27.8	internal foredeep	14	1.2991	417	1.271	408	0.0278	2068		103		24
ROMsan99_28		28	46.802751881	26.4044273	400	sandstone	33.9-23.03	internal foredeep	22	0.2069	113	0.2228	11o	0.0261	1944		155		30
ROMsan99_30		30	46.180911009	26.43326629	380	sandstone	23.03-15.9	Marginal fold	64	0.2813	745	0.9826	2602	0.0278	2068		47		4
ROMsan99_31		31	45.598723997	26.14487639	700	sandstone	100-66	Marginal fold	29	0.0351	53	1.1012	1661	0.0278	2068		5		1

ROMsan99_32		32	45.88711387	25.27249693	700	sandstone		Bucovinian nappe	22	0.2893	175	0.3257	197	0.0255	2273	134	18
ROMsan99_33		33	45.74652379	25.2761018	700	sandstone	33.9-23.03	Bucovinian nappe	32	0.5923	529	0.9909	885	0.0255	2273	88	8
ROMsan99_34		34	45.665414133	25.27069449	700	sandstone		Bucovinian nappe	25	0.7503	1067	2.0208	2874	0.0255	2273	56	4
ROMsan99_45		45	45.631167833	25.5302454	800	sandstone	110-93	Ceahlau-severin	81	0.3916	1947	0.8223	4089	0.0255	2273	72	5
ROMsan99_47		47	46.072764877	25.38244558	700	sandstone	23.03-5.33	Vadar	I00	0.6456	2273	1.1072	3898	0.0255	2273	85	6
ROMsan99_48		48	47.615650855	24.86334375	1280	sandstone	56-33.9	Marginal fold	84	0.0692	206	0.916	2728	0.0255	2273	12	1
ROMsan99_51		5I#	47.529133888	24.43436377	590	sandstone	33.9-27.8	Bucovinian nappe	45	0.1641	358	2.6352	5749	2.5342	46II	9	2
ROMsan99_52		52#	47.579602122	24.6506562	2130	sandstone		Bucovinian nappe	51	0,0124	41	0.1449	478	2.5342	4611	12	4
ROMsan99_64		64#	45.407665666	26.32512008	430	sandstone	66-56	Marginal fold	92	0.1993	660	1.0593	3508	2.5342	4611	27	7
ROMsan99_65		65#	45.46894851	26.27645428	500	sandstone	56-33.9	Marginal fold	55	0.2684	487	1.6385	2973	2.5342	4611	21	6
ROMsan99_66		66#	45.508602122	26.22778848	620	sandstone	33.9-23.03	Marginal fold	100	0.1955	938	1.1586	5558	2.5342	4611	24	6
ROMsan99_67		67#	45.544650866	26.17732025	630	sandstone	56-33.9	Marginal fold	115	0.1302	533	1.39	5689	2.5342	4611	12	3

ROMsan99_68		68#	45.66180926	26.07998866	680	sandstone	113-100	audia nappe	44	0.1191	351	1.0055	2963	2.5342	4611	16	4
ROMsan99_70		70#	46.28545243	26.74869275	250	sandstone	23.03-13.82	external foredeep	53	0.5087	2044	1.4264	5732	2.5342	4611	52	13
ROMsan99_72		72#	46.4747083	26.30889814	520	sandstone	145-66	internal foredeep	75	0.0768	282	0.9685	3609	2.5342	4611	11	3
ROMsan99_73		73#	46.55401552	26.08900084	680	sandstone	133-100	Marginal fold	52	0.063	164	0.9855	2566	2.5342	4611	9	2
ROMsan99_77		77#	47.60483623	23.99997648	600	sandstone	56-33.9	valais	73	0.0732	291	0.6646	2643	2.5342	4611	16	4
ROMsan99_78		78#	47.61745329	24.06486421	600	sandstone	33.9-23.03	Bucovinian nappe	45	0.108	266	1.84	4531	2.5342	4611	8	2
ROMsan99_80		80	46.739666522	25.62937943	835	schist		Bucovinian nappe	44	0.3434	896	1.9314	5040	0.026	2009	28	2
ROMsan99_81		81	46.782925001	25.72310615	1240	schist		Ceahlau-severin	27	0.2472	511	0.6985	1444	0.026	2009	53	4
ROMsan99_82		82	46.84060299	25.85288161	620	schist		Marginal fold	38	0.1484	386	0.3422	890	0.026	2009	50	9
ROMsan99_85		85	46.997415	25.78078413	620	schist		audia nappe	41	0.0616	I67	1.113	2868	0.026	2009	9	1
ROMsan99_86		86	46.525176519	26.16470319	640	sandstone	145-100	Marginal fold	9	0.7294	439	0.6347	382	0.026	2009	76	31
ROMsan99_88		88	46.824381006	26.46390772	380	tuff	23.03-11.63	external foredeep	36	0.1272	343	1.384	3731	0.026	2009	14	1

ROMsan99_89		89	46.81717131	26.27825672	600	tuff	33.9-5.33	internal foredeep	8	0.076	67	0.5926	369	0.026	2009		27		5
ROMwil01_RE19	Willingshofer 2001	RE19	45.5344083	22.90171488	530	sandstone	69-66	Infrabucivinian	25	0.9112	2075	4.801	5467			1	56		4
ROMwil01_HA10		HA10	45.5405268	23.01184772	500	sandstone	83.6-72.1	Infrabucivinian	30	0.8161	23042	2.767	3971			1	84		11
ROMwil01_HA3		HA3	45.53455577	23.08490408	500	sandstone	86.3-84	Infrabucivinian	30	0.6434	619	1.775	854			1	102		11
POLzat11_PL10	Zattin 2011	PL10	49.3425	21.33721667	356		41.2-33.9-33.9-27.82	valais	20	0.142	57	3.04	1216	1.27	6042	98	10.9	±	1.5
POLzat11_PL12		PL12	49.759	21.79416667	373		86-56	Marginal fold	19	0.345	232	1.77	1188	1.17	5557	55.4	50.1	±	3.8
POLzat11_PL14		PL14	49.86233333	21.74196667	231		23.03-5.33	Marginal fold	20	0.044	188	1.78	763	1.1	5210	30.8	48.7	±	6.5
POLzat11_PL16		PL16	49.66466667	19.10665	468		152-129		13	0.113	62	1.59	873	1.33	6320	77.2	17.4	±	2.4
POLzat11_PL18		PL18	49.66333333	19.0451	626		93-83		20	0.03	109	4.09	1492	1.32	6250	99.7	17.6	±	1.8
POLzat11_PL19		PL19	49.54833333	18.97558333	825		33.9-23.03		20	0.02	108	2.31	1229	1.08	5140	1.9	19.5	±	2.4
POLzat11_PL20		PL20	49.57083333	19.055	495		33.9-23.04		20	0.013	95	1.58	1128	1.3	6181	69.9	19.6	±	2.4

POLzat11_PL22		PL22	49.61283333	19.27311667	530	152-129		20	0.041	142	4.21	1453	1.26	5973	87.3	23.3	± 2.1
POLzat11_PL23		PL23	49.66866667	19.76306667	504	45-33.9		15	0.171	82	2.17	1038	1.12	5348	86.4	16.3	± 1.9
POLzat11_PL24		PL24	49.692	19.9548	434	45-33.10		20	0.066	271	4.24	1741	1.15	5487	0.2	34.5	± 3.6
POLzat11_PL26		PL26	49.584	20.13208333	699	45-27.82		16	0.022	87	3.83	1484	1.13	5376	60.5	12.1	± 1.4
POLzat11_PL27		PL27	49.70183333	20.17743333	692	45-27.83		20	0.02	81	2.29	925	1.12	5347	66.9	19.1	± 2.3
POLzat11_PL29		PL29	49.50366667	19.67461667	639	41.2-27.82		33	0.052	619	2.88	3398	1.14	5418	0	37.1	± 3.3
POLzat11_PL4		PL34	49.608	20.34813333	602	41.2-27.83		22	0.023	124	3.26	1728	1.11	5289	25.5	13.8	± 1.9
POLzat11_PL35		PL35	49.6755	20.6242	427	27.82-23.03	audia nappe	11	0.114	36	1.47	464	1.21	5765	97.6	17.2	± 3
POLzat11_PL36		PL36	49.735166667	20.51463333	478	45-33.9	audia nappe	29	0.047	312	3.31	2189	1.2	5695	0	34	± 4.7
POLzat11_PL37		PL37	49.79666667	20.35293333	357	145-66		20	0.082	362	2.45	1076	1.18	5626	0	77.5	± 10.3
POLzat11_PL38		PL38	49.81233333	20.36413333	316	33.9-27.82		15	0.013	312	5.39	1320	1.11	5279	0	53.3	± 7.4
POLzat11_PL39		PL39	49.27033333	23.40176667	402	56-33.9		11	0.012	252	4	766	1.24	5903	0.2	73	± 9.1

POLzat11_PL44		PL44	49.61366667	21.37998333	3780		27.82-23.03	audia nappe	20	0.037	163	2.49	1105	1.1	5231	6.1	29.1	±	3.3
SLOanc15_8-01	Anczkiewicz 2015	8 01	49.2332	19.82705	1290	sandstone	-	-	14	0.1306	77	0.9361	552	1.029	3010	69.2	24.9	±	3.2
SLOanc15_9-01		9 01	49.24215	19.77305	1522	sandstone	-	-	19	0.2304	328	1.6876	2402	1.024	3010	0	28.1	±	2.9
SLOanc15_10-01		10 01	49.23285	19.76745	1629	gneiss	-	-	20	0.2695	169	1.6775	1052	1.111	5137	99.98	30.6	±	2.6
SLOanc15_11-01		11 01	49.23258333	19.76766667	1629	gneiss	-	-	20	0.0979	79	0.6347	512	0.9809	4816	100	26	±	3.2
SLOanc15_12-01		12 01	49.22643333	19.767	1646	gneiss	-	-	20	0.1805	129	1.3911	994	1.066	3232	100	23.8	±	2.3
SLOanc15_1-01		1 01	49.21643333	19.75833333	1879	gneiss	-	-	20	0.2851	161	1.9036	1075	1.096	5137	100	28.2	±	2.4
SLOanc15_14-01		14 01	49.2131	19.75158333	1879	granite	-	-	19	0.6025	298	4.4925	2222	1.11	3232	100	25.6	±	1.7
SLOanc15_17-01		17 01	49.19798333	19.80061667	2176	gneiss	-	-	19	0.2662	158	2.2948	1362	1.095	3232	100	21.8	±	1.9
SLOanc15_26-01		26 01	49.24133333	19.97611667	1652	granite	-	-	20	0.3412	233	3.1061	2121	1.065	5137	100	20.1	±	1.4
SLOanc15_27-01		27 01	49.1899	20.07095	1610	granite	-	-	20	0.1723	135	1.5555	1219	1.075	5137	100	20.4	±	1.9
SLOanc15_28-01		28 01	49.19375	20.07296667	1436	granite	-	-	20	0.1655	110	1.6416	1091	1.14	5492	100	19.7	±	2

SLOanc15_29-01		29 01	49.23453333	20.08738333	1080	granite	-	-	20	0.0935	75	0.8554	686	1.054	5137	100	19.8	±	2.4
SLOanc15_34-01		34 01	49.20066667	19.75858333	2078	granite	-	-	20	0.1226	75	1.2259	750	1.135	5492	100	19.5	±	2.4
SLOanc15_38-01		38/01	49.118	19.73736667	760	sandstone	-	-	19	0.1263	57	1.09	492	1.117	5137	100	22.2	±	3.1
SLOanc15_39-01		39/01	49.13815	19.74295	916	schist	-	-	20	0.1859	120	1.7323	1118	1.14	5492	100	21	±	2.1
SLOanc15_40-01		40/01	49.14118333	19.74266667	940	gneiss	-	-	18	0.1176	63	1.267	679	0.999	4816	100	15.9	±	2.1
SLOanc15_41-01		41/01	49.15005	19.74003333	1248	gneiss	-	-	20	0.1294	83	1.9999	1283	0.9962	4816	100	11.1	±	1.3
SLOanc15_43-01		43/01	49.18973333	20.19938333	2003	granite	-	-	20	0.087	53	1.6111	981	1	4816	100	9.3	±	1.3
SLOanc15_T2		T2	49.20421667	19.83521667	1880	granite	-	-	20	0.6406	352	6.3919	3512	1.205	5912	12.55	20.8	±	1.3
SLOanc15_T3		T3	49.20421667	19.83521667	1880	schist	-	-	20	0.4561	375	5.2963	4355	1.206	5912	0.69	18.4	±	1.3
SLOanc15_T4		T4	49.21451667	19.83785	1867	granite	-	-	20	0.1544	133	1.2339	1063	1.073	3232	99.35	23	±	2.2
SLOanc15_T5		T5	49.22168333	20.01915	1820	granite	-	-	20	0.1021	82	1.9072	1532	1.215	5912	57	11.2	±	1.3
SLOanc15_T6		T6	49.22446667	20.02281667	1800	granite	-	-	20	0.0808	50	1.506	932	1.214	5912	37.46	11.2	±	1.7

SLOanc15_T7		T7	49.22976667	20.02603333	1670	granite	-	-	20	0.0739	52	1.4003	985	1.231	5912	97.01	11.2	±	1.6
SLOanc15_27-02		27 02	49.1899	19.7529	2021	schist	-	-	20	0.1328	62	1.9689	919	1.142	5492	100	13.2	±	1.8
SLOanc15_28-02		28 02	49.1735	19.7407	2185	granite	-	-	20	0.1398	58	1.2389	514	1.137	5492	100	22	±	3.1
SLOanc15_30-02		30/02	49.1753	20.14548333	2428	granite	-	-	20	0.0956	63	1.4237	938	1.137	5492	100	13.1	±	1.7
SLOanc15_32-02		32/02	49.1469	20.04025	1970	granite	-	-	20	0.0789	37	1.3485	632	1.134	5492	100	11.4	±	1.9
SLOanc15_33-02		33/02	49.16448333	20.00253333	2495	granite	-	-	20	0.0789	36	1.4051	641	1.141	5492	100	11	±	1.9
SLOanc15_34-02		34/02	49.18645	19.91665	1100	granite	-	-	20	0.0798	44	0.9796	540	1.139	5492	100	15.9	±	2.5
SLOanc15_36-02		36/02	49.17953333	20.08811667	2499	granite	-	-	20	0.1771	82	1.8621	862	1.085	5137	100	17.7	±	2.1
SLOanc15_38-02		38/02	49.18058333	20.08406667	2224	granite	-	-	20	0.1002	59	1.2128	714	1.138	5492	100	16.2	±	2.2
SLOanc15_39-02		39/02	49.18123333	20.08088333	2035	granite	-	-	20	0.1467	83	1.7324	980	1.049	5137	100	15.3	±	1.8
SLOanc15_47-02		47/02	49.21656667	20.30385	800	mudstone	-	-	20	0.1911	89	1.7218	802	0.989	4816	100	18.9	±	2.1
ROMboj98_AB6	Bojar 1998	AB6	44.8131411	22.51890827	400	gneiss		Danubian	20	0.369	337	0.557	508	0.5216	3156#	86	60		4

ROMboj98_AB22		AB22	45.09008687	22.7764872	420	gneiss	danubian	17	0.916	192	1.29	271	0.5216	3156#	85	64	4
ROMboj98_AB25		AB25	44.71630692	22.49954143	150	gneiss	Danubian	17	0.148	58	0.557	218	0.5216	3156#	92	24	4
ROMboj98_AB30		AB30	44.68144661	22.36784694	170	micaschist	Infrabucivinian	20	0.389	170	0.62	271	0.5216	3156#	87	56	6
ROMboj98_AB33		AB33	44.73180039	22.47630123	150	grenschist	Danubian	15	0.388	78	0.681	137	0.5216	3156#	55	51	7
ROMboj98_AB35		AB35	44.69113003	22.53827511	140	micaschist	Ceahlau-severin	20	0.235	253	0.508	424	0.5216	3156#	22	50	4
ROMboj98_AB36		AB36	44.84412804	22.54795853	400	gneiss	Ceahlau-severin	40	0.733	445	0.96	583	0.5216	3156#	97	68	5
ROMboj98_AB135		AB135			150	micaschist		16	0.079	109	0.368	515	0.7212	3534	59	28	3
ROMboj98_AB137		AB137	44.99906273	22.90043496	320	gneiss	danubian	17	0.781	684	1.29	1132	0.6763	2864	68	74	4
ROMboj98_AB138		AB138	45.01842957	22.86363797	320	gneiss	danubian	17	0.555	467	1.14	956	0.6763	2864	72	61	4
ROMboj98_AB152		AB152	44.73567375	22.43563087	160	gneiss	Infrabucivinian	8	0.094	40	1.47	624	0.7212	3534	<5	9	1
ROMboj98_AB156		AB156	44.78796421	22.5034148	200	amphibolite	Danubian	20	0.0196	15	0.229	176	0.7212	3534	67	11	3
ROMboj98_AB37		AB37	44.93515217	22.71838669	380	sandstone	danubian	28	0.421	187	0.69	306	0.5216	3156#	93	55	5

ROMboj98_AB142		AB142	45.08234013	22.73775353	410	sandstone	Ceahlau-severin	14	0.256	131	0.756	322	0.7212	3534	79	50	5
ROMboj98_AB16		AB16	45.02036626	22.52471832	450	sandstone	Infrabucivinian	17	0.153	100	0.639	418	0.5216	3156#	95	22	2
ROMboj98_AB150		AB150			440	sandstone		18	0.127	117	2.56	2351	0.7212	3534	1	7	1
ROMboj98_AB172		AB172	45.10364365	22.41432735	290	sandstone	Infrabucivinian	20	0.757	623	1.67	1375	0.6763	2864	1	55	3
ROMboj98_AB140		AB140	45.03973309	22.81134751	350	granite	danubian	21	0.14	88	1.21	762	0.7212	3534	42	15	2
ROMboj98_AB144		AB144	45.10364365	22.66803291	910	granite	danubian	19	0.186	106	0.705	401	0.7212	3534	38	35	4
ROMboj98_AB145		AB145	45.10751702	22.64091934	930	granite	Infrabucivinian	24	0.172	124	0.616	445	0.7212	3534	14	36	4
ROMboj98_AB146		AB146	45.10364365	22.61380577	770	granite	Infrabucivinian	15	0.328	248	1.25	945	0.7212	3534	51	32	2
ROMboj98_AB149		AB149			460	granite		18	0.13	60	0.917	424	0.7212	3534	12	19	3
ROMboj98_AB153		AB153	44.77053406	22.35041679	260	granite	danubian	21	0.437	248	2.06	1171	0.7212	3534	50	28	2
ROMboj98_AB154		AB154	44.78215416	22.41432735	260	granite	Infrabucivinian	24	0.359	276	1.33	1025	0.7212	3534	<5	36	2
ROMboj98_ABR3		ABR3	45.61105478	23.03987618	300	chlorite schist	Bucovinian nappe	20	0.081	127	0.609	919	0.6763	2865	57	17	2

ROMboj98_AB171		AB171	45.09202355	22.59637562	200	gneiss		Infrabucivinian	10	0.209	93	1.35	599	0.6763	2864	<5	19	2
SLOdan08_RO-6	Danisik 2008	RO-6	48.69472222	20.29194444	167	granite		North Meliata	30	0.1863	351	11,765	2216	7,214	4959	>95	17,5	1,1
SLOdan08_KVP-3		KVP-3	48.70083333	20.29277778	–324	granite		North Meliata	35	0.2159	464	13,947	2997	7,230	4959	>95	17,1	0,9
SLOdan08_KVH-3		KVH-3	48.70083333	20.29277778	–975	granite		North Meliata	25	0.1646	273	14,120	2342	7,262	4959	>95	12,9	0,9
SLOdanfeb08_DA-1	Danisik feb2008	DA-1	48.773	18.719	360	sandstone	26-20	CCPB	50	0.8151	2223	0.9449	2577	0.5286	3675	99.9	73.2	2.7
SLOdanfeb08_DA-2		DA-2	48.771	18.761	400	sandstone	33-26	CCPB	50	0.876	1974	1.5547	3502	0.5474	3675	93.2	49.6	1.8
SLOdanfeb08_DA-3		DA-3	48.812	18.714	440	granite	358-298	crystalline basement	25	0.5541	902	1.6641	2709	0.5624	3675	47.5	30.2	1.4
SLOdanfeb08_DA-5		DA-5	48.85	18.757	510	granite	358-298	crystalline basement	30	0.2878	310	1.126	1213	0.5924	3675	96.5	24.4	1.7
SLOdanfeb08_DA-6		DA-6	48.836	18.727	378	granite	358-298	crystalline basement	30	0.1955	294	0.5599	842	0.6186	3675	88.1	33.7	2.7
SLOdanmay11_NT-1	Danisik may2011	NT-1	48.9813	19.584	1,156	granite	-	-	25	0.9436	1206	2.4051	3074	0.6255	5,426	69	40.3	1.7
SLOdanmay11_NT-2		NT-2	48.9716	19.6153	1,200	granite	-	-	20	1.6916	977	3.9927	2306	0.6052	5,426	95	42.1	1.9
SLOdanmay11_NT-3		NT-3	48.9496	19.6282	1,700	granite	-	-	20	1.0613	614	2.5669	1485	0.6457	5,426	84	43.9	2.4

SLOdanmay11_NT-4		NT-4	48.9363	19.6401	2,043	granite	-	-	20	0.3824	359	0.9277	871	0.6119	5,426	95	41.5	2.8
SLOdanmay11_NT-5		NT-5	48.93	19.651	1,750	granite	-	-	20	0.5145	532	1.264	1307	0.5984	5,426	95	40	2.3
RTCdansep08_S	Danisik 2008	S	49.68194444	18.27638889	335	teschenite	-	tesin nappe	25	0.0931	112	2,344	282	0.5736	3929	95	36,7	4,2
RTCdansep08_T		T	49.56527778	18.23888889	400	teschenite	-	godula nappe	25	0.0419	89	1,860	395	0.5773	3929	95	21,0	2,5
SLOsmi16_G_01	Smigelski 2016	G_01	49.18510857	20.05788182	2075	crystalline	-	Tatric basement	20	0.158	175	2.783	3080	1.518	14313	99.9	16.5	1.3
SLOsmi16_G_02		G_02	49.18510857	20.05788182	1962	crystalline	-	Tatric basement	21	0.134	1665	2.344	1665	1.613	14313	25.7	16.9	1.8
SLOsmi16_G_03		G_03	49.18510857	20.05788182	1849	crystalline	-	Tatric basement	11	0.288	111	4.916	1898	1.614	14313	1.9	17.3	1.7
SLOsmi16_G_04		G_04	49.18510857	20.05788182	1736	crystalline	-	Tatric basement	20	0.116	136	2.062	2420	2.062	14313	99.9	16.6	1.5
SLOsmi16_G_05		G_05	49.18510857	20.05788182	1623	crystalline	-	Tatric basement	20	0.221	225	4.392	4467	1.61	14313	38.9	14.8	1.1
SLOsmi16_G_06		G_06	49.18510857	20.05788182	1510	crystalline	-	Tatric basement	19	0.252	131	5	2601	1.61	14313	99.9	14.9	1.4
SLOsmi16_G_07		G_07	49.18510857	20.05788182	1397	crystalline	-	Tatric basement	20	0.143	184	2.864	3675	1.61	14313	5.8	14.9	1.2
SLOsmi16_G_10		G_10	49.2354749	20.07412924	1656	crystalline	-	Tatric basement	19	0.182	111	3.116	1897	1.611	14313	99.1	17.3	1.7

SLOsmi16_G_11		G_11	49.16888882	20.05068343	2178	crystalline	-	Tatric basement	20	0.202	219	2.885	3131	1.55	10014	99.9	19.9	1.5
SLOsmi16_G_12		G_12	49.15575917	20.06099959	2135	crystalline	-	Tatric basement	20	0.115	103	1.782	1596	1.53	10014	99.9	18.1	1.9
SLOsmi16_G_13		G_13	49.13278228	20.06006175	1404	crystalline	-	Tatric basement	20	0.102	99	1.569	1520	1.53	10014	99.9	18.3	1.9
SLOsmi16_G_14		G_15	49.14028494	19.90953969	978	crystalline	-	Tatric basement	20	0.093	141	1.754	1662	1.54	10014	99.5	15	1.3
SLOsmi16_G_15		G_16	49.1332512	19.98034602	1297	crystalline	-	Tatric basement	20	0.143	209	2.681	3919	1.51	10014	99.9	14.8	1.1
POLcas16_PL72	Castelluccio 2016	PL72	49.32298	19.53182	586	sediment	86-56		20	0.228	167	12.36	906	11.15	4798	0.2	45.8	7.7
POLcas16_PL75		PL75	49.31235	19.48207	570	sediment	86-56		7	0.118	32	31.09	839	11.69	4798	64.4	8.8	1.7
POLcas16_PL82		PL82	49.30322	20.79382	608	sediment	100-66		20	0.576	432	25.42	1906	11.73	4798	0	49.8	7.1
POLcas16_PL86		PL86	49.4257	20.4413	423	sediment	56-33.9		8	0.059	15	12.15	311	11.07	4798	51	10.5	2.9
POLcas16_PL87		PL87	49.40512	20.53657	569	sediment	86-33.9		20	0.165	160	30.02	2917	11.86	4798	11.4	13.3	1.8
UKRnak18_4	Nakapelyukh 2018	4	48.491955	24.749508	490	sandstone	E2	external foredeep	45		1450		1564	0.749		0	108 ±	8
UKRnak18_5		5	48.496304	24.739237	488	sandstone	N1	external foredeep	19		565		690	0.764		0	89 ±	12

UKRnak18_6		6	48.495136	24.703566	444	sandstone	N1	external foredeep	40	1694	1622	0.779	0	116 ± 9
UKRnak18_15		15	48.229164	24.321117	627	sandstone	K1	Marginal fold	5	20	245	0.788	0.92	9.8 ± 2.3
UKRnak18_17-1		17_1	48.168125	24.257879	686	basalt	J3-K1	Marginal fold	28	172	1888	0.858	1	11.9 ± 1
UKRnak18_17-2		17_2	48.168125	24.257879	686	basalt	J3-K1	Marginal fold	40	268	2878	0.859	1	12.2 ± 0.8
UKRnak18_19		19	48.168518	24.279127	545	sandstone	K2	Marginal fold	40	237	2854	0.797	0.1	10.3 ± 0.8
UKRnak18_21		21	48.07803	24.239872	499	sandstone	K1	audia nappe	30	127	1339	0.808	0.56	11.7 ± 1.1
UKRnak18_26		26	48.049057	23.707657	269	sandstone	N1	Ceahlau-severin	40	991	3719	0.815	0	29.8 ± 3.7
UKRnak18_27		27	48.179707	23.735151	706	basalt	J3-K1	audia nappe	39	2082	3094	0.849	0.1	103 ± 4
UKRnak18_49		49	49.152622	23.264681	506	sandstone	E3	Marginal fold	47	981	4887	0.852	0	28.2 ± 1.9
UKRnak18_53		53	49.175201	23.284088	473	sandstone	K2	internal foredeep	17	1166	891	0.857	0	152 ± 17
UKRnak18_54		54	49.174561	23.28964	456	sandstone	K1-2	internal foredeep	34	4861	4299	0.858	0	140 ± 11
UKRnak18_55		55	49.282589	23.408575	362	sandstone	N1	internal foredeep	29	1113	2989	0.784	0	48.5 ± 5.5

UKRnak18_59		59	48.553703	22.981636	193	sandstone	E2	audia nappe	25		272		2687	0.837		1	12.9	±	0.8			
UKRnak18_61		61	48.635166	23.048437	301	sandstone	K2-E	audia nappe	20		225		1772	0.831		1	12.6	±	1			
UKRnak18_62		62	48.647114	23.053745	308	sandstone	K2-E2	audia nappe	14		207		2951	0.823		1	8.8	±	0.6			
UKRnak18_63		63	48.724419	23.046808	355	sandstone	K2-E2	audia nappe	15		119		1542	0.814		0.96	9.6	±	0.9			
UKRnak18_CX15		CX15	49.226885	22.358774	−4500	sandstone	E2	audia nappe	13		156		948	0.805		0	16.3	±	3.7			
SLOanc13_1-02	Anczkiewicz 2013	1 02	49.28333333	20.03722222	1040	bentonite	56-33.9		25	0.1393	84	1.8039	1088	1.044	5137	99.69	13.8		1.6			
SLOanc13_2-02		2 02	49.28333333	20.05444444	1020	bentonite	56-33.9		10	0.1127	25	1.6497	366	1.136	5492	100	13.3		2.8			
SLOanc13_3-02		3 02	49.29583333	19.85333333	760	sandstone	33.9-23.03		30	0.0876	63	1.2609	907	1.06	5137	100	12.7		1.7			
SLOanc13_4-02		4 02	49.31944444	19.90305556	970	sandstone	33.9-23.03		29	0.0801	50	1.1181	698	0.992	4816	75.99	12.2	2	1.8			
SLOanc13_5-02		5 02	49.36527778	19.85	760	sandstone	33.9-23.03		30	0.3092	223	2.5081	1809	1.142	5492	0.01	31		4.3			
SLOanc13_9-02		9 02	49.39888889	20.28916667	520	sandstone	56-23.03		30	0.0547	39	1.0959	782	1.028	5137	100	8.8		1.5			
SLOanc13_10-02		10 02	49.36722222	20.29166667	580	sandstone	33.9-23.03		30	0.0894	60	1.9141	1285	1.034	5137	100	8.3		1.1			

SLOanc13_11-02		11 02	49.39722222	20.21416667	630	sandstone	56-23.03	28	0.0875	40	1.8353	839	0.9865	4816	99.95	8.1	1
SLOanc13_12-02		12 02	49.42361111	20.075	620	sandstone	56-23.03	18	0.1005	52	1.6304	844	1.138	5492	100	12	1.7
SLOanc13_13-02		13 02	49.38722222	20.13583333	740	sandstone	33.9-23.03	29	0.1088	42	1.5075	582	0.9976	4816	100	12.4	2
SLOanc13_14-02		14 02	49.31944444	20.15166667	850	sandstone	33.9-23.03	30	0.0602	35	1.0516	611	0.9948	4816	100	9.8	1.7
SLOanc13_15-02		15 02	49.32861111	20.04916667	840	sandstone	33.9-23.03	22	0.089	44	1.9672	973	0.9795	4816	99.82	7.6	1.2
SLOanc13_17-02		17 02	49.27555556	20.12638889	960	sandstone	33.9-23.03	30	0.08	58	1.7653	1280	1.106	5137	100	8.6	1.2
SLOanc13_18-02		18 02	49.28861111	20.07222222	920	sandstone	33.9-23.03	26	0.1105	52	2.0166	949	1.07	5137	99.55	10.1	1.5
SLOanc13_19-02		19 02	49.28194444	19.95555556	900	sandstone	33.9-23.03	30	0.0751	61	1.6923	1375	1.139	5492	100	8.7	1.1
SLOanc13_21-02		21 02	49.28166667	19.85138889	930	sandstone	33.9-23.03	20	0.1582	67	2.6963	1142	1.003	4816	24.8	10.1	1
SLOanc13_22-02		22 02	49.285	19.83888889	910	sandstone	33.9-23.03	30	0.2999	125	4.4264	1845	1.136	5492	0	26.9	4.7
SLOanc13_22-01		22 01	49.28277778	19.8825	950	sandstone	33.9-23.03	20	0.0674	44	1.6813	1098	1.088	3232	100	7.5	1.2
SLOanc13_23-02		23 02	49.35083333	20.44583333	650	sandstone	45-23.03	19	0.0578	83	1.5186	2179	0.9823	4816	99.99	6.4	0.7

SLOanc13_24-02		24 02	49.35416667	20.48611111	840	sandstone	45-23.03		19	0.0855	57	1.5709	1047	0.9934	4816	99.96	9.3		1.3
SLOanc13_42-02		42/02	49.27027778	20.48611111	620	sandstone	41.2-23.03		20	0.1025	84	1.9323	1583	1.002	4816	99.99	9.1		1
SLOanc13_43-02		43/02	49.28333333	20.41055556	800	sandstone	41.2-23.03		23	0.0556	28	0.9717	489	1.135	5492	99.56	11.2		2.2
SLOanc13_44-02		44/02	49.24333333	20.35138889	940	sandstone	41.2-23.03		20	0.0635	36	1.4807	839	1.101	5137	100	8.1		1.4
SLOanc13_45-02		45/02	49.26305556	20.30166667	860	sandstone	41.2-23.03		18	0.0715	23	1.265	407	1.141	5492	98.52	11.1		2.4
SLOanc13_49-02		49/02	49.34222222	20.1075	504*	sandstone	33.9-23.03		30	0.0604	47	1.1312	880	1.08	5137	100	9.9		1.5
SLOanc13_50-02		50/02	49.34222222	20.1075	1005*	sandstone	33.9-23.03		30	0.0539	52	1.0858	1048	0.9879	4816	100	8.4		1.2
SLOanc13_51-02		51/02	49.34222222	20.1075	1540*	sandstone	41.2-27.82		30	0.0561	45	1.4951	1199	1.143	5492	100	8.4		1.1
SLOanc13_52-02		52/02	49.34222222	20.1075	2044*	sandstone	41.2-27.82		24	0.0283	21	0.7856	584	0.9907	4816	99.99	8.4		1.4
SLOanc13_F9		F9	49.34194444	19.99888889	825	sandstone	66-45		27	0.0747	44	1.6018	943	1.027	3010	99.96	8.4		1.3
SLOanc13_F8		F8	49.33305556	20.04444444	875	sandstone	33.9-23.03		30	0.0675	40	1.7949	1063	1.212	5912	100	8.4	±	1.2
ROMsch98_96-07	Schmid 1998	96-07	45.33142899	23.87412049	1900	-	-	Infrabucivinian	17	0.1461	132	2.319	2095	1.38	1857	98	15.5		1.4

ROMsch98_96-24		96-24	45.23788941	23.39285212	350	-	-	danubian	18	0.3496	209	2.232	1334	1.311	1857	84	36.6	2.8
ROMsch98_96-27		96-27	45.25000594	23.37928161	700	-	-	danubian	10	0.0268	44	1.349	287	1.365	1857	52	37.2	6.1
ROMsch98_96-40		96-40	45.40364347	23.91289337	1100	-	-	Infrabucivinian	19	0.1972	117	2.629	1560	1.357	1857	96	18.1	1.8
ROMsch98_96-41		96-41	45.43417712	23.90853142	750	-	-	Infrabucivinian	19	0.2763	220	3.22	2564	1.35	1857	91	20.6	1.5
ROMmos05_HH-75	Moser 2005	HH-75	45.53777778	23.90694444	2100	gneiss		bucovinian nappe	20	0.553	1307	0.782	1847	0.408	12045	26	53.7	2.2
ROMmos05_HH-76		HH-76	45.55222222	24.92527778	1978	gneiss		bucovinian nappe	25	0.619	1385	0.908	2034	0.408	12045	4	51.9	2.4
ROMmos05_HH-73		HH-73	45.58805556	23.915	1195	gneiss		bucovinian nappe	26	0.392	797	0.591	1203	0.408	12045	96	50.3	2.5
ROMmos05_XXVII		XXVII	45.59166667	23.92	800	gneiss		bucovinian nappe	22	0.525	768	0.84	1230	0.497	12211	47	57.7	2.9
ROMmos05_HH-77		HH-77	45.31611111	23.32444444	1668	gneiss		Infrabucivinian	25	0.468	789	0.695	1172	0.408	12045	28	51.1	2.6
ROMmos05_XXI		XXI	45.3125	23.31638889	950	gneiss		Infrabucivinian	25	0.561	838	0.924	1381	0.497	12211	47	56	2.7
ROMmos05_XXII		XXII	45.30333333	23.32083333	800	gneiss		Infrabucivinian	20	0.614	825	1.08	1461	0.497	12211	49	52.2	2.5

ROMmos05_HR-1		HR-1	45.3125	23.28555556	285	gneiss		Infrabucivinian	21	0.474	385	0.973	790	0.408	12045	14	37	2.4
ROMmos05_RB-14		RB-14	45.38777778	23.41666667	900	sandstone	33.9-5.33	Infrabucivinian	74	0.35	1107	0.8	2519	0.51	4938	4	46.2	5.2
ROMmos05_RB-4		RB-4	45.38888889	23.40055556	700	sandstone	33.9-5.33	Infrabucivinian	100	0.48	2208	0.77	3538	0.51	4938	0	62.5	7.1
ROMmos05_RB-5		RB-5	45.38638889	23.3975	640	sandstone	33.9-5.33	Infrabucivinian	90	0.49	1424	0.84	2438	0.51	4938	0	61.2	7.2
ROMmos05_RB-6		RB-6	45.38666667	23.39305556	620	sandstone	33.9-5.33	Infrabucivinian	97	0.5	2436	0.72	3479	0.51	4938	0	76.6	3.7
ROMmos05_RB-7		RB-7	45.39083333	23.38638889	660	sandstone	33.9-5.33	Infrabucivinian	99	0.55	1580	0.79	2285	0.51	4938	7	72.5	7.9
ROMmos05_RB-11		RB-11	45.39777778	23.32111111	580	sandstone	33.9-5.33	Infrabucivinian	100	0.46	2213	0.71	3533	0.51	4938	0	64.2	7.1
ROMmos05_RB-12		RB-12	45.39777778	23.32111111	580	sandstone	33.9-5.33	Infrabucivinian	100	0.41	1891	0.72	3291	0.51	4938	0	61.8	7
ROMmos05_RB-17		RB-17	45.30527778	23.025	820	sandstone	33.9-5.33	Infrabucivinian	90	0.41	1117	0.72	1994	0.51	4938	0	58.7	6.9
ROMmos05_RB-18		RB-18	45.30277778	23.02694444	780	sandstone	33.9-5.33	Infrabucivinian	100	0.51	2302	0.89	4028	0.51	4938	0	59.4	6.6
ROMfug05_96-20	Fugenschuh	96-20	45.29888889	23.59416667	1150			Infrabucivinian	20	4.154	297	36.59	2616	0.148	2167	95	29.9	1.9
ROMfug05_97-11		97-11	45.36194444	23.75	1300			Infrabucivinian	11	0.1781	68	4.687	1790	1.711	1879	64	7.9	1

ROMfug05_97-23		97-23	45.4225	23.22055556	800			Infrabucivinian	20	0.2005	187	2.891	2697	1.155	1879	75	14.3		1.1
ROMfug05_97-24		97-24	45.27722222	22.93972222	1050			Danubian	11	1.283	78	6.778	412	0.9904	3089	98	33.4		4.2
ROMfug05_97-25		97-25	45.31527778	23.08916667	950			Infrabucivinian	20	1.731	1988	3.69	4237	1.138	1879	5	94		5
ROMfug05_97-26		97-26	45.48638889	22.82722222	600			Infrabucivinian	20	2.075	1718	7.632	6320	1.122	1879	5	55.4		3
ROMfug05_97-27		97-27	45.46833333	22.89694444	700			Infrabucivinian	20	0.1534	242	1.148	1812	1.202	2400	95	28.6		2
ROMfug05_97-30		97-30	45.471944444	22.90972222	700			Infrabucivinian	20	5.463	1197	11.67	2556	0.9872	3089	80	82		3.2
ROMfug05_97-31		97-31	45.4475	23.06	600			Infrabucivinian	20	1.998	239	18.99	2271	1.404	2167	82	26.3		1.9
ROMfug05_97-33		97-33	45.45277778	23.05638889	600			Infrabucivinian	15	0.5753	257	2.046	914	0.9841	3089	81	49.2		3.6
ROMsan98_carp-1	Sanders 1998 (merten chap 5)	Carp-1	47.27784752	23.67340505	450	sandstone	33.9-5.8	bucovinian nappe	20								53	±	7
ROMsan98_carp-3		Carp-3	47.33487639	24.05834993	500	sandstone	23.8-5.8	bucovinian nappe	20								37	±	4
ROMsan98_carp-50		Carp-50	47.39665767	24.29834643	600	sandstone	23.8-16.4	bucovinian nappe	72								38	±	10
ROMsan98_carp-5		Carp-5	47.28022372	24.48606647	400	sandstone	21.5-16.0	bucovinian nappe	20								25	±	5

ROMsan98_carp-4		Carp-4	47.29923335	24.47893786	400	sandstone	21.5-16.0	bucovinian nappe	20		7 ± 2
ROMsan98_carp-6		Carp-6	47.21606624	24.69754854	600	dej tuff	16.0-12.5	bucovinian nappe	20		23 ± 3
ROMsan98_carp-107		Carp-107	47.28972854	24.94467365	1030	sandstone	28.4-23.8	bucovinian nappe	86		22 ± 2
ROMsan98_carp-106		Carp-106	47.41329109	25.13239368	900	sandstone	33.9-28.4	bucovinian nappe	48		13 ± 1
ROMsan98_carp-60		Carp-60	47.46794376	25.24169902	830	schist		bucovinian nappe	46		17 ± 5
ROMsan98_carp-58		Carp-58	47.52734883	25.35338056	770	schist		internal foredeep	45		11 ± 4
ROMsan98_carp-18I		Carp-18 I	47.54398225	25.42704285	1000	quartzite	150.8-130.0	internal foredeep	27		5 ± 2
ROMsan98_carp-18II		Carp-18 II	47.54398225	25.42704285	1000	quartzite	150.8-130.1	internal foredeep	11		25 ± 9
ROMsan98_carp-17		Carp-17	47.42754831	25.55773402	800	schist		internal foredeep	22		27 ± 9
ROMsan98_carp-19b		Carp-19b	47.53447744	25.54110059	700	sandstone	145.5-99.6	internal foredeep	42		9 ± 1
ROMsan98_carp-19		Carp-19	47.53922985	25.51971477	700	sandstone	145.5-99.7	internal foredeep	19		26 ± 6
ROMsan98_carp-56		Carp-56	47.59388252	25.62902201	450	sandstone	65.5-40.4	external foredeep	18		126 ± 18

ROMsan98_carp-57		Carp-57	47.59388252	25.88089762	530	sandstone	37.2-23.0	plateforme	7		115 ± 22
ROMsan98_carp-69		Carp-69	46.21568479	26.49158179	370	sandstone	65.5-40.4	internal foredeep	77		30 ± 8
ROMsan98_carp-44		Carp-44	45.69054393	24.55735256	900	schist		bucovinian nappe	41		36 ± 4
ROMsan98_carp-42		Carp-42	45.65727709	24.56923357	1410	schist		bucovinian nappe	10		46 ± 22
ROMsan98_carp-41		Carp-41	45.62163404	24.58349079	1580	schist		bucovinian nappe	32		26 ± 7
ROMsan98_carp-40		Carp-40	45.63589126	24.57398598	1800	schist		bucovinian nappe	37		53 ± 9
ROMsan98_carp-39		Carp-39	45.60262442	24.59537181	2050	schist		bucovinian nappe	35		64 ± 10
ROMsan98_carp-38		Carp-38	45.57886239	24.58586699	1520	schist		bucovinian nappe	34		34 ± 5
ROMsan98_carp-37		Carp-37	45.55510036	24.5882432	1220	schist		bucovinian nappe	27		23 ± 8
ROMsan98_carp-36		Carp-36	45.5099525	24.58349079	1000	schist		bucovinian nappe	30		79 ± 5
ROMsan98_carp-35		Carp-35	45.45054743	24.59537181	870	schist		bucovinian nappe	24		50 ± 4
ROMsan98_carp-103		Carp-103	45.58361479	23.78746279	2240	gneiss		Getic nappe	34		61 ± 3

ROMsan98_carp-104		Carp-104	45.56698137	23.81360103	1200	gneiss	getic nappe	37		41 ± 3
ROMnec10_O1	Necea thesis 2010	O1	45.88640341	25.74070116	675		Ceahlau-severin			76
ROMnec10_O3		O3	45.90509388	25.94629635	748		audia nappe			44
ROMnec10_O6		O6	45.90883198	25.49847263	565		Ceahlau-severin			103
ROMnec10_O7		O7	45.90509388	25.48352026	567		Ceahlau-severin			119
ROMnec10_O8		O8	45.89911293	25.46632502	688		Ceahlau-severin			101
ROMnec10_O13		O13	45.90285102	25.45286788	799		Ceahlau-severin			118
ROMnec10_P4		P4	45.93425102	26.60420098	752		internal foredeep			10
ROMnec10_P6		P6	45.87070341	26.78288189	464		external foredeep			91
ROMnec10_P7		P7	45.92378435	26.69391524	423		external foredeep			136
ROMnec10_P8		P8	45.91107483	26.74176285	398		external foredeep			72
ROMnec10_P9		P9	45.89761769	26.75447237	403		external foredeep			

ROMnec10_P10		P10	45.88416055	26.79708665	436		external foredeep									72	
ROMnec10_P11		P11	45.88939388	26.80605808	358		external foredeep									31	
ROMnec10_P12		P12	45.89088912	26.83297236	323		external foredeep									27	
ROMnec10_P13		P13	45.8938796	26.84867235	292		external foredeep									24	
ROMnec10_P14		P14	45.89911293	26.8740914	279		external foredeep										
ROMnec10_P18		P18	45.91929864	26.91820091	261		external foredeep									35	
ROMnec10_P20		P20	45.94023197	26.56532479	842		internal foredeep									17	
ROMnec10_P25		P25	45.95368911	26.37542959	1188		Marginal fold									15	
ROMnec10_P26		P26	45.94770816	26.25730581	771		Marginal fold									12	
ROMnec10_P27		P27	45.89687007	26.32384389	898		Marginal fold									18	
ROMnec10_P28		P28	45.91481293	26.33356294	1007		Marginal fold									14	
POLmaz10_PL1	Mazolli	PL1	49.31401	22.286563	702	27.82-23.03	audia nappe	20	0.084	78	2.04	1891	0.92	4368	92.6	7	0.8

POLmaz10_PL4		PL4	49.265616	22.170643	797		27.82-23.03	audia nappe	14	0.052	17	1.22	398	0.92	4355	86.9	7.2 1.8
POLmaz10_PL5		PL5	49.541347	21.050835	490		56-33.9	audia nappe	20	0.321	132	2.51	1034	0.91	4343	92.9	21.3 2
POLmaz10_PL6		PL6	49.580738	21.041832	350		27.82-23.03	audia nappe	20	0.126	90	2.08	1491	0.91	4306	76.4	10 1.1
POLmaz10_PL7		PL7	49.644887	21.160002	335		33.9-27.82	audia nappe	16	1.06	405	1.92	733	0.91	4331	0	75.7 12.8
POLmaz10_PL8		PL8	49.537971	21.421103	448		33.9-27.82	audia nappe	15	0.074	40	1.73	933	0.91	4318	92.5	7.2 1.2
POLanc08_00/13	Anczkiewicz and swierczewska 2008	00/13	49.969013	20.332808	227		23.03-5.33	Carpathian foredeep									
POLanc08_00/18		00/18	49.750678	20.704201	265		145-66	Silesian Nappe									
POLanc08_SK1/00		Sk 1/00	49.865473	19.883759	344		33.9-23.03	Silesian Nappe									
POLanc08_TA00/1		Ta 00/1	49.657267	20.134731	599		33.9-23.03	Dukla nappe									
POLanc08_Ni00/1		Ni00/1	49.643762	20.069456	526		33.9-23.03	Dukla nappe									
POLanc08_MA00/1		Ma00/1	49.532344	20.479114	447		56-33.9	Magura nappe									

POLanc08_Ba00/1		Ba 00/1	49.501957	20.399209	391	56-33.9	Magura nappe		
POLanc08_Rz00/1		Rz 00/1	49.514337	20.409337	381	56-33.9	Magura nappe		
POLanc08_Cze00/1		Cze 00/1	49.527842	20.392456	575	56-33.9	Magura nappe		
POLanc08_SN00/1		SN 00/1	49.682027	20.219139	610	56-23.03	Magura nappe		
POLanc08_DO00/2		DO 00/2	49.695532	20.237146	507	56-33.9	Magura nappe		
POLanc08_Kl01-1		Kl 01_1	18-févr	20.045822	956	56-33.9	Magura nappe		
POLanc08_04-01		04_01	49.389414	20.50725	737	182-170	PKB Grajcarek unit		
POLanc08_05-01		05_01	49.395041	20.495996	674	182-170	PKB Grajcarek unit		
POLanc08_07-01		07_01	49.383787	20.426219	478	201-66	PKB Klippen sucession		

ZFT COMPILATION																				
Coordinates									Calculation								Age (Ma)			
Database Name	Author	Sample	Age (Ma)	lat	long	Elevation (m)	Lithology	stratigraphic	Tectonic unit	nb gr	ρs (10^6/cm²)	Ns	ρi (10^6/cm²)	Ni	ρd (10^6/cm²)	Nd	P(χ²)(%)	Age (Ma)		Sd (1σ)
SLOdan10_MF-1	Danisik 2010	MF-1	143.7	49.1486111	18.8258333	658	granite	420 - 298	North Meliata	21	16.719	1671	4.6926	469	0.6601	3089	95	143.7		8.3
SLOdan10_MF-2		MF-2	45.2	49.0886111	18.8611111	802	granite	420 - 298	Tatricum	20	11.87	1289	10.4887	1139	0.64896	3089	86	45.2		2.1
SLOdan10MF-3		MF-3	135	49.0833333	18.7375	606	granite	420 - 298	North Meliata	20	30.57	2188	8.9074	642	0.4896	3089	95	135		6.9
SLOdan10_MF-6		MF-6	143.7	49.0844444	18.7494444	672	granite	420 - 298	North Meliata	20	20.266	1188	5.6976	334	0.66114	3089	95	143.7		9.6
SLOkra14_B1	Kralikova 2014	B1	69.6	49.0473056	18.8656944	518	Granite pebbles	5.33 - 2.58	Tatricum	20	86.21	1844	61.2	1309	5.232	3078	86	69.6	±	5.2
SLOkra14_B2		B2	65.9	49.04725	18.8673056	503	Granite pebbles	5.33 - 2.58	Tatricum	21	104	2518	78.65	1904	5.275	3078	83	65.9	±	4.7

SLOkra14_ZGT3		ZGT3	60.2	49.0366944	18.9233333	−2458	mylonite	145-66	Tatricum	30	69.3	1931	56.38	1571	5.182	3078	100	60.2	±	4.4
ROMwil01_HA26	willingshofer 2001	HA26	52	45.4762826	22.8252337	600	conglomerate	72-23.03	Infrabucovinian	17	8.86	1500	11.6	982	0.2271	4689	1	52		4
ROMwil01_HA28		HA28	82	45.4732234	22.824214	600	conglomerate	72-23.03	Infrabucovinian	5	11.6	551	9.729	231	0.2271	4689	85	82		10
ROMwil01_RE19		RE19	74	45.5344083	22.9017149	530	sandstone	69-66	Infrabucovinian	19	6.218	2067	5.902	981	0.2271	4689	10	74		6
ROMwil01_RE20		RE20	259	45.5150331	23.0577364	500	sandstone	72-70	Infrabucovinian	17	17.36	5813	5.059	846	0.2271	4689	1	259		15
ROMwil01_HA20		HA20	80	45.6108894	22.7558908	600	volcaniclastic	72.1-66	Bucovinian Nappe	20	10.34	4589	8.191	1818	0.2271	4689	1	80		9
ROMwil01_HA10		HA10	211	45.5405268	23.0118477	500	sandstone	83.6-72.1	Infrabucovinian	20	16.77	6352	5.421	1027	0.2271	4689	61	211		16
ROMwil01_HA1		HA1	104	45.5127681	23.0863566	500	sandstone	87-86.3	Infrabucovinian	7	7.205	952	3.678	243	0.2271	4689	1	104		22
ROMwil01_HA11		HA11	132	45.4943696	23.1037867	500	sandstone	93.9-89.8	Infrabucovinian	20	12.42	3565	6.767	971	0.2271	4689	1	132		13
SLOanc15_41/01	Anczk	41/01	55.2	49.15005	19.1567	1248	gneiss	-	Tatricum	16	0.7039	4942	397.5469	551	411.9769	571	4.48	55.2	±	4.3

ROMboj98_ZAB40	Bojar	ZAB40	190	44.8974169	22.7355283	320	sandstone		Ceahlau-severin	8	9.474	506	2.771	148	0.9981	2728	10	190		23
ROMboj98_ZAB139	Bojar	ZAB139	220	45.0170762	22.8843727	380	liassic sandstone		Danubian	10	18.546	518	4.511	126	0.9614	3533	80	220		27
ROMboj98_ZAB141	Bojar	ZAB141	173	45.0637725	22.7851431	390	sandstone		Danubian	10	17.542	557	5.433	173	0.9614	3533	97	173		19
ROMboj98_ZAB145	Bojar	ZAB145	42	45.1075471	22.6883487	930	granite		Infrabucovinian	12	6.143	301	5.449	267	0.6567	3218	22	42		5
ROMboj98_ZABR2	Bojar	ZABR2	67	45.44399	23.2582418	400	greenschist		Infrabucovinian	9	7.706	438	6.193	352	0.9614	3633	33	67		7
SLOdanfeb08_DA-3	Danisik feb2008	DA-3	109.1	48.812	18.714	440	granite	145-66	Tatricum	25	13.3764	1504	4.9539	557	0.691	6973	81.5	109.1		5.9
SLOdanfeb08_DA-5		DA-5	92.1	48.85	18.757	510	granite	145-66	Tatricum	25	9.2452	1155	4.0343	504	0.6551	6973	97.5	92.1		5.3
SLOdanfeb08_DA-6		DA-6	92.1	48.836	18.727	378	granite	145-66	Tatricum	26	10.2176	1846	4.4668	807	0.6561	6973	100	92.1		4.3
SLOdanmay11_NT-2z	Danisik may2011	NT-2z	132.1	48.9716	19.6153	1200	granite	-	North Meliata	25	19.1115	1,304	5.7159	390	0.6459	3,089	95	132.1		8.3
SLOdanmay11_NT-3z		NT-3z	155.1	48.9496	19.6282	1700	granite	-	Tatricum	20	20.2393	778	5.2029	200	0.653	3,089	95	155.1		12.9
SLOdanmay11_NT-4z		NT-4z	146.8	48.9363	19.6401	2043	granite	-	Tatricum	30	19.0123	1,754	5.1162	472	0.6479	3,089	48	146.8		8.6

SLOdanmay11_NT-5z		NT-5z	144.9	48.93	19.651	1750	granite	-	Tatricum	20	17.343	900	4.7982	249	0.6561	3,089	95	144.9		11
SLOpal07_KB-1	Palisenka 2007	KB-1	74.7	48.841346	20.5153443	847	granite	-	North Meliata	16	5.93	490	4.52	373	0.935	6008	67.3	74.7	±	5.6
SLOpal07_KB-2		KB-2	70.4	48.7377988	20.5333526	651	granite	-	North Meliata	14	10.78	1420	8.84	1165	0.939	6008	0	70.4	±	5.4
SLOpal07_KB-3		KB-3	71.3	48.692778	20.173186	711	granite	-	North Meliata	24	11.66	1822	9.49	1483	0.959	6008	1.61	71.3	±	3.9
SLOpal07_KB-4		KB-4	74.2	48.692778	20.173186	711	granite	-	North Meliata	32	12.91	2665	10.23	2111	0.964	6008	0.16	74.2	±	3.7
SLOpal07_KB-5		KB-5	64.9	48.6882759	19.6329362	909	tonalite	-	North Meliata	13	9.08	473	7.91	412	0.929	6008	63.56	64.9	±	4.8
SLOpal07_KB-6		KB-6	87.7	48.7940748	20.5761224	980	granite	-	North Meliata	22	11.68	1355	7.52	872	0.924	6008	0.55	87.7	±	5.9
SLOpal07_KB-7		KB-7	61.7	48.7377988	21.0128243	770	granite	-	North Meliata	30	8.26	1737	7.52	1582	0.915	6008	0.93	61.7	±	3.4
ROMgro08_M01	Groger thesis 2008	M01	96.6	47.72979	24.49667	540			Bucovinian Nappe	10	17.637	1291	4.932	361	0.385	3065	34	96.6		7.6
ROMgro08_M02		M02	95.7	47.75372	24.56071	580			Bucovinian Nappe	4	10.939	367	3.01	101	0.377	3065	13	95.7		13.5
ROMgro08_M03		M03	99.7	47.77254	24.58664	630			Bucovinian Nappe	20	8.688	1468	3.545	599	0.58	3605	81	99.7		6.8
ROMgro08_M04		M04	96.1	47.79145	24.6281	680			Bucovinian Nappe	10	7.007	436	3.054	190	0.597	3605	84	96.1		9.5

ROMgro08_M05		M05	107.5	47.8043	24.66709	745			Bucovinian Nappe	20	9.844	2366	3.72	894	0.586	3605	<5	107.5	7.4
ROMgro08_M06		M06	162.3	47.79085	24.69859	790			Bucovinian Nappe	20	12.907	2543	3.335	657	0.591	3605	<5	162.3	13
ROMgro08_M07		MO7	146.1	47.77364	24.73684	835			Bucovinian Nappe	20	8.663	2193	2.501	633	0.614	3605	10	146.1	10.5
ROMgro08_M08		MO8	61.3	47.690263	24.770543	820			Bucovinian Nappe	20	12.309	2703	5.232	1149	0.369	3065	<5	61.3	4.7
ROMgro08_M09		M09	96.2	47.647505	24.833619	1660			Bucovinian Nappe	20	12.615	2501	3.218	638	0.35	3065	22	96.2	6.5
ROMgro08_M12		M12	139.7	47.603497	25.112014	985	granite	541	Bucovinian Nappe	3	13.443	164	2.541	31	0.377	3065	21	139.7	29.5
ROMgro08_M13		M13	107.6	47.571246	25.12822	930	granite	541	Bucovinian Nappe	14	25.389	1812	5.871	419	0.354	3065	23	107.6	8.5
ROMgro08_M14		M14	107	47.478662	25.27951	850	granite	541	Bucovinian Nappe	20	13.767	2830	3.06	629	0.338	3065	<5	107	9.1
ROMgro08_P1		P1	82.8	47.430957	23.57476	315			Bucovinian Nappe	14	7.96	1010	2.522	320	0.373	3065	55	82.8	6.6
ROMgro08_P2		P2	78.8	47.509842	23.628772	215			Bucovinian Nappe	16	15.574	1919	4.74	584	0.342	3065	38	78.8	5.6
ROMgro08_P3		P3	84.5	47.488712	23.686807	610			Bucovinian Nappe	35	12.838	3336	4.087	1062	0.381	3065	<5	84.5	5.5
ROMgro08_R1-1		R1-1	71.8	47.59786	24.55936	1550			Infrabucovinian	17	9.173	996	3.113	338	0.346	2967	25	71.8	6.1

ROMgro08_R2-2		R2-2	100.1	47.41492	24.59726	1105	Bucovinian Nappe	20	8.041	981	3.238	395	0.574	3605	78	100.1	7.6
ROMgro08_R2-3		R2-3	68.2	47.41571	24.59586	885	Bucovinian Nappe	14	9.881	1326	3.622	486	0.357	2967	<5	68.2	6.4
ROMgro08_R2-4		R2-4	82.8	47.4193	24.59043	705	Bucovinian Nappe	26	11.52	2312	3.443	691	0.352	2967	12	82.8	5.9
ROMgro08_R2-5		R2-5	84.7	47.42124	24.58348	600	Bucovinian Nappe	17	12.109	1625	3.368	452	0.335	2967	49	84.7	6.1
ROMgro08_R3-1		R3-1	79.5	47.533782	24.620652	2020	Infrabucovinian	20	18.83	2550	5.568	754	0.335	3065	47	79.5	5.1
ROMgro08_R3-2		R3-2	83	47.42329	24.58285	1465	Bucovinian Nappe	20	7.415	1642	3.902	864	0.625	3605	62	83	5.5
ROMgro08_R3-3		R3-3	85.6	47.52893	24.60899	1310	Infrabucovinian	13	7.626	842	3.877	428	0.62	3605	37	85.6	6.8
ROMgro08_R3-4		R3-4	68.1	47.52633	24.60445	1155	Infrabucovinian	7	9.477	607	6.011	385	0.614	3605	50	68.1	5.5
ROMgro08_R3-5		R3-5	84.9	47.5232	24.59763	1005	Infrabucovinian	20	11.482	1751	5.705	870	0.608	3605	14	84.9	5.9
ROMgro08_R3-6		R3-6	78.5	47.51869	24.58798	945	Infrabucovinian	20	9.224	934	4.977	504	0.603	3605	11	78.5	6.4
ROMgro08_R4-1		R4-1	87.8	47.5008	24.92015	1638	Bucovinian Nappe	16	7.516	1710	2.193	499	0.366	3065	28	87.8	6.3
ROMgro08_R4-3		R4-3	80	47.49471	24.94101	980	Bucovinian Nappe	2	11.694	107	3.716	34	0.362	3065	86	80	16.2

ROMgro08_R4-4		R4-4	77	47.49043	24.96023	700		Bucovinian Nappe	20	13.472	1923	4.589	655	0.369	3065	<5	77	5.8
ROMgro08_R5-1		R5-1	86.2	47.552021	24.546451	1150		Infrabucovinian	8	20.411	635	5.754	179	0.346	3065	47	86.2	8.4
ROMgro08_R5-2		R5-2	64,4	47.460078	24.449131	1245		Bucovinian Nappe	18	15.094	1556	5.345	551	0.324	2967	90	64,4	4.5
ROMgro08_R5-4		R5-4	81.2	47.59616	24.87287	1270		Bucovinian Nappe	20	16.118	2517	5.033	786	0.358	3065	10	81.2	5.5
ROMsch98_96-07	Schmid 1998	96-07	29.9	45.331429	23.874120	1900	-	- Danubian	4	5.263	352	5.308	355	0.1736	1292	41	29.9	2.4
ROMsch98_96-11		96-11	59.1	45.3280364	23.884783	1900	-	- Danubian	9	15.74	466	7.94	235	0.1722	1292	98	59.1	5
ROMsch98_96-24		96-24	39.9	45.2378894	23.3928521	350	-	- Danubian	13	4.867	1231	3.582	906	0.1694	1292	50	39.9	2.1
ROMsch98_96-27		96-27	46.1	45.2500059	23.3792816	700	-	- Danubian	12	7.383	613	4.661	387	0.168	1292	35	46.1	3.3
ROMsch98_96-40		96-40	29.4	45.4036435	23.9128934	1100	-	- Infrabucovinian	15	10.55	1111	9.58	1009	0.1539	1292	88	29.4	1.5
ROMsch98_96-41		96-41	64.3	45.434171	23.9085314	750	-	- Infrabucovinian	13	8.164	659	3.63	293	0.1652	1292	99	64.3	4.9
ROMfug05_96-16	Fuge	96-16	83.4	45.2155556	23.7447222	680		Danubian	16	12.46	1403	4.377	493	0.1708	1292	12	83.4	5.7

ROMfug05_97-11		97-11	21.4	45.3619444	23.75	1300	Infrabucovinian	16	8.175	670	7.028	576	0.106	2605	97	21.4	1.3
ROMfug05_97-13		97-13	88.3	45.2211111	23.6708333	570	Danubian	12	10.4	1448	2.036	283	0.1041	2605	5	88.3	8.5
ROMfug05_97-17		97-17	50.3	45.3777778	23.7230556	1900	Infrabucovinian	20	9.58	915	3.371	322	0.1022	2605	99	50.3	3.4
ROMfug05_97-18		97-18	25.6	45.4144444	23.4486111	900	Infrabucovinian	20	8.499	618	5.79	421	0.1003	2605	93	25.6	1.7
ROMfug05_97-20		97-20	55.7	45.425	23.4525	900	Infrabucovinian	20	8.11	2124	3.712	972	0.1472	2282	81	55.7	2.5
ROMfug05_97-24		97-24	37.5	45.2772222	22.9397222	1050	Danubian	7	6.329	312	4.341	214	0.1483	2282	58	37.5	3.4
ROMfug05_97-25		97-25	145	45.3152778	23.0891667	950	Danubian	9	12.19	1315	2.114	228	0.1461	2282	81	145	10.8
ROMfug05_97-27		97-27	44	45.4683333	22.8969444	700	Infrabucovinian	15	4.717	593	2.697	339	0.1449	2282	85	44	3.1
ROMfug05_97-30		97-30	112	45.4719444	22.9097222	700	Infrabucovinian	17	13.56	1253	2.997	277	0.1438	2282	74	112	7.9
ROMfug05_97-31		97-31	39.8	45.4475	23.06	600	Infrabucovinian	13	9.156	1433	5.45	853	0.1426	2282	7	39.8	2.5
ROMfug05_97-33		97-33	128	45.4527778	23.0563889	600	Infrabucovinian	20	12.01	2065	2.28	392	0.1415	2282	91	128	7.6
ROMfug05_97-34		97-34	41.7	45.2047222	23.2627778	450	Danubian	6	4.552	216	2.656	126	0.1404	2282	74	41.7	4.8

ROMfug05_97-36		97-36	105	45.1558333	23.229444	400	Danubian	15	14.09	1268	3.212	289	0.1392	2282	20	105	8		

AHe AND ZHe COMPILATION

Name	Authors	Sample	Corrected age	coordinates		Elevation (m)	lithology	stratigraphic age	Tectonic unit	A/Z	replicates	Ngr	232Th (ng)	± (%)	238U (ng)	± (%)	He (ncc)	± (%)	Th/U	Raw age (ma)	± (ma)	Ft	± (%)	Corrected age (ma)	± (ma)	Weighted average	error
SLOancl5_1 1-01	Anczkiewicz 2015	11_ 01	40. 9	49.23 25833 3	19.76 76667	16 29	gneiss			Z	11_01_1	1	0.11	1.7	0.24	2.2	0.78 9	1.2	0.45	24.4	0.6	0.6	5	40.9	2.2	47.3	4.2
			51. 6							Z	11_01_2	1	0.16 2	1.6	0.34 3	2.1	1.54 2	1.2	0.47	33.2	0.7	0.64	5	51.6	2.8	47.3	4.2
			47. 5							Z	11_01_3	1	0.18	1.6	0.25 7	2.2	1.07 7	1.2	0.69	29.5	0.7	0.62	5	47.5	2.5	47.3	4.2
			50. 5							Z	11_01_4	1	0.05 6	1.9	0.35 8	2.1	1.39 1	1.2	0.15	30.8	0.7	0.61	5	50.5	2.7	47.3	4.2
			49. 3							Z	11_01_5	1	0.19 7	1.6	0.29 5	2.1	1.23 5	1.2	0.66	29.7	0.7	0.6	5	49.3	2.6	47.3	4.2
SLOancl5_1 3-01		13_ 01	52. 5	49.216 43333	19.75 83333	18 79	gneiss			Z	13_01_1	1	0.16 8	1.6	0.83	2.2	4.40 6	1.2	0.2	41.5	1	0.79	5	52.5	2.8	50.4	7.3
			51. 2							Z	13_01_2	1	0.19 4	1.6	1.20 1	2	6.31 9	1.2	0.16	41.5	1	0.81	5	51.2	2.7	50.4	7.3
			51							Z	13_01_3	1	0.31 4	1.6	1.93 5	2.2	10.0 42	1.2	0.16	41	1	0.8	5	51	2.7	50.4	7.3
			62. 8							Z	13_01_4	1	0.13 9	1.6	0.94 3	2.1	6.38 4	1.2	0.15	53.5	1.2	0.85	5	62.8	3.4	50.4	7.3

			42.4					Z	13_01_5	1	0.197	1.6	1.156	2.1	5.036	1.2	0.17	34.3	0.8	0.81	5	42.4	2.3	50.4	7.3
SLOanc15_27-01		27_01	28.6	49.1899	20.07095	1610	granite			Z	27_01_1	1	0.157	1.6	1.873	2	5.12	1.2	0.08	22	0.5	0.77	5	28.6	1.5	29	4.4
			36.7							Z	27_01_2	1	0.177	1.6	2.399	2.1	8.532	1.2	0.07	28.7	0.7	0.78	5	36.7	2	29	4.4
			24.5							Z	27_01_3	1	0.17	1.6	0.621	2.1	1.448	1.2	0.27	18	0.4	0.73	5	24.5	1.3	29	4.4
			29.5							Z	27_01_4	1	0.113	1.7	2.117	2	5.827	1.2	0.05	22.3	0.5	0.76	5	29.5	1.6	29	4.4
			30.7							Z	27_01_5	1	0.317	1.6	1.525	2.1	4.621	1.2	0.21	23.7	0.5	0.77	5	30.7	1.6	29	4.4
SLOanc15_28-01		28_01	35.7	49.19375	20.072966	1436	granite			Z	28_01_1	1	0.154	1.6	1.084	2.1	2.822	1.2	0.14	20.7	0.5	0.58	10	35.7	3.6	31.8	6.4
			32.6							Z	28_01_2	1	0.13	1.6	0.86	2	1.994	1.2	0.15	18.4	0.4	0.56	10	32.6	3.3	31.8	6.4
			39.3							Z	28_01_3	1	0.221	1.6	0.684	2.1	2.25	1.2	0.32	25.1	0.6	0.64	5	39.3	2.1	31.8	6.4
			23.3							Z	28_01_4	1	0.082	2	0.728	2.7	1.119	1.2	0.11	12.3	0.4	0.53	10	23.3	2.4	31.8	6.4
			27.5							Z	28_01_5	1	0.134	1.6	0.733	2.1	1.482	1.2	0.18	15.9	0.4	0.58	10	27.5	2.8	31.8	6.4

SLOanc15_39-01		39/01	22.4	49.13815	19.74295	916	schist			Z	39/01-1	1	0.371	1.6	1.418	2.1	2.916	1.2	0.26	15.9	0.4	0.71	5	22.4	1.2	22.3	2
			23							Z	39/01-2	1	0.382	1.6	0.888	2.2	2.004	1.2	0.43	16.8	0.4	0.73	5	23	1.2	22.3	2
			22.9							Z	39/01-3	1	0.175	1.6	0.857	2.1	1.812	1.2	0.2	16.6	0.4	0.73	5	22.9	1.2	22.3	2
			25.1							Z	39/01-4	1	0.385	1.6	1.065	2	2.682	1.2	0.36	19.1	0.4	0.76	5	25.1	1.4	22.3	2
			19.5							Z	39/01-5	1	0.102	1.7	0.395	2.1	0.675	1.2	0.26	13.2	0.3	0.68	5	19.5	1.1	22.3	2
SLOanc15_41-01		41/01	21.3	49.15005	19.740033	1248	gneiss			Z	41/01-1	1	0.327	1.6	1.524	2.1	3.368	1.4	0.21	17.3	0.4	0.81	5	21.3	1.1	18.7	2
			18.3							Z	41/01-2	1	0.109	1.7	0.951	2	1.615	1.4	0.11	13.6	0.3	0.74	5	18.3	1	18.7	2
			19.3							Z	41/01-3	1	0.081	1.7	0.923	2.1	1.833	1.4	0.09	16	0.4	0.83	5	19.3	1	18.7	2
			20.4							Z	41/01-4	1	0.066	1.8	1.176	2.1	2.286	1.4	0.06	15.8	0.4	0.77	5	20.4	1.1	18.7	2
			16.1							Z	41/01-5	1	0.079	1.7	0.694	2	1.115	1.4	0.11	12.8	0.3	0.8	5	16.1	0.9	18.7	2

SLOanc15_43-01		43/01	15.8	49.1897333 3	20.199383 3	2003	granite			Z	43/01-1	1	0.23	1.6	2.455	2.1	3.532	1.2	0.09	11.6	0.3	0.73	5	15.8	0.8	15.4	4.1
			14							Z	43/01-2	1	0.84	1.6	1.888	2	2.619	1.2	0.44	10.3	0.2	0.74	5	14	0.7	15.4	4.1
			21.9							Z	43/01-3	1	0.207	1.6	0.607	2	1.449	1.2	0.34	18.2	0.4	0.83	5	21.9	1.2	15.4	4.1
			12.3							Z	43/01-4	1	0.119	1.7	0.671	2.1	0.76	1.2	0.18	8.9	0.2	0.73	5	12.3	0.7	15.4	4.1
			20.4							Z	43/01-5	1	0.336	1.6	1.28	2	2.617	1.2	0.26	15.8	0.4	0.77	5	20.4	1.1	15.4	4.1
SLOanc15_T5		T5	31.1	49.22168333	20.01915	1820	granite			Z	T5-1	1	0.243	1.6	0.86	2.1	2.141	1.2	0.28	19.2	0.4	0.62	5	31.1	1.7	36	3.9
			38							Z	T5-2	1	0.835	1.6	0.363	2.1	1.734	1.2	2.29	25.5	0.5	0.67	5	38	2.1	36	3.9
			38.7							Z	T5-3	1	0.124	1.7	1.079	2.3	3.407	1.2	0.11	25.2	0.6	0.65	5	38.7	2.1	36	3.9
			41.2							Z	T5-4	1	0.095	1.7	0.681	2.1	2.398	1.2	0.14	28	0.6	0.68	5	41.2	2.2	36	3.9
			34.6							Z	T5-5	1	0.129	1.7	0.823	2.1	2.332	1.2	0.16	22.4	0.5	0.65	5	34.6	1.9	36	3.9

SLOanc15_T6		T6	45.5	49.2244667	20.0228167	1800	granite			Z	T6-1	1	0.112	1.7	0.439	2.1	1.809	1.2	0.25	31.9	0.7	0.7	5	45.5	2.4	43	7.8
			52.9							Z	T6-2	1	0.052	1.9	0.531	2.1	2.522	1.2	0.1	38.1	0.9	0.72	5	52.9	2.8	43	7.8
			51							Z	T6-3	1	0.116	1.7	0.51	2.1	2.375	1.2	0.23	36.2	0.9	0.71	5	51	2.7	43	7.8
			33.1							Z	T6-4	1	0.218	1.6	0.974	2.1	2.651	1.2	0.22	21.2	0.5	0.64	5	33.1	1.8	43	7.8
			43.9							Z	T6-5	1	0.193	1.6	0.62	2	2.455	1.2	0.31	30.3	0.7	0.69	5	43.9	2.4	43	7.8
SLOanc15_27-02		27_02	48.2	49.1899	19.7529	2021	schist			Z	27_02_1	1	0.686	1.6	1.352	2	6.859	1.2	0.5	37.2	0.8	0.77	5	48.2	2.6	44.6	2.3
			42.5							Z	27_02_2	1	0.418	1.6	0.621	2.1	2.745	1.2	0.67	31.3	0.7	0.74	5	42.5	2.3	44.6	2.3
			46.3							Z	27_02_3	1	0.66	1.6	0.778	2.1	3.846	1.2	0.84	33.8	0.7	0.73	5	46.3	2.5	44.6	2.3
			44							Z	27_02_4	1	0.089	1.7	1.225	2.2	4.893	1.2	0.07	32.2	0.8	0.73	5	44	2.4	44.6	2.3
			43.2							Z	27_02_5	1	0.591	1.6	1.611	2	6.592	1.2	0.36	30.9	0.7	0.72	5	43.2	2.3	44.6	2.3

SLOanc15_28-02		28_02	42.4	49.1735	19.7407	2185	granite			Z	28_02_1	1	0.136	1.7	1.984	2.2	7.753	1.4	0.07	31.5	0.8	0.74	5	42.4	2.3	40.8	2.6
			42.7							Z	28_02_2	1	0.162	1.6	1.473	2	5.987	1.4	0.11	32.5	0.8	0.76	5	42.7	2.3	40.8	2.6
			89.6							Z	28_02_3	1	0.196	1.6	0.841	2	7.488	1.4	0.23	69	1.6	0.77	5	89.6	4.8	40.8	2.6
			69.2							Z	28_02_4	1	0.192	1.6	1.585	2.1	10.141	1.4	0.12	50.9	1.3	0.74	5	69.2	3.7	40.8	2.6
			38							Z	28_02_5	1	0.097	1.7	0.892	2	3.144	1.4	0.11	28.2	0.7	0.74	5	38	2	40.8	2.6
SLOanc15_30-02		30_02	36.6	49.1753	20.145483	2428	granite			Z	30_02_1	1	0.3	1.6	0.837	2.1	3.336	1.2	0.36	30.1	0.7	0.82	5	36.6	2	28.6	4.2
			28.7							Z	30_02_2	1	0.165	1.6	0.876	2.1	2.453	1.2	0.19	22	0.5	0.77	5	28.7	1.5	28.6	4.2
			27.5							Z	30_02_3	1	0.217	1.6	0.871	2.1	2.421	1.2	0.25	21.5	0.5	0.78	5	27.5	1.5	28.6	4.2
			28.9							Z	30_02_4	1	0.271	1.6	0.909	2.1	2.719	1.2	0.3	22.9	0.5	0.79	5	28.9	1.5	28.6	4.2
			25.5							Z	30_02_5	1	0.19	1.6	0.572	2.1	1.503	1.2	0.33	20	0.5	0.79	5	25.5	1.4	28.6	4.2

SLOancl5_32-02		32/02	33.2	49.1469	20.04025	1970	granite			Z	32/02-1	1	0.382	1.6	0.681	2.1	2.709	1.2	0.56	28.8	0.6	0.87	5	33.2	1.8	30	3.8
			29.2							Z	32/02-2	1	0.324	1.6	2.096	2	6.257	1.2	0.15	23.6	0.6	0.81	5	29.2	1.6	30	3.8
			25							Z	32/02-3	1	0.498	1.6	2.86	2	7.215	1.2	0.17	19.9	0.5	0.8	5	25	1.4	30	3.8
			34.1							Z	32/02-4	1	0.193	1.6	2.992	2	10.37	1.2	0.06	28	0.7	0.82	5	34.1	1.8	30	3.8
			32.6							Z	32/02-5	1	0.417	1.6	1.721	2	5.976	1.2	0.24	27	0.6	0.83	5	32.6	1.8	30	3.8
SLOancl5_38-02		38/02	28.9	49.1805833	20.084066	2224	granite			Z	38/02-1	1	0.114	1.7	1.036	2.1	2.748	1.4	0.11	21.2	0.5	0.73	5	28.9	1.5	31.3	6.4
			38.9							Z	38/02-2	1	0.595	1.6	0.978	2	3.924	1.4	0.6	28.8	0.6	0.74	5	38.9	2.1	31.3	6.4
			38.2							Z	38/02-3	1	0.31	1.6	1.191	2	4.381	1.4	0.26	28.4	0.7	0.74	5	38.2	2	31.3	6.4
			26.4							Z	38/02-4	1	0.529	1.6	1.401	2	3.514	1.4	0.38	18.9	0.4	0.72	5	26.4	1.4	31.3	6.4
SLOancl5_39-02		39/02	34.7	49.18123333	20.080883	2035	granite			Z	39/02-1	1	0.256	1.6	1.81	2	5.405	1.2	0.14	23.7	0.5	0.68	5	34.7	1.9	29.9	3.9

			212.6						Z	39/02-2*	1	0.26	1.6	0.415	2.1	7.765	1.2	0.62	132.4	2.9	0.62	5	212.6	11.4	29.9	3.9
			31.8						Z	39/02-3	1	0.167	1.6	1.796	2.1	4.61	1.2	0.09	20.6	0.5	0.65	5	31.8	1.7	29.9	3.9
			31.4						Z	39/02-4	1	1.092	1.6	1.672	2	4.898	1.2	0.65	20.8	0.4	0.66	5	31.4	1.7	29.9	3.9
			25.3						Z	39/02-5	1	0.14	1.6	0.479	2.1	1.022	1.2	0.29	16.4	0.4	0.65	5	25.3	1.4	29.9	3.9
SLOancl5_47-02		47/02	19.5	49.21656667	20.30385	800	mudstone		Z	47/02-1	1	0.507	1.6	2.967	2	4.939	1.4	0.17	13.1	0.3	0.67	5	19.5	1.1	18.6	4.1
			26.5						Z	47/02-2	1	0.3	1.6	1.284	2	3.325	1.4	0.23	20.1	0.5	0.76	5	26.5	1.4	18.6	4.1
			18.6						Z	47/02-3	1	0.858	1.6	1.288	2	2.348	1.4	0.66	12.9	0.3	0.7	5	18.6	1	18.6	4.1
			18.7						Z	47/02-4	1	0.893	1.6	2.946	2.1	4.957	1.4	0.3	12.9	0.3	0.69	5	18.7	1	18.6	4.1
			15.3						Z	47/02-5	1	0.543	1.6	1.866	2.1	2.432	1.4	0.29	10	0.2	0.65	5	15.3	0.8	18.6	4.1
	Merten 2010															ccSTP										
ROMmer10_RO-02		RO-02	7.4	45.1264855	26.454895	339	sandstone	11.5-10.5		p1-Sd		0.055	10%	0.016	5%	1.66E-11	10%	3.6	4.7		0.64		7.4	0.6	9.2	0.6

			8.9						p2-S	0.081	7%	0.022	4%	2.83E-11	6%	3.8	5.7	0.64	8.9	1.3		
			9.4						p3-S	0.069	8%	0.017	5%	2.39E-11	7%	4.2	5.9	0.63	9.4	1.6		
			9						p1-L	0.095	6%	0.044	2%	4.84E-11	7%	2.2	6	0.67	9	0.9		
			9.5						p2-L	0.094	6%	0.024	4%	3.60E-11	9%	4	6.4	0.68	9.5	2.5		
			10.7						p3-L	0.169	3%	0.069	1%	9.50E-11	3%	2.5	7.2	0.67	10.7	2		
ROMmer10_RO-04		RO-04	29.7	45.2995194	26.359366	285	sandstone	10.5-8.5														
			9.6						p1-Sd	0.032	16%	0.032	3%	9.17E-11	2%	1	19.2	0.65	29.7	2.2	9.9	0.8
			13.9						p2-S	0.01	36%	0.002	28%	3.36E-12	36%	4.6	5.7	0.6	9.6	0.8		
									p3-S	0.098	6%	0.137	1%	1.60E-10	1%	0.7	8.2	0.59	13.9	2.9		
ROMmer10_RO-05		RO-05	3.7	45.3860364	26.3215152	357	sandstone	37.2-23.0														

			3.8						p1-S	0.082	7%	0.054	2%	2.08E-11	8%	1.6	2.3	0.62	3.7	0.7	3.3	0.4
			2.8						p2-S	0.049	11%	0.022	4%	9.43E-12	16%	2.3	2.3	0.6	3.8	0.9		
									p3-S	0.076	7%	0.017	5%	6.79E-12	21%	4.7	1.6	0.57	2.8	0.5		
ROMmer10_RO-06		RO-06	2.1	45.447 31927	26.27 46518	892	sandstone	65.5-40.4														
			1.7						p1-S	0.15	4%	0.081	1%	1.91E-11	9%	1.9	1.3	0.65	2.1	0.3	1.9	0.1
			1.8						p2-S	0.026	19%	0.007	11%	1.84E-12	50%	3.6	1.1	0.67	1.7	0.3		
			5.4						p3-S	0.089	6%	0.065	1%	1.15E-11	14%	1.4	1.1	0.61	1.8	0.3		
			3.1						p1-Ld	0.023	20%	0.008	10%	6.57E-12	34%	2.9	3.9	0.72	5.4	0.5		
			1.9						p2-Ld	0.49	1%	0.307	0%	1.12E-10	3%	1.6	2.2	0.71	3.1	0.4		
									p3-L	0.295	2%	0.377	0%	7.57E-11	4%	0.8	1.4	0.74	1.9	0.3		

ROMmer10_RO-07		RO-07	2.7	45.57168741	26.1737154	873	sandstone	65.5-40.4															
			1.8								p1-S	0.16	4%	0.13	1%	3.44E-11	5%	1.3	1.7	0.62	2.7	0.4	2.2	0.1
			2.8								p2-S	0.133	4%	0.013	7%	5.81E-12	24%	10.7	1.1	0.61	1.8	0.2		
			2.7								p3-S	0.216	3%	0.107	1%	3.30E-11	5%	2.1	1.7	0.61	2.8	0.5		
			2.7								p1-L	0.342	2%	0.089	1%	3.81E-11	8%	4	1.8	0.68	2.7	0.5		
			2.2								p2-L	0.538	1%	0.105	1%	5.22E-11	6%	5.2	1.8	0.68	2.7	0.4		
											p3-L	0.306	2%	0.071	1%	2.69E-11	11%	4.5	1.5	0.7	2.2	0.3		
ROMmer10_RO-09		RO-09	105.6	45.8420529 5	25.429308 9	922	conglomerate	98.9-93.5															
			53.7								p1-Sd	0.016	28%	0.04	2%	3.35E-10	1%	0.4	63.5	0.6	105.6	6.3		
			149								p2-Sd	0.014	31%	0.02	4%	9.44E-11	2%	0.7	33.3	0.62	53.7	5.8		

			16.3						p3-Sd	0.035	15%	0.051	2%	6.70E-10	0%	0.7	92.6	0.62	149	24.3		
			17						p1-Ld	0.013	31%	0.006	13%	1.31E-11	21%	2.2	11.4	0.7	16.3	1.2		
			105.8						p2-Ld	0.016	27%	0.007	11%	1.42E-11	20%	2.3	10.5	0.62	17	3.7		
									p3-Ld	0.014	30%	0.051	2%	4.60E-10	1%	0.3	69.3	0.66	105.8	13.4		
ROMmer10_RO-10		RO-10	90.4	45.85106513	25.272496	520	schist															
			146.5						p1-Sd	0.014	30%	B.D.	84%	2.38E-11	7%	-	55.9	0.62	90.4	155.5		
			99.1						p2-Sd	0.011	35%	B.D.	69%	3.22E-11	5%	-	85.7	0.58	146.5	22.5		
									p3-Sd	0.015	28%	B.D.	100%	2.73E-11	6%	-	61.4	0.62	99.1	11.1		
ROMmer10_RO-11		RO-11	38.7	45.997062	25.198597	470	sandstone	16.0-12.5														
			28.7						p1-S	0.097	6%	0.048	2%	1.96E-10	1%	2.1	22.5	0.58	38.7	5.3	32	2.4

			32.3						p2-S	0.017	26%	0.095	1%	2.14E-10	1%	0.2	17.7	0.62	28.7	3.1		
			57.7						p1-L	0.198	3%	0.062	1%	2.77E-10	1%	3.3	20.9	0.65	32.3	6.7		
			38.5						p2-Ld	0.221	3%	0.077	1%	7.32E-10	0%	2.9	46.3	0.8	57.7	5.8		
									p3-L	0.268	2%	0.092	1%	4.63E-10	1%	3	24.5	0.63	38.5	8.6		
ROMmer10_RO-12		RO-12	11.8	45.8690895	25.7014769	763	conglomerate	125.0-112.0												11.8	2.4	13.8	0.8
			13.9						p1-S	0.04	13%	0.003	21%	1.05E-11	15%	11.9	6.7	0.57	13.9	0.8		
			14.8						p2-S	0.028	18%	0.014	6%	2.07E-11	8%	2	8.1	0.59	14.8	2.5		
									p1-L	0.039	13%	0.016	5%	3.07E-11	6%	2.5	10.1	0.69				
ROMmer10_carp31		Carp31	4.5	45.5987239 7	26.144876 4	700	sandstone	85-66	audia nappe											4.5	0.4	4.3	0.2

			5.1							p1		0.033	15%	0.036	2%	1.81E-11	9%	0.9	3.4		0.76	5.1	0.4			
			3.5							p2		0.017	26%	0.009	9%	5.33E-12	29%	1.9	3.2		0.63	3.5	0.4			
										p3		0.023	20%	0.051	2%	1.62E-11	10%	0.5	2.4		0.68					
SLOdan11_BTZ-217	Danisik 2011	BTZ-217	72.2	49.013	20.901	878	granite	145-66	tatris crystalline basement	Z	BTZ-217-1	1	0.288	4.3	2.294	4.3	14.182	0.5	0.12	49.2	2.1	0.68	72.2	4.8	65.5	6.1
			60.3							Z	BTZ-217-2	1	0.128	4.3	1.199	4.3	6.001	0.5	0.11	40	1.7	0.66	60.3	4		
			64.5							Z	BTZ-217-4	1	0.173	4.3	1.437	4.2	7.963	0.5	0.12	44.1	1.9	0.68	64.5	4.2		
SLOdan11_BTZ-222		BTZ-222	47.6	49.004	20.879	757	tonalitic gneiss	145-66	tatris crystalline basement	Z	BTZ-222-1	1	0.294	4.5	3.304	4.3	14.117	0.5	0.09	34.3	1.5	0.72	47.6	3.1	50	3.2
			53.7							Z	BTZ-222-2	1	0.386	4.3	2.637	4.3	13.954	0.6	0.15	41.9	1.8	0.78	53.7	3.5		
			48.9							Z	BTZ-222-3	1	0.27	4.3	4.319	4.3	20.225	0.6	0.06	37.8	1.6	0.77	48.9	3.2		

SLOdan11_BTZ-485		BTZ-485	48.8	49.011	20.913	733	tonalite	145-66	tatris crystalline basement	Z	BTZ-485-1	1	2.072	4	4.306	4	26.412	0.6	0.48	45.1	1.7	0.93		48.8	3	50.2	4.3
			55.1							Z	BTZ-485-2	1	1.967	4	4.952	4	34.297	0.6	0.39	51.9	1.9	0.94		55.1	3.4		
			47							Z	BTZ-485-3	1	0.671	4	3.516	4	18.772	0.6	0.19	41.9	1.6	0.89		47	3		
SLOdan11_BTZ-487		BTZ-487	50	49.023	20.876	966	granodiorite	145-66	tatris crystalline basement	Z	BTZ-487-2	1	2.02	3.9	3.936	4	22.296	0.6	0.51	41.4	1.5	0.83		50	3.1	52.2	3.1
			51							Z	BTZ-487-3	1	0.32	4	1.599	4	8.689	0.6	0.2	42.5	1.7	0.83		51	3.2		
			55.9							Z	BTZ-487-4	1	1.493	4	7.504	4.1	47.982	0.6	0.2	50	2	0.89		55.9	3.5		
SLOdan11_BTA-217		BTA-217	16.9	49.013	20.901	878	granite	145-66	tatris crystalline basement	A	BTA-217-1	1	0.146	3.7	0.341	3.9	0.608	0.5	0.43	13.3	0.5	0.79		16.9	1.1	15.7	1.4
			17							A	BTA-217-2	1	0.1	3.8	0.222	3.9	0.391	0.6	0.45	13.1	0.5	0.77		17	1.1		

			14.3					A	BTA-217-3	1	0.324	3.7	0.485	3.9	0.773	0.5	0.66	11.3	0.4	0.79		14.3	0.9		
			14.8					A	BTA-217-4	1	0.171	3.7	0.25	3.9	0.399	0.5	0.68	11.3	0.4	0.76		14.8	0.9		
SLOdan11_BTA-222		BTA-222	11.1	49.004	20.879	757	tonalitic gneiss	145-66	tatris crystalline basement	A	BTA-222-1	1	0.002	7.3	0.057	3.9	0.054	1.2	0.04	7.7	0.3	0.69		11.1	0.7	12.3	0.9
			13					A	BTA-222-2	1	0.003	5.4	0.068	3.9	0.076	1	0.05	9	0.4	0.69		13	0.8		
			13.3					A	BTA-222-4	1	0.01	4	0.298	3.8	0.385	0.9	0.03	10.5	0.4	0.79		13.3	0.8		
			12.2					A	BTA-222-5	1	0.017	3.8	0.404	3.9	0.511	0.9	0.04	10.3	0.4	0.84		12.2	0.8		
			12.2					A	BTA-222-6	1	0.024	3.8	0.546	3.9	0.683	0.9	0.04	10.2	0.4	0.83		12.2	0.8		
SLOdan11_BTA-485		BTA-485	13	49.011	20.913	733	tonalite	145-66	tatris crystalline basement	A	BTA-485-1	1	0.171	3.7	0.261	3.9	0.391	0.6	0.65	10.7	0.4	0.82		13	0.8	14.9	1.5
			15.4					A	BTA-485-2	1	0.114	3.7	0.206	3.9	0.307	0.6	0.55	10.8	0.4	0.7		15.4	1		
			16.5					A	BTA-485-3	1	0.122	3.8	0.241	3.9	0.389	0.6	0.5	11.8	0.5	0.72		16.5	1		

			15						A	BTA-485-5	1	0.105	3.8	0.122	3.9	0.21	0.6	0.86	11.7	0.5	0.78	15	0.9		
SLOdan11_BTA-487		BTA-487	17.7	49.023	20.876	966	granodiorite	145-66	tatris crystalline basement	A	BTA-487-1x	1	0.005	5.9	0.041	3.8	0.064	0.6	0.11	12.5	0.5	0.71	17.7	1.1	16.7	2.5
			19.6							A	BTA-487-2x	1	0.009	4.4	0.044	3.9	0.096	0.6	0.2	17.3	0.7	0.88	19.6	1.3		
			18.9							A	BTA-487-3x	1	0.005	5.1	0.065	3.9	0.127	0.6	0.08	15.6	0.6	0.83	18.9	1.2		
			13.3							A	BTA-487-3	1	0.25	3.7	0.269	3.9	0.412	1	0.92	10.3	0.4	0.77	13.3	0.9		
			17.3							A	BTA-487-4	1	0.178	3.7	0.269	3.9	0.546	1	0.66	14.4	0.6	0.83	17.3	1.1		
			14.3							A	BTA-487-5	1	0.099	3.7	0.15	3.9	0.23	0.6	0.66	10.9	0.4	0.76	14.3	0.9		
ROMmer11_RO-02		RO-02	7.4	45.1264855	26.454895	339	sandstone	11.5-10.5	foredeep	A	p1-Se		0.055	10%	0.016	5%	1.66E-11	10%	3.6	4.7	0.2	0.64	7.4	0.6	9.2	0.6
			8.9							A	p2-S		0.081	7%	0.022	4%	2.83E-11	6%	3.8	5.7	0.2	0.64	8.9	1.3		
			9.4							A	p3-S		0.069	8%	0.017	5%	2.39E-11	7%	4.2	5.9	0.2	0.63	9.4	1.6		

			9					A	p1-L	0.095	6%	0.044	2%	4.84E-11	7%	2.2	6	0.2	0.67	9	0.9		
			9.5					A	p2-L	0.094	6%	0.024	4%	3.60E-11	9%	4	6.4	0.3	0.68	9.5	2.5		
			10.7					A	p3-L	0.169	3%	0.069	1%	9.50E-11	3%	2.5	7.2	0.3	0.67	10.7	2		
ROMmer11_RO-04		RO-04	29.7	45.2995194	26.359366 4	285	sandstone	10.5-8.5	Foredeep	A	p1-Se	0.032	16%	0.032	3%	9.17E-11	2%	1	19.2	0.7	0.65	29.7	2.2	9.9	0.8
			9.6					A	p2-S	0.01	36%	0.002	28%	3.36E-12	36%	4.6	5.7	0.4	0.6	9.6	0.8		
			13.9					A	p3-S	0.098	6%	0.137	1%	1.60E-10	1%	0.7	8.2	0.3	0.59	13.9	2.9		
ROMmer11_RO-05		RO-05	3.7	45.3860364 1	26.3215152	357	sandstone	37.2-23.0	Tarcau nappe	A	p1-S	0.082	7%	0.054	2%	2.08E-11	8%	1.6	2.3	0.1	0.62	3.7	0.7	3.3	0.4
			3.8					A	p2-S	0.049	11%	0.022	4%	9.43E-12	16%	2.3	2.3	0.1	0.6	3.8	0.9		
			2.8					A	p3-S	0.076	7%	0.017	5%	6.79E-12	21%	4.7	1.6	0.1	0.57	2.8	0.5		
ROMmer11_RO-06		RO-06	2.1	45.44731927	26.2746518	892	sandstone	65.5-40.4	Tarcau nappe	A	p1-S	0.15	4%	0.081	1%	1.91E-11	9%	1.9	1.3	0.1	0.65	2.1	0.3	1.9	0.1

			1.7					A	p2-S	0.026	19%	0.007	11%	1.84E-12	50%	3.6	1.1	0	0.67		1.7	0.3		
			1.8					A	p3-S	0.089	6%	0.065	1%	1.15E-11	14%	1.4	1.1	0	0.61		1.8	0.3		
			5.4					A	p1-Le	0.023	20%	0.008	10%	6.57E-12	34%	2.9	3.9	0.2	0.72		5.4	0.5		
			3.1					A	p2-Le	0.49	1%	0.307	0%	1.12E-10	3%	1.6	2.2	0.1	0.71		3.1	0.4		
			1.9					A	p3-L	0.295	2%	0.377	0%	7.57E-11	4%	0.8	1.4	0	0.74		1.9	0.3		
ROMmerl1_RO-07		RO-07	2.7	45.57168741	26.1737154	873	sandstone	65.5-40.4	Tarcau nappe	A	p1-S	0.16	4%	0.13	1%	3.44E-11	5%	1.3	1.7	0.1	0.62		2.7	0.4	2.2	0.1
			1.8					A	p2-S	0.133	4%	0.013	7%	5.81E-12	24%	10.7	1.1	0	0.61		1.8	0.2		
			2.8					A	p3-S	0.216	3%	0.107	1%	3.30E-11	5%	2.1	1.7	0.1	0.61		2.8	0.5		
			2.7					A	p1-L	0.342	2%	0.089	1%	3.81E-11	8%	4	1.8	0.1	0.68		2.7	0.5		
			2.7					A	p2-L	0.538	1%	0.105	1%	5.22E-11	6%	5.2	1.8	0.1	0.68		2.7	0.4		
			2.2					A	p3-L	0.306	2%	0.071	1%	2.69E-11	11%	4.5	1.5	0.1	0.7		2.2	0.3		

ROMmerl1_RO-09		RO-09	105.6	45.8420529 5	25.429308 9	922	conglomerate	98.9-93.5	post-cretaceous cover	A	p1-Se	0.016	28%	0.04	2%	3.35E-10	1%	0.4	63.5	2.4	0.6	105.6	6.3
			53.7							A	p2-Se	0.014	31%	0.02	4%	9.44E-11	2%	0.7	33.3	1.3	0.62	53.7	5.8
			149							A	p3-Se	0.035	15%	0.051	2%	6.70E-10	0%	0.7	92.6	3.3	0.62	149	24.3
			16.3							A	p1-Le	0.013	31%	0.006	13%	1.31E-11	21%	2.2	11.4	0.5	0.7	16.3	1.2
			17							A	p2-Le	0.016	27%	0.007	11%	1.42E-11	20%	2.3	10.5	0.5	0.62	17	3.7
			105.8							A	p3-Le	0.014	30%	0.051	2%	4.60E-10	1%	0.3	69.3	2.5	0.66	105.8	13.4
ROMmerl1_RO-10		RO-10	90.4	45.85106513	25.272496 9	520	schist		Bucovinian nappe	A	p1-Sf	0.014	30%	B.D.	84%	2.38E-11	7%	-	55.9	95.9	0.62	90.4	155.5
			146.5							A	p2-Sf	0.011	35%	B.D.	69%	3.22E-11	5%	-	85.7	8.7	0.58	146.5	22.5
			99.1							A	p3-Sf	0.015	28%	B.D.	100%	2.73E-11	6%	-	61.4	5.6	0.62	99.1	11.1

ROMmer11_RO-11		RO-11	38.7	45.9970625 2	25.198597	470	sandstone	16.0-12.5	transylvanian hinterland	A	p1-S	0.097	6%	0.048	2%	1.96E-10	1%	2.1	22.5	0.8	0.58	38.7	5.3	32	2.4
			28.7							A	p2-S	0.017	26%	0.095	1%	2.14E-10	1%	0.2	17.7	0.6	0.62	28.7	3.1		
			32.3							A	p1-L	0.198	3%	0.062	1%	2.77E-10	1%	3.3	20.9	0.8	0.65	32.3	6.7		
			57.7							A	p2-Le	0.221	3%	0.077	1%	7.32E-10	0%	2.9	46.3	1.7	0.8	57.7	5.8		
			38.5							A	p3-L	0.268	2%	0.092	1%	4.63E-10	1%	3	24.5	0.9	0.63	38.5	8.6		
ROMmer11_RO-12		RO-12	11.8	45.8690895	25.7014769	763	conglomerate	125.0-112.0	Baraolt nappe	A	p1-S	0.04	13%	0.003	21%	1.05E-11	15%	11.9	6.7	0.3	0.57	11.8	2.4	13.8	0.8
			13.9							A	p2-S	0.028	18%	0.014	6%	2.07E-11	8%	2	8.1	0.3	0.59	13.9	0.8		
			14.8							A	p1-L	0.039	13%	0.016	5%	3.07E-11	6%	2.5	10.1	0.4	0.69	14.8	2.5		

ROMmer11_carp31		Carp31	4.5	45.5987239 7	26.144876 4	700	sandstone	85-66	audia nappe	A	p1	0.033	15%	0.036	2%	1.81E-11	9%	0.9	3.4	0.1	0.76	4.5	0.4	4.3	0.2
			5.1							A	p2	0.017	26%	0.009	9%	5.33E-12	29%	1.9	3.2	0.1	0.63	5.1	0.4		
			3.5							A	p3	0.023	20%	0.051	2%	1.62E-11	10%	0.5	2.4	0.1	0.68	3.5	0.4		
ROMmer11_carp34		Carp34	38.9	45.6654141 3	25.270694 5	700	sandstone		sub-bucovinian nappe	A	p1	0.005	25%	0.075	2%	2.63E-10	3%	0.1	28.2	1.3	0.73	38.9	6.9	39.3	6
			40.4							A	p2	0.012	13%	0.076	2%	2.67E-10	3%	0.2	27.9	1.2	0.69	40.4	11.8		
ROMmer11_carp45		Carp45	16.6	45.631 16783	25.530245 4	800	sandstone	110-93.9	cretaceous post tectocover	A	p1e	0.033	5%	0.033	4%	5.99E-11	11%	1	12.1	1	0.73	16.6	4.6		
			48.4							A	p3f	0.016	10%	B.D.	100%	1.36E-11	35%	7.1	31	16.8	0.64	48.4	29.7		
			32.2							A	p4e	0.037	5%	0.005	21%	3.89E-11	17%	7.3	22.7	3	0.71	32.2	5.9		

ROMmerl1_carp68		Carp68	11.9	45.66180926	26.079887	680	sandstone	113-100	Convolute flysch nappe	A	p2	0.066	3%	0.004	24%	1.69E-11	31%	15.1	7	1.4	0.58	11.9	2.8	12.1	2.3
			12.4							A	p3	0.06	3%	0.007	16%	1.86E-11	11%	8.2	7.1	1.4	0.57	12.4	4.2		
			19.9							A	p4e	0.085	2%	0.004	26%	3.37E-11	7%	21.7	11.5	1.4	0.57	19.9	6.1		
ROMmerl1_carp67		Carp67	1.8	45.546508 6	26.1773203	630	sandstone	56-33.9	Tarcau nappe	A	p1	0.866	0%	1.218	0%	2.45E-10	2%	0.7	1.4	0.1	0.78	1.8	0.2	2	0.1
			2							A	p2	0.643	0%	0.602	0%	1.42E-10	3%	1.1	1.6	0.1	0.77	2	0.2		
			6.4							A	p4e	0.07	2%	0.007	17%	1.19E-11	28%	10.2	4.2	1.1	0.65	6.4	1.7		
			2.5							A	p5	0.223	1%	0.245	1%	5.93E-11	7%	0.9	1.6	0.1	0.65	2.5	0.5		
ROMmerl1_carp66		Carp66	6.3	45.508602 12	26.2277885	620	sandstone	33.9-23.03	Tarcau nappe	A	p1	0.183	1%	0.035	4%	3.33E-11	12%	5.4	3.5	0.3	0.56	6.3	4.5	3.2	0.5
			43.3							A	p2e	0.075	2%	0.014	9%	1.00E-10	5%	5.5	26.1	1.7	0.6	43.3	11		

			3.1						A	p4	0.483	0%	0.097	1%	5.37 E-11	8%	5.1	2.1	0.1	0.67	3.1	0.5		
ROMmer11_carp64		Carp64	5.3	45.40766566	26.3251201	430	sandstone	66-56	Tarcau nappe	A	p1	0.117	2%	0.037	4%	2.47 E-11	17%	3.3	3.2	0.3	0.6	5.3	1.4	3.4	0.4
			3.4							A	p2	0.113	2%	0.124	1%	3.74 E-11	7%	0.9	2	0.1	0.6	3.4	1.3		
			3.2							A	p4	0.11	2%	0.162	1%	4.84 E-11	6%	0.7	2.1	0.1	0.67	3.2	0.4		
ROMmer11_carp5		Carp5	23.8	47.2802237 2	24.4860665	400	sandstone	21.5-16.0	Transylvanian hinterland	A	p1e	0.025	7%	0.005	22%	1.82 E-11	25%	5	13.7	2	0.58	23.8	3.6	14	1.3
			14							A	p2	0.11	2%	0.071	2%	9.87 E-11	6%	1.6	8.3	0.4	0.6	14	1.4		
			13.8							A	p3	0.315	1%	0.094	1%	1.67 E-10	4%	3.4	8.1	0.3	0.59	13.8	3.1		
ROMmer11_carp6		Carp6	18.8	47.21606624	24.6975485	600	dej tuff	16.0-12.5	Transylvanian hinterland	A	p1	0.042	4%	0.011	11%	3.15 E-11	20%	3.7	12.2	2	0.65	18.8	4.5	20.2	2.2
			19.1							A	p2	0.023	7%	0.008	14%	1.96 E-11	26%	2.9	11.7	1.3	0.61	19.1	4.7		

			23.2					A	p3	0.033	5%	0.013	10%	3.66E-11	16%	2.7	14.6	1.1	0.63	23.2	4.7		
			19.9					A	p4	0.031	6%	0.006	18%	2.14E-11	30%	5	13	1.8	0.65	19.9	4.2		
ROMmer11_carp107		Carp 107	21.8	47.2897285 4	24.9446737	1030	sandstone	28.4-23.8	Transylvanian hinterland	A	p1	0.151	1%	0.048	3%	1.49E-10	6%	3.2	14.6	0.7	0.67	21.8	1.2	18.7	0.9
			116.4					A	p2e	0.154	1%	0.008	14%	4.36E-10	3%	18.9	80	4.9	0.69	116.4	9.1		
			14.5					A	p3	0.228	1%	0.007	16%	7.80E-11	8%	31.6	10.5	1	0.72	14.5	1.4		
ROMmer11_carp60		Carp 60	75.4	47.46794376	25.241699	830	schist		sub-bucovinian nappe	A	p1f	0.005	28%	0.001	60%	9.27E-12	57%	5.1	37.5	44.2	0.5	75.4	89		
			41.2					A	p2e	0.01	16%	0.003	32%	1.72E-11	28%	3.3	26.6	10.9	0.64	41.2	13.3		
			475.5					A	p3e	0.015	11%	0.002	46%	1.83E-10	4%	9.3	283.8	79.9	0.6	475.5	192.7		

ROMmerl1_carp19b		Carp 19b	14.1	47.534 47744	25.54 11006	700	sandstone	145.5-99.6	audia nappe	A	p1	0.266	1%	0.125	1%	2.40E-10	4%	2.2	10.5	0.5	0.74	14.1	2.6	15.5	2.2
			19.5							A	p2	0.181	1%	0.021	6%	9.64E-11	9%	8.8	12.4	0.7	0.64	19.5	4.3		
ROMmerl1_carp19b		Carp 19	51.3	47.539 22985	25.51 97148	700	sandstone	145.5-99.7	audia nappe	A	p1f	0.005	26%	0.001	51%	7.12E-12	35%	3.9	22.9	17.4	0.45	51.3	41.3	32.4	4.8
			32.4							A	p2	0.002	42%	0.022	6%	3.94E-11	19%	0.1	14.3	1.5	0.44	32.4	4.8		
ROMmerl1_carp69		Carp69	8	46.215 68479	26.49 15818	370	sandstone	65.5-40.4	Tarcau nappe	A	p1e	0.213	3%	0.056	2%	5.88E-11	5%	3.9	4.6	0.2	0.57	8	1.8	5.7	0.5
			4.5							A	p2	0.24	2%	0.236	0%	1.01E-10	3%	1	2.8	0.1	0.63	4.5	1		
			6							A	p3	0.114	5%	0.008	10%	1.52E-11	17%	14.8	3.6	0.1	0.6	6	0.6		
ROMmerl1_carp36		Carp 36	57.3	45.50 99525	24.58 3490 8	1000	schist		supragetic nappe	A	p1	0.006	16%	0.179	1%	9.48E-10	1%	0	43.1	1.2	0.75	57.3	4.3	62.9	2.8

			64.6						A	p2		0.004	22%	0.115	1%	6.45E-10	1%	0	45.5	1.2	0.7		64.6	4.2		
			74.9						A	p3		0.003	25%	0.1	1%	6.19E-10	1%	0	50.4	1.7	0.67		74.9	7.6		
SLOdan08_RO-6	Danisik 2008	RO-6	11,8	48.6947222	20.2919444	167	granite		tatric basement		RO-6#1	1	0,111	2,1	0,074	3,1	0,102	0,9	1,51	8,4	0,2	0,71		11,8	0.7	12,9	1,8
			12,5								RO-6#2	1	0,393	1,8	0,178	3,3	0,319	0,9	2,20	9,7	0,2	0,78		12,5	0,7		
			10,7								RO-6#3	1	0,346	1,9	0,169	2,5	0,221	0,9	2,04	7,3	0,2	0,68		10,7	0,6		
			14,7								RO-6#4	1	0,364	2,2	0,198	1,7	0,404	0,9	1,84	11,7	0,3	0,80		14,7	0,8		
			14,9								RO-6#5	1	0,298	2,5	0,171	2,6	0,344	0,9	1,75	11,8	0,3	0,79		14,9	0,8		
SLOdan08_KVP-3		KVP-3	11,4	48.7008333	20.2927778	-324	granite		tatric basement		KVP-3#1	1	0,130	1,95	0,052	3,30	0,071	1,0	2,48	7,1	0,2	0,63		11,4	0.6	11,6	0,4
			11,8								KVP-3#2	1	0,359	2,73	0,145	2,40	0,238	0,9	2,48	8,6	0,2	0,73		11,8	0,7		
			12,1								KVP-3#3	1	0,173	2,14	0,065	3,51	0,101	0,9	2,67	7,9	0,2	0,66		12,1	0,7		

			11,2							KVP-3#4	1	0,410	2,16	0,145	2,59	0,240	0,9	2,82	8,2	0,2	0,73		11,2	0,6		
SLOdan08_KVH-3		KVH-3	10,4	48.7008333	20.2927778	-975	granite		tatric basement		KVH-3#1	1	0,392	2,3	0,185	2,52	0,274	0,9	2,12	8,1	0,2	0,78		10,4	0.6	11,3	0,8
			12,4							KVH-3#2	1	0,178	2,3	0,137	3,27	0,220	0,9	1,30	10,1	0,3	0,82		12,4	0,7		
			11,4							KVH-3#3	1	0,350	2,6	0,151	2,56	0,245	0,9	2,32	8,7	0,2	0,76		11,4	0,7		
			11,2							KVH-3#4	1	0,498	1,8	0,202	2,41	0,332	0,9	2,46	8,6	0,2	0,77		11,2	0,6		
RTCdansep08 T	Danisik sep2008	T	9,1	49.5652777 8	18.2388889	400	tesche nite		tesin nappe		T#1	1	0,424	1,8	0,0649	3,1	0,148	2,6	6,54	7,4	0,2	0,81		9,1	0,5	9,0	0,2
			8,8							T#2	2	0,395	2,1	0,0631	4,1	0,135	3,4	6,27	7,2	0,3	0,82		8,8	0,6		
			9,0							T#4	1	0,290	1,1	0,0474	3,6	0,099	4,1	6,13	7,1	0,3	0,79		9,0	0,6		
RTCdansep08 S		S	23,0	49.6819444 4	18.2763889	335	tesche nite		godula nappe		S#1	3	1,189	1,4	0,154	2,8	0,997	4,0	7,73	18,9	0,8	0,82		23,0	1,5	18,6	3,3
			19,5							S#2	5	1,780	1,2	0,231	2,5	1,176	1,2	7,70	14,9	0,3	0,76		19,5	1,0		

			15,3						S#4	4	1,486	1,2	0,190	2,0	0,786	1,4	7,83	12,0	0,2	0,79		15,3	0,8		
			22,9						S#11	1	0,450	2,8	0,053	3,4	0,367	0,9	8,42	19,0	0,6	0,83		22,9	1,3		
			18,1						S#14	1	0,358	3,5	0,035	7,7	0,200	0,9	10,30	13,9	0,6	0,77		18,1	1,2		
			16,1						S#20	1	0,564	2,6	0,078	4,7	0,304	0,9	7,22	11,9	0,4	0,74		16,1	0,9		
			15,4						S#21	1	0,358	3,0	0,045	3,6	0,180	0,9	7,94	11,4	0,4	0,74		15,4	0,9		
SLOsmi16_G-01	Smigielski 2016	G_01	40.7	49.185 10857	20.05 78818	20 75	crystal line	-	Tatric basement	Z	1		0.126	8.30 %	0.521	1.20 %	746.7	0.50 %	0.24	24.8		0.61		40.7	0.6	43.7	4.4
			46.9							Z	2		0.395	2.80 %	20.695	1.10 %	1929	0.50 %	0.15	33.8		0.72		46.9	0.6		
SLOsmi16_G-06		G_06	37.9	49.185 10857	20.05 78818	15 10	crystal line	-	Tatric basement	Z	1		0.394	1.60 %	1.532	1.60 %	891.4	0.50 %	0.26	24.3		0.64		37.9	0.6	41.1	3.1
			44							Z	4		0.235	2.30 %	0.62	1.30 %	755.8	0.50 %	0.38	22.9		0.52		44	0.6		
			41.7							Z	2		0.284	2.00 %	0.778	1.30 %	662.1	0.50 %	0.37	24.2		0.58		41.7	0.6		

SLOsmi16_G-10		G_10	23.4	49.2354749	20.0741292	1656	crystal line	-	Tatric basement	Z	1	0.062	16.50%	0.331	1.40%	345.5	0.50%	0.19	13.3	0.57	23.4	0.4	40.7	13.1
			38.2							Z	2	0.102	10.00%	0.919	1.20%	1275.8	0.50%	0.11	23.3	0.61	38.2	0.5		
			53.7							Z	3	0.044	23.20%	0.48	1.20%	1095.2	0.50%	0.09	29.5	0.55	53.7	0.8		
			37.3							Z	4	0.668	2.50%	2.823	1.20%	656.4	0.50%	0.24	29.8	0.8	37.3	0.5		
			41.8							Z	5	0.496	2.60%	1.634	1.20%	904.7	0.50%	0.3	30.9	0.74	41.8	0.5		
			33.5							Z	6	0.314	3.40%	3.628	1.10%	1295.6	0.40%	0.09	25.1	0.75	33.5	0.4		
			69							Z	7	0.293	3.50%	0.921	1.10%	965.4	0.50%	0.32	51.1	0.74	69	0.8		
			37.1							Z	8	0.734	2.40%	2.798	1.20%	2020.4	0.50%	0.26	24.9	0.67	37.1	0.4		
			47.8							Z	9	0.326	3.30%	1.865	1.20%	1370.3	0.50%	0.17	34.4	0.72	47.8	0.6		
SLOsmi16_G-11		G_11	44.7	49.1688888882	20.0506834	2178	crystal line	-	Tatric basement	Z	4	1.115	2.20%	3.3	1.20%	1386.1	0.50%	0.34	34	0.76	44.7	0.6	37.7	6.5
			31.8							Z	5	0.528	2.60%	2.4	1.20%	1134.3	0.50%	0.22	23.2	0.73	31.8	0.4		

			33.3					Z	6	0.386	2.90%	2.173	1.10%	923	0.50%	0.18	24.6	0.74	33.3	0.4		
			42.6					Z	7	0.399	2.80%	2.087	1.20%	1369.7	0.50%	0.19	30.7	0.72	42.6	0.5		
SLOsmi16_G-12		G_12	24.1	49.15575917	20.060999	6 2135	crystal line	-	Tatric basement	Z	2	0.125	8.20%	0.604	1.20%	414.6	0.50%	0.21	15.9	0.66	24.1	0.3	21.1	3.5
			23.9					Z	3	0.18	5.80%	0.817	1.20%	437.5	0.50%	0.22	16.3	0.68	23.9	0.3		
			20.6					Z	4	0.218	4.20%	0.668	1.20%	199.8	0.50%	0.33	15	0.73	20.6	0.3		
			16.7					Z	5	0.161	5.10%	1.416	1.10%	318.5	0.50%	0.11	12.4	0.74	16.7	0.2		
SLOsmi16_G-13		G_13	19.8	49.13278228	20.060061	8 1404	crystal line	-	Tatric basement	Z	5	0.191	4.40%	5.586	1.30%	1216.8	0.50%	0.03	14.9	0.75	19.8	0.3	22.6	6.1
			30.4					Z	7	0.933	2.40%	8.858	2.20%	1345.7	0.50%	0.11	24.6	0.81	30.4	0.7		
			16.8					Z	2	0.191	5.50%	0.775	1.20%	350.3	0.50%	0.25	10.9	0.65	16.8	0.2		
			19.8					Z	3	0.271	3.90%	2.041	1.20%	336.4	0.50%	0.13	15.6	0.79	19.8	0.2		
			29.2					Z	4	0.467	2.60%	7.49	1.10%	923.9	0.50%	0.06	24.2	0.83	29.2	0.4		

UKRand14_PL39	Andreucci 2014	PL39	27.82	23.406	49.278	402	sandstone	56.0-33.9		A		27.82 0.51
UKRand14_PL50		PL50	90.73	23.59728	49.10535	394	sandstone	41.2-23.03		A		90.73 1.14
UKRand14_PL52		PL52	5.55	23.01528	48.7549	375	sandstone	89.8-66.0		A		5.55 0.11
UKRand14_PL53		PL53	8.67	23.03987	48.69062	334	sandstone	56.0-33.9		A		8.67 0.12
UKRand14_PL54		PL54	6.92	23.11432	48.85612	754	sandstone	33.9-23.03		A		6.92 0.1
UKRand14_PL55		PL55	8.06	23.38268	48.9642	577	sandstone	33.9-23.03		A		8.06 0.2

UKRand14_PL56		PL56	12.8	24.57653	48.65198	408	basement	23.03-11.63		A		12.8 0.19
UKRand14_PL58		PL58	10.38	24.18608	48.0019	442	basement	420-298		A		10.38 0.13
UKRand14_PL59		PL59	8.35	24.10122	47.92877	358	sandstone	420-298		A		8.35 0.15
UKRand14_PL60		PL60	6.03	24.02183	47.98445	312	sandstone	56.0-33.9		A		6.03 0.12
UKRand14_PL61		PL61	8.37	24.18275	48.06155	582	sandstone	145-125		A		8.37 0.21
UKRand14_PL62		PL62	10.64	24.2403	48.07738	471	sandstone	145-125		A		10.64 0.17

UKRand14_PL63		PL63	9	24.27502	48.1651	551	sandstone	145-125		A		9 0.1
UKRand14_PL64		PL64	7.64	24.3037	48.19787	577	sandstone	89.8-56		A		7.64 0.09
UKRand14_PL65		PL65	7.25	24.44802	48.30572	877	sandstone	33.9-23.03		A		7.25 0.09
UKRand14_PL67		PL67	7.08	23.55803	48.22262	206	sandstone	56.0-33.9		A		7.08 0.16
UKRand14_PL68		PL68	8.68	23.59305	48.31918	423	sandstone	89.8-56		A		8.68 0.11
UKRand14_PL69		PL69	5.68	23.61838	48.3542	459	sandstone	145-125		A		5.68 0.09
UKRand14_PL70		PL70	6.93	23.65317	48.39232	530	sandstone	56.0-33.9		A		6.93 0.09

UKRand14_PL50		PL50	156.83	23.59728	49.10535	394	sandstone	45-23.03		Z		156.83	140.55
UKRand14_PL52		PL52	49.43	23.01528	48.7549	375	sandstone	85-66		Z		49.43	26.44
UKRand14_PL55		PL55	246.41	23.38268	48.9642	577	sandstone	33.9-23.03		Z		246.41	152.64
UKRand14_PL59		PL59	40.27	24.10122	47.92877	358	basement	358-298		Z		40.27	9.18
UKRand14_PL60		PL60	109.21	24.02183	47.98445	312	sandstone	56-33.9		Z		109.21	14.2
UKRand14_PL62		PL62	173.54	24.2403	48.07738	471	sandstone	145-129		Z		173.54	36.89
UKRand14_PL63		PL63	92.83	24.27502	48.1651	551	sandstone	145-129		Z		92.83	27.33

UKRand14_PL65		PL65	73.68	24.44802	48.30572	877	sandstone	33.9-23.03		Z													73.68	22.55
UKRand14_PL67		PL67	241.01	23.55803	48.22262	206	sandstone	56-33.9		Z													241.01	9.2
UKRand14_PL70		PL70	53.21	23.65317	48.39232	530	sandstone	56-33.9		Z													53.21	12.98
POLcas16_PL72		PL72	10.32	49.32298	19.53182	586	sediment	85-56		A	13A156_AC_PL72_Ap1	93.42	1.35	22.87	0.34	1.62	0.08	4.19	6.63	0.35			10.32	0.54	7.95	0.14
			7.74							A	13A157_AC_PL72_Ap2	75.29	1.07	9.62	0.15	0.74	0.01	8.02	4.98	0.1			7.74	0.16		
			14.78b							A	13A158_AC_PL72_Ap3	0.16	0	0.06	0	0.01	0	2.73	10.58	0.24			14.78b	0.34b		
			66.76b							A	13A159_AC_PL72_Ap4	138.21	2.01	95.35	1.37	27.99	0.32	1.49	40.16	0.63			66.76b	1.06b		

			26.71b						A	13A160_AC_PL72_Ap5	89.39	1.29	88.2	1.26	10.22	0.16	1.04	17.23	0.33		26.71b	0.51b		
POLcas16_PL75		PL75	9.12	49.31235	19.48207	570	sediment	85-56		A	13A161_AC_PL75_Ap1	2.58	0.04	1	0.01	0.07	0	2.63	8.18	0.19		9.12	0.22	8.11	0.09
			11.24							A	13A162_AC_PL75_Ap2	176.33	2.51	26.51	0.38	2.92	0.04	6.82	7.88	0.14		11.24	0.2		
			7.27							A	13A163_AC_PL75_Ap3	136.4	1.94	18.59	0.27	1.28	0.03	7.53	4.59	0.11		7.27	0.17		
			7.65							A	13A164_AC_PL75_Ap4	172.9	2.48	12.35	0.18	1.42	0.06	14.36	4.92	0.22		7.65	0.33		
			7.08							A	12A165_AC_PL75_Ap5	143.33	2.05	12.86	0.18	1.14	0.02	11.44	4.47	0.1		7.08	0.15		
POLcas16_PL82		PL82	11.36	49.30322	20.79382	608	sediment	85-66		A	13A166_AC_PL82_Ap1	98.5	1.41	6.31	0.09	1.35	0.02	16	8.3	0.15		11.36	0.21	11.63	0.11

			11.76					A	13A167_AC_PL82_Ap2	70.24	1.02	25.71	0.37	1.58	0.07	2.8	6.82	0.3		11.76	0.52		
			9.31					A	13A168_AC_PL82_Ap3	111.08	1.6	19.57	0.29	1.3	0.03	5.82	5.18	0.12		9.31	0.21		
			49.60 b					A	13A169_AC_PL82_Ap4	18.53	0.26	9.46	0.14	2.77	0.04	2.01	36.57	0.63		49.60 b	0.85 b		
			11.86					A	13A170_AC_PL82_Ap5	66.49	0.95	48.7	0.69	2.96	0.03	1.4	8.38	0.13		11.86	0.19		
POLcas16_PL86		PL86	11.12	49.4257	20.4413	423	sediment	56-33.9		A	13A176_AC_PL86_Ap1	95.65	1.37	34.1	0.49	2.22	0.13	2.88	7.2	0.42		11.12	0.65	10.5	0.12
			11.97					A	13A177_AC_PL86_Ap2	194.15	2.79	13.72	0.2	2.61	0.07	14.52	8.05	0.23		11.97	0.34		
			10.29					A	13A178_AC_PL86_Ap3	354.44	5.04	8.75	0.13	3.42	0.04	41.56	6.82	0.11		10.29	0.17		

			7.85					A	13A179_AC_PL86_Ap4	146.78	2.09	5.45	0.1	1.08	0.03	27.64	4.97	0.17	7.85	0.27		
			17.52b					A	13A180_AC_PL86_Ap5	256.43	3.67	65.62	0.95	6.84	0.17	4.01	10	0.27	17.52b	0.48b		
POLcas16_PL87		PL87	8.67	49.40512	20.53657	569	sediment	85-33.9		A	13A181_AC_PL87_Ap1	44.27	0.64	8.83	0.13	0.63	0.02	5.14	5.98	0.17	8.67	0.24	8.62	0.15
			18.36b					A	13A182_AC_PL87_Ap2	72.83	1.06	12.12	0.17	1.97	0.07	6.16	12.26	0.44	18.36b	0.66b		
			6					A	13A183_AC_PL87_Ap3	16.74	0.24	2.26	0.04	0.15	0.01	7.6	4.39	0.27	6	0.36		
			7.97					A	13A184_AC_PL87_Ap4	33.12	0.48	16.16	0.23	0.76	0.02	2.1	5.84	0.18	7.97	0.25		
			11.42					A	13A185_AC_PL87_Ap5	44.68	0.64	5.84	0.08	0.74	0.04	7.84	8.28	0.44	11.42	0.61		

POLand13_PL1	Andreucci 2013	PL1	10.16	49.31048333	22.2675833	615	sandstone	27.82-23.03		A	BA Pll_Ol	13.46	7.3	0.2	10.16	0.27
			11.06							A	BA PL1_05	0.74	7 .3	0.1	11.06	0.22
			9.53							A	BA PL1_07	19.23	6 .0	0 .2	9 .53	0.36
			6.3							A	BA PL1_09	22.44	4.1	0.2	6.3	0.36
			9.23							A	BA PL1_10	3.99	6.1	0.1	9 .23	0.15
POLand13_PL5		PL5	16.09	49.5644833 3	21.0831333	523	sandstone	56-33.9		A	BA PL5_01	0.42	9.5	0.2	16.09	0.32
			24.19							A	BA PL5_07	0.15	15.8	0.3	24.19	0.48
			16.5							A	BA_ PL5_06	0.14	10	0.3	16.5	0.45
			12.07							A	BA_ PL5_08	2.23	8 .0	0.2	12.07	0.37
POLand13_PL6		PL6	11.59	49.5992833 3	21.0168167	373	sandstone	27.82-23.03		A	BA PL6_02	5.81	7 .1	0.1	11.59	0.16

			13.19					A	BA PL6_04	12.53	8 .0	0 .1	13.19	0 .20	
			8.82					A	BA_PL 6_05	35.99	5.7	0.1	8.82	0.2	
POLand13_ PL10		PL 10	10.2	49.34265	21.3372167	356	sandstone	56-23.03	A	BA_ PL10_01	6.52	6 .0	1.6	10.2	2.78
			6.16					A	BA_ PL10_02	7 .73	4 .2	0.2	6.16	0.29	
			9 .18					A	BA_pl10_03	15.43	6 .3	0.5	9 .18	0 .76	
POLandl3_PL 11		PL 11	8.58	49.52851667	21.6677667	459	sandstone	33.9-23.03	A	BA_Pll 1_Ol	4.62	5.8	0.3	8.58	0.4
			10					A	BA_PL 11_03	5 .82	7 .5	0.2	10	0 .22	
			6 .65					A	BA_ PL11_04	8 .14	4 .4	0 .3	6 .65	0 .51	
POLandl3_ PL12		PL 12	44.4	49.7591	21.7844167	373	sandstone	85-56	A	BA_PL 12_01	4.29	29.7	1	44.4	1.52

			102.65					A	BA_PL12_04	0.26	59.5	1.9	102.65	3.2	
			106.57					A	BA_PL12_06	0.70	65.9	1.8	106.57	2.85	
POLand13_PL13		PL13	106.85	49.7689666 7	21.846866 7	315	sandstone	85-56	A	BA_PL13_01	0.14	68.3	1.5	106.85	2.4
			119.95					A	BA_PL13_04	0.11	83.5	1.6	119.95	2.36	
			120.14					A	BA_PL13_05	0.02	76	1.5	120.14	2.43	
POLand13_PL14		PL14	102.4	49.86235	21.7419667	231	sandstone	23.03-5.33	A	BA_PL14_01	2.85	63.1	2.6	102.4	4.17
			30.95					A	BA_PL14_02	10.86	23.2	0.6	30.95	0.82	
			34.56					A	BA_PL14_03	12.7	24.4	1	34.56	1.44	
POLand13_PL15		PL15	18.91	49.6816333 3	19.19695	364			A	BA_pl15_03	17.79	11.4	0.4	18.91	0.72

			16.66					A	BA_PL15_05	17.54	10.2	0 .5	16.66	0 .85		
			20.5					A	BA_PL15_06	19.58	12.4	0.4	20.5	0 .59		
POLandI3_PL16		PL16	13.28	49.6646666 7	19.10665	468	sandstone	152-129		A	BA_PL16_06	1.77	9.1	0.2	13.28	0 .33
			15.54					A	BA_PL16_07	4.19	10.5	6.6	15.54	0.8		
POLandI3_PL18		PL18	34.32	49.6633833 3	19.0451	626	sandstone	93-66		A	BA_pl18_02	0.31	22.4	0.5	34.32	0 .70
			11.54					A	BA_PL18_04	6.31	8	0.5	11.54	0 .35		
			14.2					A	BA_PL18_05	24.67	10	0 .2	14.2	0.31		
			12.09					A	BA_PL18_06	2.03	8 .8	0 .2	12.09	0 .24		
POLandI3_PL19		PL19	12.73	49.5484166 7	18.9755833	825	sandstone	33.9-23.03		A	BA_PL19_01	7.91	7.7	0 .2	12.73	0 .35

			6.96					A	BA_PL19_03	19.08	4 .8	0.2	6.96	0.16		
			12.91					A	BA_PL19_04	3 .45	8 .6	0 .1	12.91	0 .72		
			10.64					A	BA_PL19_05	133.83	7 .1	0 .5	10.64	0 .83		
POLandl3_PL20		PL20	8.95	49.5709667	19.055	495	sandstone	33.9-23.03	A	BA_PL20_01	37.03	5 .1	0.6	8.95	0.26	
			11					A	BA_pl20_02	13.62	6.8	0.2	11	0 .19		
			13.32					A	BA_PL20_04	10.93	8.7	0.1	13.32	0 .35		
POLandl3_PL21		PL21	11.72	49.6596333 3	19.3066	414	sandstone	85-66	A	BA_PL21_03	12.41	7 .4	0.2	11.72	0.26	
			12.37					A	BA_PL21_01	14.51	7 .1	0.2	12.37	0 .22		
			12.34					A	BA_PL21_02	13.13	6.8	0 .1	12.34	0 .23		

POLand13_PL22		PL22	14.56	49.6129	19.2731167	530	sandstone	152-129		A	BA_PL22_01	1.26	10.7	0.2	14.56	0.27
			17.6							A	BA_PL22_02	0.02	10.2	0.3	17.6	0.51
			17.38							A	BA_PL22_04	0.16	11.8	0.4	17.38	0.62
			15.52							A	BA_PL22_06	5.34	9.7	0.5	15.52	0.87
POLand13_PL23		PL23	13.84	49.6687666 7	19.7630667	504	sandstone	41-33.9		A	BA_PL23_01	2.44	9.6	0.3	13.84	0.46
			15.4							A	BA_PL23_02	4.39	10.7	0.9	15.4	1.26
			15.52							A	BA_PL23_03	1.05	11.3	2.3	15.52	3.11
POLand13_PL24		PL24	35.12	49.69205	19.9548	434	sandstone	41-33.9		A	BA_PL24_01	0.19	25.3	0.5	35.12	0.68

			14.13					A	BA_PL24_03	1.23	8.7	0.2	14.13	0.32		
			15.65					A	BA_pl24_04	3.62	10.8	0.5	15.65	0.76		
			22.46					A	BA_PL24_07	0.3	15.8	0.6	22.46	0.85		
POLand13_PL25		PL25	13.35	49.62108333	20.0834167	492	sandstone	27.82-15.97		A	BA_PL25_01	0.40	9.5	0.2	13.35	0.31
			10.37						A	BA_pl25_02	2.19	5.9	1	10.37	1.72	
POLand13_PL26		PL26	15.34	49.58405	20.132083	699	sandstone	41-27.83		A	BA_PL26_01	0.98	10	0.5	15.34	0.7
			15.06						A	BA_PL26_04	0.42	11.2	0.2	15.06	0.30	
			12.04						A	BA_PL26_05	3.45	8.5	0.2	12.04	0.25	
POLand13_PL27		PL27	19.48	49.70183333	20.1774333	692	sandstone	41-27.83		A	BA_PL27_01	0.47	12.4	0.3	19.48	0.46

			15.16					A	BA_PL27_03	1.04	10.1	0.3	15.16	0.44
			15.75					A	BA_PL27_07	5.43	11.3	0.9	15.75	1.19
POLand13_PL28		PL28	17.56	49.5532333	20.1774333	1058	sandstone	41-27.83	A	BA_PL28_01	1.49	13.6	0.3	17.56	0.34
			14.4					A	BA_PL28_02	2.54	9.0	0.2	14.4	0.35
			18.65					A	BA_PL28_03	1.42	11.9	0.2	18.65	0.35
			17.6					A	BA PL28 04	1.64	11.7	0.3	17.6	0.5
POLand13_PL29		PL29	18.76	49.5037666 7	19.6746167	639	sandstone	41-27.83	A	BA_PL29_01	4.15	11.9	1.2	18.76	1.86
			15.26					A	BA_PL29_02	1.35	10.5	0.5	15.26	0.69
			14.38					A	BA_pl29_03	7.76	9.6	0.6	14.38	0.93

POLand13_PL30		PL-30	20.45	49.47753333	19.63232333	621	sandstone	23.03-5.33		A	BA_PL30_01	6.4	12.9	0.5	20.45	0.77
			20.68							A	BA_PL30_02	5	14.2	2.1	20.68	3.12
			14.92							A	BA_pl30_03	9.11	11.4	0.3	14.92	0.39
POLand13_PL32		PL32	13.15	49.6013	20.2962167	608	sandstone	41-27.83		A	BA_pl32_03	41.56	8.4	0.2	13.15	0.36
			13.27							A	BA_PL32_04	7.64	8.6	0.3	13.27	0.43
POLand13_PL33		PL33	8.95	49.607	20.29715	521	sandstone	33.9-23.03		A	BA_PL33_01	77.71	5.8	0.2	8.95	0.33
			13.47							A	BA_pl33_02	18.43	8.3	0.6	13.47	0.93
			17.56							A	BA_pl33_03	2.14	10.4	1	17.56	1.67
			20.79							A	BA_pl33_05	3.38	14.2	0.6	20.79	0.81

POLand13_PL34		PL34	14.16	49.6080333	20.3481333	602	sandstone	41-27.83		A	BA_PL34_01	3.17	9.2	0.3	14.16	0.39
			14.86							A	BA_pl34_04	1.19	10.6	0.3	14.86	0.37
			12.39							A	BA_pl34_05	11.32	9.1	0.3	12.39	0.4
POLand13_PL35		PL35	12.75	49.67555	20.6242	427	sandstone	27.82-23.03		A	BA_pl35_01	3.13	8.9	0.2	12.75	0.28
			10.87							A	BA_PL35_02	3	7.7	0.5	10.87	0.76
			12.49							A	BA_PL35_03	7.68	8.3	0.6	12.49	0.88
POLand13_PL36		PL36	13.95	49.7353	20.5146333	478	sandstone	41-23.03		A	BA_pl36_02	2.34	10.2	0.2	13.95	0.25
			15.15							A	BA_pl36_03	2.77	11.5	0.2	15.15	0.22
			18.92							A	BA_pl36_05	0.95	12.1	0.6	18.92	0.89

POLand13_PL37		PL37	12.46	49.7967166 7	20.352933 3	357	Sandstone	145-66		A	BA_pl37_01	5.57	7.6	0.2	12.46	0.30
			17.03							A	BA_PL37_02	1.94	11	0.1	17.03	0.23
			14.90							A	BA_PL37_04	1.46	9.9	0.2	14.90	0.26
POLand13_PL38		PL38	18.32	49.8123666 7	20.3641333	316	sandstone	33.9-27.82		A	BA_pl38_01	1.18	13.2	0.2	18.32	0.32
			22.81							A	BA_PL38_04	1.91	14.5	0.3	22.81	0.42
			84.86							A	BA_PL38_05	3.17	59.6	0.8	84.86	1.16
			56.89							A	BA_pl38_06	1.51	40.6	0.7	56.89	1
POLand13_PL39		PL39	24.32	49.267283	23.4118667	402	sandstone	56-33.9		A	BA_PL39_01	2.19	14.5	0.5	24.32	0.90
			67.42							A	BA_PL39_02	1.59	42.8	0.6	67.42	0.95
			97.62							A	BA_PL39_03	0.17	69.1	1.2	97.62	1.66

			17.95						A	BA_pl39_04	0.79	11.3	0.3	17.95	0.51
POLand13_PL40		PL40	12.63	49.3724	19.8118667	757	sandstone	41.2-33.9		A	BA_PL40_01	5.8	8	0.1	12.63	0.2
			10.5							A	BA_PL40_02	7.68	6.5	0.3	10.5	0.45
			14.98							A	BA_pl40_03	5.55	9	0.1	14.98	0.22
POLand13_PL41		PL41	8.27	49.6103333333	20.06395	520	sandstone	27.82-15.97		A	BA_pl41_01	38.42	4.4	0.1	8.27	0.26
			12.81							A	BA_pl41_02	8.62	8.9	0.1	12.81	0.19
			13.21							A	BA_PL41_03	1.99	7.9	0.2	13.21	0.31
POLand13_PL42		PL42	14.37	49.5973166 7	20.0620333	562	sandstone	41-27.83		A	BA_pl42_01	0.6	10.4	0.3	14.37	0.43
			17.88							A	BA_pl42_02	8.87	11.4	0.5	17.88	0.73
			13.51							A	BA_pl42_04	4.02	10	0.3	13.51	0.37

POLand13_PL43		PL43	100.3	49.6201333	21.2968	428	sandstone	33.9-23.03		A	BA_pl43_01	0.02	58.1	3.4	100.3	5.84
POLand13_PL44		PL44	12.68	49.6137	21.379983	378	sandstone	27.82-23.03		A	BA_pl44_03	2.37	8.3	0.2	12.68	0.36
			32.61							A	BA_pl44_04	1	22.1	0.7	32.61	1.01
POLand13_PL46		PL46	14.44	49.42295	21.66365	513	sandstone	27.82-23.03		A	BA_pl46_01	1.5	9.1	0.3	14.44	0.4
			20.93							A	BA_pl46_02	5.96	12.7	0.4	20.93	0.62
			19.38							A	BA_pl46_03	0.28	12.4	0.4	19.38	0.68
			15.87							A	BA_PL46_04	0.13	10.1	0.4	15.87	0.68
POLand13_PL47		PL47	86.1	49.467683 3	22.35785	376	sandstone	27.82-23.03		A	BA_pl47_01	8.11	49.8	2.1	86.1	3.58
			11.06							A	BA_pl47_03	6.18	6.5	1.3	11.06	2.25

			28.99						A	BA_PL47_04	4.02	20.3	0.6	28.99	0.86
			54.71						A	BA_PL47_05	0.59	33.7	0.9	54.71	1.52
			16.34						A	BA_PL47_06	1.75	9.9	0.3	16.34	0.51
POLand13_PL48		PL48	9.87	49.22805	22.3645167	542	sandstone	27.82-23.03		A	BA_PL48_01	0.84	6.6	0.3	9.87	0.51
			10.53						A	BA_PL48_02	1.74	6.4	0.3	10.53	0.47
			13.24						A	BA_PL48_03	6.1	8.1	0.9	13.24	1.41
			10.28						A	BA_PL48_04	6.05	6.8	0.3	10.28	0.46
ROMnec10_O1	Necea thesis 2010	O1	23	45.8864034 1	25.7407012	675									23	
ROMnec10_O3		O3	26	45.9050938 8	25.946296 4	748									26	

ROMnec10_O6		O6	27	45.9088319 8	25.498472 6	565					27
ROMnec10_O7		O7	47	45.9050938 8	25.483520 3	567					47
ROMnec10_O8		O8	44	45.8991129 3	25.466325	688					44
ROMnec10_O13		O13	29	45.9028510 2	25.452867 9	799					29
ROMnec10_P14		P4	1	45.9342510 2	26.604201	752					1
ROMnec10_P6		P6	27	45.8707034 1	26.782881 9	464					27
ROMnec10_P7		P7	35	45.9237843 5	26.6939152	423					35

ROMnec10_P8		P8	7	45.91107483	26.7417629	398						7
ROMnec10_P9		P9	14	45.897617669	26.754472 4	403						14
ROMnec10_P10		P10	7	45.884160555	26.7970867	436						7
ROMnec10_P11		P11	4	45.889393888	26.8060581	358						4
ROMnec10_P21		P12	21	45.890889122	26.832972 4	323						21
ROMnec10_P13		P13	9	45.8938796	26.848672 4	292						9
ROMnec10_P14		P14	9	45.8991129 3	26.874091 4	279						9

ROMnec10_P18		P18	10	45.91929864	26.918200 9	261																	10		
ROMnec10_P20		P20		45.94023197	26.565324 8	842																			
ROMnec10_P25		P25	12	45.95368911	26.375429 6	1188																	12		
ROMnec10_P26		P26	36	45.94770816	26.2573058	771																	36		
ROMnec10_P27		P27	8	45.8968700 7	26.323843 9	898																	8		
ROMnec10_P28		P28	8	45.91481293	26.333562 9	1007																	8		
SLOdan11_NT-1		NT-1	15.8	48.9813	19.584	1,156	granite			A	NT-1#1	1	0.139	2.4	0.244	0.2	0.417	0.9	0.56	11.9	0.3	0.75		15.8	0.9	17.5	1.5
			18.1							A	NT-1#2	1	0.077	2.5	0.207	1.9	0.373	0.9	0.37	13.1	0.3	0.72		18.1	1.1		

			18.6						A	NT-1#3	1	0.138	2.4	0.234	1.9	0.453	0.9	0.59	13.4	0.3	0.72		18.6	1.1		
SLOdan11_NT-2		NT-2	15.6	48.9716	19.6153	1,200	granite			A	NT-2#0	2	0.132	1.1	0.286	1.7	0.443	2.6	0.46	11.5	0.4	0.74		15.6	0.9	18	2.2
			16.1							A	NT-2#1	1	0.137	1.5	0.166	1.2	0.284	4.5	0.82	11.8	0.6	0.73		16.1	1.1		
			20.6							A	NT-2#2	1	0.015	2.9	0.186	1.9	0.294	0.9	0.08	12.5	0.3	0.61		20.6	1.2		
			20							A	NT-2#3	1	0.014	2.9	0.14	2	0.23	0.9	0.1	12.9	0.3	0.65		20	1.2		
			18.2							A	NT-2#4	1	0.017	2.8	0.251	1.9	0.39	0.9	0.07	12.3	0.3	0.67		18.2	1.1		
SLOdan11_NT-3		NT-3	25.5	48.9496	19.6282	1,700	granite			A	NT-3#1	1	0.028	2.7	0.071	2.6	0.158	0.9	0.38	15.9	0.6	0.62		25.5	1.6	20.2	4.9
			15.8							A	NT-3#2	1	0.016	2.9	0.054	3.2	0.076	0.9	0.3	10.2	0.4	0.65		15.8	1		
			20.4							A	NT-3#3	1	0.019	2.8	0.056	3	0.107	0.9	0.34	13.8	0.5	0.68		20.4	1.3		
SLOdan11_NT-4		NT-4	21.9	48.9363	19.6401	2,043	granite			A	NT-4#1	1	0.017	2.9	0.031	4.5	0.068	0.9	0.55	15.4	0.7	0.71		21.9	1.5	20.6	1.8

			19.3						A	NT-4#2	1	0.017	2.9	0.041	3.5	0.074	0.9	0.42	13.1	0.5	0.68		19.3	1.2		
SLOdan11_NT-5		NT-5	20.9	48.93	19.651	1,750	granite			A	NT-5#1	1	0.043	2.6	0.185	1.9	0.362	0.9	0.23	14.6	0.5	0.7		20.9	1.2	20.2	0.7
			19.6						A	NT-5#2	1	0.021	2.8	0.118	2.1	0.236	0.9	0.18	14.7	0.6	0.75		19.6	1.2		
SLOdan11_NT-2		NT-2	72.6	48.9716	19.6153	1,200	granite			Z	NT-2#1*	1	0.875	5.3	4.884	4.3	36.589	0.5	0.18	58.8	2.6	0.81		72.6	4.8	58.2	14.5
			52.1						Z	NT-2#2	1	1.207	5.3	5.339	4.3	29.953	0.5	0.23	43.6	1.9	0.84		52.1	3.5	49.3	5.7
			77.1						Z	NT-2#3*	1	1.27	5.3	3.467	4.3	30.424	0.5	0.37	66.1	2.9	0.86		77.1	5.1		
			53.4						Z	NT-2#4	1	0.596	4.6	1.336	4.8	8.177	1.2	0.45	45.4	2.2	0.85		53.4	3.8		
			43						Z	NT-2#5	1	0.557	4.5	0.82	4.8	3.985	1.2	0.68	34.4	1.7	0.8		43	3		
SLOdan11_NT-3		NT-3	52.6	48.9496	19.6282	1,700	granite			Z	NT-3#1	1	0.895	5.3	2.486	4.3	14.666	0.5	0.36	44.6	2	0.85		52.6	3.5	55.4	12.1
			77.8						Z	NT-3#2*	1	1.822	5.3	4.074	4.3	36.657	0.6	0.45	66.6	2.9	0.86		77.8	5.2	50.9	1.6

			49.8					Z	NT-3#3	1	1.273	5.3	4.871	4.3	26.945	0.5	0.26	42.7	1.9	0.86	49.8	3.3		
			49.4					Z	NT-3#4	1	0.232	4.4	1.917	4.8	10.273	1.2	0.12	42.7	2.1	0.87	49.4	3.5		
			51.9					Z	NT-3#5	1	0.274	4.4	0.822	4.8	4.832	0.9	0.33	44.6	2.2	0.86	51.9	3.6		
SLOdan11_NT-4		NT-4	39.4	48.9363	19.6401	2,043	granite			Z	NT-4#1	1	0.278	5.3	4.58	4.3	15.118	0.5	0.06	26.7	1.2	0.68	39.4	2.6	48	9.8
			43.3					Z	NT-4#2	1	0.638	5.3	6.505	4.3	23.758	0.5	0.1	29.3	1.3	0.68	43.3	2.9	44.5	4.3
			46.4					Z	NT-4#3	1	0.034	4.8	0.669	4.8	2.919	0.9	0.05	35.3	1.7	0.76	46.4	3.2		
			65					Z	NT-4#4*	1	0.465	5.3	3.097	4.3	20.458	0.5	0.15	52.2	2.3	0.8	65	4.3		
			49.6					Z	NT-4#5	1	0.206	4.7	1.755	4.9	7.845	0.9	0.12	35.7	1.8	0.72	49.6	3.5		
SLOdan11_NT-5		NT-5	42.1	48.93	19.651	1,750	granite			Z	NT-5#1	1	0.583	5.3	6.019	4.3	24.474	0.5	0.1	32.6	1.4	0.77	42.1	2.8	46.3	6.9
			47.6					Z	NT-5#2	1	0.656	5.3	7.432	4.3	36.121	0.5	0.09	39	1.7	0.82	47.6	3.2	43.7	2.8
			41.4					Z	NT-5#3	1	0.639	5.3	3.162	4.3	13	0.5	0.2	32.2	1.4	0.78	41.4	2.7		

			58.3					Z	NT-5#4*	1	0.079	4.6	0.706	4.9	4.343	0.9	0.11	49	2.4	0.84		58.3	4.1	
			44					Z	NT-5#5	1	0.113	4.4	0.634	4.8	2.733	0.9	0.18	33.9	1.7	0.77		44	3.1	
SLOput14_BUC-1	Putis 2014	BUC-1	107.1					Z	a		1.422	1.4	2.433	1.9	26.138	1.5	0.58	77.1	1.7	0.72	5	107.1	5.9	
			114					Z	b		0.778	1.4	0.821	1.8	10.648	1.2	0.94	86.6	1.7	0.76	5	114	6.1	
			99.5					Z	c		0.664	1.4	1.212	1.8	12.497	1.2	0.54	74.6	1.5	0.75	5	99.5	5.4	
			95.2					Z	d		0.882	1.4	0.886	1.9	8.661	1.2	0.99	64.8	1.3	0.68	5	95.2	5.1	
			102.4					Z	e		0.524	1.4	1.029	1.8	10.539	2	0.51	74.7	1.5	0.73	5	102.4	5.5	
SLOput14_JAK-5		JAK-5	74					Z	a		0.074	1.6	0.461	1.9	2.98	1.2	0.16	51.1	1.1	0.69	5	74	4	
			77					Z	b		0.125	1.5	0.489	1.8	3.46	1.2	0.25	54.7	1.2	0.71	5	77	4.2	
			69.8					Z	c		0.217	1.5	0.533	1.9	3.435	1.2	0.4	48.2	1	0.69	5	69.8	3.8	
			80.2					Z	d		0.181	1.5	1.191	1.9	8.461	1.2	0.15	56.1	1.2	0.7	5	80.2	4.4	

			74					Z	e	0.475	1.4	1.274	1.9	8.135	1.2	0.37	48.1	1	0.65	5	74	4
SLOput14_OS-1		OS-1	65					Z	a	0.229	1.5	0.624	1.8	3.817	1.2	0.37	46.1	1	0.71	5	65	3.5
			66.9					Z	b	0.169	1.5	0.601	1.9	3.453	1.2	0.28	44.2	0.9	0.66	5	66.9	3.6
			68.3					Z	c	0.218	1.5	0.808	1.9	4.801	1.2	0.27	45.8	1	0.67	5	68.3	3.7
			73.5					Z	d	0.318	1.5	1.239	1.9	7.661	1.2	0.26	47.8	1	0.65	5	73.5	4
			89.2					Z	e	0.311	1.5	0.551	1.8	5.177	1.2	0.56	67.8	1.4	0.76	5	89.2	4.8
SLOput14_JAS-1		JAS-1	118.6					Z	a	1.327	1.4	2.867	1.8	33.728	1.2	0.46	86.6	1.7	0.73	5	118.6	6.4
			120.6					Z	b	0.689	1.4	0.958	1.8	12.588	1.2	0.71	91.7	1.8	0.76	5	120.6	6.5
			128.6					Z	c	0.411	1.4	0.942	1.8	12.287	1.2	0.43	96.5	2	0.75	5	128.6	6.9
			125.7					Z	d	0.232	1.5	0.604	1.8	7.712	1.2	0.38	95.6	2	0.76	5	125.7	6.8
			131					Z	e	0.492	1.4	1.707	1.8	23.159	1.2	0.29	103.5	2.1	0.79	5.1	131	7.1

SLOput14_Do-111		Do-111	10.3					A	a	0.009	5.9	0.00024	6.5	0.002	12.9	35.96	8	1.1	0.78	5	10.3	1.5
			49.4					A	b	0.005	4.7	0.00169	4.8	0.013	2.6	3.15	35.8	1.5	0.73	5	49.4	3.2
			34					A	c	0.01	4.3	0.00015	10.6	0.007	2.2	63.47	24.1	1.1	0.71	5	34	2.3
			21.4					A	d	0.009	4.3	0.00053	5.6	0.005	2	16.39	17.1	0.7	0.8	5	21.4	1.4
			63.1					A	e	0.008	4.3	0.00117	4.9	0.017	1.9	7.17	45	1.7	0.71	5	63.1	3.9
			30.4					A	f	0.004	5.6	0.0022	4.7	0.009	2.5	1.67	24.1	1.1	0.79	5	30.4	2
			39.4					A	g	0.009	4.4	0.00068	6.4	0.009	2.2	13.32	27.6	1.2	0.7	5	39.4	2.6
			11.2					A	h	0.011	4.2	0.00004	40	0.002	3.3	250.44	7.5	0.4	0.67	5	11.2	0.8
ROMmer11_carp97	Merten thesis	Carp97	143.1	apuseni mountain				A	p1e	0.014	30%	0.027	3%	3.45E-10	1%	0.5	93.7	3.5	0.65		143.1	21.6
			90.5					A	p2e	0.017	26%	0.045	2%	3.56E-10	1%	0.4	59.4	2.3	0.66		90.5	18.8

			140.5					A	p3e	0.014	31%	0.025	3%	2.99E-10	1%	0.6	86	3.3	0.61		140.5	18.2			
ROMmerl1_carp100		Carp100	44.6	apuseni mountain				A	p1	0.151	4%	0.101	1%	5.08E-10	0%	1.5	30.5	1.1	0.68		44.6	4.6	46	3	
			55.4					A	p2	0.145	4%	0.115	1%	7.21E-10	0%	1.3	39.7	1.4	0.72		55.4	5.4			
			35.9					A	p3	0.223	3%	0.168	1%	6.92E-10	0%	1.4	25.8	0.9	0.72		35.9	6.3			
ROMmerl1_carp105		Carp105	38.6	apuseni mountain				A	p1	0.107	5%	0.042	2%	1.94E-10	1%	2.6	23.6	0.8	0.61		38.6	2.6	42	1.9	
			45.8					A	p2	0.096	6%	0.038	2%	2.16E-10	1%	2.6	29.2	1.1	0.64		45.8	3.5			
			45.3					A	p3	0.153	4%	0.045	2%	2.67E-10	1%	3.5	27.1	1	0.6		45.3	4.3			
ROMmerl1_carp92a		Carp92a	54.8	apuseni mountain				A	p1	0.046	2%	0.018	5%	1.20E-10	5%	2.6	34.2	1.8	0.62		54.8	7.5	52.8	3.4	

			61.4					A	p2	0.062	2%	0.019	5%	1.50E-10	4%	3.3	36.5	1.7	0.59		61.4	10.8		
			50.9					A	p3	0.075	1%	0.026	3%	1.88E-10	3%	2.9	35	1.4	0.69		50.9	4.1		
ROMmer11_RO-13b		RO-13b	34	apuseni mountain				A	p1	0.066	1%	0.035	1%	1.28E-10	26%	1.9	20.8	4.6	0.61		34	7.9	29.9	6.5
			26.3					A	p2f	0.035	2%	0.011	4%	3.77E-11	54%	3.3	16	10.6	0.61		26.3	17.4		
			21.9					A	p3	0.05	2%	0.017	3%	4.95E-11	47%	3	14.2	7.2	0.65		21.9	11.1		
			8.1					A	p4f	0.031	3%	0.01	4%	9.73E-12	82%	3.2	4.7	11.9	0.58		8.1	20.6		
ROMmer11_RO-22b		RO-22b	283.7	apuseni mountain				A	p1g	0.017	4%	0.01	4%	3.44E-10	11%	1.8	200.9	21.2	0.71		283.7	34.2		
			24.3					A	p2g	0.006	3%	0.055	1%	1.11E-10	29%	0.1	16.3	4.2	0.67		24.3	6.9		
			46.5					A	p3f	0.006	12%	0.007	6%	2.72E-11	62%	0.9	28.1	25.9	0.61		46.5	42.9		

ROMmerl1_RO-27b		RO-27b	55.1	apuseni mountain				A	p1	0.094	1%	0.031	1%	2.63E-10	15%	3.1	40.4	4.9	0.73	55.1	9.8	65.6	7.2
			70.7					A	p2	0.126	1%	0.031	1%	3.77E-10	11%	4.1	50.7	4.6	0.72	70.7	22.7		
			76.3					A	p3	0.144	1%	0.014	3%	2.92E-10	13%	10.6	49.9	4.9	0.65	76.3	20.5		
			81.9					A	p4	0.045	2%	0.012	4%	1.54E-10	22%	3.8	55.9	9.6	0.68	81.9	14.8		
ROMmerl1_RO-28b		RO-28b	105.1	apuseni mountain				A	p1g	0.023	3%	0.009	5%	1.17E-10	28%	2.7	68.1	15.1	0.65	105.1	28		
			157.7					A	p2g	0.033	2%	0.012	4%	2.49E-10	15%	2.9	105.4	12.2	0.67	157.7	21.7		
			69.9					A	p3g	0.022	4%	0.007	6%	6.37E-11	41%	3	41.6	16.4	0.6	69.9	29.7		
ROMmerl1_RO-34b		RO-34b	27	apuseni mountain				A	p1f	0.001	48%	0.012	4%	2.76E-11	62%	0.1	18.9	17.1	0.7	27	24.5		

			120					A	p2f	B.D.	100%	0.002	20%	1.87E-11	71%	-	84.5	113.8	0.7		120	162.4			
			48.3					A	p3f	0.001	59%	0.012	4%	4.68E-11	49%	0	32.9	17.6	0.68		48.3	26.9			
ROMmer11_RO-35b		RO-35b	37.6	apuseni mountain				A	p1f	B.D.	72%	0.016	3%	4.93E-11	48%	-	25.1	12.9	0.67		37.6	19.8	40.4	13.8	
			152.9					A	p2f	B.D.	100%	0.011	4%	1.35E-10	25%	-	96.8	20.2	0.63		152.9	36.3			
			141.3					A	p3f	B.D.	100%	0.009	5%	1.02E-10	30%	-	94.7	25.9	0.67		141.3	39.4			
			40.4					A	p4	0.002	32%	0.023	2%	7.74E-11	37%	0.1	26.9	8.9	0.66		40.4	13.8			

South-eastern Carpathians exhumation in Sarmatian?

In the LT thermochronometer database, more data are dated in the SE Carpathians than in the Eastern Carpathians of Romania. Therefore, our exhumation model better constrains the exhumation of the SE Carpathians in this region specifically. Previous studies of SE Carpathian exhumation have performed a T-t run of their samples and constrained the overall exhumation of the region (Merten et al., 2010; Necea et al., 2021).

In Merten et al., 2010, exhumation of Tarcau nappe samples is constrained with a Sarmatian exhumation phase based on geologic evidence of Sarmatian thrusting in the SE Carpathians (Matenco

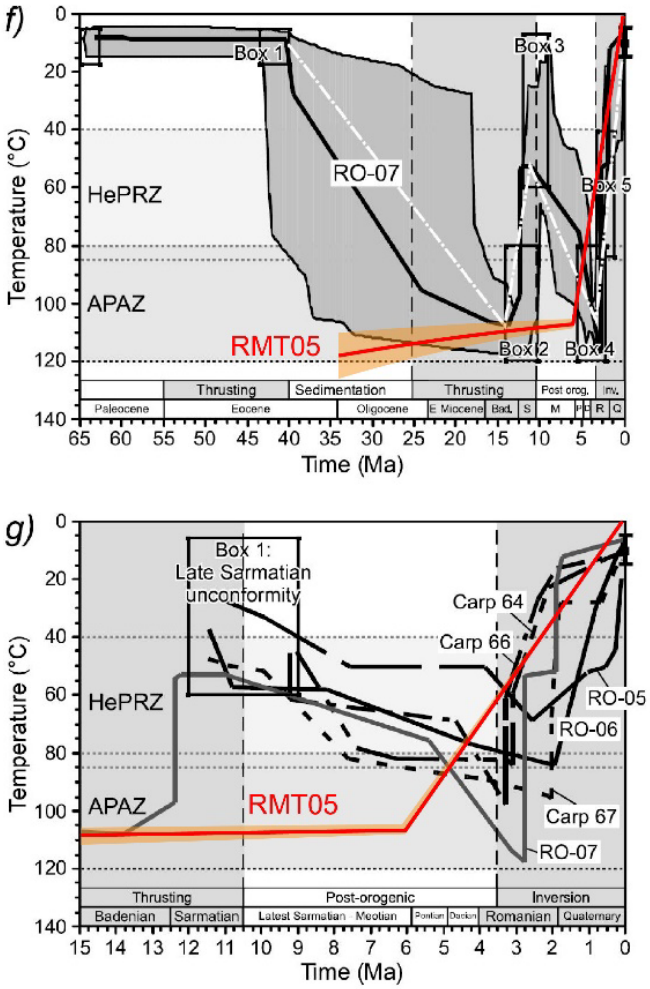

From Merten et al., 2010 as their figure 6. f) display RO-07 samples T-t path modelled with HEfTy (Ketcham, 2005) with AFT population ages (box 2 and 4) and AHe ages (box 5). In red and orange are the RMT05 mean value and standard error on the model we constrained with Pecube-NA inversions. The box 3 is a geological constrain of the observed Sarmatian unconformity sealing the frontal thrust in the SE Carpathians. The burial phase is not constrained in our model of exhumation. g) is the T-t path of all the AHe samples of the Tarcau nappe from Merten et al. (2010), and the RMT05 model in red and orange.

and Bertotti 2000). Models of "Sarmatian unconfromity" show an exhumation of ~2-3 km for the Tarcau nappe in the SE region (Merten et al., 2010). However, exhumation rate calculations for the Tarcau and Marginal folds nappe in our model (RMT05), is consistent with all T-t constraints displayed except for the Sarmatian exhumation phase (Figure X).

Geologic constraints on the Sarmatian unconformity are assumed by the sealing of the frontal thrust in the SE region by Sarmatian sediments in the foreland basin. Nevertheless, geologic sections of the belt (Matenco and Bertotti, 2000) also show Sarmatian sediments embedded in the Tarcau nappe, in agreement with the stratigraphy further south of the RO-07 sample area. Lateral variation in accretion in the belt may explain this diachronicity in the very close proximities and age shift of the sediments sealing the faults.

Our exhumation model does not constrain Sarmatian exhumation, as the general trend is presumably different from local effects in this specific region of the South-eastern Carpathians. Another possibility is proposed by Necea et al. (2021): the Sarmatian exhumation phase could not always be reproduced because the sensitivity of thermochronometers does not allow resolution of exhumation phases smaller than 2-3 km depending on the geothermal gradient. Although working in the same region of the Southeast Carpathians, the T-t plot of Necea et al. (2021) did not reproduce the Sarmatian exhumation, nor did they constrain the plot to display such exhumation pattern.